



**HAL**  
open science

**Influence of fluid-rock interaction processes and strain  
on strike-slip zones properties : an analogue-based  
multidisciplinary approach : fractured granitic  
geothermal reservoirs applications**

Johanne Klee

► **To cite this version:**

Johanne Klee. Influence of fluid-rock interaction processes and strain on strike-slip zones properties : an analogue-based multidisciplinary approach : fractured granitic geothermal reservoirs applications. Earth Sciences. Université de Picardie Jules Verne, 2021. English. NNT : 2021AMIE0074 . tel-03953776

**HAL Id: tel-03953776**

**<https://theses.hal.science/tel-03953776v1>**

Submitted on 24 Jan 2023

**HAL** is a multi-disciplinary open access archive for the deposit and dissemination of scientific research documents, whether they are published or not. The documents may come from teaching and research institutions in France or abroad, or from public or private research centers.

L'archive ouverte pluridisciplinaire **HAL**, est destinée au dépôt et à la diffusion de documents scientifiques de niveau recherche, publiés ou non, émanant des établissements d'enseignement et de recherche français ou étrangers, des laboratoires publics ou privés.



# Thèse de Doctorat

*Mention Sciences de la Terre  
Spécialité Géosciences*

Présentée à l'Ecole Doctorale en Sciences, Technologie et Santé (ED 585)

De l'Université de Picardie Jules Verne

par

**Johanne Klee**

Pour obtenir le grade de Docteur

***Influence des processus d'interaction fluide-roche et de la déformation sur les propriétés des systèmes décrochants : Une approche multidisciplinaire basée sur des analogues. Applications aux réservoirs géothermiques granitiques fracturés.***

Soutenue le 26 novembre 2021, après avis des rapporteurs, devant le jury d'examen :

Rafael FERREIRO MÄHLMANN  
Gioia FALCONE  
Domenico LIOTTA  
David BRUHN  
Juliet NEWSON  
Ingo SASS  
Pascal BARRIER  
Ghislain TRULLENQUE  
Sébastien POTEL  
Béatrice LEDESERT  
Terry PAVLIS

Professeur HDR, Université de Darmstadt  
Professeur, Université de Glasgow  
Enseignant-chercheur, Université de Bari  
Professeur, Université de Delft  
Directrice, School Energy Islande  
Professeur, Université de Darmstadt  
Enseignant-Chercheur HDR, UniLaSalle  
Enseignant-Chercheur, UniLaSalle  
Directeur de recherche HDR, UniLaSalle  
Professeur HDR, Cergy Paris Université  
Professeur, Université du Texas El Paso

Rapporteur-Président de jury  
Rapporteur  
Examinateur  
Examinateur  
Examinateur  
Examinateur  
Directeur  
Co-Directeur  
Invité  
Invité  
Invité







## Doctoral Thesis

*Mention Earth Sciences  
Specialization Geosciences*

Presented at the *Doctoral School of Science, Technology and Health (ED 585)*

**Of the University of Picardie Jules Verne**

by

**Johanne Klee**

For the grade of Doctor

***Influence of fluid-rock interaction processes and strain on  
strike-slip zones properties:  
An analogue-based multidisciplinary approach.  
Fractured granitic geothermal reservoirs applications.***

Presented on the 26 of November 2021 in front of the judging panel:

Rafael FERREIRO MÄHLMANN  
Gioia FALCONE  
Domenico LIOTTA  
David BRUHN  
Juliet NEWSON  
Ingo SASS  
Pascal BARRIER  
Ghislain TRULLENQUE  
Sébastien POTEL  
Béatrice LEDESERT  
Terry PAVLIS

Professor, Universität Darmstadt  
Professor, University of Glasgow  
Associate Professor, Università di Bari  
Professor, Universität Delft  
Director, Iceland School Energy  
Professor, Universität Darmstadt  
Associate Professor, UniLaSalle  
Associate Professor, UniLaSalle  
Research Director, UniLaSalle  
Professor, Cergy Paris University  
Professor, University of Texas El Paso

Jury president–Rapporteur  
Judge–Rapporteur  
Judge–Examinateur  
Judge–Examinateur  
Judge–Examinateur  
Judge–Examinateur  
Director  
Co-Director  
Collaborator–Guest  
Collaborator–Guest  
Collaborator–Guest





A ma grand-mère,



## REMERCIEMENTS

---

C'est avec beaucoup de nostalgie que j'écris ces dernières pages afin de remercier l'ensemble des personnes ayant contribué de près ou de loin à ces 3 années d'aventure. Elles auront été riches autant d'un point de vu scientifique, humain, que professionnel et personnel.

Je tiens à remercier dans un premier temps la team Death Valley (Ghislain Trullenque, Arezki Chabani alias Kiki, Sébastien Potel alias Seb, Béatrice Ledésert alias Béa le Coyote et Ronan Hébert). Merci de m'avoir accompagnée sur ce projet du terrain au labo en passant par tous ces moments conviviaux. Merci de m'avoir fait grandir scientifiquement en partageant vos expériences et connaissances. De manière plus individuelle :

- Merci Ghislain pour cette opportunité que tu m'as offerte, de réaliser cette thèse, de suivre une aventure que j'ai toujours voulue faire. Merci pour tes conseils, m'avoir poussée pour donner le meilleur de moi-même, pour ta confiance et ta rigueur scientifique. Merci pour ces moments partagés sur le terrain... je crois que GOML s'en souviendra longtemps !! « This is the gouge of life !! », cette expédition dans les Owlshead etc... Quoi de mieux que d'attaquer un affleurement à la scie ! Merci de m'avoir permis de vivre cette grande aventure qu'est la thèse et vive la margarita, le mojito et le Denny's !!
- Merci Kiki pour ta présence, ton soutien, ton énergie et ta bonne humeur. Merci d'avoir été à mon écoute dans les moments durs comme les plus excitants. Merci de m'avoir supportée jusqu'à la fin. Comme tu le disais souvent ...« A un moment donné.... », cette phrase va beaucoup me manquer ! Ces soirées passées avec les coupains !! les terrains dans les mines ! la découverte ensemble de l'acceptation de mon premier papier (j'aurais pu crier dans le resto ce soir là).
- Merci à toi Seb pour ta gentillesse, ta bienveillance et m'avoir initiée aux argiles. Merci d'avoir répondu à toutes mes « petites questions ». Qui sait peut-être qu'il y en aura d'autres... Les pauses cafés vont clairement me manquer. Quel bon moment d'avoir partagé cette soirée raclette... en étant dans le respect du couvre-feu bien entendu ! et toutes les autres soirées ! Un réel plaisir d'avoir partagé cette dernière Sainte-Barbe avec toi !
- Merci Béa pour ta présence, ton écoute, ton partage de connaissances, ta bienveillance et tes bons conseils. Merci pour tous ces Teams qui pouvaient parfois se terminer à 1h du mat... (ouf ta petite famille ne m'a pas détestée). Merci pour tous ces bons moments, scanlines sur le terrain en formation pingouin (et oui il peut faire froid en pleine journée

dans le désert !), notre atelier couture et rafistolage avec les moyens du bord (qui aura révélé notre âme d'artiste !!), nos Teams potins et j'en oublie.. tu auras été un Super Coyote !!!

- Merci Ronan pour ton partage de connaissances, d'expériences, pour tes conseils, ton soutien et ta sagesse. Tu es un réel maître zen ! Merci pour ces bons moments, sur le terrain (mon risotto t'aura marqué), durant les discussions scientifiques.... Mais aussi un bon souvenir d'avoir flané dans les rues et les casinos de Vegas ! Toi et Béa formez un duo du tonnerre et je suis ravie d'avoir partagé ce bout important de ma vie avec vous !

Je te remercie Pascal (Barrier) tout d'abord pour avoir permis de réaliser cette thèse au sein d'UniLasalle, mais aussi pour ta bienveillance tout au long de ces trois années.

Thank you so much to the European commission and the Hauts-de-France region for financing and supporting the realization of the MEET Project which allowed the financing of my thesis. I would like to thank all the MEET consortium for their help and scientific advices, but also thank you for all the good moments spent together during the different meetings. It was an unforgettable experience to have the chance to participate in such a large project with such wonderful people. A special dedication to my two MEET companions Katie and Aysegul. So good memories together (meetings, Teams breaks to speak about everything). Thank you for being there!

Merci à UniLaSalle et tout particulièrement à l'équipe B2R pour leur accueil et votre soutien humain et logistique. Merci de m'avoir fait rentrer dans la famille et m'avoir fait découvrir ce qu'est une vraie Sainte-Barbe !!! Merci à Damien Paisnel pour son aide à la réalisation de toutes ces lames minces !!

Un special merci à la team plateforme GEOS ! Les coupains !! (Elise Chenot et Barbara Clausmann avec Sébastien Potel et Arezki Chabani) pour cette belle ambiance de travail, mais aussi de potins. Un merci tout particulier à ma Babs : ma coupine d'amour, tu as été mon rayon de soleil durant cette thèse. Je te réponds à tes remerciements dans ton manuscrit par ces mots... cette these sans toi.... (tu connais également la suite !)

Many thanks to Prof. Gioia Falcone, Prof. Rafael Ferreira Mählmann, Dr. Domenico Liotta, Prof. David Bruhn, Dr. Juliet Newson, Prof. Ingo Sass for being part of the judging panel and for their time spent to read, listen and judge this work!

Merci aux membres de mon comité de thèse (Gianreto Manatschal, Alexandre Tarantola accompagnés de Albert Genter, Béatrice Ledésert et Sébastien Potel) pour leur écoute, soutien et importants conseils.

Thank you to Terry Pavlis for accompanying us on field missions to Death Valley and for sharing his knowledge of this unusual place with us.

Ich bedanke mich herzlich bei den Mitarbeitern der Grube Schauinsland (Schwarzwald), Finstergrund, die uns den Zugang zu den Stollen ermöglicht haben.

Un grand remerciement également à M. Jacquot qui nous a gentilement accueillis et présenté la mine de Gabe-Gottes près de Sainte-Marie-aux-Mines dans les Vosges.

I would like to thank you very much Thi Tuyen, Elena, Armand, Mahdi, Benjamin, Carl and Chloé for their precious help and good mood! Merci Merci !!

Malheureusement citer tout le monde serait trop long, mais.... Un très grand merci à ces personnes formidables qui m'ont soutenue : les coupains de Beauvais : Babs, Kiki, Sandra, FX, Mika, Elise, JuB, Seb... ; les amis de Strasbourg : Manon (ma coupine chérie, ma solution... toutes ces heures passées au téléphone pour me conseiller, me rassurer... Merci ! C'est qui le patron ???), Simon, Arnaud, Robin, Lise, Romain... ; les amis d'enfance.... Merci à toi Antoine pour avoir été présent et m'avoir soutenue et réconfortée.

Enfin, je remercie et suis reconnaissante du soutien infaillible de ma famille et leur fierté. Tout d'abord, merci à vous Maman et Papa. D'aussi loin que je puisse me souvenir, j'ai toujours voulu être géologue et dans cette voie vous m'avez toujours poussée et encouragée. Merci pour la force que vous me procurez jour après jour, vos conseils et vos encouragements à persévérer pour aller jusqu'au bout de mes rêves. A toi Thomas, mon ptit frère, merci pour ta présence et ton soutien. Papou, merci d'être là pour moi mon Pap' Taxi, merci pour ces petits bouts de journaux que tu me ramènes dès qu'il y a des news sur la géothermie, merci pour être venu jusqu'à Beauvais pour me voir et assister à ma soutenance. Enfin, le meilleur conseil que tu m'as donné « l'autodérision est une arme redoutable ! ». Une grosse pensée pour mamou qui est toujours là au plus près du cœur. Papi, Mamie, merci à vous deux pour votre foi en moi, votre présence, votre soutien, pour ces sessions de Schwarzer Peter, pour votre goût des choses simples de la vie à savourer chaque instant.

**UN GRAND MERCI A VOUS TOUS !**



# TABLE OF CONTENT

---

<b>Remerciements</b> .....	<b>7</b>
<b>Table of content</b> .....	<b>11</b>
<b>List of figures</b> .....	<b>17</b>
<b>List of tables</b> .....	<b>35</b>
<b>Abbreviations</b> .....	<b>37</b>
<b>CHAPTER 1 Scope of the study and scientific objectives</b> .....	<b>39</b>
I. Geothermal Energy.....	39
I.1. Deep geothermal.....	40
I.2. Geothermal energy in the world .....	42
I.3. Deep geothermal development in Europe .....	46
II. The MEET project.....	47
III. Scope of the PhD.....	48
<b>CHAPTER 2 Geological setting</b> .....	<b>51</b>
I. Death Valley –The Noble Hills range.....	51
I.1. Tectonic setting of the Great Basin.....	51
I.2. Death Valley structural setting.....	55
I.3. The Noble Hills range .....	59
I.3.1. Previous work.....	59
I.3.2. Revisited geological map .....	61
II. Upper Rhine Graben – Soultz-sous-Forêts geothermal site .....	63
II.1. Geodynamic evolution of the Upper Rhine Graben.....	63
II.2. The Soultz-sous-Forêts geothermal site.....	67
<b>CHAPTER 3 State of the art</b> .....	<b>71</b>
I. Deformation mechanisms .....	71
I.1. Introduction.....	71
I.2. Brittle deformation.....	72
I.3. Ductile deformation.....	78
II. Fluid-rock interactions in granitic rocks and fracture zone properties.....	81
<b>CHAPTER 4 Fluid-Rock Interactions in a Paleo-Geothermal Reservoir (Noble Hills Granite, California, USA). Part 1: Granite Pervasive Alteration Processes away from Fracture Zones</b> .....	<b>87</b>

I. Abstract.....	88
II. Introduction .....	89
III. Geological Setting.....	91
III.1. Death Valley.....	91
III.2. Noble Hills .....	92
IV. Material and Methods.....	95
IV.1. Material and Sampling Strategy.....	95
IV.2. Methods.....	95
IV.2.1. Microscopic Observations.....	95
IV.2.2. Fractures Density.....	96
IV.2.3. SEM-EDS .....	96
IV.2.4. X-ray Diffraction (XRD).....	97
IV.2.4.1. Experimental Conditions.....	97
IV.2.4.2. Determination of Illite Crystallinity and Kübler Index .....	97
IV.2.5. ICP-MS—ICP-AES .....	98
IV.2.6. Manocalcimetry .....	99
IV.2.7. Ethanol Saturation Porosimetry .....	99
V. Results .....	100
V.1. Petrographic Description .....	100
V.1.1. The Owlshead Granite .....	100
V.1.2. The Noble Hills Granite.....	104
V.1.3. Clay Minerals Identification and Kübler INDEX.....	108
V.1.3.1. Owlshead Mountains.....	108
V.1.3.2. Noble Hills.....	109
V.2. Geochemical Analyses .....	112
V.2.1. Major Element Bulk Rock Chemistry .....	112
V.2.2. Trace Element and REE Bulk Chemistry .....	114
V.3. Calcimetry and Porosimetry .....	116
VI. Discussion.....	117
VI.1. Petrogenesis of the OM and NH Granites .....	117
VI.2. Thermal Evolution of the NH Granite .....	118
VI.3. Alteration Parageneses.....	119

VI.3.1. Propylitic Alteration.....	120
VI.3.2. Argillic Alteration.....	121
VI.3.3. Evidences of Weathering .....	123
VI.3.4. Alteration Stage Occurrences.....	123
VI.4. Effects of Alteration on Petrographic and Petrophysical Behaviour.....	124
VI.5. The NH: A Paleo-Geothermal Reservoir? .....	125
VII. Conclusions .....	126
VIII. Acknowledgments .....	127
<b>CHAPTER 5 Fluid-Rock Interactions in a Paleo-Geothermal Reservoir (Noble Hills Granite, California, USA). Part 2: The Influence of Fracturing on Granite Alteration Processes and Fluid Circulation at Low to Moderate Regional Strain.....</b>	<b>129</b>
I. Abstract.....	130
II. Introduction .....	130
III. Geological Setting.....	132
IV. Materials and Methods .....	134
IV.1. Material and Sample selection .....	134
IV.2. Methods.....	135
IV.2.1. Fracture Network Parameters.....	135
IV.2.2. Petrographic Characterization.....	135
IV.2.3. X-ray Diffraction (XRD).....	136
IV.2.4. Manocalcimetry .....	138
IV.2.5. Ethanol Saturation Porosimetry .....	138
IV.2.6. Bulk Rock Geochemical Analyzes .....	138
IV.2.7. Mass-balance using Gresens Method .....	139
V. Results .....	139
V.1. Noble Hills structural overview.....	139
V.2. Petrographic Description .....	141
V.3. Fracturing and Fluid Circulation.....	144
V.3.1. Opening related structures with minimum shear displacement .....	146
V.3.2. Infill of fractures developed with a confirmed lateral shear displacement.....	147
V.3.2.1. Sample NH_31 .....	147
V.3.2.2. Sample NH_36 .....	154
V.3.2.3. Sample NH_23 .....	157

V.4. Geochemical Analyses .....	162
V.5. Calcite Content.....	164
V.6. Porosity and Mass-balance .....	165
V.7. Temperature Conditions.....	167
VI. Discussion.....	170
VI.1. Argillic Alteration Dominance .....	170
VI.2. Thermal Evolution Toward Fracture Zones.....	171
VI.3. A Multi-Stage Paleo-fluid Circulation.....	172
VI.4. Fluid Circulation and Argillic Alteration Effects on Petrographic and Petrophysical Behavior .....	173
VI.5. Relation Between Fluid Circulation, Alteration and Fracture Density.....	174
VI.6. Implication of Alteration in Terms of Geothermal Reservoir Properties.....	179
VII. Conclusion .....	180
VIII. Acknowledgments .....	181
<b>CHAPTER 6 The role of inherited structures on fluid circulation within a pre-structured reservoir at high strain .....</b>	<b>183</b>
I. Introduction.....	183
II. Case of highly strained rocks developing a fault structure from an inherited stacked basement/sedimentary pile: The Noble Hills range .....	185
II.1. Introduction.....	185
II.2. Material and Methods .....	186
II.2.1. Material and sampling strategy .....	186
II.2.2. Methods.....	189
II.2.2.1. Field sampling .....	189
II.2.2.2. Petrographic characterization.....	189
II.2.2.3. X-ray diffraction and Kübler Index .....	190
II.2.2.4. Manocalcimetry and ethanol saturation porosimetry.....	191
II.2.2.5. Bulk-rock geochemical analyses.....	191
II.2.2.6. K-Ar illite dating.....	191
II.3. Results .....	192
II.3.1. Field results .....	192
II.3.2. Petrographical description .....	193
II.3.2.1. Granite – Sample NH_40.....	193

II.3.2.2. The gneiss/fault core limit and the gneiss – Sample NH_44 and NH_45....	196
II.3.2.3. The fault core .....	202
II.3.3. Geochemistry.....	209
II.3.4. Temperature conditions .....	211
II.4. Discussion .....	211
II.4.1. The fault gouge protolith .....	211
II.4.2. Fluid-rock interactions and fluid circulation at high strain .....	212
II.4.3. Gouge microstructural evolution associating fluid circulation and high strain ..	215
II.4.4. Implication of high strain zones in terms of geothermal reservoir properties ...	216
II.5. Conclusion .....	217
III. Case of highly strained rocks developing a fault structure from a single basement protolith: Insights from outcrops at Upper Rhine Graben shoulders .....	218
III.1. Introduction.....	218
III.2. Vosges Mountains – Gabe Gottes Mine.....	220
III.3. Black Forest – Schauinsland Mine.....	227
III.4. Conclusion .....	233
IV. General conclusion of this chapter 6.....	234
<b>CHAPTER 7 The Noble Hills granite and the Upper Rhine Graben shoulders crystalline basement: analogues of the Soultz-sous-Forêts geothermal reservoir .....</b>	<b>237</b>
I. Introduction.....	237
II. Fracture network connectivity.....	239
III. Analogy in terms of Hydrothermal alteration between the Upper Rhine Graben and the Noble Hills range .....	244
IV. Analogy in terms of fracture zone properties at low to moderate strain .....	247
V. Influence of highly sheared zones and inherited structures on fluid circulation.....	255
VI. Conclusion to chapter 7.....	258
<b>CHAPTER 8 Conclusions and Perspectives .....</b>	<b>261</b>
I. Major outcomes for research .....	261
I.1. Hydrothermal alteration and its indicators .....	261
I.2. Relation between amount of deformation and fluid circulation .....	262
II. Major outcomes for the geothermal industry .....	267
III. Perspectives.....	269
III.1. High strain zones in-depth characterization.....	269

III.2. Paleo-fluid characterization .....	270
<b>References.....</b>	<b>271</b>
<b>Appendices.....</b>	<b>297</b>
<b>Résumé étendu.....</b>	<b>345</b>
I. Chapitre 1 : Intérêt de l'étude et objectifs scientifiques .....	345
II. Chapitre 2 : Contexte géologique.....	349
III. Chapitre 3 : Etat de l'art.....	350
IV. Chapitre 4 : Interactions fluide-roche dans un réservoir paléo-géothermique (Granite de Noble Hills, Californie, USA). Partie 1 : Processus d'altération généralisée du granite loin des zones de fractures.....	350
V. Chapitre 5 : Interactions fluide-roche dans un réservoir paléo-géothermique (Granite de Noble Hills, Californie, USA). Partie 2 : L'influence de la fracturation sur les processus d'altération du granite et la circulation des fluides à une déformation régionale faible à modérée .....	351
VI. Chapitre 6 : Le rôle de la structuration héritée sur la circulation des fluides à dans un réservoir pré-structuré sous forte contrainte.....	351
VII. Chapitre 7 : Le granite de Noble Hills et le socle cristallin des épaules du fossé du Rhin supérieur : des analogues du réservoir géothermique de Soultz-sous-Forêts.....	352
VIII. Chapitre 8 : Conclusions et perspectives.....	352
VIII.1. Résultats majeurs pour la recherche .....	352
VIII.1.1. Les altérations hydrothermales et leurs indicateurs dans les NH.....	352
VIII.1.2. Relation entre la quantité de déformation et les circulations de fluides.....	353
VIII.2. Résultats majeurs pour les industriels.....	357
VIII.3. Perspectives .....	359
VIII.3.1. Caractérisation approfondie des zones de forte déformation.....	359
VIII.3.2. Caractérisation des paléo-fluides .....	360
<b>Abstract.....</b>	<b>362</b>
<b>Résumé.....</b>	<b>362</b>

## LIST OF FIGURES

---

Figure 1-1. Geothermal play types with example geothermal fields installed worldwide from Moeck (2014): CV–Convection dominated heat transfer, CD–Conduction dominated heat transfer .....	40
Figure 1-2. Heat exploitation system by a geothermal power plant modified after ( <a href="http://www.afpg.asso.fr">http://www.afpg.asso.fr</a> ) .....	42
Figure 1-3. Installed capacity of geothermal energy across the world in 2020 .....	43
Figure 1-4. (a) Geothermal fields in the Great Basin region after Faulds et al. (2004). Geothermal fields cluster in the Sevier Desert (SD), Humboldt structural zone (HSZ), Black Rock Desert (BRD), Surprise Valley (SV), and Walker Lane (WLG) belts. The northwestern Great Basin, directly northeast of the northwest terminus of the Walker Lane, contains the greatest concentration of fields. White circles are geothermal systems with maximum temperatures of 100-160°C; grey circles have maximum temperatures >160°C. ECSZ, eastern California shear zone. (b) Density of known geothermal systems ( $\geq 37^{\circ}\text{C}$ ) in the Great Basin region plotted on a map showing strain rates after Faulds and Hinz (2015). .....	45
Figure 1-5. Schematic overview of the four representative European Variscan geotectonic settings including the demonstration sites, the analogue sites and the investigation methods according to Trullenque et al. (2018). Our case study is framed in red.....	48
Figure 2-1. Scheme cataloging the convection dominated geothermal play systems based on geological controls. 1–Play type, 2–Typus locality, 3–Plate tectonic setting, 4–Geological habitat of potential geothermal reservoirs, 5–Heat transfer type and 6–Geologic control after Moeck (2014). .....	51
Figure 2-2. Cenozoic tectonic evolution, western North America after Faulds et al. (2004). The box surrounds the locus of geothermal activity in the northwestern Great Basin. MTJ, Mendocino triple junction; SAF, San Andreas fault; WL, Walker Lane. ....	52
Figure 2-3. Simplified tectonic map of the western USA Cordillera showing the modern plate boundaries and tectonic provinces after Nagorsen-Rinke et al. (2013). Basin and Range Province is in medium gray; Central Nevada seismic belt (CNSB), eastern California shear zone (ECSZ), Intermountain seismic belt (ISB), and Walker Lane belt (WLB) are in light gray; Mina deflection (MD) is in dark gray.....	53

Figure 2-4. Shaded relief index map of Quaternary faults, roads, towns, and field trip stops in the eastern California shear zone after Frankel et al. (2008). Most faults are from the U.S. Geological Survey Quaternary fault and fold database (<http://earthquake.usgs.gov/regional/qfaults>). Arrows indicate relative fault motion for strike slip faults. Bar and circle indicate the hanging wall of normal faults. AHF—Ash Hill fault; ALF—Airport Lake fault; B—Bishop; BF—Blackwater fault; BLF—Bicycle Lake fault; BM—Black Mountains; BP—Big Pine; Br—Baker; Bw—Barstow; By—Beatty; CA—California; CF—Cady fault; CLF—Coyote Lake fault; CoF—Calico fault; CRF—Camp Rock fault; DSF—Deep Springs fault; DV-FLVF—Death Valley–Fish Lake Valley fault; EPF—Emigrant Peak fault; EV—Eureka Valley; FIF—Fort Irwin fault; FM—Funeral Mountains; GF—Garlock fault; GFL—Goldstone Lake fault; GM—Grapevine Mountains; HF—Helendale fault; HLF—Harper Lake fault; HMSVF—Hunter Mountain–Saline Valley fault; I—Independence; LF—Lenwood fault; LLF—Lavic Lake fault; LoF—Lockhart fault; LP—Lone Pine; LuF—Ludlow fault; LV—Las Vegas; M—Mojave; MF—Manix fault; NV—Nevada; O—Olancho; OL—Owens Lake; OVF—Owens Valley fault; P—Pahrump; PF—Pisgah fault; PV—Panamint Valley; PVF—Panamint Valley fault; R—Ridgecrest; S—Shoshone; SAF—San Andreas fault; SDVF—southern Death Valley fault; SLF—Stateline fault; SPLM—Silver Peak–Lone Mountain extensional complex; SNF—Sierra Nevada frontal fault; SP—Silver Peak Range; T—Tonopah; TF—Tiefort Mountain fault; TMF—Tin Mountain fault; TPF—Towne Pass fault; WMF—White Mountains fault; YM—Yucca Mountain..... 54

Figure 2-5. (a) Generalized map of the Death Valley region showing the fault systems and their relationship to the Garlock Fault Zone from (Butler et al., 1988). (b) A model of the Death Valley “pull-apart” basin from (Burchfiel and Stewart, 1966). (c) Sub-basins of modern Death Valley from (Miller and Wright, 2015) after (Blakely et al., 1999)..... 56

Figure 2-6. Geologic map of Death Valley area after Miller (2005). Numbers and arrows depict corresponding photo location and direction of view. Abbreviations for mountain ranges are as follows: B: Black Mountains; C: Cottonwood Mountains; F: Funeral Mountains; G: Grapevine Mountains; L: Last Chance Range; N: Nopah Range; O: Owlshead Mountains; P: Panamint Mountains; R: Resting Spring Range. Abbreviations on location map of California are as follows: CA: California; DV: Death Valley National Park; LA: Los Angeles; NV: Nevada; SF: San Francisco; SN: Sierra Nevada Mountains..... 57

Figure 2-7. (a) Generalized stratigraphy of the Pahrump Group in the Death Valley region revised by Mahon et al. (2014a). (b) Generalized columnar section of Precambrian to Lower Cambrian, Death Valley region from Wright et al. (1974) ..... 58

Figure 2-8. (a) Location of the Death Valley and the Noble Hills range, modified after (Norton, 2011). (b) Satellite view of the Noble Hills range. SDVFZ–Southern Death Valley Fault Zone, GFZ–Garlock Fault Zone.....	59
Figure 2-9. Geological map of the Noble Hills range from Klee et al. (2021a) and modified after Klee et al. (2020) and Niles (2016). The quaternary is not displayed and available on Niles (2016) map (Appendix 2). NHF–Noble Hills Formation .....	62
Figure 2-10. Conceptual scheme (a) at regional scale and (b) at the Noble Hills scale of the spatial arrangement of the Noble Hills fracture network from Chabani et al. (2021).....	63
Figure 2-11. (a) Location map of the European Cenozoic rift system (ECRIS) in the Alpine and Pyrenean foreland, showing Cenozoic fault systems (black lines), rift-related sedimentary basins (light gray), Variscan massifs (cross pattern) and volcanic fields (black). Solid barbed line: Variscan deformation front; stippled barbed line: Alpine deformation front. BF, Black Forest; BG, Bresse Graben; EG, Eger (Ohre) Graben; FP, Franconian Platform; HG, Hessian Grabens; LG, Limagne Graben, LRG, Lower Rhine (Roer Valley) Graben; URG, Upper Rhine Graben; OW, Odenwald; VG, Vosges after Cloetingh et al. (2005) and Dèzes et al. (2004). (b) Map of the deep geothermal sites operating or under development in 2020, also representing the major oilfields and the isotherms at 2000 m depth from Glaas (2021) .....	64
Figure 2-12. Geological W-E cross-section through the URG at Sultz-sous-Forêts latitude from Dezayes and Lerouge (2019a) .....	65
Figure 2-13. (a) Synthesis of the main brittle tectonic phases and associated fracture set since the Hercynian orogenesis to the URG formation from Glaas (2021). (b) Synthetic block diagrams showing the four tectonic phases that occurred during the Cenozoic rifting of the Rhine Graben from Villemin and Bergerat (1987). A–N–S compression phase (Eocene); B–E–W extensional phase (Oligocene); C–NE–SW compressional phase (Oligocene) and D–NW–SE compressional phase (Miocene).....	66
Figure 2-14. Temperature distribution at 2000 m TVD in the URG derived from 3D interpolation of 6531 temperature data from 1600 boreholes in the URG and adjacent areas, from Baillieux et al. (2013). The locations of the two main petroleum and geothermal areas at Pechelbronn/Sultz-sous-Forêts and Landau are indicated. Boreholes with a depth >2000 m TVD are indicated by triangles. VM, Vosges Mountains; BFM, Black Forest Mountains; OM, Odenwald Mountains; KV, Kaiserstuhl volcanic massif.....	67
Figure 2-15. The Sultz-sous-Forêts EGS with the pilot plant from (Ledésert and Hébert, 2020). -1400 m: depth of the basement roff; -2200 m: bottom of EPS-1 borehole.....	68

Figure 3-1. (a) Brittle to (b-c) brittle-ductile to (d) ductile deformation after Van der Pluijm and Marshak, (2004).....	72
Figure 3-2. Types of brittle deformation. (a) Orientation of the remote principal stress directions on an intact rock body. (b) A tensile crack, forming parallel to $\sigma_1$ and perpendicular to $\sigma_3$ . (c) A shear fracture forming at an angle of about $30^\circ$ to $\sigma_1$ . (d) A tensile crack that has been reoriented with respect to the remote stresses and becomes a fault by undergoing frictional sliding. (e) A tensile crack which has been reactivated as a cataclastic shear zone. (f) A shear fracture that has evolved into a fault. (g) A shear fracture that has evolved into a cataclastic shear zone. Figure is from Van der Pluijm and Marshak (2004).....	73
Figure 3-3. Conceptual block-diagram of a fault zone from Choi et al. (2016) showing the main components of a fault zone architecture and structural elements and features in each component.....	74
Figure 3-4. Architecture and structural elements of a fault zone in a crystalline rock with a fault core (FC) composed of breccia and fault gouge and damage zone (DZ) with increased fracture density (Caine et al., 1996). Figure from Bauer et al. (2015) .....	74
Figure 3-5. Schemes of typical strike-slip structures showing (a) a single fault core and (b) a multiple fault core, with associated damage zone from Mitchell and Faulkner (2009) .....	75
Figure 3-6. Schemes of the multiscale aspect of a fault zone from Le Garzic et al. (2011) .....	76
Figure 3-7. Schemes showing different types of commonly fragmented porphyroclasts after Passchier and Trouw (2005).....	77
Figure 3-8. (a) The effect of changing the confining pressure on various rock types. (b) The effect of changing temperature on the compressive strength of some rocks and minerals after Van der Pluijm and Marshak (2004). .....	78
Figure 3-9. Schemes of shear-sense indicators in a dextral ductile shear zone from Van der Pluijm and Marshak (2004) distinguishable from thin section to outcrop scale.....	80
Figure 3-10. (a) Irregularly distributed dislocations. (b) Rearranged dislocations by glide and climb to form a tilt boundary (or dislocation wall) that separates subgrains. Figure from Van der Pluijm and Marshak (2004).....	81
Figure 3-11. Fracture density and porosity profiles in a conceptual lithofacies granite zonation of hydrothermally altered and fractured granite modified from Genter et al. (2000) and Glaas (2021).....	83
Figure 3-12. Conceptual scheme for fault-related fluid flow from Caine et al. (1996).....	84

Figure 4-1. (a) Simplified tectonic map of the Great Basin region (western U.S. Cordillera) showing the tectonic provinces (modified after Nagorsen-Rinke et al. (2013)). WLB—Walker Lane Belt; ECSZ—Eastern California Shear Zone; GFZ—Garlock Fault Zone. The Basin and Range Province is represented in dark grey and the WLB/ECSZ in light grey. The red dashed line marks the limit between these both domains. The dark lines within the Basin and Range Province and in the WLB-ECSZ zone represent the main faults. (b) Structural setting of the Death Valley region (modified after Miller and Wright (2015); Rämö et al. (2002)). AM—Avawatz Mountains; BM—Black Mountains; BMF—Black Mountains Fault; CM—Cottonwood Mountain; FM—Funeral Mountains; GM—Grapevine Mountains; OM—Owlshead Mountains; PM—Panamint Mountains; GFZ—Garlock Fault Zone; NDVFZ—Northern Death Valley Fault Zone; SDVFZ—Southern Death Valley Fault Zone. .... 92

Figure 4-2. (a) Map presenting the structural setting of the southern part of the Death Valley region and the location of the Noble Hills range (NH) and the location of samples in the Owlshead Mountains (OM) represented by the white dots. (b) A scheme showing the displacement of the NH granite from the OM along the SDVFZ described by Pavlis and Trullenque (2021). (c) The geological map of the Noble Hills range, modified after (Klee et al., 2020; Niles, 2016). The quaternary is not displayed but available on Niles (2016) map. In (a,b), samples location for this study are represented by the white dots; the blue star corresponds to a sample from Rämö et al. (2002). NHF—Noble Hills Formation. .... 94

Figure 4-3. Macroscale to microscale photographs illustrating (a–c) the Owlshead and (d–f) the Noble Hills granites. (a,d) Hand specimens for each granite showing their different aspects. (b,e) Thin section mosaics realized for each granite under optical microscope in polarized—analyzed light and showing the difference in terms of grain size and microfracturing. (c,f) Thin sections zooms of each granite mosaic in polarized—analyzed light showing the difference in terms of alteration degree. Abbreviations (except for “Wm”) after Kretz (1983): Bt—Biotite, Kfs—K-feldspar, Wm—K-white mica, Pl—Plagioclase, Qtz—Quartz. .... 102

Figure 4-4. Photomicrographs of the Owlshead granite in polarized-analyzed and polarized—non-analyzed light showing (a,b) perthitic and unaltered orthoclase, unaltered quartz presenting a slight undulatory extinction and calcite veinlets at grain boundaries. (c,d) Plagioclase alteration with the formation of K-white mica. (e,f) Incipient biotite alteration associated to hematite and epidote formation. Abbreviations (except for “Wm”) after Kretz (1983): Bt—Biotite, Cal—Calcite, Ep—Epidote, Hem—Hematite, Kfs—K-feldspar, Wm—K-white mica, Pl—Plagioclase, Qtz—Quartz. .... 104

Figure 4-5. Photomicrographs showing the plagioclase transformation progress in the Noble Hills granite. (a) Progressive illitization of plagioclase initiating in the core of the mineral under optical microscope in polarized–analyzed light. (b) Needles shape illite replacing plagioclase in polarized–analyzed light under optical microscope. (c) Back-scattered electron image of needles/flakes shape illite replacing plagioclase. (d) Plagioclase completely replaced by illite, kaolinite and calcite and non-altered K-feldspar under optical microscope in polarized–analyzed light. (e) Back-scattered electron image showing a fan shape kaolinite, calcite and oxide veinlet. (f) Back-scattered electron image showing a magnified view of a single mineral of kaolinite under SEM. Abbreviations (except for “Ox”) after Kretz (1983): Ap–Apatite, Bt–Biotite, Cal–Calcite, Ill–Illite, Kln–Kaolinite, Kfs–K-feldspar, Ox–Oxides, Pl–Plagioclase, Qtz–Quartz.....107

Figure 4-6. Photomicrographs showing a biotite completely altered and replaced by oxides and K-white mica (essentially illite) according to the cleavage planes (a) in polarized–analyzed light under optical microscope and (b) in polarized–analyzed light under optical microscope. Abbreviations (except for “Ox and Wm”) after Kretz (1983): Bt–Biotite, Cal–Calcite, Kfs–K-feldspar, Wm–K-white mica, Ox–Oxides, Pl–Plagioclase, Qtz–Quartz.....107

Figure 4-7. Normative composition of one sample from the OM and 4 samples from the NH in a QAP (Quartz-Alkali-feldspar-Plagioclase) ternary diagram (Streckeisen, 1973). .....108

Figure 4-8. XRD result obtained for the clay fraction < 2  $\mu\text{m}$  in Air-Dried (AD), Glycolated (G) and Heated (H) of the samples in the OM granite and showing a montmorillonite (Mnt) pattern. ....109

Figure 4-9. XRD patterns obtained for the clay fraction < 2 $\mu\text{m}$  in Air-Dried (AD), Glycolated (G) and Heated (H) for the NH granite and showing the clay composition of the samples in the NH granite: (a) corrensite (Cor), a chlorite/smectite mixed-layer, and (b) illite/smectite mixed-layer (I/S). Abbreviations (except for “Cor and I/S”) after Kretz (1983): Bt–Biotite, Kln–Kaolinite, Qtz–Quartz, Ill–Illite.....110

Figure 4-10. Geological map (see Figure 4-2b) representing the Kübler Index (KI) in air dried conditions of each sample and the corresponding metamorphic zone showed by the color of the dots for (a) the fraction < 2 $\mu\text{m}$  and (b) the fraction 2–6  $\mu\text{m}$ . .....111

Figure 4-11. (a) Total alkali versus silica diagram ((Cox, 1979) adopted for plutonic rocks by (Wilson, 1989)). (b) AFM (Alkali-Fe<sub>2</sub>O<sub>3</sub>-MgO) classification diagram established by Jensen (1976). (c) A/CNK (Al<sub>2</sub>O<sub>3</sub>/(CaO + Na<sub>2</sub>O + K<sub>2</sub>O)) versus silica diagram. The blue star corresponds to a sample from the OM analyzed by Rämö et al. (2002). .....112

Figure 4-12. Harker diagrams showing the variation of (a) K <sub>2</sub> O (Le Maître et al., 1989) and (b) Al <sub>2</sub> O <sub>3</sub> in the OM and NH granites. A sample from the OM analyzed by Rämö et al. (2002) is represented by the blue star .....	113
Figure 4-13. Plot of selected major element oxides (SiO <sub>2</sub> , K <sub>2</sub> O, Al <sub>2</sub> O <sub>3</sub> , Na <sub>2</sub> O, CaO and MgO) versus LOI (loss on ignition). .....	114
Figure 4-14. (a) Chondrite-normalized (values from [77]) rare earth element (REE) patterns of samples from the OM and the NH. (b) Primitive mantle-normalized (values from McDonough et al. (1992)'s slight revision of Sun and McDonough (1989)) multi-element diagram showing trace element patterns of samples from the OM and the NH. ....	116
Figure 4-15. (a) Plot of the porosity versus the calcite content. (b) Plot of calcite content versus LOI (Loss on ignition). (c) Plot of porosity versus LOI. ....	117
Figure 4-16. Paragenesis sequence and alteration evolution in the OM and NH granite.....	119
Figure 4-17. Schematic representation of the different alteration processes which can be observed in the OM and NH granites. (a) Fresh granite non-affected by alteration. (b) Granite affected by the propylitic alteration showing the slight chloritization of biotite and the crystallization of K-white micas in the core of plagioclase. (c) Granite affected by the argillic alteration and localized along fractures where fluid has circulated. Biotite are locally completely transformed into illite and plagioclase into illite, calcite and/or kaolinite. Perthites and inclusions in K-feldspars can also be altered. Abbreviations (except for "Ox and Wm") after Kretz (1983): Bt—Biotite, Cal—Calcite, Chl—Chlorite, Ep—Epidote, Ill—Illite, Kln—Kaolinite, Kfs—K-feldspar, Ox—Oxide, Pl—Plagioclase, Qtz—Quartz, Wm—K-white mica. ....	121
Figure 4-18. Back-scattered image showing a magnified view of plagioclase dissolution pits under SEM (15 kV 5.3 mm x 1.7 k BSECOMP). .....	122
Figure 5-1. (a) Location of the Noble Hills on the western USA satellite map. SAFZ – San Andreas Fault Zone, GFZ – Garlock Fault Zone and DV – Death Valley. (b) The geological map of the Noble Hills range, modified after Klee et al. (2020), Niles (2016) and Klee et al. (2021a). The quaternary is not displayed but available on the map provided by Niles (2016). Sample locations are represented by the white dots. The asterisk shows the samples used as case studies in this work. NHF – Noble Hills Formation. ....	133
Figure 5-2. (a) Satellite view of the NH range showing a deformation gradient increasing southeastward, represented by the yellow dashed lines. (b and c) Map view zooms on the Proterozoic units along the NH strike showing the strain increase from (b) to (c), where basal CS sedimentary sequence appears increasingly stretched and boudinated.....	141

- Figure 5-3. Two examples of XRD patterns obtained for the clay fraction  $< 2 \mu\text{m}$  in Air-Dried (AD-dark), after Glycol solvation (G-blue) and Heated (H-red) conditions for the NH granite, which were not identified in the fresh granite described by (Klee et al., 2021a), and showing different clay compositions. (a) Illite, kaolinite and quartz. (b) Vermiculite, illite, kaolinite and quartz. .... 144
- Figure 5-4. (a) Photograph and digitization showing representative hydrothermalized fracture zones observed on the field. (b) Photograph and digitization of granite crosscutting by multiple carbonate veins (veins network) altering pervasively the rock. .... 145
- Figure 5-5. (a) Photograph and digitization of a brecciated and recrystallized vein also developing a gradient of alteration. Location of the sample NH\_31 used as a case study in this section. (b) Photograph and digitization of a mylonitic vein developing a gradient of alteration. Location of the sample NH\_23 used as a case study in this section. .... 146
- Figure 5-6. (a) Photomicrograph of a quartz veinlets intersected by an illite veinlets under optical microscope in polarized-analyzed light. (b) Photomicrograph showing an illite vein crosscutting K-feldspar and illitized plagioclase under optical microscope in polarized-analyzed light. (c) Back-scattered image showing the different phases presented in (b). (c) Photomicrograph showing dolomite intersecting illite under optical microscope in polarized-analyzed light. (d) Back-scattered image of a dolomite, siderite and calcite showing their chronology. (e) Hydraulic fracturing with calcite precipitating around clasts of quartz placed like a fan under optical microscope in polarized-analyzed light. (f) Photomicrograph under optical microscope in polarized-analyzed light of a microfracture intersecting an altered plagioclase which borders are made of pure kaolinite whereas the plagioclase was recrystallized into kaolinite and illite. (g) Photomicrograph under optical microscope in polarized-analyzed light showing illite developing on the walls of an open microfracture and dolomite filling this open space. .... 147
- Figure 5-7. (a) Photo and the respective digitalization of the sample NH\_31, gathering NH\_31\_1\_2 and NH\_31\_3, showing the different compartments that compose it, as well as the two scanlines realized in the host rock of the vein. (b) Plots of the cumulative frequency percentage against distance percentage for both scanlines. The diagonal represents an uniform distribution. (c) Stick plots showing the fracture position along the scanlines and for which the fracture density ( $P_{10}$ ) and the coefficient of variation (Cv) are given. .... 148
- Figure 5-8. (a) Thin sections location on the sample NH\_31. (b) Thin section mosaics showing the position and orientation of the scanlines. (c) Plots of the cumulative frequency percentage against distance percentage for each scanline. The diagonal represents a uniform distribution.

Dashed lines indicate a zone where a rapid increase of the number of fractures is observed (slope threshold > 2). (d) Stick plots showing the position of the fracture along the scanlines and for which the fracture density ( $P_{10}$ ) and the coefficient of variation (Cv) are given. ....151

Figure 5-9. Photomicrographs of the different compartments of the sample NH\_31 and their location in the sample. (a-b) Respectively back-scattered image and CL images of calcite veins composed of 2 phases (Cal A and Cal B) crosscutting quartz, crosscut by a phase made of a carbonate/oxide matrix (calcite, dolomite, ankerite) with barium patches and transported clasts of quartz, K-feldspars and few biotite, crosscut by later calcite veins (Cal C). (c-d) Zoom on the first generation of calcite vein and crosscutting quartz under optical microscope in polarized-analyzed light and showing two phases under CL. (e) A chemical quantification map realized under SEM of the carbonate/oxide matrix with barium and clasts. Different colors show a relative abundance of specific chemical elements (counts). (f,g) A photomicrograph under optical microscope in polarized-analyzed and under SEM respectively of the contact with the granite showing a dolomite matrix with transported clasts intersected by a calcite vein, the whole intersected by a carbonate/oxide matrix with transported clasts and barium precipitation patches. (h) The altered granite close to the brecciated vein showing a completely altered plagioclase replaced by calcite, kaolinite and illite, a completely altered biotite replaced by illite and oxides and non-altered K-feldspar and quartz under optical microscope in polarized-analyzed light. (i) The altered granite close to the brecciated vein presented in (h) under CL showing illite with no luminescence, in light blue an unaltered K-feldspar, in red some calcite and apatite in yellow. (j) The altered granite away from the brecciated vein showing a plagioclase partially replaced by calcite, kaolinite and illite, biotites partially replaced by illite and oxides and unaltered quartz under optical microscope in polarized-analyzed light. (k) The altered granite away from the brecciated vein presented in (j) under CL showing kaolinite in dark blue, calcite in red, apatite in yellow and illite, quartz and biotite with no luminescence. ....153

Figure 5-10. (a) Photograph of the sample NH\_36 showing the scanline and the emplacement of the two thin sections made in the sample. (b) Plot of the cumulative frequency percentage against distance percentage for the scanline. The diagonal line represents an uniform distribution. Dashed lines indicate a cluster, meaning a zone where a rapid increase of the number of fractures is observed (slope threshold > 2). (c) Stick plot showing the fracture position along the scanline and for which the fracture density ( $P_{10}$ ) and the coefficient of variation (Cv) are given. (d) Thin section mosaics showing the position and the orientation of the scanlines. (e) Plots of the cumulative frequency percentage against distance percentage for each scanline. The diagonal line represents again an uniform distribution and the dashed lines

delimit a fracture cluster. (f) Stick plot showing the fracture position along the scanline and for which the fracture density ( $P_{10}$ ) and the coefficient of variation (Cv) are given. Data were provided by (Chabani et al., 2021). .....154

Figure 5-11. (a) Sample NH\_36 collected close to a fault zone showing the location of the two thin sections. (b) A mosaic of the thin section NH\_36\_1 showing a breccia. (c) A mosaic of the thin section NH\_36\_2 showing the limit between a breccia and the almost preserved granite. (d) A microphotograph of the NH\_36\_1 thin section showing a brecciated and slightly altered plagioclase, a brecciated quartz with a significant undulatory extinction starting to recrystallized into subgrains, a brecciated biotite and calcite crystallizing in the microfractures. (e) A micrograph of thin section NH\_36\_1 showing brecciated and non-altered K-feldspar and quartz with dolomite and calcite deposits between the clasts. (f) A microphotograph zooming in the preserved granitic zone visible of the thin section NH\_36\_2 and showing a brecciated and partially replaced plagioclase into kaolinite and brecciated but unaltered quartz and biotite. (g) A microphotograph zooming in the brecciated part of the thin section NH\_36\_2 and showing a carbonate matrix composed of dolomite and calcite transported clasts from the granite.....157

Figure 5-12. (a) A photo and the corresponding digitalization of the sample NH\_23 showing the different compartments that compose it, as well as the two scanlines realized in the host rock of the vein. (b) Plots of the cumulative frequency percentage against distance percentage for both scanlines. The diagonal represents a uniform distribution. Dashed lines indicate a zone where a rapid increase of the number of fractures is observed (slope threshold  $> 2$ ). (c) Stick plots showing the fracture position along the scanlines and for which the fracture density ( $P_{10}$ ) and the coefficient of variation (Cv) are given. ....158

Figure 5-13. (a) Thin section location on the sample NH\_23. (b) Thin section mosaics showing the position and orientation of the scanlines. (c) Plots of the cumulative frequency percentage against distance percentage for each scanline. The diagonal represents a uniform distribution. Dashed lines indicate a zone where a rapid increase of the number of fractures is observed (slope threshold  $> 2$ ). (d) Stick plots showing the position of the fractures along the scanlines and for which the fracture density ( $P_{10}$ ) and the coefficient of variation (Cv) are given. ....160

Figure 5-14. Photomicrographs of the different compartments of the sample and their location in the sample. (a) Veins of ankerite and calcite crosscutting the major quartzitic/feldspathic vein of the sample under optical microscope in polarized-analyzed light. (b) Back-scattered electron image of the photomicrograph (a). (c) Photomicrograph of the ankerite-granite interlayering zone under optical microscope in polarized-analyzed light. (d) A zoom image of the ankerite vein, under optical microscope in polarized-analyzed light, presented in (c) and showing a

sigmoid of ankerite with a swell of automorphic crystals crushed and stretched in the pinches.	
(e) The altered granite close to the vein showing a completely altered plagioclase and biotite both replaced by illite and oxides and partially altered K-feldspar under optical microscope in polarized-analyzed light. (f) The altered granite away from the vein showing a completely altered plagioclase replaced by illite and kaolinite, biotite partially replaced by illite and oxides, an unaltered K-feldspar and calcite veinlets under optical microscope in polarized-analyzed light.....	162
Figure 5-15. Plot of selected major element oxides ( $\text{Na}_2\text{O}$ , $\text{K}_2\text{O}$ , $\text{Al}_2\text{O}_3$ , $\text{CaO}$ , $\text{MgO}$ , $\text{Fe}_2\text{O}_3$ and $\text{SiO}_2$ ) versus LOI (loss on ignition) of samples from this study in orange and from Klee et al. (2021a) in grey. The dashed arrows show the different trends observed.....	164
Figure 5-16. NH geological map showing the location and the associated calcite content of samples from this study represented by the white dots and of samples from Klee et al. (2021a) by the grey dots.....	165
Figure 5-17. Geological map representing the Kübler Index (KI) in air dried conditions of each sample from this study (Dots) and from Klee et al. (2021a) (Triangles) and the corresponding metamorphic zone represented by the different colors indicated in the legend for (a) the fraction $< 2\mu\text{m}$ and (b) the fraction $2-6\mu\text{m}$ .....	169
Figure 5-18. (a) Diagrams showing Kübler Index (KI) values versus kaolinite crystallinity index (KCI) for the clay fractions $<2\mu\text{m}$ and $2-6\mu\text{m}$ . (b) Diagram showing positive correlations between KI and KCI for the clay fractions $<2\mu\text{m}$ and $2-6\mu\text{m}$ excluding samples NH_6, NH_8 and NH_31_1_2.....	170
Figure 5-19. Synthetic scheme showing, from low to moderate strain, the interaction between the fluid and the granite in the cases of a very low fluid/rock ratio. (a) Open fractures with an incipient alteration of the surrounding rock. (b) Brecciated zones with a carbonated matrix and no change of alteration degree. No scale is given for this scheme, because it can represent fracture zones of several order of magnitude. ....	176
Figure 5-20. Synthetic scheme showing, from low to moderate strain, the interaction between the fluid and the granite in the cases of a high fluid/rock ratio observed in the field. (a) An open fracture with an incipient alteration gradient at the border. (b) A sealed fracture with a slight alteration gradient. (c) A brecciated vein induced from fracture reactivation and showing an alteration gradient but no fracturing gradient. (d) A mylonite made of carbonates and granitic lenses showing an alteration gradient and a fracturing gradient. NH_31 and NH_23 show a	

similar fracture density (Fd). No scale is given for this scheme, because it can represent fracture zones of several order of magnitude. ....	178
Figure 6-1. Block diagram, with no scale, representing the conceptual model of a fault zone according to Caine et al., 1996. We can differentiate three major zones: (a) the fault core, (b) the damage zone, and (c) the protolith. Secondary fractures (d) can react as conduit for fluid flow if they are not sealed by secondary minerals. ....	184
Figure 6-2. (a) Satellite map of the western USA showing the location of the Noble Hills range (black hollow rectangle). SAFZ – San Andreas Fault Zone, GFZ – Garlock Fault Zone and DV – Death Valley. (b) Geological map modified after Niles (2016) and Klee et al. (2021b), showing the studied location (white dot) on a major clay-bearing fault zone (orange line). The Quaternary is not displayed but it is available on the map provided by Niles, 2016. ....	186
Figure 6-3. (a) A photograph of the outcropping fault zone. (b) The digitization of the outcrop showing the fault core in dark grey, the granite on the left, the gneiss on the right and the location of the different collected samples. (c) Photographs of the different collected samples. DZ – Damage Zone. ....	187
Figure 6-4. Sampling methodology. (a) Application of a film of fiberglass and epoxy resin on the outcrop surface for consolidation purposes and hole drilling to delimitate the sample. (b) Extraction after complete drilling. (c) Site of the extracted sample. All epoxy resin remnants have been carefully removed from the sampling area after sample extraction. ....	189
Figure 6-5. (a) Schematic cross-section of the Proterozoic sequence stacking with granite intrusions west of the Pipeline Wash (Figure 6-2b). The violet square represents the area that will be reactivated by the SDVFZ to obtain the fault gouge. (b) Schematic cross-section fault gouge after having been stretched by the SDVFZ. CBS–Crystalline Bedrock Slice after Brady (1984). ....	193
Figure 6-6. (a) Photograph of the granitic part of the outcrop with a perpendicular view to the fault core noundary. (b) Digitization of the outcrop presented in (a) showing the fracturing, the veins and the granitic sample location. (c,d) Photograph and digitization of the granitic sample NH_40 showing a magmatic texture and alteration halos at main fracture walls. ....	194
Figure 6-7. Microphotographs and back-scattered images of the sample NH_40 (a) Microphotograph of the whole thin section made in the sample under polarized-analyzed light. (b-c) Microphotographs showing an altered plagioclase replaced by illite in the core and kaolinite in the borders and slightly altered biotite in polarized-analyzed light (b) and under SEM (c). (d) Microphotograph of a plagioclase transformed into kaolinite intersected by illite veinlets	

under polarized-analyzed light. (e) Back-scattered image of an illite veinlet developed through the porosity created by plagioclase kaolinization. The ellipsoids 1 and to show the diffusion of illite from the veinlet through the porosity. (f-g) Microphotograph under polarized-analyzed light and back-scattered image of a microfracture, with kaolinized walls, crosscutting an altered plagioclase replaced by kaolinite, illite and calcite. The limit between kaolinite from plagioclase alteration and kaolinite related to the microfracture is represented by the white dashed line. ....195

Figure 6-8. (a) Digitized photograph of the studied outcrop showing the location of the samples NH\_44 and NH\_45. (b) Photograph of the sample NH\_44 showing four different phases. The dashed yellow lines represent the limit between the gneissic part and the fault core. (c) Photograph of sample NH\_45 collected away from the fault core. Both samples show the evolution of alteration and deformation approaching the gouge.....197

Figure 6-9. (a) Microphotographs under polarized-non-analyzed light of global thin sections realized in sample NH\_45. (b-d) Microphotographs under polarized-non-analyzed light of global thin sections realized in sample NH\_44 showing the microstructure and alteration evolution with deformation through the gneissic part. (e) Microphotographs under polarized-non-analyzed light of global thin section made in the fault core considered as a mix between Proterozoic sediments, basement and Mesozoic granite. (f-m) Microphotographs zooms under polarized-analyzed light from each thin section. (f) Brecciated quartz showing an undulatory extinction and new grains, almost unaltered biotite and fractures filled by calcite. (g) Plagioclase partially altered into illite and almost unaltered biotite oriented following the gneiss foliation. (h) Brecciated quartz showing an undulatory extinction and sub-grain rotation. (i) Brecciated K-feldspar and quartz with fractures filled by calcite. (j) Grain size reduction and development of an illite+dolomite matrix containing still a lot of biotite partially altered. (k) Important amount of dolomite which partially filled the fractures. (l) K-feldspar and plagioclase completely altered into illite forming the matrix with dolomite and embedded quartz clasts and few biotite. (m) Illite+dolomite matrix where only little clasts of quartz are still visible. ....199

Figure 6-10. (a) Photograph zoom of the fault core. (b) Digitization of the outcrop (a) showing the different fault core compartments made of gneiss lenses taken in a clay-bearing fault gouge delimited by dashed red lines, the whole surrounded by granite and gneiss, as well as the location of the different sample collected in the fault core.....202

Figure 6-11. Photograph and digitization of sample NH\_41 collected from the clay-bearing gouge affected by shear deformation showed by boudinated structures, foliated material and sigmoid.....203

Figure 6-12. (a-g) Microphotographs under polarized-analyzed light from the different compartment composing the sample NH\_41: (a) brecciated dolomite, (b) automorphous gypsum, (c) brecciated and deformed quartz crystal presenting a strong undulatory extinction and sub-grain rotation, (d) slightly altered but deformed biotite presenting as mica fishes and showing an undulatory extinction, (e-g) reduction of the grain size and increase of dolomite and illite content with (e) highly brecciated quartz, K-feldspar and biotite and a little dolomite, (f) reduction of the grain size and development of an illite/dolomite matrix and illite matrix and (g) reduction of the grain size and prevalence of the illite matrix. (h-i) Back-scattered images zooming in the illite matrix and showing the illite crystallographic preferential orientation.

Po – Porosity.....205

Figure 6-13. Photographs and digitizations of (a) sample NH\_42 and (b) sample NH\_43 showing the transition between the gneiss lens from the central part of the fault core and the clay gouge, represented by black dashed line.....207

Figure 6-14. (a) Microphotograph of the entire thin section from sample NH\_42 in polarized-analyzed light. (b) Microphotograph in polarized-analyzed light showing the preserved texture of the gneiss which is highly altered. (c) Microphotograph zoom in polarized-analyzed light on the gneiss showing completely altered plagioclase into illite, altered biotite into illite following the initial foliation. (d) Microphotograph in polarized-analyzed light of the transition between the gneiss (brecciated quartz) and the gouge (illite matrix embedding quartz clasts). In the gouge: (e) Microphotograph in polarized-analyzed light of the matrix made of dolomite and illite containing quartz sigmoid with its associated pressure shadow, (f) Microphotograph in polarized-analyzed light of a quartz clast pressure shadow made of illite, and (g) Back-scattered image of a quartz clast with its associated pressure shadow made of illite and kaolinite in a clay rich matrix embedding dolomite and quartz clasts.....208

Figure 6-15. (a) Chondrite-normalized (values from Boynton (1984)) rare earth elements (REE) patterns of samples from this study (colored lines) and from Klee et al. (2021a) (grey area). (b) Primitive mantle-normalized (values from McDonough et al. (1992)'s slight revision of Sun and McDonough (1989)) multi-element diagram showing trace element pattern of samples from this study and from Klee et al. (2021a).....210

Figure 6-16. (a) The fault gouge outcrop showing the samples locations. The gouge being composed of two branches, it is considered that the left branch present equivalent values than NH\_41 and thus marked by a dashed square. (b) Extrapolated evolution of the amount of illite in comparison to kaolinite. (c) Extrapolated evolution of the porosity, LOI and calcite content

percentages through the fault zone. (d) KI values of the fraction <math><2 \mu\text{m}</math> and <math>2\text{--}6 \mu\text{m}</math> along the fault zone profile.....	213
Figure 6-17. (a) Markstein basin location in the URG modified after (Edel et al., 2007; Ledésert and Hébert, 2020). (b) Geological map showing sediment slices pinched between blocks of granite due to shear displacement identified in the vicinity of the Markstein basin in the URG (infoterre). .....	217
Figure 6-18. Structural map of the European Cenozoic rift system showing the tectonic setting of the Upper Rhine Graben (URG in the rectangle) after Schumacher (2002) .....	219
Figure 6-19. Location and simplified geological map of the Upper Rhine Graben modified after Ledésert and Hébert (2020) and Rotstein et al. (2006) showing the location of the two investigated mines. LRG - Lower Rhine Graben, URG - Upper Rhine Graben and BG - Brest Graben. ....	220
Figure 6-20. Tectonics phases of the Vosges mountain since the Carboniferous to the end of the Miocene (Hafeznia et al., 2015).....	221
Figure 6-21. Geological map of the Gabe Gottes mine with fault analysis data .....	222
Figure 6-22. Interaction between a sheared zone and euhedral-geodic veins.....	223
Figure 6-23. Development of euhedral quartz within the shear zone, showing no sign of deformation .....	224
Figure 6-24. (a) Photograph of the sheared zone showing the euhedral quartz veins interlayered and making bridges in the sheared basement. (b) Zoom showing an euhedral quartz veinlets crosscutting the highly deformed basement using plans of weakness. ....	224
Figure 6-25. Microphotographs under optical microscope of samples collected according to a profile through a shear fault zone with (a) the wall rock, (b-d) the outer zone of the fault core and (e-g) the fault core. (a) The surrounding rock highly altered with feldspar transformed into illite associated to carbonates, altered biotite into illite and oxides and unaltered quartz partially dynamically recrystallized (grain boundary migration) at the grain borders. (b,c) Highly deformed basement showing sigma clasts of illite and carbonates, layers of dynamically recrystallized quartz by grain boundary migration and illite-carbonate rich layers. (d) Layer of recrystallized quartz by grain boundary migration. (e,f) Veins of euhedral secondary quartz crosscutting highly deformed zones of illite and carbonates presenting a CPO. (g) Example of a geode filled by quartz observed in the core of the high strain zone.....	226

Figure 6-26. Geological map of the Black Forest. In red the location of the detailed geological map of the Schauinsland area, translated after Wittenbrink (1999).....	228
Figure 6-27. Geological map of Schauinsland mostly composed of pre-Cambrian gneissic rocks, the blue dotted lines correspond to the mineral veins, modified from Wittenbrink (1999).....	229
Figure 6-28. Ore mineral vein in Schauinsland showing evidence of brine circulation pulses .....	230
Figure 6-29. N-S cross-section of Schauinsland showing the Schumachersche Ruschel cross-cutting the Schauinsland massif, modified after Wittenbrink 1999). .....	230
Figure 6-30. Geological map of the gallery, the studied area corresponds to the red rectangle where the beginning of the gallery is on the left, modified and translated after Wittenbrink (1999).....	231
Figure 6-31. (a) Photogrammetric model of the portion of the gallery showing the fault gouge. (b) Photo of a branch of the fault gouge showing flows of hydrozincite.....	232
Figure 6-32. Scheme of the extinction of the mineral vein when encountering the highly strained shear zone (Werner, 2002). .....	233
Figure 6-33. (a) Scheme of the interaction between the competent sheared zone and the vein observed in the Gabe-Gottes mine. (b) Scheme of the interaction between the sheared fault gouge and the vein observed in the Schauinsland mine.....	234
Figure 7-1. (a) Geological sketch map of the western Variscides. (b) Geological sketch map derived from the processed gravity maps illustrating the sinistral strike-slip motions along the NE-SW faults, modified after Edel et al. (2007). .....	238
Figure 7-2. (a) Schematic large-scale W-E cross-section of the URG with interpretation of the fault orders from Bertrand et al. (2018). (b) Conceptual scheme presenting the spatial arrangement of the NH fracture network at (1) regional scale, (2) NH scale, (3) outcrop scale from Chabani et al. (2021). .....	241
Figure 7-3. Scheme of a crystalline basement outcrop in the internal part of a 3 <sup>rd</sup> -4 <sup>th</sup> order structural block with the fault core (FC), the damage zone (DZ) and the intra-block fracturing corridor from Bertrand, 2017. ....	243
Figure 7-4. Fault zone architecture in sandstone, weathered top basement, hydrothermally altered granite and deep granite identified at Soultz-sous-Forêts in Vidal and Genter, 2018. FZ– Fault Zone, FC–Fault Core, DZ–Damage Zone.....	248

- Figure 7-5. Block diagram from Glaas et al. (2019) representing the fluid circulation in a complex system of fracture zones. Three zones are distinguished: (a) the fault core, which can be a pathway for fluid if illite and quartz veins do not totally seal the zone, (b) the damage zone, which can be sealed or opened with small-scale fractures that act as fluid pathways, and (c) the unaltered granite, which generally shows very low matrix and fracture permeability.....250
- Figure 7-6. (a) Examples of mineralogical assemblages of the granitic basement observed in SsF cores (middle) and in RTH cuttings (right); these assemblages define the different hydrothermal alteration grades (left). GRAN: unaltered granite; HLOW: low hydrothermal alteration; HMOD: moderate hydrothermal alteration; HHIG: high hydrothermal alteration; HEXT: extreme hydrothermal alteration; VEIN: secondary drusy quartz vein from Glaas et al. (2019). (b) Examples of mineralogical assemblages of the granitic basement observed in the NH (right) defining different hydrothermal alteration grades (left).....251
- Figure 7-7. (a) Scan of a core (laid flat and doubled) of a major permeable fracture zone from EPS-1 well at SsF with the original scan and the zones characterizing the core (modified after Vidal and Genter (2018)). (b) Photo and respective digitization of the sample NH\_31 showing the different zones characterizing the sample. QV-Quartz vein, CG-Cataclased granite, HG-Hydrothermalized granite, PG-Porphyrific granite, CZ-Cataclastic Zone.....252
- Figure 7-8. Cross-section of the Soultz-sous-Forêts geothermal system showing the different boreholes (EPS1, GPK1, GPK2, GPK3 and GPK4) from Ledésert and Hébert (2020) .....254
- Figure 7-9. (a) Photographs of a longitudinal core section of a sheared and sealed fracture from EPS-1 well at SsF showing the different zonation characterizing the core. HG-Hydrothermalized granite; MQ-Mylonitic quartz as relicts; MOC-Mylonitic oxides and clays. (b) Photograph of an outcrop in the NH showing a high strain zone characterized as a fault gouge. (c) Photogrammetric model of a fault gouge from the Schauinsland mine in the Black Forest.....256
- Figure 7-10. Fault gouge outcrop from in the Noble Hills range. ....257
- Figure 7-11. Geodic vein intersecting a shear zone by using weakness planes in the Gabe-Gottes mine (Vosges Mountains) .....258
- Figure 7-12. A synthetic scheme showing what might be the complexity of a granitic geothermal reservoir by representing the different types of fault zones and fractures that might exist, modified and enhanced after Glaas et al. (2019). Three zones are visible: (1) fault cores, which can be open or sealed by secondary minerals, (2) the damage zone which can be sealed or

opened with small-scale fractures acting as fluid pathways, and (3) the unaltered granite showing generally a very low matrix and fracture porosity and permeability. ....259

Figure 8-1. Synthetic scheme showing the interaction between the fluid and the granite at different amount of strain. (a) Initiation of a fracture in a granite affected by propylitic alteration. (b) Open fractures with an incipient alteration of the surrounding rock. (c) Brecciated zones with a carbonated matrix and no change of alteration degree. (d) An open fracture with an incipient alteration gradient at the border. (e) Mineral crystallization at the border of the vein. (f) A sealed fracture with a slight alteration gradient. (g) A brecciated vein induced from fracture reactivation and showing an alteration gradient but no fracturing gradient. (h) A mylonite made of carbonates and granitic lenses showing an alteration gradient and a fracturing gradient. (g) and (h) show a similar fracture density ( $F_d$ ). (i) A fault gouge resulted into the deformation of inherited pinched Proterozoic basement and sediments. (j) Gabe-Gottes mine case, deviation of the vein with the shear zone. (k) Schauinsland case, the vein is stopped by the clay gouge. No scale is given for this scheme, because it can represent fracture zones of several order of magnitude. The supposed geothermal exploitation potential is indicated by smileys of different colors.....265

## LIST OF TABLES

---

Table 1-1. Summary by region and continent of direct-use geothermal data worldwide in 2019 after Lund and Toth (2021) .....	44
Table 4-1. Metamorphic zone boundaries (Merriman and Frey, 1998) for Kübler Index (KI) values (Warr and Mähmann, 2015) and temperatures (Abad, 2007).....	98
Table 4-2. List of samples collected in the field with their mineralogical composition determined after microscopic observations and XRD analysis (primary minerals, alteration phases for plagioclase, biotite and K-feldspar, other secondary minerals and microfissuring after Castaing and Rabu scale). Abbreviations (except for “Ox and Wm”) after Kretz (1983): Qtz—Quartz, Pl—Plagioclase, Mc—Microcline, Or—Orthoclase, Bt—Biotite, Kln—Kaolinite, Ep—Epidote, Ox—Oxide (when it could not be determined precisely), Wm—K-white mica, Cal—Calcite, Dol—Dolomite, Hem-Hematite, Gp—Gypsum, Fd—Fracture density.....	103
Table 4-3. List of samples with their respective clay minerals composition, FWHM and Kübler Index (KI) for the fractions < 2µm and 2–6 µm. Abbreviations (except for “Cor”) after [45]: Ill—Illite, Kln—Kaolinite, Cor—Corrensite, I/S—Illite/Smectite, Vrm—Dioctahedral Vermiculite, Bt—Biotite, Mnt—Montmorillonite, AD—Air-dried. ....	106
Table 4-4. Major elements of the Owlshead and Noble Hills granites.....	112
Table 4-5. Loss on ignition values compared to the alteration degree of plagioclase and biotite estimated under optical microscope.....	114
Table 4-6. Trace elements chemical composition of the Owlshead and Noble Hills granites. ....	115
Table 5-1. List of samples collected in the field with their mineralogical composition determined after microscopic observations (Optical-microscope and SEM-EDS) and XRD analysis (primary minerals and secondary minerals), their degree of microfracturing after Castaing and Rabu (1981) and their clay minerals composition for the fractions < 2 µm and 2–6 µm. Abbreviations after Kretz (1983), except for the following: Olg - Oligoclase, Ox - Oxide, I/S - Illite/Smectite, C/S - Corrensite, n.m. - not measured, n.a. - not analyzed. ....	142
Table 5-2. Spatial fractures analysis. Scanline length: total length of each scanline; Fracture number, Mean spacing, P <sub>10</sub> and Cv value by scanline and fracture distribution tendency by scanline.....	149

Table 5-3. Major elements and loss on ignition (LOI) weight percentage (wt%) for the NH granite.....	163
Table 5-4. Porosity values, recalculated bulk-rock major element weight percentage, altered rock density/fresh rock density ratio, volume factor ( $F_v$ ) assuming the immobility of $Al_2O_3$ ( $X_{Al_2O_3} = 0$ ). .....	166
Table 5-5. Results of mass-balance calculations assuming $F_v = 1$ . .....	167
Table 5-6. List of samples with their respective FWHM and Kübler Index (KI) values in air dried (AD) conditions for the fractions < 2 $\mu$ m and 2-6 $\mu$ m. n.m. - not measured.....	167
Table 6-1. List of samples collected on the outcrop with their mineralogical composition and clay mineral composition for the fractions <2 $\mu$ m and 2-6 $\mu$ m determined after microscopic observations (OM and SEM-EDS) and XRD analyses (primary minerals and secondary minerals) .....	195
Table 6-2. Loss on ignition values and major elements, trace elements and rare earth elements chemical composition. ....	209
Table 6-3. List of samples with their respective FWHM and Kübler Index (KI) values in air dried (AD) conditions for the fraction <2 $\mu$ m and 2-6 $\mu$ m. n.m.-not measured.....	211
Table 7-1. Primary minerals, secondary minerals (from propylitic and argillic alterations) and fracture infills for both Upper Rhine Graben and Noble Hills range. Bold writing indicates the differences between SsF and NH. ....	246

# ABBREVIATIONS

---

**AM:** Avawatz Mountains

**CBS:** Crystalline Bedrock Slice

**CSF:** Crystal Spring Formation

**DV:** Death Valley

**ECRIS:** European Cenozoic Rift System

**ECSZ:** Eastern California Shear Zone

**EGS:** Enhanced Geothermal System

**FCFZ:** Furnace Creek Fault Zone

**GFZ:** Garlock Fault Zone

**HDR:** Hot Dry Rock

**MEET:** Multidisciplinary and multi-context demonstration of Enhanced Geothermal Systems exploration and Exploitation Techniques and potentials

**MTJ:** Mendocino Triple Junction

**NDVFZ:** Northern Death Valley Fault Zone

**NH:** Noble Hills

**NHF:** Noble Hills Formation

**OM:** Owlshead Mountains

**RTH:** Rittershoffen

**SAF:** San Andreas Fault

**SDVFZ:** Southern Death Valley Fault Zone

**SR:** Schuhmachersche Ruschel

**SsF:** Soultz-sous-Forêts

**TVD:** True Vertical Depth

**URG:** Upper Rhine Graben

**WLB:** Walker Lane Belt



# CHAPTER 1

## Scope of the study and scientific objectives

---

### I. GEOTHERMAL ENERGY

Geothermal comes from the Greek geo (“the Earth”) and thermos (“the heat”). A geothermal system, defined by Williams et al. (2011) is: “any localized geological setting where portions of the Earth’s thermal energy may be extracted from a circulating fluid and transported to a point of use”. The use of geothermal resources can be broken down into two main categories: (1) electricity production and (2) heat production. Depending on the resource, the technique used and the needs, there are multiple applications. The criterion that serves as a guide to properly identify the sector is the temperature. The temperature of the fluid depends on the natural geothermal gradient and the depth at which the fluid is collected. Thus, geothermal energy is qualified according to three types: (1) surface geothermal, (2) medium depth geothermal and (3) deep geothermal.

Geothermal systems can be subdivided according to their geological characteristics referred to as geothermal plays by Moeck (2014) (Figure 1-1):

1. magmatic volcanic field and plutonic type
2. extensional domains
3. igneous basement type
4. intracratonic basins and orogenic belts

The geological setting has an important influence on the reservoir characteristics, the fluid composition, the temperature and whether the geothermal play is a conductive or convective system (Moeck, 2014).

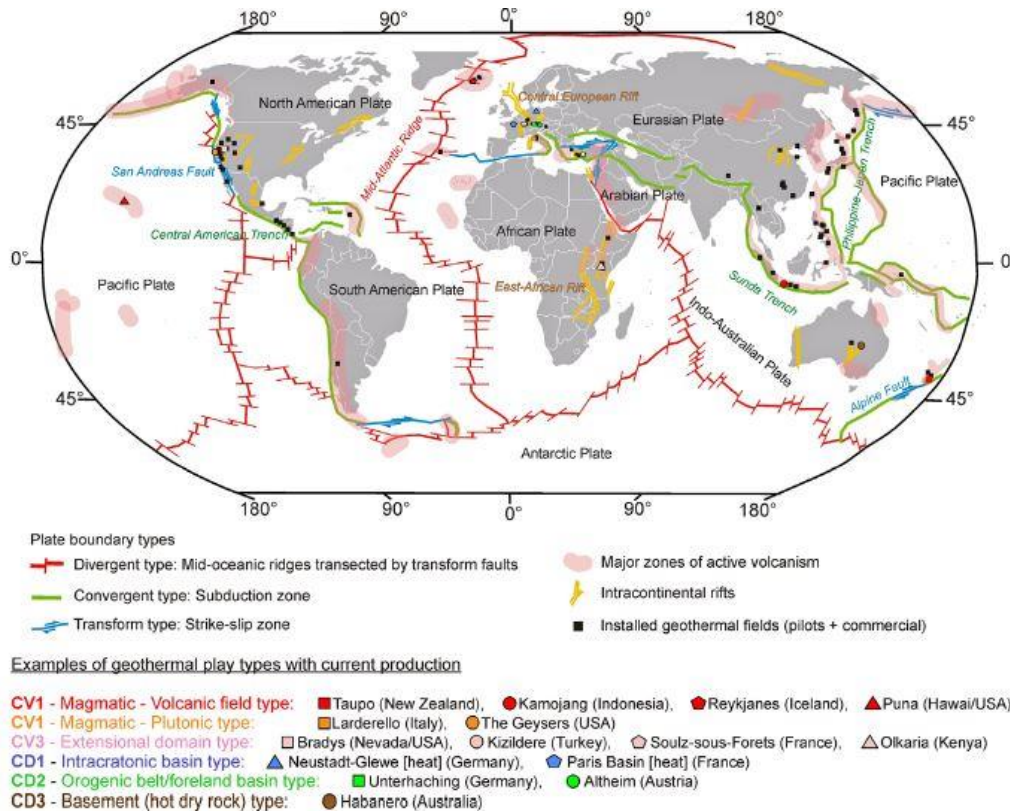


Figure 1-1. Geothermal play types with example geothermal fields installed worldwide from Moeck (2014): CV-Convection dominated heat transfer, CD-Conduction dominated heat transfer

## 1.1. Deep geothermal

Deep geothermal reservoirs are located between 2000 and 5000 meters deep. They are found in volcanic or magmatic fractured rocks affected by an anomalous temperature gradient, reaching from 150°C to super critical temperatures in some cases. These resources can be used to generate electricity, or heat can be used directly. Cogeneration of heat and electricity is an efficient way to use this type of resource.

Deep geothermal energy from fractured reservoirs aims to capture geothermal fluids present in naturally fractured reservoirs. Even if the reservoir rock themselves have practically zero permeability, the reservoir itself is made locally permeable by faulted zones created by tectonic movements that may have affected them throughout their geological history.

Enhanced or Engineered Geothermal Systems (EGS) technique is used in deep geothermal exploitation, not to fracture the surrounding rock, but to enhance the circulation of the fluid already present in the fractures of the reservoir by taking advantage of the permeability and the natural circulation present in the existing network of faults (Olasolo et al., 2016). Contrary to conventional hydrothermal reservoirs, EGS requires stimulation as thermal, hydraulic and or chemical stimulation to re-open fractures mechanically, enhance the hydraulic connectivity

between fractures and/or dissolving sealed fractures, to allow economic heat recovery (Bruhn et al., 2010; Gérard et al., 2006). The geothermal fluids thus play the role of heat transfer fluids. A good circulation of these geothermal fluids is essential to allow their ascent, via convective loops within this fault network and authorize an exploitation of the geothermal resource at acceptable depths. In such an environment a variety of factors (fracturing intensity, stress field, rock petrophysical properties) play a capital role to present interesting geothermal characteristics. The density of the fractures, their openings and their interconnections must be sufficient to present a context favorable to an economically viable geothermal exploitation (<http://www.afpg.asso.fr>).

Thus, the concept of geothermal system was revised by Moeck (2014): "A geothermal system is any localized geologic setting where portions of the Earth's thermal energy may be extracted from natural or artificially induced circulating fluids transported to a point of use. Enhanced Geothermal Systems are portions of the Earth crust where the ratio of flow rate and fluid temperature is naturally too low for economic use, and therefore the flow rate must be increased to a sufficient flow rate/temperature ratio by enhancing the natural permeability through technological solutions".

Geothermal exploitation consists into the extraction of a fluid heated at depth, generally a saline brine (Aquilina et al., 1997; Sanjuan et al., 2010), circulating through the crust fracture network. Once the fluid is at the surface, heat is recovered through a heat exchangers. The cooled fluid is then reinjected in the reservoir in order to maintain the pressure (Figure 1-2). The resource can directly be used for districts heating or used to generate electricity through turbines.

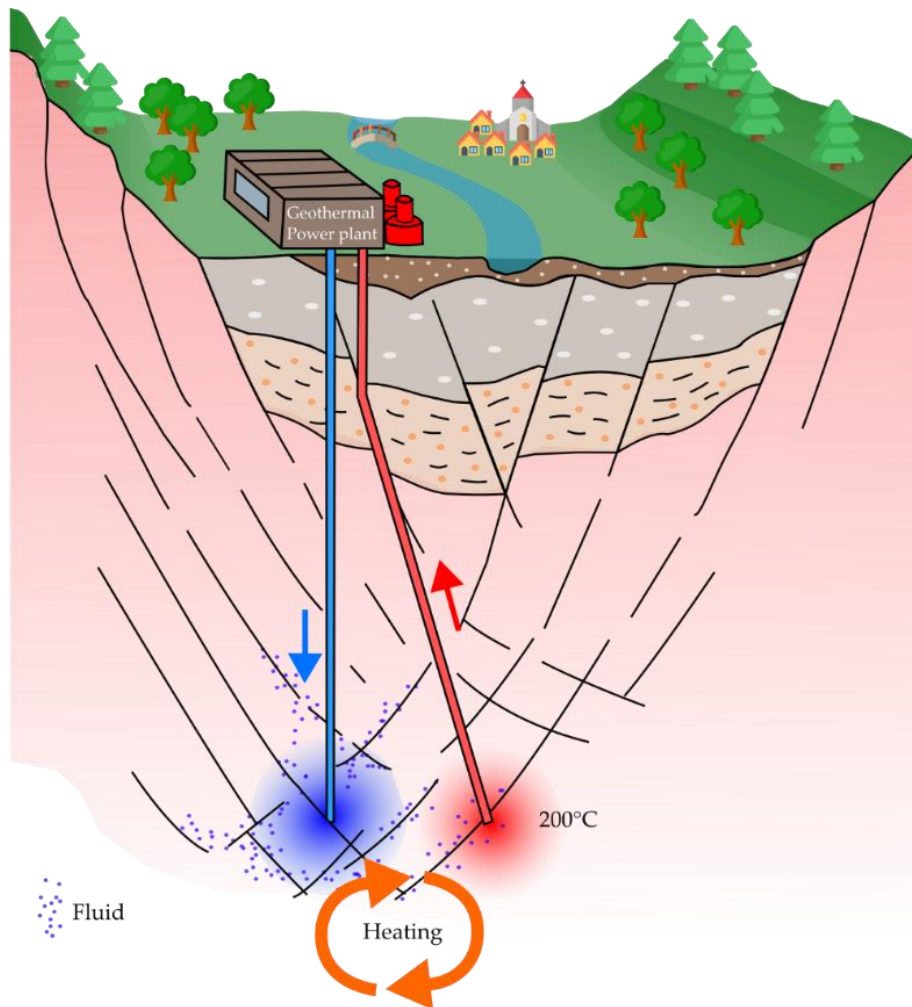


Figure 1-2. Heat exploitation system by a geothermal power plant modified after (<http://www.afpg.asso.fr>)

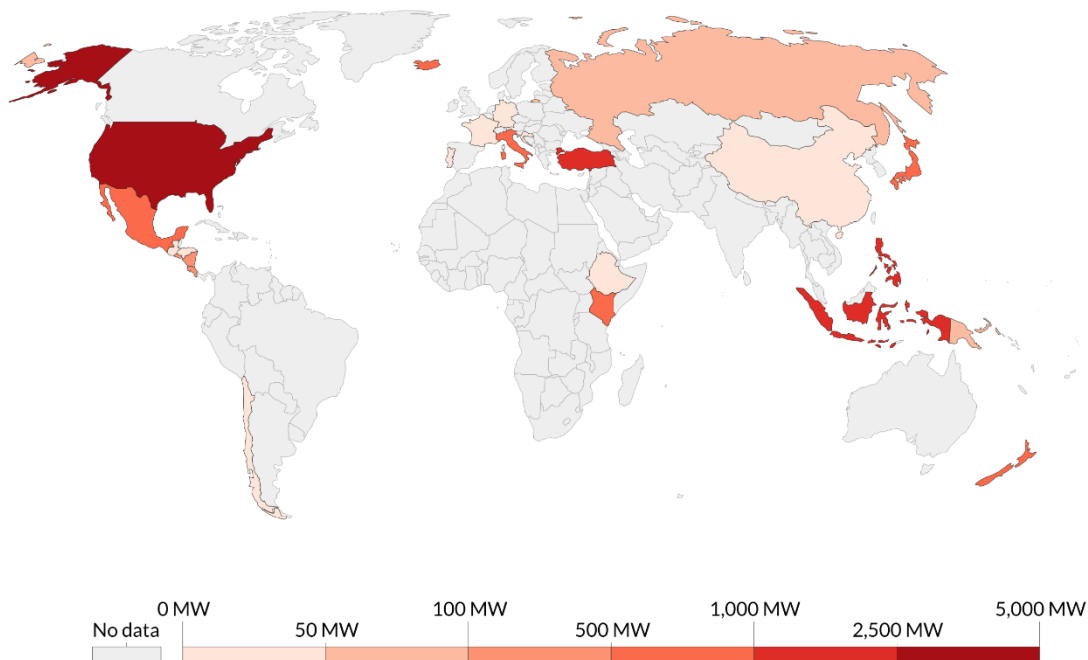
## 1.2. Geothermal energy in the world

The first geothermally generated electricity was produced in Larderello, Italy, in 1904. Nowadays, the power plant produced 545 MW of electricity. The second geothermal power plant developed in the world was in Wairakei, New Zealand in 1958, with 54 production wells with a depth of around 800 m. It produces about 1,550 GWh of geothermal electricity. It was followed by the pilot project in Pathe (Mexico) in 1959 and by “The Geysers” project in 1960 in the USA. The United States is the world’s largest producer. “The Geysers” north of San Francisco in California is the largest geothermal field in the world comprising 22 geothermal power plants (Quick et al., 2010). Iceland is one of the pioneers in the use of geothermal energy for space heating. Currently, geothermal sources accounts for 66% of Iceland’s primary energy use and 25% of the country’s total electricity production is generated by geothermal power facilities (<https://nea.is/geothermal/>).

Geothermal energy is generated in around 88 countries (Figure 1-1; Figure 1-3). Several countries stand out as major producers and consumers of geothermal fluids for direct use as China, USA, Sweden, Turkey, Japan, Germany, Iceland, Finland, France and Canada. However, in most of them the development has been slow.

### Installed geothermal energy capacity

Cumulative installed capacity of geothermal energy, measured in megawatts.



Source: Statistical Review of World Energy - BP (2021)

OurWorldInData.org/renewable-energy • CC BY

Figure 1-3. Installed capacity of geothermal energy across the world in 2020

At the end of 2019, the reported total installed capacity for geothermal direct utilization worldwide is 107.727 GWt, with a total annual energy use about 283,580 GWh), which represent an increase of 72.3% over 2015 (Lund and Toth, 2021) (Table 1-1).

Table 1-1. Summary by region and continent of direct-use geothermal data worldwide in 2019 after Lund and Toth (2021)

Region/Continent (#countries/regions)	MWt	TJ/year	GWh/year	Capacity Factor
Africa (11)	198	3730	1036	0.597
Americas (17)	23,330	180,414	50,115	0.245
Central America and Caribbean (5)	9	195	54	0.687
North America (4)	22,700	171,510	47,642	0.24
South America (8)	621	8709	2419	0.445
Asia (18)	49,079	545,019	151,394	0.352
Commonwealth of Independent States (5)	2121	15,907	4419	0.238
Europe (34)	32,386	264,843	73,568	0.259
Central and Eastern Europe (17)	3439	28,098	7805	0.259
Western and Northern Europe (17)	28,947	236,745	65,762	0.259
Oceania (3)	613	10,974	3048	0.568
<b>Total (88)</b>	<b>107,727</b>	<b>1,020,887</b>	<b>283,580</b>	<b>0.300</b>

In the generation of geothermal power, the USA leads the world with a total installed capacity of ~3,700 MWe in 2019 (Huttrer, 2020) (Figure 1-3). California and Nevada are the primary states generating geothermal power with respectively 2,683 MWe and 795 MWe. Geothermal power comprises about 0.4% of the total national power generation and about 2% of all renewable sources (Huttrer, 2020). The Great Basin region, in the western USA is an example of a region that hosts predominantly fault controlled geothermal plays (Faulds et al., 2010; Moeck, 2014). This Great Basin region was affected by large magnitude crustal transtension and thinning, as well as emplacement of metamorphic core complexes during the Cenozoic. This caused heat flow elevation facilitating prolific geothermal activity in the western part of the region (Faulds et al., 2010; Moeck, 2014). Seismic data indicate a crustal thickness lower than 24 km along the NW-SE trending Walker Lane. In this area, relative crustal thinning means that the Moho has moved closer to the surface and the heat flow has increased. Fluids circulate deep within the crust and seem to be of meteoric origin (Lutz et al., 2002) and of Pleistocene age (Moeck, 2014). Thus, abundant geothermal fields are clustered following NNE to NE-trending belts across the northern Great Basin (Faulds et al., 2010, 2004) (Figure 1-4). The most favorable setting, hosting around 32 % of the systems are step-overs or relay ramps in normal

fault zones. Other settings are present such as intersections between normal faults and strike-slip or oblique-slip faults (22%), normal fault terminations or tip-lines (22%), accommodation zones like oppositely dipping normal faults (8%), major normal faults (6%), displacement transfer zones (5%) and pull-aparts in strike-slip faults (4%) (Faulds et al., 2012).

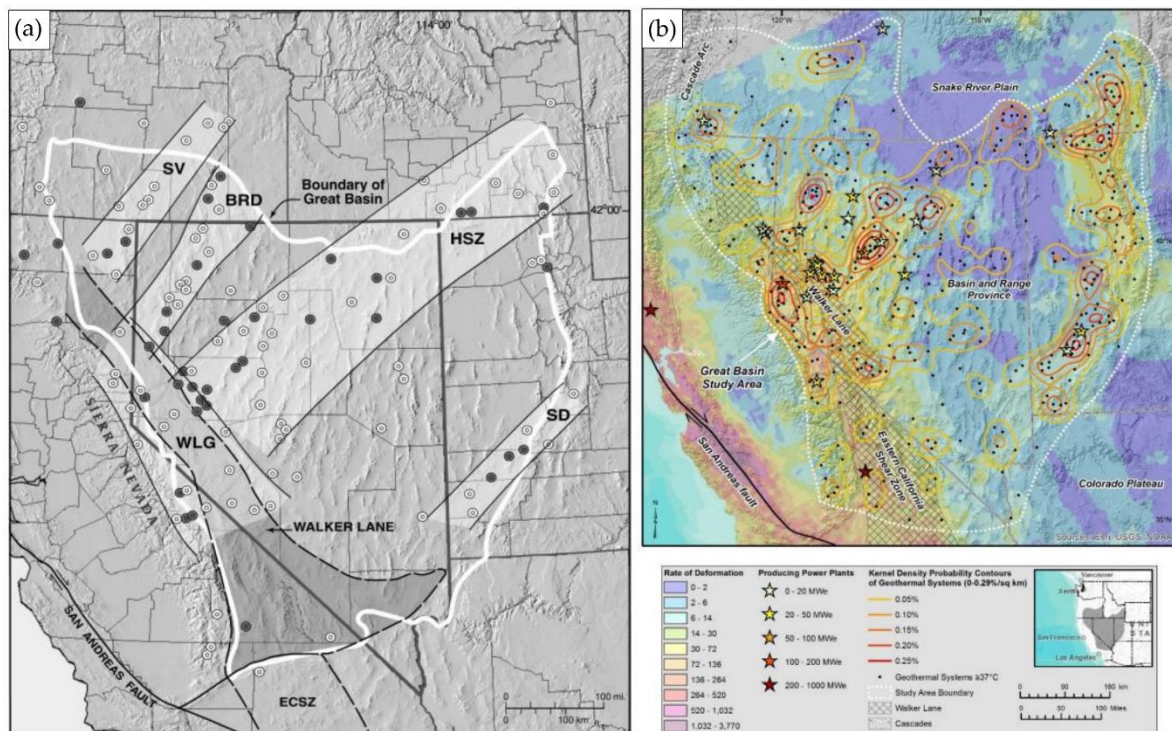


Figure 1-4. (a) Geothermal fields in the Great Basin region after Faulds et al. (2004). Geothermal fields cluster in the Sevier Desert (SD), Humboldt structural zone (HSZ), Black Rock Desert (BRD), Surprise Valley (SV), and Walker Lane (WLG) belts. The northwestern Great Basin, directly northeast of the northwest terminus of the Walker Lane, contains the greatest concentration of fields. White circles are geothermal systems with maximum temperatures of 100-160°C; grey circles have maximum temperatures  $>160^\circ\text{C}$ . ECSZ, eastern California shear zone. (b) Density of known geothermal systems ( $\geq 37^\circ\text{C}$ ) in the Great Basin region plotted on a map showing strain rates after Faulds and Hinz (2015).

Geothermal energy leads for many countries to a reduction in their dependence on imported fuels, but for all it leads to the elimination of pollutants such as carbon particles and greenhouse gases. US \$22.262 billion were invested in geothermal projects by 53 countries in the period 2015-2019 for both direct-use and electric power. Energy savings represents 81.0 million tons of equivalent oil annually, which prevent 78.1 million tons of carbon and 252.6 million tons of  $\text{CO}_2$  from being releasing in the atmosphere (Lund and Toth, 2021). However, as other industrial processes, geothermal power production leads to direct environmental impacts (geological hazards, waste heat, atmospheric emissions, solid waste, water consumption, noise and impact on biodiversity) or indirect environmental impacts (impacts coming due to materials and energy required over the power generation process life cycle). Thus, an evaluation allowing an

environmentally sustainable management can be conducted using Life Cycle Assessment (LCA) (Tomasini-Montenegro et al., 2017).

### I.3. Deep geothermal development in Europe

In Europe, 257 geothermal district heating systems with total installed capacity of 4.6 GWt are present and the total installed capacity for geothermal electricity was about 2.2 GWe, generated by 84 power plants. The total installed capacity could increase to reach 1,400 TWh/year by 2050, half of it being produced by EGS plants (European Commission, 2016). To make possible enhancement of deep geothermal development in Europe, a SET-Plan (Strategic Energy Technology Plan) has been created by the European Commission (2016) presenting 6 main strategic targets:

1. Increase reservoir performance resulting in power demand of reservoir pumps to below 10% of gross energy generation and in sustainable yield predicted for at least 30 years by 2030.
2. Improve the overall conversion efficiency, including bottoming cycle, of geothermal installations at different thermodynamic conditions by 10% in 2030 and 20% in 2050
3. Reduce production costs of geothermal energy (including from unconventional resources, EGS, and/or from hybrid solutions which couple geothermal with other renewable energy sources) below 10 €/ct/kWhe for electricity and 5 €/ct/kWhth for heat by 2025.
4. Reduce the exploration costs by 25% in 2025, and by 50% in 2050 compared to 2015
5. Reduce the unit cost of drilling (€/MWh) by 15% in 2020, 30% in 2030 and by 50% in 2050 compared to 2015.
6. Demonstrate the technical and economic feasibility of responding to commands from a grid operator, at any time, to increase or decrease output ramp up and down from 60% – 110% of nominal power.

The European Union pays special attention to geothermal energy in respect to the Paris Agreement (COP 21, 2015). Within the Horizon 2020 Framework Program, about €90 million worth were funded by the European Commission, granted for Research and Development on geothermal technology during the period 2014-2020 (Hoogland et al., 2019). One of the funded projects is the MEET Project, which aims at demonstrate the viability of EGS with electric and thermal power generation in all main kinds of geological settings (crystalline, sedimentary, metamorphic, volcanic).

## II. THE MEET PROJECT

Europe is sleeping over a giant but largely underused source of geothermal energy. The consequent amount of natural heat coming from Earth is underground, below the European citizen's feet. To boost the market penetration of geothermal power in Europe, the MEET project (**M**ultidisciplinary and multi-context demonstration of **E**GS exploration and **E**xploitation Techniques and potentials) (<https://www.meet-h2020.com>). It received funding from the European Union's Horizon 2020 research and innovation program under grant agreement No. 792037 and brings together 16 partners (universities and industries) from France, Germany, Belgium, Croatia and Iceland. The MEET project was created with the main goal of demonstrating the viability of Enhanced Geothermal Systems (EGS) with electrical and thermal power generation in all main kinds of Variscan geological settings (volcanic, metamorphic, sedimentary and crystalline). The concept of the EGS approach is to exploit the heat which is trapped in any geological settings (different tectonic setting, stress field and rock composition) where fluid circulate.

The main objectives of the MEET project are:

- To gather knowledge of EGS heat and power production in various geological settings
- To increase heat production from existing plants and to convert oil wells into geothermal wells
- To enhance heat-to-power conversion at low temperature (60-90°C) by using smart mobile Organic Rankine Cycle (ORC) units
- To replicate the technology by promoting the penetration EGS power and/or heat

Applying EGS techniques to Variscan domains are particularly challenging for a variety of reasons like (1) the complex geological history of the Variscan orogeny itself, (2) tectonic overprint by subsequent orogenic cycles and (3) the high anisotropy of the metamorphic rocks.

The Variscan domain very often outcrops in Europe and is not yet recognized for its large geothermal potential. In order to structure the project approach, the Variscan domain has been divided in four main parts depending on the nature of the encountered rocks (Figure 1-5):

- Variscan metamorphic (metasedimentary and metavolcanic) successions overprinted by younger (mostly Cenozoic) extensional tectonics (rift system)
- Variscan metamorphic (metasedimentary and metavolcanic) successions not overprinted by younger extensional tectonics
- Variscan granitic basement overprinted by post-variscan extensional faults

- Variscan granitic basement not overprinted by post-variscan extensional faults

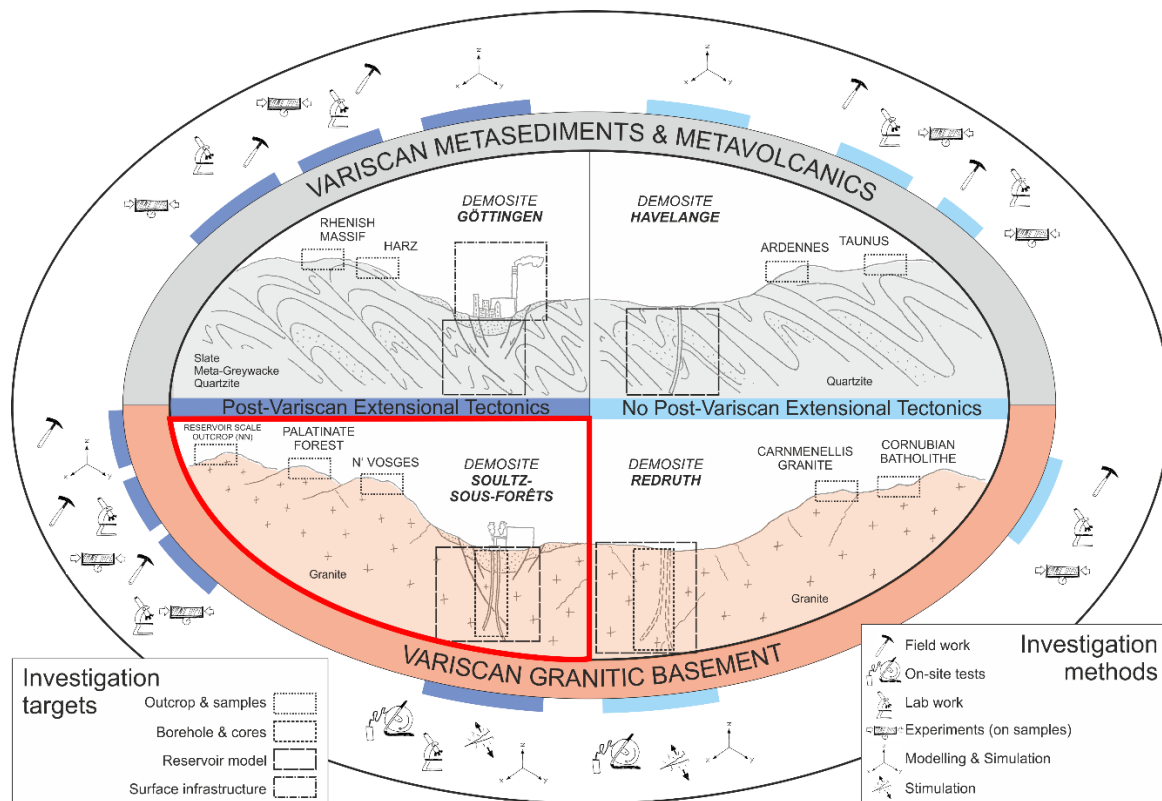


Figure 1-5. Schematic overview of the four representative European Variscan geotectonic settings including the demonstration sites, the analogue sites and the investigation methods according to Trullenque et al. (2018). Our case study is framed in red.

A multidisciplinary input is therefore chosen and reservoir geologists play here a role of primary importance. The major difficulties for them consist in the lack of large-scale outcropping units since information are restricted to borehole data and indirect geophysical methods. Despite several decades of research and development efforts, the large-scale structure of geothermal reservoirs remains not fully understood at present.

This work focus on the study of granitic reservoirs affected by extensional tectonics as framed in red on Figure 1-5. The Upper Rhine Graben (URG, France), with the active geothermal site of Soutz-sous-Forêts, was considered as the reference for this study in terms of exploited granitic reservoir.

### III. SCOPE OF THE PHD

Normal faults, related to the URG formation, are the main structures actually targeted for geothermal exploitations in the URG, being the major drains in the granitic reservoir (Genter, 1989; Glaas, 2021; Vidal, 2017). Up to know, the conceptual model of a fault zone infer the

development of an impermeable fault core, which does not favor reservoir connectivity and acting as a barrier to fluid circulation (Caine et al., 1996).

It is known that the URG is affected by reactivated strike-slip faults through geophysical methods (Edel et al., 2007) and fieldwork (Dezayes et al., 2021). Strike-slip faults are still underestimated and poorly studied in geothermal. In transtensional zones, fault connectivity is naturally enhanced by cross-cutting relationships between the normal faults and the accommodating strike-slip structures between them (Bailleux et al., 2011; Curewitz and Karson, 1997). The evolution in time and space of strike-slip structures within crystalline basement rocks affected by varying amounts of deformation and associated fluid-rock interactions appears of primary importance regarding reservoir understanding.

This research work aims to address the following questions:

- What are the effects of alteration processes in terms of geothermal reservoir properties approaching fracture zones?
- What is the relation between fracture density, alteration and fluid circulation?
- What is the interplay between deformation intensity and fault rock petrophysical properties?
- How the structural heritage impacts the reservoir properties and connectivity?

There is thus a crucial need to investigate beyond the 1D vision provided by the deep boreholes, by evaluating relevant granite naturally exhumed reservoirs considered as analogues. This approach is quite common in geothermal (Aretz et al., 2016; Bertrand, 2017; Chabani, 2019; Le Garzic, 2010; Place, 2010) and oil and gas (Grammer et al., 2004, Sidle and Lee, 2010) literature and has proven to bring a valuable contribution in reservoir understanding. In oil and gas, the analogy is applied in petroleum reserves estimation and classification and used in resources assessment (Sidle and Lee, 2010). A reservoir analogue need to have similar rock and fluid properties, reservoir conditions, geological formation, structure and drive mechanisms (Sidle and Lee, 2010). In geothermal, analogues consist into outcrops allowing the fracture network characterization at large scale because some of the attributes cannot be measured using wellbores, but also the mineralizations, fluid-rock interactions and petrophysical properties (Bertrand, 2017; Chabani, 2019; Ukar et al., 2019, Dezayes et al., 2021). Analogues are also valuable because (1) they provide 2D and 3D high quality datasets unaffected by borehole sampling bias, (2) it is much less expensive, (3) it requires simple means for data acquisition and (4) the study can be done at different scales, from satellite imagery to thin sections.

The concept of analogue can have different approaches. **It is here emphasized on the adopted definition of an analogue as a site to gain input in understanding the evolution of given key processes at depth on certain types of geological structures. It is believed that one of these processes are fluid-rock interactions and their evolution depending on the amount of deformation in transcurrent structures affecting the crystalline basement.**

**Under such a concept, Demonstration and Analogue sites do not need to be directly comparable in terms of specific geological record like timing and amounts of deformation. The study never had the purpose to establish a clear regional geology comparison between the two objects.**

For this work the analogue should at least satisfy the three main following conditions:

1. Present an array of converging similarities in terms of large-scale tectonic setting
2. Have similar crystalline rock petrographic characteristics
3. Allow access to exceptionally outcropping conditions where deformation gradients and fluid rock interaction processes are particularly well developed and preserved

The Soultz-sous-Forêts (SsF) granitic geothermal reservoir, located in the URG, is considered in this study as the demonstration site located in a granitic basement overprinted by extensional tectonics (Figure 1-5, red box). The Noble Hills (NH) range, located along a portion of the Southern Death Valley Fault Zone (CA, USA) forming the Death Valley basin, has been chosen as the main granitic analogue. The goal is to establish a model showing the evolution of transcurrent structures in terms of fluid-rock interactions and amount of strain considering the geological and structural heritage. Knowing the presence of strike-slip faults in the URG shoulders (close to the demonstration site), it is highly probable that these structures are found within the graben. Thus, mines in the URG shoulders (Vosges Mountains and Black Forest), dug in the gneiss, have been preliminary investigated in order to transpose the observations made in the NH. Even if both analogues (NH and URG mines) do not present exactly the same rock nature, granite and gneiss are both crystalline rocks with a similar mineralogical and chemical composition. The combination of data from both sites is thus realistic in order to better understand the SsF reservoir.

This work is a multidisciplinary methodology approach combining fieldwork and laboratory analyses like petrographic, petrophysical, geochemical and fracture distribution analyses.

This research work has been carried out at UniLaSalle Beauvais, in the U2R 7511 Basins-Reservoirs-Resources (B2R) research unit, under the European H2020 MEET Project.

# CHAPTER 2

## Geological setting

One goal of the MEET Project is to gather knowledge of geothermal reservoirs in various geological settings by studying analogues. This work focuses on fault controlled convective dominated domains, i.e. extensional domain types (Figure 2-1). Some of the typical targets are convergent settings containing a variety of extensional domains including pull-apart basins or graben structures (Moeck, 2014).

The demonstration site is the Soultz-sous-Forêts (SsF) geothermal reservoir located in the Upper Rhine Graben (URG). The primary attributed analogue is the Noble Hills range (NH) located in Death Valley (DV). URG shoulders have been preliminary investigated as a near-field analogue of the SsF reservoir.

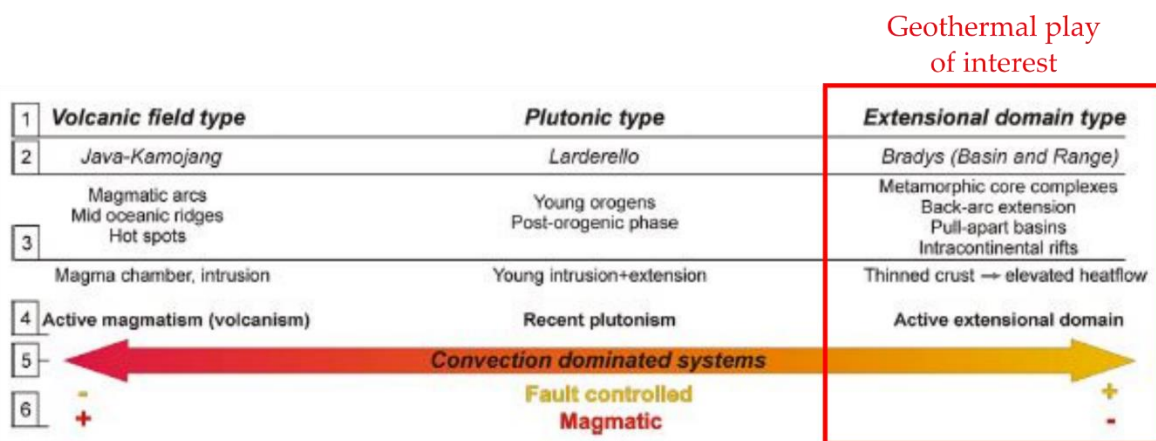


Figure 2-1. Scheme cataloging the convection dominated geothermal play systems based on geological controls. 1-Play type, 2-Typus locality, 3-Plate tectonic setting, 4-Geological habitat of potential geothermal reservoirs, 5-Heat transfer type and 6-Geologic control after Moeck (2014).

## I. DEATH VALLEY –THE NOBLE HILLS RANGE

### I.1. Tectonic setting of the Great Basin

In response to subduction of the last vestiges of the Farallon plate, the Pacific plate came into contact with the western margin of North American around 30 Ma, creating the San Andreas fault (SAF) system (Figure 2-2). By progressively disappearing into the subduction zone of the Farallon plate, the contact between the Pacific plate and the North American plate is enlarged, letting only a remnant of the Farallon plate (Juan de Fuca plate) appearing. The SAF is then lengthened towards the southeast and the northwest where a triple junction is observed

between the Juan de Fuca plate, the Pacific plate and the North American plate. This point has migrated northwest during the past 30 million years and nowadays called the Mendocino Triple Junction (MTJ) (Faulds et al., 2004).

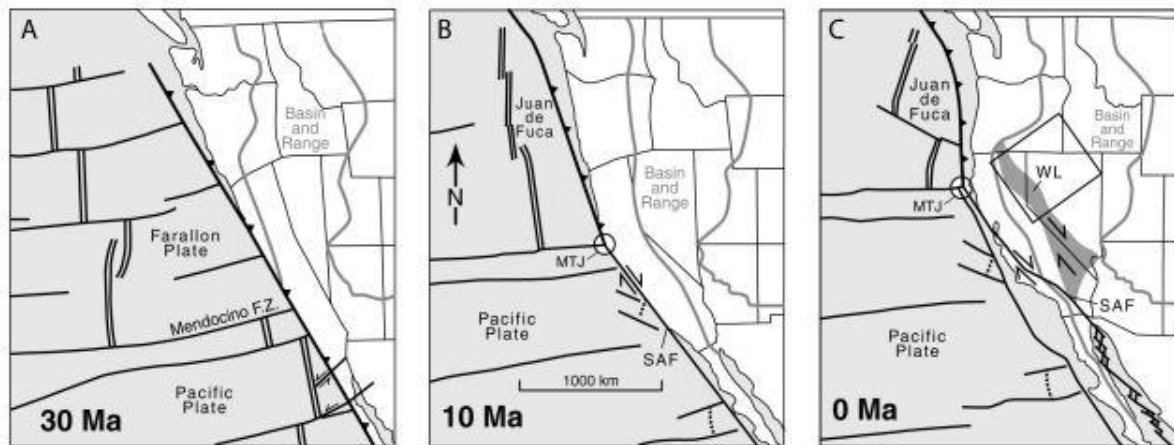


Figure 2-2. Cenozoic tectonic evolution, western North America after Faulds et al. (2004). The box surrounds the locus of geothermal activity in the northwestern Great Basin. MTJ, Mendocino triple junction; SAF, San Andreas fault; WL, Walker Lane.

As the San Andreas fault system has grown through time, it has periodically stepped inland (Faulds et al., 2004). Today, a broad zone of distributed dextral shear zones is identifiable from the San Andreas fault system to the Basin and Range province (Faulds et al., 2004) (Figure 2-2C and Figure 2-3). This zone is the Walker Lane Belt/Eastern California Shear Zone (WLB/ECSZ) (Dokka and Travis, 1990). The important geothermal activity probably results from a NW-trending dextral shear transfer in the WLB to WNW extension in the northern Great Basin (Faulds et al., 2010). The WLB is well known as a system of right-lateral strike-slip faults which accommodated about 20% of the dextral motion between the Pacific and the North American plates (Faulds et al., 2012, 2004; Stewart and Ernst, 1988). This principal system of northwest-striking, right-lateral faults accommodates 4 to 12 mm/yr of dextral motion between the Sierra Nevada block and the central parts of the Great Basin (Faulds et al., 2004; Stewart and Ernst, 1988). According to the dextral motion of the WLB, the Sierra Nevada has been decoupling from the Great Basin (Faulds et al., 2004).

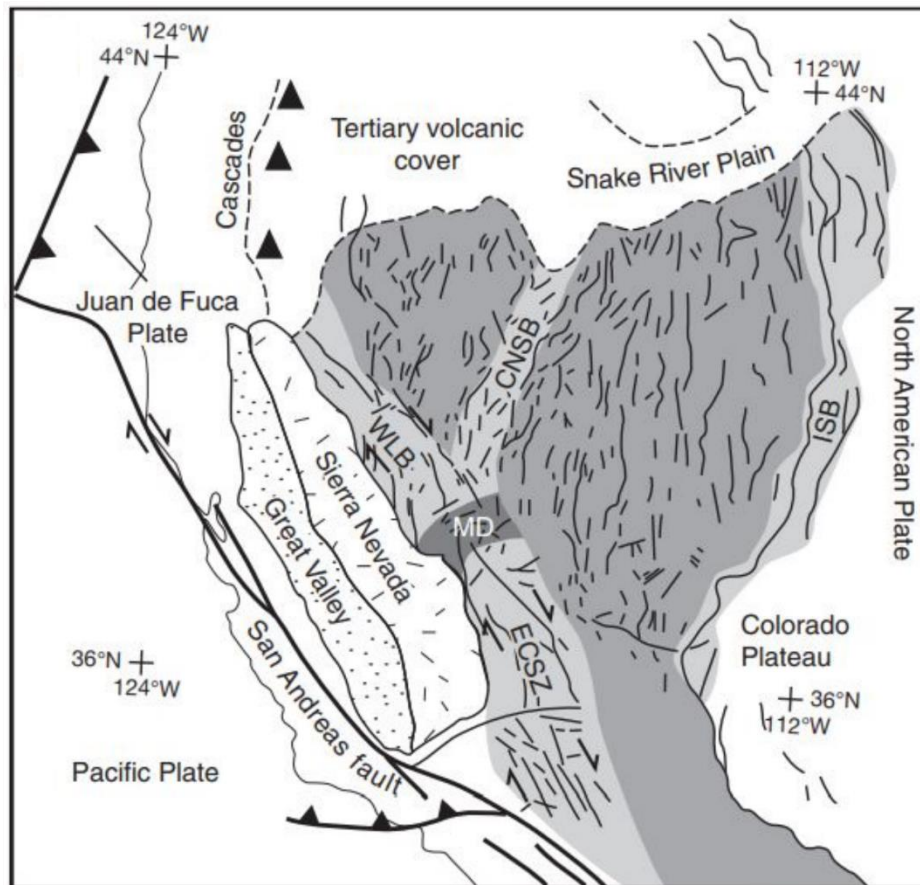


Figure 2-3. Simplified tectonic map of the western USA Cordillera showing the modern plate boundaries and tectonic provinces after Nagorsen-Rinke et al. (2013). Basin and Range Province is in medium gray; Central Nevada seismic belt (CNSB), eastern California shear zone (ECSZ), Intermountain seismic belt (ISB), and Walker Lane belt (WLB) are in light gray; Mina deflection (MD) is in dark gray.

The WLB merged at its southern part with the ECSZ that connects with the SAF system. The ECSZ consists into a broad network of Cenozoic right-lateral strike-slip faults linked to the rotation of the Mojave Desert Block (Dokka and Travis, 1990). As for the WLB, the ECSZ accommodate ~20-25% of total relative motion between the Pacific plate and North American plate. It goes northward through the Mojave Desert for ~500 km and along the western edge of the Basin and Range Province, east of the Sierra Nevada (Frankel et al., 2008) (Figure 2-4). According to Dokka and Travis (1990) the ECSZ became active no earlier than 20 Ma and no later than 6 Ma. Thus, an initiation time is considered to be most likely between ~10 and 6 Ma. It overprints the Basin and Range rifting structure which dates around 17 Ma ago and occupy the space between the Cascade Ranges and Rocky Mountains in the North and the Sierra Nevada and the Colorado Plateau in the south (Eaton, 1982; Parsons, 2006) (Figure 2-3). This province is a classic example of the Miocene to Holocene development of mountains and basins by relative uplift and depression on bounding normal faults (Hill and Troxel, 1966).

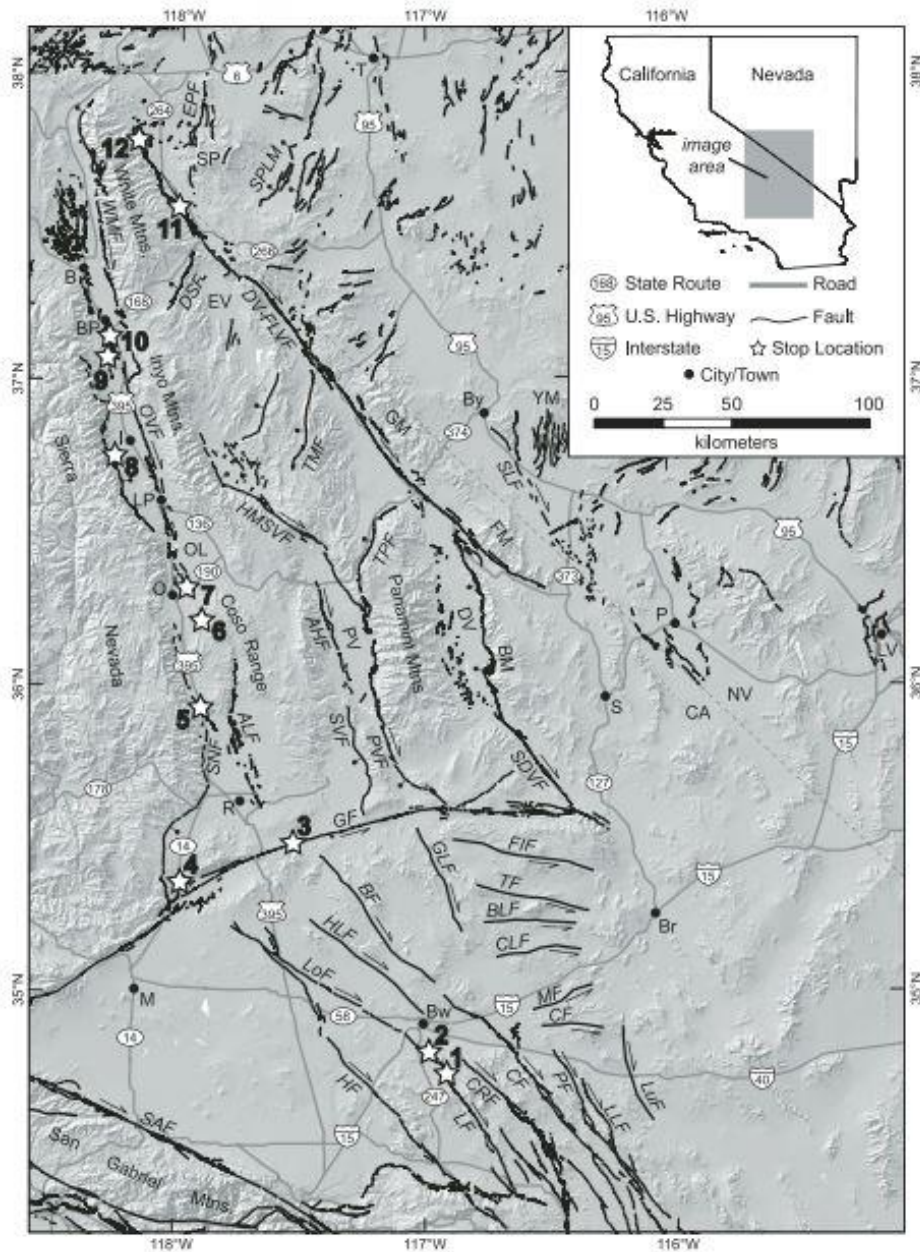


Figure 2-4. Shaded relief index map of Quaternary faults, roads, towns, and field trip stops in the eastern California shear zone after Frankel et al. (2008). Most faults are from the U.S. Geological Survey Quaternary fault and fold database (<http://earthquake.usgs.gov/regional/qfaults>). Arrows indicate relative fault motion for strike slip faults. Bar and circle indicate the hanging wall of normal faults. AHF—Ash Hill fault; ALF—Airport Lake fault; B—Bishop; BF—Blackwater fault; BLF—Bicycle Lake fault; BM—Black Mountains; BP—Big Pine; Br—Baker; Bw—Barstow; By—Beatty; CA—California; CF—Cady fault; CLF—Coyote Lake fault; CoF—Calico fault; CRF—Camp Rock fault; DSF—Deep Springs fault; DV-FLVF—Death Valley–Fish Lake Valley fault; EPF—Emigrant Peak fault; EV—Eureka Valley; FIF—Fort Irwin fault; FM—Funeral Mountains; GF—Garlock fault; GFL—Goldstone Lake fault; GM—Grapevine Mountains; HF—Helendale fault; HLF—Harper Lake fault; HMSVF—Hunter Mountain–Saline Valley fault; I—Independence; LF—Lenwood fault; LLF—Lavic Lake fault; LoF—Lockhart fault; LP—Lone Pine; LuF—Ludlow fault; LV—Las Vegas; M—Mojave; MF—Manix fault; NV—Nevada; O—Olancho; OL—Owens Lake; OVF—Owens Valley fault; P—Pahrump; PF—Pisgah fault; PV—Panamint Valley; PVF—Panamint Valley fault; R—Ridgcrest; S—Shoshone; SAF—San Andreas fault; SDVF—southern Death Valley fault; SLF—Stateline fault; SPLM—Silver Peak–Lone Mountain extensional complex; SNF—Sierra Nevada frontal fault; SP—Silver Peak Range; T—Tonopah; TF—Tiefert Mountain fault; TMF—Tin Mountain fault; TPF—Towner Pass fault; WMF—White Mountains fault; YM—Yucca Mountain.

## 1.2. Death Valley structural setting

The Death Valley (DV) region, extending northwestward on ~200 km from the Garlock Fault Zone (GFZ), stands out from the adjacent regions in its structural setting and in the timing of Basin and Range extension (Fridrich and Thompson, 2011). It is a structural depression bounded by the Panamint Range on the west and by the Black Mountains on the east (Hill and Troxel, 1966)(Figure 2-5a). The Death Valley region is one of the youngest regions of large-scale crustal extension within the Basin and Range province (Calzia and Rämö, 2000). Hill and Troxel (1966) have suggested that the DV region is essentially a strike-slip fault system, with major and minor strain axes approximately horizontal. However, Burchfiel and Stewart (1966) suggested that the central part of DV is related to tension along a strike-slip fault segment which is slightly oblique to the main trend of the fault zone. This tension was caused by the right-lateral movement along the Northern Death Valley-Furnace Creek Fault Zone (NDVFZ-FCFZ) and the Southern Death Valley Fault Zone (SDVFZ) (Burchfiel and Stewart, 1966; Hill and Troxel, 1966). Thus, both sides of DV have been pull-apart and a graben produced between (Burchfiel and Stewart, 1966) (Figure 2-5b). Along with the NDFVZ, the SDVFZ appears to be related to extension within the southern Basin and Range province (Stewart, 1983) and so makes up the southern component of the Death Valley fault system (Machette et al., 2001). Blakely et al. (1999) suggest that the basin along DV is composed of northwest trending small pull-apart structures forming subbasins (Figure 2-5c). The authors put in evidence these subbasins by identifying a right-lateral offset between the Badwater Basin and the Mormon Point Basin (Blakely et al., 1999) (Figure 2-5c). Normal and associated strike-slip faulting accompanied by the extensional DV basin formation began < 15 Ma and continuous today (Calzia and Rämö, 2000). Pavlis and Trullenque (2021) comfort with regional evidence that dextral transtension began by ca. 12 Ma.

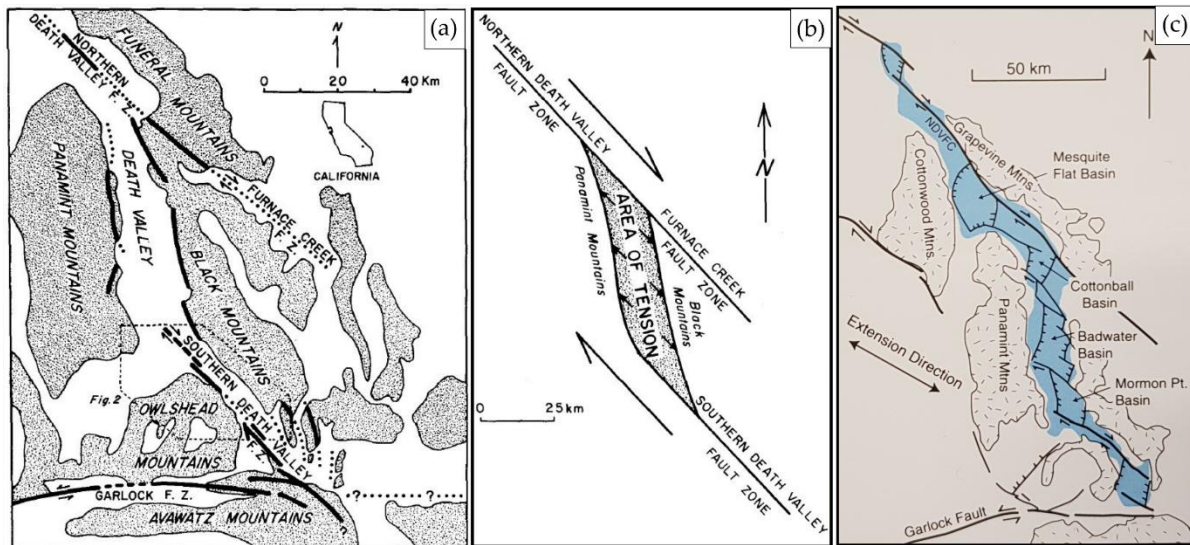


Figure 2-5. (a) Generalized map of the Death Valley region showing the fault systems and their relationship to the Garlock Fault Zone from (Butler et al., 1988). (b) A model of the Death Valley “pull-apart” basin from (Burchfiel and Stewart, 1966). (c) Sub-basins of modern Death Valley from (Miller and Wright, 2015) after (Blakely et al., 1999).

A right-lateral offset of ~35 km has been defined along the SDVFZ, based on matching offset alluvial fan ravel with its source area (Butler et al., 1988). It refined earlier estimates of 8 to 80 km of movement for the SDVFZ and is consistent with the geometry of a pull-apart basin model for central Death Valley defined by Burchfiel and Stewart (1966). The pull-apart model fits with the regional geology showing series of different rock compositions on both sides of the valley (Figure 2-6).

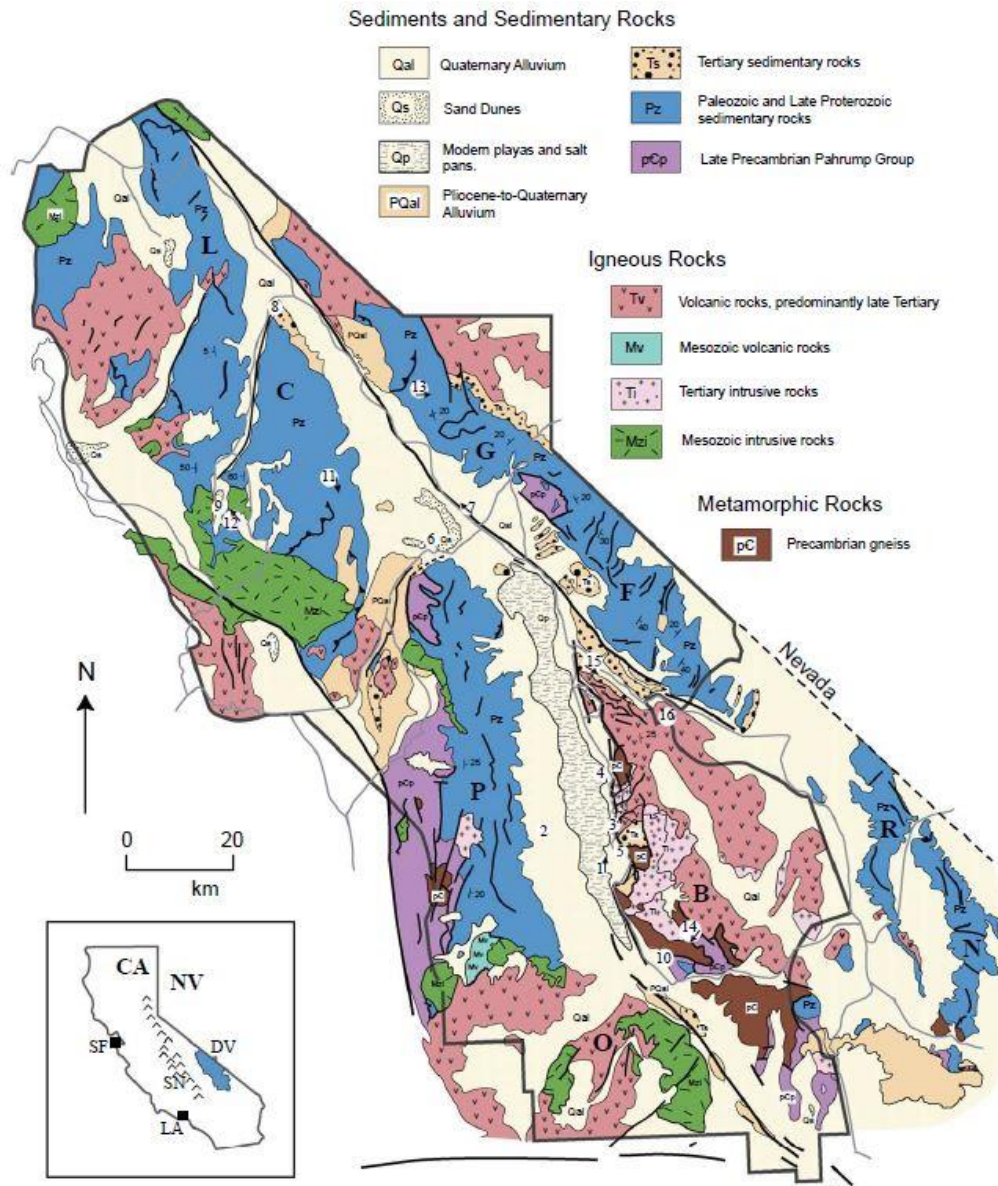


Figure 2-6. Geologic map of Death Valley area after Miller (2005). Numbers and arrows depict corresponding photo location and direction of view. Abbreviations for mountain ranges are as follows: B: Black Mountains; C: Cottonwood Mountains; F: Funeral Mountains; G: Grapevine Mountains; L: Last Chance Range; N: Nopah Range; O: Owlshead Mountains; P: Panamint Mountains; R: Resting Spring Range. Abbreviations on location map of California are as follows: CA: California; DV: Death Valley National Park; LA: Los Angeles; NV: Nevada; SF: San Francisco; SN: Sierra Nevada Mountains.

In this region the pre-Cenozoic stratigraphy consists of Early Proterozoic cratonic rocks and Middle Proterozoic sedimentary paragneiss, schist, and quartzite intruded by 1.7 Ga orthogneiss and 1.4 Ga anorogenic granites (Wooden and Miller, 1990). The Middle Proterozoic Pahrump Group (Figure 2-7a) unconformably overlies the cratonic rocks and is overlain by 3000-5000 m of Late Proterozoic and Paleozoic miogeoclinal deposits.

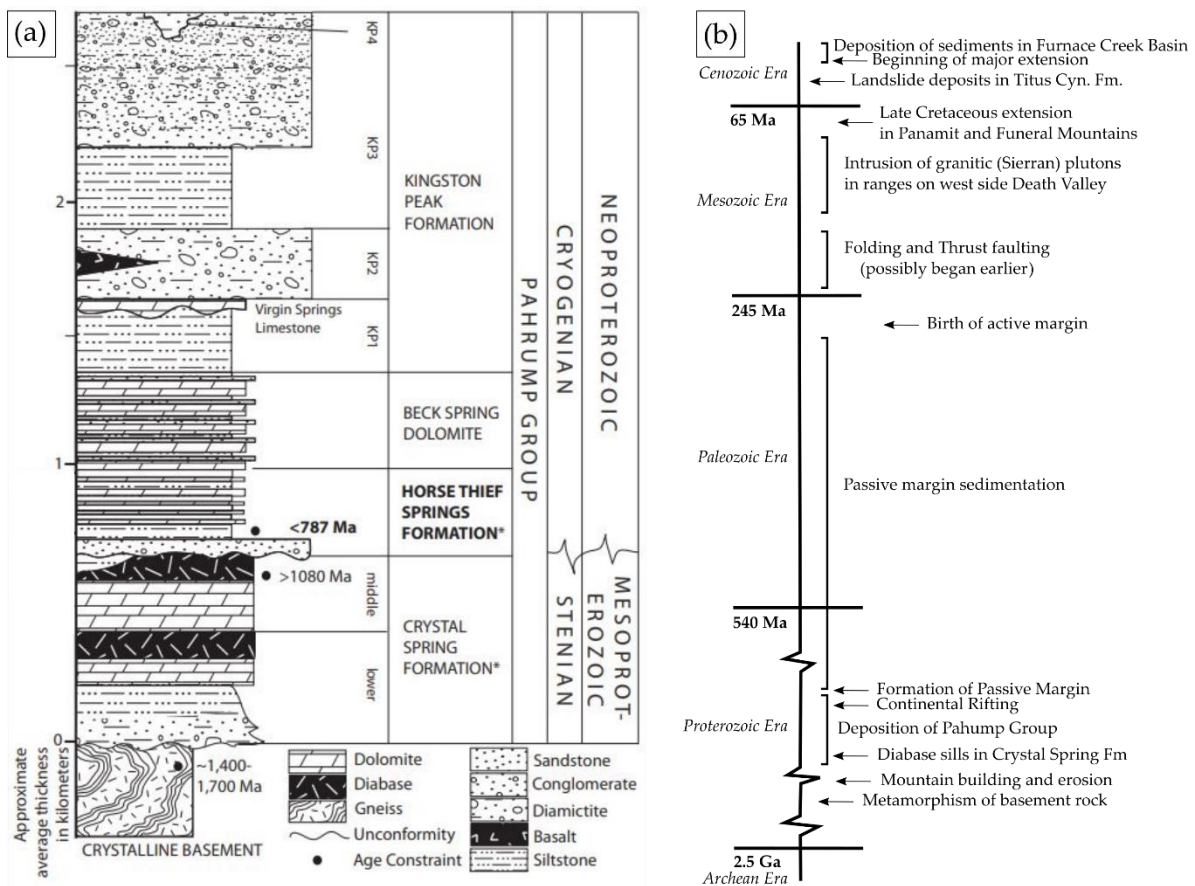


Figure 2-7. (a) Generalized stratigraphy of the Pahrump Group in the Death Valley region revised by Mahon et al. (2014a). (b) Generalized columnar section of Precambrian to Lower Cambrian, Death Valley region from Wright et al. (1974)

These deposits consist of ~2100 m of conglomerate, sandstone, shale, and carbonate rocks divided into three formations: the Crystal Spring Formation, Beck Spring Dolomite, and Kingstone Peak Formation. After several revision of its composition, the Crystal Spring Formation (CSF) in ascending stratigraphic order includes: the arkosic sandstone, feldspathic sandstone, mudstone, dolomite and algal dolomite-siltstone according to Mahon et al. (2014a) (Figure 2-7a). The CSF is intruded by diabase sills that yielded an age of 1.08 Ga (Heaman and Grotzinger, 1992). Metamorphic reactions between the diabase and dolomite of the Crystal Spring Formation produced large deposits of talc, which have been mined throughout the Death Valley region (Miller, 2005). Most of the Proterozoic and Paleozoic rocks are intruded by calc-alkaline granitoids, related to the emplacement of the Sierra Nevada Batholith. These are formed above the eastward dipping subduction zone along the western margin of the North American continent from Late Triassic to Late Cretaceous time (DeCelles, 2004) (Figure 2-7b). All these rocks are overlain by later Tertiary sedimentary and volcanic rocks and Quaternary alluvial deposits. Note that numerous granitic plutons, dikes, and sills are synchronous with extension (Calzia and Rämö, 2000).

### 1.3. The Noble Hills range

#### 1.3.1. Previous work

The area of interest for this work is the Noble Hills (NH) range located at the southern part of the SDVFZ (Figure 2-8). It extends 17 km northwest from the Avawatz Mountains (AM) (Niles, 2016) and form the main feature trending parallel to the SDVFZ (Jennings et al., 1963). The SDVFZ formed the NH, at its southernmost part, by vertical displacement (Brady III, 1986; Brady et al., 1989; Troxel and Butler, 1979).

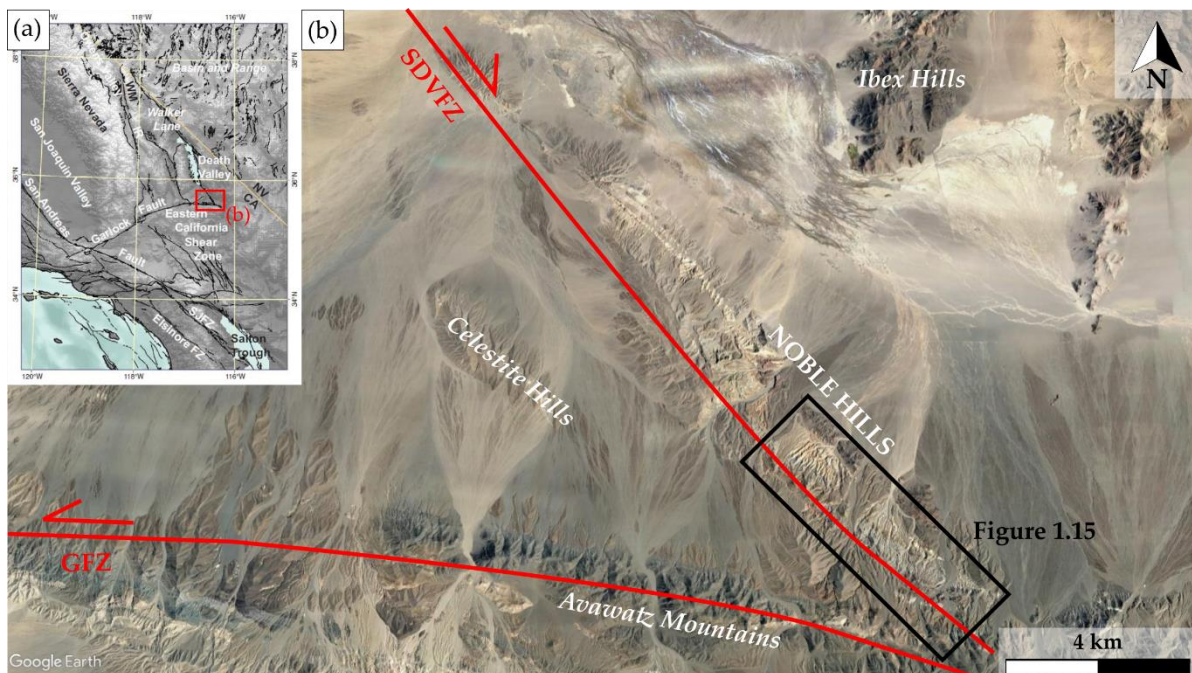


Figure 2-8. (a) Location of the Death Valley and the Noble Hills range, modified after (Norton, 2011). (b) Satellite view of the Noble Hills range. SDVFZ–Southern Death Valley Fault Zone, GFZ–Garlock Fault Zone.

It contains six sub-parallel, overlapping nearly vertical right-lateral fault branches juxtaposing crystalline basement rocks, called the “Crystalline Bedrock Slice” (CBS) or “Axial crystalline ridge”, with Tertiary and Quaternary sedimentary strata outcropping in the NH (Brady III, 1986; Troxel and Butler, 1979). The CBS comprises Precambrian CSF locally intruded by the 1.08 Ga diabase sills and Mesozoic granitic rocks. The SDVFZ intersects the east-trending left lateral Garlock Fault Zone (GFZ), which is linked to the San Andreas Fault (Calzia and Rämö, 2000) (Figure 2-5a) and became active around 10 Ma (Andrew et al., 2015; Chinn, 2013; McGill et al., 2009). With regard on the kinematics according to Brady III (1986) and Verosub et al. (1989), the GFZ terminates as an east-vergent reverse fault in the eastern AM. Thus, it does not continue east of the SDVFZ, however, the SDVFZ changes its strike to wrap around the AM foothills (Chinn, 2013). Thrust faults were observed at the AM foothills by Chinn (2013) and interpreted as the results of the activity of the GFZ uplifting the AM foothills. Likewise, Brady

III (1986) also identified an uplift which increases towards the southeast and seems deformed the crystalline basement rocks and Tertiary sediments, exhuming them from beneath a cover of Quaternary sediments. Recently, Pavlis and Trullenque (2021) have proposed a net amount of 40 to 41 km strike-slip along the SDVFZ based on correlation of a set of geological markers between the Owlshead Mountains (OM) and the southern termination of the Noble Hills. Thus, the granite composing the CBS must be a transported part of the Cretaceous granitic pluton (~95 Ma), forming the OM (Pavlis and Trullenque, 2021; Rämö et al., 2002). Brittle shearing and large-scale boudinage characterize a brittle deformation, showing generally subhorizontal axes, which is prevalent within the Cretaceous granitic intrusion and Precambrian roof pendants (Niles, 2016). Contractional deformation involving all members of the NHF is characterized along the NH and increases in intensity southeast toward the intersection with the GFZ (Niles, 2016).

Few geological mapping has been conducted in the NH (Brady III, 1986; Brady, 1984; Brady and Troxel, 1986b; Troxel and Butler, 1979). More recently, a revised geological map of the NH was realized by Niles (2016), who mainly focused his study on the structural geology and the Tertiary stratigraphy (Appendix 2). From all these investigations performed by the previously cited authors, the CBS was poorly studied. It was only defined as quartz monzonite (Troxel and Butler, 1979) or leucocratic adamellite (Stamm, 1981). Later, Brady III (1986) completed the description as a medium to coarse equigranular grained to slightly porphyritic leucocratic rock. Brady III (1986) also mentioned the presence of mineralization throughout the crystalline basement rocks as veins up to 150 cm thick and 100 m long, composed of barite crystals from 1 to 10 mm long embedded in a dark brown amorphous matrix consisting into a mixture of manganese and iron oxides. This represents a sign of fluids circulation. These types of mineralizations are most numerous in the southeastern part of the range. Niles (2016) also mentioned the sporadic presence of mineralization through the crystalline basement rocks indicative of hydrothermal alteration. After the exhumation and the displacement of the CBS, ~3.34 Ma Pliocene sediments of the Noble Hills Formation (NHF) were deposited, as well as Quaternary alluvium (Niles, 2016). The NHF is composed of a lower sandstone-siltstone member, a gypsiferous member, a halitic mudstone member, a conglomerate member, an upper sandstone, siltstone and gypsiferous member, a megabreccia member and a granite bearing conglomerate (Niles, 2016). These alteration visible in the crystalline basement rocks being not present in the Pliocene strata, Niles (2016) suggested that the deformation of the crystalline basement rocks predates the Pliocene deformation.

### 1.3.2. Revisited geological map

A GIS assisted field work mapping was conducted in order to obtain a new geological map of the NH focused on the CBS (Figure 2-9) (Klee et al., 2021a, 2020 (Appendix 3), 2021b). Fieldwork revealed a complex geometry that was not previously identified by Niles (2016). The Proterozoic sequences outcropping northwest of the Pipeline Wash was investigated (Klee et al., 2021b). The plutonic contact between the Proterozoic sequences and the granite is confirmed. However, the Proterozoic sequences present multiple evidences of deformation with a tectonically induced duplication of the sequences between each granite is present and a lateral bending, stretching and boudinage of this stacked series towards the southeast (Klee et al., 2021b). Thus, a clear deformation gradient has been identified through the range and is presented in Chapter 5. Initially mapped sedimentary contact by Niles (2016) in the rear part of the range and in the front between the CBS (Proterozoic sequences and granite) were mapped as tectonic contacts (Klee et al., 2021a, 2020, 2021b). Likewise, Tertiary volcanism has been identified in the rear southeast part of the range.

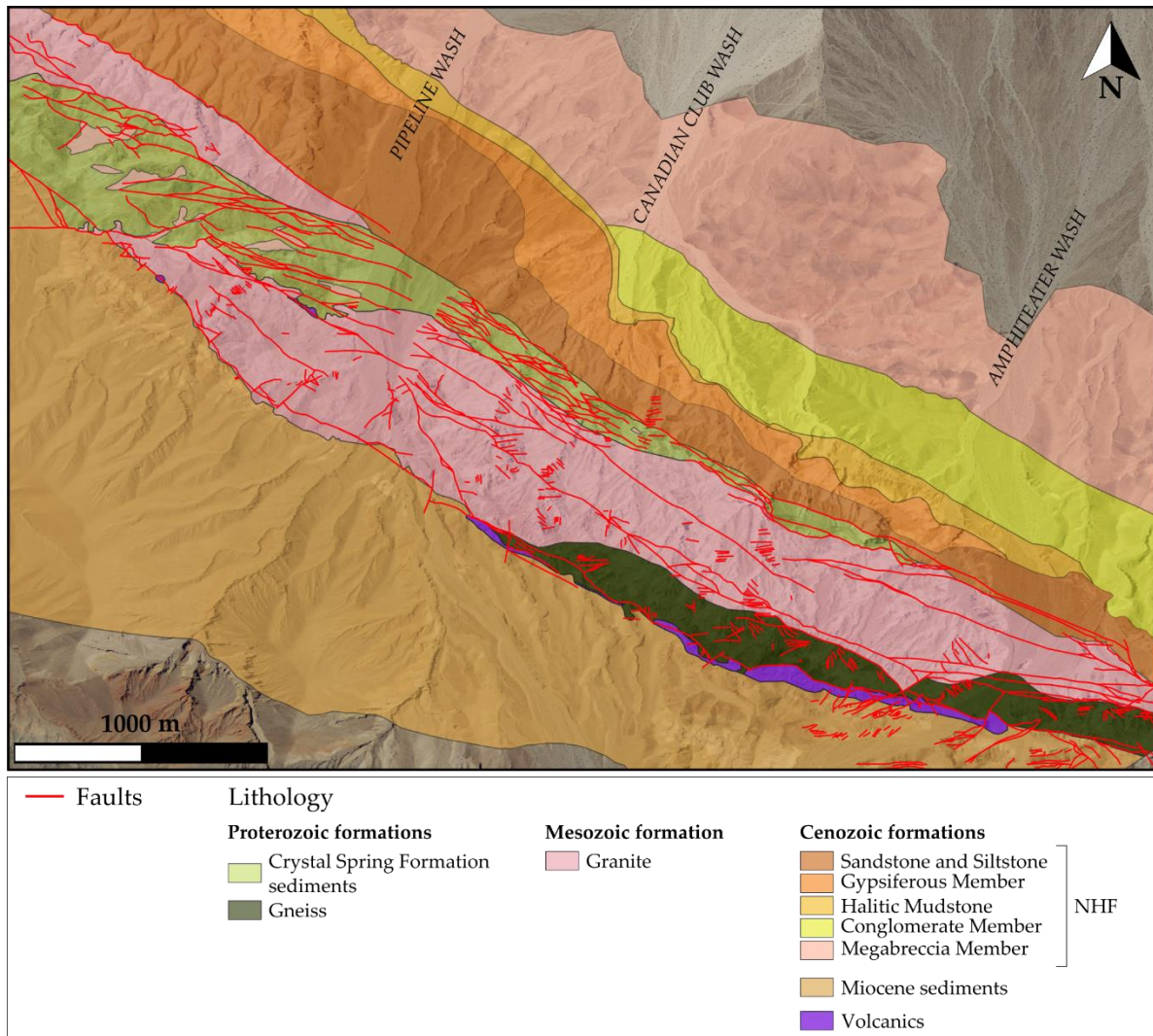


Figure 2-9. Geological map of the Noble Hills range from Klee et al. (2021a) and modified after Klee et al. (2020) and Niles (2016). The quaternary is not displayed and available on Niles (2016) map (Appendix 2). NHF—Noble Hills Formation

A precise fracture pattern characterization of the area has been performed by Chabani et al. (2021), through a multiscale approach, from the regional scale to the microscopic scale. The authors have shown that the NH structure is mainly controlled by the SDVFZ (NW-SE oriented), but also by E-W structures at lower order of scale as moving southeastward. These structures seem to be related to the activity of the GFZ.

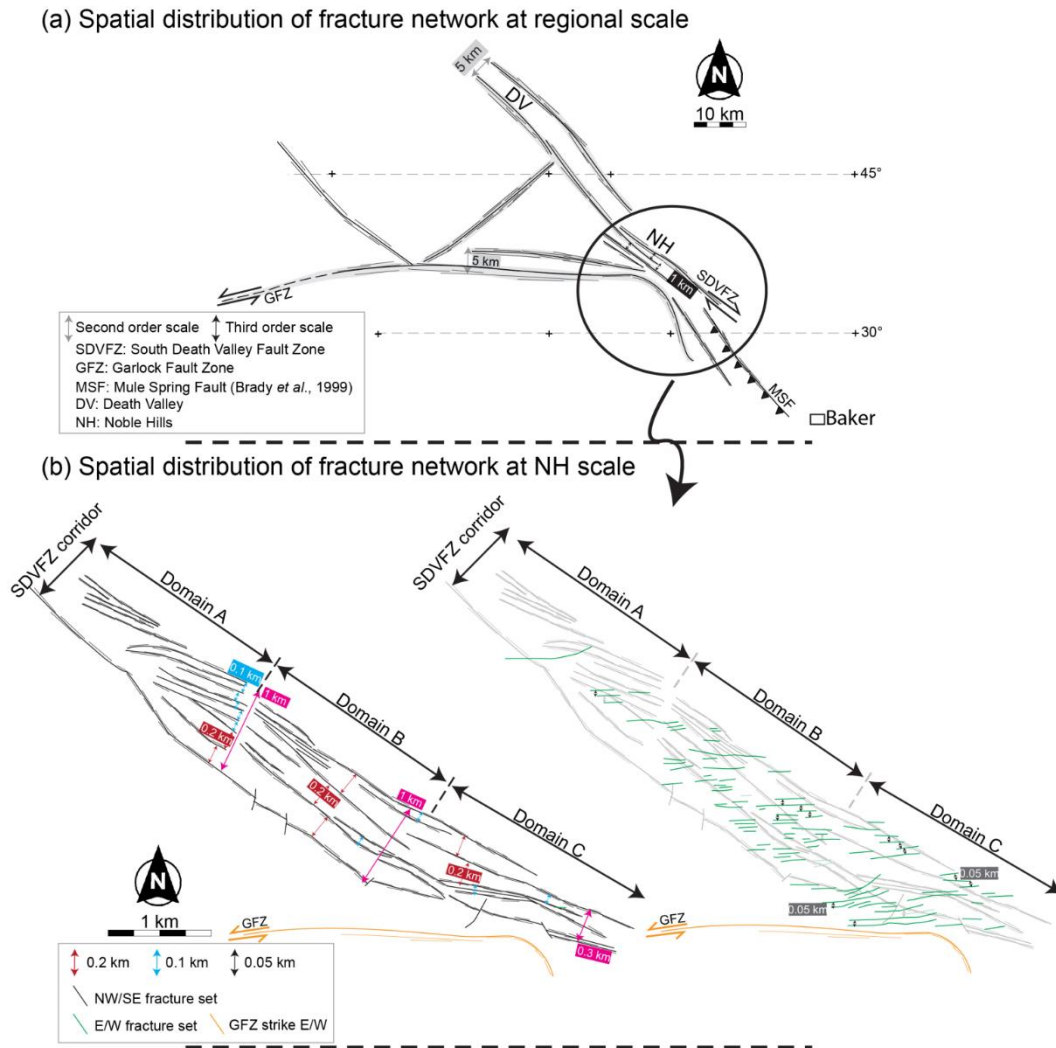


Figure 2-10. Conceptual scheme (a) at regional scale and (b) at the Noble Hills scale of the spatial arrangement of the Noble Hills fracture network from Chabani *et al.* (2021)

## II. UPPER RHINE GRABEN – SOULTZ-SOUS-FORETS GEOTHERMAL SITE

### II.1. Geodynamic evolution of the Upper Rhine Graben

The Upper Rhine Graben (URG) is the central segment of the European Cenozoic Rift System (ECRIS) (Dèzes *et al.*, 2004; Ziegler, 1992) (Figure 2-11a). It extends on 300 km length according to a SSW-NNE direction and on 30-40 km width (Schumacher, 2002) (Figure 2-11b). It is limited by the Rhenish massif in the north and the Jura Mountains to the south, but also by the Vosges Paleozoic crystalline massif in the southwest and by the Black forest crystalline massif in the southeast.

The URG is mainly characterized by normal faults on its borders and internal part. The western part is delimited by the western Rhenian and Vosgian faults, the eastern part is delimited by the eastern Rhenian and Black Forest faults (Figure 2-11b). The normal faults in the internal part are combined to left-lateral strike-slip movements oriented parallel to the graben but also 120°

transverse to the graben axis (Illies, 1972). It is composed of a Paleozoic crystalline basement rocks overlain by 1400 m of Mesozoic and Cenozoic sediments (Illies, 1972; Vidal, 2017) (Figure 2-12). The URG presents a geometry of asymmetric half-grabens with opposing tilt directions (Derer et al., 2005). Likewise, in both half-graben, a generally eastward tilted graben floor, locally offset with variable displacements, enhances an overall graben asymmetry (Grimmer et al., 2017) (Figure 2-12).

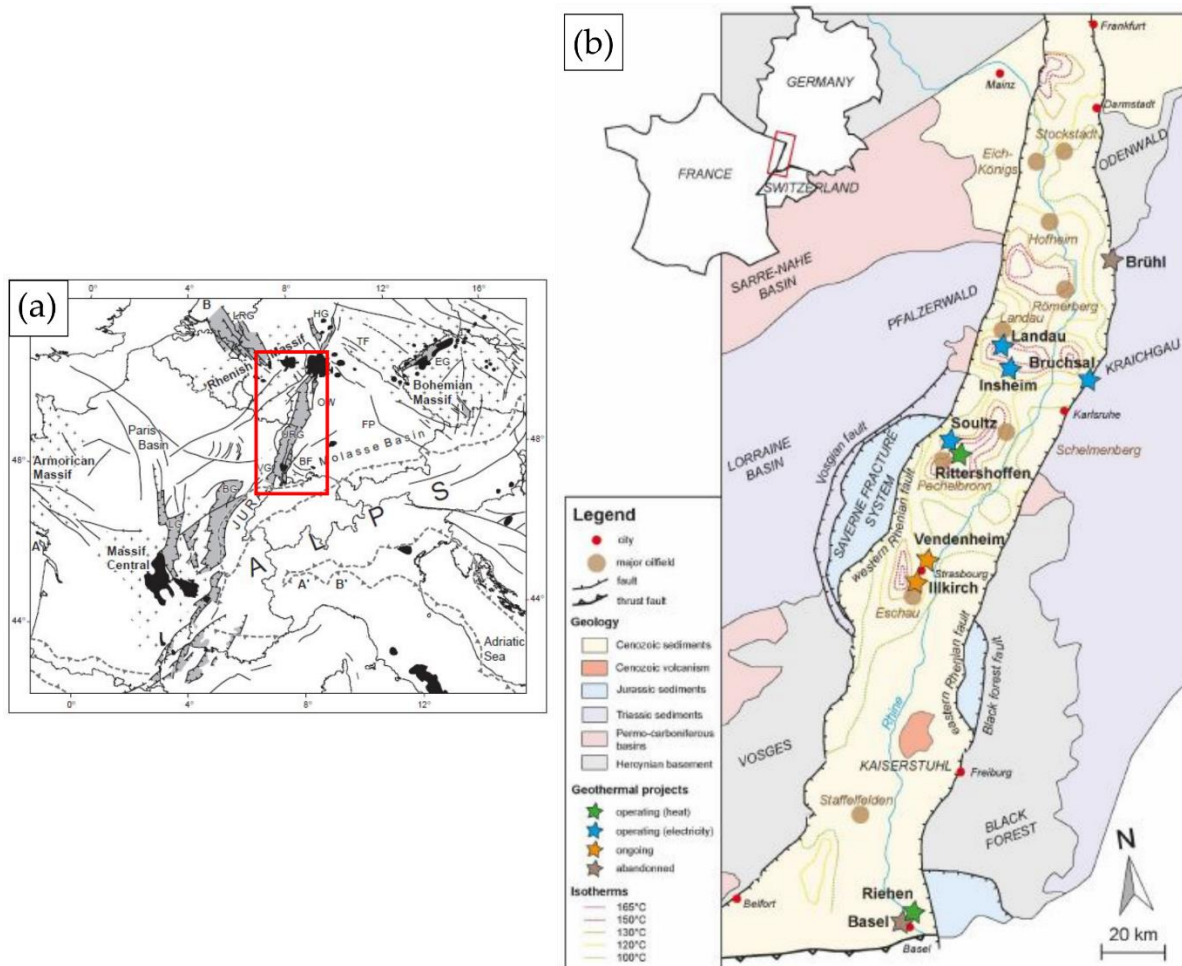


Figure 2-11. (a) Location map of the European Cenozoic rift system (ECRIS) in the Alpine and Pyrenean foreland, showing Cenozoic fault systems (black lines), rift-related sedimentary basins (light gray), Variscan massifs (cross pattern) and volcanic fields (black). Solid barbed line: Variscan deformation front; stippled barbed line: Alpine deformation front. BF, Black Forest; BG, Bresse Graben; EG, Eger (Ohre) Graben; FP, Franconian Platform; HG, Hessian Grabens; LG, Limagne Graben, LRG, Lower Rhine (Roer Valley) Graben; URG, Upper Rhine Graben; OW, Odenwald; VG, Vosges after Cloetingh et al. (2005) and Dèzes et al. (2004). (b) Map of the deep geothermal sites operating or under development in 2020, also representing the major oilfields and the isotherms at 2000 m depth from Glaas (2021)

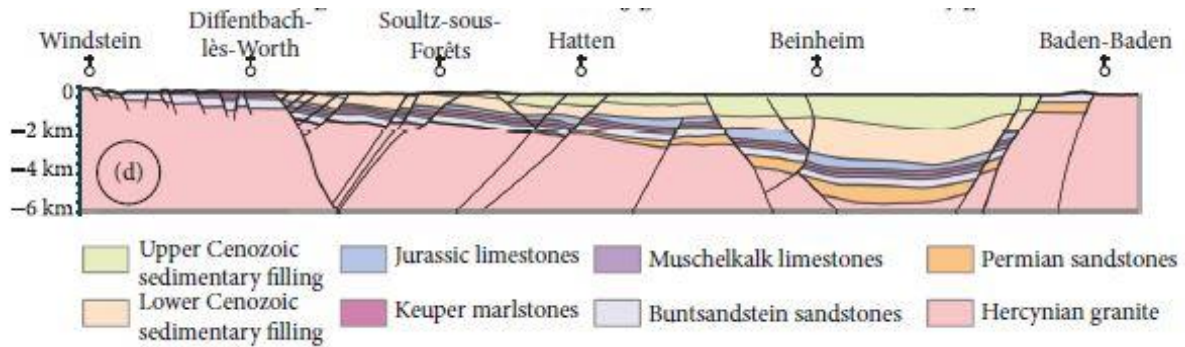


Figure 2-12. Geological W-E cross-section through the URG at Sultz-sous-Forêts latitude from Dezayes and Lerouge (2019a)

The URG structuration is directly related to the Hercynian orogeny followed by the Alpine orogeny. The crystalline basement is characterized by three major terranes: the Rheno-Hercynian, the Saxo-Thuringian, and the Moldanubian which were accreted by subduction during the Carboniferous (the Sudete phase) and Permian (the Saalian phase) along NE-SW sutures as the Lalaye-Lubine fault (Schumacher, 2002). The Variscan cycle is also characterized by the intrusion of granitoids from -340 Ma to -270 Ma following the NE to NNE axis (Altherr et al., 2000, 1999). The Sudete phase was linked to a N-S compression marking the structuration of the orogeny, generating NE-SW sinistral and NW-SE dextral shear faults and to NE-SW compressional thrusting events (Edel and Schulmann, 2009) (Figure 2-13a). These phases caused brittle tectonics with primary fracture sets oriented N45°E, N135°E, and N-S for the Carboniferous phase and N60°E to N90 ° E and N120°E for the Permian phase (Dezayes and Lerouge, 2019a). Both phases are separated by an orogenesis relaxation episode conducted to an extension along an NNE-SSW axis (Figure 2-13a).

A N-S extension occurred during the Late Permian and extended during the Mesozoic. At the same time, until Early Cretaceous, the sedimentation of the Buntsandstein sandstone, Muschelkalk limestone and Keuper evaporites followed by the graben surrection and the erosion of the Late Jurassic layers (Figure 2-13a). This basin subsidence induced NW directed faults in the Vosges and the Black Forest massif (Dezayes and Lerouge, 2019a).

The post-hercynian cycle refers to the Cenozoic rifting (ECRIS) described into 4 phases (Figure 2-13b):

1. A compressional sheared N-S phase at the Early Eocene influenced by the Alpine and Pyrenean thrusting, which reactivated the ENE-WSW and NNE-SSW inherited structures playing an important role in the initiation of the rifting phase (Dèzes et al., 2004; Schumacher, 2002; Villemin and Bergerat, 1987; Ziegler, 1992).

2. An extension phase occurred from the Late Eocene to the Early Oligocene marking the main rifting phase dominated by an E-W extension combined to reactivated NNE-SSW normal faults and reactivated sheared NE-SW and NW-SE faults (Villemin and Bergerat, 1987).
3. A NE-SW compression phase occurred at the Late Oligocene which reactivated the borders faults with dextral shear (Villemin and Bergerat, 1987).
4. The final NW-SE compression phase occurred at the Early Miocene and still active is influenced by the Pyrenean thrusting transforming the URG into a shear zone. This change of strain is accompanied by the uplift and the erosion the Vosges and Black Forest crystalline horsts linked to the Alpine thrusting (Illies and Greiner, 1979; Villemin and Bergerat, 1987). The URG is still influenced by this Alpine thrusting reactivating in shearing N-S and NE-SW inherited hercynian faults (Edel et al., 2007).

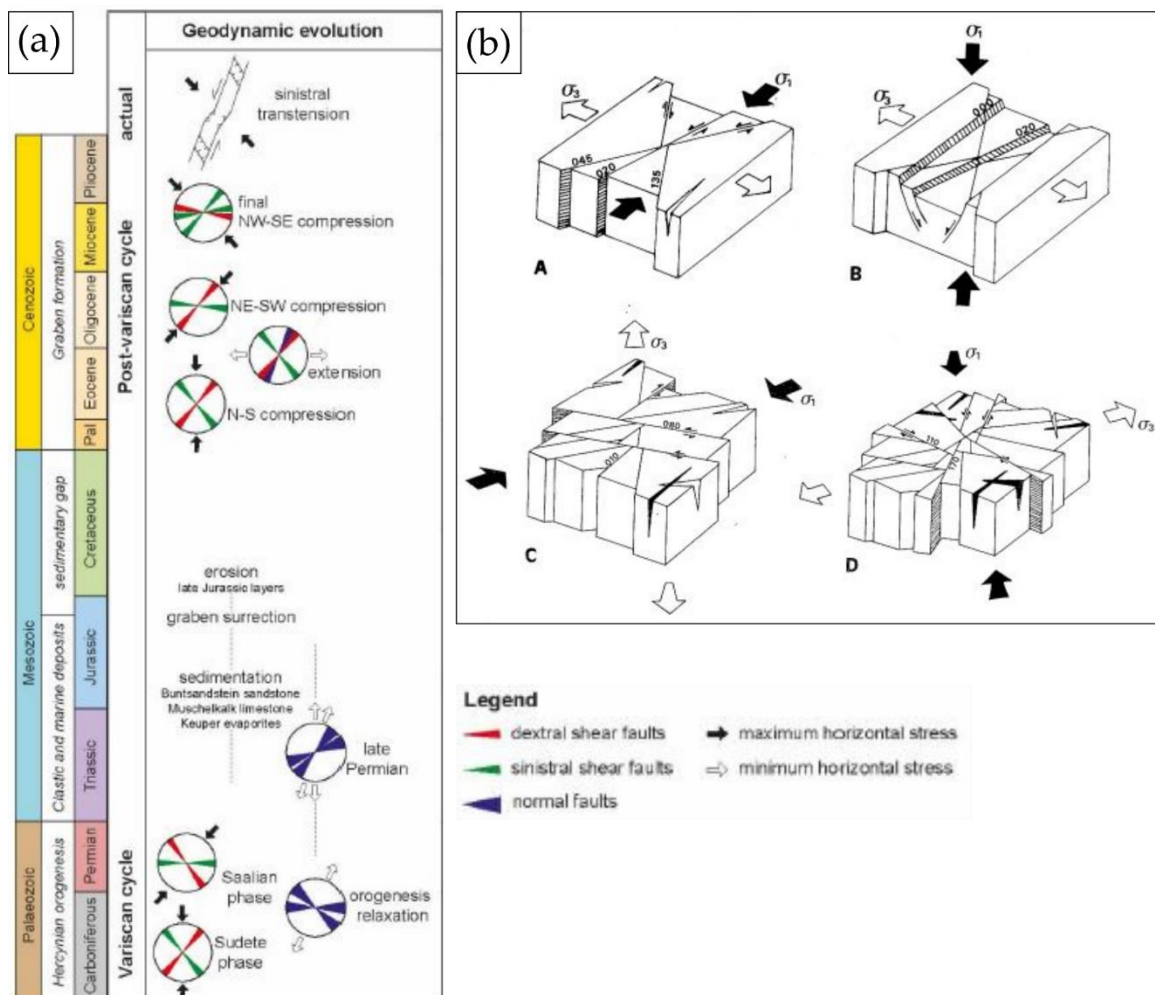


Figure 2-13. (a) Synthesis of the main brittle tectonic phases and associated fracture set since the Hercynian orogenesis to the URG formation from Glaas (2021). (b) Synthetic block diagrams showing the four tectonic phases that occurred during the Cenozoic rifting of the Rhine Graben from Villemin and Bergerat (1987). A–N-S compression phase (Eocene); B–E-W extensional phase (Oligocene); C–NE-SW compressional phase (Oligocene) and D–NW-SE compressional phase (Miocene)

The thinning of the lithosphere due to the ECRIS phase is well represented by thermal anomalies which are heterogeneously distributed along the URG (Baillieux et al., 2013). The local highest temperatures, higher than 150°C at 2000 m True Vertical Depth (TVD), are concentrated in the northern part of the URG (Figure 2-14). These temperature anomalies heat the fluid circulating through the fracture network, which can be extracted for electricity generation as at Soultz-sous-Forêts (Ledésert and Hébert, 2020).

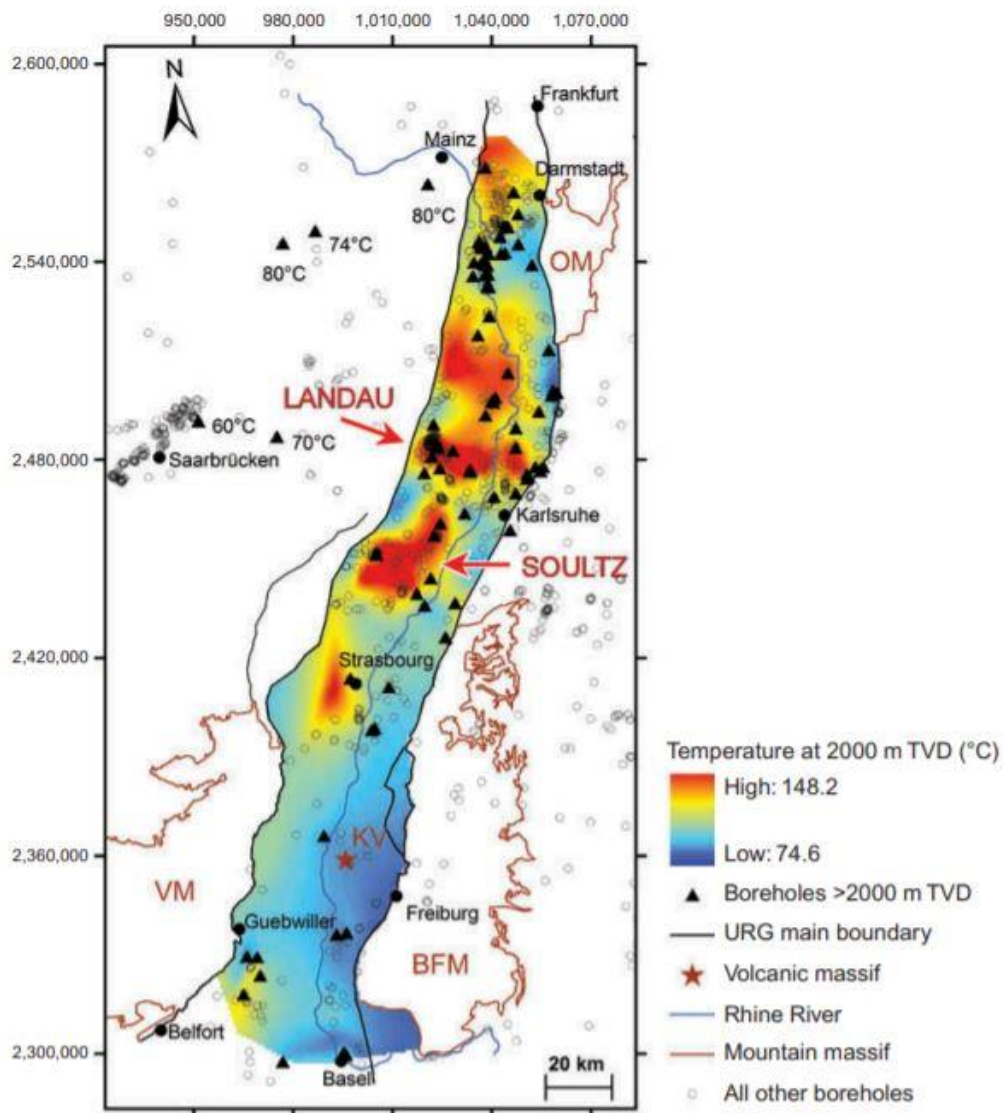


Figure 2-14. Temperature distribution at 2000 m TVD in the URG derived from 3D interpolation of 6531 temperature data from 1600 boreholes in the URG and adjacent areas, from Baillieux et al. (2013). The locations of the two main petroleum and geothermal areas at Pechelbronn/Soultz-sous-Forêts and Landau are indicated. Boreholes with a depth >2000 m TVD are indicated by triangles. VM, Vosges Mountains; BFM, Black Forest Mountains; OM, Odenwald Mountains; KV, Kaiserstuhl volcanic massif.

## II.2. The Soultz-sous-Forêts geothermal site

The Soultz-sous-Forêts (SsF) site is located in the northern part of the URG. Based on oil exploration, an intense thermal anomaly was known in the area (Haas and Hoffmann, 1929). At

the end of the industrial oil exploitation (1970) and after numerous geological data acquisition, preliminary studies of deep geothermal began. SsF has been chosen initially as the location for the European Hot Dry Rock (HDR) research project, which started in 1987 by the drilling of the first well, GPK1. The project continued by the deepening and the coring of the old oil well EPS1 in 1990/1991 in order to characterize the granitic reservoir, following by the deepening of the GPK1 well in 1992. This well became the first well of a doublet, the second one, GPK2 having been drilled in 1995. In 1999, the GPK2 well was deepened and two new wells were drilled (GPK3 and GPK4) in 2002 and 2004 respectively, creating a triplet of deviated wells. All the wells drilled in SsF penetrated the granitic basement with depth ranging from 3.6 to 5 km (Figure 2-15), where a hot brine circulates through a natural fracture network. In order to enhance the permeability of the rock mass needed for commercial energy production, thermal, hydraulic and chemical stimulations were performed, upgrading the SsF site to EGS technology known today. Since 2014, the SsF site was converted to an industrial project operated by the GEIE (Exploitation Minière de la Chaleur). A review paper from present state of knowledge at SsF is given by Ledésert and Hébert (2012).

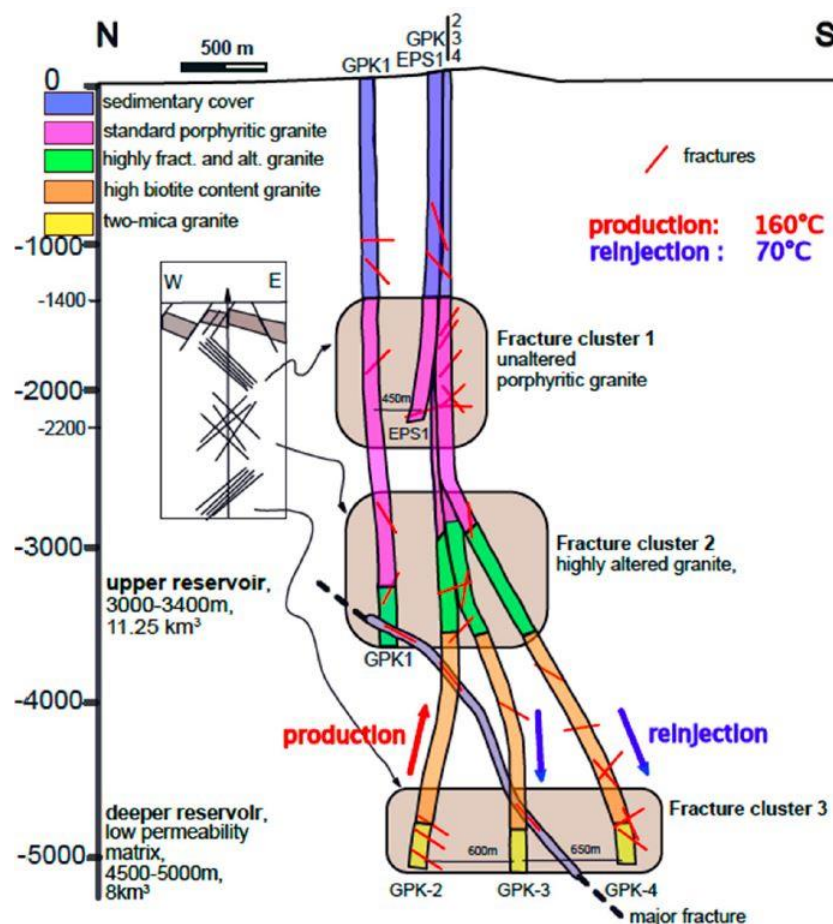


Figure 2-15. The Soultz-sous-Forêts EGS with the pilot plant from (Ledésert and Hébert, 2020). -1400 m: depth of the basement rock; -2200 m: bottom of EPS-1 borehole.

It has been shown that the thermal anomalies appear as hot zones along faults, oriented N30°E in the case of SsF mostly linked to convection phenomenon, but also to radiogenic production from the granitic basement (Baillieux et al., 2013). They are interpreted as vertical fluid circulation per ascensum of meteoric waters (Pribnow and Schellschmidt, 2000). Through the drilling, a temperature profile was realized: a thermal gradient of 110°C/km is visible the first kilometer of conductive type. It is followed by a lower thermal gradient of 5°C/km until 3.3 km at the interface granite-sediments presenting a convective regime. The profile ends at 5 km in the granite showing a thermal gradient of 30°C/km indicating again a conductive regime (Vidal, 2017).

Along the 5 km, three fracture clusters were identified, whose 60% of fractures belong to two sets striking N-S and dipping the west and to the east (Figure 2-15) (Dezayes et al., 2010a, 2010b):

1. Cluster 1 (1800-2000 m TVD) is located in the unaltered porphyritic granite. The main fracture set dips to the east. It was permeable prior to any stimulation operation.
2. Cluster 2 (3000-3400 m TVD) is located within the fractured and altered granite characterized by high pervasive alteration related to small-scale fractures, but also by at least one thick fracture with a significant hydrothermal alteration halo. A high proportion of clay and hydrothermal minerals are present in this facies. The two conjugate sets of fracture are equally represented deeping eastward and westward.
3. Cluster 3 (4500-5000 m TVD) is located in a deep massive granite characterized by a low pervasive alteration, which needed to be stimulated. The westward fracture set is dominant.

The normal N-S-striking faults are the most productive fractures at SsF as presented above due to their high permeability (Bächler et al., 2003).

Note that in its upper part (1420-1550 m), at the top of the massif, the granite is strongly weathered with numerous signs of clay mineral development and hematization. Deeper, two main types of hydrothermal alteration were seen: (1) an early stage of pervasive alteration and (2) subsequent stages of vein alteration (Genter and Traineau, 1995).



# CHAPTER 3

## State of the art

---

### I. DEFORMATION MECHANISMS

#### I.1. Introduction

**Deformation** refers to the transformation (changes in shape, position or orientation) of an object which is the result from the application of a differential stress (Van der Pluijm and Marshak, 2004; Bouchez and Nicolas, 2021). It consists of three components: (1) rotation, (2) translation and (3) distortion or strain. The strain path corresponds to the succession of tectonic events like extension, compression and strike-slip (Bouchez and Nicolas, 2021). Deformation can be continuous and homogeneous, continuous and heterogeneous or discontinuous with discontinuities that can be a grain-boundary, a joint or a fault. Moreover, depending on the scale, deformation may be different (i.e. continuous at the massif scale and discontinuous at the sample or thin section scale) (Bouchez and Nicolas, 2021).

In geology, the ability of stressed rocks to deform or to flow is described by the **rheology** of the rock by using fundamental parameters such as strain rate, elasticity, plasticity and viscosity (Van der Pluijm and Marshak, 2004).

- The ability of rocks to deform elastically resides in nonpermanent distortions of the crystal lattice, but the magnitude is relatively small. Once the stress applied is released, the atomic structure returns to its energetically most stable configuration (the lowest potential energy). Thus, **elastic behavior** is characterized by recoverable strain.
- The **plastic behavior** is a response to stress such that when the yield strength of the material is exceeded, it develops a strain without loss of continuity (i.e., without formation of fractures).
- The **viscous behavior** consists into the accumulation of strain as function of time (i.e. the strain rate). It is irreversible and thus produces a non-recoverable strain.

Natural deformation can be more generally divided into two types: brittle deformation and ductile deformation including a brittle-ductile transition (Figure 3-1).

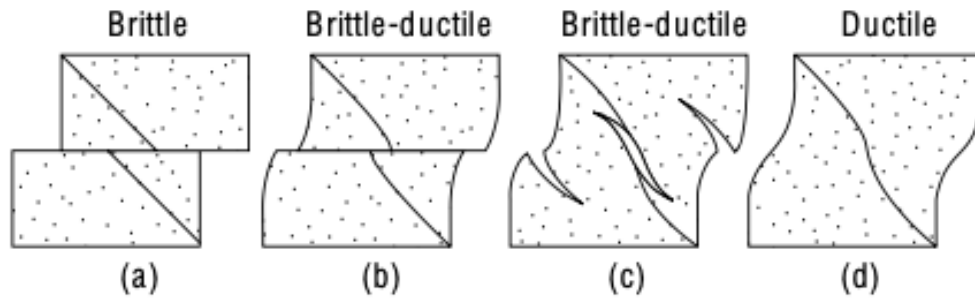


Figure 3-1. (a) Brittle to (b-c) brittle-ductile to (d) ductile deformation after Van der Pluijm and Marshak, (2004)

Deformation in rocks is achieved by a large number of processes depending on (1) factors such as mineralogy, grain size, lattice preferred orientation, porosity and permeability and (2) on external controls such as temperature, differential stress, lithostatic pressure, fluid pressure and external imposed strain rate.

## 1.2. Brittle deformation

Van der Pluijm and Marshak (2004) defined the **brittle behavior** as: “A response of a solid material to stress during which the rock loses continuity (cohesion). It occurs only when stresses exceed a critical value, and thus after the body has already undergone some elastic or/and plastic behavior. Brittle behavior generally does not occur at high temperatures.”. The **brittle deformation mechanisms** is the permanent change that occurs in a solid material due to fracture growth (joint formation and shear rupture formation) and/or frictional sliding (faulting). If those mechanisms occur at grain scale, the resulting deformation is called **cataclasis** (distributed fracturing, crushing, and frictional sliding of rocks or rock fragments) (Figure 3-2). According to Van der Pluijm and Marshak (2004), a **fracture** is any surface of discontinuity, leaning a surface across which the material is no longer bonded. If a fracture is filled with secondary minerals, it is a **vein**. A **joint**, also called cracks or tensile fractures, is a natural fracture in the rock showing no measurable shear displacement. In contrast, **shear fractures** are mesoscopic fractures presenting signs of displacement. In the case where the displacement is easily measurable, it is called a fault.

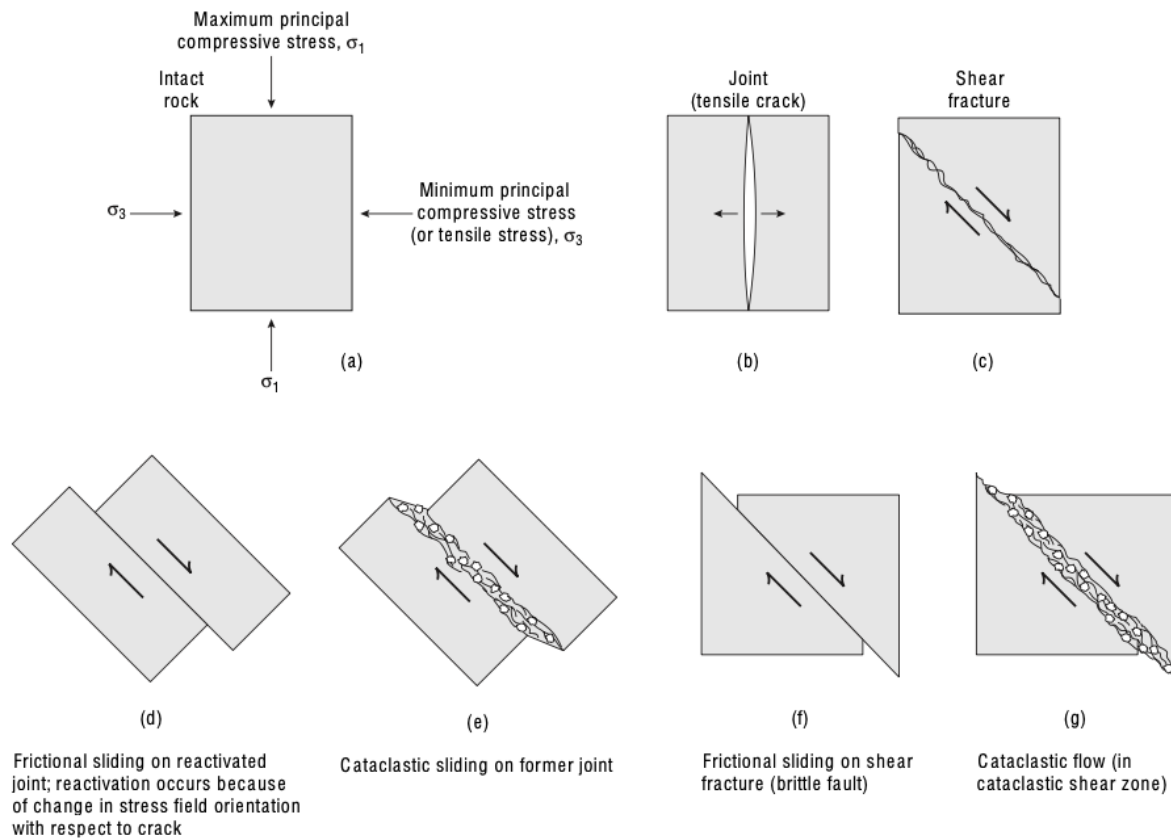


Figure 3-2. Types of brittle deformation. (a) Orientation of the remote principal stress directions on an intact rock body. (b) A tensile crack, forming parallel to  $\sigma_1$  and perpendicular to  $\sigma_3$ . (c) A shear fracture forming at an angle of about  $30^\circ$  to  $\sigma_1$ . (d) A tensile crack that has been reoriented with respect to the remote stresses and becomes a fault by undergoing frictional sliding. (e) A tensile crack which has been reactivated as a cataclastic shear zone. (f) A shear fracture that has evolved into a fault. (g) A shear fracture that has evolved into a cataclastic shear zone. Figure is from Van der Pluijm and Marshak (2004).

A **fault** is a fracture surface on which there has been sliding. Thus, a **fault zone** refers either to a band of finite width across which the displacement is partitioned among many smaller faults, or to the zone of rock bordering the fault that has fractured during faulting. A fault zone architecture is more complex than a simple plan and depends on different factors as the deformation mode (normal, inverse or shear fault), the rheology, the inherited fracture reactivation, etc. A fault zone is thus characterized by three distinct components (Figure 3-3):

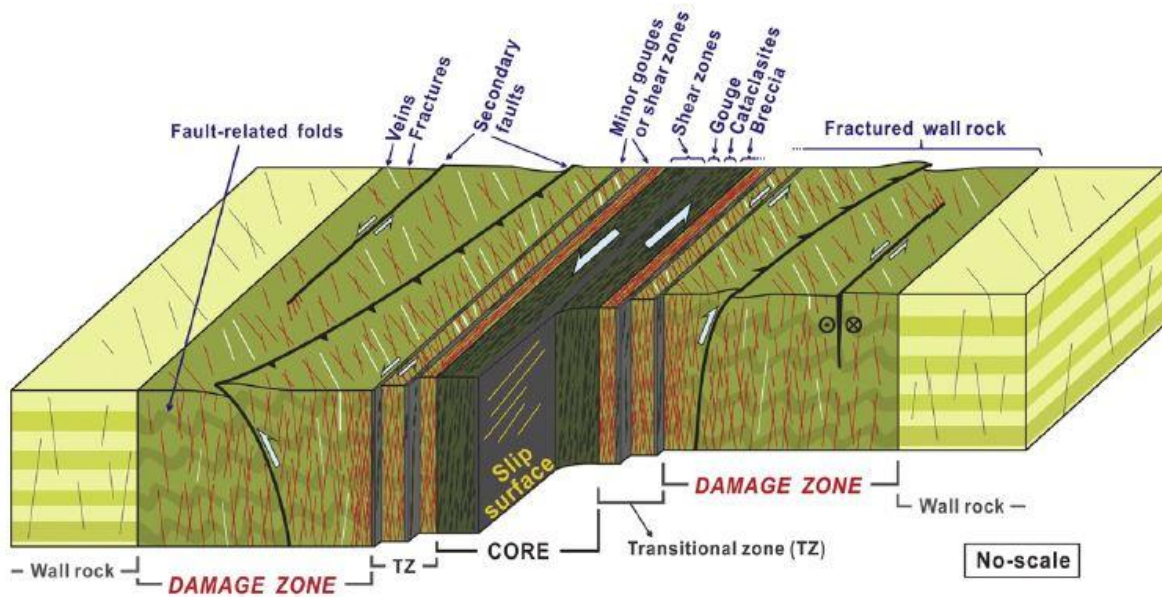


Figure 3-3. Conceptual block-diagram of a fault zone from Choi et al. (2016) showing the main components of a fault zone architecture and structural elements and features in each component

- a **fault core**, which is defined as the portion where most of the displacement is accommodated. It may include clay gouge, breccia, cataclasite, mylonite (Figure 3-4). The core may act as a conduit during deformation and as a barrier when it is filled by newly formed minerals following deformation (Caine et al., 2010, 1996; Evans et al., 1997; Faulkner et al., 2010)

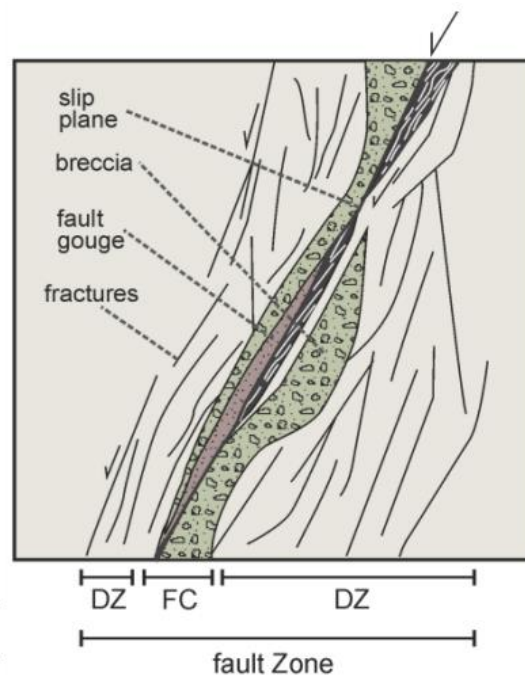


Figure 3-4. Architecture and structural elements of a fault zone in a crystalline rock with a fault core (FC) composed of breccia and fault gouge and damage zone (DZ) with increased fracture density (Caine et al., 1996). Figure from Bauer et al. (2015)

- a **damage zone**, which is composed of a distributed zone of enhanced subsidiary fracturing, faulting and veining surrounding the fault core, with a width proportional to the displacement (Caine et al., 2010, 1996; Choi et al., 2016; Faulkner et al., 2010; Wallace and Morris, 1986). The fracture networks have orientations mechanically related to the main fault (Caine and Forster, 1999). It can be a high permeability channel and become the main fluids pathway if the fault core is completely sealed by secondary minerals (Géraud et al., 2010).
- a relatively undeformed **protolith or wall rock** where fault related permeability structures are absent (Caine et al., 1996).

However, a fault core can occur as a relative narrow and localized slip zone containing high strain product as presented above (Figure 3-5a), or as a wider zone containing multiple strands of fault cores (Figure 3-5b) (Mitchell and Faulkner, 2009).

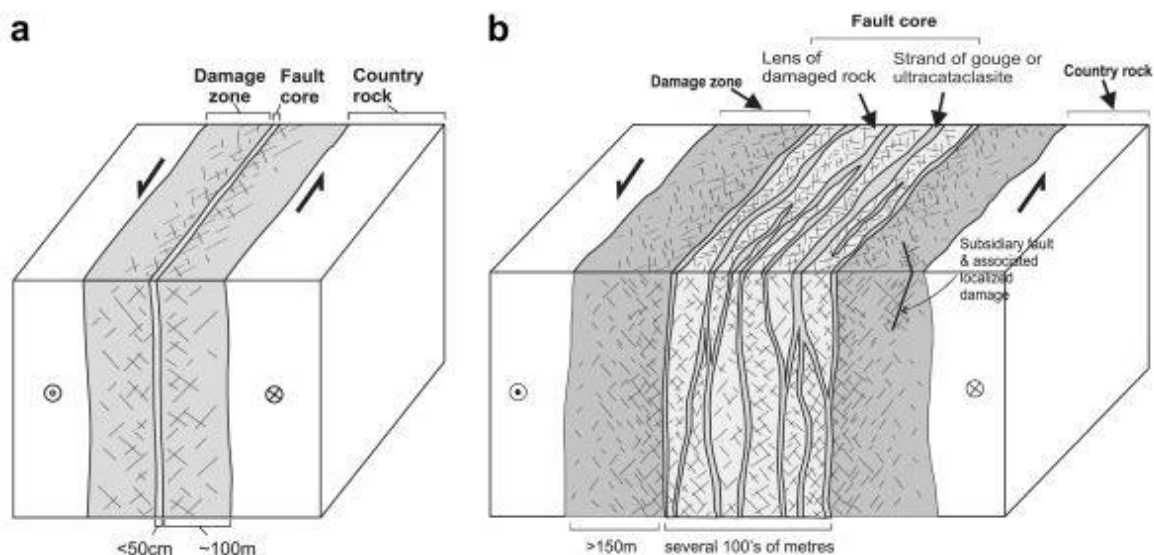


Figure 3-5. Schemes of typical strike-slip structures showing (a) a single fault core and (b) a multiple fault core, with associated damage zone from Mitchell and Faulkner (2009)

The notion of scaling when defining a fault zone has to be considered. A fault zone, as described above, contains in its damage zone several fault zones of low order having their own fault core and their own damage zone (Figure 3-6) (Le Garzic et al., 2011). They will have their own morphology not necessarily representative of the higher order fault zone. Thus, the synthetic schemes of fracture zones presented in this manuscript will have no scale, because they can represent fracture zones at several order of magnitude.

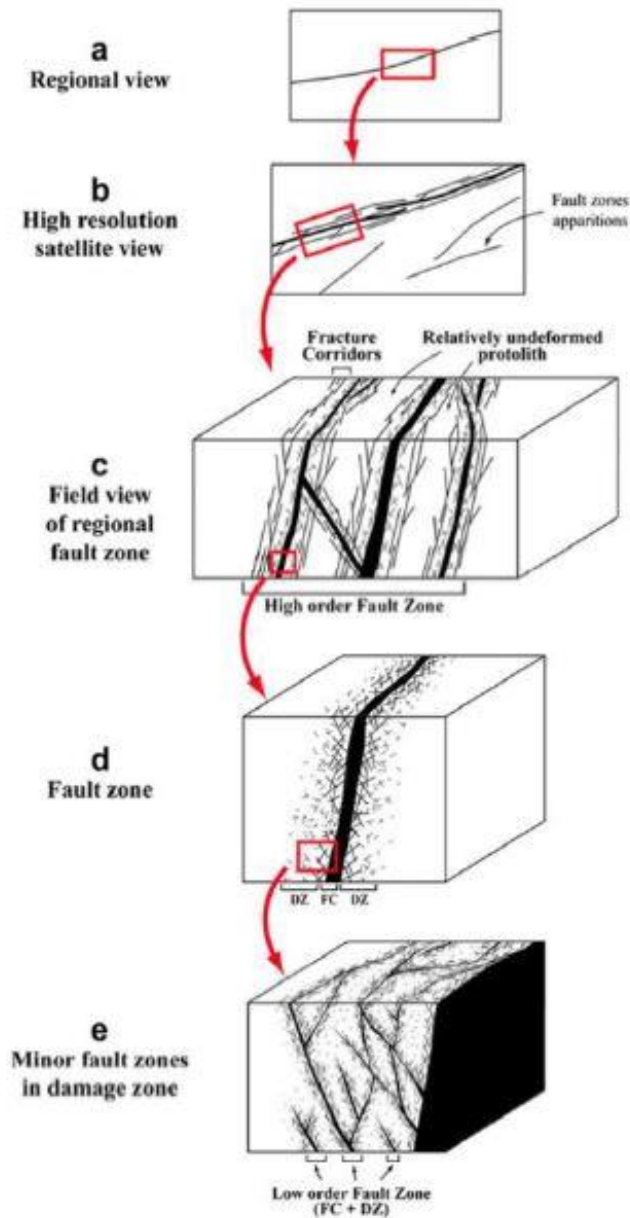


Figure 3-6. Schemes of the multiscale aspect of a fault zone from Le Garzic et al. (2011)

A **shear zone** is a high-strain zone in which deformation contains a rotation component that reflect the lateral displacement of all rock segments (Passchier and Trouw, 2005). It is characterized by a band of finite width in which the ductile shear strain is significantly greater than in the surrounding rock (Van der Pluijm and Marshak, 2004). A shear zone can be subdivided into two zones: (1) brittle zones or faults and (2) ductile zones. Most of the shear zones have both brittle and ductile segments (Passchier and Trouw, 2005).

Sliding on faults and fracturing of wall rock forms a volume of brittle fault rock along a fault plane (Passchier and Trouw, 2005). A **fault rock** is a rock that consists of fragments produced by the crushing and grinding which can be cohesive or noncohesive and accompanies a

dislocation. It is often found along the fault plane. The major fault rocks and their associated processes are defined below (Bouchez and Nicolas, 2018; Van der Pluijm and Marshak, 2004):

- A tectonic **breccia** is considered as a cohesive or noncohesive fault rock with fragments that make up >30% of the rock mass in a fine grain matrix. In the case of a cohesive breccia is that the nature of the rock is due to dissolution-precipitation-crystallization of minerals.
- A **cataclasite** is a cohesive or noncohesive fault rock generally with fragments that make up <30% of the rock mass in a fine grain matrix. It commonly shows evidences of abundant pressure solution and precipitation effects.
- A **fault gouge** is a fault rock consists into a rock composed of material whose grain size has been mechanically reduced. Few large fragments of the rock occur isolated in the matrix. Grains are less than about 1 mm in diameter. Shearing of gouge along a fault surface during progressive movement may create foliation within the gouge and fragments can have a lensoid shape. Clay formed by alteration of silicate minerals in fault zones may be difficult to distinguish from true gouge.

Minerals such as feldspar can be separated into aggregates of fragments by fracturing along crystallographic directions with a geometry similar to asymmetric boudins, separated by seams cataclasite. Domino and mosaic fragmented porphyroclasts are more common (Figure 3-7). They allow to determine the shear sense from their displacement (Passchier and Trouw, 2005; Van der Pluijm and Marshak, 2004).

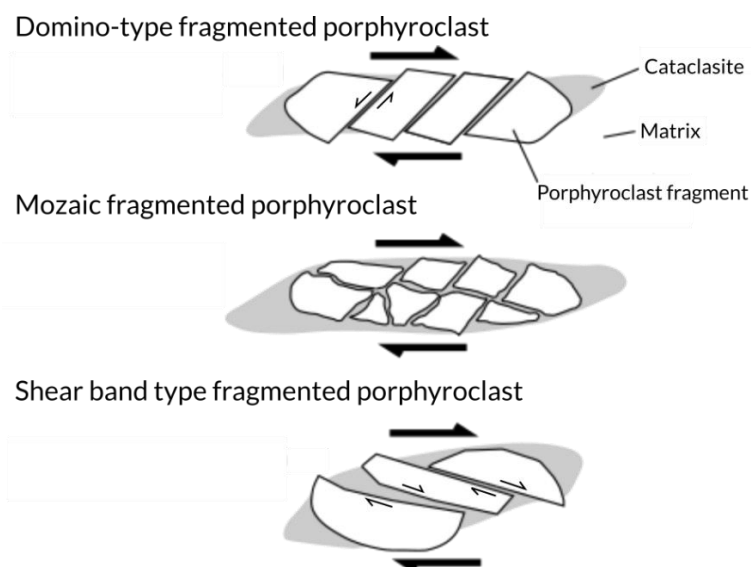


Figure 3-7. Schemes showing different types of commonly fragmented porphyroclasts after Passchier and Trouw (2005).

In a granitic body, the rocks on either side of a shear zone are indistinguishable. That is why shear-sense indicators are prevalent.

The ability of a fault to propagate is influenced by many processes such as the regional stress field, the geometry of the rock units, fluid pressure and the interaction of the brittle fault rock with fluids (Passchier and Trouw, 2005). The mechanical behavior of a fault is strongly influenced by the infiltrated fluids. Fluid may cause (1) the weakening of the fault by reaction of strong phases to weaker minerals in fault rocks (e.g. clay forms in fault zones due to alteration of feldspar by the fluid) or (2) fault rock strengthening by vein precipitation cementing fault rock fragments together.

When the temperature increases, the elastic portion of strain decreases, while the ductility increases. This is most noticeable at elevated confining pressures. Likewise, the yield strength (i.e. maximum stress supported by a rock until it flows) decreases with increasing temperature. Thus, the behavior of various rock types and minerals reacts differently under conditions of increasing temperature and confining pressure (Figure 3-8) (Van der Pluijm and Marshak, 2004).

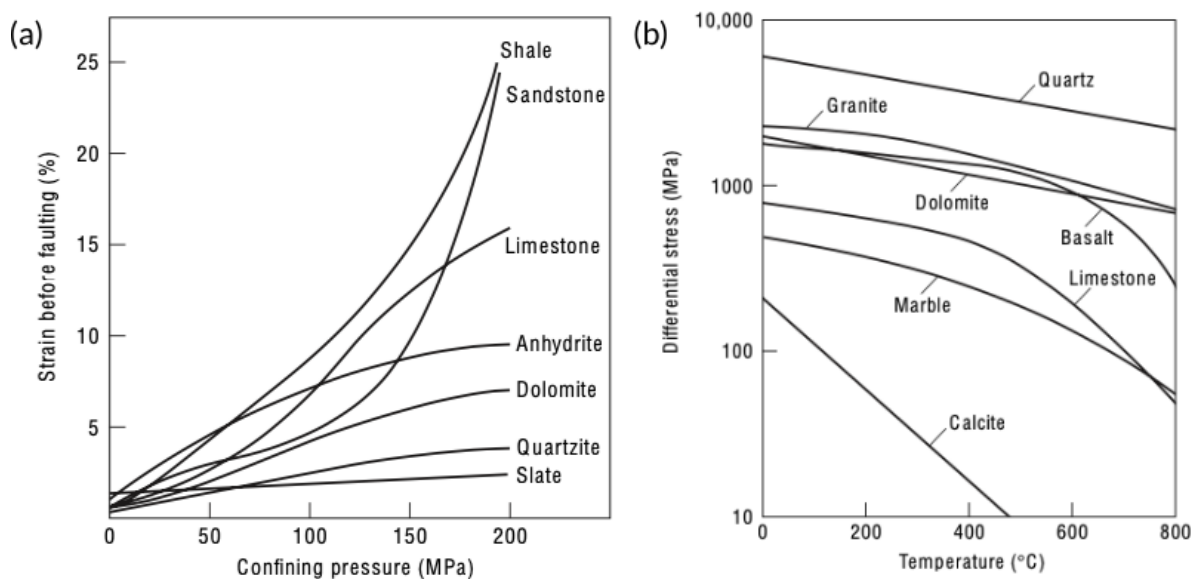


Figure 3-8. (a) The effect of changing the confining pressure on various rock types. (b) The effect of changing temperature on the compressive strength of some rocks and minerals after Van der Pluijm and Marshak (2004).

### 1.3. Ductile deformation

Van der Pluijm and Marshak (2004) defined the **ductile behavior** as the ability of a rock to accumulate significant permanent strain with deformation distributed on the mesoscopic scale. The distortions that occur must be a result of permanent changes. Ductile behavior is

distinguished from the brittle behavior by the fact that the strain is distributed over the body rather than localized. However, the scale of observation needs to be considered. Strain that appears homogeneous on one scale can represent heterogeneity on another. Down to the mesoscopic scale (hand specimen), the ductile behavior can be considered as uniform flow. Three fundamental mechanisms producing ductile behavior in rocks and minerals can be distinguished (Van der Pluijm and Marshak, 2004):

- **Cataclastic flow:** It is distributed fracturing, crushing, and frictional sliding of grains of rock or rock fragments. Thus, it is mesoscopic ductile behavior, yet the process by which it occurs is microscopic brittle fracturing and frictional sliding. It is typically found in fault zones.
- **Crystal plasticity:** Ductile behavior can be achieved by the motion of crystal defects (point defects, line defects or dislocations and planar defects). Crystal plasticity corresponds to the associated distortion of solid phases. Dislocations through the crystal lattice may occur by glide, glide and climb combination (creep) or twinning and if the activation energy for movement is achieved.
- **Diffusional mass transfer:** It is a flow of rocks that occurs by the transfer of material. It exists three diffusion-related deformation mechanisms (1) pressure solution, (2) grain-boundary diffusion (Coble creep) and (3) volume diffusion (Nabarro-Herring creep). Volume and grain-boundary diffusions correspond respectively to the vacancies diffusion (permanent shape change) through the entire body or at its grain boundary along a narrow region. Pressure solution process is similar to grain-boundary diffusion, but evolves at lower temperatures on grain boundaries the presence of a fluid film.

Shear zones can also be ductile and are this time characterized as a tabular band in which the strain is considerably higher compared to the surrounding rock. This strain is thus accumulated by ductile processes from cataclasis, to crystal-plasticity, to diffusion and no throughgoing fracture is formed (Van der Pluijm and Marshak, 2004). A mylonite is a foliated and usually lineated rock dominated by the crystal-plastic processes producing another characteristic of deformed rocks, a texture or crystallographic-preferred fabrics (Van der Pluijm and Marshak, 2004; Passchier and Trouw, 2005). Conditions of mylonitization are reached at various temperature, stress and strain rate depending on the minerals in the rock (Van der Pluijm and Marshak, 2004).

Mylonites usually contain large grains surrounded by a finer matrix. These grains may have tails of materials that differ from the matrix, such that are distinguishable and allow to identify the sense of shear (Van der Pluijm and Marshak, 2004). Two types of grain-tail complexes are

recognizable (1)  $\sigma$ -type and (2)  $\delta$ -type (Figure 3-9). Phyllosilicate grains, such as mica, can show a stair-stepping geometry in the direction of the shear and look like scales on a fish, thus called mica-fish (Figure 3-9). Mylonites show at least one major foliation at low-angle to the shear zone boundary known as the S-foliation (S from French word “schistosité”) (Figure 3-9). At some point, it may be hard to distinguish this foliation from a foliation parallel to the shear zone known as the C-foliation (C from French word “cisaillement”) (Figure 3-9). A third foliation oblique to the shear boundary can be identified as discrete shear displacement and known as the C'-foliation or shear band (Figure 3-9). These foliations reflect discrete shear surfaces or grain-shape fabrics distinguishable at different scales from thin section up to outcrop scale (Van der Pluijm and Marshak, 2004).

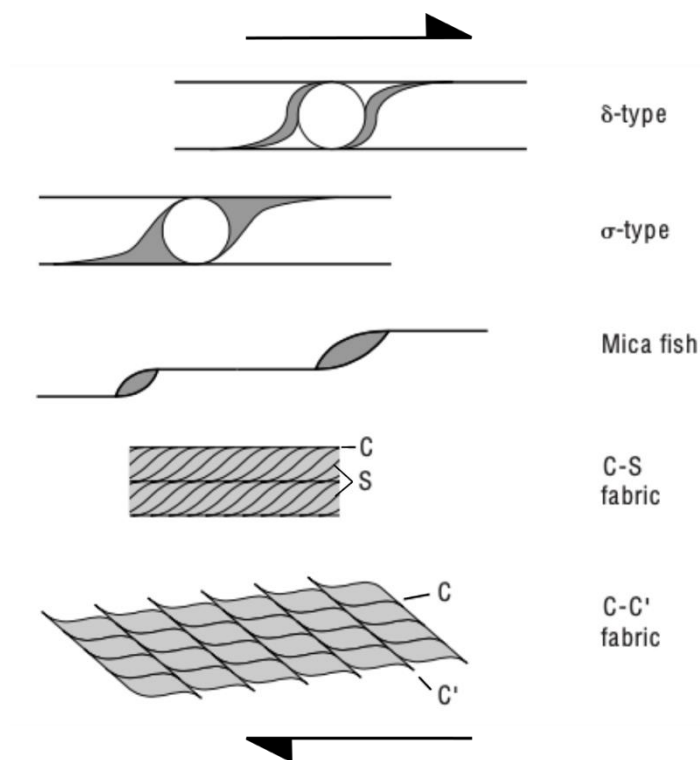


Figure 3-9. Schemes of shear-sense indicators in a dextral ductile shear zone from Van der Pluijm and Marshak (2004) distinguishable from thin section to outcrop scale.

Microstructures at the grain scale in deformed rocks result from three different mechanisms after Van der Pluijm and Marshak (2004): recovery, recrystallization and superplastic creep.

- The process of **recovery** consists into a way to change the internal strain energy of a grain by (1) an irregular distribution of dislocations distorting the crystal lattice (e.g. undulose extinction) (Figure 3-10a) or (2) a rearrangement of these dislocations to form a dislocation wall or tilt boundary by glide and climb separating subgrains (low-angle grain boundaries) (Figure 3-10b).

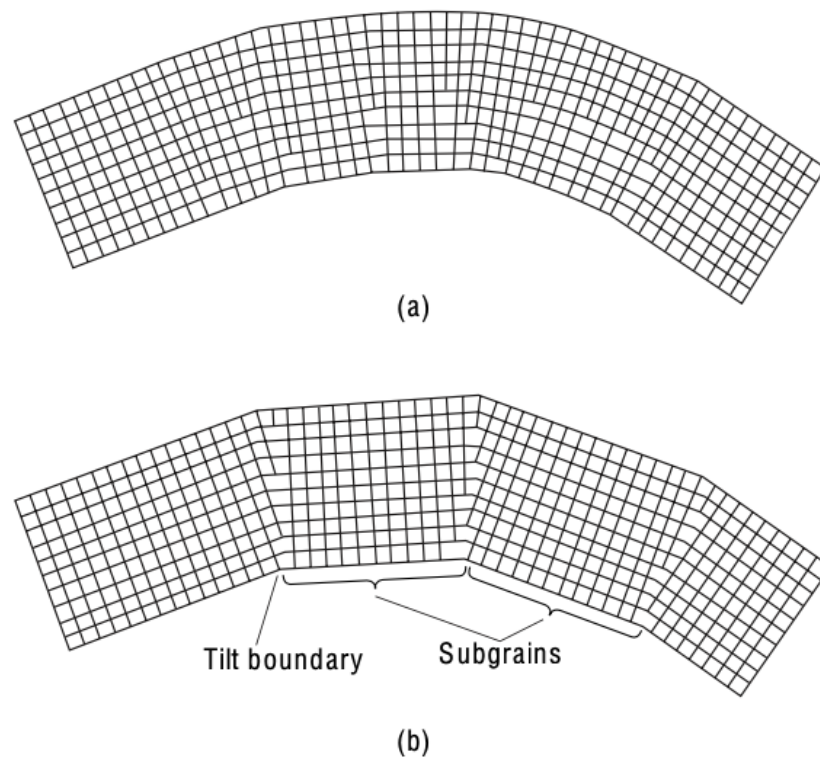


Figure 3-10. (a) Irregularly distributed dislocations. (b) Rearranged dislocations by glide and climb to form a tilt boundary (or dislocation wall) that separates subgrains. Figure from Van der Pluijm and Marshak (2004).

- **Recrystallization** is the process that removes the internal strain energy remaining in grains after recovery and forms high-angle grain boundaries which separate strain-free grains from each other. These new grains present no undulatory extinction and straight borders. Within an anisotropic stress field, recrystallization is called dynamic recrystallization (bulging, subgrain rotation and grain boundary migration (Stipp and Kunze, 2008)). Within an isotropic stress field, it is called static recrystallization or annealing.
- **Superplastic creep** is a deformation mechanism that changes the grains shape allowing them to slide past one another without friction. In other words, it is the ability of a rock to accumulate a high amount of strain without mesoscopic breaking.

## II. FLUID-ROCK INTERACTIONS IN GRANITIC ROCKS AND FRACTURE ZONE PROPERTIES

Mineralogical, geochemical and textural changes are caused by penetration of a hydrothermal fluid along fractures and its interaction with the host rock. These phenomena are also called hydrothermal alteration processes (Nishimoto and Yoshida, 2010; Fulignati, 2020). Primary mineral phases constituting the host rock are chemically attacked by the fluid. In the case of a granitic rock usually composed of quartz (Qtz), plagioclase (Pl), K-feldspar (Kfs, in this study we

consider this abbreviation for perthitic orthoclase) and biotite (Bt), all of these minerals can be altered but very rarely quartz. In order to re-equilibrate with the system, new mineralogical assemblages are generated as hydrous minerals, with clay minerals being prevalent like smectite, kaolinite, illite, chlorite, mixed-layers (chlorite/smectite also called corrensite, illite/smectite and biotite/vermiculite) etc... (Fulignati, 2020). The new minerals form in response to pressure, temperature and composition of the altering fluids (Creasey, 1966). The dissolution of primary rock-forming minerals and the secondary minerals precipitation change the in situ conditions with respect to the rock mechanical strength (Meller and Kohl, 2014).

Hydrothermal alterations are important to the EGS because (1) the mineralogy, the porosity and the permeability of the rock are modified, (2) indications about the nature and the temperature of the fluid flowing in the rock are provided and (3) an idea about the spatial and temporal scale of fluid circulation is given (Ledésert et al., 2010).

According to different authors, different types of alteration processes of alteration facies are described representing different mineral assemblages giving different nomenclatures for hydrothermal alteration types (e.g. Burnham, 1962; Creasey, 1966; Nishimoto and Yoshida, 2010). A general acceptance was made for the terms propylitic and argillic alterations even if some authors prefer to use mineral assemblages.

The propylitic type of alteration is distinguished by the prominence of lime-bearing minerals, such as calcite and epidote and of corrensite (Creasey, 1966; Velde 1977). This alteration is characterized as a pervasive alteration by interstitial fluids trapped into the grain boundaries affecting an important volume of rock during the cooling of the pluton (Genter, 1989). The transformation of some of the primary minerals (plagioclase and biotite) is often partial or selective.

The argillic alteration is distinguished by the prominence of clay minerals like illite, kaolinite and illite/smectite mixed-layer in conjunction with leaching of CaO (Creasey, 1966; Que and Allen, 1996; Ledésert et al., 1999; Środoń, 1999). This alteration is characterized by (1) an important leaching and transformation of the primary minerals (plagioclase, biotite and sometimes K-feldspar) localized on both sides of fractures related to the interaction of fluids, that circulate through the fracture network, with the surrounding rock and (2) fracture fillings of different natures (Genter, 1989; Nishimoto and Yoshida, 2010). The argillic alteration is thus also called vein alteration.

Crystalline rocks are known for their low matrix porosity and permeability. Thus, natural permeability is mainly controlled by the fracture network at different scales where fluid

circulates (Evans et al., 2005). Fracture and fault development is an important factor in terms of fluid circulation and thus of hydrothermal alteration. Higher is the fracture density, higher is the alteration amount (Nishimoto and Yoshida, 2010). The complexity and the difference of physical properties of a fault zone could explain chemical and petrophysical processes during fluid-rock interactions (Choi et al., 2016; Faulkner et al., 2010). The fault core and damage zone of a fault zone control the fluid flow near and within a fault zone. More precisely, as defined by Caine et al. (1996), the fault core is the seat of secondary minerals precipitation where most of the displacement occurs. With distance of the fault core, a strong decrease of the fracture density is observed (Mitchell and Faulkner, 2012) (Figure 3-11). Moreover, the damage zone composing of hundreds of fractures appears highly altered and more porous (Caine, 1996; Genter et al., 2000) (Figure 3-11).

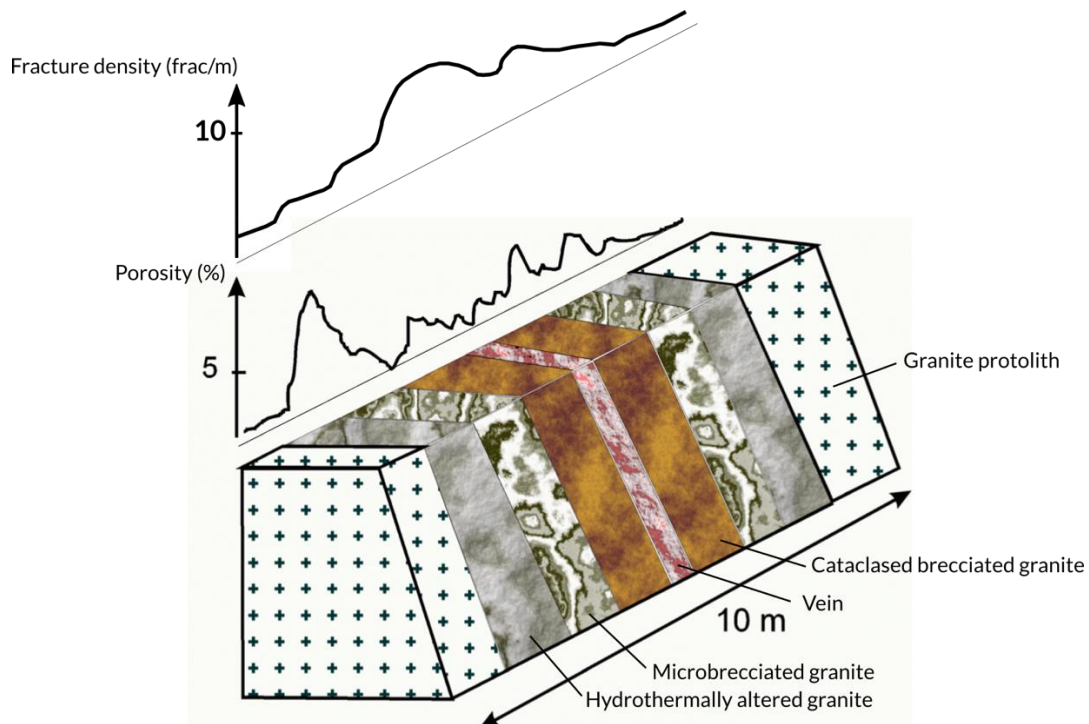


Figure 3-11. Fracture density and porosity profiles in a conceptual lithofacies granite zonation of hydrothermally altered and fractured granite modified from Genter et al. (2000) and Glaas (2021).

Géraud et al. (2010) described the physical properties across a fault zone as an increase of permeability within the damage zone, from the protolith to the fault core due to fracturing and the dissolution of the primary minerals (secondary porosity). However, toward the fault core, the permeability is reduced due to secondary mineral precipitation sealing the fracture. Thus, the damage zone would show the highest permeability. In the case of an occasional free space between both surfaces of the fault plane, the fault core could represent a high fluid flow conduit.

A fault zone may act as conduits, barriers or combined conduit-barrier systems enhancing or impeding fluid flow (Figure 3-12) (Caine et al., 1996; Seebeck et al., 2014).

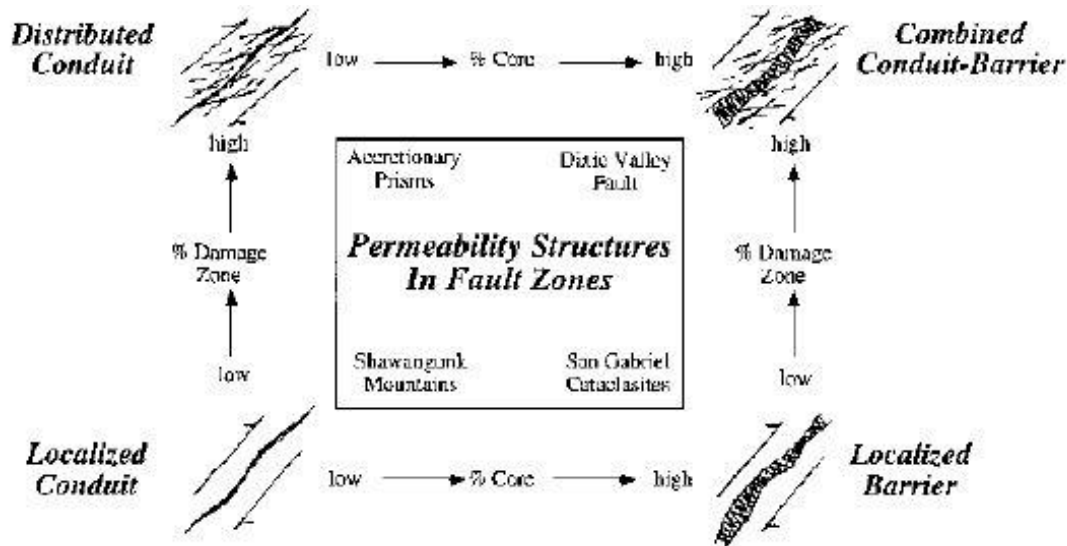


Figure 3-12. Conceptual scheme for fault-related fluid flow from Caine et al. (1996).

The grain size reduction in a fault core in the case of a unique protolith as presented by Caine et al. (1996) leads to the decrease of porosity and permeability providing an across-fault barrier to flow (Faulkner et al., 2010; Goddard and Evans, 1995; Song et al., 2017). This permeability decrease depends mainly on the amount of clay composing the fault core. The presence of clay also leads to an increase of the permeability anisotropy according to the fault plan direction (Bertrand, 2017). Fault zones rich in phyllosilicate material as illite tend to have lower permeabilities than quartz and/or framework silicate-rich gouges (Faulkner et al., 2010). The fractured damage zone is visualized as an along/up-fault conduit, control the fluid circulation depending on its thickness and its fracture density (Choi et al., 2016; Faulkner et al., 2010). Moreover, the fracture network visible in a whole massif allowed to estimate the extent of the fracture connection that allowed fluid to flow. Meller and Kohl (2014) also showed that hydrothermal alteration lowers the mechanical strength of the SsF granite and its fractures and thus can change the local stress regime.

Géraud et al. (2005) observed a clear correlation between the alteration type and the porosity with low porosity value corresponding to the propylitic alteration and high porosity value for the argillic alteration. However, they also observed that the permeability of very porous samples can be very low. Permeability and porosity are not always correlated.

Clay minerals type, structure and preferred orientation can play an important role on fault behaviors in terms of frictional (depending on their structure and water content) and hydrological properties, permeability and porosity evolution, but also in terms of slip rate of the fault (Buatier et al., 2012; Meller and Kohl, 2014). A reduction of frictional strength was observed by Crawford et al. (2008) with an increase of the clay fraction. As well as, low friction coefficients were obtained on fault gouges rich in phyllosilicates which are aligned (Ikari et al., 2009; Buatier et al., 2012). Clay minerals may contribute to a fault slip weakening behavior (Buatier et al., 2012).

The link between deformation and fluid-rock interactions is of primary importance in order to better understand a geothermal reservoir and it is the main goal of this work.



# CHAPTER 4

## Fluid-Rock Interactions in a Paleo-Geothermal Reservoir (Noble Hills Granite, California, USA).

### Part 1: Granite Pervasive Alteration Processes away from Fracture Zones

---

This chapter is a published contribution to the *Geosciences Journal*, in the 2021 special issue “Enhanced Geothermal Systems and other Deep Geothermal Applications throughout Europe: The MEET Project”.

The published version is available at the following link:  
<https://doi.org/10.3390/geosciences11080325>

**Keywords:** Noble Hills granite; Owlshead Mountains granite; metamorphic grade; fluid/rock interactions; newly formed minerals; element variations; geothermal reservoir

# Fluid-Rock Interactions in a Paleo-Geothermal Reservoir (Noble Hills Granite, California, USA). Part 1: Granite Pervasive Alteration Processes away from Fracture Zones

Johanne Klee <sup>1,\*</sup>, Sébastien Potel <sup>1</sup>, Béatrice A. Ledésert <sup>2</sup>, Ronan L. Hébert <sup>2</sup>, Arezki Chabani <sup>1</sup>, Pascal Barrier <sup>1</sup> and Ghislain Trullenque <sup>1</sup>

<sup>1</sup>B2R, Geosciences Department, Institut Polytechnique UniLaSalle Beauvais, 19 Rue Pierre Waguët, F-60026 Beauvais, France; sebastien.potel@unilasalle.fr (S.P.); arezki.chabani@unilasalle.fr (A.C.); pascal.barrier@unilasalle.fr (P.B.); ghislain.trullenque@unilasalle.fr (G.T.)

<sup>2</sup>Geosciences and Environment Cergy, CY Cergy Paris Université, 1 Rue Descartes, F-95000 Neuville-sur-Oise, France; beatrice.ledesert@cyu.fr (B.A.L.); ronan.hebert@cyu.fr (R.L.H.)

## I. ABSTRACT

Only few data from geothermal exploited reservoirs are available due to the restricted accessibility by drilling, which limits the understanding of the entire reservoir. Thus, analogue investigations are needed and were performed in the framework of the H2020 MEET project. The Noble Hills range, located along the southern branch of the Death Valley pull-apart (CA, USA), has been selected as a possible granitic paleo-reservoir. The aim is to characterize the pervasive alteration processes affecting this granite, away from the influence of the faults, in terms of mineralogical, petrophysical and chemical changes. Various methods were used as petrographic, geochemical and petrophysical analyses. Mineral changes, clay mineralogy, bulk rock chemical composition, calcite content and porosity were determined on different granite samples, collected in the Noble Hills granite, far from the faults and in the Owlshead Mountains, north of the Noble Hills, considered as its protolith. In order to complete the granite characterization, the metamorphic grade has been studied through the Noble Hills granite body. This complete characterization has allowed distinguishing the occurrence of three stages of alteration: (1) a pervasive propylitic alteration characterized by calcite-corrensite-epidote-K-white mica assemblage, (2) a more local one, only present in the Noble Hills granite, producing illite, kaolinite, illite/smectite, calcite and oxides, characteristic of the argillic alteration, which overprints the propylitic alteration and (3) weathering evidenced by the presence of montmorillonite in the Owlshead Mountains, which is considered as negligible in both granites. Alteration was also outlined by the correlation of the loss on ignition, representing the hydration rate, to porosity, calcite content and chemical composition. Moreover, the Kübler Index calculated from illite crystals allowed to identify a NW-SE temperature gradient in the Noble Hills.

## II. INTRODUCTION

Geothermal systems occur in different geological settings such as active volcanic fields, plutonic provinces, extensional domains, intracratonic basins and orogenic belts, i.e., anywhere with heat and fluids that are able to flow through the rocks (Williams et al., 2011). The exploitation of geothermal energy is expanding worldwide due to the abundant resources and the progress of the technology that lead to Enhanced Geothermal Systems (EGS). EGS (1) defines a reservoir where the natural permeability of the rocks needs to be enhanced through stimulations in order to obtain a sufficient temperature/flow rate ratio (Moeck, 2014) and (2) aims at transforming efficiently the geothermal resource into heat and electricity for human consumption (Olasolo et al., 2016).

The present study is part of the MEET H2020 project (Multidisciplinary and multi-context demonstration of EGS exploration and Exploitation Techniques and potentials) (Trullenque et al., 2018). One aim of this project is to provide a characterization method of a geothermal granitic reservoir in a geological extensive context, such as the Great Basin region (USA), where normal fault zones also act as the most favorable structural setting for geothermal fluid flow (Faulds et al., 2013). In the Great Basin, other notable structural settings control fluid flow such as the intersection between normal faults and other structures like strike-slip faults (~22%), as well as pull-apart structures (4%) (Faulds et al., 2013). The fluid-rock interaction along and inside fracture zones results in hydrothermal alterations. They lead to geochemical, mineralogical and petrophysical (porosity and permeability) modifications of the rocks (Nishimoto and Yoshida, 2010). In granitic rocks, fluid circulations usually occur through the fracture network at different scales (Dezayes and Lerouge, 2019a; Nishimoto and Yoshida, 2010) involving a pervasive alteration which may influence up to cubic kilometers of rock (Plumper and Putnis, 2009). Thus, an intense fluid/rock interaction (Inoue, 1995) can significantly change the mineralogy, the chemistry and the texture of the bulk-rock (Dezayes and Lerouge, 2019a) among which the common formation of clay minerals, including illite. Exploited geothermal reservoirs are located at depth, and the only and limited available data come from drillings (cores, cuttings) and seismic surveys. Studying exhumed geothermal reservoirs allows better understanding of the 3D features of the reservoir. To do so, the Noble Hills range (NH, Death Valley, CA, USA) has been selected as a possible granitic geothermal reservoir in a trans-tensional context. The NH are located in the southwestern part of the Great Basin region along the Southern Death Valley Fault Zone (SDVFZ), which constitutes the southern branch of the Death Valley pull-apart (Burchfiel and Stewart, 1966). They extend over an area of 7 km long and 2 km wide and contain a part of the Cretaceous granitic pluton (~95 Ma) forming the Owshead Mountains (OM) (Pavlis

and Trullenque, 2021). The arid climate prevents from a thick vegetal cover and the deep canyons that crosscut the range allow a thorough 3D investigation in order to characterize the evolution of the granite at the kilometer scale.

This paper aims at characterizing the pervasive alteration processes affecting the NH granite. This massif is considered as a possible paleo-geothermal reservoir. The study is based on the analysis of (1) rock mineralogical and related petrophysical properties changes and (2) associated chemical transfers between host rock and percolating fluids. All samples have been collected away from fractures described by Chabani et al. (2021) in order to avoid the influence of strain and massive fluid flow. This sampling strategy ascertains the preservation of the protolith initial magmatic texture and mineralogy. A second paper (Klee et al., 2021b) focuses on the role of deformation on hydrothermal alteration close to fractures. Data collected from the NH granite samples are directly compared to those obtained for the granite samples collected in the OM pluton, which is considered as the protolith. Analyses performed on targeted areas include macroscopic and microscopic petrographic studies, mineralogical characterization by X-ray diffraction (XRD) on whole rock and clay minerals, bulk rock chemical characterization by Inductively Coupled Plasma (ICP)–Mass Spectrometry (MS) and–Atomic Emission Spectrometry (AES), Scanning Electron Microscopy coupled with Energy Dispersive Spectrometry (SEM-EDS) for structural observation and local chemical analyses, as well as calcimetry and porosimetry analyses. To help at the granite characterization, the metamorphic evolution can be estimated through the Kübler Index (KI). Indeed, the temperature range of illite formation can be estimated thanks to the KI (Árkai et al., 2003a; Kisch, 1987) based on illite “crystallinity” (IC). Temperature is thought to be the main factor controlling the IC evolution, but the lithology also has important effects (Árkai et al., 2002; Ferreiro Mählmann et al., 2012; Frey, 1987; Mullis et al., 2017). Working at constant lithology, here granitic rock, allows us to avoid this effect. During the NH range formation, minerals could be transformed similarly as diagenetic reactions observed in feldspathic sandstones (Ledésert et al., 1999). Inoue (1995) has also shown that the rock alteration resulting from hot fluid storage during a long geological period, heated in-situ and in equilibrium with the surrounding rock is usually considered as diagenesis or metamorphism. Therefore, the terms defined by Kisch (1987) for each diagenetic and metamorphic zones are considered in this study as eligible for granitic context.

### III. GEOLOGICAL SETTING

#### III.1. Death Valley

The area of interest for this study is the southern part of the Death Valley (DV) region, which extends for about 200 km. It is located southwest of the Basin and Range province (Wernicke et al., 1988), in the Eastern California Shear Zone/Walker Lane Belt (ECSZ/WLB) (Stewart, 1983; Wernicke et al., 1982; Wright, 1976) (Figure 4-1a). DV is considered as one of the youngest regions where strike-slip deformation contemporaneously occurs with large-scale crustal extension within the Basin and Range province (Calzia and Rämö, 2000; Luckow et al., 2005; Norton, 2011). This extensional basin formation accompanying normal and associated strike-slip faulting would be active since 15 Ma according to (Calzia and Rämö, 2000). It corresponds to a structural depression between the Panamint Range and the Black and Funeral Mountains (Hill and Troxel, 1966) (Figure 4-1), generally NNW-SSE oriented. This depression is related to tension along a segment of two strike-slip faults. Those two strike-slip faults consisting in the Northern Death Valley Fault Zone (NDVFZ) and the Southern Death Valley Fault Zone (SDVFZ), are characterized by en echelon traces (Butler et al., 1988) (Figure 4-1b). They have a general right-lateral movement, NW-SE oriented, from which results a “pull-apart” structure forming a N-S oriented basin (Burchfiel and Stewart, 1966) (Figure 4-1b).

The SDVFZ is composed of several branches. The SDVFZ formed the NH, at its southernmost part, by vertical displacement (Brady III, 1986; Brady et al., 1989) (Figure 4-2a). It intersects the east-trending left lateral Garlock Fault Zone (GFZ), which ends at its western termination by the northwest-striking San Andreas fault zone (Butler et al., 1988) (Figure 4-1a). Recently, (Pavlis and Trullenque, 2021) suggested a net dextral slip along the SDVFZ of 40–41 km based on the offset positions of the granite-basement contact from the OM to the Avawatz Mountains. Much of the dextral slip, occurring before the deposition of the 6–8 Ma Neogene cover, is indicated by stratigraphic overlaps on fault rocks. This suggests an occurrence of the dextral slip during the main extension. The authors challenge the young feature of the DV pull-apart (Norton, 2011), by opting to a long-lived pull-apart which is consistent with regional evidence of the initiation in the middle Miocene of the dextral trans-tension in the ECSZ/WLB (Lifton et al., 2013).

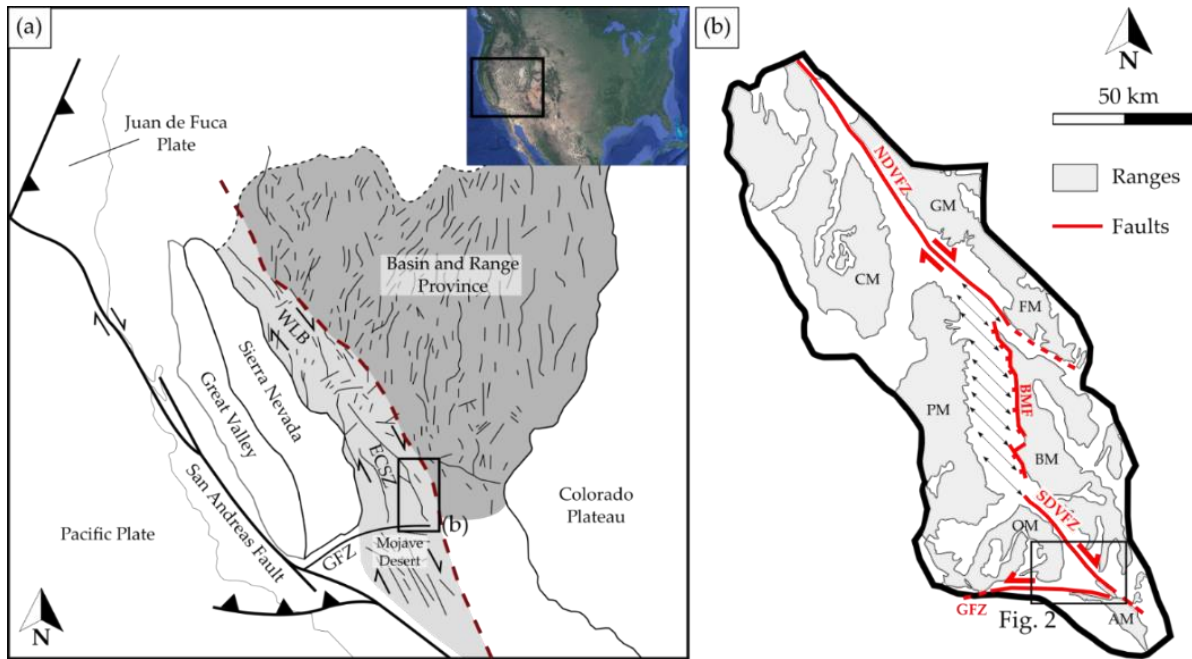


Figure 4-1. (a) Simplified tectonic map of the Great Basin region (western U.S. Cordillera) showing the tectonic provinces (modified after Nagorsen-Rinke et al. (2013)). WLB—Walker Lane Belt; ECSZ—Eastern California Shear Zone; GFZ—Garlock Fault Zone. The Basin and Range Province is represented in dark grey and the WLB/ECSZ in light grey. The red dashed line marks the limit between these both domains. The dark lines within the Basin and Range Province and in the WLB-ECSZ zone represent the main faults. (b) Structural setting of the Death Valley region (modified after Miller and Wright (2015); Rämö et al. (2002)). AM—Avawatz Mountains; BM—Black Mountains; BMF—Black Mountains Fault; CM—Cottonwood Mountain; FM—Funeral Mountains; GM—Grapevine Mountains; OM—Owlshead Mountains; PM—Panamint Mountains; GFZ—Garlock Fault Zone; NDVFZ—Northern Death Valley Fault Zone; SDVFZ—Southern Death Valley Fault Zone.

### III.2. Noble Hills

The NH extend 14 km northwest of the northern Avawatz Mountains (Brady et al., 1989) (Figure 4-2a,b). A first general geological map of the NH was provided by Troxel and Butler (1979), and later completed by Brady III (1986), Brady and Troxel (1986b), Butler (1984) and Niles (2016). They show that Precambrian gneiss covered by Crystal Spring Formation (CSF), a siliclastic-carbonate unit (Mahon et al., 2014b) of the Pahrump Group, were first intruded by 1.1 Ga diabase sills then by Mesozoic granitic rocks. All of these facies form the axial crystalline ridge defined by Brady III (1986).

The NH granite was poorly studied previously. It is part of the calc-alkaline granitoid intrusion related to the emplacement of the Sierra Nevada batholith, which was formed due to the eastward dipping subduction of the Pacific plate under the North American continent (DeCelles, 2004). It was only defined as both quartz monzonite (Troxel and Butler, 1979) and leucocratic adamellite (Stamm, 1981). Brady III (1986) completed the description as a medium to coarse equigranular grained to slightly porphyritic leucocratic rock containing few biotite and

little or no hornblende. The presence of sporadic mineralization due to hydrothermal alteration was also raised by Niles (2016). After the emplacement of the granite and its exhumation, ~3.34 Ma Pliocene sediments of the Noble Hills Formation (NHF) were deposited (Niles, 2016). The NHF consists in interbedded fine-grained clastic and evaporitic rocks, alluvial conglomerates, minor limestone and megabreccia. Recent work done by Klee et al. (2020) in the NH has shown a more complex geometry of the axial ridge than described until now (Figure 4-2c). The undifferentiated Precambrian and Paleozoic rocks facies were described by Klee et al. (2020) as a stacking of different CSF series, intruded by the Mesozoic granite. They seem to be dragged and stretched southeastward against the granite following the SDVFZ trend. Tertiary volcanism was also highlighted at the back of the range.

Based on the geology along the SDVFZ trace, Pavlis and Trullenque (2021) suggest that the NH axial crystalline ridge must be a transported part of the Cretaceous granitic pluton (~95 Ma), forming the OM (Rämö et al., 2002), which is relatively weakly deformed internally at its southern part (Luckow et al., 2005). This piece would have moved a minimum of 8 km according to Brady III (1986) and Brady and Troxel (1986b) and around 28 km according to Troxel (1994) along the SDVFZ (Figure 2b). Brittle shearing and large-scale *boudinage* characterize a brittle deformation, showing generally subhorizontal axes, which is prevalent within the Cretaceous granitic intrusion and Precambrian roof pendants (Figure 4-2c). Contractional deformation involving all members of the NHF is characterized along the NH and increases in intensity southeast toward the intersection with the GFZ (Niles, 2016).

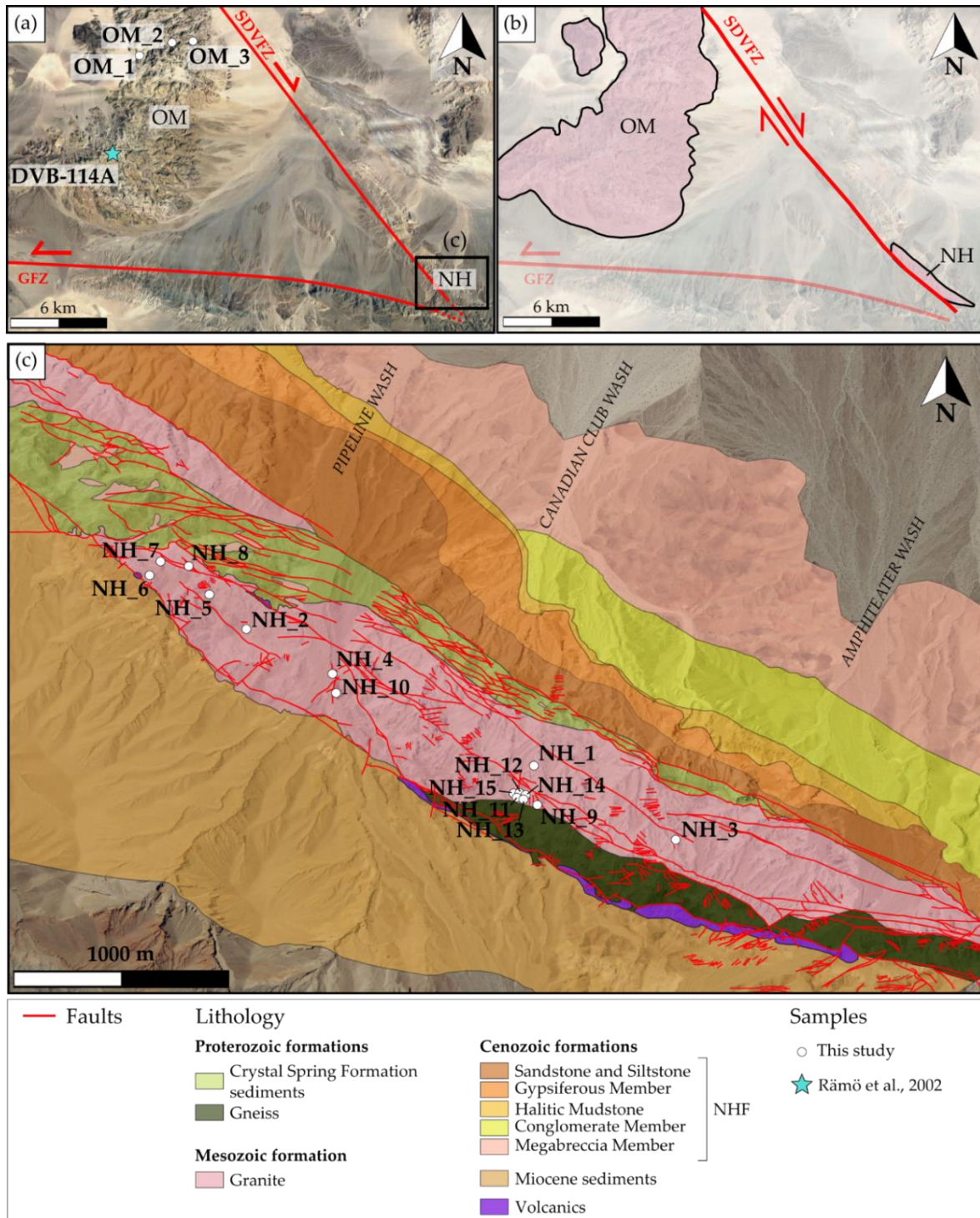


Figure 4-2. (a) Map presenting the structural setting of the southern part of the Death Valley region and the location of the Noble Hills range (NH) and the location of samples in the Owlshead Mountains (OM) represented by the white dots. (b) A scheme showing the displacement of the NH granite from the OM along the SDVZF described by Pavlis and Trullenque (2021). (c) The geological map of the Noble Hills range, modified after (Klee et al., 2020; Niles, 2016). The quaternary is not displayed but available on Niles (2016) map. In (a,b), samples location for this study are represented by the white dots; the blue star corresponds to a sample from Rämö et al. (2002). NHF—Noble Hills Formation.

## IV. MATERIAL AND METHODS

### IV.1. Material and Sampling Strategy

Fifteen samples from the NH granite and three samples from the OM granite (Figure 4-2) were collected in order to perform petrographical, mineralogical and geochemical characterizations. Hand specimens of centimetric size were collected in the two granite bodies (OM and NH) in order to characterize their mineralogical changes.

The selection of those samples through the NH was done under one scope, consisting of target zones away from the faults in order to avoid their influence. In that case, the magmatic texture is preserved. These faults are striking mainly NW/SE (SDVFZ direction) (Chabani et al., 2021). In order to be more precise in the sample selection, this latter was also based on the degrees of microfracturing defined by Castaing and Rabu (1981), from microscopical observations. This scale was improved by attributing a value of fracture density, based on scanlines realized on thin section mosaics, for each degree of microfracturing, which is described in the Methods section.

All the samples are georeferenced for database supply as well as located precisely (Figure 4-2). The OM being considered as the same batholith as the NH granite (Pavlis and Trullenque, 2021), samples were collected in an area unaffected by the SDVFZ activity in order to have a reference protolith of the studied area. Thin sections as well as powders were prepared to perform the following analyses.

### IV.2. Methods

#### IV.2.1. Microscopic Observations

A petrographical study performed on covered and polished thin-sections of 15 samples from the NH and two samples from the OM (OM\_1 and OM\_3), was realized at Institut Polytechnique UniLaSalle in Beauvais, using a Leica DM4500-P optical microscope equipped with a Leica DFC450C camera. Images were acquired thanks to the software Leica Application Suite (LAS) v4.11.0. The system is also equipped with a multistep acquisition program to perform thin section mosaics. It consists in the acquisition of several photos that follow each other in order to scan the whole thin section. At the end, the pictures are merged to obtain the mosaic. All the mineral abbreviations used in this paper refer to mineral symbols defined by Kretz (1983). The degree of mineral transformation into secondary minerals was defined based on optical observations.

### IV.2.2. Fractures Density

The studied samples were selected away from fracture zones, but also according to a certain degree of microfracturing based on the scale defined by Castaing and Rabu (1981). For this study, fractures density values were calculated for each degree of microfracturing by using thin section mosaics. For each mosaic, two scanlines (Bisdorn et al., 2014; Gillespie et al., 1993) perpendicular to the main fractures were realized by digitalizing fractures along both lines. The  $P_{10}$  (Bisdorn et al., 2014) has been calculated for each scanline. It consists in the number of fracture intersects per line length of scanline. The average was calculated to obtain a value of fracture density attributed to each thin section mosaic and corresponding to each microfracturing degree defined by Castaing and Rabu (1981):

$F_{d0} < 1687$  fracs/m—no to very low microfracturing

$F_{d1} = 1687$  fracs/m—microfracturing of order less than the grain size

$F_{d2} = 2694$  fracs/m, with a multiplier factor of 1.6—microfracturing of grain size order with interconnections

$F_{d3} = 3549$  fracs/m, with a multiplier factor of 1.3—abundant microfracturing

$F_{d4} \geq 5140$  fracs/m (Chabani et al., 2021), with a multiplier factor of 1.4—very abundant microfracturing

Samples selected for this study have so a fracture density lower or equal to  $F_{d2}$ .

### IV.2.3. SEM-EDS

Scanning Electron Microscope (Hitachi S-3400N SEM) equipped with a Thermo Ultradry Energy Dispersive X-ray Spectrometer (EDS) probe was used on two polished thin sections and one hand specimen at Institut Polytechnique UniLaSalle in Beauvais. It aimed at analyzing the microstructure characteristics and to perform qualitative and semi-quantitative chemical analyses of various selected mineral phases.

A NORAN-type correction (©Thermo Fisher Scientific, Waltham, MA, USA) procedure was used for all data and all Fe was assumed to be ferrous for simplification. Polished thin sections were analyzed using a 50  $\mu$ A beam current, an accelerating voltage of 20 kV and an acquisition time of 30 s.

#### IV.2.4. X-ray Diffraction (XRD)

##### IV.2.4.1. Experimental Conditions

XRD analyses were performed at Institut UniLaSalle Beauvais on the 15 samples from the NH and one sample from the OM (OM\_2) using a D8-Advance Bruker-AXS (Siemens, Munich, Germany) diffractometer with a Ni-filtered  $\text{CuK}\alpha$  radiation at 40 kV and 40 mA, a primary soller slit of  $2.5^\circ$ , divergence slit of 0.6 mm and a secondary soller slit of  $2.5^\circ$ , with a detector slit of 0.1 mm and an antiscattering slit of 0.6 mm. Samples were crushed with an agate pestle and mortar. Quantitative phase analysis based on Reference Intensity Ratio values were performed on randomly oriented bulk rock powders with a step length of  $0.5^\circ$  and a scan speed of  $0.014^\circ/\text{s}$  over the range  $3^\circ$ – $70^\circ 2\theta$  for bulk rocks composition. The uncertainty is estimated to be around 5%.

##### IV.2.4.2. Determination of Illite Crystallinity and Kübler Index

XRD investigations were carried out on bulk rock powder specimens and clay fractions of 16 samples in order to identify and determine the relative abundance of mineral phases (semi-quantitative, around 3–5%) observed upstream under the optical microscope and the SEM. Clay mineral separation was conducted using techniques described by Schmidt et al. (1997), following the recommendations of Kisch (1991), and according to the standard techniques suggested by Ferreiro Mählmann and Frey (2012). It consists into the collection of the  $<2\ \mu\text{m}$  and  $2$ – $6\ \mu\text{m}$  fractions from the sample powders put in suspension into water in decantation tubes. Oriented slides were then prepared by pipetting suspension onto glass slides ( $5\ \text{mg}/\text{cm}^2$ ) and air-drying. XRD measurements were then performed at air dried, solvated with ethylene glycol, and after heating ( $550\ ^\circ\text{C}$ ) conditions with a step length of  $0.5^\circ$  and a speed of  $0.01^\circ/\text{s}$  per step over the range  $3^\circ$ – $35^\circ 2\theta$ . The clay minerals identification, which is based on d-values and the relative intensity of their 00l peak reflections, was undertaken referring to Moore and Reynolds (1989) and Starkey et al. (1984). The illite “crystallinity” (IC), defined as the full width at half maximum (FWHM) of the  $10\ \text{Å}$  (001) peak of illite, was calculated using the software DIFFRAC EVA v 4.2 (by ©Bruker AXS, Billerica, MA, USA). The obtained values were standardized using the crystallinity index-standard (CIS) samples of Warr and Rice (1994a) in order to calculate the Kübler Index (KI).

The KI values of raw data expressed in  $\Delta^{\circ}2\theta$ , were measured into three slots, corresponding to different campaigns, inducing the three following standardizations:

$$KI_{(ULS1)} = 1.6987 \times IC_{\text{measured}} - 0.0842 \quad (R^2 = 0.9724) \quad (1)$$

$$KI_{(ULS2)} = 1.5501 \times IC_{\text{measured}} - 0.0512 \quad (R^2 = 0.9944) \quad (2)$$

$$KI_{(ULS3)} = 1.5337 \times IC_{\text{measured}} - 0.0498 \quad (R^2 = 0.9975) \quad (3)$$

KI was used to define the limits of metamorphic zones (Kübler, 1967), following the recommendations for Kübler-Index calibration of (Ferreiro Mählmann and Frey, 2012) and the CIS-KI transformation formalism of (Warr and Mählmann, 2015). In siliciclastic rocks, the transitions from non-metamorphic to low-grade (referring to the term greenschist facies (Winkler, 1979)) and from the very low-grade (chlorite zone (Tilley, 1925)) to low-grade metamorphic zone (biotite zone (Barrow, 1893)) take place through three zones defined by Kisch (1987): the diagenetic zone, the anchizone and the epizone. The zone boundary values are presented in Table 4-1. The smallest FWHM able to be measured by our diffractometer (limit detection) is  $0.08 \Delta^{\circ}2\theta$ .

Table 4-1. Metamorphic zone boundaries (Merriman and Frey, 1998) for Kübler Index (KI) values (Warr and Mählmann, 2015) and temperatures (Abad, 2007).

Metamorphic Zone	KI ( $\Delta^{\circ}2\theta$ )	Temperature ( $^{\circ}\text{C}$ )
Low Diagenesis	>1	~100
High Diagenesis	0.42–1	~200
Low Anchizone	0.30–0.42	
High Anchizone	0.25–0.30	
Epizone	<0.25	~300

#### IV.2.5. ICP-MS—ICP-AES

The analyses of major, trace and rare earth elements were completed on five selected samples from the NH (NH\_1, NH\_2, NH\_3, NH\_4 and NH\_12) and one from the OM (OM\_3) by Bureau Veritas Minerals (Vancouver, Canada) using ICP-ES and ICP-MS.

Samples were crushed and mixed with  $\text{LiBO}_2/\text{LiB}_4\text{O}_7$  flux. Crucibles were fused in a furnace at  $980 \text{ }^{\circ}\text{C}$ . Then, the cooled bead was dissolved in ACS grade nitric acid and analyzed by ICP-AES and/or ICP-MS. Loss on ignition (LOI) was determined by igniting the samples split then measuring the weight loss.

#### IV.2.6. Manocalcimetry

Calcite contents were determined using an OFITE 152-95 manocalcimeter. The analyses were performed on 15 samples from the NH and one sample from the OM at CY Cergy Paris University in the Geosciences and Environment Cergy (GEC) laboratory. It provides an indication of the total carbonate content in a sample and allows to assess the influence of calcite on permeability of the fluid pathways. This is achieved by measuring the rate of response of 10% hydrochloric acid on the samples. Calcimetry has also proved to be an efficient, easy and low-cost method to better understand the hydrothermal sealing of a reservoir (Ledésert et al., 2009).

Manocalcimetry consists into the measurements of CO<sub>2</sub> partial pressure when calcite is dissolved by HCl. The reaction that occurs is:



The calcimeter, composed of a glass flask and a high precision manometer calibrated with pure calcite reduced into fine powder. This allows us to determine the calcimeter coefficient. Variation of temperature and pressure can cause uncertainty on measurements, which was considered to obtain high quality results with a precision around 0.5 wt.%.

Prior to measurements, sample preparation was done according to Ledésert et al. (2009). The samples were reduced into powder in an agate mortar and put in the oven at 60 °C for 24 h. Then, 1.000 g of each sample was weighed and put in a sample holder, itself put in the calcimeter with a little glass filled with HCl. The amount of HCl is in excess in order to dissolve all the calcite present in the sample. The maximum value reached during the measurement was read on the manometer and the CaCO<sub>3</sub> percentage was determined as follows:

$$\% \text{CaCO}_3 = (\text{Measured value} \times 100) / \text{Calcimeter coefficient} \quad (5)$$

Two replicates were performed for each sample in order to check the reproducibility of the results, which is considered as good when the difference between the two results is lower than 0.5 wt.%, corresponding to the precision interval mentioned above.

#### IV.2.7. Ethanol Saturation Porosimetry

The estimation of available volume for fluid storage is fundamental and can be quantified by porosity measurements (Dullien, 1979). The connected porosity was measured on 6 samples from the NH and one from the OM by the triple weighing method (Navelot et al., 2018) defined

by the RILEM standard (test n°I.1, 1978). It consists in the saturation of the samples after vacuum degassing. The measurements were carried out at CY Cergy Paris University in the Laboratory of Mechanics and Materials for Civil Engineering (L2MGC).

In this study, ethanol has been chosen instead of water, as used in classical methods, in order to avoid possible clay swelling (Gates et al., 2004), which could lead to the destruction of the sample and biased results. Even though ethanol (0.469 nm) is a molecule larger than that of water (0.343 nm), the pore volume is not estimated to be under-evaluated, as the pore size is much larger than that of ethanol molecules. The samples were first oven-dried at approximately 40 °C until obtaining a constant weight (W1). Samples were then soaked by capillary action with ethanol after staying for 12 h under a vacuum. When the samples were completely immersed, the vacuum was stopped and the samples left in the ethanol for 24 h. Finally, they were weighted twice: (1) weighing of saturated samples, W2; and (2) weighing of samples under “ethanostatic” conditions (suspended into ethanol under the balance), W3. The connected porosity  $\phi$  is then calculated:

$$\phi(\%) = (W2 - W1/W2 - W3) \times 100 \quad (6)$$

## V. RESULTS

### V.1. Petrographic Description

#### V.1.1. The Owlshead Granite

Samples of the OM granite appear rather fresh, meaning that primary minerals seem not transformed into secondary ones and present no sign of deformation. They show a light grey/whitish and yellowish granite (Figure 4-3a) with equant medium-size grains (0.1–1 cm). Primary assemblage is composed of plagioclase, quartz, K-feldspar and biotite. Biotite is generally surrounded by a yellowish oxide halo, showing its incipient alteration.

OM granite microscopic observations (Figure 4-3b,c, Table 4-2) confirm the freshness of the rock as well as the very low to absent microfracturing. Figure 4-3b shows a microfracturing around F<sub>d</sub>1 (Table 4-2). Most of the fractures are open and a few of them are filled by calcite. Calcite is also present at the grain boundaries (Figure 4-4a,b).

Regarding mineralogical composition, plagioclase (35%, modal composition) occurs subautomorphous crystals, up to 5 mm, of oligoclase composition with an oscillatory zonation (Bard, 1980) (Figure 4-3b). Quartz (35%) forms up to 2 cm polycrystalline clusters of anhedral crystals which range up to 1 cm and present a slight rolling extinction. K-feldspar (25%) occurs

as centimetric subautomorphous crystals of microcline and orthoclase with a Carlsbad twin, rich in perthites (albite vein or braid/patch shape (Bard, 1980) (Figure 4-4a,b). K-feldspar crystals can contain plagioclase and biotite inclusions. Biotite (5%) of around 2 mm in length is euhedral. Primary opaque minerals (<1%) are also found in this granite.

The core of plagioclase is slightly transformed into K-white mica (Figure 4-3c and Figure 4-4c,d). They will be represented as Wm. Quartz and K-feldspar are not affected by the alteration and are only little undeformed as seen on quartz showing undulatory extinction (Figure 4-4a). Biotite can be slightly altered. Few epidotes are present nearby the biotite (Figure 4-4e,f).

Microscopic observations of samples OM\_3 and OM\_1 are consistent with whole rock XRD analyses performed on the sample OM\_2 from the OM granite. The three samples have a similar mineralogical composition and are grouped together in Table 4-2.

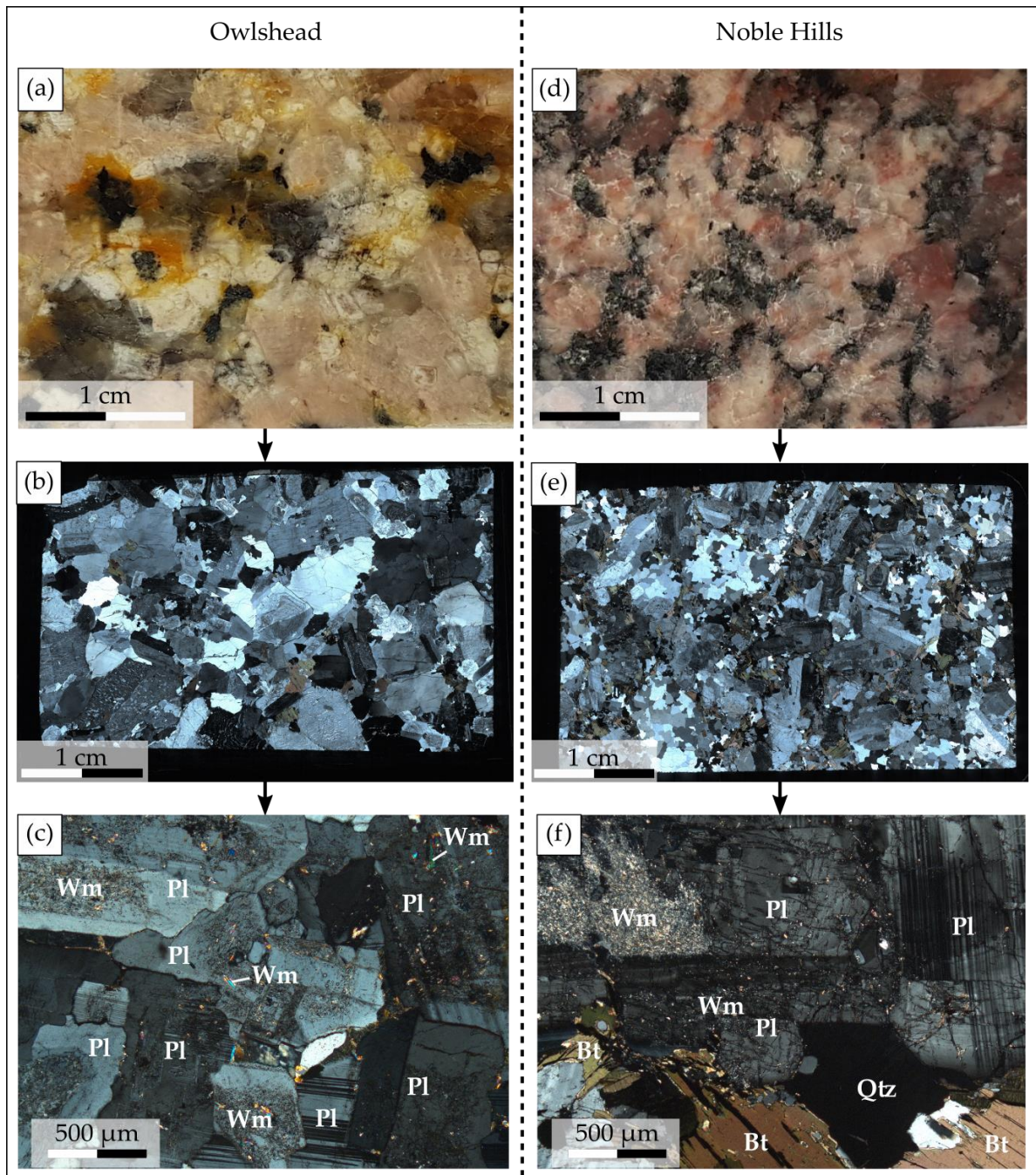


Figure 4-3. Macroscale to microscale photographs illustrating (a–c) the Owlshead and (d–f) the Noble Hills granites. (a,d) Hand specimens for each granite showing their different aspects. (b,e) Thin section mosaics realized for each granite under optical microscope in polarized–analyzed light and showing the difference in terms of grain size and microfracturing. (c,f) Thin sections zooms of each granite mosaic in polarized–analyzed light showing the difference in terms of alteration degree. Abbreviations (except for “Wm”) after Kretz (1983): Bt–Biotite, Kfs–K-feldspar, Wm–K-white mica, Pl–Plagioclase, Qtz–Quartz.

Table 4-2. List of samples collected in the field with their mineralogical composition determined after microscopic observations and XRD analysis (primary minerals, alteration phases for plagioclase, biotite and K-feldspar, other secondary minerals and microfissuring after Castaing and Rabu scale). Abbreviations (except for "Ox and Wm") after Kretz (1983): Qtz—Quartz, Pl—Plagioclase, Mc—Microcline, Or—Orthoclase, Bt—Biotite, Kln—Kaolinite, Ep—Epidote, Ox—Oxide (when it could not be determined precisely), Wm—K-white mica, Cal—Calcite, Dol—Dolomite, Hem—Hematite, Gp—Gypsum, Fd—Fracture density.

Sample ID	Primary Minerals	Major Secondary Phases Within					Other Secondary Minerals	Microfracturing	
		Pl			Bt				Kfs
		Wm	Kln	Cal	Wm	Ox			Wm
OM_1_2_3	Qtz, Pl, Mc, Or, Bt, Ox	✓					Ep, Ox, Wm, Cal	Fd1	
NH_1	Qtz, Pl, Mc, Or, Bt, Ox	✓	✓		✓	✓	Cal, Dol, Wm	Fd1	
NH_2	Qtz, Pl, Or, Bt, Ox	✓	✓			✓	Dol, Wm	Fd1	
NH_3	Qtz, Pl, Or, Bt, Ox	✓	✓		✓	✓	✓	Cal, Dol, Wm	Fd1-2
NH_4	Qtz, Pl, Or, Bt, Ox	✓	✓	✓	✓	✓		Cal, Hem	Fd0-1
NH_5	Qtz, Pl, Or, Bt, Ox	✓	✓			✓		Hem, Wm	Fd0-1
NH_6	Qtz, Pl, Or, Bt, Ox	✓	✓	✓	✓	✓		Cal, Hem, Wm	Fd1-2
NH_7	Qtz, Pl, Or, Bt, Ox	✓	✓		✓	✓		Cal, Ox, Wm	Fd1
NH_8	Qtz, Pl, Or, Bt, Ox	✓	✓	✓	✓	✓		Cal, Ox, Wm	Fd1-2
NH_9	Qtz, Pl, Or, Bt, Ox	✓	✓					Cal, Ox, Wm	Fd0-1
NH_10	Qtz, Pl, Or, Bt, Ox	✓	✓	✓	✓	✓		Cal, Hem, Wm, Ep	Fd2
NH_11	Qtz, Pl, Or, Bt, Ox	✓	✓	✓	✓	✓		Cal, Hem, Wm	Fd1-2
NH_12	Qtz, Pl, Mc, Or, Bt, Ox	✓	✓	✓	✓	✓		Cal, Hem, Gp, Wm	Fd0-1
NH_13	Qtz, Pl, Mc, Or, Bt, Ox	✓	✓	✓	✓	✓		Cal, Hem, Gp, Wm	Fd0-1
NH_14	Qtz, Pl, Mc, Or, Bt, Ox	✓	✓	✓	✓	✓		Cal, Hem, Gp, Wm	Fd0-1
NH_15	Qtz, Pl, Or, Bt, Ox	✓	✓		✓	✓		Cal, Mag, Wm	Fd1-2

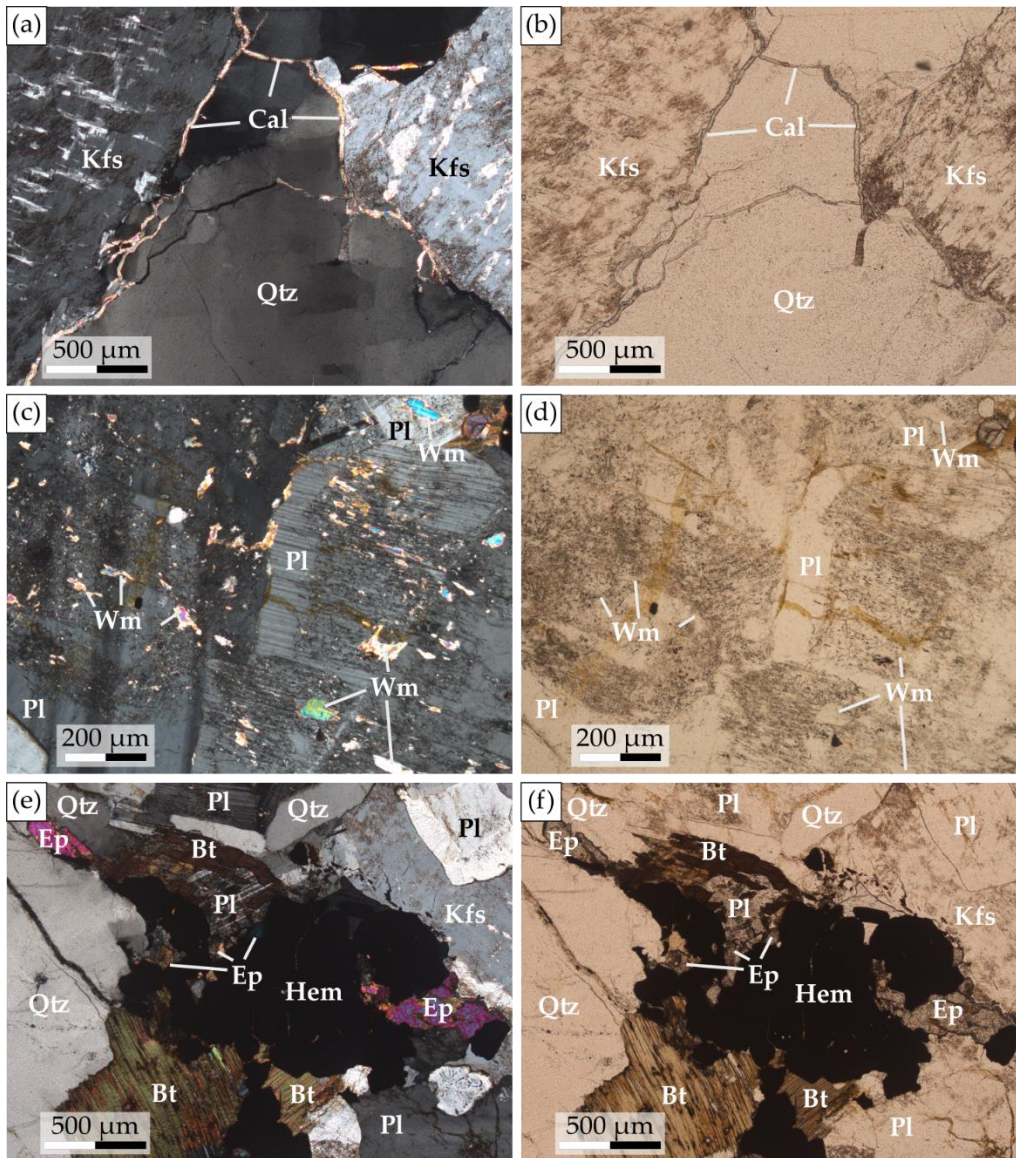


Figure 4-4. Photomicrographs of the Owlshhead granite in polarized-analyzed and polarized–non-analyzed light showing (a,b) perthitic and unaltered orthoclase, unaltered quartz presenting a slight undulatory extinction and calcite veinlets at grain boundaries. (c,d) Plagioclase alteration with the formation of K-white mica. (e,f) Incipient biotite alteration associated to hematite and epidote formation. Abbreviations (except for “Wm”) after Kretz (1983): Bt–Biotite, Cal–Calcite, Ep–Epidote, Hem–Hematite, Kfs–K-feldspar, Wm–K-white mica, Pl–Plagioclase, Qtz–Quartz.

### V.1.2. The Noble Hills Granite

Far from the major faults, the NH granite appears, as a whole, microfractured and altered. with preserved “fresh” zones. The collected hand specimens (Figure 4-2b) are equant to slightly porphyritic and display a pinkish color (Figure 4-3d) or a whitish color for the samples with evidences of alteration. Primary assemblage, as for the OM granite, is made of plagioclase, quartz, K-feldspar and biotite.

At the microscale, the degree of microfracturing ranges from  $F_d0-1$  to  $F_d2$  (Table 4-2). As for the OM granite, the microfractures can be opened or filled by carbonates. As regards mineralogical composition, plagioclase (~35%, oligoclase in composition) occurs as sub-anhedral to euhedral crystals (up to 5 mm in length) showing growth zonation (see Figure 4-3f) and (Bard, 1980)). Quartz (~30%) forms polycrystalline euhedral clusters of around 1 cm in size made of 3-mm-wide crystals with sometimes a slight undulatory extinction linked to low deformation. K-feldspar (~25%) is made of sub-anhedral to euhedral orthoclase (up to 1 cm in length) with vein shaped perthites (Bard, 1980). Microcline is only present in the samples NH\_12 and NH\_14, in the southern part of the range (Figure 4-2 and Table 4-2). Some K-feldspar crystals contain inclusions of plagioclase or/and biotite. Depending on the samples, the amount of plagioclase can be equivalent to that of K-feldspar (~30% each), but most of the time, plagioclase dominate. Myrmekite can be observed at the interface between plagioclase and K-feldspar. Biotite (~10%) appears euhedral with crystals ~ 2 mm in length. Accessory minerals (<1%) as apatite are also observed. More rarely, primary muscovite, as well as primary opaque minerals (oxides) are observed in the granite. A comparison between the NH and the OM granites highlights a grain size difference. Quartz and K-feldspar crystals are smaller in the NH granite (up to 3 mm and 1 cm respectively, Figure 4-3e) than in the OM granite (up to 1 cm and centimetric crystals respectively, Figure 4-3b).

Primary minerals, function of their sensitivity to alteration (Bard, 1980), recrystallized into secondary minerals which are shown in Table 4-2. This is related to differences into chemical properties (Goldich, 1938). In the plagioclase, which is the most altered mineral (Figure 4-5), recrystallization propagate from the core of the crystal to the more albitic rim (Figure 4-5a) (Que and Allen, 1996). When alteration is intense, plagioclase is entirely replaced by newly formed minerals leaving only the pseudomorph of the plagioclase to subsist (Figure 4-5d). The newly formed minerals are the following:

- Illite is the most frequent and occurs as tiny flakes or needles 0.5 to 8  $\mu\text{m}$  width and up to 40  $\mu\text{m}$  long (Streckeisen, 1973) (Figure 4-5b,c).
- Kaolinite is present as fan shape (Figure 5e,f) of 25  $\mu\text{m}$  to 40  $\mu\text{m}$  in diameter. Under SEM (Figure 4-5f), well crystallized kaolinite presents a porous structure which can contribute to the porosity of the rock. It is only present in the NH granite (Table 4-3) indicating that the NH granite has undergone a different alteration from that of the OM granite.
- Calcite, which occurs as small spots, is mainly associated with kaolinite (Figure 4-5d,e). It crystallizes in the porosity created by plagioclase dissolution.

- Illite and kaolinite can be present together in the same sample (Figure 4-5d).
- The K-feldspar remains always unaffected (Figure 4-5d), but when the alteration is relatively pronounced, perthites can be altered as well as the mineral inclusions like in sample NH\_3 (Table 4-2). Biotite is progressively replaced by K-white mica (illite) as compared to the biotite in the OM granite (Table 4-2). K-white mica crystallizes along the cleavages and can be associated to the crystallization of oxides, as hematite, also along the cleavages (Figure 4-6).

Table 4-3. List of samples with their respective clay minerals composition, FWHM and Kübler Index (KI) for the fractions < 2 $\mu$ m and 2–6  $\mu$ m. Abbreviations (except for “Cor”) after [45]: Ill–Illite, Kln–Kaolinite, Cor–Corrensite, I/S–Illite/Smectite, Vrm–Dioctahedral Vermiculite, Bt–Biotite, Mnt–Montmorillonite, AD–Air-dried.

Sample ID	<2 $\mu$ m					2–6 $\mu$ m						<2 $\mu$ m (AD)		2–6 $\mu$ m (AD)	
	Ill	Kln	Cor	I/S	Bt	Ill	Kln	Cor	I/S	Mnt	Bt	FWHM	KI	FWHM	KI
OM_2	no material					-								0.18 0.22	
NH_1	+	-			++	-	+				++	0.48	0.69	0.34	0.46
NH_2	--	-			++	--	-				++	0.31	0.43	0.32	0.44
NH_3	+	+	++			+	+	++				0.63	0.92	0.59	0.87
NH_4	++	+	-			++	+	-				0.81	1.29	0.73	1.16
NH_5	+	-	-			-	-	-			+	0.69	1.09	0.37	0.55
NH_6	+	++		-		+	++		-			1.37	2.25	1.15	1.87
NH_7	+	+		-		+	+		-		+	1.01	1.63	0.71	1.13
NH_8	+	+	+			+	++	+				1.10	1.79	1.18	1.93
NH_9	+	+	++			+	+	++				0.85	1.36	0.56	0.87
NH_10	+	-			++	+	-				++	0.46	0.65	0.51	0.73
NH_11	++	-	+			++	+	+				0.67	1.05	0.62	0.97
NH_12	++	+		-		++	+		-			0.57	0.89	0.46	0.69
NH_13	+	-	+			+	-	+				0.46	0.69	0.38	0.56
NH_14	+	--	-		+	+	--	-			+	0.59	0.92	0.44	0.66
NH_15	+	-	+			+	-	-				0.69	1.08	0.50	0.77

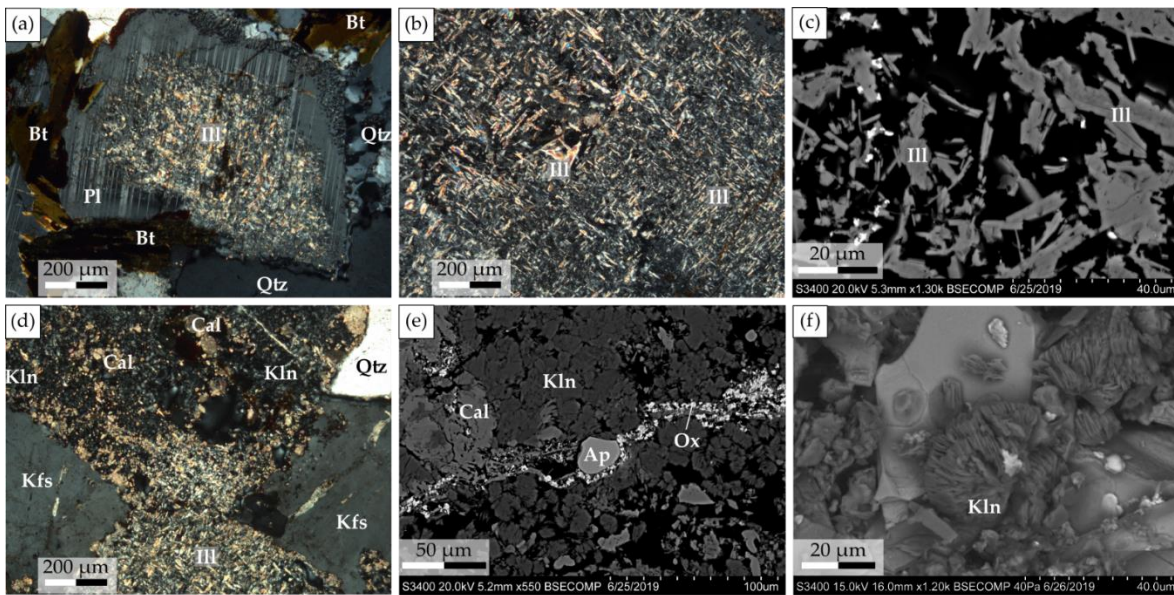


Figure 4-5. Photomicrographs showing the plagioclase transformation progress in the Noble Hills granite. (a) Progressive illitization of plagioclase initiating in the core of the mineral under optical microscope in polarized–analyzed light. (b) Needles shape illite replacing plagioclase in polarized–analyzed light under optical microscope. (c) Back-scattered electron image of needles/flakes shape illite replacing plagioclase. (d) Plagioclase completely replaced by illite, kaolinite and calcite and non-altered K-feldspar under optical microscope in polarized–analyzed light. (e) Back-scattered electron image showing a fan shape kaolinite, calcite and oxide veinlet. (f) Back-scattered electron image showing a magnified view of a single mineral of kaolinite under SEM. Abbreviations (except for “Ox”) after Kretz (1983): Ap–Apatite, Bt–Biotite, Cal–Calcite, Ill–Illite, Kln–Kaolinite, Kfs–K-feldspar, Ox–Oxides, Pl–Plagioclase, Qtz–Quartz.

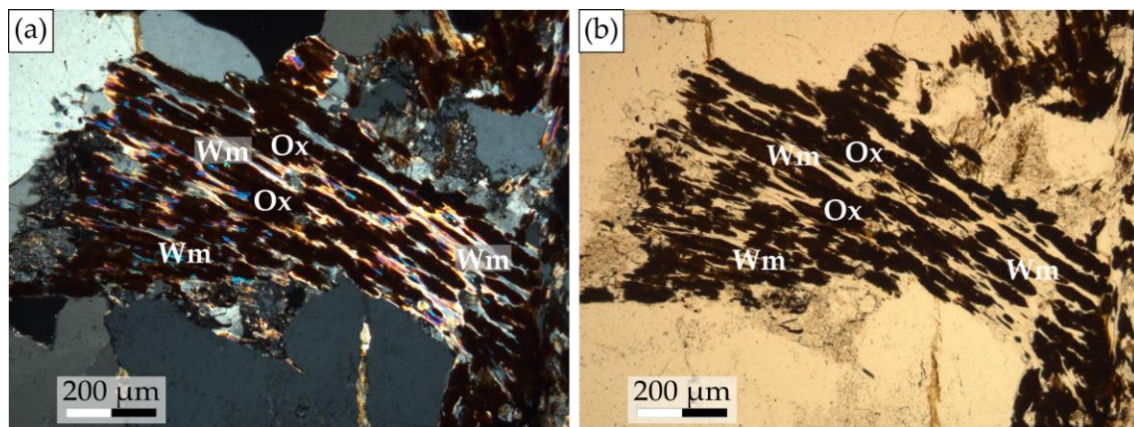


Figure 4-6. Photomicrographs showing a biotite completely altered and replaced by oxides and K-white mica (essentially illite) according to the cleavage planes (a) in polarized–analyzed light under optical microscope and (b) in polarized–analyzed light under optical microscope. Abbreviations (except for “Ox and Wm”) after Kretz (1983): Bt–Biotite, Cal–Calcite, Kfs–K-feldspar, Wm–K-white mica, Ox–Oxides, Pl–Plagioclase, Qtz–Quartz.

All the samples are plotted in the Streckeisen ternary diagram (Figure 4-7) (Streckeisen, 1973). The OM and NH granites of this study are both defined as monzogranites. The OM sample analyzed by Rämö et al. (2002) (Figure 4-2a, blue star) shows a different composition (Figure

4-7, blue star). It is rather a monzonite, as defined by Rämö et al. (2002), than a monzogranite, as defined in this study.

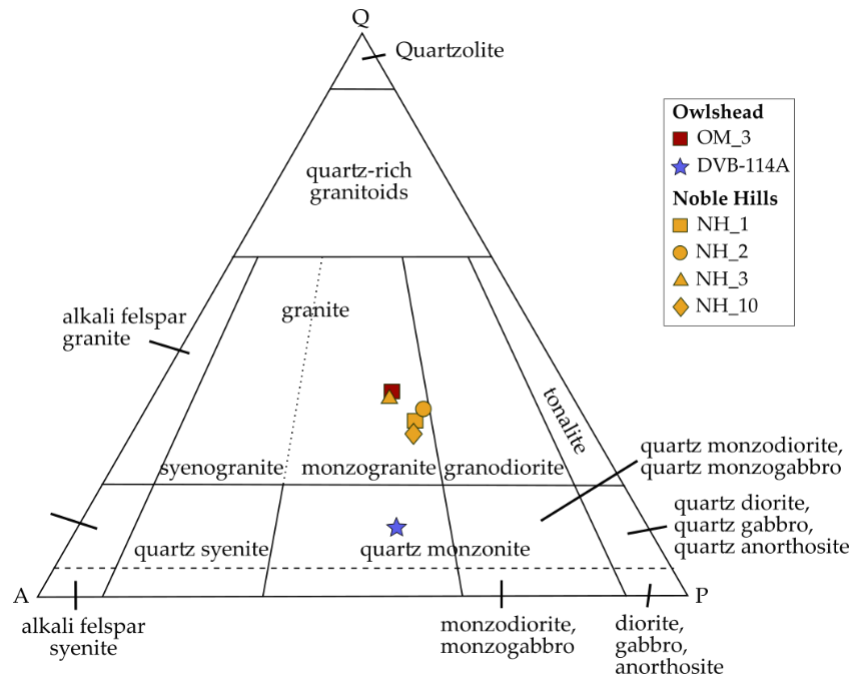


Figure 4-7. Normative composition of one sample from the OM and 4 samples from the NH in a QAP (Quartz-Alkali-feldspar-Plagioclase) ternary diagram (Streckeisen, 1973).

### V.1.3. Clay Minerals Identification and Kübler INDEX

Clay minerals from the <2  $\mu\text{m}$  and 2–6  $\mu\text{m}$  fractions were separated. The clay composition of both fractions of each studied sample (OM and NH) is given in Table 4-3, based on Moore and Reynolds (1989).

#### V.1.3.1. Owlshead Mountains

The OM sample clay analyses confirm the presence of illite observed under optical microscope. They also reveal the pattern of montmorillonite (Mnt) (Moore and Reynolds, 1989), a common smectite (Figure 4-8). Its very intense 001 peak allows the determination of its amount representing 15% of the clay fraction. This peak is characterized by a shift from 14.87 Å (air-dried) to 16.90 Å after glycol solvation and it collapses at 10.09 Å after heating. After glycol solvation, new peaks appear at 5.61 Å and 8.46 Å.

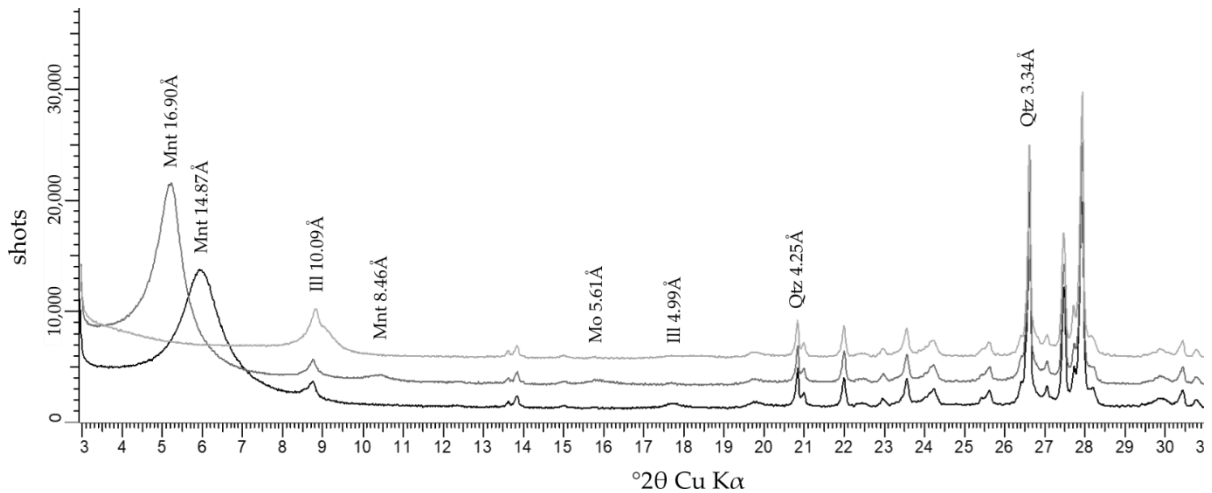


Figure 4-8. XRD result obtained for the clay fraction  $< 2 \mu\text{m}$  in Air-Dried (AD), Glycolated (G) and Heated (H) of the samples in the OM granite and showing a montmorillonite (Mnt) pattern.

### V.1.3.2. Noble Hills

Two typical XRD patterns of clay minerals are identified in the NH samples for the  $< 2 \mu\text{m}$  fraction (Figure 4-9):

- Corrensite, kaolinite and illite are identified in the first pattern, where corrensite is well known as the trioctahedral variety of regular 50:50 mixed-layer chlorite/smectite (Beaufort et al., 1997) (Figure 4-9a). It is characterized by (1) the peak at  $13.60 \text{ \AA}$  in air-dried conditions, shifting to  $15.62 \text{ \AA}$  after glycol solvation and collapses to  $11.72 \text{ \AA}$  after heating, and (2) new peaks at  $7.78 \text{ \AA}$ ,  $5.15 \text{ \AA}$  and  $3.44 \text{ \AA}$  appear after glycol solvation and disappear after heating. The corrensite found in the NH granite is considered as a low charge corrensite after Moore and Reynolds (1989).
- Illite/smectite (I/S) mixed-layer, kaolinite and illite (Figure 4-9b) are identified in the second pattern, where I/S is illite-rich (R3), with more than 90% of illite and R representing the Reichweite parameter (Jagodzinski, 1949). I/S is characterized by a large peak at  $10.08 \text{ \AA}$  in air-dried, becoming narrower when it collapses to  $9.93 \text{ \AA}$  after glycol solvation and by a peak at  $5 \text{ \AA}$  swelling after glycol solvation.

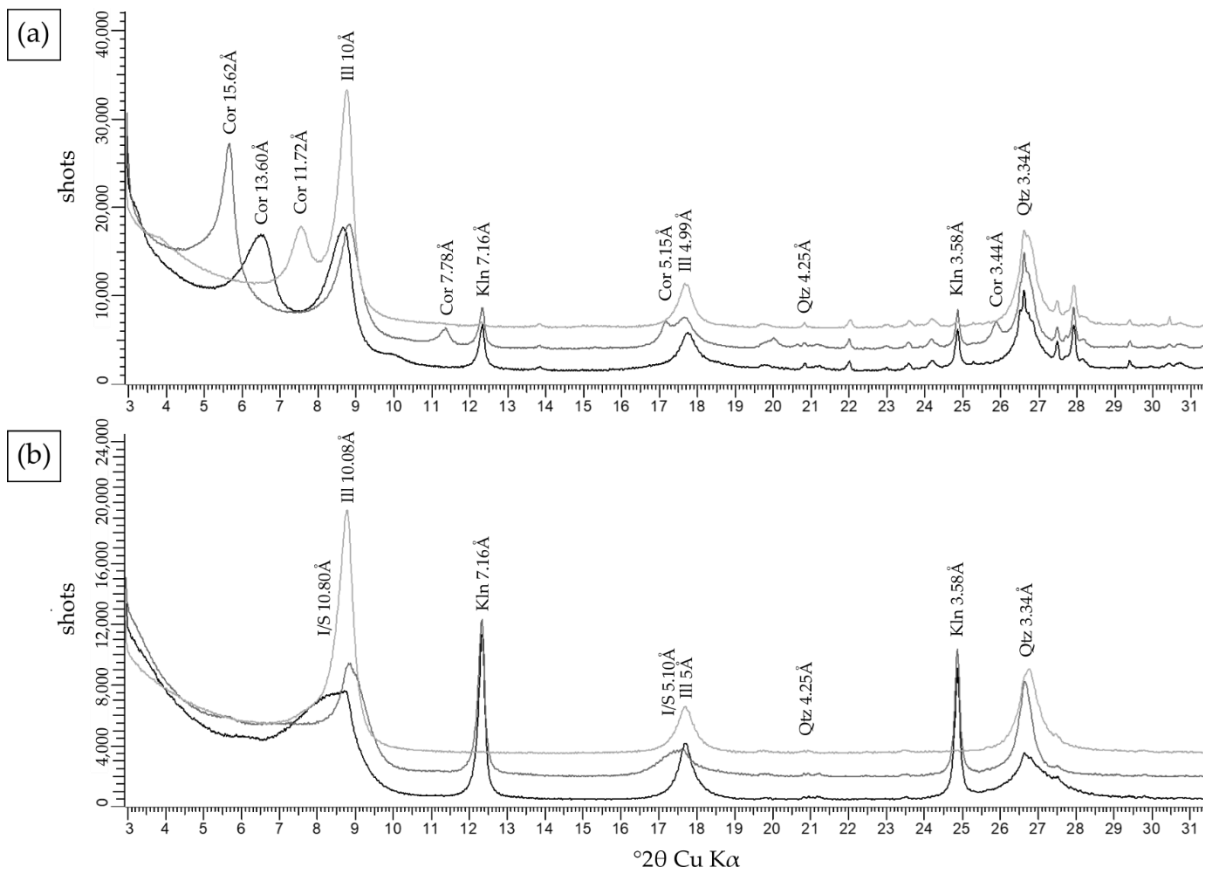


Figure 4-9. XRD patterns obtained for the clay fraction  $< 2\mu\text{m}$  in Air-Dried (AD), Glycolated (G) and Heated (H) for the NH granite and showing the clay composition of the samples in the NH granite: (a) corrensite (Cor), a chlorite/smectite mixed-layer, and (b) illite/smectite mixed-layer (I/S). Abbreviations (except for "Cor and I/S") after Kretz (1983): Bt—Biotite, Kln—Kaolinite, Qtz—Quartz, Ill—Illite.

In the NH KI values range from  $2.25^{\circ}2\theta$  to  $0.43^{\circ}2\theta$  for the  $< 2\mu\text{m}$  fraction and from  $1.93^{\circ}2\theta$  to  $0.44^{\circ}2\theta$  for the  $2\text{--}6\mu\text{m}$  fraction (Table 4-3). The spatial distribution of the samples and the KI values are shown in Figure 10. A NW to SE decrease in KI values in the main granitic body is distinguishable in the  $< 2\mu\text{m}$  fraction (Figure 4-10a) and confirmed in the  $2\text{--}6\mu\text{m}$  fraction (Figure 4-10b).

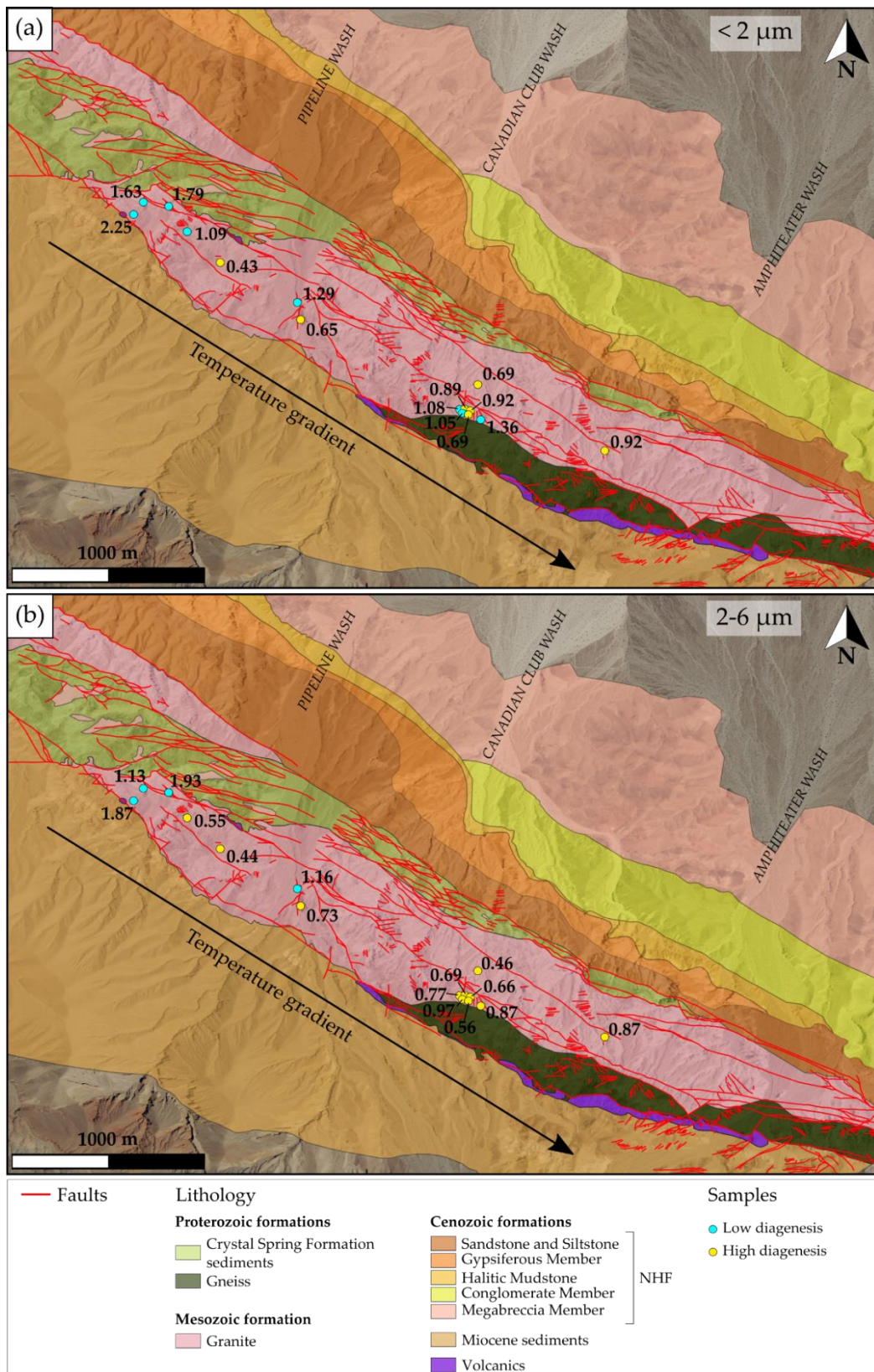


Figure 4-10. Geological map (see Figure 4-2b) representing the Kübler Index (KI) in air dried conditions of each sample and the corresponding metamorphic zone showed by the color of the dots for (a) the fraction < 2 μm and (b) the fraction 2-6 μm.

## V.2. Geochemical Analyses

### V.2.1. Major Element Bulk Rock Chemistry

Major element geochemistry (Table 4-4) allows classifying the granite samples in different diagrams (Figure 4-11 and Figure 4-12).

Table 4-4. Major elements of the Owlshead and Noble Hills granites.

Sample ID	OM_3	NH_10	NH_1	NH_2	NH_3
Oxides (weight %)					
SiO <sub>2</sub>	74.65	68.54	69.56	68.69	68.78
Al <sub>2</sub> O <sub>3</sub>	12.90	15.36	14.93	14.53	14.99
Fe <sub>2</sub> O <sub>3</sub>	1.83	3.02	2.83	4.29	2.95
MgO	0.31	0.57	0.56	1.15	0.78
CaO	1.09	2.62	2.20	2.50	1.99
Na <sub>2</sub> O	3.51	3.31	3.42	3.19	2.78
K <sub>2</sub> O	4.43	4.31	4.10	3.60	4.22
TiO <sub>2</sub>	0.20	0.29	0.26	0.46	0.28
P <sub>2</sub> O <sub>5</sub>	0.07	0.14	0.13	0.20	0.14
MnO	0.08	0.09	0.08	0.12	0.08

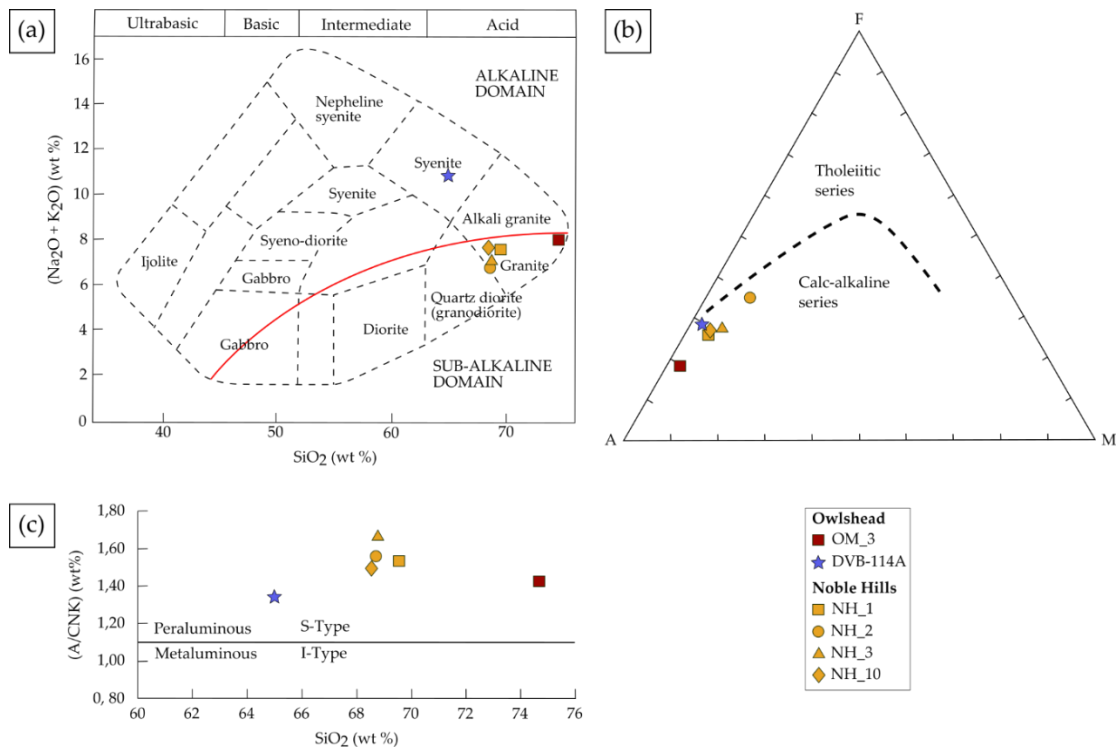


Figure 4-11. (a) Total alkali versus silica diagram ((Cox, 1979) adopted for plutonic rocks by (Wilson, 1989)). (b) AFM (Alkali-Fe<sub>2</sub>O<sub>3</sub>-MgO) classification diagram established by Jensen (1976). (c) A/CNK

( $Al_2O_3/(CaO + Na_2O + K_2O)$ ) versus silica diagram. The blue star corresponds to a sample from the OM analyzed by Rämö et al. (2002).

In the  $Na_2O + K_2O$  versus  $SiO_2$  classification (called TAS) diagram of Cox (1979), modified after Wilson (1989) for plutonic rocks, all the samples plot in the sub-alkalic domain. They all have a granite composition close to the granodiorite zone (Figure 4-11a). However, the sample from Rämö et al. (2002) plots in the syenite field, while it plots in the monzonite field in the Streckeisen diagram (Figure 4-7). The AFM triangular plot classifies all the samples as calc-alkaline (Figure 4-11b). The silica content of the OM granite 74.65 wt.% is higher than that of the NH granite which ranges from 68.54 to 69.56 wt.%. According to the  $SiO_2$  versus A/CNK diagram (Figure 4-11c) (White and Chappell, 1983), all the samples are peraluminous rocks, and are found rather far from the boundary with metaluminous S-type granites, with a A/CNK between 1.4 and 1.6 wt.%. Harker diagrams complete the information by showing a high content of  $K_2O$  ranging from 3.6 to 4.43 wt.%, and plot the samples in the high-K calc-alkaline domain (Figure 4-12a) which limits were defined by Le Maître et al. (1989). However, the OM sample has a lower  $Al_2O_3$  content (12.9 wt.%) than the NH samples (14.53–15.36 wt.%) forming a separate cluster (Figure 4-12b). Again, the sample from Kretz (1983) (DVB-114A—blue star) shows a large difference in composition compared to OM\_3.

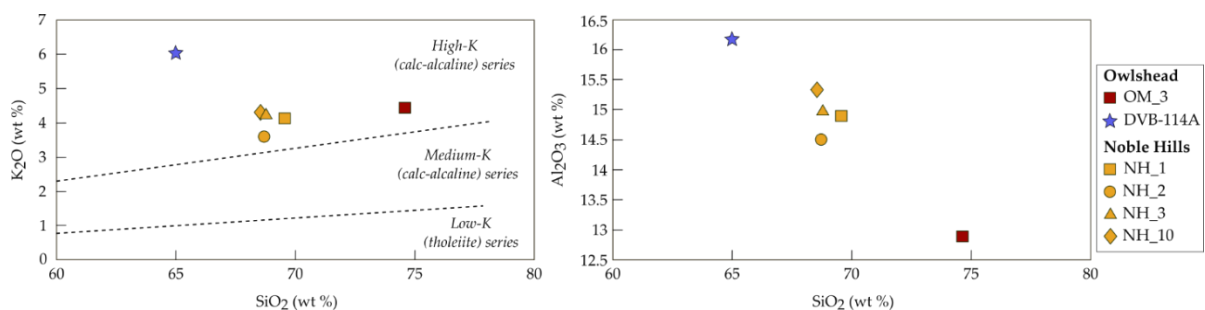


Figure 4-12. Harker diagrams showing the variation of (a)  $K_2O$  (Le Maître et al., 1989) and (b)  $Al_2O_3$  in the OM and NH granites. A sample from the OM analyzed by Rämö et al. (2002) is represented by the blue star

The loss on ignition (LOI) is of 0.7 wt.% for the OM granite and ranges from 1.1 to 2.8 wt.% for the NH granite (Table 4-5), showing that the OM granite contains less volatile elements than the NH granite, even for the freshest samples (NH\_10, NH\_1 and NH\_2). By comparing the alteration degree of each sample estimated from optical observations of plagioclase and biotite (Table 4-5) and the LOI values, we note that a low LOI corresponds to a slight alteration, e.g., OM\_3 or NH\_2 and a high LOI corresponds to a more pronounced alteration, e.g., NH\_3.

Table 4-5. Loss on ignition values compared to the alteration degree of plagioclase and biotite estimated under optical microscope.

Sample ID	OM_3	NH_10	NH_1	NH_2	NH_3
Loss on ignition (LOI) (wt.%)	0.7	1.5	1.7	1.1	2.8
Alteration degree (%)	2	10	9	4	18
Plagioclase alteration (%)	5	20	20	10	40
Biotite alteration (%)	0	15	10	0	20

In diagrams representing selected major elements versus the LOI (Figure 4-13), LOI values of NH samples show a positive correlation with  $K_2O$  and a negative correlation with  $Na_2O$  and  $CaO$ .  $SiO_2$  and  $Al_2O_3$  contents are approximately constant, 68.54–69.56 wt.% and 14.53–15.36 wt.% respectively.  $MgO$  content varies a lot (0.56–1.15 wt.%) showing no clear correlation with the LOI.  $K_2O$  and  $Na_2O$  contents of the OM granite are equivalent to those of the freshest NH granites (NH\_2, NH\_10 and NH\_1). However, the OM granite sample presents a higher amount of  $SiO_2$  and a lower amount of  $Al_2O_3$ ,  $CaO$  and  $MgO$ . The chemistry of the OM granite seems different from that of the NH granite regarding Figure 4-12 and Figure 4-13 even though, according to Pavlis and Trullenque (2021), the NH granite derived from the OM granite.

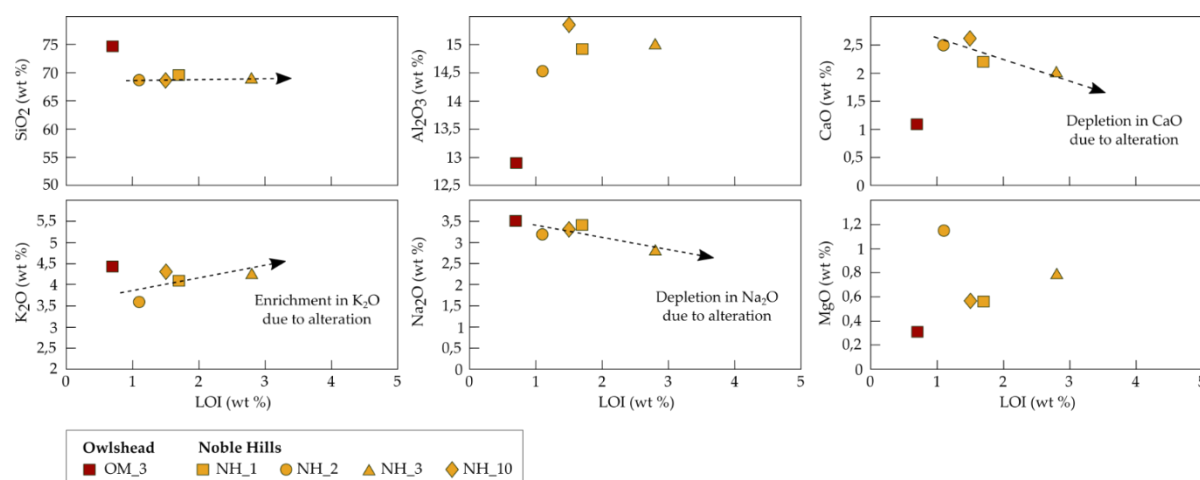


Figure 4-13. Plot of selected major element oxides ( $SiO_2$ ,  $K_2O$ ,  $Al_2O_3$ ,  $Na_2O$ ,  $CaO$  and  $MgO$ ) versus LOI (loss on ignition).

### V.2.2. Trace Element and REE Bulk Chemistry

Trace elements and Rare Earth Elements (REE) (Table 4-6) analyses were performed on the same samples as for major elements.

Table 4-6. Trace elements chemical composition of the Owlshead and Noble Hills granites.

Sample ID	OM_3	NH_10	NH_1	NH_2	NH_3
Trace elements (ppm)					
Be	2	2	2	3	2
Co	1.5	4.2	2.9	6.4	3.5
Cs	1.6	2.4	1.1	3.4	1.8
Ga	15.6	16.7	16.0	17.2	14.1
Hf	4.3	3.6	4.1	4.6	4.6
Nb	22.3	13.8	11.4	18.9	10.5
Rb	154.7	144.9	103.0	139.9	115.7
Sn	2	1	<1	2	<1
Sr	116.2	275.2	237.5	268.2	182.7
Ta	1.6	0.9	0.7	1.3	0.6
Th	19.3	11.4	10.2	9.0	11.0
U	1.8	2.2	1.5	1.4	1.5
V	16	33	22	40	25
W	<0.5	<0.5	0.7	<0.5	<0.5
Zr	139.8	134.2	156.6	180.6	159.0
Y	19.7	22.5	17.5	21.4	17.0
Ba	554	1009	845	704	772
Ni	<20	<20	<20	<20	<20
Sc	4	5	4	8	4
Cr <sub>2</sub> O <sub>3</sub>	<0.002	<0.002	<0.002	<0.002	<0.002
Be	2	2	2	3	2
Rare Earth Elements (ppm)					
La	52.1	28.3	26.2	21.7	26.8
Ce	97.0	53.0	48.1	40.8	52.2
Pr	9.97	5.93	5.31	4.59	5.62
Nd	31.7	20.6	18.8	16.6	19.5
Sm	5.29	3.82	3.51	3.56	3.48
Eu	0.53	0.89	0.89	0.81	0.81
Gd	4.24	3.66	3.14	3.60	3.22
Tb	0.65	0.59	0.51	0.59	0.51
Dy	3.66	3.63	3.05	3.65	2.96
Ho	0.69	0.78	0.62	0.73	0.59
Er	2.05	2.25	1.87	2.18	1.81
Tm	0.30	0.33	0.28	0.33	0.27
Yb	2.08	2.32	1.77	2.16	1.86
Lu	0.33	0.37	0.28	0.36	0.28
TOT/C	0.02	0.14	0.21	0.04	0.26
TOT/S	<0.02	<0.02	<0.02	<0.02	<0.02

Chondrite-normalized REE patterns (Figure 4-14a) present enriched samples in light rare earth elements (LREE) relative to heavy rare earth elements (HREE) in both granites. However, the OW granite shows a higher abundance of LREE and a stronger negative Eu anomaly than the NH samples. In spite of different degrees of mineral alteration, all the NH samples follow the same trend. The primitive mantle-normalized multi-element diagram (Figure 4-14b) is characterized by distinct negative anomalies for Nb and Sr and high Th and U contents, typical for upper crustal composition (Rollinson, 1993). They also show variable but high Cs, Rb and Ba contents. More generally, samples are relatively rich in large-ion lithophile elements (LILEs) such as Rb, Ba, Th and U, with Sr having the greatest depletion relative to the LILEs. High field strength elements (HFSEs) such as Ta, Nb, Zr and Hf are depleted compared to the LILEs. The OW granite shows, once again, a different trend compared to the NH samples. It has higher Th, Ta, Nb, La, Ce, Nd and Sm contents and a lower Ba content. On both diagrams of Figure 14, the sample DVB-114A (Rämö et al., 2002) shows a different pattern compared to OM\_3.

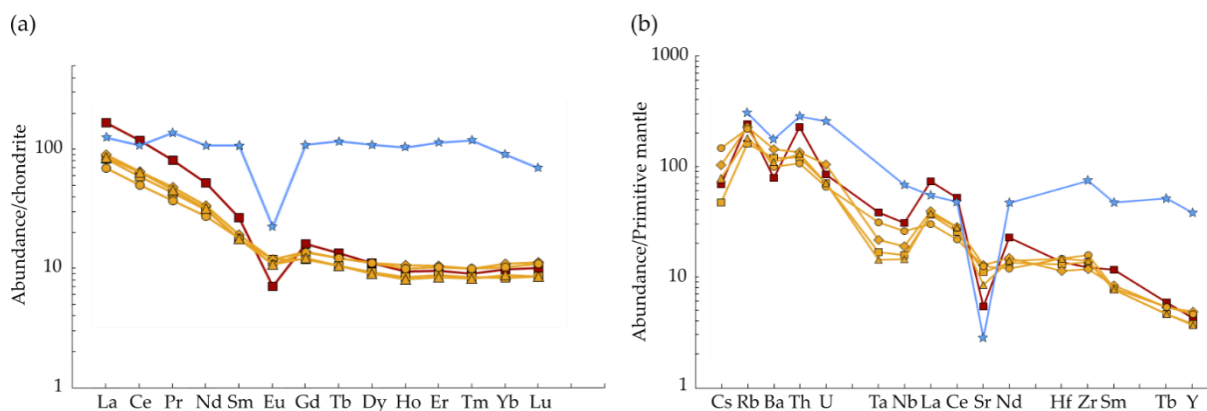


Figure 4-14. (a) Chondrite-normalized (values from [77]) rare earth element (REE) patterns of samples from the OM and the NH. (b) Primitive mantle-normalized (values from McDonough et al. (1992)'s slight revision of Sun and McDonough (1989)) multi-element diagram showing trace element patterns of samples from the OM and the NH.

### V.3. Calcimetry and Porosimetry

Calcite is present in all the samples, essentially linked to the alteration of the plagioclase. The calcite content is of 0.55% for the OM granite and ranges from 0.55 to 6.53% for the NH granite, with an average of 2.2% and a standard deviation of 1.64%. The porosity is of 2.28% for the OM granite and ranges from 2.21 to 5.17% for the NH granite. A clear positive correlation can be seen between the calcite content and the LOI (Figure 4-15a). Positive correlations are also visible between the porosity and the LOI and between the porosity and the calcite content (Figure 4-15b,c). However, the sample NH\_7 in Figure 4-15c is different. Having a low calcite content, it presents a higher porosity compared to the others. Those

diagrams show that a low LOI corresponds to a low amount of calcite and a low porosity and that a low amount of calcite fits with a low porosity except for NH\_7.

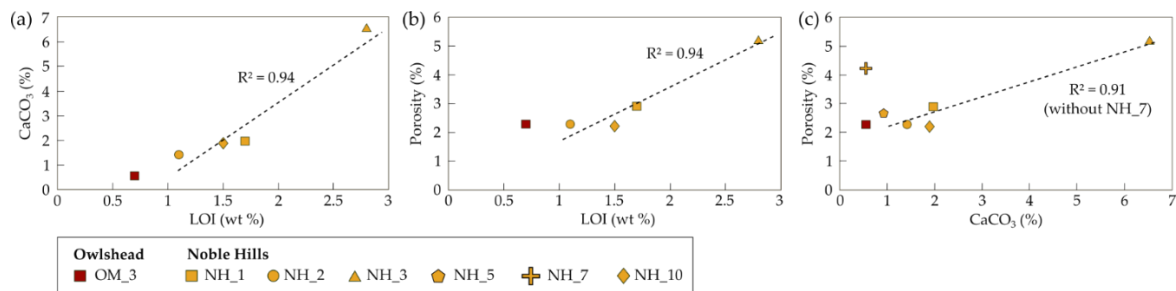


Figure 4-15. (a) Plot of the porosity versus the calcite content. (b) Plot of calcite content versus LOI (Loss on ignition). (c) Plot of porosity versus LOI.

## VI. DISCUSSION

### VI.1. Petrogenesis of the OM and NH Granites

Bulk rock analyses of the OM and NH granites indicate for both of them a calc-alkaline, monzogranite composition, S-type in character (Figure 4-11). (Rämö et al., 2002) also investigated the OM in the same batholith, but south of our sampling area (blue star in Figure 4-2a). The comparison of geochemical data from their sample with the samples studied here, shows differences in terms of chemical composition (Figure 4-7, Figure 4-11, Figure 4-12 and Figure 4-14). The OM seems to be a heterogeneous pluton.

Chondrite-normalized REE patterns for the NH granite samples show the same trend (Figure 4-14a), but are different from the OM granite one. REE are relatively immobile during low-grade metamorphism and hydrothermal alteration (Rollinson, 1993). The enrichment of the LREE and the depletion of Eu indicate the degree of magmatic differentiation the rock underwent. The Eu negative anomaly is attributed to the plagioclase fractionation involved in the setting of granites (Koljonen and Rosenberg, 1974). However, the breakdown of plagioclase and biotite can release some REE except Eu, which can be accommodated by illite formation (Alderton et al., 1980).

The same observations were done through the primitive mantle-normalized spider diagrams, which shows variations in Ta and Nb contents of the NH samples (Figure 4-14b). Those variations are in good correlation with the LOI: the higher the LOI, the lower the Nb and Ta contents. Li et al. (2013) observed Nb/Ta ratios in altered domains in granitic rocks due to the Nb and Ta decreasing content during the illitization stage. The LOI is directly related to the percentage of alteration, the same phenomenon is observed in our samples. The depletion of

Sr in the NH granite might be due to the alteration of magmatic primary plagioclase (Li et al., 2013). However, Sr content in OM is relatively low.

Those diagrams show and confirm the difference in terms of chemical composition between the NH and the OM, which was suspected during thin sections observations. A comparison between our own chemical data within the OM and the data presented by Rämö et al. (2002) show substantial differences meaning that the OM granite is not homogeneous. Given the fact that the NH granite is considered as a transported part of the OM (Pavlis and Trullenque, 2021), it is therefore not surprising that the NH granite presents local composition variations. The OM samples are considered as representing the protolith prior to the mineral transformations identified in the NH granite.

Microcline was identified in the OM granite and only in the southern part of the NH indicating that this part of the range might have undergone a slower cooling than the northern part of the range or a warming.

## VI.2. Thermal Evolution of the NH Granite

Petrographic investigations have shown that plagioclase and sometimes biotite are replaced by illite. A recent study from Warr and Cox (2016) has confirmed that IC provides a useful method for characterizing regional grades of diagenesis and low-grade metamorphism. As already mentioned, in some conditions the alteration of a granite, resulting from fluid circulation, shows similarities with diagenetic reactions present in feldspathic sandstones (Ledéseret et al., 1999), meaning that it is possible to characterize a regional grade by using the KI values obtained in granitic rocks.

As shown in Figure 4-2, the NH range is a structure stretched NW-SE. The KI values display a trend following this direction with decreasing values towards the south-east (Figure 4-10). KI values can be associated to different metamorphic zones corresponding to ranges of temperature (Table 4-1, (Abad, 2007)). The northwestern part of the range, characterized by high KI values, reveals mostly low-grade diagenesis tending progressively to high-grade diagenesis roughly toward the SE. A decrease of KI values indicates an increase in temperature (Merriman and Frey, 1998). Thus, this tendency reflects a temperature gradient increasing from the NW toward the SE. The elevation being higher in the south-east, with a higher temperature in this zone might indicate that the southern part of the range was more buried than the rest of the range and has been exhumed. A northeast-vergent contractional deformation is well expressed along the NH range in addition to the strike-slip deformation. It increases in intensity

where the NH range converges with the Avawatz mountains ((Niles, 2016) and references therein), at the intersection between the SDVFZ and the GFZ (Brady et al., 1989). Chabani et al. (2021) have identified E-W structures in this area and they suppose that these structures are linked to the activity of the GFZ and the convergence of the Avawatz and the NH range. It is tempting to propose that this convergence implied the elevation of the topography at the southern part of the NH range. A work is in progress about exhumation history reconstruction by means of isotopic dating.

### VI.3. Alteration Parageneses

The OM and NH granites characterization reveals the presence of various secondary minerals as oxides, epidote, corrensite, K-white mica, calcite, kaolinite, illite/smectite mixed-layer and montmorillonite. Those minerals are well known as being the product of alteration processes due to the interaction of a circulating fluid with the surrounding rock. They are in equilibrium with the new environment in response to temperature, pressure and composition of the altering fluid (Creasey, 1966; Fulignati, 2020; Nishimoto and Yoshida, 2010; Traineau et al., 1991). In the OM and the NH granites, only plagioclase and biotite are affected. In the case of intense circulation, some primary minerals like plagioclase or biotite may be completely replaced. The newly formed minerals consist mainly in clay minerals (Inoue, 1995). According to optical observations, SEM-EDS and XRD analyses, two types of alteration processes have been identified in the OM and NH granites which are classified as (1) propylitic alteration and (2) argillic alteration. The characterization of the paragenesis and the alteration processes of the granites investigated in this study help to refine a part of the history of the OM and NH granitic basements (Figure 4-16).

PARAGENESIS	IGNEOUS STAGE	PROPYLITIC ALTERATION	ARGILLIC ALTERATION
Quartz	-----		
K-feldspar	-----		
Plagioclase	-----		
Biotite	-----		
Oxide 1	-----		
Corrensite		-----	
Epidote		-----	
K-white micas			-----
Calcite			-----
Kaolinite			-----
Illite/Smectite			-----
Oxide 2			-----

Figure 4-16. Paragenesis sequence and alteration evolution in the OM and NH granite.

### VI.3.1. Propylitic Alteration

The newly formed minerals depend on the composition of the host mineral. Corrensite, epidote, K-white micas, calcite and iron oxides were identified in the OM and NH granites (Figure 4-16) by means of optical observations, SEM-EDS and XRD analyses:

1. The calcite as in the OM granite occurs as infills of the microcracks without interacting with the surrounding rock, as well as at grain boundaries.
2. Mixed-layer clay minerals are the intermediate products of reactions involving end-member clays (Środoń, 1999). Corrensite, a chlorite/trioctahedral smectite mixed-layer phyllosilicate is considered as a stable mineral and also as an indicator of propylitic alteration (Burnham, 1962; Genter, 1989; Traineau et al., 1991). It replaces partially biotite and occurs between 160–250 °C in geothermal fields (Fulignati, 2020; Nishimoto and Yoshida, 2010; Velde, 1977).
3. Epidote crystallization occurs around 220 °C (Traineau et al., 1991). It is also one major indicator of the propylitic alteration with corrensite (Burnham, 1962).
4. The presence of K-white mica flakes allows to fix temperatures around 230 °C up to 350 °C (Fulignati, 2020; Steiner, 1968).

All those secondary minerals occur at temperatures between approximately 160 °C and 350 °C. The presence of corrensite and epidote is the major indicator of a stage of propylitic alteration. The propylitic alteration (Figure 17b) is considered as an earlier pervasive alteration stage. It is common at the margins of alteration zones produced at low fluid/rock ratio (Nishimoto and Yoshida, 2010) and it takes place at the end of the crystallization of the granite (Ledésert et al., 2010). The propylitic alteration results in the partial recrystallization of primary minerals (biotite and plagioclase) in secondary propylitic assemblages by interstitial fluids trapped into the grain boundaries during the cooling of the pluton (Genter, 1989). Its effects are discrete, but both the OM and NH massifs are affected.

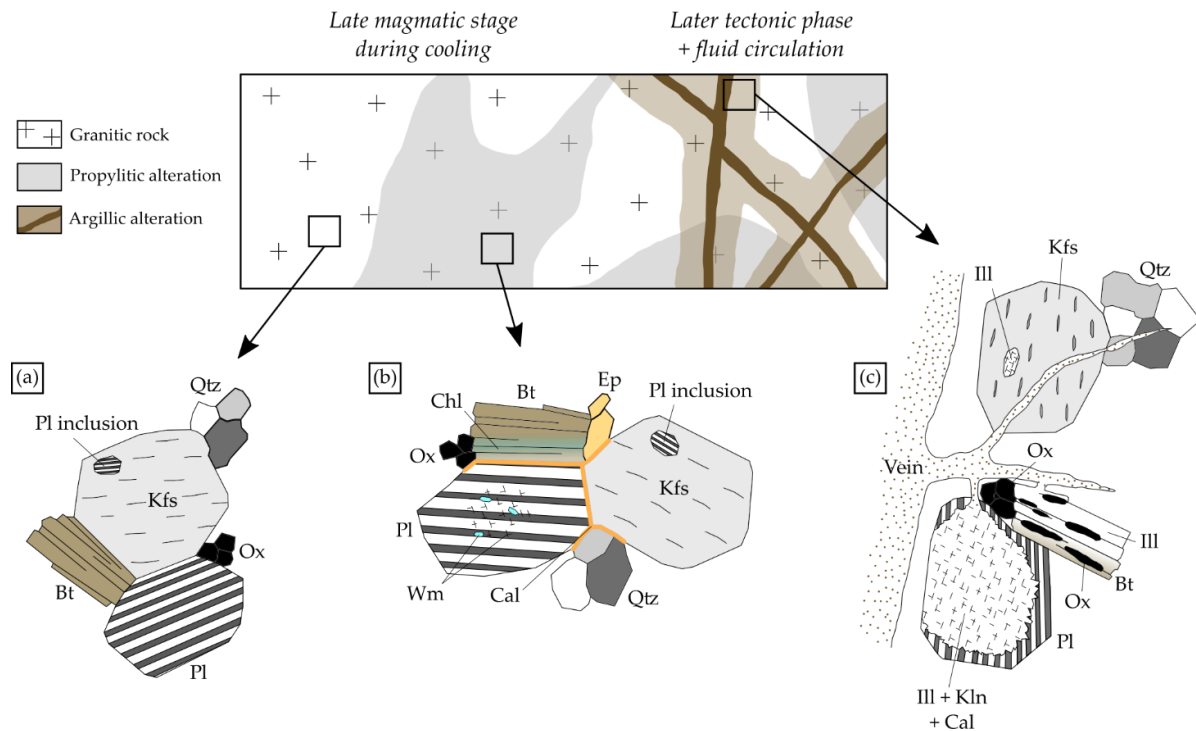


Figure 4-17. Schematic representation of the different alteration processes which can be observed in the OM and NH granites. (a) Fresh granite non-affected by alteration. (b) Granite affected by the propylitic alteration showing the slight chloritization of biotite and the crystallization of K-white micas in the core of plagioclase. (c) Granite affected by the argillic alteration and localized along fractures where fluid has circulated. Biotite are locally completely transformed into illite and plagioclase into illite, calcite and/or kaolinite. Perthites and inclusions in K-feldspars can also be altered. Abbreviations (except for “Ox and Wm”) after Kretz (1983): Bt–Biotite, Cal–Calcite, Chl–Chlorite, Ep–Epidote, Ill–Illite, Kln–Kaolinite, Kfs–K-feldspar, Ox–Oxide, Pl–Plagioclase, Qtz–Quartz, Wm–K-white mica.

### VI.3.2. Argillic Alteration

Other newly formed mineral assemblages were identified only in the NH granite. They consist in illite + kaolinite + mixed-layers as illite/smectite (I/S) + calcite and oxide (Figure 4-16):

1. Illitic minerals are well known to be indicators of fluid circulation as well as paleo-circulation systems (Vidal et al., 2018). (Ledésert et al., 1999; Ledésert and Hébert, 2020) show that illite crystallization episodes can occur, for example, in a temperature range of 120 to 160 °C, corresponding to the argillic alteration facies. The illitization process mainly develops in plagioclase and biotite. It is a form of alteration product found extensively in granitoids, and felsic rocks, whereas K-feldspar remains relatively unaltered (Creasey, 1966; Plummer and Putnis, 2009; Que and Allen, 1996).
2. According to Fulignati (2020), the presence of kaolinite in alteration paragenesis indicates a fluid temperature lower than 200–150 °C. Kaolinite is stable under more acidic conditions than illite, with pH values ranging from about 4.5 to 6. It also

represents a more advanced product of hydrolysis reaction due to a high  $H^+$  activity in hydrothermal fluids.

3. The illite-rich (R3) I/S mixed-layer form around 150 °C (Fulignati, 2020; Środoń, 1999), with more than 90% of illite based on Moore and Reynolds (1989).
4. Plagioclase, oligoclase in composition, presents patches of calcite. Those patches are interpreted as a product of Ca release due to plagioclase alteration.
5. Oxides can be present along the cleavages of the altered biotite. They are interpreted as the result of Mg and Fe release during biotite alteration.

Plagioclase and quartz form an interconnected skeleton through the texture. The difference of physical and chemical behaviors between both minerals results in different types of porosity. Quartz shows microcracks and plagioclase shows dissolution pits (Figure 4-18). Sardini et al. (1997) observed the same in the Soultz-sous-Forêts granite. They also showed that the exchange surface between plagioclase and a fluid is around 20 times higher than in quartz. As a consequence, they assume that all the pores are interconnected in plagioclase. They considered this mineral as the main path for fluid flow. Thus, this can be also available in the NH granite. K-feldspar is not affected by the alteration, but perthites and mineral inclusions present in the K-feldspars can be dissolved.

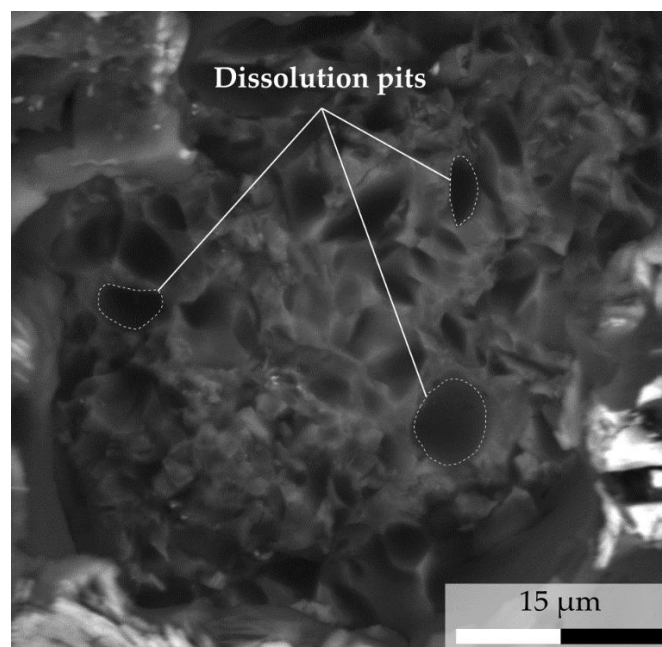


Figure 4-18. Back-scattered image showing a magnified view of plagioclase dissolution pits under SEM (15 kV 5.3 mm x 1.7 k BSECOMP).

The crystallization of these minerals occurs at temperature between 130 and 200 °C. This range of temperature corresponds to the stage of argillic alteration (Fulignati, 2020). The argillic

alteration (Figure 4-17c) consists into the chemical leaching and clay enrichment processes produced at lower temperatures (Genter, 1989; Glaas et al., 2021; Ledésert et al., 1999). This alteration is known as a vein alteration organized in the vicinity of fractures where fluids have circulated (Genter, 1989; Traineau et al., 1991).

### VI.3.3. Evidences of Weathering

XRD analyses on an oriented sample of the clay fraction from the OM reveal the presence of Montmorillonite (Mnt) (Figure 4-8). Mnt, a common smectite pattern, results either from argillic (vein) alteration (Burnham, 1962; Fulignati, 2020) or from weathering (Meunier et al., 1983; Tardy et al., 1970). As described above, the OM granite appears as “fresh” from (1) field observations: no veins were observed at outcrop scale and macro-scale and the granite appears competent, (2) thin-section analyzes: no veins or veinlets, calcite crystallizations are only present at grain boundaries, and (3) geochemical analyzes, which indicate a very low LOI (0.7 wt.%). No vein was observed at any scale and secondary minerals are all characteristic of propylitic alteration. Those data show that the Mnt cannot result from argillic alteration. In the case of the OM granite, the Mnt is interpreted as a signature of weathering. As its amount is low (15% of the clay fraction), the global alteration of the granite is considered as being dominated by the propylitic alteration. With the OM being considered as the protolith, weathering can be considered negligible in both OM and NH granites.

### VI.3.4. Alteration Stage Occurrences

The OM granite presents evidence of propylitic alteration only, while the NH granite presents both propylitic and argillic facies. The argillic facies seems most of the time to overprinting the propylitic facies. However, some samples present only evidence of argillic alteration. In those cases, either the propylitic facies have either completely disappeared, or some zones were not initially affected by the propylitic alteration. Some minerals, such as illite and kaolinite, crystallize during the argillic alteration under different conditions (Fulignati, 2020). This suggests that several episodes of alteration could have occurred in the NH granite. Afterward, weathering can occur at ambient temperature, when the granite was exhumed. These alteration overprints result also in a retrograde evolution in terms of temperature (T) with  $T_{\text{propylitic}} > T_{\text{argillic}} > T_{\text{weathering}}$ .

In the NH granite, the argillic alteration seems to be associated to fracturing. A fresh granitic rock is not permeable enough to allow fluid circulation (Nishimoto and Yoshida, 2010). This suggests that the development of fractures is an important factor allowing fluid to circulate

(Nishimoto and Yoshida, 2010), the observation that the freshest NH granite is more altered than the one from the OM (Figure 4-3) can be related to the fact that the NH lie along an important shear corridor. None of NH samples considered in the present study are fracture free, even though they were collected far from the faults, and each of them shows evidences of argillic alteration. In spite of the low fracture density the existing number of microfractures is enough to allow fluid to significantly percolate through the host rocks and chemically interact with it. A second paper (PART 2, this issue) focusses on the role of the fracture system on the granite alteration processes.

#### VI.4. Effects of Alteration on Petrographic and Petrophysical Behaviour

Petrographic observations and the range of LOI (0.7–4.1 wt.%) values confirm that the NH granite experienced alteration. LOI is so directly related to the degree of mineral alteration as done by Chambefort et al. (2007) and Liu et al. (2018). Mineral changes being related to the propylitic and argillic alterations, the LOI can be defined in this study as a monitor for alteration processes. The effects of alteration on element transfers can be evaluated thanks to the diagrams plotting  $\text{SiO}_2$ ,  $\text{Al}_2\text{O}_3$ ,  $\text{CaO}$ ,  $\text{K}_2\text{O}$ ,  $\text{Na}_2\text{O}$  and  $\text{MgO}$  against LOI (Figure 4-13). In Figure 13, the  $\text{K}_2\text{O}$ ,  $\text{Na}_2\text{O}$ ,  $\text{CaO}$  and  $\text{MgO}$  define a broad correlation with LOI, indicating that they may have been mobile during alteration (Liu et al., 2018). The NH granite shows that  $\text{Na}_2\text{O}$  and  $\text{CaO}$  have a negative correlation which can be related to the alteration of the plagioclase (oligoclase initial composition). Indeed, plagioclase can be depleted in Na and Ca mobile elements when it interacts with a fluid (Garrels and MacKenzie, 1967). Likewise, the  $\text{K}_2\text{O}$  is observed in alteration products of plagioclase as illite and shows an enrichment with the LOI increase. Newly formed minerals, as presented above, are related to the recrystallization of the plagioclase as a result of its interaction with the fluid. As for the  $\text{CaO}$  and  $\text{MgO}$  contents, they remain high compared to the OM granite. This can be linked to an external contribution. In a whole, the NH granite was affected by an alkali alteration, which results in major compositional changes. Thus, all the elements, Si and Al excepted, have partly left the system, meaning that the system is open. Their content differences in the NH granite compared to the OM granite could be explained by the depletion of the most mobile elements during the alteration of the NH granite. This can so influence the percentage of each element. Otherwise, it can be suggested that the visible variations of  $\text{SiO}_2$  and  $\text{Al}_2\text{O}_3$  were controlled by protolith composition rather than alteration processes.

Link alteration degree and amount of calcite is difficult since petrographic analyses of the samples is qualitative. However, Figure 4-15a shows a positive correlation between LOI and

calcite content. Ledésert et al. (2009) show that calcite can be encountered in high amount in altered zones. Thus, in the NH, the correlation shows that the higher the calcite content, the higher the degree of alteration and vice versa. In the same way, LOI can be related to porosity (Figure 4-15b) with a low LOI linked to low porosity (NH\_1, NH\_2 and NH\_10) and high LOI linked to as high porosity (NH\_3). Therefore, the increase of porosity is also linked to the increase of alteration. Studies (Cassiaux et al., 2006; Rosener and Géraud, 2007) showed that the porosity increases from unaltered to altered granite. Figure 4-15c shows a similar correlation between the calcite content and the porosity. Samples having a low calcite content (NH1, NH\_2, NH\_5 and NH\_10) present a low porosity, while NH\_3 has a high calcite content associated with a high porosity. One exception can be observed. The sample NH\_7 presents a low calcite content for a high porosity. This can be explained by the presence of larger microfractures compared to the other samples, which increase the porosity. Thus, it is not always possible to link the porosity to the calcite content. According to White et al. (2005), the average calcite content of a fresh granite is 0.252 wt.%, and does not exceed 1.8 wt.%. As a consequence, measurements over this last value can be regarded as a calcite anomaly, and so are representative of a granite affected by argillic alteration, which may be a sign of paleo fluid flow (Ledésert and Hébert, 2020). Ten samples out of fifteen from the NH have a calcite content higher than 1.8 wt.%. This suggests that the OM and some zones of the NH were not affected by the argillic alteration, but only by the propylitic one. By considering the calcite content average of 2.2% for the NH, those data also indicate that even if the samples were collected far from the major faults, the granite can be affected by argillic alteration.

### VI.5. The NH: A Paleo-Geothermal Reservoir?

In the present contribution we have given numerous pieces of evidences for a pervasive alteration of the NH granite. Ubiquitous argillic alteration affecting plagioclase and biotite is present. The K-feldspar being unaltered, potassium enrichment by incoming fluids is necessary to produce abundant amount of illite. The high concentration of calcite, in some samples, requires an external input of Ca, which cannot come only from the plagioclase alteration. Due to this alteration, the rock porosity was drastically enhanced by dissolution of the plagioclase. Porosity is also enhanced by the microfracturing well visible in quartz and K-feldspar, which is related to the activity of the SDVFZ. It is believed that this microfracturing drastically enhanced interaction surfaces between minerals and fluids allowing chemical elements exchanges between hydrothermal fluids and the granite. The strain is not homogeneously distributed in the NH. The NH granite is affected either by non-localized deformation (samples from this

study) or by strain concentrations along fault zones that will be presented in the accompanying contribution (PART 2, this issue).

Our results have shown that an alteration of vast volumes of rocks is thus possible, even outside localized high strain zones. All these data are in favor of a hydrothermal fluid percolation, which is encountered in an exploited geothermal reservoir (Ledésert et al., 1999; Nishimoto and Yoshida, 2010). A geothermal reservoir consisting into a flow system where a high amount of hot fluid is stored and circulates through the rock, and our results encourage to consider the NH as a paleo-geothermal reservoir.

## VII. CONCLUSIONS

The NH were chosen in the framework of the H2020 MEET project as being an opportunity to characterize a granitic paleo-geothermal reservoir in a trans-tensional context. Arid conditions and a 3D exposure were important criteria allowing the thorough characterization of the granite. The aim of this study was to characterize the granite pervasive alteration processes, away from the fractures, in terms of changes of mineralogical, geochemical and related petrophysical properties.

Illite was identified by XRD in all the NH samples, allowing to obtain KI values which revealed a NW-SE temperature gradient through the range. This gradient might be considered as a sign of a possible exhumation of the southern part of the range due to the interaction with the Avawatz Mountains.

The partial recrystallization of plagioclase and biotite into newly formed minerals, due to fluid/rock interactions, was identified as reflecting three types of alteration:

1. A pervasive propylitic alteration. This alteration is present in the OM granite (the freshest one considered as the protolith) and in the NH granite and characterized by the presence of corrensite and/or epidote.
2. A local argillic alteration. This alteration was identified only locally in the NH granite by the occurrence of clay minerals such as kaolinite, illite/smectite mixed-layers and illite, all of which crystallize at a lower temperature than the propylitic alteration. Kaolinite and illite might reflect a different amount of leaching or different pH, meaning that several fluids have circulated.
3. Weathering identified in the OM granite by the presence of montmorillonite, thus formed at surface temperature.

The NH granite alteration was highlighted by optical observations. In addition, geochemistry also provided data to support them. Indeed, depletion of Na and Ca was observed with the increase of LOI, considered as a good indicator of the amount of alteration of plagioclase alteration. At the same time, K enrichment was observed with the increase of LOI, and linked to illite crystallization. Calcimetry performed on the NH granite samples showed a calcite content often higher than the 1.8% value, admitted as being the maximum in a fresh granite. These values tend to increase with the LOI, confirming that the NH granite underwent alteration. Porosity also shows a positive correlation with the LOI indicating that the porosity increases with the amount of alteration. However, its correlation with the calcite content is less obvious, as calcite might crystallize in the porosity and thus reduce it.

The NH granite underwent up to two stages of alteration before being exposed to surface conditions, showing a retrograde evolution. It was observed petrographically that the argillic alteration overprinted the propylitic alteration, until its signature is lost. The weathering signal is low (~15% of the clay fraction) and considered as negligible in the OM. The OM being considered as the protolith of the NH, the contribution of weathering is also considered as negligible in the NH granite, where no montmorillonite was found. The newly formed minerals are thus considered as being the product of hydrothermal alteration and not of weathering.

This study provides multiple evidence allowing the consideration of the NH granite as a paleo-geothermal reservoir.

The activity of a geothermal reservoir is a combination of pervasive circulation within nearly strain-free zones (as shown in the present contribution), as well as fractured domains where high strain is accumulated. Our study is therefore completed by a PART 2 (this issue), in which the same investigation approach is dedicated to samples taken within visibly fractured zones.

## VIII. ACKNOWLEDGMENTS

This manuscript was prepared as a contribution to the PhD thesis (Institut Polytechnique UniLaSalle Beauvais) of Johanne Klee, which was funded by the European Union's Horizon 2020 research and innovation program under grant agreement No 792037 (H2020 MEET project). The authors are grateful to Terry Pavlis for his knowledge and helpful discussions about the regional geology of Death Valley and the Noble Hills. We also acknowledge Albert Genter for the fruitful exchanges about granite alteration processes. We thank Thi Tuyen Nguyen, Elena Pavlovskaja, Carl Tixier and Chloé Gindrat for their help for analyses. Helpful comments and the validation of the manuscript by the H2020 MEET consortium are gratefully

acknowledged. We finally would like to thank Catherine Lerouge and the anonymous reviewer for their help and remarks to improve this manuscript.

# CHAPTER 5

## Fluid-Rock Interactions in a Paleo-Geothermal Reservoir (Noble Hills Granite, California, USA).

### Part 2: The Influence of Fracturing on Granite Alteration Processes and Fluid Circulation at Low to Moderate Regional Strain

---

This chapter is a published contribution to the *Geosciences Journal*, in the 2021 special issue “Enhanced Geothermal Systems and other Deep Geothermal Applications throughout Europe: The MEET Project”.

The published version is available at the following link:

<https://doi.org/10.3390/geosciences11110433>

**Keywords:** Fracturing processes, fluid circulation, granite alteration, low to moderate regional strain, geothermal reservoir

# Fluid-Rock Interactions in a Paleo-Geothermal Reservoir (Noble Hills Granite, California, USA). Part 2: The Influence of Fracturing on Granite Alteration Processes and Fluid Circulation at Low to Moderate Regional Strain

Johanne Klee <sup>1,\*</sup>, Arezki Chabani<sup>1</sup>, Béatrice A. Ledésert<sup>2</sup>, Sébastien Potel<sup>1</sup>, Ronan L. Hébert<sup>2</sup> and Ghislain Trullenque<sup>1</sup>

<sup>1</sup>B2R, Geosciences Department, Institut Polytechnique UniLaSalle Beauvais, 19 Rue Pierre Waguët, F-60026 Beauvais, France; arezki.chabani@unilasalle.fr (A.C.); sebastien.potel@unilasalle.fr (S.P.); ghislain.trullenque@unilasalle.fr (G.T.)

<sup>2</sup>Geosciences and Environment Cergy, CY Cergy Paris Université, 1 Rue Descartes, F-95000 Neuville-sur-Oise, France; beatrice.ledesert@cyu.fr (B.A.L.); ronan.hebert@cyu.fr (R.L.H.)

## I. ABSTRACT

Fracture connectivity within fractured granitic basement geothermal reservoirs is an important factor controlling their permeability. This study aims to improve the understanding of fluid-rock interaction processes at low to moderate regional strain. The Noble Hills range (Death Valley, CA, USA) was chosen as a naturally exhumed paleo geothermal reservoir. A series of petrographic, petrophysical and geochemical investigations combined with a fracture distribution analysis are carried out on samples collected across fracture zones. Our results indicate that several generations of fluids have percolated through the reservoir. An increase of (1) the alteration degree, (2) the porosity values and (3) the calcite content is observed when approaching fracture zones. No correlation was identified either between the alteration degree, or the porosity, or the calcite content. At local scale, samples showed that the degree of alteration does not necessarily depend either on fracture density, or on amount of strain. It is concluded that combined influence of strain and coeval fluid-rock interaction processes drastically influence the petrophysical properties of fracture zones, which in turn impacts geothermal production potential.

## II. INTRODUCTION

Long term exploitation of geothermal resources is closely linked to reservoir rock petrophysical properties and regional geological setting (Williams et al., 2011). Due to the low matrix porosity and permeability of granitic rocks, underground granitic units are considered as a reservoir only when fractures are present. These fractures provide the essential reservoir permeability and

porosity for fluid flow (Gentier et al., 2000; Gillespie et al., 2020) and are therefore of primary importance regarding geothermal exploitation (Bauer et al., 2015; Callahan et al., 2019; Curewitz and Karson, 1997; Dezayes and Lerouge, 2019b; Vidal and Genter, 2018). These structures control the deep flow at the reservoir scale, in case of a good connectivity (Faulkner et al., 2010; Gentier et al., 2000; Géraud et al., 2010, 2005; Gillespie et al., 2020), which is one of the most important controls on the permeability (Long and Witherspoon, 1985). Several granitic reservoirs, as Soultz-sous-Forêts in the Upper Rhine Graben, France (Ledésert et al., 2010; Vidal and Genter, 2018) or the Cooper Basin in Australia (Kuncoro, 2015), give invaluable experience in terms of exploration and exploitation feedback. In addition to these datasets gained from data limited to boreholes and indirect geophysical methods, studies of surface reservoir analogues are common (Dalmais et al., 2019; Dezayes et al., 2021; Turpault et al., 1992). The MEET H2020 project (Multidisciplinary and multi-context demonstration of EGS exploration and Exploitation Techniques and potentials) (Trullenque et al., 2018) aims at developing Enhanced Geothermal Systems throughout Europe. Within this project, the Noble Hills (NH) range, located in the southern termination of the Death Valley (DV, California, USA), has been chosen as an analogue of fractured granitic basements in a context of transtensional deformation (Klee et al., 2021a). Klee et al. (2021a) highlighted numerous evidences of hydrothermal alterations: (1) a propylitic alteration affecting pervasively a large volume of rock during the cooling of the pluton and (2) an argillic alteration, also called vein alteration (Genter, 1989; Klee et al., 2021a; Ledésert et al., 1999; Meunier, 1995; Traineau et al., 1991), inducing changes of the bulk-rock chemical and mineralogical compositions and of physical properties (Bonorino, 1959; Callahan et al., 2019).

A vast amount of literature (Caine et al., 2010; Faulkner et al., 2010; Géraud et al., 2010) has proven that increasing amounts of strain within fault zones drastically change their petrophysical properties. The present paper focuses on the influence of fractures on the fluid circulation and alteration processes at low to moderate regional strain.

The present study aims at:

1. A characterization of the relation between varying amounts of strain, fracture density and alteration degree at the NH scale, as well as sample scale through case studies.
2. A characterization of variations in (1) chemical elements concentration, (2) calcite content, (3) porosity and (4) temperature conditions variations when approaching fracture zones.
3. An identification of different fluid circulation episodes through the granite body.

Macroscopic and microscopic petrographic studies, XRD mineralogical characterization of whole rock and clay minerals, bulk rock chemical analyses by Inductively Coupled Plasma (ICP) – Mass Spectrometry (MS) and – Atomic Emission Spectrometry (AES), Scanning Electron Microscopy coupled with Energy Dispersive Spectrometry (SEM-EDS) for structural observation and local chemical analyses, mass balance calculations, fracture density calculations, calcimetry and porosimetry were performed on samples collected in the vicinity of fracture zones within areas of the NH affected by low to moderate regional transcurrent strain. The results will be discussed and compared with the protolith studied by (Klee et al., 2021a).

### III. GEOLOGICAL SETTING

The Death Valley (DV, Figure 5-1a) is located in the core of a Cenozoic distributed system of dextral strike-slips about 700 km long comprising the Walker Lane Belt and the Eastern California Shear Zone (ECSZ/WLB) (Dokka and Travis, 1990; Lifton et al., 2013; Norton, 2011; Stewart and Ernst, 1988). This narrow northwest-trending system, lying between the Basin and Range region to the east and the Sierra Nevada batholith to the west (Stewart and Ernst, 1988), accommodates today ~25% of the Pacific-North America relative motion (Miller et al., 2001; Norton, 2011). DV is a structural depression, NNW-SSE oriented, bounded by the Black and Funeral Mountains to the west and by the Panamint Range to the east (Hill and Troxel, 1966). It has been formed by a right-lateral movement giving a pull-apart structure (Burchfiel and Stewart, 1966).

The area of interest for this study is the Noble Hills range (NH, Figure 5-1b). It is located in the southernmost part of the DV region and trends parallel to the NW-striking SDVFZ at its southern end. Geological markers along the SDVFZ trace, Pavlis and Trullenque (2021) suggest that the NH correspond to a transported fragment of the frontal part of the Owlshead Mountains (OM) a Cretaceous (~95 Ma, (Rämö et al., 2002)) granitic pluton at a 40-41 km distance to the SE. Several attempts have been made and discussed in the literature to give insights on the geological setting of the NH and structural relationships between SDVFZ and GFZ (Chinn, 2013; Reinert, 2004; Spencer, 1990). A particular emphasis has been given to detailed description of sedimentary sequence deposits on each side of the NH Crystalline Bedrock Slice (CBS) (Brady, 1984; Niles, 2016). The CBS is composed of Proterozoic sediments with upward younging direction the Crystal Spring (CS) quartzite, CS dolomite, detrital flysch and carbonate sequences possibly part of the Parhump group, intruded by 1.1 Ga diabase sills, the whole intruded by Mesozoic granite (Troxel and Butler, 1979). However, a detailed structural analysis of the CBS itself is missing. Thus, Section V.1 of this

study will give new elements improving the observations made by Klee et al. (2020) and Niles (2016) concerning the NH structure. A precise fracture patterns characterization of the NH was performed by Chabani et al. (2021), through a wide-ranging analysis scale from the microscopic scale to the regional scale. These authors showed that the NH fracture network geometry has been controlled by the SDVFZ and the GFZ.

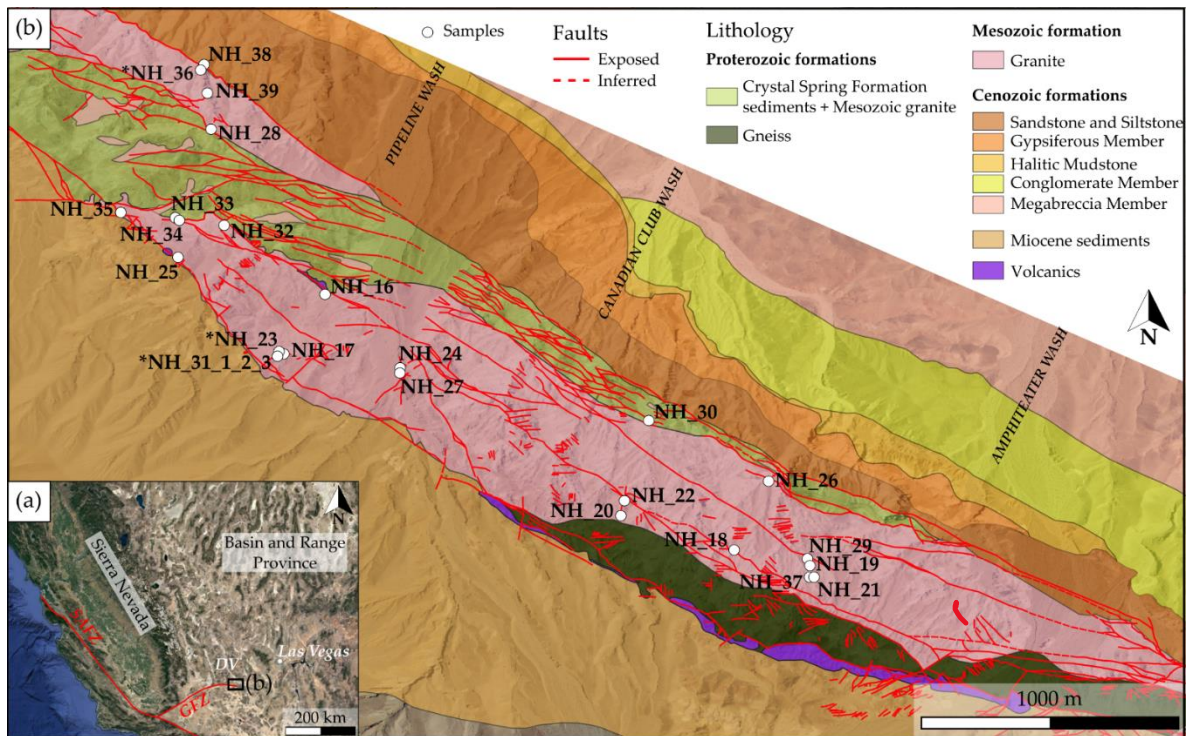


Figure 5-1. (a) Location of the Noble Hills on the western USA satellite map. SAFZ – San Andreas Fault Zone, GFZ – Garlock Fault Zone and DV – Death Valley. (b) The geological map of the Noble Hills range, modified after Klee et al. (2020), Niles (2016) and Klee et al. (2021a). The quaternary is not displayed but available on the map provided by Niles (2016). Sample locations are represented by the white dots. The asterisk shows the samples used as case studies in this work. NHF – Noble Hills Formation.

The NH granite was poorly studied in terms of microstructure, petrography and geochemistry. A recent study conducted by Klee et al. (2021a) characterized the granite as a leucocratic equigranular monzogranite (S-type), ranging in the high-K calc-alkaline and peraluminous domains. The NH granite is composed of primary plagioclase, quartz, K-feldspar and biotite. Klee et al. (2021a) also have shown that the NH granite underwent two alteration stages forming secondary minerals that recorded the chemical and paleo-thermal conditions of the system: (1) a pervasive, propylitic alteration linked to the cooling of the pluton and (2) a more local alteration corresponding to the argillic alteration (illitization and sometimes kaolinitization) which overprints the propylitic alteration. Among the primary minerals, optical observations and geochemical data show that only plagioclase and biotite are affected by those alteration processes.

## IV. MATERIALS AND METHODS

### IV.1. Material and Sample selection

Digital field mapping techniques have been used in the field, these include the use of portable rugged tablet laptop with internal GPS. The QGIS software has been used for sample location, geological digitization and structural data acquisition. Georeferenced topographic maps and ortho-imagery were the initial input of the database.

A detailed petrographic, mineralogical, geochemical and petrophysical characterization was conducted on 25 samples from the NH granite, based on fieldwork and laboratory analyses.

Samples were selected by targeting fracture zones located in CBS areas that have been affected by low to moderate strain. It aims to characterize the influence of fracturing on fluid circulations and the associated argillic alteration, mentioned only by Klee et al. (2021a) until now. Thus, the collected samples consist of altered granite presenting open fractures, veins, reactivated veins and breccias. All the samples are georeferenced for precise location as well as database supply (Figure 5-1c). The selection took into account ranges of fracture density ( $F_d$ ) defined by Klee et al. (2021a) from scanlines realized on thin sections, based on Castaing and Rabu (1981):

$F_d 0 < 1687$  fracs/m – no to very low microfracturing,

$F_d 1 = 1687$  fracs/m – microfracturing of order less than the grain size,

$F_d 2 = 2694$  fracs/m, with a multiplier factor of 1.6 compared to  $F_d 1$  – microfracturing of grain size order with interconnections,

$F_d 3 = 3549$  fracs/m, with a multiplier factor of 1.3 compared to  $F_d 2$  – abundant microfracturing,

$F_d 4 \geq 5140$  fracs/m ((Chabani et al., 2021) this issue), with a multiplier factor of 1.4 compared to  $F_d 3$  – very abundant microfracturing,

Samples selected for this study have a fracture density higher than 2694 fracs/m meaning they fall into categories from  $F_d 2$  to  $F_d 4$ .  $F_d 4$  corresponds to highly strained zones in which granite becomes a breccia. In order to correlate the fracture density with the amount of alteration, 3 hand specimens and 7 thin sections, located in the granite body, are used for fracture extraction and analysis. These fracture characterizations are based on the scanline method, described in section 3.1. Data from Chabani et al. (2021) (this issue) will be used to complete the characterization.

## IV.2. Methods

### IV.2.1. Fracture Network Parameters

Fracture networks can be characterized by their spatial arrangement (Laubach et al., 2018). The fracture network geometry is used to predict fluid circulation (Laubach et al., 2018) and evidence of structural growth processes (Olson, 1993). Spacing measurements through the 1D-scanline method are widely used to characterize arrangements (Bisdorn et al., 2014; Gillespie et al., 1993; Priest and Hudson, 1976; Sanderson and Peacock, 2019). It consists in the digitization of fractures along those lines, in order to calculate the linear fracture density  $P_{10}$  characterized by the number of fractures per length calculated along the scanline (Bisdorn et al., 2014; Gillespie et al., 1993). The Terzaghi correction has been applied (Terzaghi, 1965). Two parallel scanlines were performed on the hand specimens, perpendicular to a major fracture. For each oriented thin section mosaic, two scanlines were realized perpendicular to the main structures. For each scanline, stick plots and cumulative frequency diagrams were realized to describe the fractures spatial distribution (Sanderson and Peacock, 2019). A coefficient of variation  $C_v$  was computed for each scanline in order to quantify the fracture distribution (Gillespie et al., 1993):  $C_v < 1$  indicates a regular fracture spacing,  $C_v \sim 1$  indicates a random distribution and  $C_v > 1$  indicates a clustered distribution. Fracture density data obtained by Chabani et al. (2021) on selected samples will be used in this study.

### IV.2.2. Petrographic Characterization

Twenty-four samples were selected to prepare 31 covered and polished thin sections, for petrographic observations. Optical microscopy is used to study the mineralogical assemblage, the alteration paragenesis, the microfabric and the degree of microfracturing. The thin sections were observed under a Leica DM4500-P optical microscope, equipped with a Leica DFC450C camera at Institut Polytechnique UniLaSalle (ULS, Beauvais, France). Large field area imaging under polarized-analyzed and polarized-non-analyzed light was gained using Leica automatized stage facility and Leica Application Suite (LAS) v4.11.0 software (Klee et al., 2021a).

Based on optical microscopical observations, microsites were selected on 9 thin sections for Energy Dispersive X-ray Spectrometry (EDS) analyses (Zhou and Wang, 2007) performed at ULS. These were conducted with a Hitachi S-3400N Scanning Electron Microscope (SEM) equipped with a Thermo Ultradry EDS (K. Kanda, 1991) and associated with NSS thermal scientific software. These analyses aimed to obtain qualitative and semi-quantitative chemical compositions and to characterize the microstructure of different selected phases. The analytical

conditions consisted of 50  $\mu\text{A}$  beam current, an accelerating voltage of 20 kV and an acquisition time of 30 s. A NORAN-type correction procedure was used.

In addition, cathodoluminescence (CL) analyses (Götze, 2000) was performed on 8 thin sections from 4 samples. CL imaging was performed (1) at the University of Göttingen using a “hot-cathode” cathodoluminescence microscope HC3-LM apparatus and (2) at CY Cergy Paris University in the Geosciences and Environment Cergy (GEC) laboratory, using a cathodoluminescence Olympus BX50. CL of minerals is predominantly a “defect luminescence”. It allows the detection of distribution patterns of certain trace elements like iron (Fe) which is the most efficient quencher element and manganese (Mn) which is the most important activator element. Many minerals show visible CL colors like quartz (blue-purple), K-feldspar (blue when fresh and brownish when weathered), plagioclase (green +blue-purple when highly affected by hydrothermal alteration), calcite (yellow or yellow-orange when resulting from hydrothermal alteration), dolomite (orange-red), magnesite (red), apatite (yellow), kaolinite (dark blue) (Götze, 2012, 2000). Illite shows no luminescence (Götze, 2012, 2000).

Most of the mineral abbreviations used in this paper refer to Kretz (1983) mineral symbols and only a few others were defined by the authors.

#### IV.2.3. X-ray Diffraction (XRD)

XRD analyses were carried out to identify and determine the mineral phases (semi-quantitative, around 3-5%). The analyses were performed at (1) ULS using a D8-Advance Bruker-AXS (Siemens) diffractometer with a Ni-filtered  $\text{CuK}\alpha$  radiation at 40 kV and 40 mA, a primary soller slit of  $2.5^\circ$ , divergence slit of 0.6 mm and a secondary soller slit of  $2.5^\circ$ , with a detector slit of 0.1 mm and an antiscattering slit of 0.6 mm and (2) University of Göttingen using a PHILIPS PW1800 diffractometer with a Cu-anode and an automatic divergence slit. Whole rock powders and oriented clay fractions (2-6  $\mu\text{m}$  and  $< 2 \mu\text{m}$ ) analyses were performed on 12 samples. Quantitative phase analysis based on Reference Intensity Ratio values were performed on randomly oriented whole-rock powders with a step length of  $0.5^\circ$  and a scan speed of  $0.014^\circ/\text{sec}$  over the range  $3^\circ$ - $70^\circ 2\theta$  for whole rocks composition. The uncertainty is estimated to be  $\pm 5\%$ . Clay mineral separation was conducted using a technique described by Klee et al. (2021a), based on Schmidt et al. (1997) and Kisch (1991), according to the standard techniques suggested by Ferreiro Mählmann and Frey (2012). For the XRD analyses of both fractions, oriented specimens were measured at air dried (AD), solvated with ethylene glycol (G), and after heating at  $550^\circ\text{C}$  (H) conditions. These three analytical steps are routinely used

to better determine clay minerals content and swelling properties (Callahan et al., 2019). The clay minerals identification, which is based on d-values and the relative intensity of their 00l reflections, was undertaken referencing to (Moore and Reynolds, 1989; Starkey et al., 1984). These measurements were performed with a step length of  $0.5^\circ$  and a speed of  $0.01^\circ/\text{s}$  per step over the range  $3^\circ$ - $35^\circ 2\theta$ . The interpretations of the data obtained at ULS were performed using the DIFFRAC EVA v4.2 (©Bruker AXS) software. Two fractions were collected in order to (1) separate the last produced or neoformed clay minerals (fraction  $< 2 \mu\text{m}$ ), which could be assimilated to the result of the last fluid circulation event, from the fraction  $2$ - $6 \mu\text{m}$  assimilated to old grains recrystallization or to possible mix between detrital and neoformed clay minerals, (2) obtained the respective clay composition, and (3) obtained the temperature conditions.

### ***Kübler Index and Kaolinite Crystallinity Index determination***

The Kübler Index (KI) was used to define the limits of metamorphic zones (diagenetic zone, anchizone and epizone) (Klee et al., 2021a; Kübler, 1967), following the recommendations for Kübler-Index calibration of Ferreiro Mählmann and Frey (2012) and the CIS-KI transformation formalism of Warr and Mählmann (2015), as well as the temperature of illite formation (Árkai et al., 2003b, 2003a; Kisch, 1987). The KI was calculated from the illite crystallinity (IC) which is defined as the full width at half maximum (FWHM) of the (001)  $10\text{\AA}$  peak of illite, on the AD oriented clay fractions. A recent study (Warr and Cox, 2016) has confirmed that IC provides a useful method for characterizing regional grades of diagenesis and low-grade metamorphism. Temperature is thought to be the main factor controlling IC, but other parameters such as lithology also have important effects (Árkai et al., 2002; Frey, 1987; Mullis et al., 2017). Working at constant lithology allows this effect to be avoided. In some conditions, an altered granite shows similarities with diagenetic reactions present in feldspathic sandstones (Ledéser et al., 1999). Thus, it is possible to characterize temperature ranges by using the KI values obtained for granitic rocks. The values obtained by IC were thus standardized using the crystallinity index-standard (CIS) samples provided by Warr and Rice (1994a) in order to calculate the KI. The KI values of raw data expressed in  $\Delta^\circ 2\theta$ , were measured into three slots, corresponding to different campaigns, which induced three standardizations given by Klee et al. (2021a). The Kaolinite Crystallinity Index (KCI) was calculated and put in parallel with the KI in order to identify any correlation between both and to determine temperature evolution as an indicator for samples free of illite. The KCI is defined as the FWHM of the (001)  $7\text{\AA}$  peak of kaolinite on the AD oriented clay fraction.

#### IV.2.4. Manocalcimetry

Manocalcimetry is used as an indicator of the total calcite content in a rock sample and to assess its possible influence on permeability and consequently better understand the hydrothermal sealing of a reservoir (Ledésert et al., 2009). Calcite content was determined using an OFITE 152-95 manocalcimeter composed of a glass flask and a high precision manometer. The analyses were performed on 15 samples at CY-GEC. High quality results are obtained with an accuracy of  $\pm 0.5$  wt.%. Prior to measurement, sample preparation was done according to Ledésert et al. (2009). Two replicates were performed for each sample, following the protocol described by Klee et al. (2021a), in order to check the reproducibility of the results. This procedure is considered to be good when the difference between the two results is lower than 0.5 wt.%, corresponding to the precision mentioned above. The  $\text{CaCO}_3$  percentage was calculated according to Klee et al. (2021a). The average calcite content of a fresh granite is 0.252 wt.% and does not exceed 1.8 wt.% (White et al., 2005). As a consequence, measurements above this last value can be regarded as a calcite anomaly (Ledésert et al., 2009), thus due to hydrothermal alteration.

#### IV.2.5. Ethanol Saturation Porosimetry

Porosity measurement quantify the available volume for fluid storage (Dullien, 1979). The connected porosity was measured on 3 samples by the triple weighing method (Klee et al., 2021a; Navelot et al., 2018) defined by the RILEM standard (test n°1.1, 1978). The measurements were carried out at CY Cergy Paris University in the Mechanics and Material for Civil Engineering laboratory (L2MGC). They consist in the saturation of the samples after vacuum degassing. The analyses and calculations were conducted using technique described by Klee et al. (2021a). Ethanol has been chosen instead of water in classical methods, in order to avoid possible clay swelling (Gates et al., 2004), which could lead to the destruction of the sample and bias to porosity values. Even though ethanol (0.469 nm) is a larger molecule than water (0.343 nm), the pore volume is not estimated to be under evaluated, because the pore size is likely much larger than that of ethanol molecules.

#### IV.2.6. Bulk Rock Geochemical Analyzes

Chemical analyzes of the major element oxides, rare earth elements and trace elements were conducted on 5 samples, selected as case studies in this paper. Analyzes were performed at Bureau Veritas Minerals (Vancouver, Canada) using Inductively Coupled Plasma Emission Spectrometry or Mass Spectrometry (ICP-ES and ICP-MS respectively). Samples were crushed

and mixed with  $\text{LiBO}_2/\text{LiB}_4\text{O}_7$  flux. Crucibles were fused in a furnace at  $980^\circ\text{C}$ . The obtained cooled bead was dissolved in ACS grade nitric acid and analyzed. Loss on ignition (LOI) was determined by igniting the samples split then measuring the weight loss. These chemical analyses were performed in order to determine the element transfers and the degree of alteration.

#### IV.2.7. Mass-balance using Gresens Method

Bulk-rock mass-balance were used to establish element transfers during hydrothermal alteration by applying the Gresens mass-balance procedure (Gresens, 1967). It consists of the quantification of gains and losses of major elements by comparing unaltered and altered samples. NH\_2 is considered as the reference because it is the freshest sample collected in the area by Klee et al. (2021a) and 3 altered samples were selected from this study (NH\_20, NH\_28, NH\_32\_3 and NH\_37). The following equation defined by Gresens (1967) relates the composition and volume of altered rocks to unaltered/fresh rocks:

$$X_n = F_v \times (d_A/d_F) \times C_n^A - C_n^B \quad (1)$$

With  $X_n$  corresponding to the gain or loss of a considered element  $n$  (absolute mobility (%)),  $F_v$  the volume factor,  $d_A$  and  $d_F$  the density (in  $\text{g}/\text{cm}^3$ ) of the altered (A) and the fresh (F) rocks respectively, and  $C_n^A$  and  $C_n^B$  the oxide percentage of the element  $n$  for the altered (A) and the fresh (F) rocks respectively, which were given by the bulk geochemical analyses, recalculated without the LOI. The densities were calculated from the sample masses obtained during the porosity measurements. The  $F_v$  was calculated for each altered sample by considering  $X_{\text{Al}_2\text{O}_3} = 0$  following the analysis of the values.  $X_n$  was calculated for each element. Then, the obtained  $F_v$  values being very close to 1, the  $X_n$  values were recalculated by considering  $F_v = 1$  (constant volume). Hence,  $X_n$  values  $> 0$  (positive values) represent the gains and  $X_n$  values  $< 0$  (negative values) represent the losses for the considered elements. This calculation was applied for the major elements in each sample.

## V. RESULTS

### V.1. Noble Hills structural overview

We investigated the geometry of outcropping Proterozoic sequences between Pipeline and Cave Spring washes (Figure 5-2a) and confirm at first the plutonic nature of the contact at the base of the Proterozoic sequence with the underlying Mesozoic granite by metamorphic halos (Troxel and Butler, 1979). The whole architecture of the NH presents signs of deformation

affecting both Proterozoic and granitic units. Proterozoic units present much evidences of deformation with (1) several tectonically induced duplications of the stratigraphic sequence (Figure 5-2b) and (2) a lateral bending, stretching and boudinage of this Proterozoic cover nappe stack (Klee et al., 2020). Boudinage has been identified in the field and in map view where progressive dismantling of stratigraphic markers is observed (Figure 5-2b,c). Development of synthetic, oblique dextral shears (Figure 5-2c), offsetting along the CBS strike and accommodating the deformation, have also been identified. The age and tectonic significance of the nappe stack described in (1) is still unclear at present and possibly predates Mesozoic magmatic intrusion as it does not appear intensively deformed along the basal contacts of the nappes. Lateral bending and stretching mentioned in (2) and depicted in Figure 5-2b,c are to be related to SDVFZ activity since all kinematic indicators are consistent with progressive southeast oriented dextral shearing. This feature is ubiquitous within the NH as described by Pavlis and Trullenque (2021). Given these new findings dealing with internal CBS structural organization, it is expected that areas along the rear southern limit of the CBS have recorded less transcurrent shear compared to areas situated along its northern front. Thus, the CBS gives an opportunity to study the effects of progressive transcurrent shearing within a granitic geothermal analogue. The above considerations have important implications regarding strain distribution within the NH and in turn concerning the sampling strategy. Given the above-mentioned findings, we consider the CBS as an exceptional example of large scale cataclastic flow in which rock masses of the northern domain are dragged as a continuous body into a transcurrent deformation corridor (Figure 5-2a). No signs of a discrete, large scale deformation structure appear on the map presented in Figure 5-2, where yellow dashed lines show instead a continuous flow accommodated by brittle deformation processes.

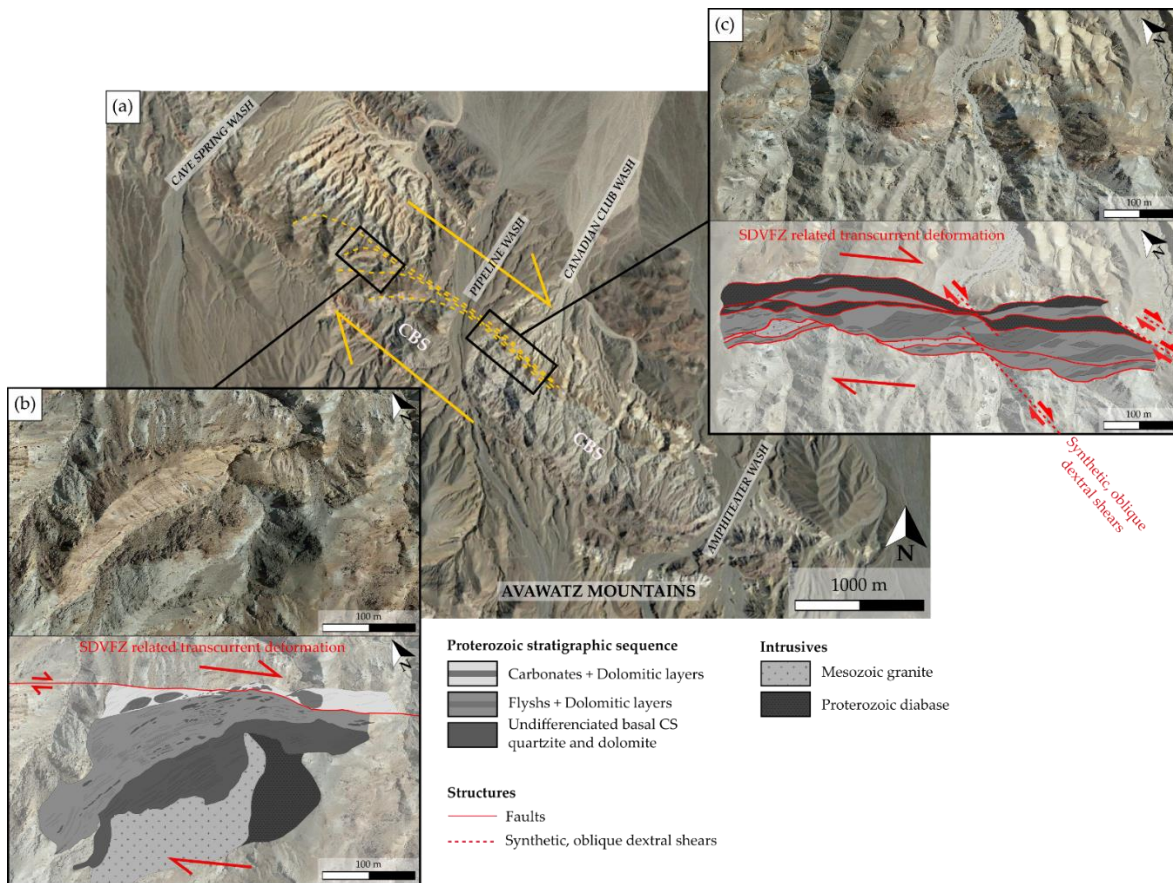


Figure 5-2. (a) Satellite view of the NH range showing a deformation gradient increasing southeastward, represented by the yellow dashed lines. (b and c) Map view zooms on the Proterozoic units along the NH strike showing the strain increase from (b) to (c), where basal CS sedimentary sequence appears increasingly stretched and boudinated.

## V.2. Petrographic Description

As described by Klee et al. (2021a), the primary assemblage of the NH granite is made of plagioclase (mainly oligoclase in composition), quartz, K-feldspar (perthitic orthoclase and sometimes microcline) and biotite. The granitic samples collected for this study show strong evidences of intense alteration, especially on plagioclase and biotite. Plagioclase transformed into illite, kaolinite and/or calcite and biotite into illite and oxides. In rare samples, K-feldspar perthites can be partially altered into illite. However, the magmatic texture is almost preserved except in the case of breccias, which are not necessarily highly altered. For all the samples, the alteration product is always the same, but the relative proportions of the different secondary phases might vary. The mineralogical composition and the degree of fracturing of each sample is given in Table 5-1.

Table 5-1. List of samples collected in the field with their mineralogical composition determined after microscopic observations (Optical-microscope and SEM-EDS) and XRD analysis (primary minerals and secondary minerals), their degree of microfracturing after Castaing and Rabu (1981) and their clay minerals composition for the fractions < 2  $\mu\text{m}$  and 2–6  $\mu\text{m}$ . Abbreviations after Kretz (1983), except for the following: Olg – Oligoclase, Ox – Oxide, I/S – Illite/Smectite, C/S – Corrensite, n.m. – not measured, n.a. – not analyzed.

Sample name	Primary minerals	Secondary minerals	Clay fraction < 2 $\mu\text{m}$						Clay fraction 2-6 $\mu\text{m}$						Microfracturing	
			Ill/Ms	Kln	C/S	I/S	Vrm	Bt	Ill/Ms	Kln	C/S	I/S	Vrm	Bt		
NH_16	Qtz, Or, Bt, Olg	Cal, Clays	+	-	--					+	+	--				Fd2
NH_17	Qtz, Or, Ab, Ap	Gp, Clays	n.m.						+	-		--				Fd2
NH_18	Qtz, Or, Olg, Bt	Clays	++	--						++	--					Fd2
NH_19	Mc, Or, Olg, Bt, Qtz, Ms	Dol, Cal, Clays	+							+						Fd2-3
NH_20	Qtz, Or, Olg, Bt	Cal, Ox, Clays	n.a.						n.a.						Fd2-3	
NH_21	Qtz, Or, Olg	Cal, Dol, Sd, Ox, Clays	n.a.						n.a.						Fd3	
NH_22	Qtz, Or, Bt, Olg	Cal, Hem, (Dol), Clays	+	-						+	-				-	Fd3
NH_23	Qtz, Or, Olg, Bt	Cal, Ox, Clays	n.a.						n.a.						Fd3	
NH_24	Qtz, Or, Olg, Bt	Cal, Clays	+	+		-	-			-	+		-	-		Fd3
NH_25	Qtz, Or, Bt, Ep	Cal, Ox, Clays	++							++						Fd3
NH_26	Qtz, Or, Bt, Olg, Mc	Clays	-	++			+	+		-	++			+	+	Fd3
NH_27	Qtz, Or, Bt	Ank, Cal, Clays	+	++	-			-		+	++	-			-	Fd3
NH_28	Qtz, Or, Mc, Olg, Bt, Ms	Cal, Ox, (Dol), Clays		++							++					Fd3
NH_29	Qtz, Or, Olg, Ab, Bt	Cal, Dol, Clays	n.a.						n.a.						Fd3	
NH_30	Qtz, Or, Mc, Olg, Ab, Bt, Ms	Cal, (Ox, Dol), Clays	n.a.						n.a.						Fd3	
NH_31_1_2	Qtz, Or, Olg, Bt	Clays	+	+		-				+	++		-			Fd3
NH_31_3	Qtz, Or, Ab, Bt	Gp, Cal, Clays	n.m.						++	--						Fd3
NH_32	Qtz, Or, Bt	Cal, Ox, (Dol), Clays	+	++	-					+	++	-				Fd4
NH_33	Qtz, Or, Bt, Ab	Cal, Clays	--	++				-		--	++				-	Fd4
NH_34	Qtz, Or, Mc, Ab, Ap, Bt	Gp, Cal, Hem, Clays	n.m.						--	++			--			Fd4
NH_35	Qtz, Or, Mc, Bt	Cal, Clays	n.a.						n.a.						Fd4	
NH_36	Qtz, Or, Bt, Olg	Cal, Gp, Hl, Clays		+				+			++				-	Fd4
NH_37	Qtz, Or	Cal, Dol, Ank, Ox, Clays	n.a.						n.a.						Fd4	
NH_38	Qtz, Or, Mc, Olg, Bt	Cal, Clays		++							++					Fd4
NH_39	Qtz, Or, Mc, Olg, Bt	Cal, Clays		++							++					Fd4

The clay mineral composition of some samples has been precisely determined for the  $< 2 \mu\text{m}$  and  $2\text{--}6 \mu\text{m}$  (Table 5-1). It reveals the presence of Illite/Smectite (I/S) mixed-layers in three samples (NH\_17, NH\_24 and NH31\_1\_2) in both fractions when it was measurable. The I/S identified is always illite-rich (R3), with more than 90% of illite (Moore and Reynolds, 1989), where R represents the Reichweite parameter (Moore and Reynolds, 1989). A small amount of corrensite (trioctahedral variety of regular 50:50 chlorite/smectite mixed-layer (C/S) (Beaufort et al., 1997)) was also identified in the samples NH\_16, NH\_27 and NH\_32. Both mixed-layers (I/S and C/S) were already identified by Klee et al. (2021a) in the sampled granite away from the fracture zones. Two new patterns were identified in this study (Figure 5-3):

- The first pattern (Figure 5-3a) shows illite characterized by peaks at  $10.1\text{\AA}$  and  $4.99\text{\AA}$ , which supports the previous results (Klee et al., 2021a). Illite is present in almost all the samples except NH\_28, NH\_36, NH\_38 and NH\_39. Kaolinite is also present and could be associated to illite or not.
- The second pattern (Figure 5-3b) shows the presence of dioctahedral vermiculite. It is characterized by a peak at  $14.32\text{\AA}$  in air-dried condition, which slightly swells up to  $14.59\text{\AA}$  after glycol solvation and slightly collapses to  $12.26\text{\AA}$  after heating. It was identified only in samples NH\_24, NH\_26 and NH\_33, where it is associated to illite and kaolinite.

The high proportion of illite and kaolinite being characteristic of the argillic alteration (Klee et al., 2021a). Argillic alteration is prevalent in the vicinity of fracture zones (Table 5-1). Vermiculite can be interpreted as either hydrothermal alteration or weathering. This will be discussed in the section 5.1.

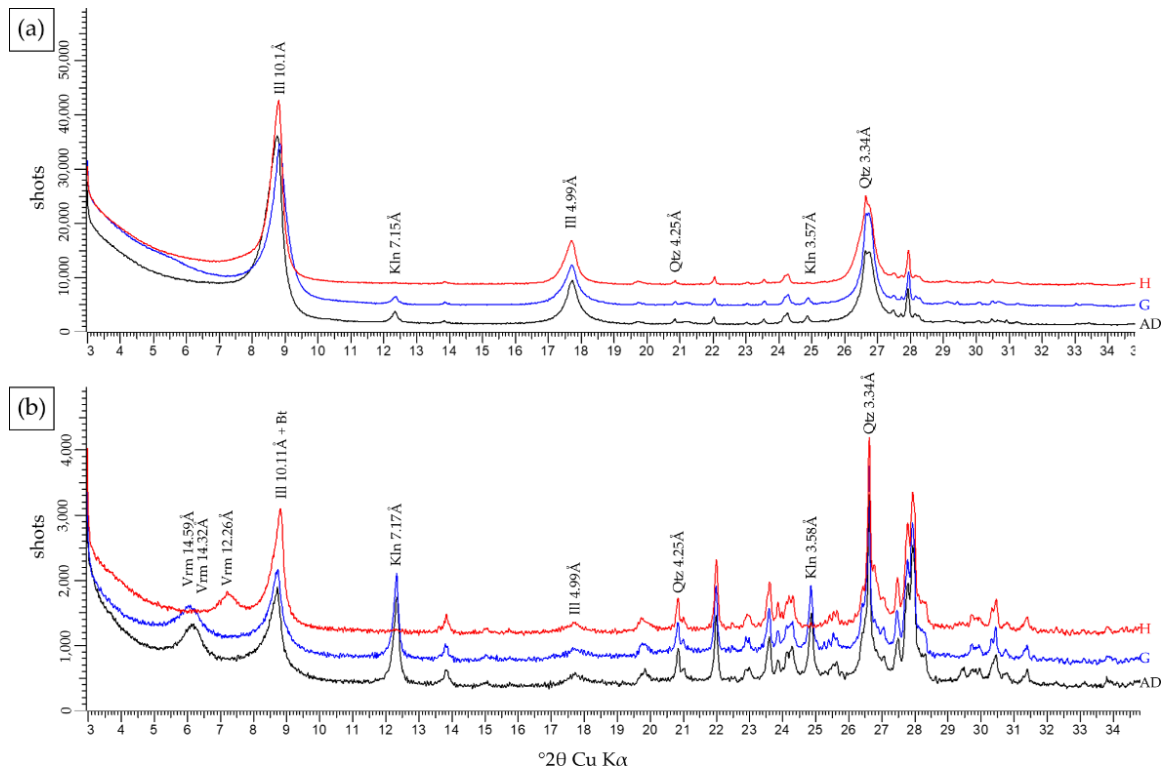


Figure 5-3. Two examples of XRD patterns obtained for the clay fraction  $< 2 \mu\text{m}$  in Air-Dried (AD-dark), after Glycol solvation (G-blue) and Heated (H-red) conditions for the NH granite, which were not identified in the fresh granite described by (Klee et al., 2021a), and showing different clay compositions. (a) Illite, kaolinite and quartz. (b) Vermiculite, illite, kaolinite and quartz.

Microscopic observations and SEM-EDS analyses have shown that in almost all the samples, carbonates (dolomite, siderite, ankerite and calcite) and oxides are present as veins and or in replacement of plagioclase. Moreover, XRD analyses revealed the presence of gypsum and/or halite in minor amounts in few samples (Table 5-1). Halite only occurred in sample NH\_36 and gypsum is found in samples NH\_17, NH31\_3, NH\_34 and also NH\_36.

### V.3. Fracturing and Fluid Circulation

The NH granite presents ubiquitous signs of both fracturing and alteration due to its location along the SDVFZ major fault corridor. The area lies along a deformation corridor governed by transcurrent deformation along the SDVFZ. In addition to the present contribution, Klee et al. (2020) argue in favor of a deformation gradient affecting the CBS. At low to moderate strain, the system presents fracture zones composed of a fault core in which fractures are branching and where most of the displacement is concentrated (Figure 5-4a). These fracture zones affect the surrounding rock, creating an important fracture network (the damage zone, DMZ). Open fractures and veins are observed in this DMZ (Figure 5-4b).

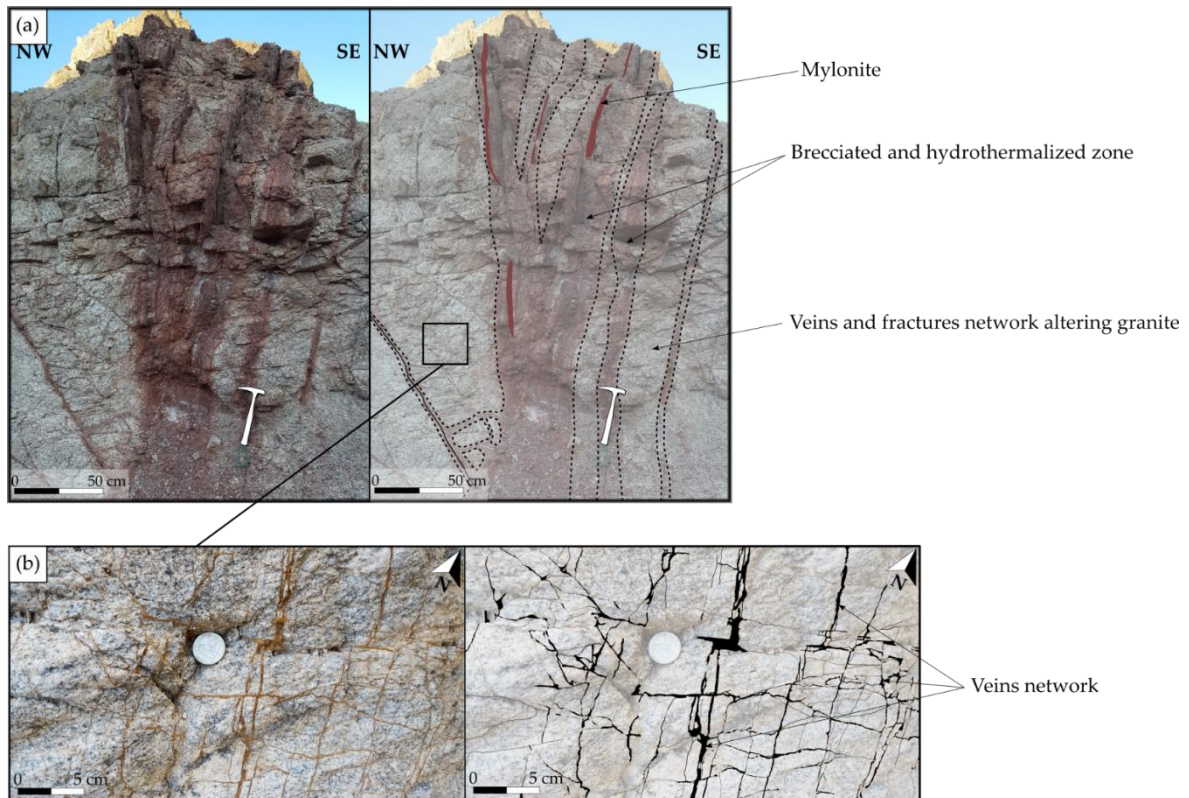


Figure 5-4. (a) Photograph and digitization showing representative hydrothermalized fracture zones observed on the field. (b) Photograph and digitization of granite crosscutting by multiple carbonate veins (veins network) altering pervasively the rock.

Fault zones may act as a channel when connected and open fractures are present or as a barrier when fracture are sealed by mineralization. The distinction is made between (1) zones of opening related structures (i.e. where no signs of displacement are recognized between the two borders of the vein, Figure 5-4b) and (2) zones of lateral displacement (i.e. indicative of a shear displacement is observable) through three samples used as case studies (NH\_31 (Figure 5-5a), NH\_36 and NH\_23 (Figure 5-5b)). Note that these samples are spaced at 2 m and are almost perpendicular to each other.

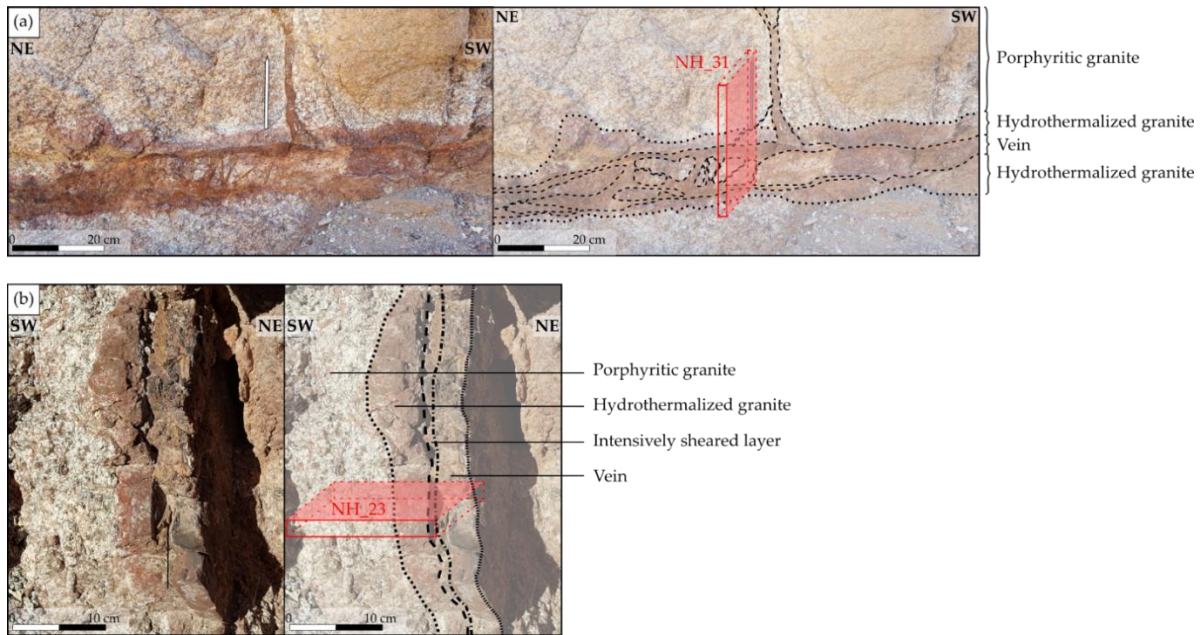


Figure 5-5. (a) Photograph and digitization of a brecciated and recrystallized vein also developing a gradient of alteration. Location of the sample NH\_31 used as a case study in this section. (b) Photograph and digitization of a mylonitic vein developing a gradient of alteration. Location of the sample NH\_23 used as a case study in this section.

### V.3.1. Opening related structures with minimum shear displacement

A significant number of veins, veinlets and microfractures were identified in the different samples and outcrops investigated. Veinlets of various mineralization natures ( $\leq 100 \mu\text{m}$  wide) were also identified in the samples. This variety of fracture infills shows different fluid circulation episodes. Rare veinlets of quartz were observed and intersected by illite veinlets (Figure 5-6a), which can be contemporaneous to kaolinite veinlets. Illite development is dependent on host mineral properties in terms of mechanical resistance and chemical stability. In that sense, quartz and K-feldspar, which remains unaltered, presents sharp open fractures in which illite precipitates (Figure 5-6b). Plagioclase, which is altered, presents blurred vein borders and start to spread out pervasively, due to the secondary porosity created by the alteration process (Figure 5-6b). These veinlets are generally intersected by carbonate veins (Figure 5-6c). These veins, the size of which ranges between  $500 \mu\text{m}$  width up to centimetric scales are composed of dolomite, siderite, ankerite and calcite. Most of the time, dolomite and ankerite appear contemporaneous. When siderite is present, it alters dolomite borders and crystallizes in it or crosscut it (Figure 5-6d). Then, calcite veins intersect the dolomite/ankerite and siderite veins (Figure 5-6d). Calcite can crystallize around angular clasts arranged in a fan shape characteristic of hydraulic fracturing (Figure 5-6e). Open microfractures present in the samples can show altered walls with kaolinite (Figure 5-6f) and/or illite (Figure 5-6g) indicating an influence of microfractures on mineral alteration.

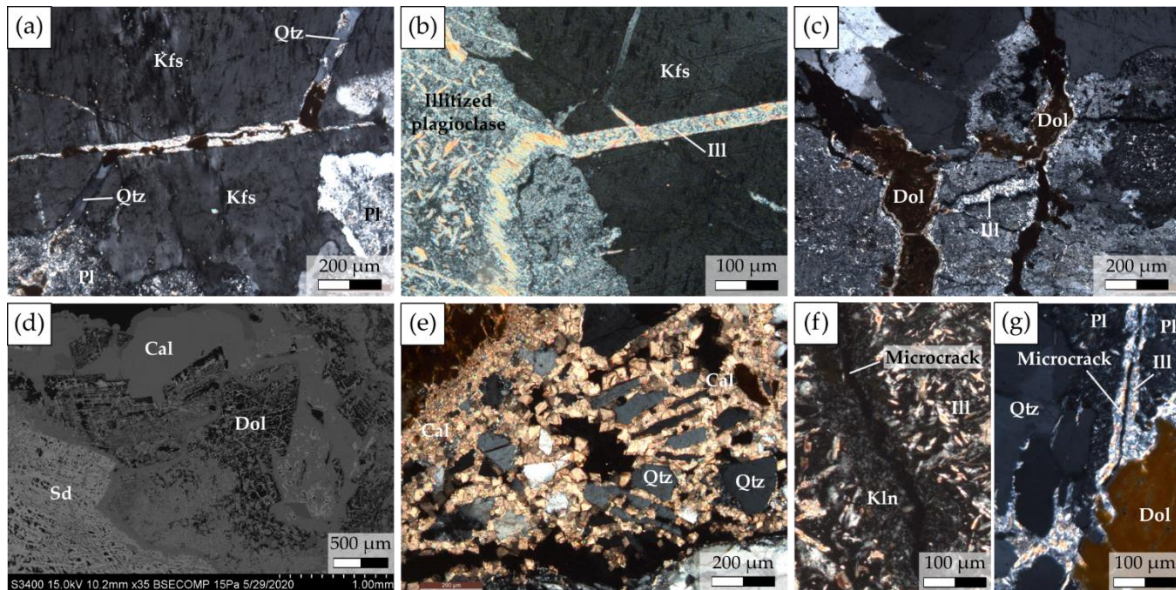


Figure 5-6. (a) Photomicrograph of a quartz veinlets intersected by an illite veinlets under optical microscope in polarized-analyzed light. (b) Photomicrograph showing an illite vein crosscutting K-feldspar and illitized plagioclase under optical microscope in polarized-analyzed light. (c) Back-scattered image showing the different phases presented in (b). (c) Photomicrograph showing dolomite intersecting illite under optical microscope in polarized-analyzed light. (d) Back-scattered image of a dolomite, siderite and calcite showing their chronology. (e) Hydraulic fracturing with calcite precipitating around clasts of quartz placed like a fan under optical microscope in polarized-analyzed light. (f) Photomicrograph under optical microscope in polarized-analyzed light of a microfracture intersecting an altered plagioclase which borders are made of pure kaolinite whereas the plagioclase was recrystallized into kaolinite and illite. (g) Photomicrograph under optical microscope in polarized-analyzed light showing illite developing on the walls of an open microfracture and dolomite filling this open space.

### V.3.2. Infill of fractures developed with a confirmed lateral shear displacement

The previous section shows that all the samples in the area present a lot of fractures where fluid has circulated precipitating or not various secondary minerals. However, the area is constrained by a shear component. Three samples were selected in order to describe the relationship between the amount of strain and fluid circulation.

#### V.3.2.1. Sample NH\_31

The outcrop of the sample NH\_31 (Figure 5-5a) presents a vein around 10 cm thick crosscutting the granite and with a pinkish halo developed on each border. This halo represents the hydrothermalized zone of the granite. The sample NH\_31 (Figure 5-7a) is composed of (1) a brecciated vein presenting brecciated quartz remnants which were overprinted by a carbonate matrix and granitic clasts transported by the carbonate matrix, (2) a hydrothermalized zone which corresponds to the pinkish halo, and (3) the porphyritic granite crosscut by veinlets filled by carbonates coming from the brecciated vein. Quartz vein are scarce in the NH granite.

Fractures are dominantly rich in carbonates. It can be observed through this sample that carbonates crosscut the quartz.

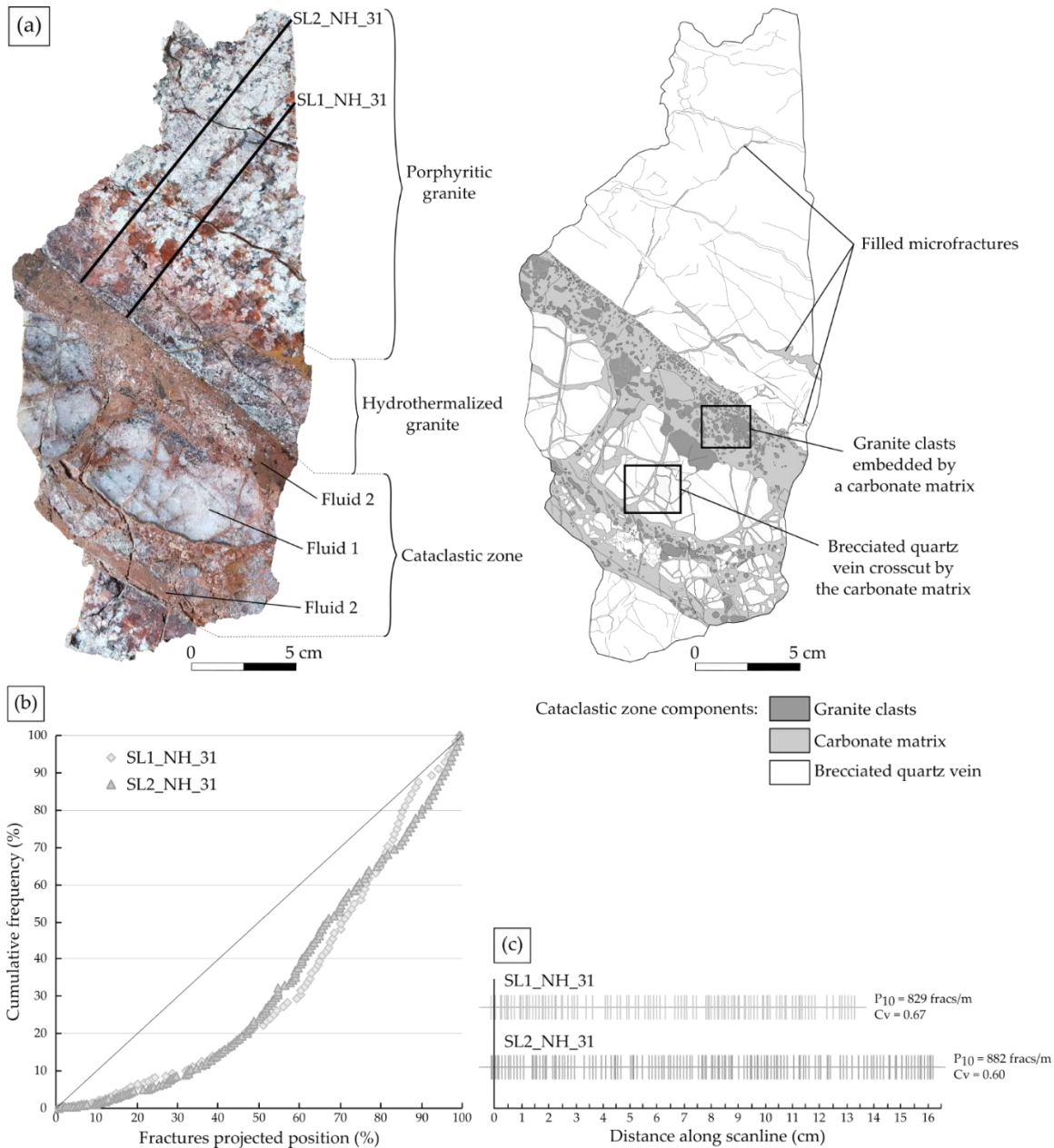


Figure 5-7. (a) Photo and the respective digitalization of the sample NH<sub>31</sub>, gathering NH<sub>31</sub>\_1\_2 and NH<sub>31</sub>\_3, showing the different compartments that compose it, as well as the two scanlines realized in the host rock of the vein. (b) Plots of the cumulative frequency percentage against distance percentage for both scanlines. The diagonal represents an uniform distribution. (c) Stick plots showing the fracture position along the scanlines and for which the fracture density ( $P_{10}$ ) and the coefficient of variation ( $Cv$ ) are given.

- Spatial fracture distribution

Two scanlines were realized in the granitic part of the sample (Figure 5-7a), from the brecciated vein towards the host rock, in order to evaluate the evolution of the fracture density along those two profiles. The spatial analysis is summarized in Table 5-2.

Table 5-2. Spatial fractures analysis. Scanline length: total length of each scanline; Fracture number, Mean spacing,  $P_{10}$  and  $C_v$  value by scanline and fracture distribution tendency by scanline.

Sample name	Scale	Scanline name	Scanline length (cm)	Fracture number	Mean spacing (cm)	$P_{10}$ (fracs/m)	$C_v$	Fracture Distribution
NH_31	Sample	SL1_NH_31	13.51	111	0.12	829	0.67	Regular - Random
		SL2_NH_31	16.44	144	0.11	882	0.60	Regular - Random
	Thin sections	SL_NH_31_1	1.60	47	0.03	2997	1.03	Random
SL_NH_31_2		2.21	87	0.02	3988	1.07	Random - Clustered	
SL_NH_31_3		2.34	118	0.02	5084	1.11	Random - Clustered	
NH_36	Samples	SL_NH_36	15.8	53	0.3	342	1.03	Random
	Thin sections	SLH_NH_36_1	2.87	153	0.02	4636	1.49	Clustered
		SLV_NH_36_1	2.06	133	0.02	6312	1.01	Random
		SLH_NH_36_2	3.35	184	0.02	5231	1.11	Random - Clustered
NH_23	Sample	SL1_NH_23	14.33	197	0.07	1382	0.68	Regular - Random
		SL2_NH_23	12.93	170	0.07	1322	0.66	Regular - Random
	Thin sections	SL_NH_23_1	2.48	117	0.02	4798	0.77	Regular - Random
		SL_NH_23_2	2.37	91	0.02	3879	1.19	Random - Clustered

The cumulative frequency plotted against the fracture projected position is presented in Figure 5-7b. The fracture frequency regularly and slowly increases over the first half part of the diagram curve, then increases regularly but more significantly. The  $C_v$  of 0.67 and 0.60 for each scanline shows a regular to random fracture arrangement which is confirmed by the stick plots in Figure 5-7c. Both scanlines present an equivalent fracture density of 829 fracs/m and 882 fracs/m.

Moreover, three thin sections were gained from the sample and one scanline was realized from each thin section (Figure 5-8a,b). As for the sample scanlines, the thin section scanlines were realized perpendicular to the vein and towards the host rock (Figure 5-8c).

SL\_NH\_31\_1 shows a fracture frequency that increases following a random arrangement ( $C_v = 1.03$ ) (Figure 5-8c,d).

The SL\_NH\_31\_2, parallel to the previous scanline, presents also an irregular distribution. The frequency increases slowly at the beginning, followed by a high fracture density zone around

0.7–1.05 (fracture cluster), then a more significant increase comprising a new fracture cluster around 2–2.2 (Figure 5-8c). The slightly higher  $C_v$  compared to the previous scanline ( $C_v = 1.07$ ) and the fracture distribution (Figure 5-8c) indicate a random to clustered arrangement of the fractures.

The last scanline SL\_NH\_31\_3, which is the furthest from the vein, shows a greater overall increase of the fracture frequency compared to the two previous scanlines (Figure 5-8c). Only one fracture cluster was identified around 1.7–1.9 cm even if the  $C_v$  is higher ( $C_v = 1.11$ ). The fracture arrangement is again considered as random to clustered.

$C_v$  values as well as fracture density values increase from the vein towards the host rock, from 1.03 to 1.11 and from 2997 fracs/m to 5084 fracs/m respectively (Figure 5-8d).

By comparing fracture analyses between sample scale and thin section scale, a clear difference is observed between  $P_{10}$ , the mean spacing and  $C_v$  values (Table 5-2). At thin section scale, the fracture density is significantly higher ( $\times 4.7$ ) than at sample scale and the mean spacing is 6 times lower. At sample scale, the  $C_v$  is lower than 1 indicating an almost regular spacing between the fractures even if there is a change of the slope (Figure 5-7c). Whereas, at thin section scale, the  $C_v$  is around 1 or slightly higher, indicating a global random distribution of the fractures along the scanlines with the appearance of few clusters (Figure 5-7c). For both, differences in the fracture distribution can be linked to a subjective bias during the data collection (Maria Tartarello and Johnson, 2019), but also to the image resolution which prevents from seeing all the fractures and so induced a bias. Thin section fracture analyses are thus more precise.

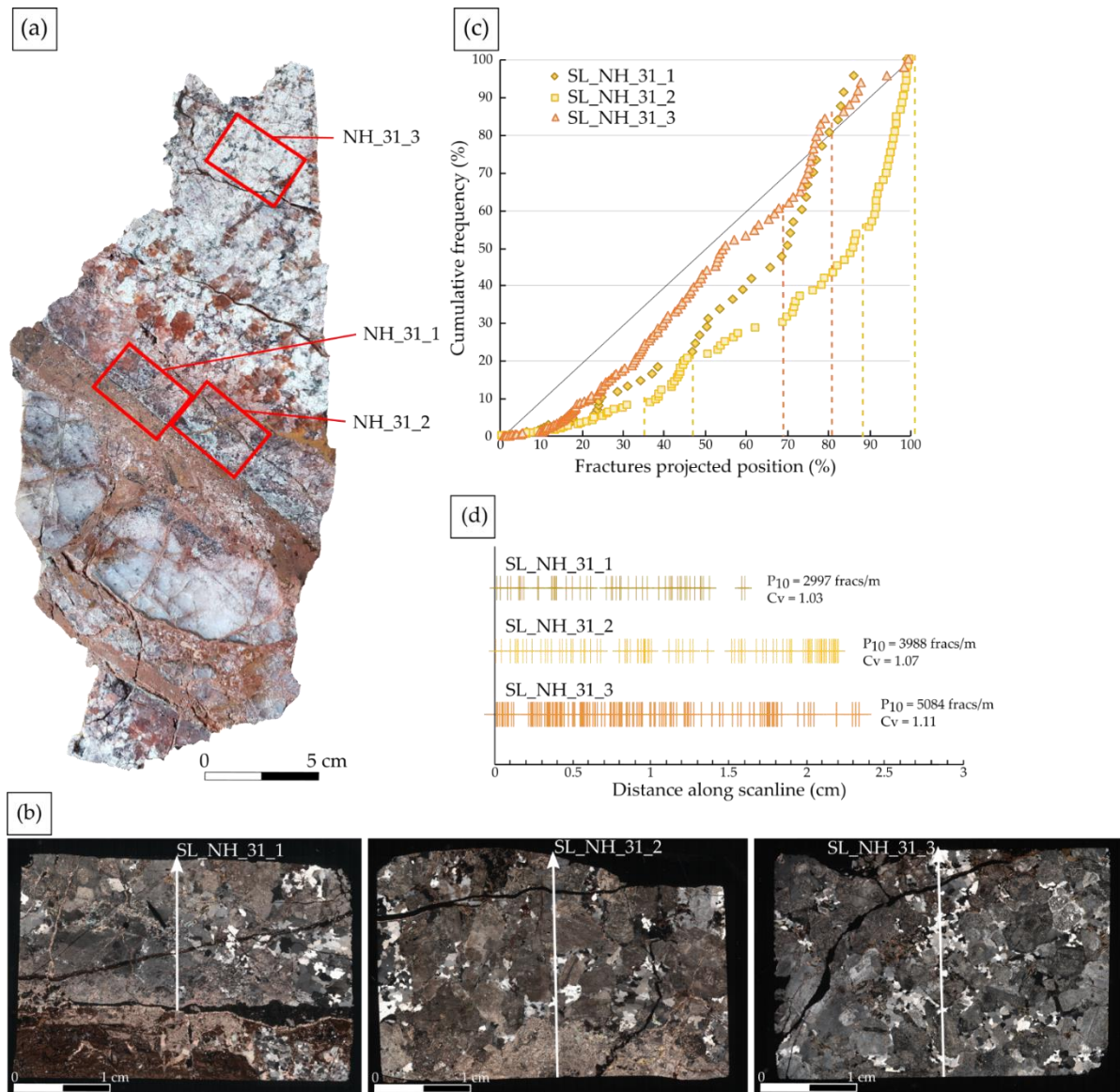


Figure 5-8. (a) Thin sections location on the sample NH<sub>31</sub>. (b) Thin section mosaics showing the position and orientation of the scanlines. (c) Plots of the cumulative frequency percentage against distance percentage for each scanline. The diagonal represents a uniform distribution. Dashed lines indicate a zone where a rapid increase of the number of fractures is observed (slope threshold > 2). (d) Stick plots showing the position of the fracture along the scanlines and for which the fracture density ( $P_{10}$ ) and the coefficient of variation ( $C_v$ ) are given.

- Petrographic and Petrophysical Characterization

The brecciated vein presents a large variety of mineralogical phases. As shown in Figure 5-7a, this zone shows a carbonate matrix containing clasts of granite, which overprints a brecciated quartz vein remnant showing an undulatory extinction but no evidence of dynamic recrystallization. The carbonate matrix is complex, composed of several phases (Figure 5-9a-g).

Focusing on the veins crosscutting the quartz porphyroclasts, three phases are identified (Figure 5-9a-e):

1. Phase 1 is composed of calcite veins crosscutting the quartz. These veins, appearing as a single phase under SEM and optical microscope (Figure 5-9a,c), present two phases under cathodoluminescence (CL): a dark phase (Cal A) in the center of the vein and an orange bright phase (Cal B) (Figure 5-9b,d). Cal B phase seems to dissolve or corrode the Cal A phase (Figure 5-9b,d). A zonation corresponding to calcite growth halos are visible in the phase A which are used as weakness zones in which the phase B can penetrate by dissolving the phase A.
2. Phase 2 is composed of a matrix rich in carbonates (calcite, dolomite, ankerite) transported clasts of quartz, K-feldspars and few biotite, but also presents barite precipitation patches (Figure 5-9e). This phase crosscuts the quartz and the calcite veins.
3. Phase 3 consists again of calcite veins. However, they crosscut the whole-rock and appear as a dark single phase (Cal C) under CL (Figure 5-9b).

Evidences of hydraulic fracturing, as presented in Figure 5-6e, have also been observed in this part of the sample.

By focusing in the carbonate matrix, at the contact with the granite, a new phase is observed, composed of dolomite embedding small clasts (mainly quartz). This phase is intersected by the phase 2, which is intersected by the phase 3 (Figure 5-9e,f). Examining the hydrothermalized granite along the brecciated vein (NH\_31\_1 and NH\_31\_2), the granite shows a preserved magmatic texture with plagioclase fully altered into illite,  $\pm$  kaolinite and calcite, completely altered biotite into illite and oxides, and unaltered perthitic K-feldspar (Figure 5-9h,i). Hematite and numerous dolomite/ankerite and calcite veinlets are present. Moving away from the brecciated vein (NH\_31\_3), the granite appears less affected by the alteration. Plagioclase and biotite are only partially altered and K-feldspar and quartz are unaltered (Figure 5-9j,k). Unlike the hydrothermalized zone, the granite presents only a few veinlets of calcite.

Bulk chemical analyses were performed on the granitic part of the sample and show a low LOI of 2.5%, a porosity of 10.1% and a calcite content of 1.86% close to the brecciated vein (NH\_31\_1\_2) and a calcite content of 1.37% away from it (NH\_31\_3).

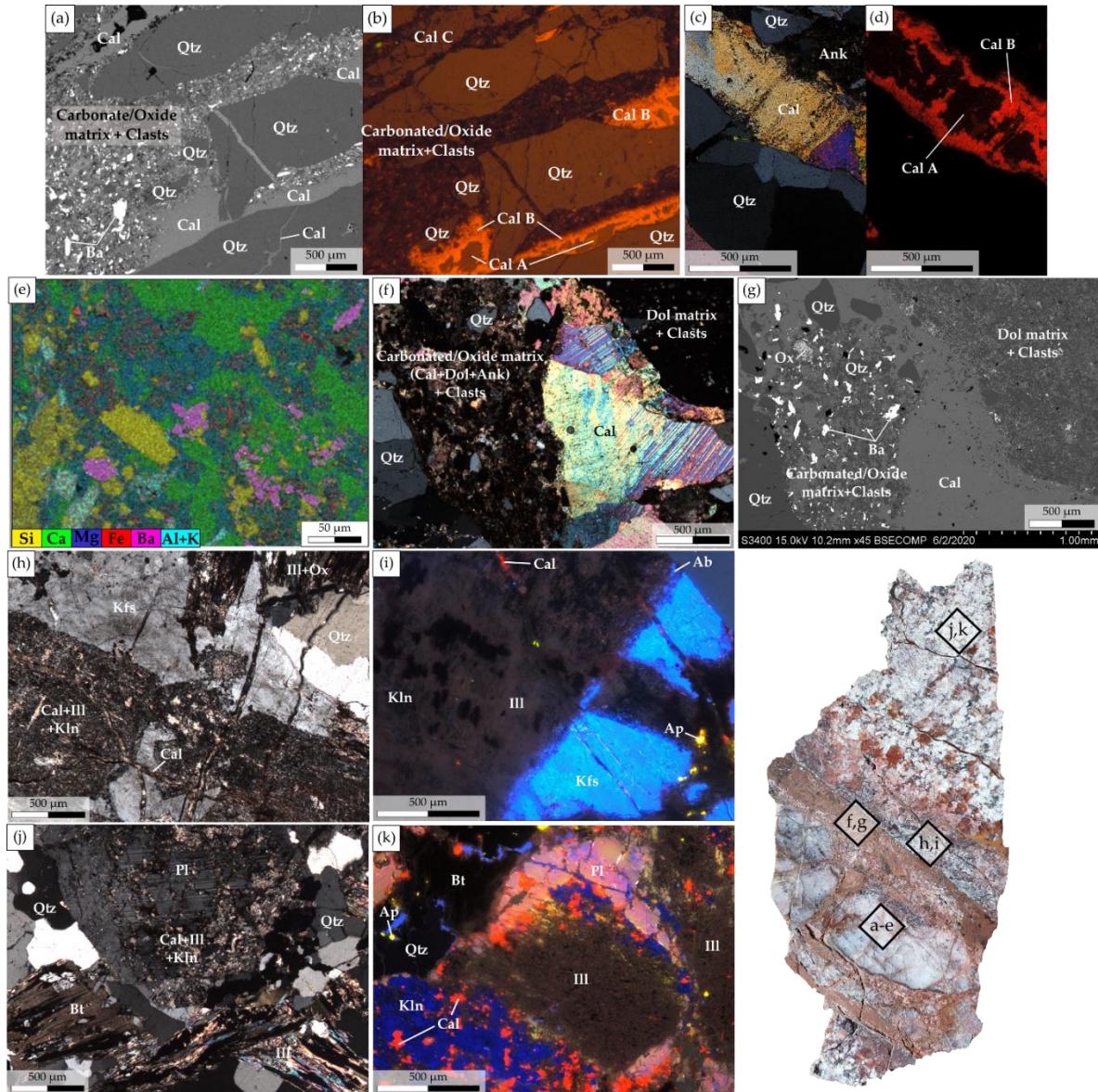


Figure 5-9. Photomicrographs of the different compartments of the sample NH\_31 and their location in the sample. (a-b) Respectively back-scattered image and CL images of calcite veins composed of 2 phases (Cal A and Cal B) crosscutting quartz, crosscut by a phase made of a carbonate/oxide matrix (calcite, dolomite, ankerite) with barium patches and transported clasts of quartz, K-feldspars and few biotite, crosscut by later calcite veins (Cal C). (c-d) Zoom on the first generation of calcite vein and crosscutting quartz under optical microscope in polarized-analyzed light and showing two phases under CL. (e) A chemical quantification map realized under SEM of the carbonate/oxide matrix with barium and clasts. Different colors show a relative abundance of specific chemical elements (counts). (f,g) A photomicrograph under optical microscope in polarized-analyzed and under SEM respectively of the contact with the granite showing a dolomite matrix with transported clasts intersected by a calcite vein, the whole intersected by a carbonate/oxide matrix with transported clasts and barium precipitation patches. (h) The altered granite close to the brecciated vein showing a completely altered plagioclase replaced by calcite, kaolinite and illite, a completely altered biotite replaced by illite and oxides and non-altered K-feldspar and quartz under optical microscope in polarized-analyzed light. (i) The altered granite close to the brecciated vein presented in (h) under CL showing illite with no luminescence, in light blue an unaltered K-feldspar, in red some calcite and apatite in yellow. (j) The altered granite away from the brecciated vein showing a plagioclase partially replaced by calcite, kaolinite and illite, biotites partially replaced by illite and oxides and unaltered quartz under optical microscope in polarized-analyzed light. (k) The altered granite away from the brecciated vein presented in (j) under CL

showing kaolinite in dark blue, calcite in red, apatite in yellow and illite, quartz and biotite with no luminescence.

V.3.2.2. Sample NH\_36

This sample (Figure 5-1c, Figure 5-10a) shows a fractured granite with a preserved magmatic texture intersected by brecciated zones. As for sample NH\_31, the fracture distribution analyses, as well as a petrographic description were realized.

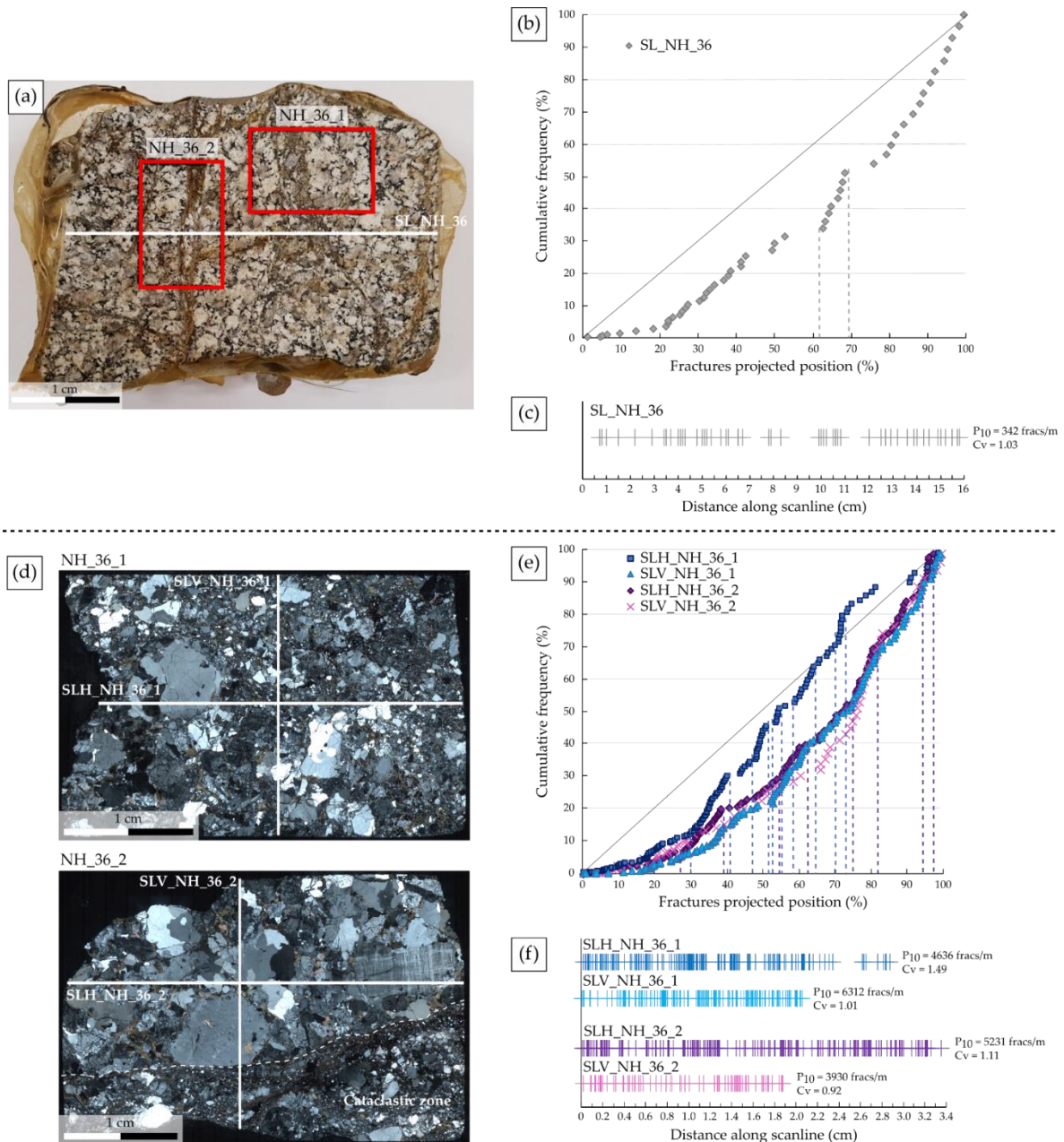


Figure 5-10. (a) Photograph of the sample NH\_36 showing the scanline and the emplacement of the two thin sections made in the sample. (b) Plot of the cumulative frequency percentage against distance percentage for the scanline. The diagonal line represents an uniform distribution. Dashed lines indicate a cluster, meaning a zone where a rapid increase of the number of fractures is observed (slope threshold > 2). (c) Stick plot showing the fracture position along the scanline and for which the fracture density (P<sub>10</sub>) and the coefficient of variation (C<sub>v</sub>) are given. (d) Thin section mosaics showing the position and the orientation

of the scanlines. (e) Plots of the cumulative frequency percentage against distance percentage for each scanline. The diagonal line represents again an uniform distribution and the dashed lines delimit a fracture cluster. (f) Stick plot showing the fracture position along the scanline and for which the fracture density ( $P_{10}$ ) and the coefficient of variation ( $C_v$ ) are given. Data were provided by (Chabani et al., 2021).

- Spatial Fracture Distribution

The spatial fracture distribution analysis was realized based on data from (Chabani et al., 2021). One scanline was realized through the sample in order to evaluate the evolution of the fracture distribution and density (Table 5-2, Figure 5-10a). The cumulative frequency against the fractures projected position presented in Figure 5-10b shows a fracture frequency slowly increasing, as well as a fracture cluster. The  $C_v$  of 1.03 indicates a random arrangement of the fractures along the scanline (Figure 5-10c). A fracture density of 342 fracs/m was compiled (Figure 5-10c).

Two thin sections were made from the sample (Figure 5-10a,d). Two perpendicular scanlines were realized on each thin section (Figure 5-10d).

Regarding the thin section NH\_36\_1, the scanline SLH\_NH\_36\_1, perpendicular to the main fractures, shows a fracture frequency increases slowly the first 30%, then increases more strongly by presenting five fracture clusters (Figure 5-10e). This fracture distribution is highlighted by a  $C_v = 1.49$ , confirming a clustered arrangement of the fractures (Figure 5-10f). The fracture clusters are respectively comprised between, 0.9–1.2 cm, 1.4–1.5 cm, 1.55–1.6 cm, 1.7–1.85 cm and 2.05–2.1 cm intervals (Figure 5-10e,f). The scanline SLV\_NH\_36\_1, parallel to the main fractures, shows a different trend. The fracture frequency increases slowly and irregularly (Figure 5-10e). This distribution is highlighted by a  $C_v = 1.01$ , indicating a random arrangement of the fractures (Figure 5-10f). Considering both scanlines, the average fracture density is of 5474 fracs/m.

Regarding thin section NH\_36\_2, the scanline SLH\_NH\_36\_2, parallel to the main fractures shows a fracture frequency trending similarly to SLV\_NH\_36\_1. Four fracture clusters were identified (Figure 5-10e), also visible in the stick plot between 0.95–1.3 cm, 1.85–2.05 cm, 2.5–2.7 cm and 3.1–3.2 cm (Figure 5-10f). The  $C_v = 1.11$  confirmed a random to clustered arrangement of the fractures. The scanline SLV\_NH\_36\_2, perpendicular to the main fractures crosscut the magmatic preserved texture of the granite and a breccia. A change of the curve inclination is visible around 65% of the scanline, where the fracture frequency strongly increases (Figure 5-10e). It corresponds to the limit between both zones (Figure 5-10d). The  $C_v = 0.92$  indicates a global regular to random fracture arrangement along this scanline (Figure 5-10f). Considering both scanlines, the average fracture density is of 4581 fracs/m.

Because fractures are difficult to recognize in the breccia of the sample NH\_36\_2, the fracture density calculated for both thin sections may be underestimated.

As for sample NH\_31, an important difference between the  $P_{10}$  values of the sample and the thin sections is observed. However, a global random arrangement of the fractures at both scales is observed. Only SLH\_NH\_36\_1 presents a clustered distribution.

- Petrographic and Petrophysical Characterization

The two thin sections (Figure 5-11a,b,c) allow petrographical characterization the sample. The first thin section, NH\_36\_1 (Figure 5-11a,b), shows a breccia of the granite with significant variations of the grain size. No crystallographic preferential orientation (CPO) is observed. Some zones show brecciated minerals with small precipitation of carbonates as calcite and dolomite in the microfractures (Figure 5-11d). Primary minerals are only slightly altered but intensively deformed. Quartz which shows a pronounced undulatory extinction and starts to dynamically recrystallize by means of sub-grain rotation processes (Figure 5-11d). Other zones show still preserved minerals but also a significant amount of carbonate, mainly calcite, between the clasts (Figure 5-11e). The second thin section, NH\_36\_2 (Figure 5-11c), shows a granite with a preserved magmatic texture but fractured, and a breccia composed of a carbonate matrix and transported clasts coming from the granite with no CPO. The preserved granite part shows a low alteration degree. Quartz, K-feldspars (orthoclase and microcline) and biotite are fractured and unaltered. Plagioclase is fractured and slightly altered and replaced by kaolinite (Figure 5-11f). The breccia shows a matrix composed of dolomite and calcite flowing through transported clasts of unaltered quartz and feldspar and lenses of kaolinite (Figure 5-11g).

Bulk analyses show a low LOI (2.6%), a calcite content of 5.95% and a porosity of 11.5%. XRD bulk and clay fraction analyses also reveal the presence of gypsum and halite.

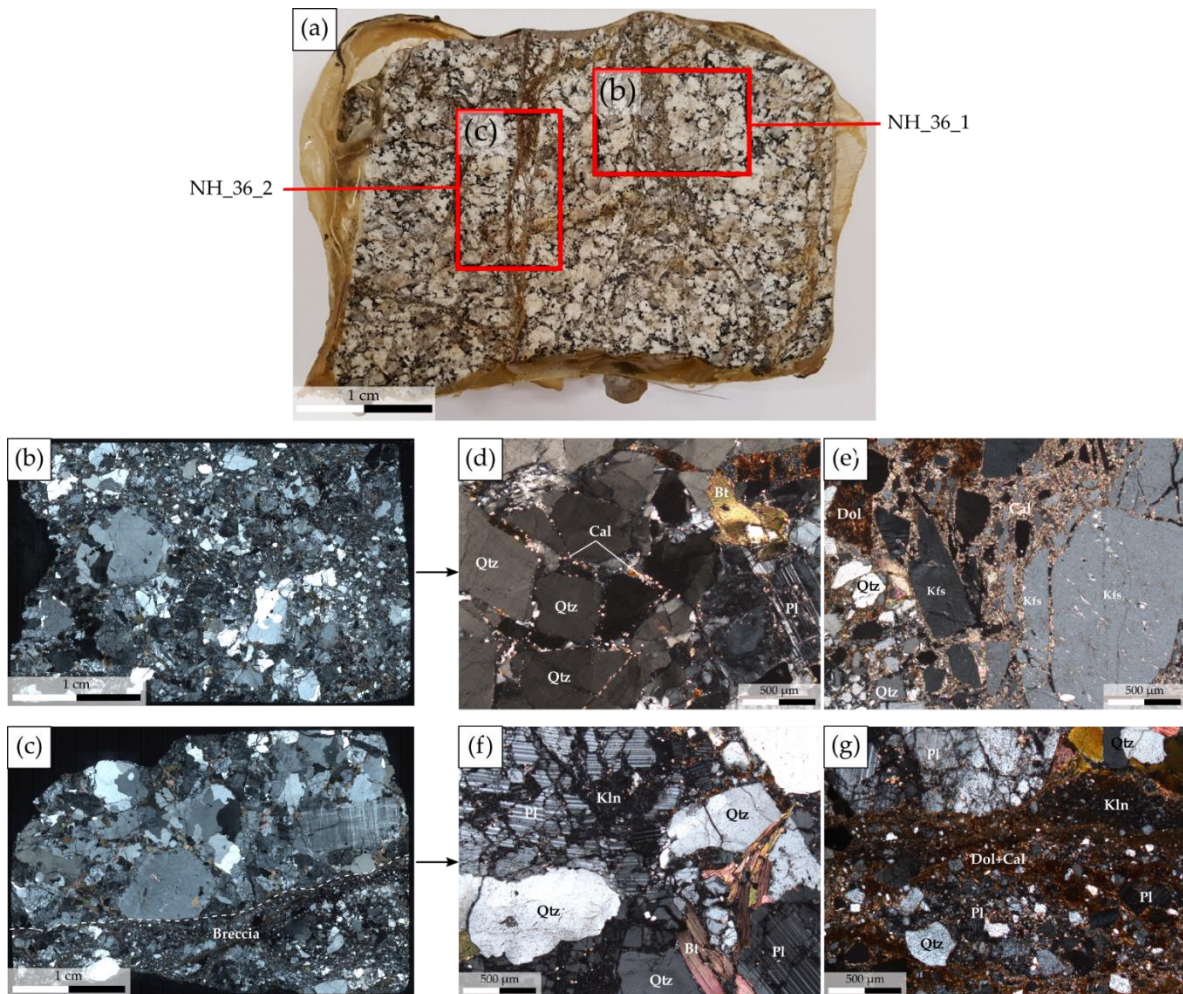


Figure 5-11. (a) Sample NH\_36 collected close to a fault zone showing the location of the two thin sections. (b) A mosaic of the thin section NH\_36\_1 showing a breccia. (c) A mosaic of the thin section NH\_36\_2 showing the limit between a breccia and the almost preserved granite. (d) A microphotograph of the NH\_36\_1 thin section showing a brecciated and slightly altered plagioclase, a brecciated quartz with a significant undulatory extinction starting to recrystallized into subgrains, a brecciated biotite and calcite crystallizing in the microfractures. (e) A micrograph of thin section NH\_36\_1 showing brecciated and non-altered K-feldspar and quartz with dolomite and calcite deposits between the clasts. (f) A microphotograph zooming in the preserved granitic zone visible of the thin section NH\_36\_2 and showing a brecciated and partially replaced plagioclase into kaolinite and brecciated but unaltered quartz and biotite. (g) A microphotograph zooming in the brecciated part of the thin section NH\_36\_2 and showing a carbonate matrix composed of dolomite and calcite transported clasts from the granite.

### V.3.2.3. Sample NH\_23

At outcrop (Figure 5-5b) and sample (Figure 5-12a) scales (Figure 5-1c), 3 compartments were identified: (1) a vein composed of a microcrystalline quartz-feldspathic unit showing signs of foliation with clear shear sense indicators bordered by a calcium rich mylonite and containing clasts of it, (3) a hydrothermalized zone in the granite along the vein represented by a pinkish halo and the porphyritic granite (Figure 5-12a).

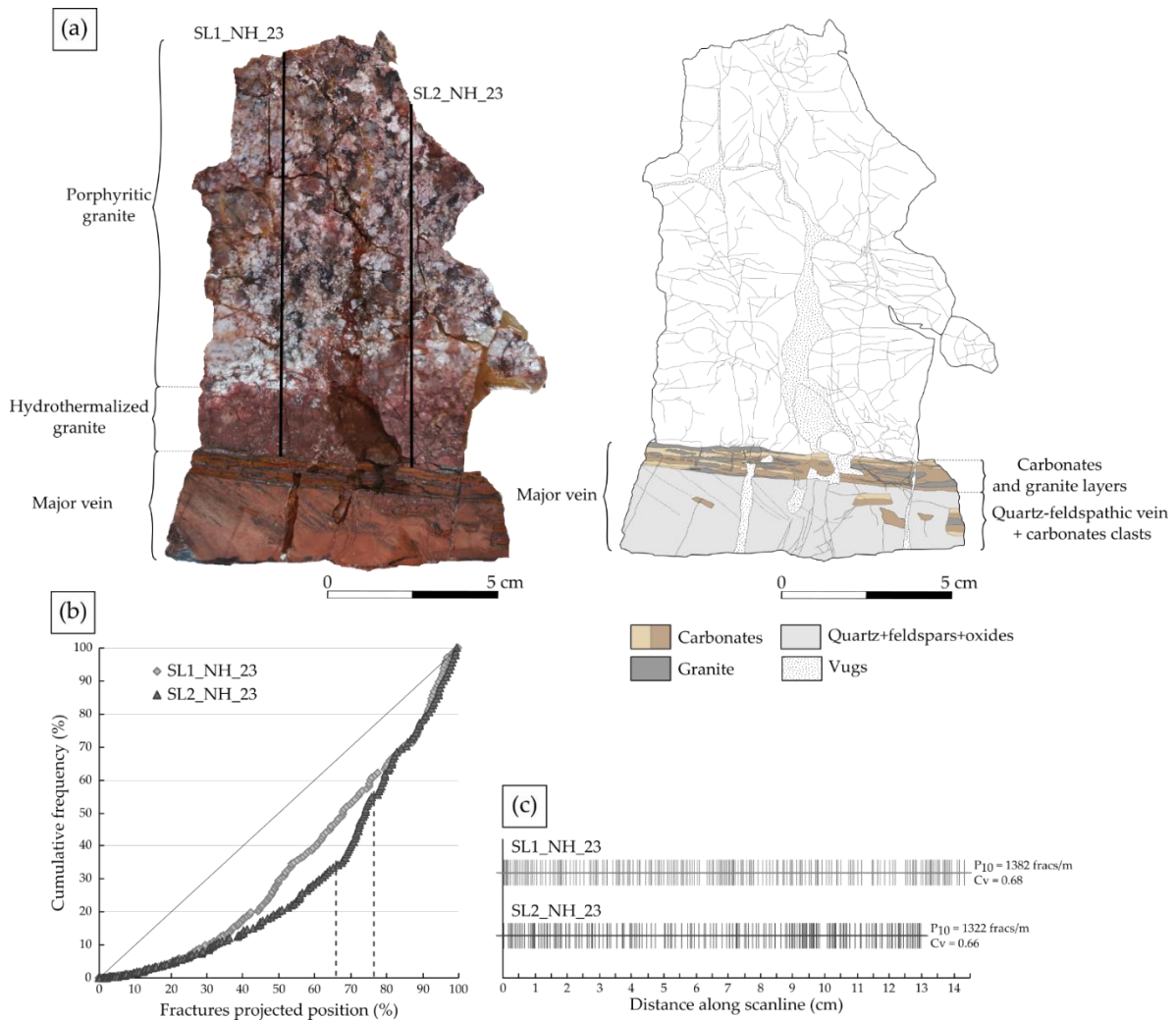


Figure 5-12. (a) A photo and the corresponding digitalization of the sample NH<sub>23</sub> showing the different compartments that compose it, as well as the two scanlines realized in the host rock of the vein. (b) Plots of the cumulative frequency percentage against distance percentage for both scanlines. The diagonal represents a uniform distribution. Dashed lines indicate a zone where a rapid increase of the number of fractures is observed (slope threshold > 2). (c) Stick plots showing the fracture position along the scanlines and for which the fracture density ( $P_{10}$ ) and the coefficient of variation ( $C_v$ ) are given.

- Spatial fracture distribution

Two scanlines were realized in the granitic part of the sample NH<sub>23</sub> to evaluate the fracture arrangement from the vein towards the host rock (Figure 5-12a). The spatial analysis is summarized in Table 5-2. Fracture distributions presented in Figure 5-12b,c for each scanline show an evolution in two steps of the fracture cumulative frequency (Figure 5-12b).

Along the SL1\_NH<sub>23</sub> scanline, the frequency slowly increases and shows a regular fracture distribution. At 40% of the scanline, the frequency slightly increases, still with a regular arrangement of the fractures. The stick plot Figure 5-12c highlights this distribution. The SL2\_NH<sub>23</sub> scanline presents a similar evolution as SL1\_NH<sub>23</sub> scanline, with an increase in

the frequency at  $\frac{3}{4}$  of the scanline. This slope change is expressed at the end by a fracture cluster around 8.7–10 cm, clearly visible on the stick plot (Figure 5-12c). The Cv of 0.68 and 0.67 for each scanline shows a regular to random arrangement of the fractures along both scanlines (Figure 5-12c, Table 5-2). Both scanlines fracture densities are equivalent, with respectively 1382 fracs/m and 1322 fracs/m (Figure 5-12c, Table 5-2).

In order to complete the dataset, the method was repeated on two thin sections from the granite. One is at the border of the vein (NH\_23\_1) and the second away from it (NH\_23\_2) (Figure 5-13a). A scanline was realized in both thin sections (Figure 5-13b), perpendicular to the major vein. The spatial analysis is presented in Table 5-2.

Along the SL\_NH\_23\_1 scanline (Figure 5-13c), a low fracture density zone is present at the beginning of the scanline, then there is an increase of frequency between 0.9–1.4 cm (fracture cluster, Figure 5-13d), followed by an irregular fracture distribution until the 0.4 last cm where a fracture cluster was identified. Three fracture clusters are present in the SL\_NH\_23\_2 scanline around 1.5 cm, between 1.7–2.1 cm and around 2.3 cm. From the first fracture cluster, the frequency increases significantly and irregularly. The scanline SL-NH\_23\_1, with the Cv = 0.77, shows a regular to random arrangement of the fractures, while the Cv = 1.19 of the scanline SL\_NH\_23\_2 indicate a random to clustered arrangement (Figure 5-13c). The fracture distribution varies with the position of the scanline and shows a P<sub>10</sub> slightly higher close to the vein (4798 fracs/m) than away from it (3879 fracs/m) (Figure 5-13d).

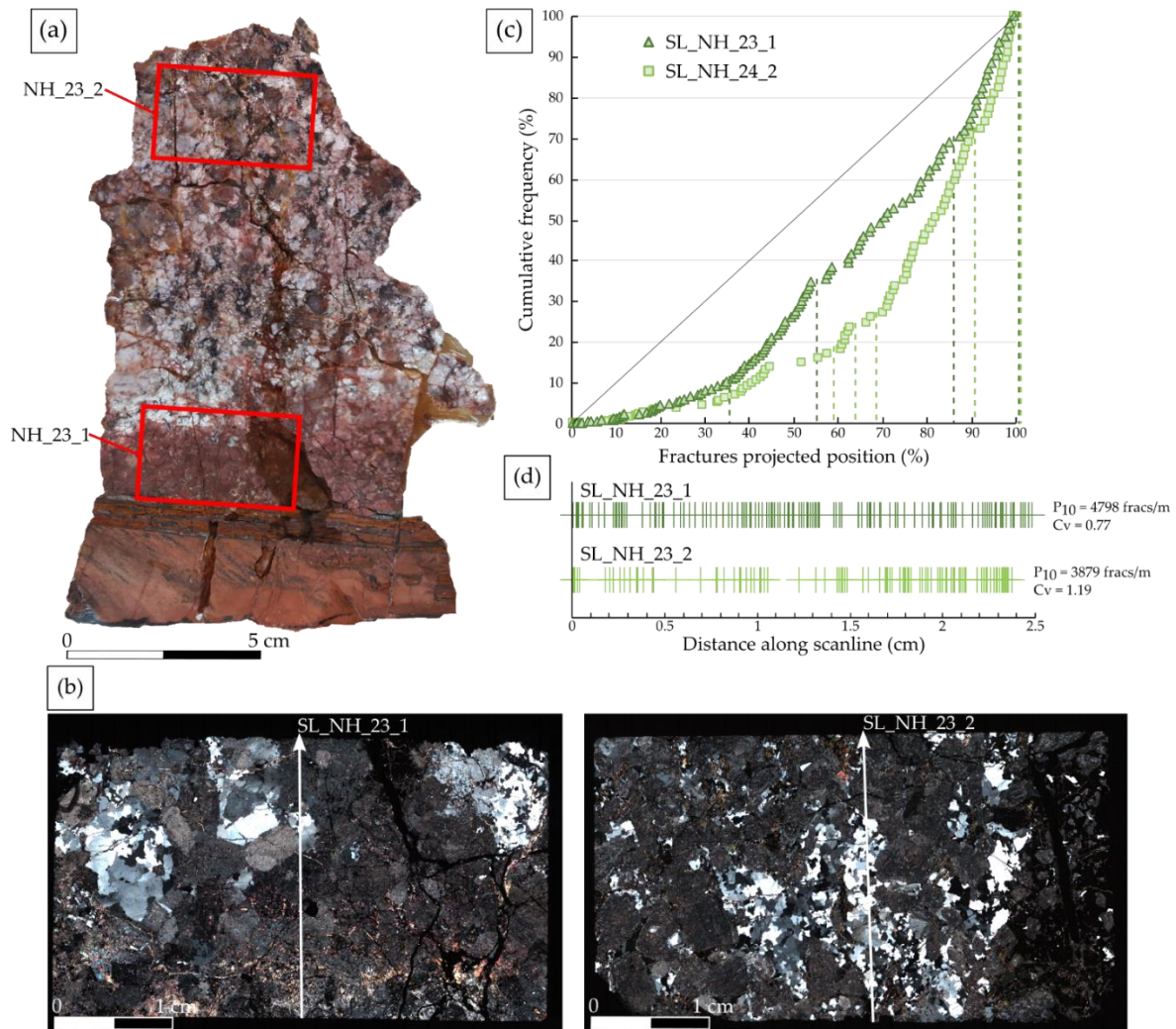


Figure 5-13. (a) Thin section location on the sample NH\_23. (b) Thin section mosaics showing the position and orientation of the scanlines. (c) Plots of the cumulative frequency percentage against distance percentage for each scanline. The diagonal represents a uniform distribution. Dashed lines indicate a zone where a rapid increase of the number of fractures is observed (slope threshold > 2). (d) Stick plots showing the position of the fractures along the scanlines and for which the fracture density ( $P_{10}$ ) and the coefficient of variation ( $C_v$ ) are given.

- Petrographic and Petrophysical Characterization

The vein of the sample NH\_23 consists of two parts. The major part is mainly composed of quartz, few feldspar and oxide minerals having no CPO. Ankerite veinlets crosscut it, and are also intersected by calcite veinlets (Figure 5-14a,b). This vein includes also clasts of carbonates having the same characteristics as the carbonate vein at the contact with the granite (Figure 5-12b). This thin carbonate vein is composed of ankerite layers and granite lenses (Figure 5-14c). By zooming in on the ankerite layer, some part of it appears as lenses with automorphic crystals in the swell which are crushed and stretched through the pinches (Figure 5-14d). Granite is pinched between these ankerite layers. Quartz clasts present in the granite lenses show an undulatory extinction, as well as some evidences of subgrain rotation phenomena.

Carbonates can deform plastically and accumulate large amount of strain at relatively low P-T conditions, from a minimum temperature of 180°C (Bestmann et al., 2000; Burkhard, 1990; Schmid et al., 1987). Quartz crystal plastic deformation is dominant from 600°C (Stipp and Kunze, 2008). Hence, in the present situation carbonates accommodate large amounts of deformation by means of crystal plasticity, while granite is being deformed by cataclastic flow, i.e. a process accommodated by brittle processes. A localized and significant amount of deformation occurred in this vein. The major vein of this sample is thus composed of (1) a highly deformed zone made of ankerite and granite lenses and (2) a siliceous vein, which contains clasts of similar composition as the carbonate vein. We suggest that the carbonate vein was the first event which was intensively deformed and then intersected by the siliceous vein tearing off pieces of the carbonate vein. Calcite and ankerite veins identified in Figure 5-14a,b intersect the carbonate vein and the siliceous vein.

As presented above, the magmatic texture of the granitic part of the sample is preserved. However, a color change of the granite is observed close to the vein. At sample scale, the granitic part along the vein (NH\_23\_1) shows a pronounced pinkish color (Figure 5-13a). In thin section, the granite appears almost completely altered. Plagioclase and biotite are no longer recognizable and are replaced by illite and oxides. Perthitic K-feldspar are not completely affected by the alteration but are partially replaced by illite (Figure 5-14e). Away from the vein (NH\_23\_2), the granite appears whitish at sample scale (Figure 5-13a). Compared to NH\_23\_1, plagioclase are completely replaced by illite and kaolinite, but biotite are only partially altered and K-feldspar are unaltered (Figure 5-14f). This indicates that the granite is more affected by the alteration along the vein, in the hydrothermally altered zone. Bulk analyses performed on the granitic part of the sample show a LOI of 5.2%. In all the granite, calcite veinlets are observed coming from the major vein.

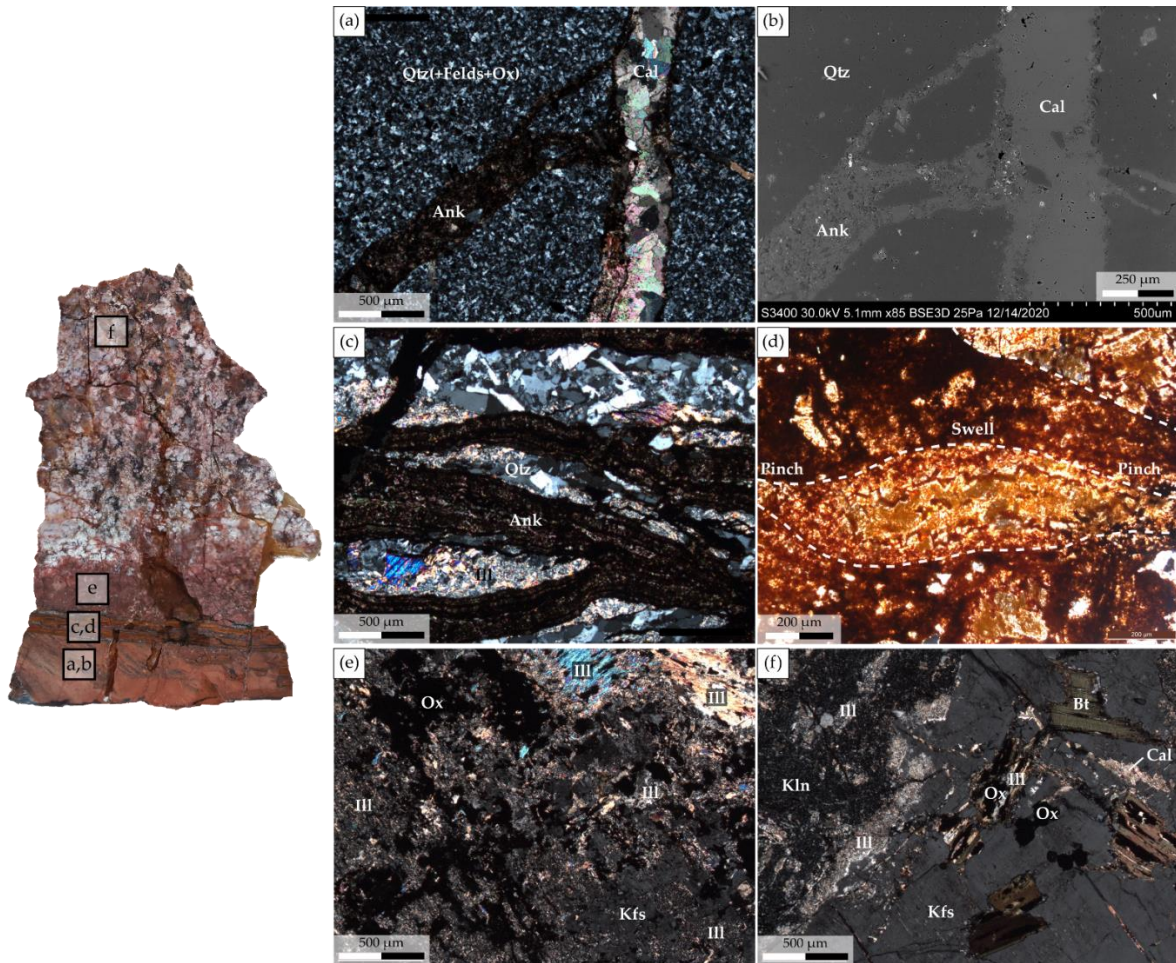


Figure 5-14. Photomicrographs of the different compartments of the sample and their location in the sample. (a) Veins of ankerite and calcite crosscutting the major quartzitic/feldspathic vein of the sample under optical microscope in polarized-analyzed light. (b) Back-scattered electron image of the photomicrograph (a). (c) Photomicrograph of the ankerite-granite interlayering zone under optical microscope in polarized-analyzed light. (d) A zoom image of the ankerite vein, under optical microscope in polarized-analyzed light, presented in (c) and showing a sigmoid of ankerite with a swell of automorphic crystals crushed and stretched in the pinches. (e) The altered granite close to the vein showing a completely altered plagioclase and biotite both replaced by illite and oxides and partially altered K-feldspar under optical microscope in polarized-analyzed light. (f) The altered granite away from the vein showing a completely altered plagioclase replaced by illite and kaolinite, biotite partially replaced by illite and oxides, an unaltered K-feldspar and calcite veinlets under optical microscope in polarized-analyzed light.

#### V.4. Geochemical Analyses

The geochemistry of major element, presented in Table 5-3, allows to establish diagrams representing selected elements versus LOI (Figure 5-15) in order to study the alteration degree of the selected samples.

Table 5-3. Major elements and loss on ignition (LOI) weight percentage (wt%) for the NH granite.

Sample ID	NH_19	NH_23	NH_27	NH_31_3	NH_36
SiO <sub>2</sub>	67.18	60.84	56.26	69.29	66.67
Al <sub>2</sub> O <sub>3</sub>	15.03	17.31	14.05	15.42	15.30
Fe <sub>2</sub> O <sub>3</sub>	2.93	4.61	3.17	2.69	3.65
MgO	0.71	1.06	0.89	0.24	0.97
CaO	1.81	2.83	9.10	2.34	3.80
Na <sub>2</sub> O	2.20	2.45	0.27	2.89	3.12
K <sub>2</sub> O	5.45	4.69	4.48	4.05	3.05
TiO <sub>2</sub>	0.23	0.39	0.29	0.24	0.34
P <sub>2</sub> O <sub>5</sub>	0.12	0.18	0.14	0.13	0.17
MnO	0.11	0.23	0.23	0.06	0.12
LOI	4.10	5.20	10.90	2.50	2.60
Sum	99.91	99.88	99.90	99.88	99.87

The LOI ranges from 2.50 to 10.90 wt% with an average around 5 wt%. The LOI values show a negative correlation with Na<sub>2</sub>O and SiO<sub>2</sub> and a positive one with K<sub>2</sub>O. The CaO content varies slightly between 1.81 wt% and 3.12 wt% except for the sample NH\_27 which CaO content is about 9.10 wt%. Al<sub>2</sub>O<sub>3</sub>, MgO and Fe<sub>2</sub>O<sub>3</sub> contents vary more widely in the ranges 14.05–17.31 wt%, 0.24–1.06 wt% and 2.69–4.61 wt%, respectively. However, a positive correlation is observed between Al<sub>2</sub>O<sub>3</sub> and LOI if the sample NH\_27 is rejected. These diagrams show that carbonate (represented by Ca and Mg) and oxide (represented by Fe) precipitations do not depend on the LOI.

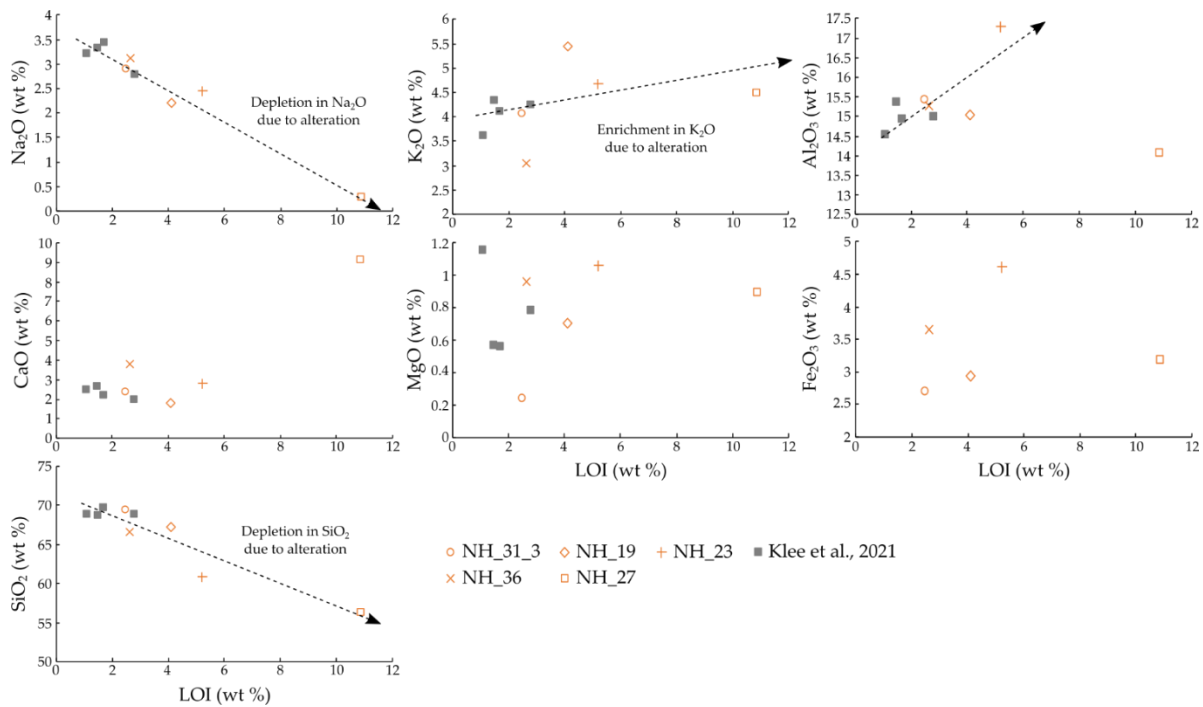


Figure 5-15. Plot of selected major element oxides ( $\text{Na}_2\text{O}$ ,  $\text{K}_2\text{O}$ ,  $\text{Al}_2\text{O}_3$ ,  $\text{CaO}$ ,  $\text{MgO}$ ,  $\text{Fe}_2\text{O}_3$  and  $\text{SiO}_2$ ) versus LOI (loss on ignition) of samples from this study in orange and from Klee et al. (2021a) in grey. The dashed arrows show the different trends observed.

## V.5. Calcite Content

Calcite is present in the majority of the samples. Samples homogeneously distributed in the studied area were selected for calcite content analyses. The calcite content is represented on the map in Figure 5-16 by the white dots and figures. The values range between 1.2% and 8.7%. Fracture zones as well as the surrounding granite present variable calcite content. However, the calcite content appears higher in the southeastern part of the range than in the northwest. All the samples except NH\_17, NH\_26 and NH\_31\_3 have a calcite content higher than 1.8%, meaning that they were affected by hydrothermal alteration according to White et al. (2005).

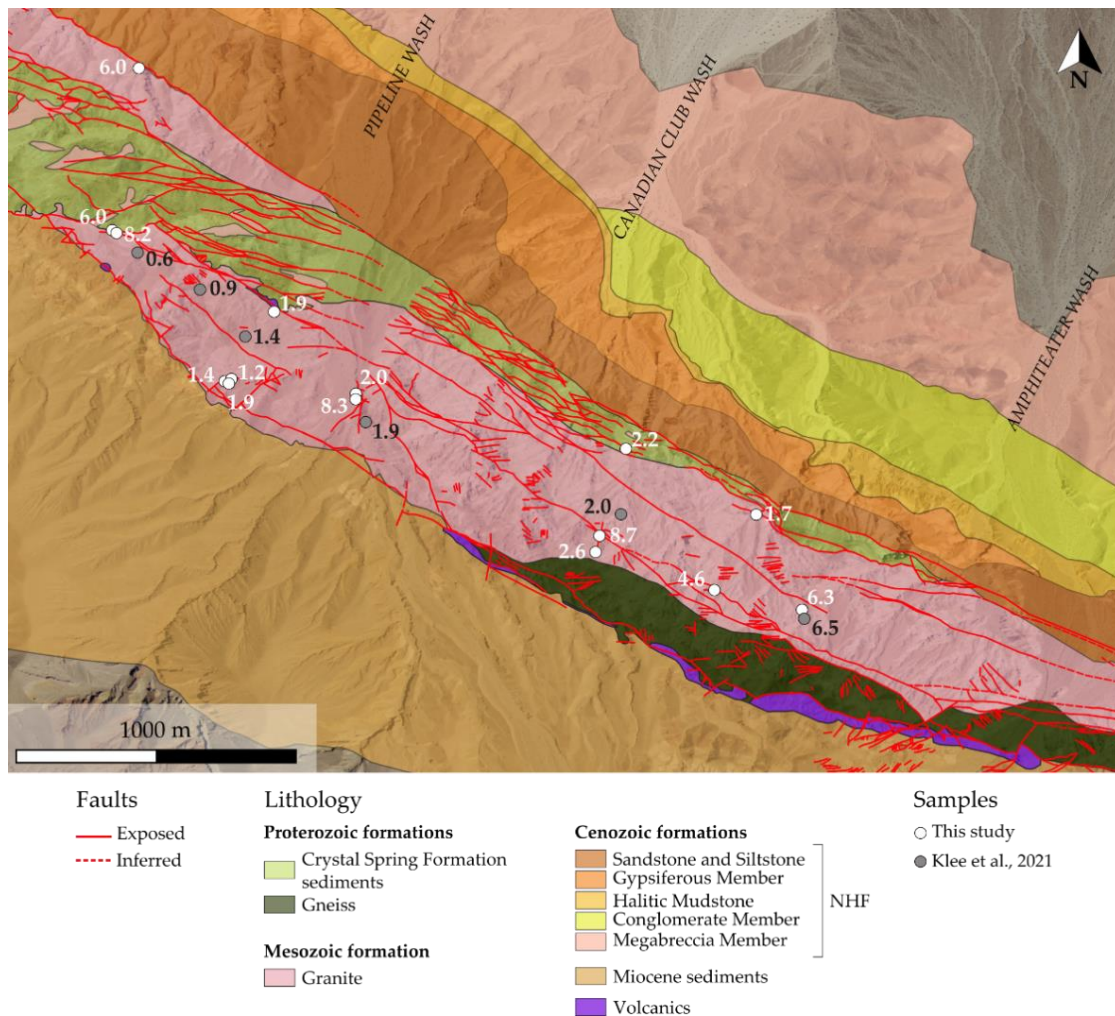


Figure 5-16. NH geological map showing the location and the associated calcite content of samples from this study represented by the white dots and of samples from Klee et al. (2021a) by the grey dots.

## V.6. Porosity and Mass-balance

Porosimetry measurement was only performed on samples NH\_27, NH\_31\_3 and NH\_36 (Table 5-4). NH\_36 is the closest to a fracture zone and has the highest porosity (11.5%). This suggests that the porosity increases with proximity to fracture zones. Porosity measurements were used to better decipher the petrophysical properties of the rock for geothermal purpose and to realize mass-balance calculations. The chemical compositions recalculated after suppression of the LOI, the densities, and volume factors ( $F_v$ ) assuming  $X_{Al_2O_3} = 0$ , of the rock samples used for mass balance calculations, are given in Table 5-4. The  $F_v$  shows values very close to 1 indicating a small change in volume between the freshest sample and the altered ones.

Table 5-4. Porosity values, recalculated bulk-rock major element weight percentage, altered rock density/fresh rock density ratio, volume factor ( $F_v$ ) assuming the immobility of  $Al_2O_3$  ( $X_{Al_2O_3} = 0$ ).

Sample ID	NH_2 <sup>1</sup>	NH_27	NH_31_3	NH_36
Porosity (%)	2.29	10.1	10.1	11.5
Oxides (weight %)				
SiO <sub>2</sub>	69.57	63.3	71.18	68.6
Al <sub>2</sub> O <sub>3</sub>	14.72	15.81	15.84	15.74
Fe <sub>2</sub> O <sub>3</sub>	4.35	3.57	2.76	3.76
MgO	1.16	1	0.25	1
CaO	2.53	10.24	2.4	3.91
Na <sub>2</sub> O	3.23	0.3	2.97	3.21
K <sub>2</sub> O	3.65	5.04	4.16	3.14
TiO <sub>2</sub>	0.47	0.33	0.25	0.35
MnO	0.12	0.26	0.06	0.12
Density ratio				
( $d_A/d_F$ )		0.93	0.92	0.92
$F_v$ ( $X_{Al_2O_3} = 0$ )	1.00	1.00	1.01	1.02

<sup>1</sup> Geochemical data recalculated from Klee et al. (2021a)

The results of mass-balance calculations, corresponding to the absolute mobility values of each element for each sample, are given in Table 5-5, by considering a constant volume,  $F_v = 1$ , as exposed by Gresens (1967). Positive values represent the gains and negative values the losses of the considered elements. Absolute mobility values indicate almost immobility of  $Al_2O_3$ ,  $TiO_2$  and  $MnO$ . They also show losses of  $SiO_2$  and  $Na_2O$ , which are three times more important in NH\_27 than in NH\_31-3 and twice that of NH\_36. The losses of  $Fe_2O_3$  and  $MgO$ , are more important in NH\_31\_3 and less important in NH\_36.  $CaO$  losses are observed in NH\_31\_3, whereas  $CaO$  gains are observed in NH\_36 and a high gain is observed in NH\_27. Finally, the results show a gain of  $K_2O$  in samples NH\_27 and NH\_31\_3 and a loss in NH\_37.

Table 5-5. Results of mass-balance calculations assuming  $F_v = 1$ .

Sample ID	NH_27	NH_31_3	NH_36
Absolute mobility (%)			
SiO <sub>2</sub>	-10,39	-3,54	-5,32
Al <sub>2</sub> O <sub>3</sub>	0,06	-0,18	-0,29
Fe <sub>2</sub> O <sub>3</sub>	-1,01	-1,77	-0,82
MgO	-0,23	-0,92	-0,22
CaO	7,04	-0,30	1,10
Na <sub>2</sub> O	-2,95	-0,47	-0,22
K <sub>2</sub> O	1,06	0,20	-0,70
TiO <sub>2</sub>	-0,16	-0,24	-0,14
MnO	0,12	-0,06	-0,01

## V.7. Temperature Conditions

The clay composition of the fractions  $< 2 \mu\text{m}$  and  $2\text{--}6 \mu\text{m}$  was given in Table 5-1. For some of the samples containing enough illite, Kübler Index (KI) was measured for both fractions (

Table 5-6). The fraction  $< 2 \mu\text{m}$  likely is supposed to represent neoformed clay minerals, thus corresponding to the youngest event. By contrast, the fraction  $2\text{--}6 \mu\text{m}$  might contain either more developed illite crystals by inherited grains recrystallization, or a mix of detrital and neoformed minerals. The KI gives information concerning the degree of metamorphism for each fraction. In some fraction, it was not possible to measure the KI due to the too low amount of illite.

Table 5-6. List of samples with their respective FWHM and Kübler Index (KI) values in air dried (AD) conditions for the fractions  $< 2 \mu\text{m}$  and  $2\text{--}6 \mu\text{m}$ . n.m. - not measured.

Sample ID	illite peak (10) $< 2 \mu\text{m}$		illite peak (10) $2\text{--}6 \mu\text{m}$	
	FWHM AD	KI AD	FWHM AD	KI AD
NH_16	0,62	0,97	0,43	0,65
NH_17	n.m.		0,80	1,27
NH_18	0,41	0,61	0,34	0,49
NH_19	0,52	0,75	0,51	0,74
NH_22	0,53	0,78	0,58	0,84
NH_24	0,83	1,32	0,70	1,11
NH_25	0,59	0,59	0,63	0,63
NH_27	0,65	0,96	0,55	0,80
NH_31_1_2	0,72	1,14	0,64	1,01
NH_31_3	n.m.		0,34	0,50
NH_32	0,29	0,29	0,21	0,21
NH_34	n.m.		0,28	0,39

KI values range from  $1.32\Delta^{\circ}2\theta$  to  $0.29\Delta^{\circ}2\theta$  for the  $<2\ \mu\text{m}$  fraction and from  $1.27\Delta^{\circ}2\theta$  to  $0.21\Delta^{\circ}2\theta$  for the  $2\text{-}6\ \mu\text{m}$  fraction (

Table 5-6). The spatial distribution of the samples and their associated KI values are shown in Figure 5-17 by the dots. In both fractions, most of the samples present KI values corresponding to the diagenetic zone except for two samples (NH\_32 and NH\_34). These samples are located in the northwestern part of the main granitic body (Figure 5-7a,b), at the contact with the Proterozoic basement. They present lower KI values of low anchizone and epizone. No significant variations in KI or trends are observed between both fractions.

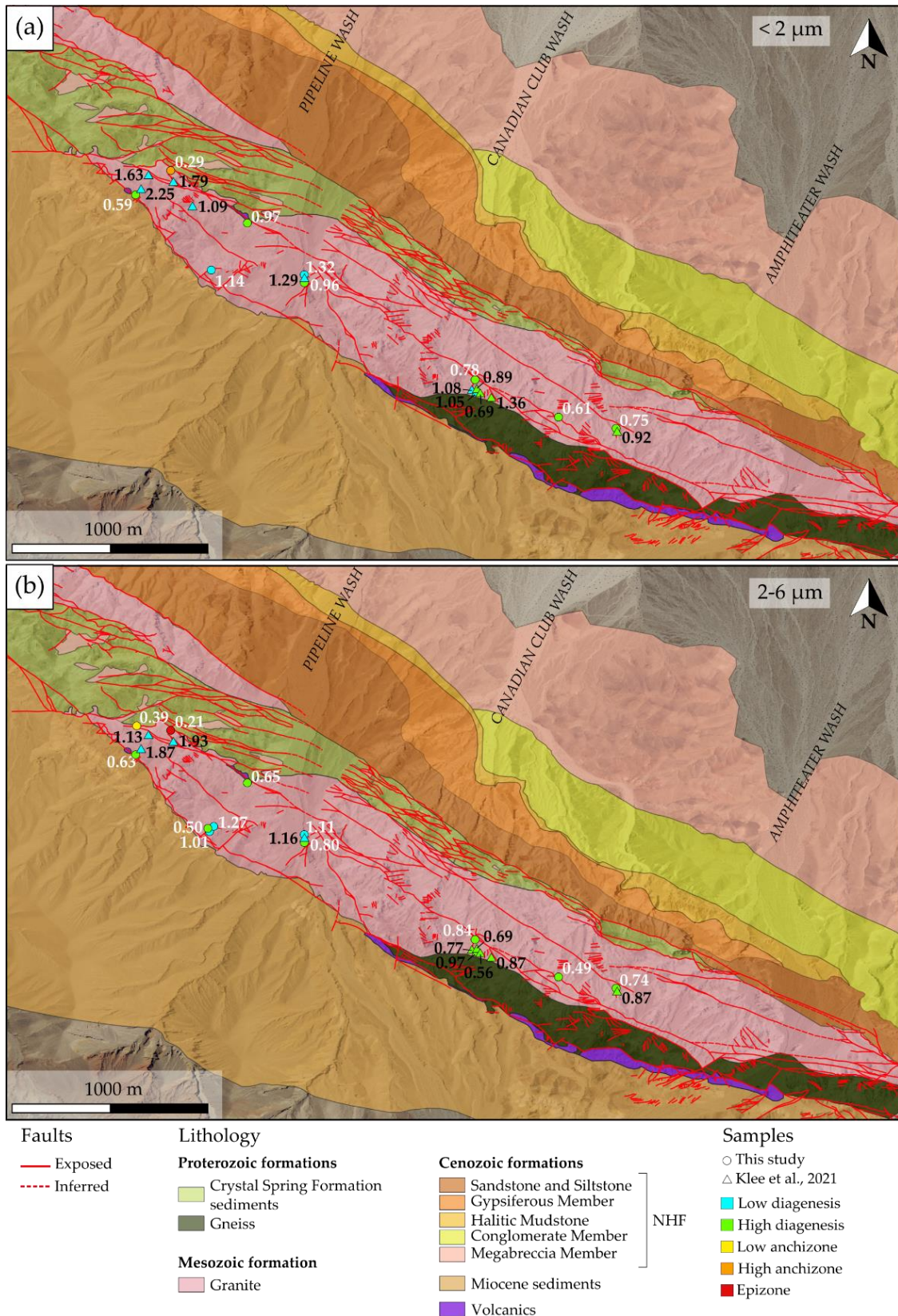


Figure 5-17. Geological map representing the Kübler Index (KI) in air dried conditions of each sample from this study (Dots) and from Klee et al. (2021a) (Triangles) and the corresponding metamorphic zone represented by the different colors indicated in the legend for (a) the fraction  $< 2\mu\text{m}$  and (b) the fraction  $2-6 \mu\text{m}$ .

Some samples contain only kaolinite and no illite. Positive trends have been identified between KI and KCI for both clay fractions  $<2\ \mu\text{m}$  and  $2\text{--}6\ \mu\text{m}$  (Figure 5-18). Samples NH\_6, NH\_8 and NH\_31\_1\_2 with out of range values, due to the presence of I/S and/or corrensite interfering with the  $7\text{\AA}$  peak, were excluded from the correlation. The trends observed in the two different fractions are similar and give more confidence into the concomitant evolution of KI and KCI. The correlation provides temperature indications for illite-free samples. Thus, samples NH\_26, NH\_33 and NH\_36 show values equivalent to diagenetic zone and anchizone conditions.

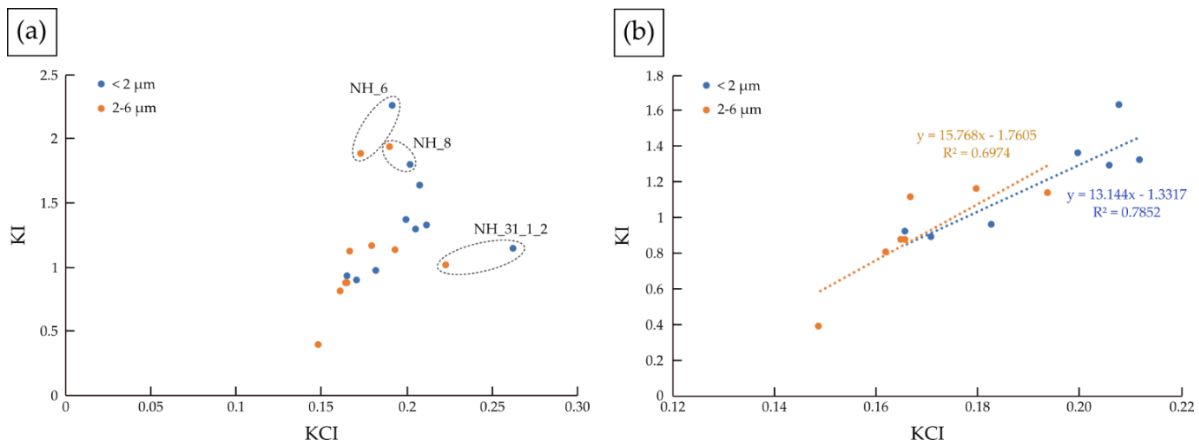


Figure 5-18. (a) Diagrams showing Kübler Index (KI) values versus kaolinite crystallinity index (KCI) for the clay fractions  $<2\ \mu\text{m}$  and  $2\text{--}6\ \mu\text{m}$ . (b) Diagram showing positive correlations between KI and KCI for the clay fractions  $<2\ \mu\text{m}$  and  $2\text{--}6\ \mu\text{m}$  excluding samples NH\_6, NH\_8 and NH\_31\_1\_2.

## VI. DISCUSSION

### VI.1. Argillic Alteration Dominance

The characterization of the NH granite alteration processes in the vicinity of fracture zones reveals the presence of various secondary minerals such as clay minerals (kaolinite, illite, I/S mixed layer, corrensite and vermiculite), carbonates (calcite, dolomite, ankerite, siderite) and oxides. Thus, two successive types of hydrothermal alteration events, characterized by (Klee et al., 2021a) in the protolith, were observed:

1. the propylitic alteration, which is an early stage of alteration affecting pervasively the granite during the cooling of the pluton (Glaas et al., 2021). It involves mainly the formation of corrensite and epidote considered as the major indicators of the propylitic alteration (Burnham, 1962; Klee et al., 2021a; Traineau et al., 1991). Only plagioclase and biotite are partially affected.
2. the argillic alteration, associated with fluid circulation through a fracture network. Thus, the argillic alteration is also called “vein” alteration (Dubois et al., 2000; Genter, 1989; Ledésert et al., 2010). It is characterized by (1) a high water/rock ratio in the

fractures/veins walls, due to fluid circulating within the fracture network (Berger and Velde, 1992; Bonorino, 1959; Genter, 1989; Ledésert et al., 1999; Marques et al., 2010; Parneix and Petit, 1991; Pauwels et al., 1993) and (2) illite + kaolinite + illite/smectite mixed layers + carbonates + oxides replacing plagioclase, biotite and more rarely, partially K-feldspar (Klee et al., 2021a). Fractures enhance the fluid circulation and thus the fluid-rock interaction. Alteration gradients are visible, increasing toward the fracture (Figure 5-7a, Figure 5-9h-k, Figure 5-12a and Figure 5-14e,f). An alteration zoning around microfractures is also presented in Figure 5-6h, which could correspond to a time dependent process controlled by a sequence of interrelated mineral reactions (Turpault et al., 1992).

However, compared to Klee et al. (2021a), the samples are more altered and corrensite is not as evident as in the samples from this study. Kaolinite and illite are the prevailing clay minerals. This confirms a significant fluid-rock interaction near fractures and a predominant argillic alteration, which has overprinted almost completely the propylitic alteration. Kaolinite being the dominant clay mineral, indicates either a more important leaching of the rock or the circulation of a more acidic fluid (Fulignati, 2020).

The samples NH\_24, NH\_26 and NH\_33 contain a small amount of vermiculite, which can be associated to hydrothermal alteration at low temperature or to weathering. It is commonly thought that most of the vermiculite is formed under supergene conditions (Fordham, 1989; Kajdas et al., 2017). In these samples, the amount of vermiculite is low and the weathering contribution already discarded by Klee et al. (2021a).

## VI.2. Thermal Evolution Toward Fracture Zones

Studied samples present KI values characteristic of the diagenetic zone, meaning temperatures lower than 200°C (Abad, 2007). However, KI values of samples NH\_32 and NH\_34 have lower KI values with anchizonal to epizonal conditions, meaning temperatures around 300°C (Abad, 2007). These two samples present the highest fracture density (Fd4) suggesting that shear heating could contribute to a local increase of temperature (Camacho et al., 2001). Moreover, KI values are similar between both clay fractions indicating the predominance of neoformed illite crystallization close to fracture zones. It is highlighted by the presence of illite veins observed microscopically. By comparing KI values from this study and from Klee et al. (2021a), the KI tends to decrease approaching fracture zones. Thus, the greater the fracturing, the higher was the temperature, except for NH\_31\_1\_2 and NH\_24. These two samples present higher KI values, meaning lower temperatures. It can be explained by the presence of I/S and vermiculite

forming at lower temperature than illite and kaolinite (Fordham, 1989; Kajdas et al., 2017; Środoń, 1999). The samples NH\_26, NH\_33 and NH\_36 present only kaolinite. KCl values correlating with KI values, these samples show temperatures estimated to be around 200°C or less, which correspond to the temperature obtained for the other samples. Likewise, the presence of kaolinite in hydrothermal alteration paragenesis indicates temperature lower than 200°C (Fulignati, 2020).

### VI.3. A Multi-Stage Paleo-fluid Circulation

Hydrothermal alteration in crystalline basement rocks induces the precipitation of secondary minerals that can seal the fractures (Gillespie et al., 2020). The argillic facies, described above, is also characterized by fractures filled by various kinds of secondary minerals, as a result of different fluid generations. Veins are formed from fluids that had reacted with granite (Bruhn et al., 1994) and transported various chemical elements. Through the petrographic analyses of the whole samples, a relative chronology between the different veins can be determined. Six vein generations, following each other, were identified (Figure 5-6 and Figure 5-9):

1. Quartz veins resulting into the precipitation of secondary quartz due to primary silicate partial dissolution.
2. Illite veinlets, which have different behaviors according to the mineral crossed. Indeed, as presented by Klee et al. (2021a) and Sardini et al. (1997), plagioclase is the main pathway for fluid flow due to their abundance in the rock and to dissolution pit porosity allowing the interconnection between the pores. In quartz and K-feldspar, however, only microfractures create the porosity allowing the fluid to circulate. This explains why veinlets look like straight lines in quartz and K-feldspar and are twisted and blurred lines in altered plagioclase. Illite veinlets can be contemporary to kaolinite veinlets.
3. A dolomitic brecciated vein embedding essentially quartz clasts, like in sample NH\_31.
4. Carbonate veins with different compositions: contemporary ankerite/dolomite veins, intersected by siderite veins and the whole intersected by later calcite veins. They are preferentially oriented NW-SE, according to the direction of the NH. It is suggested that the fluids having precipitated these carbonate veins have circulated through the fracture network formed by the activity of the SDVFZ.
5. A carbonate brecciated vein that is likely to have transported clasts of quartz, K-feldspar and biotite, and presenting precipitations of barite. This phase, but also barite itself, is only present in sample NH\_31. This phase was probably due to a later event that reactivated the main fracture composing the sample and let a new fluid circulate.

6. Calcite veins, as shown in the sample NH\_31, which are of a different composition from generation 4.

Two types of calcite veins and the carbonate vein of phase 5 were thus identified through the sample NH\_31, allowing the definition of two generations of calcite. However, they do not allow a decision if the calcite veins identified in the other samples correspond to the generation 4 or 6. CL analyses are ongoing to identify the type of calcite generation. Sample NH\_31 and the multiple vein generations show how complex the fluid circulation history was in this area.

#### VI.4. Fluid Circulation and Argillic Alteration Effects on Petrographic and Petrophysical Behavior

The effects of alteration on the element transfers are described by the diagrams plotting major element oxides against LOI (Figure 5-15) and by mass-balance calculations (Table 5-5) using the Gresens method Gresens (1967) to quantify the losses and gains of elements during hydrothermal alteration. To this end, data from this study and from Klee et al. (2021a) were used. LOI has been defined as an indicator of the alteration degree (Chambefort et al., 2007; Klee et al., 2021a; Liu et al., 2018) supporting optical observations. In this study, LOI values range from 2.5% to 10.9% (Table 5-3), whereas, Klee et al. (2021a) obtained values from 1.1% to 2.8% for the protolith. These values confirm a more pronounced alteration of the granite in the vicinity of fracture zones.

Concerning element transfers, only minor variations of  $Al_2O_3$  were observed compared to the LOI, also confirmed through mass-balance calculations. Al is thus considered as immobile. This study has shown a significant  $SiO_2$  negative correlation with LOI. This loss is confirmed by mass-balance calculations. It indicates the partial silicate alteration, explaining the presence of quartz veins and veinlets through the granite. A negative correlation with LOI was observed for  $Na_2O$ , confirmed by the loss of  $Na_2O$  obtained by mass-balance calculation. Indeed, altered plagioclase are depleted in  $Na_2O$ . No Na-bearing newly formed minerals (except little I/S and C/S) was encountered. It is likely that Na was exported out of the alteration zone. When the alteration of plagioclase is less pronounced, as in samples NH\_31\_3 and NH\_36 (Table 5-3), the  $Na_2O$  depletion is lower. However, a global enrichment of  $K_2O$  is observed linked to illite crystallization. A positive correlation is observed between amount of alteration and illite formation. K-feldspar being rarely altered, chemical modelling would be necessary to determine whether the amount of K release by biotite alteration would be sufficient to allow the rather important formation of illite.  $MgO$  and  $Fe_2O_3$  present no clear correlation with LOI. However, low depletion of  $Fe_2O_3$  and  $MgO$  compared to the protolith were identified by mass-balance

calculations. It is suggested that these depletions are linked to the alteration of biotite but they are compensated by their precipitation as oxides or in carbonates. Thus, it is likely that no Fe or Mg is exported out of the alteration zones. CaO and calcite content present no correlation with the LOI. Samples NH\_19, NH\_36 (this study) and NH\_3 (in Klee et al. (2021a)) present a similar calcite content, respectively of 6.3%, 6.0% and 6.5%, whereas they present different LOI values (4.1%, 2.6% and 2.8% respectively). The case of a high calcite content associated to a low LOI can be either explained by (1) physico-chemical fluid composition bringing Ca and not allowing a complete alteration of plagioclase and biotite into clay minerals (Glassley et al., 2016), (2) the residence time of the fluid was not sufficient (Kadko and Butterfield, 1998), (3) a non-sufficient amount of fluid to allow the transformation of plagioclase and biotite into clay minerals. CaO losses are attributed to the alteration of plagioclase. However, the amount of Ca released by the alteration of plagioclase is certainly not sufficient to explain the crystallization of large amounts of carbonate into the granite veins. We infer that Ca is related to an external source as it is gained by the system (open system). Carbonate veins being related to the SDVFZ activity, we suggest that the source of the Ca is the Proterozoic series which contain dolomite and carbonate sequences.

Fracture zones created porosity through microfractures and spaces between secondary minerals (Figure 5-6f) precipitated during primary mineral alteration. When fracturing increases, alteration increases too, as well as porosity (Géraud et al., 2005). However, the subsequent mineralization and chemical alteration can either decrease or increase the porosity of the rock (Gillespie et al., 2020). For a similar LOI, porosity values vary significantly (e.g. NH\_3 (Klee et al., 2021a), NH\_23 and NH\_31\_3). No correlation is visible between porosity and alteration or calcite content.

## VI.5. Relation Between Fluid Circulation, Alteration and Fracture Density

It is expected that areas along the rear southern limit of the CBS have recorded less transcurrent shear than areas situated along its northern front (section 4.1). Recent work by Chabani et al. (2021) has shown a structural compartmentalization occurring at the NH scale with a varying intensity that may influence fluid flow through the fracture network. Likewise, they identified a complex network of joints at outcrop scale, also encountered in this study at the sample and thin section scales, playing a key role in the fracture connectivity. The authors identified several fracture sets, among which the NW/SE and the E/W oriented sets are predominant. The NW/SE trend, following the SDVFZ direction, controls the geometry in the whole range,

whereas the E/W, set characterized by several short fractures is mostly present in the central and southeastern part of the NH. The geometrical analysis of both fracture sets showed that the connectivity is ruled by fractures of different sizes. Regarding the fracture distribution, the highest fracture density is recorded within the rear southern part with values five times higher than in the northern part. This can be explained by the complex tectonic setting and the gradient of deformation observed in the entire NH range, with evidence of extreme shearing in the southern part as already presented. Moreover, through scanline analyses along drone photogrammetric outcrop profiles and ground outcrop profiles, Chabani et al. (2021) show a clear correlation between fracture density and distance from a fault zone. The closer the fault zone, the greater the fracture density. There is no straightforward correlation between amounts of deformation and fracture density. Fracture density depends on a series of parameters notably rock competence, anisotropy of units and possible presence of detachment zones concentrating deformation in narrow areas.

This study together with that of Klee et al. (2021a) confirm the increase of fracture density towards fault zones through several samples collected at different distances from the faults. Moreover, at the NH scale, the LOI increases as the fracture zones are approached (Section VI.4). The more intense the fracturing, the higher the alteration. Likewise, porosity values obtained for samples from Klee et al. (2021a) range from 2.2% to 5.2%, whereas, porosity values for this study samples range from 10.1% to 14.0%. Close to fracture zones, samples have more than twice the porosity than the samples away from them. Calcite content (Figure 5-16) also show higher values near to fracture zones, highlighting the importance of the presence of fractures allowing fluid circulations and thus carbonate precipitation, which mainly filled and sealed the fractures (Hébert et al., 2010; Ledésert et al., 2009). Carbonate veins are present in the whole range, preferentially orientated following the NH strike, probably related to the SDVFZ activity. However, calcite content is generally higher in the southeastern part of the range. This part is characterized by a high fracture density due to complex tectonic setting, related to the GFZ activity (Chabani et al., 2021). The connectivity within this part is ruled by the small and large fractures, and an additional complex joint network leading the fluid supply toward the fault zone.

The comparison of the data from Klee et al. (2021a) with those in this study at the NH scale shows that the increase in fracture density is correlated with the increases in alteration degree, porosity and calcite content, respectively. However, no correlation is observed between alteration, porosity and calcite content all together. The sample NH\_36 (Figure 5-11) has shown that calcite content is not related to the intensity of alteration (section 5.4). This highly fractured

sample has been characterized by a specific fracture arrangement, composed mainly of fracture clusters, following the SDVFZ direction. It allows the fluid to circulate following these clusters, and then creating a flow anisotropy. However, only a low alteration degree is observed, which can either be due to (1) specific physico-chemical fluid composition (Glassley et al., 2016), (2) an equilibrium between the fluid and the surrounding rock, (3) an insufficient residence time of the fluid (Kadko and Butterfield, 1998), or (4) a non-sufficient amount of fluid. Fracture density increase does not necessarily induce the increase of alteration (Figure 5-19a,b), whereas at NH scale, a general correlation between fracture density and alteration was shown. Sample NH\_36 shows that fluid can circulate through a highly fractured granite without necessarily producing alteration (Figure 5-19b).

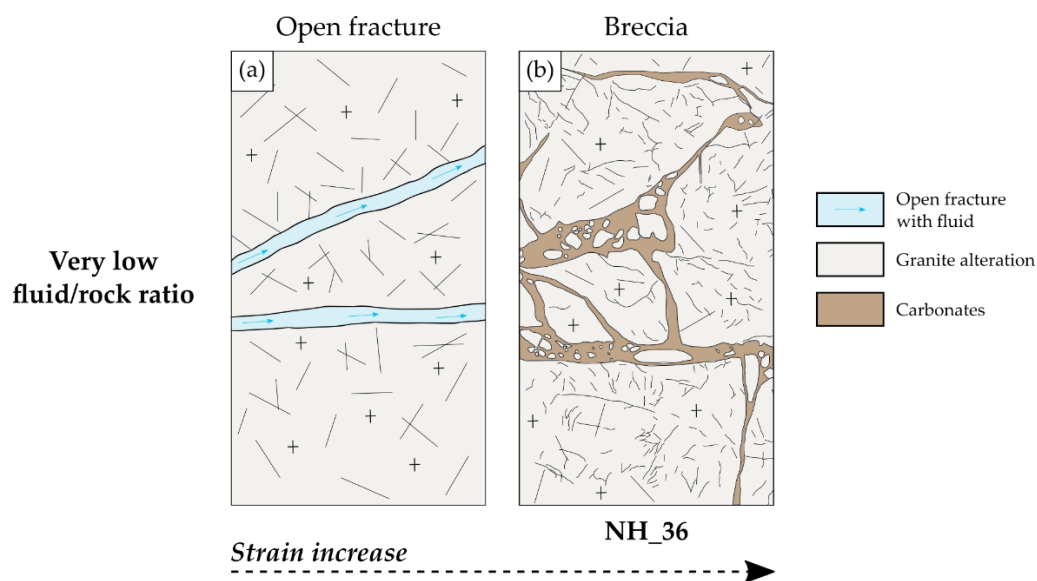


Figure 5-19. Synthetic scheme showing, from low to moderate strain, the interaction between the fluid and the granite in the cases of a very low fluid/rock ratio. (a) Open fractures with an incipient alteration of the surrounding rock. (b) Brecciated zones with a carbonated matrix and no change of alteration degree. No scale is given for this scheme, because it can represent fracture zones of several order of magnitude.

Numerous fractures and veins, showing a high fluid-rock ratio, crosscut the granite altering it consequently (Figure 5-20a,b). Faulkner et al. (2010) have shown that within crystalline rocks, the flow can be ruled by a small number of fractures within the rock surrounding a fracture zone. The fracture interconnections constitute the main parameter which can enhance the fluid circulation. Samples NH\_31 and NH\_23 showed the relation between fracturing and alteration at local scale (section 4.3.2). Thin section fracture analyses showed that the fracture density average is similar in both samples. NH\_31 consists of a brecciated vein developing an alteration gradient but no fracturing gradient (Figure 5-20c), while NH\_23, perpendicular to NH\_31, consists of a mylonite developing an alteration and a fracturing gradient (Figure 5-20d). Regarding the stress axis orientation, it is suggested that the main stress axis  $\sigma_3$  is at a very high

angle to the NH\_31 initial quartz vein. The close to normal angle between the initial quartz vein and the stress axis  $\sigma_3$  was favorable to reactivation, inducing a brecciated vein without developing a significant additional fracture gradient in the surrounding rock (Figure 5-20c). It has been shown that remnants of a quartz vein composed the NH\_31 brecciated vein. This quartz vein, developed during a past event of unknown age and origin, possibly magmatic (last crystallization fluids). It is suggested that this vein was reactivated, letting a new fluid rich in Ca circulates. Then carbonates crystallized giving a brecciated vein as a final product. The alteration gradient observed in the wall rock is especially pronounced at the borders of the brecciated vein. The proximity with the main fluid pathway induced an important leaching by the fluid. Within NH\_23 (Figure 5-20d), it is supposed that the quartz-feldspathic unit was initially a dyke crosscutting the granitic pluton. Such dykes have been observed in the surroundings. During SDVFZ activity, reactivation of this zone of weakness permitted percolation of a Ca-rich fluid. An intensive shearing induced dynamic recrystallization developing a mylonite in the borders and its associated fracturing gradient in the wall rock. In that case, the main stress axis  $\sigma_1$  would be characterized by an intermediate angle to the shear plane. A fracturing gradient is observed in the surrounding rock. The fracture density induced in the surrounding rock does not further increase. Asymmetric clasts and shear bands are observed within this mylonitic layer.

Fluid circulation and induced fracturing have promoted fluid-rock interactions and the granite alteration, which is more pronounced in NH\_23 than in NH\_31 (Figure 5-9h-k, Figure 5-14e,f). Those two samples showed that at sample and outcrop scales, fracturing and alteration are heterogeneous, but also that the alteration degree is not always related to the fracture density (Figure 5-20c,d).

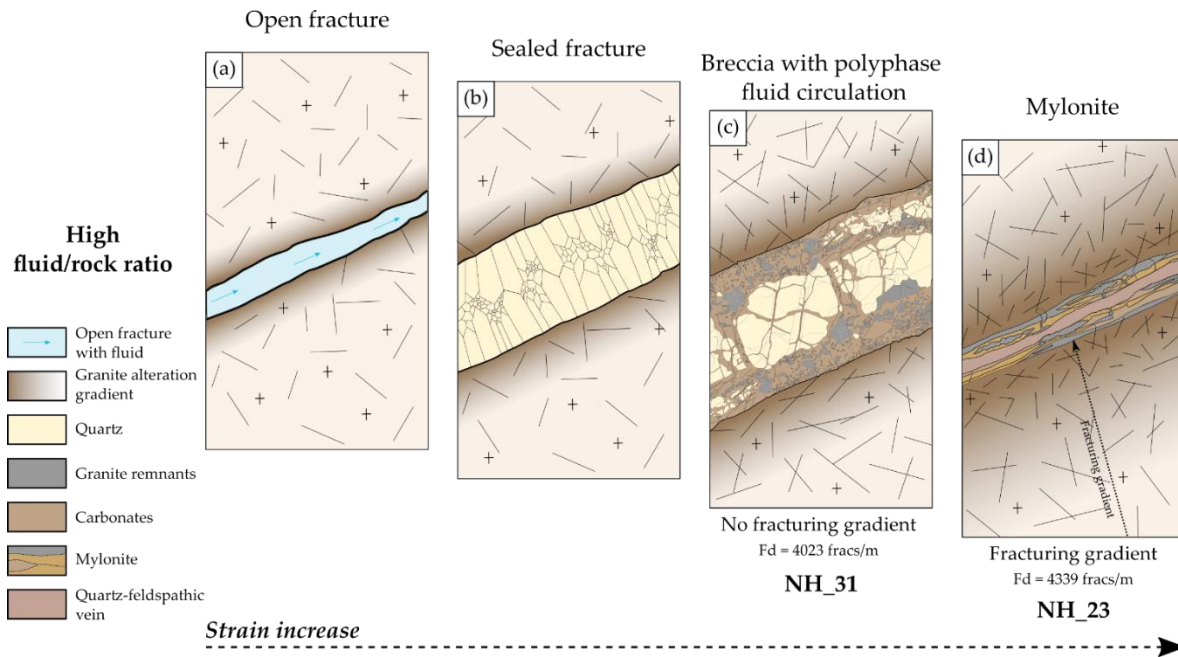


Figure 5-20. Synthetic scheme showing, from low to moderate strain, the interaction between the fluid and the granite in the cases of a high fluid/rock ratio observed in the field. (a) An open fracture with an incipient alteration gradient at the border. (b) A sealed fracture with a slight alteration gradient. (c) A brecciated vein induced from fracture reactivation and showing an alteration gradient but no fracturing gradient. (d) A mylonite made of carbonates and granitic lenses showing an alteration gradient and a fracturing gradient. NH\_31 and NH\_23 show a similar fracture density (Fd). No scale is given for this scheme, because it can represent fracture zones of several order of magnitude.

These sample analyses allowed us to study a fault zone development depending on strain, fluid-rock ratio, and material rheology. It is shown that at low to moderate regional strain, incipient local high strain concentration is present (Figure 5-20). It has been observed that:

1. The fluid interacts with the surrounding rock altering it pervasively and fractures are sealed by secondary minerals (Figure 5-20a,b). Those veins can be reactivated by shearing Dhansay et al. (2017). Thus, it creates a brecciated vein (e.g. NH\_31) or even a mylonite (e.g. NH\_23) developing an alteration gradient. Sample NH\_23, shows that mylonitic deformation appears at low to moderate regional strain when carbonates are involved. Fault reactivation tends to cause a mineral fill breakage and re-opens the fracture (Gillespie et al., 2020; Moir et al., 2010).
2. Open fractures let fluid circulate without interaction with the surrounding rock. Shearing creates a breccia without further alteration within the granite such as in NH\_36 (Figure 5-19).

At any scales, fracture density promotes fluid flow through the fracture network provided a fluid is present (Dezayes and Lerouge, 2019b; Faulkner et al., 2010). However, the alteration degree is not correlated to the fracture density.

## VI.6. Implication of Alteration in Terms of Geothermal Reservoir Properties

Fresh granite has a very low initial matrix porosity (<1%), which “does not allow” the fluid circulation, hence inducing a low permeability (Géraud et al., 2010). A granitic geothermal reservoir is considered as exploitable when it presents a connected fracture network increasing the permeability and in which a sufficient amount of hot fluid circulates (Faulkner et al., 2010; Gentier et al., 2000; Géraud et al., 2010; Gillespie et al., 2020). By flowing through fractures, the fluid interacts with the rock, increasing the matrix porosity and permeability promoted by the dissolution of the primary minerals and crystallization of newly-formed phases (Ledésert et al., 2010). However, newly-formed minerals can also crystallize in the fractures and seal them, reducing the porosity and the permeability (Laubach, 2003; Woodcock et al., 2007). Thus, sealed fractures are transformed from conduits into barriers to fluid flow (Glaas et al., 2021; Liotta et al., 2020; Vidal et al., 2018) and impact the geothermal production by decreasing the connectivity between the fractures and hence the permeability (Gillespie et al., 2020; Griffiths et al., 2016).

The NH altered granite shows an important fracture network and a high matrix porosity which allowed fluids to circulate and to interact with the surrounding rock. Indeed, numerous veins with various infills crosscut the granite indicating several successive fluid circulation events. Carbonates occupy a prominent part of the fracture system, which can be easily dissolved thanks to acid injections in order to connect the boreholes to major conductive fractures for geothermal exploitation. It is suggested that when NH were an active reservoir at depth, fractures were only partially filled and the fluid could flow through the fracture network. It has been seen that the stress field has a major impact on the fluid circulation. Indeed, drilling into fractures at a very high angle from the main stress axis  $\sigma_1$ , such as exposed by sample NH\_31, is favorable to allow fluid to circulate. In the event of geothermal exploitation, only minor chemical stimulation, if any, would have been necessary (Ito, 2003; Ledésert et al., 2010, 2009). Moreover, the alteration amount is not necessarily related to the degree of fracturing and therefore, the fracture network influence on fluid circulation is hardly predictable. Thus, due to the conduit-barrier role, the deformation gradient, the degree of fracturing, the alteration processes and the relationship between them have a large impact on geothermal production (Griffiths et al., 2016).

## VII. CONCLUSION

The Noble Hills (NH) is a newly studied area in terms of an exhumed granitic geothermal reservoir. It provides an excellent opportunity to give fundamental scientific inputs in 3D allowing a better understanding of granitic reservoir behavior in a trans-tensional context. This analogue shows how complex a granitic reservoir can be, in terms of structures, fluid circulation and fluid-rock interactions. This study proposes a geometric, petrographic, petrophysical and geochemical description in order to characterize the influence of fracturing on fluid circulation and alteration processes.

Approaching fracture zones at large scale, the NH granite shows signs of several generations of fluid circulations resulting in successive veins of various mineralization. Fluid circulation being more important in the vicinity of fracture zones, a stronger fluid-rock interaction is observed. Thus, argillic alteration prevails compared to in the protolith. It is highlighted by the increase of the LOI correlated to a Na depletion due to plagioclase alteration and a K enrichment associated to illite precipitation. Likewise, the porosity, the calcite content and the temperature increase nearer to fracture zones. However, no correlation exists between LOI, porosity and calcite content all together. Also, a high fracture density does not necessarily imply a strong alteration (e.g. sample NH\_36).

This relation between fluid circulation, alteration and fracturing is also visible at sample scale. The higher the fracture density, the more pronounced the alteration. However, samples NH\_31 and NH\_23 showed how complex this relation can be:

- NH\_31 shows a reactivated vein giving a brecciated vein (quartz and granitic clasts in a carbonate matrix) which induced no fracture gradient in the surrounding porphyritic granite, but developed an alteration gradient.
- NH\_23 shows a carbonate mylonite creeping around deformed granite lenses, which induced a fracture gradient as well as an alteration gradient in the surrounding porphyritic granite.

These two samples, showing different deformation features as a result of a different orientation within the stress field, present a similar fracture density. Strain was accumulated within a carbonate mylonite within sample NH\_23. The alteration gradient is more pronounced in this sample, but the fracture density does not change. Sample NH\_36, consisting of a granite composed of a cohesive breccia whose matrix is made of dolomite, shows a low alteration. Even

locally, alteration does not always depend either on the deformation gradient or on the fracture density.

This study shows that the deformation gradient observed at large scale is also visible locally in a context of low to moderate strain. It also highlights the importance of mineral crystallization in a geothermal reservoir. Fluid flow depends on a connected network of open and permeable fractures. In reservoirs at depth, fractures can however be sealed and act as a barrier. Stimulation techniques are needed in order to re-open them so that a drain allowing a new fluid circulation is created. The influence of fracture zones on fluid flow and alteration is difficult to be predict and yet impacts the production from the reservoir.

In order to complete this work, a future study will focus on the influence of a fault zone on fluid circulation and alteration processes, in the NH, at high strain conditions. Moreover, laboratory investigations could be performed in order to better understand the controlling parameters of the ongoing processes while fracturing of rocks.

## VIII. ACKNOWLEDGMENTS

This manuscript was prepared as a contribution to the PhD thesis (Institut Polytechnique UniLaSalle Beauvais) of Johanne Klee, which was funded by the European Union's Horizon 2020 research and innovation program under grant agreement No 792037 (H2020 MEET project). The authors greatly thank Terry Pavlis for his support and helpful exchanges about the regional geology of Death Valley and the Noble Hills. Albert Genter is thanked for the helpful discussions and knowledges about fractured granitic reservoirs. We are grateful to Klaus Wemmer for his help on XRD analyses and the fruitful discussions. We also thank Graciela Sosa and Alphonse M. Van den Kerkhof for their help on cathodoluminescence observations and acquisitions. We thank Mahdi Chettabi, Thi Tuyen Nguyen, Elena Pavlovskaja, Carl Tixier and Chloé Gindrat for their help for analyses. We acknowledge the H2020 MEET consortium for their helpful comments and the validation of the manuscript. We finally would like to thank the two anonymous reviewers for their help and remarks to improve this manuscript.



# CHAPTER 6

## The role of inherited structures on fluid circulation within a pre-structured reservoir at high strain

---

### I. INTRODUCTION

In crystalline rocks, fracture permeability depends on the fracture density and hydraulic conductivity (Barton et al., 1995). Fluid circulation is facilitated by the growth of the fracture network during deformation (Cox, 2007). Fault zones are usually associated to neo-mineralization and transformation of primary minerals composing the surrounding wall rock. These mineral transformations associated to deformation and to episodic and successive fracture reactivations induce a change in physical and hydraulic properties of a fault zone during its activity (Ikari et al., 2009; Meller and Kohl, 2014; Numelin et al., 2007). Displacement, microstructures and fluid properties play important roles in controlling chemical and physical processes in a fault zone (Song et al., 2017). These factors interact with one another and are involved in the formation of fault rocks. Movements along faults induce crushing and grinding of host rocks, promoting rocks fragment size reduction and promoting interaction with eventual fluids (Bouchez and Nicolas, 2018; Faulkner et al., 2010; Niemeijer et al., 2008; Van der Pluijm and Marshak, 2004). According to Passchier and Trouw (2005) and Van der Pluijm and Marshak (2004), depending on the mechanism, this process produces a fault rock which can be (1) a breccia (fragments that make up >30% of the rock mass in a fine grain matrix), (2) a cataclasite (fragments that make up <30% of the rock mass in a fine grain matrix), (3) a gouge (few fragments (< 1mm) of the rock occur isolated in a foliated matrix), (4) a mylonite (foliated fault rock, formed dominantly by crystal-plastic processes) or even (5) a pseudotachylite (glassy fault rock along fractures, formed by flash melting of the host rock from heat generated during frictional sliding).

According to Caine et al. (1996), a typical fault zone is composed of three compartments:

1. A fault core which accommodates the most of the displacement and may include clay-rich fault zone, breccias, cataclasite or mylonite zones and where the grain-size reduction and/or mineral precipitation yield the fault core with low porosity and permeability compared to the protolith. This generally leads to a fault core that act as barrier to fluid flow (Figure 6-1a).

2. A damage zone which is considered as a network of opened and/or sealed subsidiary fractures acting as fluid pathways. This fracture network may enhance the fault zone permeability (Figure 6-1b). Secondary fractures present in the damage zone (Figure 6-1d) can react as conduit for fluid flow if they are not sealed by secondary minerals.
3. A protolith, found in the wall-rocks of the fault, which is characterized by a low porosity and permeability compared to the damage zone (Figure 6-1c).

Secondary fractures present in the damage zone (Figure 6-1d) can react as conduit for fluid flow if they are not sealed by secondary minerals.

Caine et al. (1996) have also shown that the fault core may act as a conduit during deformation and as a barrier following deformation when the pore space is filled by secondary mineral precipitation. Thus, the description of the fault evolution stage is important for a reservoir characterization.

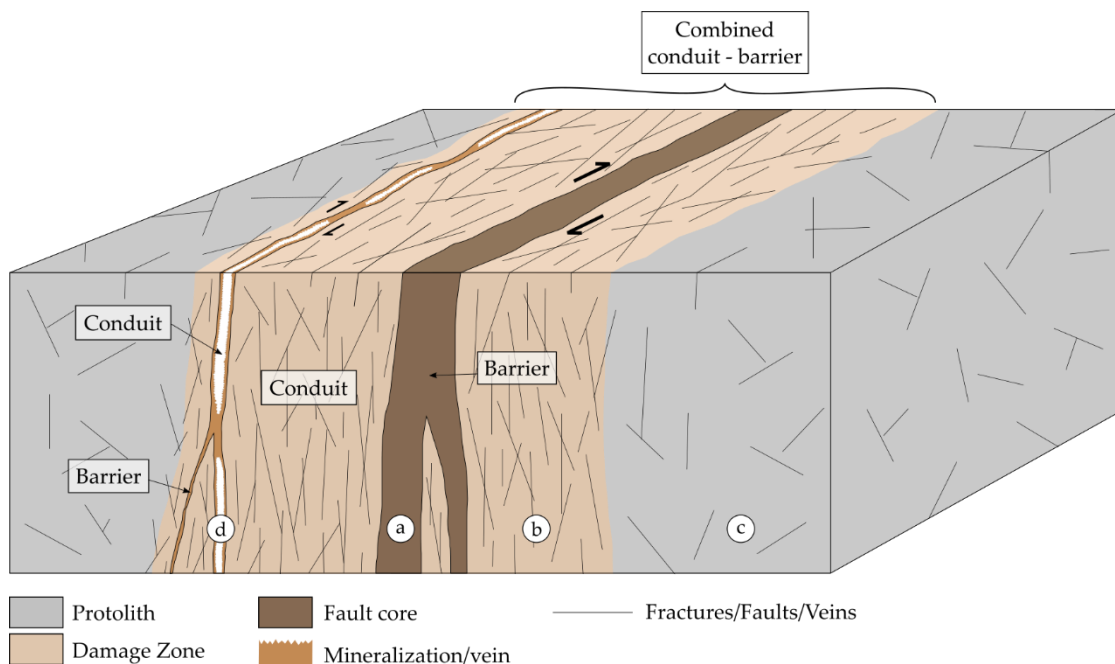


Figure 6-1. Block diagram, with no scale, representing the conceptual model of a fault zone according to Caine et al., 1996. We can differentiate three major zones: (a) the fault core, (b) the damage zone, and (c) the protolith. Secondary fractures (d) can react as conduit for fluid flow if they are not sealed by secondary minerals.

Klee et al. (2021b) have shown that fracturing influences the fluid circulation and alteration processes at low to moderate strain. The work presented in this chapter brings a step forward by focusing on the study of high strain fault zones. These are common features within crustal basement rocks and have been recognized within the Noble Hills range and in the Upper Rhine Graben shoulders.

Several case studies using far-field and near-field analogues are presented, where the concept of analogue remains the one described in the general introduction of this thesis.

The aim is to give insights on the effect of high strain fault zones on the rock reservoir petrographic evolution considering deformation and fluid-rock interactions processes. An effort is dedicated to the understanding on the role of inherited high strain structures in terms of hydraulic conductivity and fault connectivity to later fluid flow.

## II. CASE OF HIGHLY STRAINED ROCKS DEVELOPING A FAULT STRUCTURE FROM AN INHERITED STACKED BASEMENT/SEDIMENTARY PILE: THE NOBLE HILLS RANGE

### II.1. Introduction

The NH is located in the southern termination of the dextral Southern Death Valley Fault Zone (SDVFZ), which consists into the southern branch of the Death Valley pull-apart described by Burchfiel and Stewart (1966) and Niles (2016). According to Pavlis and Trullenque (2021), the NH has been transported over 40-41 km along the SDVFZ. In the previous chapters, it has been shown that the geology and the structure of the NH is more complex than what had been described until now. It is composed of a crystalline bedrock slice (CBS) (Brady, 1984) made of Proterozoic sediments, the Crystal Spring Formation (CSF), intruded by 1.1 Ga diabase sills, the whole intruded by Mesozoic granite (Troxel and Butler, 1979). Klee et al. (2021b) in contrast to Niles (2016) have shown that the outcropping Proterozoic west of the Pipeline Wash (Figure 6-2b) consists into several tectonically induced duplications of the Proterozoic sequence intruded by granite. The presence of a deformation gradient through the area was also highlighted by Klee et al. (2021b) due to a lateral bending, stretching and boudinage of this Proterozoic cover nappe stack towards the southeast. The NH has been characterized as an exhumed paleo-geothermal reservoir thanks to the evidences of fluid circulation such as numerous veins and the dominance of the argillic alteration that developed in the vicinity of fractures (Klee et al., 2021a, 2021b). Fieldwork, microstructure, petrographic, petrophysical, geochemical analyses and K-Ar dating have been performed to characterize the origin of the fault zone and its evolution in terms of microstructure, mineralogy changes, amount of alteration, element transfers, porosity and calcite content along this outcrop profile.

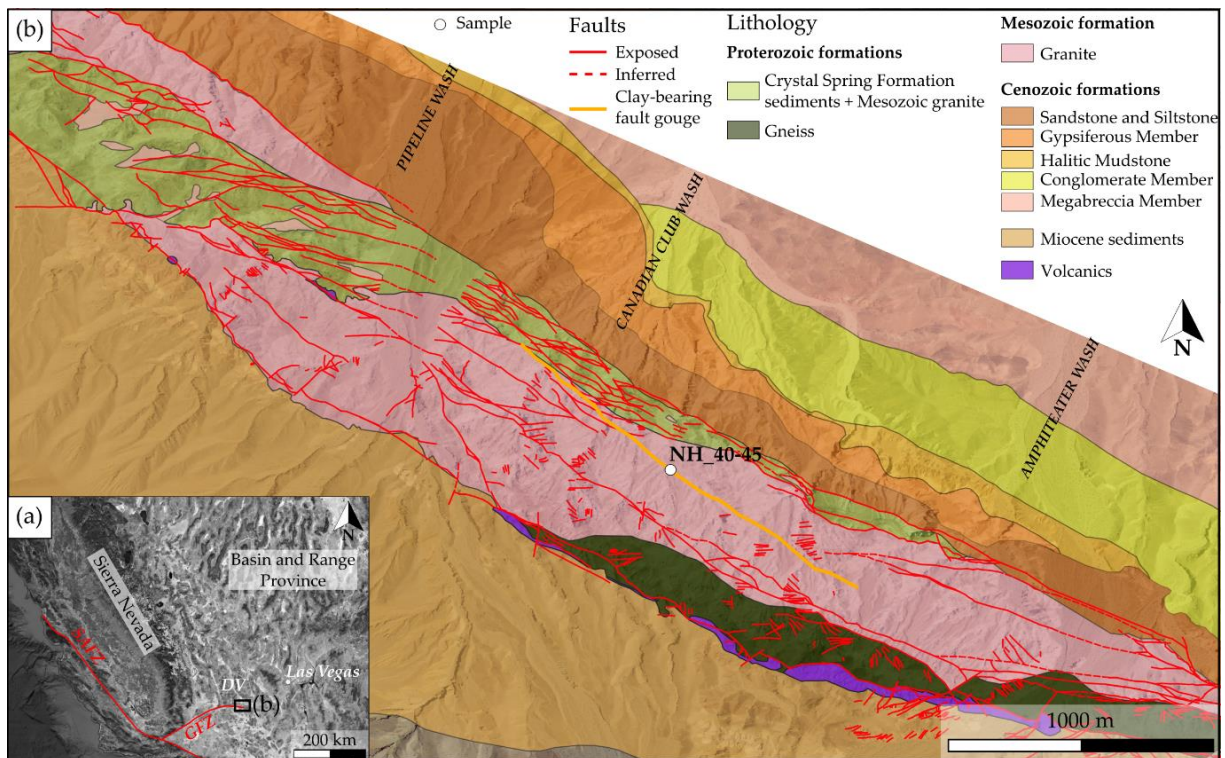


Figure 6-2. (a) Satellite map of the western USA showing the location of the Noble Hills range (black hollow rectangle). SAFZ – San Andreas Fault Zone, GFZ – Garlock Fault Zone and DV – Death Valley. (b) Geological map modified after Niles (2016) and Klee et al. (2021b), showing the studied location (white dot) on a major clay-bearing fault zone (orange line). The Quaternary is not displayed but it is available on the map provided by Niles, 2016.

## II.2. Material and Methods

### II.2.1. Material and sampling strategy

The study focuses on an outcrop (Figure 6-2b) exposing a clay-bearing fault core surrounded by granitic and gneissic rocks (Figure 6-3a,b). Figure 6-2b shows that both walls of the fault zone are granitic rocks. The eastern part of the fault zone is composed dominantly by remnants of granitic sills, deformed together with Proterozoic gneisses. Thus, the granitic facies was mapped, but a detailed mapping is under progress.

0

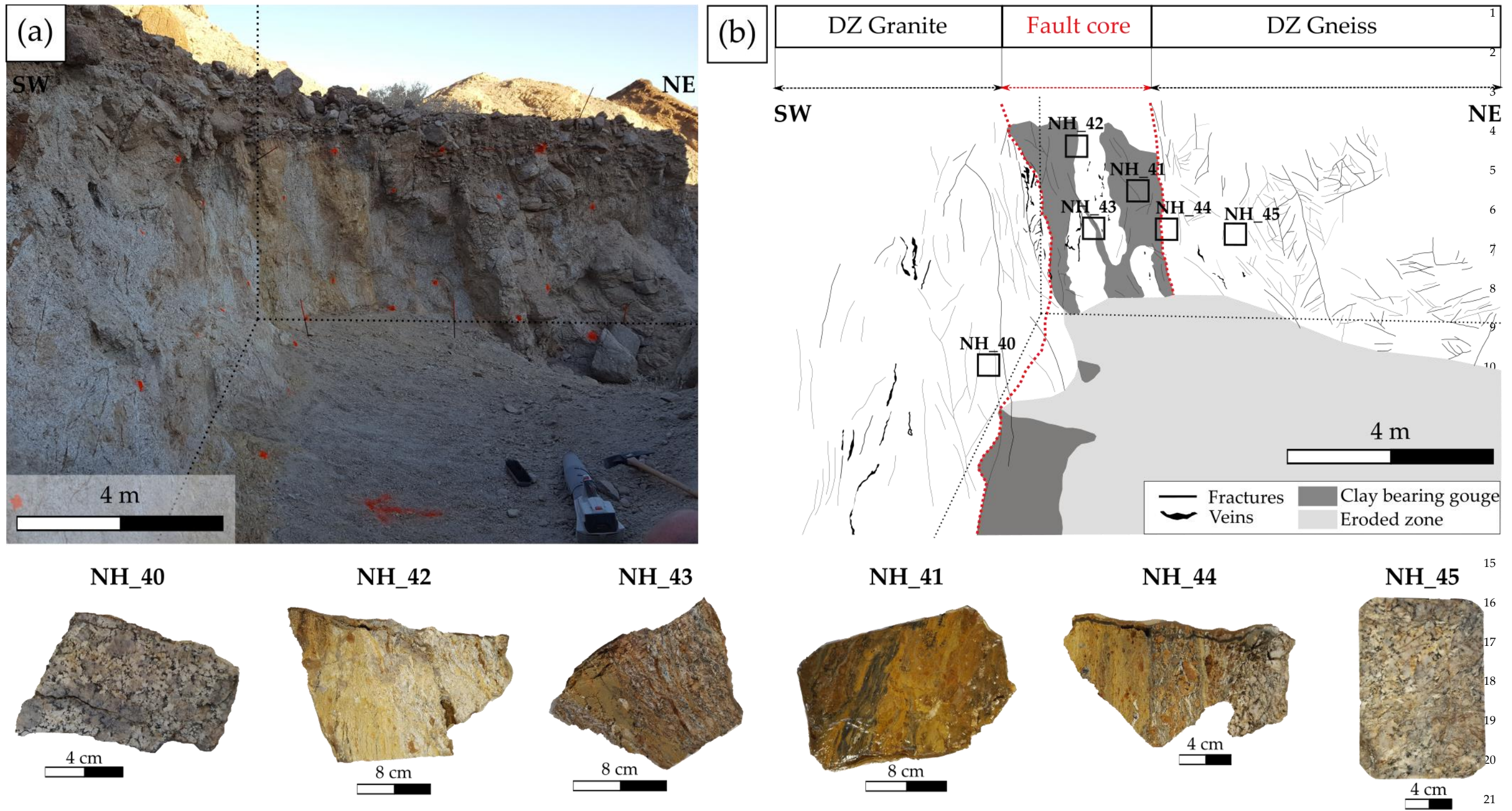


Figure 6-3. (a) A photograph of the outcropping fault zone. (b) The digitization of the outcrop showing the fault core in dark grey, the granite on the left, the gneiss on the right and the location of the different collected samples. (c) Photographs of the different collected samples. DZ - Damage Zone.

24

23



In map field (Figure 6-2b), the fault can be followed over several hundred meters. Petrographic, mineralogical, petrophysical and geochemical analyses were performed on six samples collected along a profile through the outcrop (Figure 6-3b,c). They aim at characterizing the possible variations in terms of newly-formed minerals, alteration processes, calcite content, porosity, element transfers and microfabric along this profile, related to the influence of the fault.

## II.2.2. Methods

### II.2.2.1. Field sampling

To extract the sample from the outcrop, fiber glass and epoxy resin were put on the targeted zone in order to consolidate the sample (Figure 6-4a). Once the resin hardened, a driller was used to drill around the sample delimitation until its complete extraction (Figure 6-4b,c). The outcrop was cleaned and the samples were finally wrapped in resin in order to avoid damaging during shipping.

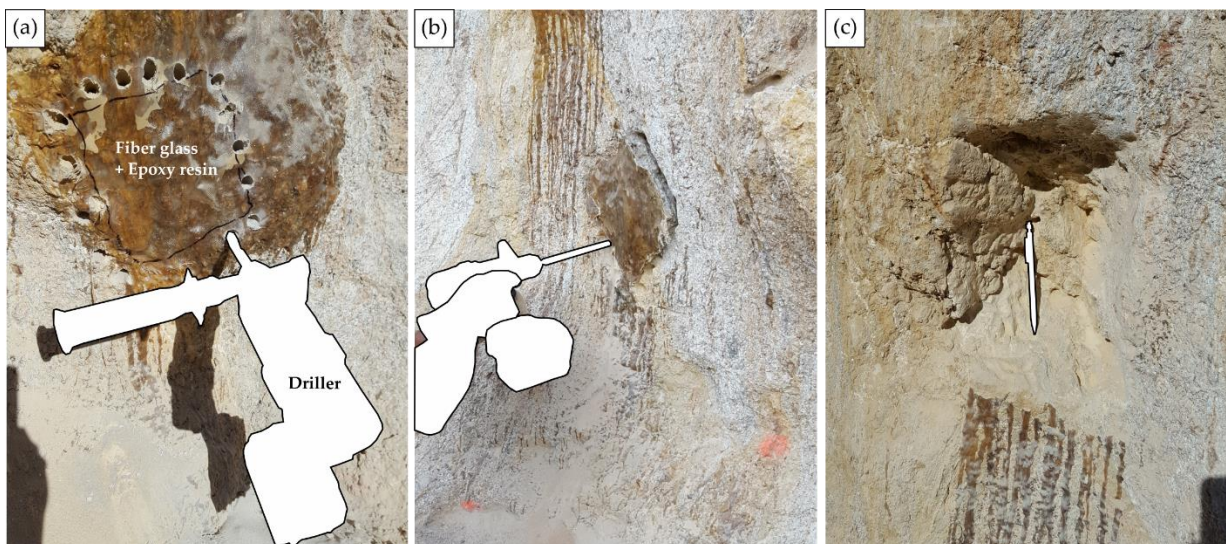


Figure 6-4. Sampling methodology. (a) Application of a film of fiberglass and epoxy resin on the outcrop surface for consolidation purposes and hole drilling to delimitate the sample. (b) Extraction after complete drilling. (c) Site of the extracted sample. All epoxy resin remnants have been carefully removed from the sampling area after sample extraction.

### II.2.2.2. Petrographic characterization

Seventeen thin sections, including 6 large thin sections (size: 10 cm × 7.5 cm) and 11 small thin sections (size: 4.8 cm × 2.8 cm), were realized on the six collected samples for petrographical analyses. Large thin sections allowed to better study the limit between the different zones identified in a sample. Large field area images were gained under polarized-analyzed light using Leica automatized stage facility microscope and Leica application Suite (LAS) v4.11.0 (Klee et

al., 2021a). Optical microscopy, using a Leica DM4500-P microscope, and Scanning Electron Microscope (SEM, Hitachi S-3400N) coupled to a Thermo Ultradry Energy Dispersive X-ray Spectrometry (EDS) (Kimio Kanda, 1991; K. Kanda, 1991) analyses were performed at Institut UniLaSalle Beauvais (ULS). These analyses aimed at characterizing the mineralogical assemblage, the chemical composition, the alteration paragenesis, the microstructure and microfabric, but also the degree of microfracturing. Most of the mineral abbreviations used in this paper refer to Kretz (1983) mineral symbols. Only few others were defined by myself as done in the two previous chapters.

### II.2.2.3. X-ray diffraction and Kübler Index

In addition to the petrographic characterization, XRD analyses were carried out at ULS using a D8-Advance Bruker-AXS (Siemens) diffractometer in order to identify the mineral phases (semi-quantitative method, with an accuracy about 3–5%). Thus, analyses were performed on whole rock powders and oriented clay fractions (<2  $\mu\text{m}$  and 2–6  $\mu\text{m}$ ) from five samples (NH\_40, NH\_41, NH\_43, NH\_44 and NH\_45). The experimental conditions are described in Klee et al. (2021a). Clay mineral separation was conducted using technique described in Klee et al. (2021a), based on Kisch (1991) and Schmidt et al. (1997), according to standard techniques suggested by Ferreiro Mählmann and Frey (2012). For both fractions, XRD measurements were done at air dried conditions (AD), solvated with ethylene glycol (G) and after heating at 550°C (H). These analytical steps allowed to distinguish the different clay minerals of (1) the last produced or newly formed clay minerals (fraction <2  $\mu\text{m}$ ), assimilated to the result of the last fluid circulation event and of (2) the fraction 2–6  $\mu\text{m}$  assimilated to possible mix between inherited material from the propylitic phase and newly formed clay minerals or inherited grains recrystallization. Their identification was undertaken referencing to Moore and Reynolds (1989) and Starkey et al. (1984) using the software DIFFRAC EVA v4.2 (©Bruker AXS). This separation in two fractions allowed to obtain the respective temperature conditions through the Kübler Index (KI) defining the limit of metamorphic zones (diagenetic zone, anchizone and epizone). An altered granite shows similarities with diagenetic reactions present in feldspathic sandstones (Ledéseret et al., 1999). Thus, it is possible to characterize temperature ranges by using the KI values obtained for granitic rocks. KI values are calculated from the illite crystallinity (IC), which corresponds to the full width at half maximum (FWHM) of the (001) 10Å peak of illite on AD conditions. The IC obtained values were standardized using the crystallinity index-standard (CIS) samples provided by Warr and Rice (1994b) in order to calculate the KI.

#### II.2.2.4. Manocalcimetry and ethanol saturation porosimetry

The calcite content of five samples (NH\_40, NH\_41, NH\_43, NH\_44 and NH\_45) was measured using an OFITE 152-95 manocalcimeter at CY Cergy Paris University in the Geosciences and Environment Cergy (GEC) laboratory. It provides an indication of the carbonate content in order to assess the influence of calcite on rock permeability and thus to better understand the fracture sealing in a reservoir (Ledésert et al., 2009). The CaCO<sub>3</sub> percentage (wt.%) was calculated as follow:

$$\%CaCO_3 = (\text{Measured value} \times 100) / \text{Calcimeter coefficient} \quad (1)$$

In order to quantify the available fluid storage volume (Dullien, 1979), porosity measurements were performed on five samples at CY Cergy Paris University in the Mechanics and Material for Civil Engineering laboratory (L2MGC). The triple weighing method was used (Klee et al., 2021a; Navelot et al., 2018) according to RILEM standard test n°1.1, 1978. Ethanol has been chosen instead of water in order to avoid possible clay swelling and thus a possible damaging of the samples (Gates et al., 2004).

#### II.2.2.5. Bulk-rock geochemical analyses

Bulk-rock geochemical analyses were performed at Bureau Veritas Minerals (Vancouver, Canada) using Inductively Coupled Plasma Emission Spectrometry or Mass Spectrometry (ICP-ES and ICP-MS respectively). Loss on ignition, major element oxides, rare earth elements and trace elements contents were obtained on 4 samples. The method is described in Klee et al., 2021a. These chemical analyses were performed in order to determine the degree of alteration and the element transfers.

#### II.2.2.6. K-Ar illite dating

K-Ar dating has been realized at the University of Göttingen on a single sample, NH\_41, corresponding to the fault core. Before dating measurements, the sample was dissolved in water. The suspension was wet-sieved using a 63 μm sieve. The fraction <63μm was used to extract the clay fractions 2-6 μm by settling in Atterberg cylinders. A second <2 μm fraction was gained the same way and used to separate the fraction <0.2μm using an ultra-centrifuge.

For each fraction, the argon isotopic composition was measured in a stainless-steel extraction and purification line coupled to a Thermo Scientific ARGUS VI™ noble gas mass spectrometer operating in static mode. The amount of radiogenic <sup>40</sup>Ar was determined by isotope dilution

method using a highly enriched  $^{38}\text{Ar}$  spike from Schumacher (1975). The spike is calibrated against the biotite standard HD-B1 (Fuhrmann et al., 1987). The age calculation was based on the constants recommended by the IUGS quoted in Steiger and Jäger (1977). Potassium was determined in duplicate by flame photometry using a BWB-XP flame photometer <sup>™</sup>. The samples were dissolved in a mixture of HF and HNO<sub>3</sub> according to the technique of Heinrichs and Herrmann, 2013. The analytical error for the K/Ar age calculation is given on a 95% confidence level ( $2\sigma$ ). Details of argon and potassium analyses made by the laboratory in Göttingen were exposed by Wemmer (1991).

## II.3. Results

### II.3.1. Field results

Field investigations have shown that the NE frontal part of the NH consists in an inherited imbricate of Proterozoic basement and Proterozoic sedimentary cover units (Klee et al., 2021b) (Figure 6-5a), visible northwest of the Pipeline Wash (Figure 6-2b). The age of this imbricate is not fully understood at present but predates Mesozoic granitic intrusives. These granites are found in the form of undeformed sills along the basal contact of the different Proterozoic basement and Proterozoic cover units (Figure 6-5a). SDVFZ activity overprints this inherited imbricate and produces intensive shearing within the weak sedimentary CSF. A localized zone of deformation concentrates strain within a narrow zone containing predominantly pinched units of Proterozoic sediments, Proterozoic basement (Figure 6-5b). Therefore, it is shown that this fault zone does not follow the fault zone model of Caine et al. (1996), who considered the fault core is due to a progressive comminution and alteration of a unique protolith. This is also noticed when comparing the east side (gneiss) and the west side (granite) of the fault core. This fault zone consisting into a mix of crystalline basement and sediments is the studied object of this section. This outcrop is a primary importance as it shows that inherited structures involving weak sediments can be involved in reservoir structuration. In the case where regional scale geological understanding of the reservoir is missing, these sediments can easily be interpreted as the product of a single protolith having suffered large amounts of deformation.

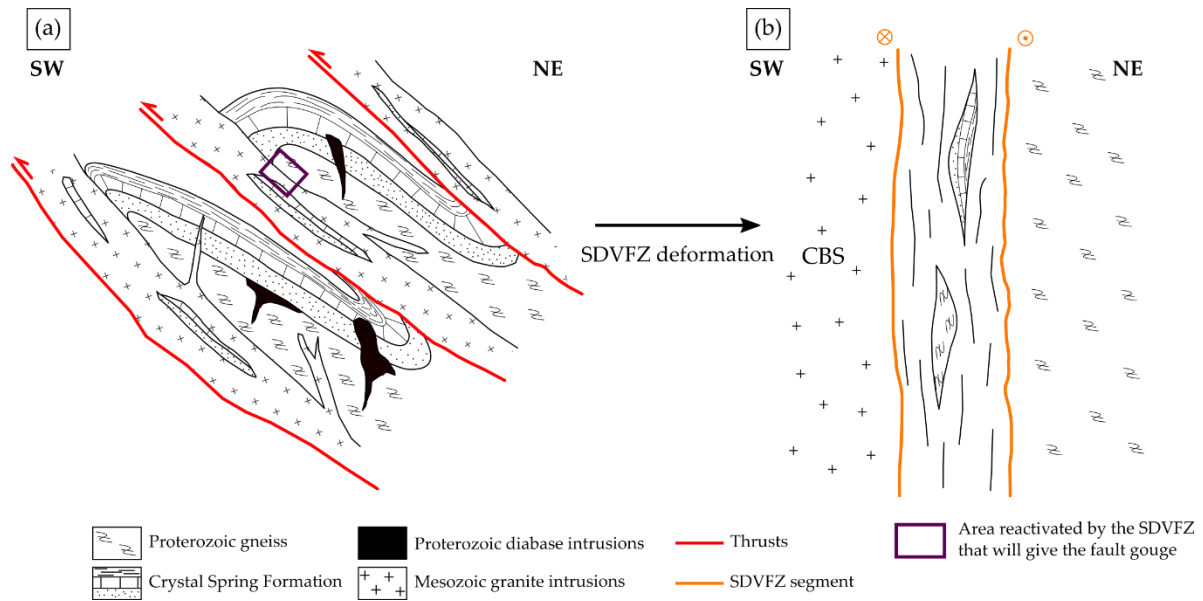


Figure 6-5. (a) Schematic cross-section of the Proterozoic sequence stacking with granite intrusions west of the Pipeline Wash (Figure 6-2b). The violet square represents the area that will be reactivated by the SDVFZ to obtain the fault gouge. (b) Schematic cross-section fault gouge after having been stretched by the SDVFZ. CBS–Crystalline Bedrock Slice after Brady (1984).

## II.3.2. Petrographical description

### II.3.2.1. Granite – Sample NH\_40

The granite on the west side of the fault core is highly fractured at outcrop scale but still preserving a magmatic texture (Figure 6-6a-c). As described in Klee et al. (2021a) the primary assemblage is composed of plagioclase (oligoclase) that appears whitish due to alteration, quartz, K-feldspar (perthitic orthoclase) and biotite. Fractures are opened but also filled by secondary minerals. Alteration halos are visible on the main fracture walls on the sample, indicating a more pronounced alteration around these fractures (Figure 6-6d).

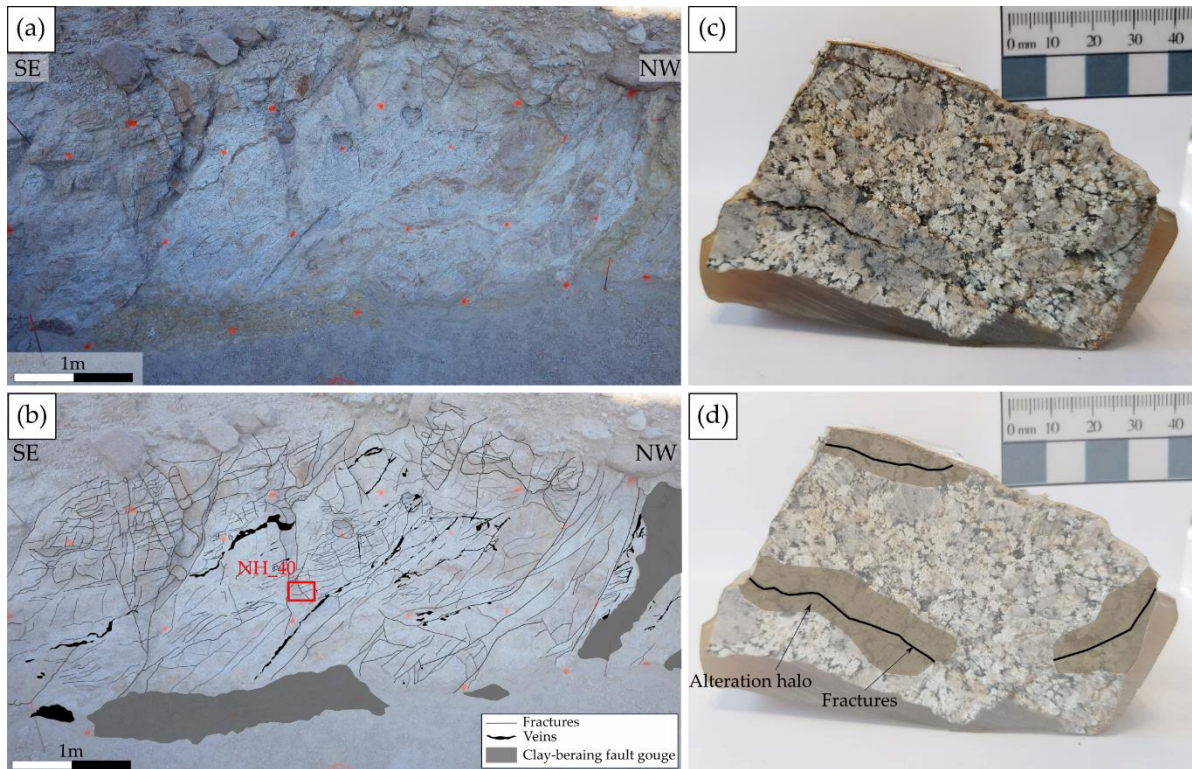


Figure 6-6. (a) Photograph of the granitic part of the outcrop with a perpendicular view to the fault core noundary. (b) Digitization of the outcrop presented in (a) showing the fracturing, the veins and the granitic sample location. (c,d) Photograph and digitization of the granitic sample NH\_40 showing a magmatic texture and alteration halos at main fracture walls.

Microscopic observations confirm the preservation of the magmatic texture but also show that the granite is altered (Figure 6-7a). Quartz and K-feldspar are unaltered with no signs of deformation. Plagioclase is the only affected phase. It is mainly transformed into kaolinite, illite and calcite. Some transformed plagioclase show an illitic core whereas borders are completely replaced by kaolinite (Figure 6-7b,c). Biotite is slightly altered and recrystallized into illite and oxides. The clay mineral composition determined by XRD, reveals the presence of corrensite (trioctahedral variety of regular 50:50 chlorite/smectite mixed-layer C/S (Beaufort et al., 1997)), which can replace biotite (Velde, 1977) as presented in Klee et al. (2021b). The predominance of kaolinite and illite indicates that the argillic alteration is prevalent on the propylitic alteration. Hematite was also identified. The mineralogical composition is given in Table 6-1.

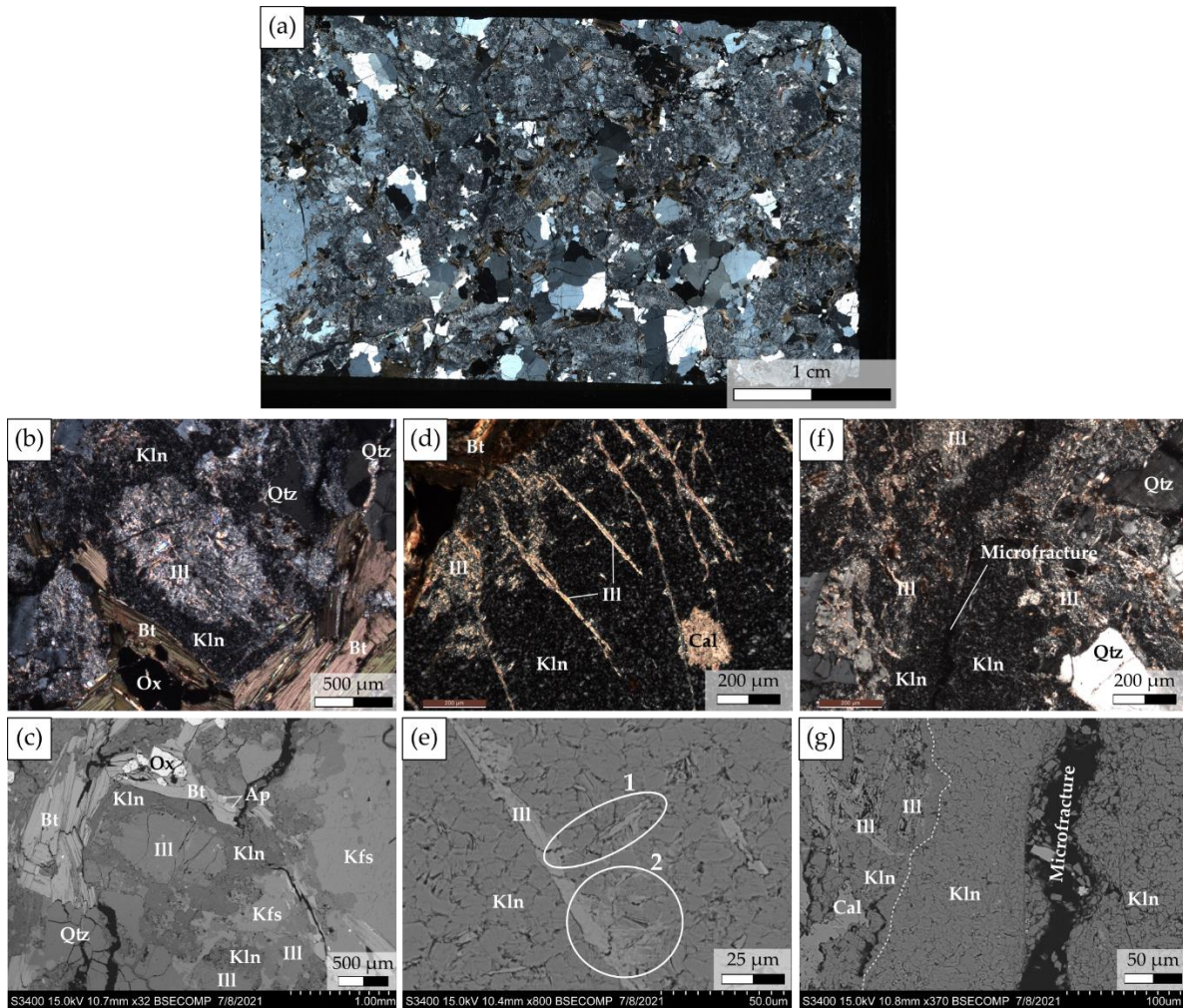


Figure 6-7. Microphotographs and back-scattered images of the sample NH\_40 (a) Microphotograph of the whole thin section made in the sample under polarized-analyzed light. (b-c) Microphotographs showing an altered plagioclase replaced by illite in the core and kaolinite in the borders and slightly altered biotite in the borders under polarized-analyzed light (b) and under SEM (c). (d) Microphotograph of a plagioclase transformed into kaolinite intersected by illite veinlets under polarized-analyzed light. (e) Back-scattered image of an illite veinlet developed through the porosity created by plagioclase kaolinitization. The ellipsoids 1 and 2 show the diffusion of illite from the veinlet through the porosity. (f-g) Microphotograph under polarized-analyzed light and back-scattered image of a microfracture, with kaolinized walls, crosscutting an altered plagioclase replaced by kaolinite, illite and calcite. The limit between kaolinite from plagioclase alteration and kaolinite related to the microfracture is represented by the white dashed line.

Table 6-1. List of samples collected on the outcrop with their mineralogical composition and clay mineral composition for the fractions  $<2\ \mu\text{m}$  and  $2-6\ \mu\text{m}$  determined after microscopic observations (OM and SEM-EDS) and XRD analyses (primary minerals and secondary minerals)

Samples	Primary minerals	Secondary minerals	clay fraction $<2\ \mu\text{m}$				clay fraction $2-6\ \mu\text{m}$			
			Ill/Ms	Kln	C/S	Bt	Ill/Ms	Kln	C/S	Bt
NH_40	Qtz, Or, Ab, Bt, Ap	Kln, Ill, Cal, Hem	+	++	+		+	++	-	
NH_41	Qtz, Or, Bt, Ap	Ill, Dol, Gp, Cal, Anh	++	--			++	-		
NH_42	Qtz, Or, Mc, Bt, Ap	Ill, Kln, Cal, Dol, Gp					n.a.			
NH_43	Qtz, Or, Mc, Ab, Bt, Ap	Kln, Ill, Cal, Gp		n.m.			+	++	+	-
NH_44	Qtz, Or, Mc, Ab, Bt, Ap	Kln, Ill, Cal, Hem, Gp		n.m.			+	++	+	+
NH_45	Qtz, Or, Mc, Olg, Bt, Ap	Kln, Ill, Cal, Hem	-	++	+	-	-	++	+	+

Multiple illite veinlets crosscut the granite (Figure 6-7d). They intersect in a clear way quartz and alkali feldspar crystals. These veinlets show blurred borders by crosscutting illitized plagioclase, but show almost clean borders by crosscutting kaolinized plagioclase. Illite veinlets have developed through the secondary porosity, between kaolinite crystals, created during plagioclase kaolinization (Figure 6-7e). From these veinlets, illite also spreads out by crystallizing pervasively in the secondary porosity (Figure 6-7e). Few carbonate veinlets (calcite and dolomite) and calcite patches related to plagioclase alteration are present. Calcite content was measured at around 5.5 wt.% in this sample. The sample presents also open microfractures crosscutting ancient plagioclase, which walls can present only kaolinite whereas the rest of the plagioclase is replaced by a mixing of kaolinite and illite (Figure 6-7f). Moreover, a slight limit can be identified between kaolinite formed by the microfracture influence and the kaolinite related to plagioclase transformation (Figure 6-7g). Hence, two kaolinite generations are observed. The porosity of this sample is  $14 \pm 0.71\%$ .

#### II.3.2.2. The gneiss/fault core limit and the gneiss – Sample NH\_44 and NH\_45

The gneiss composed the east side of the fault core (Figure 6-8a). The limit between the gneiss and the fault core is represented by the samples NH\_44 (Figure 6-8b,c). The sample NH\_45 was collected in the gneiss away from the fault core.

NH\_45 appears highly fractured at sample scale and shows an eye-shape texture, also called eye texture (Figure 6-8c). Some of the visible microfractures are filled by carbonates. The whitish color results from a significant alteration of the plagioclase. Biotite is not much altered but deformed (Figure 6-9a,f,g) and tending to keep its initial orientation. Sample NH\_44 can be divided into four zones (Figure 6-8b): (1) an altered and fractured gneissic part with a brecciated eye texture and microfractures filled by carbonates, (2) a zone which is rich in carbonates due to its brownish color, (3) an altered and foliated zone with whitish plagioclase and orange K-feldspar and quartz, and (4) a heterogeneous gouge with a clay matrix.

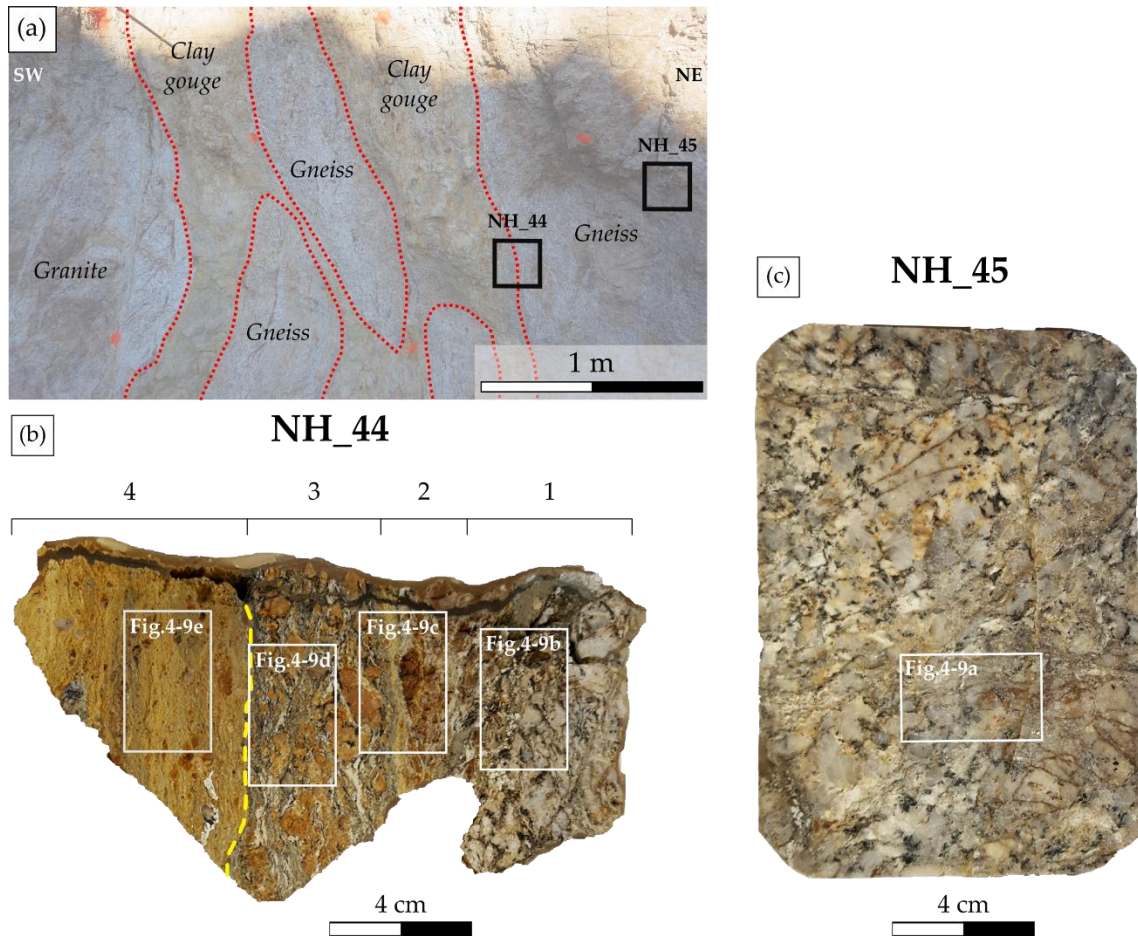


Figure 6-8. (a) Digitized photograph of the studied outcrop showing the location of the samples NH\_44 and NH\_45. (b) Photograph of the sample NH\_44 showing four different phases. The dashed yellow lines represent the limit between the gneissic part and the fault core. (c) Photograph of sample NH\_45 collected away from the fault core. Both samples show the evolution of alteration and deformation approaching the gouge.

One thin section was realized in sample NH\_45 (Figure 6-9a) and four thin sections in each identified zone of sample NH\_44, from the wall rock towards the gouge (Figure 6-9b-e).

The microscopic investigation shows that the gneiss of sample NH\_45 is highly fractured (Figure 6-9a). This initial foliation is recognizable but has been reworked. Quartz and K-feldspar are unaltered but brecciated with calcite filling some of the fractures (Figure 6-9f). The calcite content measured in this sample is about 5.16 wt.%. Primary mineral clasts are generally > 0.1 mm across. Quartz presents undulatory extinction (Figure 6-9f). Biotite is deformed and slightly altered into illite. Plagioclase (oligoclase in composition) is partially replaced by illite and kaolinite (Figure 6-9g). As for NH\_40, kaolinite is the dominant clay mineral. The obtained porosity for the sample NH\_45 is of 16.4%.



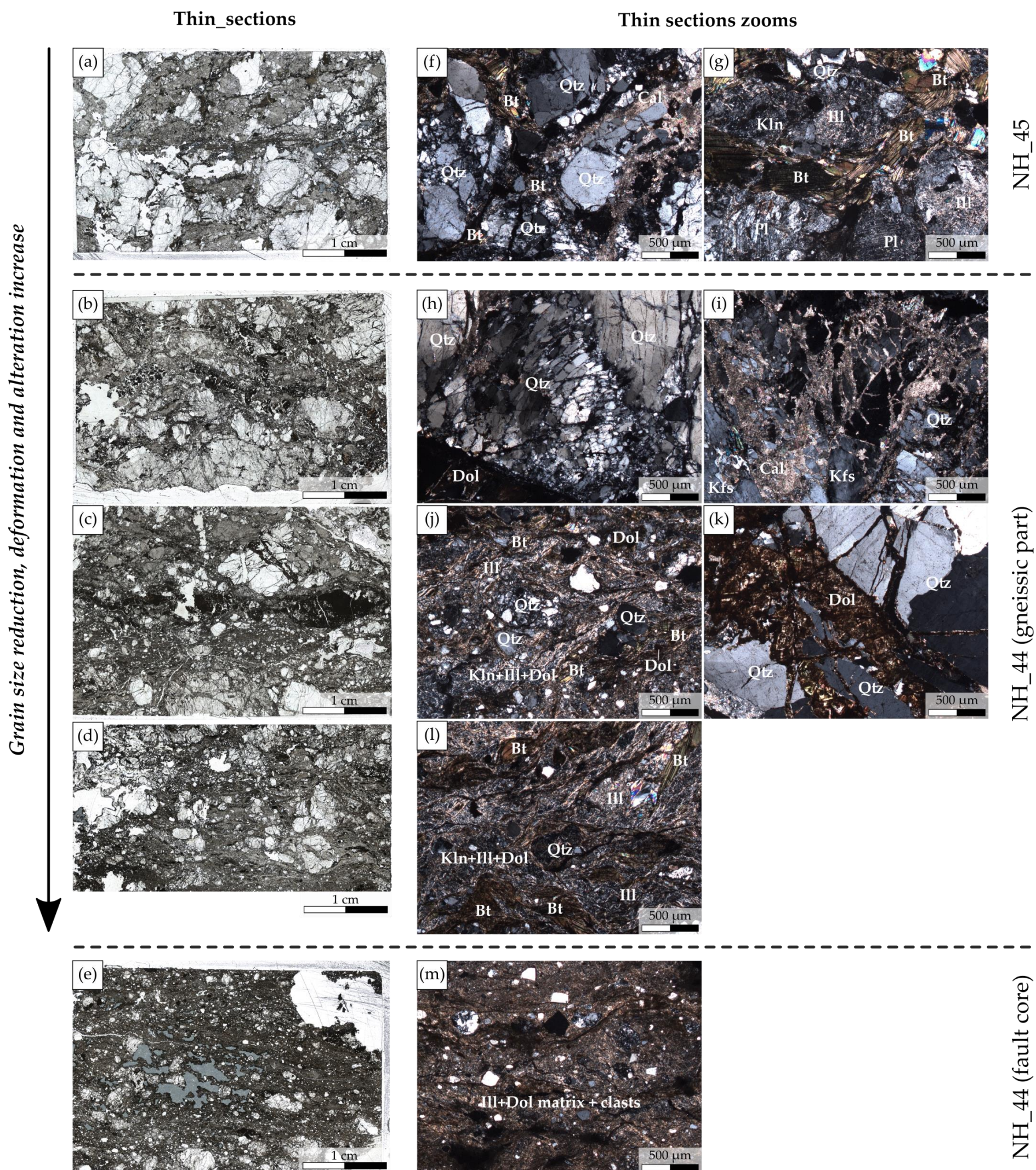


Figure 6-9. (a) Microphotographs under polarized-non-analyzed light of global thin sections realized in sample NH\_45. (b-d) Microphotographs under polarized-non-analyzed light of global thin sections realized in sample NH\_44 showing the microstructure and alteration evolution with deformation through the gneissic part. (e) Microphotographs under polarized-non-analyzed light of global thin section made in the fault core considered as a mix between Proterozoic sediments, basement and Mesozoic granite. (f-m) Microphotographs zooms under polarized-analyzed light from each thin section. (f) Brecciated quartz showing an undulatory extinction and new grains, almost unaltered biotite and fractures filled by calcite. (g) Plagioclase partially altered into illite and almost unaltered biotite oriented following the gneiss foliation. (h) Brecciated quartz showing an undulatory extinction and sub-grain rotation. (i) Brecciated K-feldspar and quartz with fractures filled by calcite. (j) Grain size reduction and development of an illite+dolomite matrix containing still a lot of biotite partially altered. (k) Important amount of dolomite which partially filled the fractures. (l) K-feldspar and plagioclase completely altered into illite forming the matrix with dolomite and embedded quartz clasts and few biotite. (m) Illite+dolomite matrix where only little clasts of quartz are still visible.



Approaching the clay-rich fault core, a gradational (1) grain size reduction, (2) deformation increase and (3) alteration increase were observed through the three compartments of the sample NH\_44 gneissic part (Figure 6-8b). From the outer part towards the fault core:

- *The section 1* (Figure 6-8b1) shows a significant grain size reduction (Figure 6-9b) compared to NH\_45. Quartz crystals are highly fragmented and show a more pronounced undulatory extinction (Figure 6-9h). As in sample NH\_45, biotite is deformed and slightly altered into illite. Plagioclase is completely altered into kaolinite and illite. The amount of carbonate visible in this portion of the gneiss is more abundant. Large clasts of dolomite are observed (~500  $\mu\text{m}$ ), as well as an important amount of calcite filling the fractures (Figure 6-9i). A calcite content of 8.27 wt.% was measured for sample NH\_44. This section is classified as a breccia (Passchier and Trouw, 2005; Van der Pluijm and Marshak, 2004).
- *The section 2* (Figure 6-8b2, Figure 6-9c) shows a grain size reduction compared to the previous section. Most of the grains are < 0.5 mm across and are still identifiable. Biotite is partially altered into illite and more deformed (Figure 6-9j). As for the previous section, a lot of carbonates, especially dolomite, are present (Figure 6-9k). Grains are embedded in a matrix made of illite and dolomite. Dolomite gives the brownish color to the matrix. This section is also classified as a breccia produced by cataclastic flow process (Passchier and Trouw, 2005; Van der Pluijm and Marshak, 2004).
- *The section 3* (Figure 6-8b3, Figure 6-9d) shows a grain size decrease from up to 1 mm to less than 200  $\mu\text{m}$  (Figure 6-9d), as well as an increase in the matrix proportion made of illite, dolomite and little kaolinite (Figure 6-9l). Biotite is intensively deformed and aligned according to a preferential orientation. In this developed cataclasite (Passchier and Trouw, 2005; Van der Pluijm and Marshak, 2004) grains are non-uniformly distributed and aligned parallel to the bounding fault plane. Few grains of up to 1 mm across embedded in the matrix are composed of single minerals, mainly quartz.
- *The section 4* (Figure 6-8b4, Figure 6-9e) corresponds to the fault core considered as a mix of Proterozoic sediments, basement and Mesozoic granite thanks to fieldwork. Few rounded grains (most of them ~100  $\mu\text{m}$ ) of quartz are found within a foliated illite+dolomite matrix (Figure 6-9e). K-feldspar is completely altered and transformed into illite. Biotite is almost completely altered and smaller in size compared to previous zones. The foliated matrix is relatively dark due to the presence of dolomite (Figure 6-9m).

### II.3.2.3. The fault core

At the studied outcrop location, the fault core is anastomosed and separated into two branches around 50 cm wide each, encompassing gneiss lenses (Figure 6-10a,b). Three samples were collected in the fault core: NH\_41 from the gouge itself, NH\_42 at the transition between the gouge and a central lens of gneiss and NH\_43 from the central gneiss lenses crosscut by a small gouge branch.

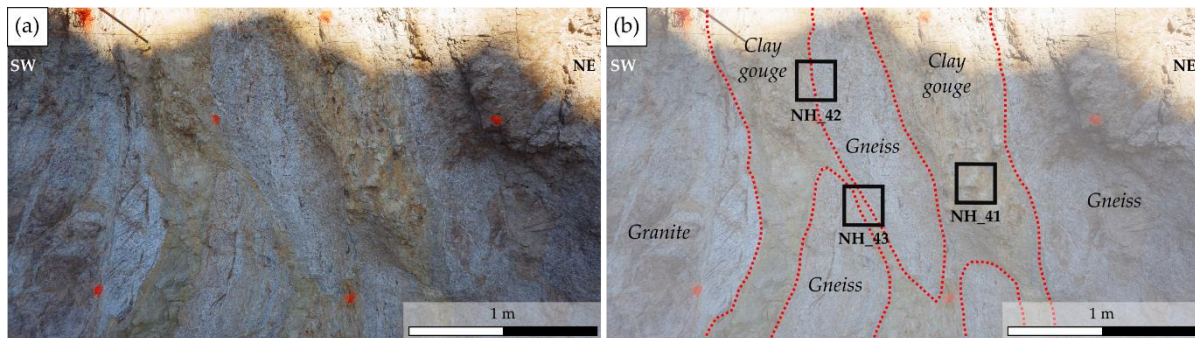


Figure 6-10. (a) Photograph zoom of the fault core. (b) Digitization of the outcrop (a) showing the different fault core compartments made of gneiss lenses taken in a clay-bearing fault gouge delimited by dashed red lines, the whole surrounded by granite and gneiss, as well as the location of the different sample collected in the fault core.

- **The clay-rich core – Sample NH\_41**

The sample NH\_41 (Figure 6-11) is mainly composed of quartz (~50%) and illite (~25%), but also of dolomite (~10%), orthoclase remnants relics (~5%), biotite (~5%) and apatite (~5%). Quartz is the most dominant mineral among the primary minerals. Illite is the predominant clay minerals, whereas kaolinite occurs as very small amount (<1%) Table 6-1. The hand specimen shows different mineral phases, showing how heterogeneous the gouge is. The yellowish-orange phase represents a clay dominant phase. Boudinated material, sigmoids and foliated structures were identified showing evidences of an intense shearing. Only a whitish material appears euhedral, identified as gypsum. The size of grains is very fine due to an intensive grinding triggered by a brittle shear deformation (sigma clasts). All the elements of the clay-rich core are deformed and oriented according to a privileged plan.



Figure 6-11. Photograph and digitization of sample NH\_41 collected from the clay-bearing gouge affected by shear deformation showed by boudinated structures, foliated material and sigmoid.

Thin sections analyses allowed to identify the different phases composing the sample NH\_41:

- The brownish phase (Figure 6-12a) corresponds to deformed fragments of dolomite associated to remnants of preserved primary rock-forming minerals (quartz, biotite and K-feldspar) and altered plagioclase into illite.
- Optical and SEM analyses of the whitish euhedral (Figure 6-12b) material confirm that it is gypsum (Figure 6-12b).
- The dark zone (Figure 6-12c,d) corresponds mainly to highly deformed biotite and brecciated remnants of quartz. Quartz grains (~50%) show a strong undulatory extinction (Figure 6-12c). They also appear as sub-angular to angular fragments of various sizes, the larger ones forming lenses. Biotite (~40%) is only slightly altered but highly deformed showing mica fish shapes (Mukherjee, 2011) (Figure 6-12d). They tend to be aligned according to a preferential orientation, thus creating a foliation. Plagioclase and K-feldspar are no more recognizable and completely transformed into illite, forming a matrix. The clay matrix embedding these fragments consists into less than 10% of the dark zone, leading to consider this dark zone as a breccia. Moreover, calcite and especially dolomite filled some fractures between the larger clasts of quartz.
- Focusing in the orange finer material, which is predominant in the sample, different zones are identified:

- Zone 1 (Figure 6-12e): It consists into a highly brecciated protolith remnant which initial texture is no more recognizable, with quartz and biotite sub-angular to angular fragments as in the darker zone. Small amounts of illite and dolomite are present between the fragments.
- Zone 2 (Figure 6-12f): It consists into smaller sub-angular grains, than in zone 1, embedded in an illite-dolomite matrix, presenting a crystallographic preferential orientation (CPO). Dolomite is also present as deformed clasts.
- Zone 3 (Figure 6-12g,h,i): This zone composed the majority of the sample. It consists into an illite-dolomite rich matrix preferentially oriented and containing smaller sub-rounded and sub-angular fragments of quartz as in zone 2 (Figure 6-12g). The matrix is the prevalent phase and is mixed with very fine-grained silica material deriving from quartz. Indeed, sigmoid and lensoid shapes are visible indicating and confirming the dextral shear that the rock has undergone. Under SEM, the clay foliation is predominant. Illite crystals show a slight deformation appearing as slight folding related to the stress imposed on illite flakes during the mineral growth. Quartz tiny fragments are oriented sub-parallel to the matrix foliation (Figure 6-12h,i).

The clasts present in this phase have globally clear boundaries. They can also show a bit of abrasion regardless of their size, giving a sub-rounded to round shape.

The material composing the facies presented Figure 6-12g,h,i) is very heterogeneous (breccia, cataclasite and gouge) (Passchier and Trouw, 2005; Van der Pluijm and Marshak, 2004).

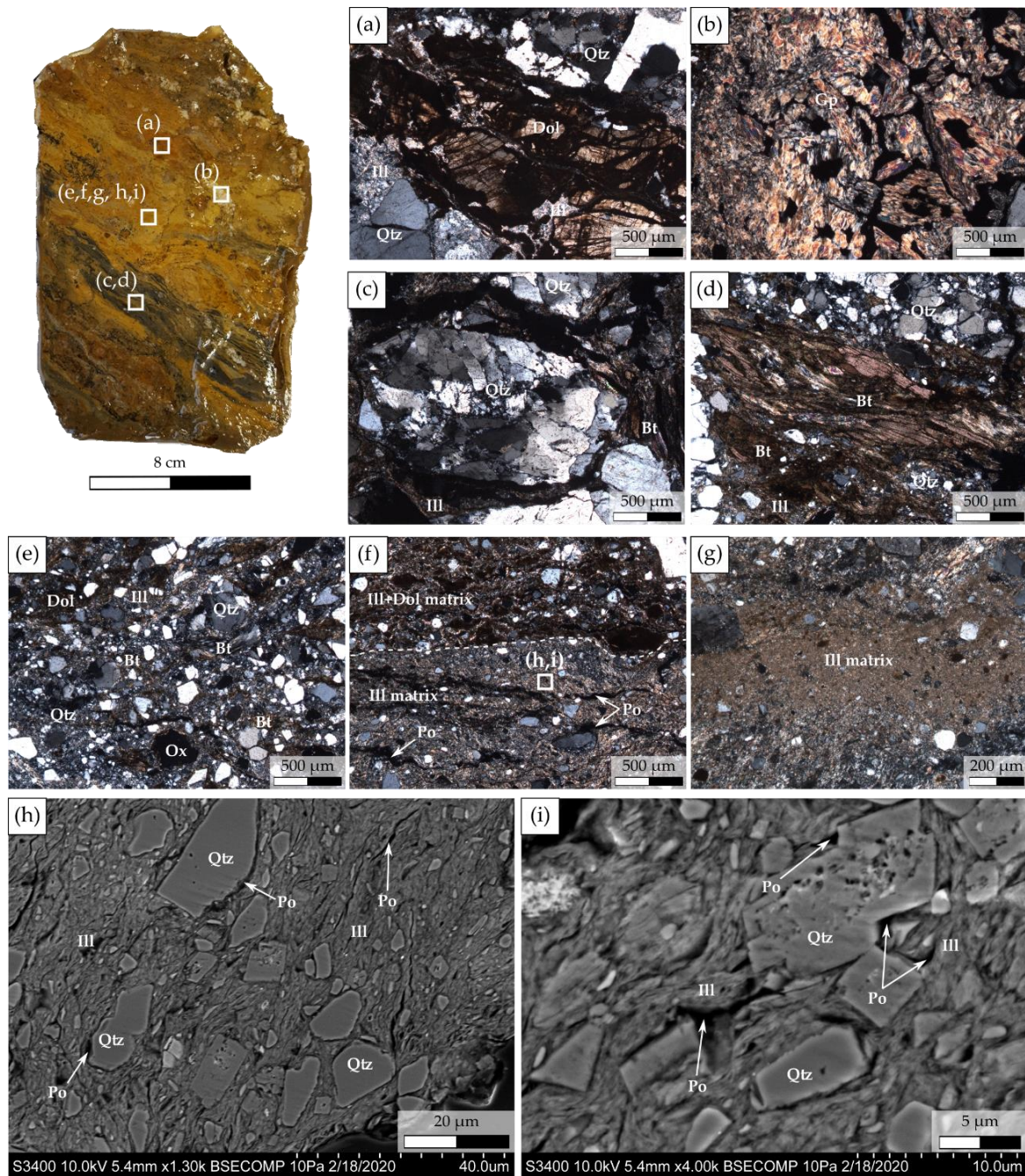


Figure 6-12. (a-g) Microphotographs under polarized-analyzed light from the different compartment composing the sample NH\_41: (a) brecciated dolomite, (b) automorphous gypsum, (c) brecciated and deformed quartz crystal presenting a strong undulatory extinction and sub-grain rotation, (d) slightly altered but deformed biotite presenting as mica fishes and showing an undulatory extinction, (e-g) reduction of the grain size and increase of dolomite and illite content with (e) highly brecciated quartz, K-feldspar and biotite and a little dolomite, (f) reduction of the grain size and development of an illite/dolomite matrix and illite matrix and (g) reduction of the grain size and prevalence of the illite matrix. (h-i) Back-scattered images zooming in the illite matrix and showing the illite crystallographic preferential orientation. Po – Porosity.

The sample NH\_41 is globally heterogeneous. However, the finer material is predominant which consists predominantly of a gouge. The entirely clay-rich part of the fault core is thus considered as a gouge.

Dolomite is present in a significant proportion in the whole sample as clasts and associated to the illite in the matrix. Calcimetry measurements were realized, giving a calcite content of 11.9%. Moreover, a porosity of 18.6% were measured for this sample. Porosity develops mostly at the boundaries between quartz grains and the matrix, along microfractures (Figure 6-12h,i) and is mostly present in les argillized phases (Figure 6-12a-e). XRD clay fractions analyses also revealed the presence of anhydrite and of a very low amount of kaolinite in the gouge (Table 6-1).

K-Ar dating has been performed on illite from the fraction  $<0.2 \mu\text{m}$ ,  $<2 \mu\text{m}$  and  $2-6 \mu\text{m}$  of this sample. The obtained ages are respectively  $6.8 \pm 0.2 \text{ Ma}$ ,  $14.5 \pm 0.3 \text{ Ma}$  and  $29.1 \pm 0.9 \text{ Ma}$ .

- **Limit between the gouge and the gneiss lens – Samples NH\_42 and NH\_43**

Samples NH\_42 and NH\_43 (Figure 6-13) show the limit between a highly deformed protolith from the central part of the fault core and the gouge. The sample NH\_43 shows a foliation, well recognizable by the biotite alignment and the eye texture resulting into few feldspar and quartz eye-shaped. Few carbonate boudins are identified in it and show that the dextral shearing affected these gneiss lenses. Carbonates also fill some fractures. Moreover, the whitish color show that gneiss was intensively affected by alteration. The fine grain phase on sample NH\_42 is similar to the gouge composing the sample NH\_41 described above. At sample scale, the limit between the gouge and the gneiss lens is relatively clear.

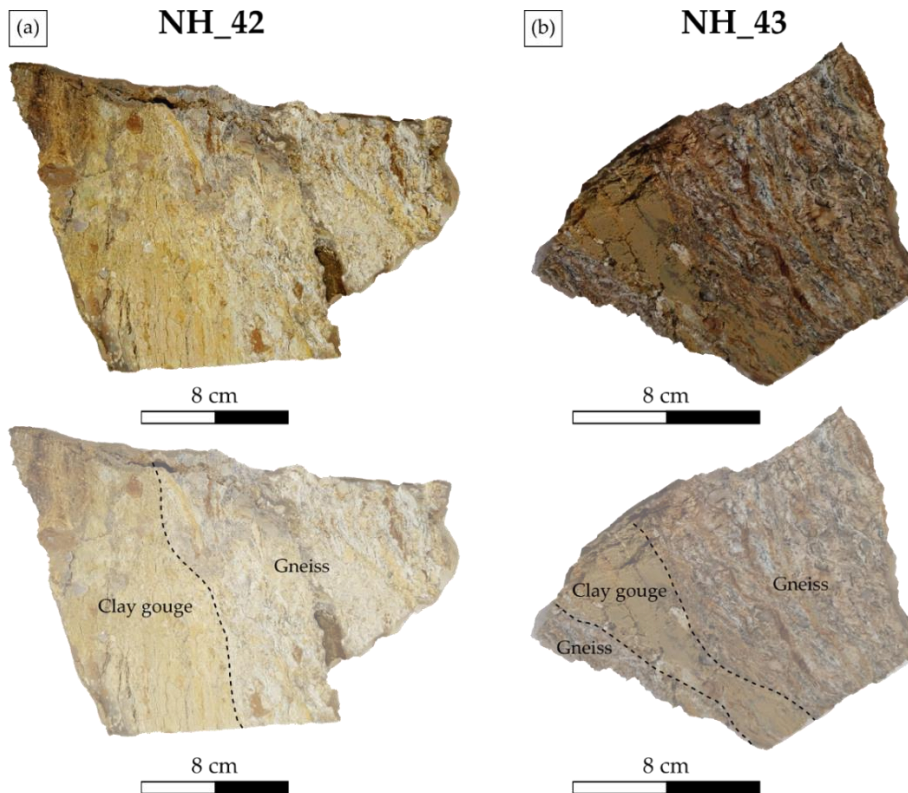


Figure 6-13. Photographs and digitizations of (a) sample NH\_42 and (b) sample NH\_43 showing the transition between the gneiss lens from the central part of the fault core and the clay gouge, represented by black dashed line.

This limit between the two phases was studied through thin sections (Figure 6-14a). In the country rock, the initial foliation is visible in both samples NH\_42 and NH\_43 (Figure 6-14b). However, the gneiss appears highly fractured and altered (Figure 6-14b,c). Plagioclases are completely transformed into illite and kaolinite (Figure 6-14c). Biotite are deformed and aligned according to a foliation and are partially replaced by illite (Figure 6-14c). XRD analyses showed that kaolinite is the prevalent clay mineral present in the gneiss lens. Likewise, the presence of corrensite indicates a propylitic signature. Quartz are brecciated and show a clear undulatory extinction as well as newly formed grains (Figure 6-14d). K-feldspars are brecciated but not altered. K-feldspar and quartz are crushed and got strung out creating sub-angular-angular to lenticular fragments representing less than 30% of the rock mass and are encompassed in illitic-dolomitic material. Thus, the sample NH\_43 and the gneissic zone of the sample NH\_42 are considered as cataclasites. Gypsum was also identified.

Carbonates, especially dolomite, are well present in this phase. A calcite content of 5.26% was measured for NH\_43. A porosity of 17% was measured for NH\_42 and of 14.6% for NH\_43.

The limit itself between both phases is almost instantaneous, a drastic grain size reduction and a significant increase of illite and carbonate content (Figure 6-14d) are observed. In the gouge

part (Figure 6-14e–g), sub-angular fine-grained silica materials are embedded in a matrix rich in illite and dolomite (Figure 6-14e) as in sample NH\_41. Only few larger fragments occur isolated in the matrix. Indeed, these fragments show a lensoid shape with pressure shadows formed by pressure-solution mechanism (Passchier and Trouw, 2005), showing a dextral shear deformation (Figure 6-14e–g). These pressure shadows are mostly made of illite (Figure 6-14f) and sometimes contain kaolinite (Figure 6-14g). As for sample NH\_41, the grain size reduction and the foliated illite-dolomite matrix show a CPO (Figure 6-14a,g). This fine grain phase is characterized as the same gouge as the NH\_41.

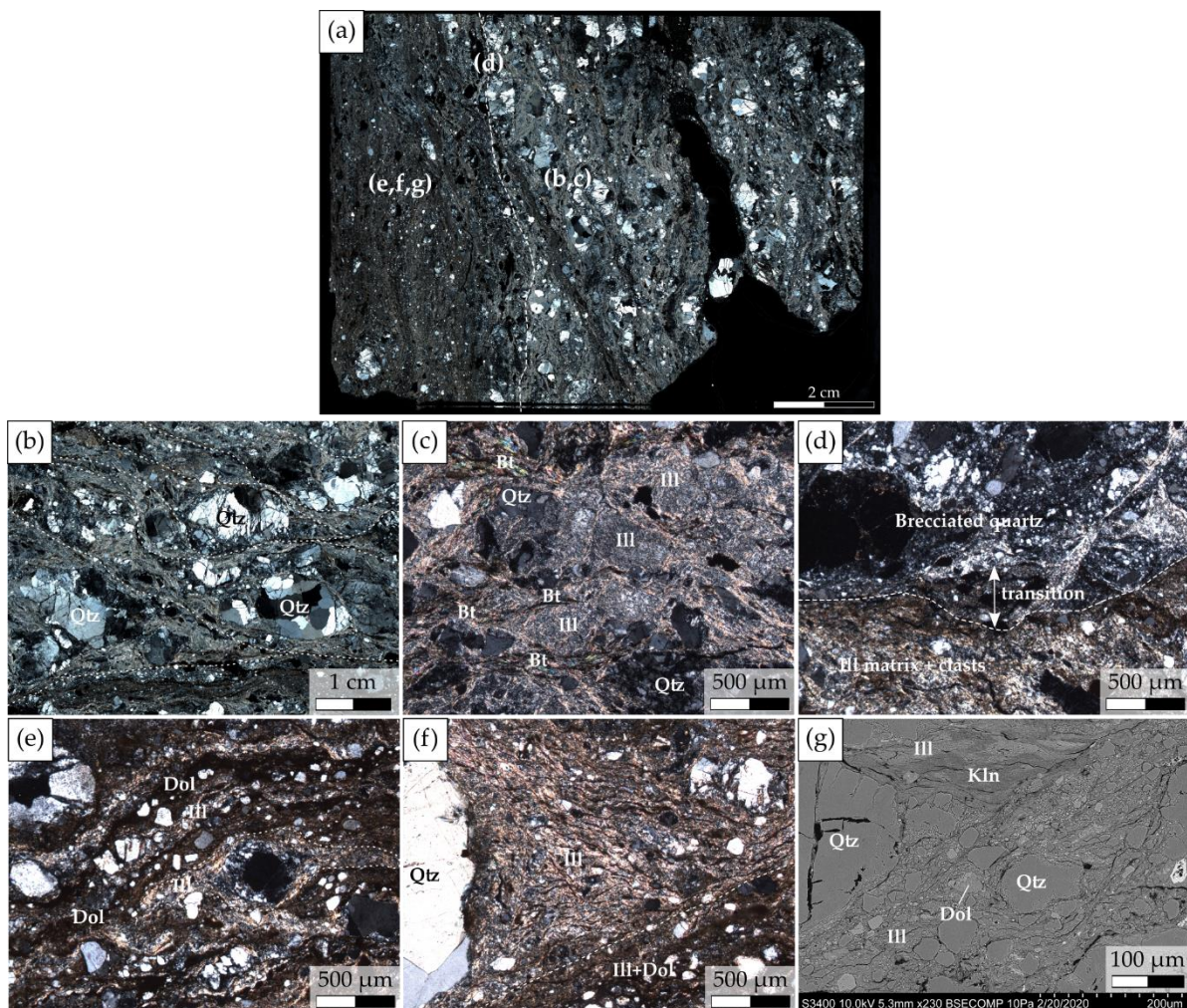


Figure 6-14. (a) Microphotograph of the entire thin section from sample NH\_42 in polarized-analyzed light. (b) Microphotograph in polarized-analyzed light showing the preserved texture of the gneiss which is highly altered. (c) Microphotograph zoom in polarized-analyzed light on the gneiss showing completely altered plagioclase into illite, altered biotite into illite following the initial foliation. (d) Microphotograph in polarized-analyzed light of the transition between the gneiss (brecciated quartz) and the gouge (illite matrix embedding quartz clasts). In the gouge: (e) Microphotograph in polarized-analyzed light of the matrix made of dolomite and illite containing quartz sigmoid with its associated pressure shadow, (f) Microphotograph in polarized-analyzed light of a quartz clast pressure shadow made of illite, and (g) Back-scattered image of a quartz clast with its associated pressure shadow made of illite and kaolinite in a clay rich matrix embedding dolomite and quartz clasts.

## II.3.3. Geochemistry

Geochemical analyses were performed on samples NH\_40, NH\_41, NH\_43 and NH\_45 in order to study the chemical as well as the loss on ignition (LOI), thus the alteration variations through a profile along the outcrop. All the data are presented in Table 6-2.

The LOI values ranges from 4.5 to 9.4 wt% (Table 6-2). The samples from the wall rocks show LOI values of 4.5 wt% for NH\_40 and of 5.9 wt% for NH\_45, which are the lowest LOI value from the profile. The fault core shows values that are almost twice as high as the values of the surrounding rocks. Indeed, the clay gouge (NH\_41) has a LOI of 9.4 wt%, which is higher than the gneiss lenses (NH\_43) with a LOI value of 7.9 wt%.

Table 6-2. Loss on ignition values and major elements, trace elements and rare earth elements chemical composition.

Sample	NH_40	NH_41	NH_43	NH_45
<b>Major elements</b>				
LOI	4.5	9.4	7.9	5.9
SiO <sub>2</sub>	65.45	63.05	62.97	62.71
Al <sub>2</sub> O <sub>3</sub>	16.17	13.02	13.70	15.61
Fe <sub>2</sub> O <sub>3</sub>	3.09	2.75	3.33	3.49
MgO	0.74	1.83	1.84	0.92
CaO	2.38	3.02	3.01	3.44
Na <sub>2</sub> O	1.66	2.24	1.85	2.02
K <sub>2</sub> O	5.17	3.95	4.69	5.08
TiO <sub>2</sub>	0.32	0.33	0.26	0.33
P <sub>2</sub> O <sub>5</sub>	0.16	0.12	0.14	0.20
MnO	0.08	0.13	0.11	0.08
Sum	99.89	99.86	99.88	99.88
<b>Trace elements</b>				
Be	3	4	2	2
Co	3.8	5.1	4.0	3.6
Cs	2.1	4.9	3.0	2.4
Ga	14.4	14.5	13.5	14.6
Hf	4.2	4.9	4.4	4.5
Nb	11.5	11.1	10.4	12.1
Rb	135.6	151.9	136.7	159.3
Sn	1	2	<1	2
Sr	166.1	319.8	256.7	202.0
Ta	0.6	0.7	0.6	0.8
Th	11.9	14.9	11.4	9.0
U	1.3	4.1	2.9	2.1
V	29	28	19	25
W	<0.5	1.0	0.6	0.8
Zr	153.6	175.4	151.1	154.6
Y	18.3	24.2	18.5	25.0
Ba	1303	320	624	1388
Ni	<20	<20	<20	<20
Sc	5	6	4	6
Cr <sub>2</sub> O <sub>3</sub>	<0.002	0.002	<0.002	<0.002

Table 2. Continued.

Sample	NH_40	NH_41	NH_43	NH_45
<b>Rare Earth Elements (REE)</b>				
La	28.6	33.9	30.8	26.3
Ce	53.7	66.0	59.1	50.5
Pr	6.11	7.45	6.49	5.58
Nd	21.7	26.3	22.5	19.6
Sm	3.92	4.89	3.85	3.65
Eu	0.84	0.97	0.90	0.90
Gd	3.67	4.54	3.49	3.73
Tb	0.56	0.69	0.53	0.66
Dy	3.19	4.06	3.19	4.01
Ho	0.61	0.88	0.65	0.88
Er	1.83	2.64	1.95	2.54
Tm	0.28	0.36	0.30	0.36
Yb	1.78	2.49	1.96	2.20
Lu	0.31	0.38	0.31	0.36
TOT/C	0.47	0.94	0.86	0.69
TOT/S	0.02	0.64	0.65	0.20

Chondrite-normalized REE patterns present enriched samples in light rare earth elements (LREE) relative to heavy rare earth elements (HREE). Likewise, all the samples present a slight negative anomaly in Eu. All the samples show a similar trend with no significant difference in element abundance between each sample. The primitive mantle-normalization multi-element diagram is characterized by (1) a clear depletion in Ba approaching the gouge (NH\_41), (2) an enrichment in Cs, U and Sr approaching the gouge and (3) a lower abundance of Hf in NH\_40 compared to the other samples.

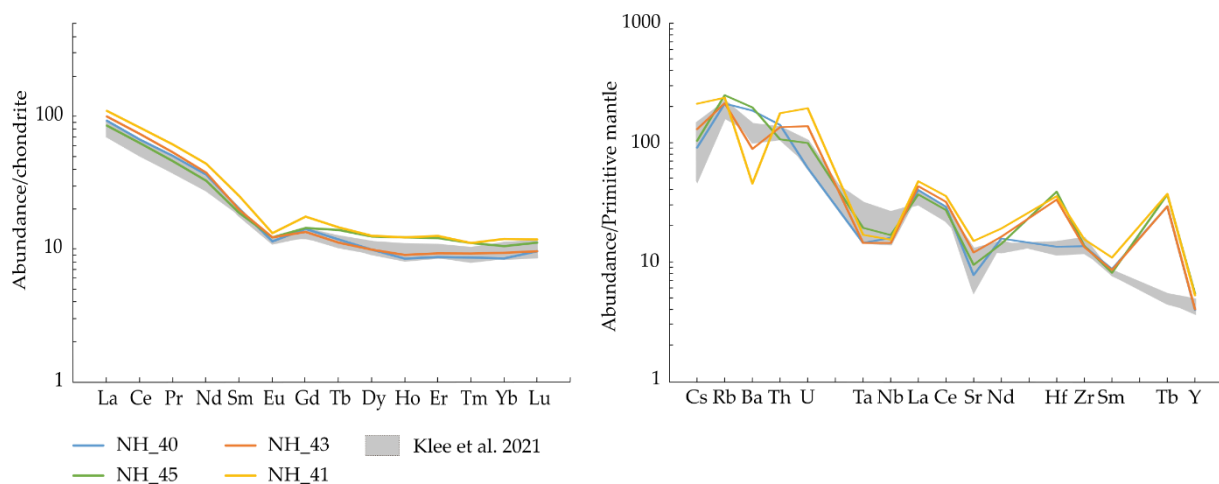


Figure 6-15. (a) Chondrite-normalized (values from Boynton (1984)) rare earth elements (REE) patterns of samples from this study (colored lines) and from Klee et al. (2021a) (grey area). (b) Primitive mantle-normalized (values from McDonough et al. (1992)'s slight revision of Sun and McDonough (1989)) multi-element diagram showing trace element pattern of samples from this study and from Klee et al. (2021a).

### II.3.4. Temperature conditions

For samples containing enough illite, the Kübler Index (KI) was calculated for the fractions <2  $\mu\text{m}$  and 2–6  $\mu\text{m}$  Table 6-3. The clay composition is given in Table 6-1. As described in Klee et al., 2021a, the fraction <2  $\mu\text{m}$  is supposed to correspond to the youngest event which crystallized neoformed illite crystals. Whereas, the fraction 2–6  $\mu\text{m}$  might represent inherited grains recrystallization into more developed illite crystals or a mix of detrital and neoformed illite. Through the KI, information about the degree of metamorphism is given for each fraction when possible. When the amount of illite was too low or the amount of biotite too high compared to the illite one (e.g. both fractions of NH\_44 and fraction 2–6  $\mu\text{m}$  for NH\_45), the KI was not measured.

Table 6-3. List of samples with their respective FWHM and Kübler Index (KI) values in air dried (AD) conditions for the fraction <2  $\mu\text{m}$  and 2–6  $\mu\text{m}$ . n.m. - not measured.

Samples	clay fraction < 2 $\mu\text{m}$ (AD)		clay fraction 2-6 $\mu\text{m}$ (AD)	
	FWHM	KI	FWHM	KI
NH_40	0,694	1,02	0,741	1,10
NH_41	0,685	1,01	0,661	0,97
NH_43	n.m.		0,43	0,62
NH_45	0,38	0,54	n.m.	

KI values range from 0.54 $\Delta^{\circ}2\theta$  to 1.02 $\Delta^{\circ}2\theta$  for the <2  $\mu\text{m}$  fraction and from 0.62 $\Delta^{\circ}2\theta$  to 1.10 $\Delta^{\circ}2\theta$  for the 2-6  $\mu\text{m}$  fraction Table 6-3. They are almost equivalent in both fractions. All the samples show KI values corresponding to the diagenetic zone. The granite (NH\_40) shows high KI values in both fractions with 1.02  $\Delta^{\circ}2\theta$  (< 2 $\mu\text{m}$ ) and 1.10  $\Delta^{\circ}2\theta$  (2–6  $\mu\text{m}$ ). The gouge (NH\_41) shows a similar KI, 1.01  $\Delta^{\circ}2\theta$ , in the fraction < 2 $\mu\text{m}$  to NH\_40, whereas the KI measured in the fraction 2–6  $\mu\text{m}$  is lower, 0.97  $\Delta^{\circ}2\theta$ . A lower KI value, 0.62  $\Delta^{\circ}2\theta$  was obtained for the fraction 2–6  $\mu\text{m}$  of the gneiss lenses sample (NH\_43). Finally, the fraction <2  $\mu\text{m}$  of the gneiss in contact with the gouge (NH\_45) shows the lowest KI value (0.54  $\Delta^{\circ}2\theta$ ). The gneissic rocks show lower diagenetic grade KI values than the granite and the gouge.

## II.4. Discussion

### II.4.1. The fault gouge protolith

Fieldwork observations have shown that the fault zone is related to SDVFZ activity overprinting previously stacked Mesozoic and Proterozoic sequences. This initial sedimentary stack has been pinched between the granite and the gneiss composing the walls of the fault core. Petrographic analyses associated to fieldwork have shown how heterogeneous the gouge is. However, geochemistry analyses showed a REE signature close to wall rocks REE signature

(Figure 6-15a). The geochemical signature of Proterozoic sediments outside of the high strain zone here presented is not available and cannot be compared to the gouge geochemical signature. By considering both fieldwork observations and geochemical signal, we consider that the gouge present a mixed geochemical signal of Proterozoic sediments, basement and Mesozoic granite. Further analyses should be performed along the entire fault zone and on the Proterozoic sediments in order to know the proportion of each rocks crushed into the fault gouge.

#### II.4.2. Fluid-rock interactions and fluid circulation at high strain

All the samples, collected according to a profile (AB) through the fault zone (Figure 6-16a), are strongly altered. As demonstrated at low to moderate regional strain in the area by Klee et al. (2021b), high strain zones show also a correlation between amount of deformation and alteration degree. An alteration gradient was observed through thin sections by the progressive complete transformation of plagioclase into kaolinite and/or illite and of biotite and K-feldspar into illite towards the gouge. The K-feldspar breakdown due to hydrothermal alteration is well represented by the decrease content of Ba and the increase of U (Figure 6-15b) (Li et al., 2013). LOI values increase (Figure 6-16b) highlights the alteration gradient which tends to increase towards the gouge (NH\_41).

The gouge presents the highest LOI indicating an important amount of hydrous minerals in it. The wall rocks granite (NH\_40) and gneiss (NH\_45) one meter from the gouge have lower LOI values. Thus, the wall rocks present a lower percentage of hydrous minerals than the fault core. The gneiss is slightly more altered than the granite due to the fact that, near the fault core, the gneiss is slightly more fractured. We cannot exclude that the gneiss fracturing is partly inherited and that further fracturing occurred during SDVFZ activity. Amount of fracturing drastically decreases in the first ten meters away from the considered fault zone. The gneiss lens (NH\_43) being more deformed than the wall rock, shows a higher LOI. NH\_43, being comparable to NH\_45 in composition, the LOI can be related to the amount of alteration. Thus, NH\_43 shows a more pronounced alteration. Geochemical analyses from this study compared to Klee et al. (2021a) show that the representative granites affected by the regional alteration fit almost perfectly with the granite from this study (NH\_40), excepted for Ba, due to a difference in the amount of alteration, and for Tb which is until now misunderstood (Figure 6-15b). Knowing that the fault core and the gneiss are more altered than the granite, the positive anomaly of Hf is difficult to explain as Hf is an immobile element under hydrothermal conditions (Figure 6-15b).

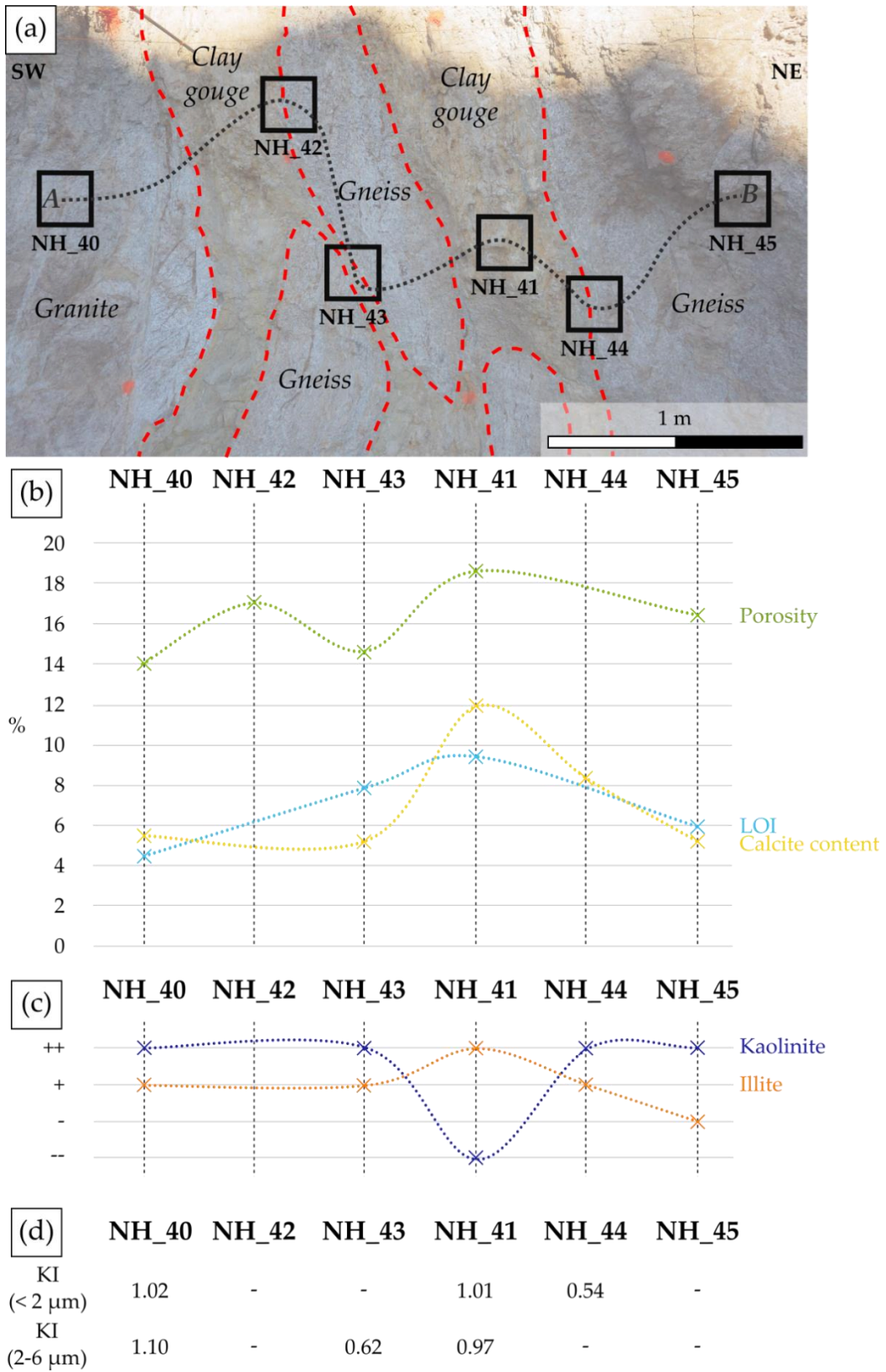


Figure 6-16. (a) The fault gouge outcrop showing the samples locations. The gouge being composed of two branches, it is considered that the left branch present equivalent values than NH\_41 and thus marked by a dashed square. (b) Extrapolated evolution of the amount of illite in comparison to kaolinite. (c) Extrapolated evolution of the porosity, LOI and calcite content percentages through the fault zone. (d) KI values of the fraction <math>< 2 \mu\text{m}</math> and <math>2-6 \mu\text{m}</math> along the fault zone profile.

Alteration inducing clay precipitation, it has been shown that kaolinite is the prevalent clay mineral in the gneiss lenses in the center of the fault gouge and in the wall rocks. Kaolinite can be related to a high fluid-rock ratio or to an acidic fluid circulation (Fulignati, 2020; Nishimoto and Yoshida, 2010). However, the wall rocks and the gneiss lenses present also corrensite indicating a propylitic signature (Burnham, 1962; Genter, 1989). Alteration being lower in these rocks than in the gouge, it is suggested that an acidic fluid has circulated through the fault zone. However, illite is the predominant clay mineral composing the gouge (Figure 6-16c). K-feldspar and biotite being almost completely leached, potassium was released. Geochemical analyses highlight this by the  $K_2O$  content decrease. Klee et al. (2021a, 2021b) have shown that in all the NH granite K-feldspar, besides the perthites, were not affected by the alteration. The complete alteration of K-feldspar in this gouge proves, in complement to LOI values, that the leaching was important. It is suggested that part of the released potassium allows the transformation of kaolinite into illite without compensates the  $K_2O$  depletion (Chermak and Rimstidt, 1990). Kaolinite can also disappears by illitization before conditions of the diagenesis-anchizone boundary are reached, unless the environment is Al-rich (Śródoń et al., 2006). The rest of the potassium has left the fault zone, allowing probably illite crystallization in the surrounding rock.

Illite content increases towards the gouge and progressively formed a matrix. The illite crystals are oriented following a preferred orientation. Pressure shadows observed under optical microscope and SEM indicate that the apparent foliation corresponds to a foliation created by a later tectonic event (SDVFZ activity) (Song et al., 2017). The similarities between KI values of fractions  $<2 \mu\text{m}$  and  $2-6 \mu\text{m}$  from the granite and the gouge emphasizes the presence of mainly neoformed illite. The fact that most of illite is neoformed is highlighted by the K-Ar illite ages of 6.8 Ma for the  $<0.2 \mu\text{m}$  fraction, considered as being representative of the last event during which illite has crystallized. Pavlis and Trullenque (2021) have shown that the activity of the SDVFZ began by ca. 12 Ma after. The young age given by the K-Ar dating on the fraction  $<0.2 \mu\text{m}$  shows that the last fluid circulation occurred more recently. The later event that occurred in the area is the compression of the Avawatz Mountains due to the activity of the Garlock Fault zone creating a new fracture set observed by Chabani et al. (2021). It is conceivable that fluid circulation during this deformation episode induced an age resetting of illites found at this locality.

High amounts of dolomite are found in this matrix as a feature highlighted by an increase of MgO (Table 6-2) and of the calcite content (Figure 6-16b) compared to the wall rocks.

Considering that carbonates derive from an external source (Klee et al., 2021b), their amount in the fault gouge (Figure 6-16b) shows that fluid circulation was mainly concentrated in the fault core.

Automorphous gypsum has also been identified in the fault core. Van Driessche et al. (2019) have shown that gypsum is most stable and precipitates at temperatures less than 40–60 °C. Thus, gypsum found in the fault core can be linked to the last fluid that has circulated when the fault activity stopped. The origin of the gypsum is still not understood. This last event could be related to the Garlock Fault Zone activity, which is younger than the SDVFZ (Andrew et al., 2015). The compression of the Avawatz Mountains could have deformed and fractured the Miocene sedimentary series rich in evaporites at the rear part of the range, as well as impacted the studied fault zone letting a fluid circulate through the sediments until the gouge. The same episode of fluid circulation might be responsible of the age resetting above mentioned.

#### II.4.3. Gouge microstructural evolution associating fluid circulation and high strain

The development of a fault core is associated to a drastic change of fault mechanical response to stress (Berg and Skar, 2005). Rock microfabric evolution along strain gradients is drastically influenced by, fluid circulation in fault zones. Interplay between progressive deformation and fluid rock interaction processes controls chemical and physical processes at each stage during fault activities (Song et al., 2017). At sample scale and under microscope, the different types of fault rocks show a general gradational increase in strain intensity from the wall rocks towards the gouge. This strain increase is accompanied by variations in terms of petrography, petrophysics, chemical (as presented above) and microfabric, which are observed through the different samples collected according to a profile (AB) through the fault zone (Figure 6-16a).

The grain size reduction, observed approaching the gouge, is influenced by the continuous deformation processes of the successive primary minerals. Quartz and feldspar grain size tend to decrease at the onset of applied deformations. Grain size reduction promotes chemical reactions during fluid circulation and thus clay minerals precipitations (Buatier et al., 2012; Song et al., 2017). Initial anisotropies like foliation in gneiss are reworked, creating a new shistosity along which biotite and illite are preferentially oriented. According to field work and petrographic analyses, a clear limit is visible at outcrop, sample and thin section scales between the fault gouge and the wall rocks. The reduction size of the quartz grains in the gouge is due to the fault activity but also due to material composing the gouge consisting into Proterozoic gneiss and sediments. The gouge contributed to a slip weakening behavior of the fault (Buatier

et al., 2012). It is suggested that the deformation was accommodated by the gouge (Bard, 1980) due to the small amount of deformation observed in the walls of the fault.

The process of grain size reduction by fracturing and attrition should reduce the microporosity (Hadizadeh et al., 2015; Song et al., 2017). However, this study shows a porosity increase towards the gouge, with a maximum porosity in the gouge itself (Figure 6-16b). Note that even if the granite presents the lowest porosity within the considered outcrop, it is much higher compared to a fresh granite (i.e. <5%) (Ledésert et al., 2010; Staněk and Géraud, 2019). Porosity is visible under optical microscope and SEM as microfractures and as spaces between the grains (Figure 6-12f,h,i). Song et al. (2017) have shown that zones where quartz grains or fragments are dominant reveal the highest porosity values. Likewise, these authors showed that pores cannot be created where dense clay minerals are present. The strong heterogeneity of the fault gouge in terms of microstructure and mineralogical composition, partly due to a protolith different from the wall rocks, observed in the gouge explains the high porosity value obtained (Figure 6-16b). Some of the porosity could have been also created by fracturing during the sample extraction and/or afterward during the sample preparation for porosity measurements.

#### II.4.4. Implication of high strain zones in terms of geothermal reservoir properties

In crystalline basement, fracturing controls the porosity and permeability allowing fluid circulation in case of a good connectivity (Gillespie et al., 2020). The mechanical and hydrologic properties of highly deformed faults are influenced by the presence of clays in fault rocks. Caine et al. (1996) has shown that a high strain zone formed exclusively due to strain and fluid-rock interactions of a unique protolith which composes the fracture zone walls. It is well known that the increase proportions of clays promotes ductile behavior and reduces frictional strength as well as reduces and prevents regeneration of permeability (Davatzes and Hickman, 2005). Likewise, grain-size reduction decreases the porosity and the permeability of the fault core compared to the adjacent protolith (Caine et al., 1996; Song et al., 2017). Thus, permeability reduction leads to fault core to act as a barrier to fluid flow in geothermal reservoirs (Caine et al., 1996; Ikari et al., 2009).

In this study fault core rocks do not derive from the bounding blocks, namely Mesozoic granite and Proterozoic gneiss but from pinched sedimentary units with interlayered gneiss. Due to its heterogeneity, its high porosity, its high calcite content and its important leaching, this fault core gathers all the element indicating that it can acts as a drain. This can be explained by the fact that (1) deformation and alteration, although pronounced, were not sufficient to produce

enough illite to seal the fault and become a barrier, but also that (2) having potential sediments wedged in the fault core may influence the petrophysical properties of the fault core. Hence, a high strain zone can still act as a drain as long as clay minerals don't have sealed the system.

At larger scale, sediment slices pinched between two blocks of basement were also identified in the URG. An example is found close to the Markstein basin in the vicinity of Colmar in the Vosges Mountains (Figure 6-17). These sediments pinches are bordered by basement units laterally transported by strike-slip structures. This hectometric size basement and sedimentary assemblage is directly comparable to the imbricate, previously described, in the NH.

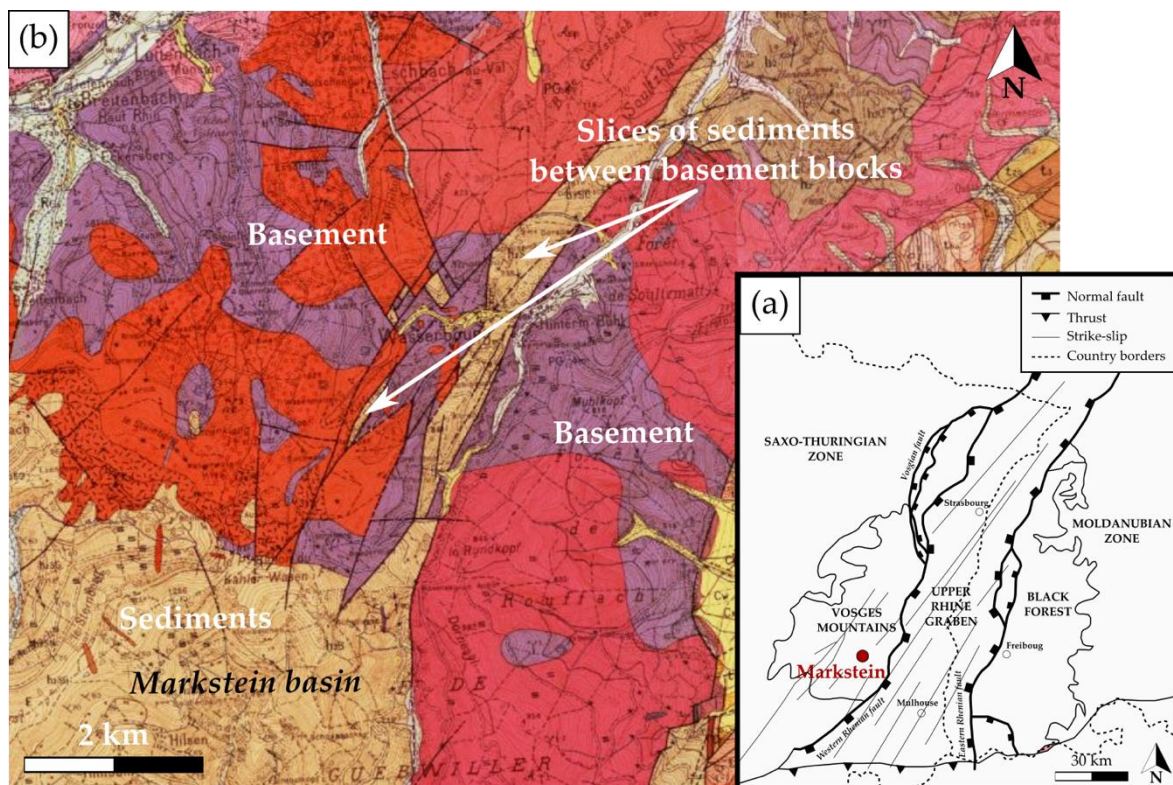


Figure 6-17. (a) Markstein basin location in the URG modified after (Edel et al., 2007; Ledésert and Hébert, 2020). (b) Geological map showing sediment slices pinched between blocks of granite due to shear displacement identified in the vicinity of the Markstein basin in the URG (infoterre).

Fault gouges identified during reservoir exploration need to be investigated because even with a lot of clay, they can be drains.

## II.5. Conclusion

Fault gouges rich in clay are not the main target in geothermal exploitation. They are generally characterized as a sealed system that act as a barrier due to grain size reduction and production of an important amount of clay which reduce the porosity and thus the permeability. However, this outcrop analogue study of a consequent fault gouge identified in the Noble Hills range has shown that a fault gouge can be a drain for fluid circulation. An important leaching and thus a

more pronounced alteration are observed in the fault core than in the wall rocks. The fault gouge being heterogeneous in terms of mineralogical composition from the protolith (mix of leached Proterozoic sediments and gneiss), presenting different size of grains, as well as a high amount of carbonates, a high porosity is induced even if a lot of clay minerals are present. This porosity can allowed the fluid to circulate. Permeability measurements are needed to confirm this hypothesis. The walls being not highly fractured, deformed and altered, it shows that the gouge has accommodated the deformation. Kaolinite being the prevalent clay mineral in the wall rocks, and not in the fault core where the leaching was the more abundant, indicates that an acid fluid has circulated through the fault zone.

Fault gouges are very complicated objects, whose structures can largely deviate from the conceptual model presented in the literature due to the structural heritage present in the reservoir (Caine et al., 1996). Thus, the view of a fault gouge in terms of drain and barrier needs to be revisited.

### III. CASE OF HIGHLY STRAINED ROCKS DEVELOPING A FAULT STRUCTURE FROM A SINGLE BASEMENT PROTOLITH: INSIGHTS FROM OUTCROPS AT UPPER RHINE GRABEN SHOULDERS

#### III.1. Introduction

The previous section described the influence of a highly sheared zone in the NH. In accordance with our adopted definition of an analogue, we consider that structures present in the URG shoulders are suited to investigate processes active in present day exploited reservoir within the central graben. In order to find optimum outcrops exposures, site visits were led in abandoned mines within the Vosges (Gabe-Gottes mines) and in the Black Forest (Schauinsland mine) massives.

Soultz-Sous-Forêts (SsF) geothermal site located in the Upper Rhine Graben (URG) produces electricity by exploiting brines in a fractured granitic basement. Geothermal wells penetrate the fractured basement and intersect fractures at varying degrees of permeability. These are partially opened and present mineralizations due to fluid circulation. Several tectonic phases occurred during the Variscan cycle leading to the actual structure of the URG.

The URG is a part of the European Cenozoic rift system and has an approximate length of 300km, a width varying from 30 to 40km and a NNE trending (Ziegler, 1992). The Rhenish Massif and the Jura Mountains delimitate respectively the Northern and Southern part of the

URG (Figure 6-18). The URG was developed in the northern Alpine foreland, it is assumed that its development is contemporaneous with the collisional phases of the Alpine and Pyrenean orogeneses (Schumacher, 2002). It is the result of continental extension beginning in the Late Eocene (Lopes Cardozo and Behrmann, 2006).

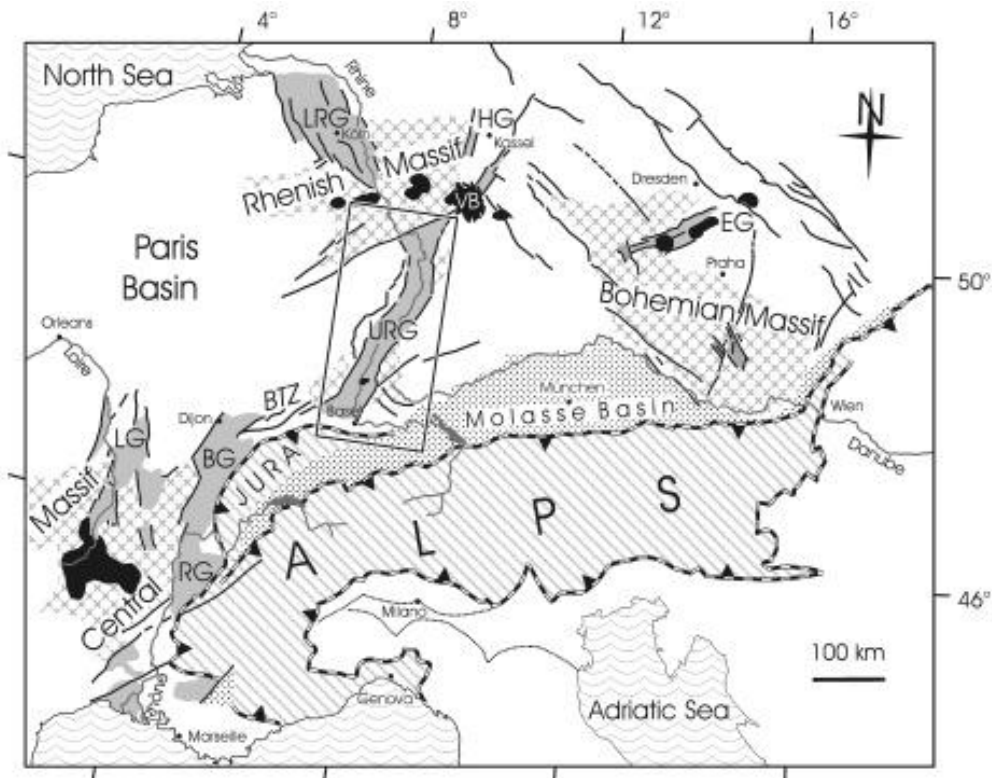


Figure 6-18. Structural map of the European Cenozoic rift system showing the tectonic setting of the Upper Rhine Graben (URG in the rectangle) after Schumacher (2002)

At the regional scale, Cenozoic sediments fill the graben in its central part (Figure 6-19). Triassic and Jurassic sediments are lying under the Cenozoic sediment and can outcrop at some places. The structure is composed of normal faults on its internal part and borders on the eastern and western sides, which delimitate the Vosges Mountain and the Black Forest. Those mountains are composed of Hercynian crystalline basement rocks. Basement rock from the Paleozoic are overlain by 1400 m of Mesozoic and Cenozoic sediments (Illies, 1972; Vidal, 2017). Main regional directions can be observed in the URG. The ENE-WSW to NE-SW direction related to the Variscan sutures was activated at the Carboniferous, a NNE-SSW direction also activated at the Carboniferous and a NW-SE direction linked to dextral strike-slip movement related to the Alpine orogeny (Vidal, 2017).

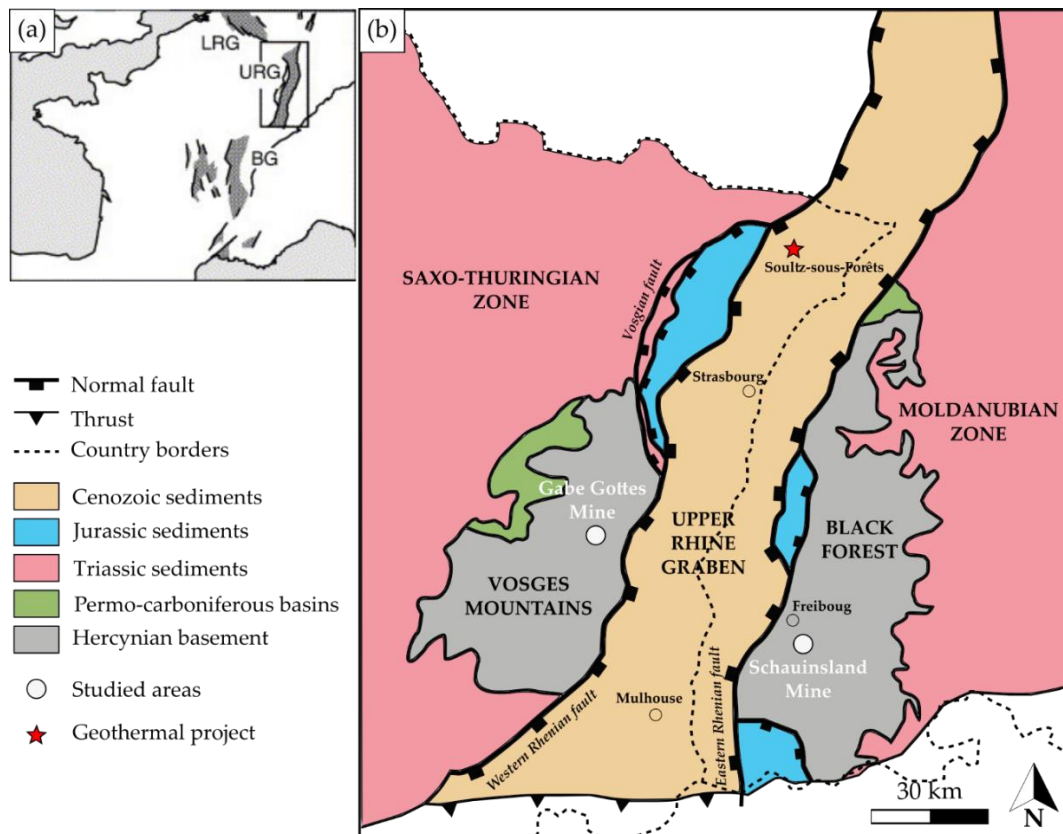


Figure 6-19. Location and simplified geological map of the Upper Rhine Graben modified after Ledésert and Hébert (2020) and Rotstein et al. (2006) showing the location of the two investigated mines. LRG – Lower Rhine Graben, URG – Upper Rhine Graben and BG – Brest Graben.

### III.2. Vosges Mountains – Gabe Gottes Mine

Gabe Gottes mines is located next to Sainte-Marie-aux-Mines in France (Figure 6-19) in the Vosges massif. The Vosges massif, being one of the URG shoulders, were subject to a several stress state changes through the geological periods (Figure 6-20). Distension and compression events occurred in the Carboniferous, the Permian was a distension period with different orientation of the minimum stress applied. In the Upper Eocene, a N-S compression took place. The Oligocene corresponds to the opening phase of the Rhine Graben. In the Miocene, the Vosges mountains were subject to compression.

The Gabe Gottes mine was exploited from the 10th to the 20th century for various ore minerals, and native silver. The mineralized veins occur in the “Varied gneiss group” which is composed of various lithologies including “pearl” gneiss, migmatitic gneiss and garnet gneiss locally intercalated with amphibolite and limestone (Hafeznia et al., 2015).

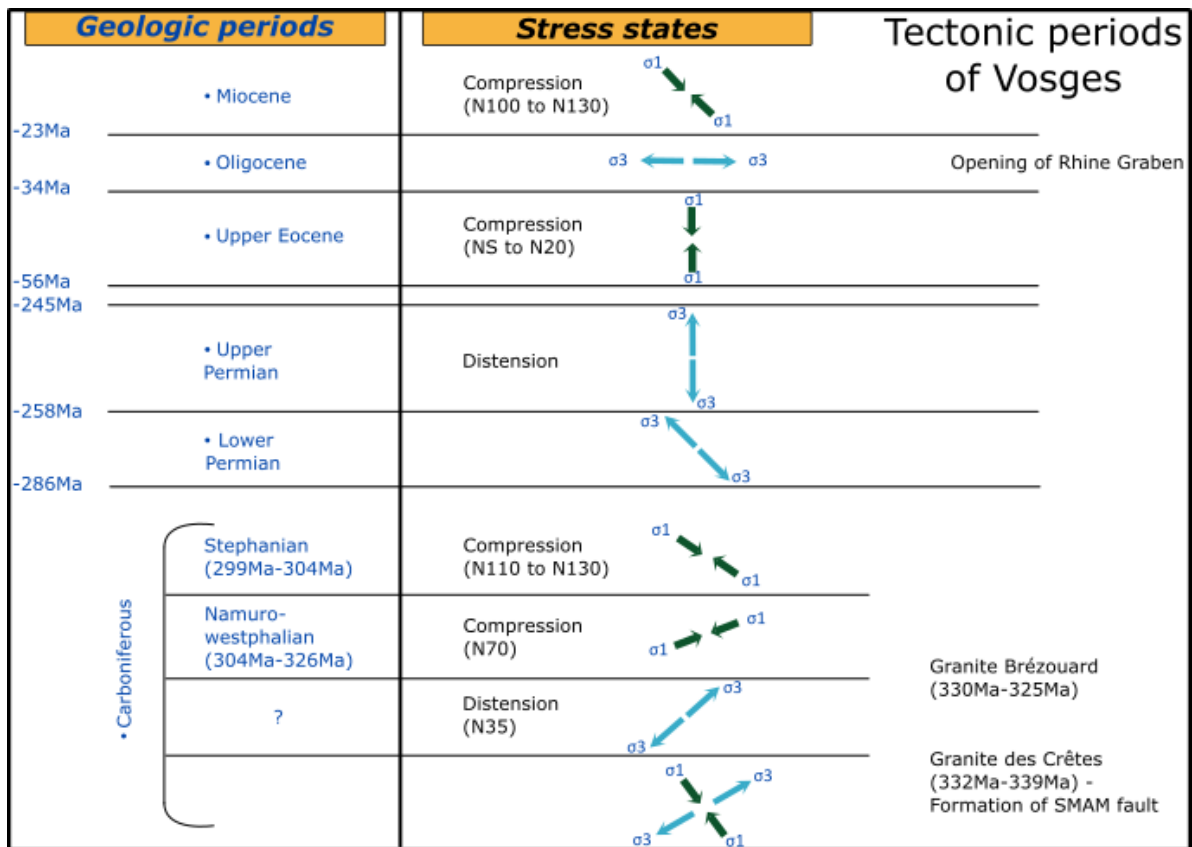


Figure 6-20. Tectonics phases of the Vosges mountain since the Carboniferous to the end of the Miocene (Hafeznia et al., 2015).

During the investigation, a focus was made on the P-west gallery (Figure 6-21). In this gallery was observed a highly deformed subvertical fault zone (Figure 6-22). This fault zone corresponds to a dextral shear zone with an E-W orientation (the Saint-Jacques fault system, Figure 6-21) which can be followed along the gallery. The shear zone appears highly deformed with stretched and boudinated basement rock elements preferentially orientated parallel to schistosity. Numerous movement indicators in the form of striations, mineral lineations and slickenslides confirm the transcurrent nature of this deformation zone ((Hafeznia et al., 2015) and own data).

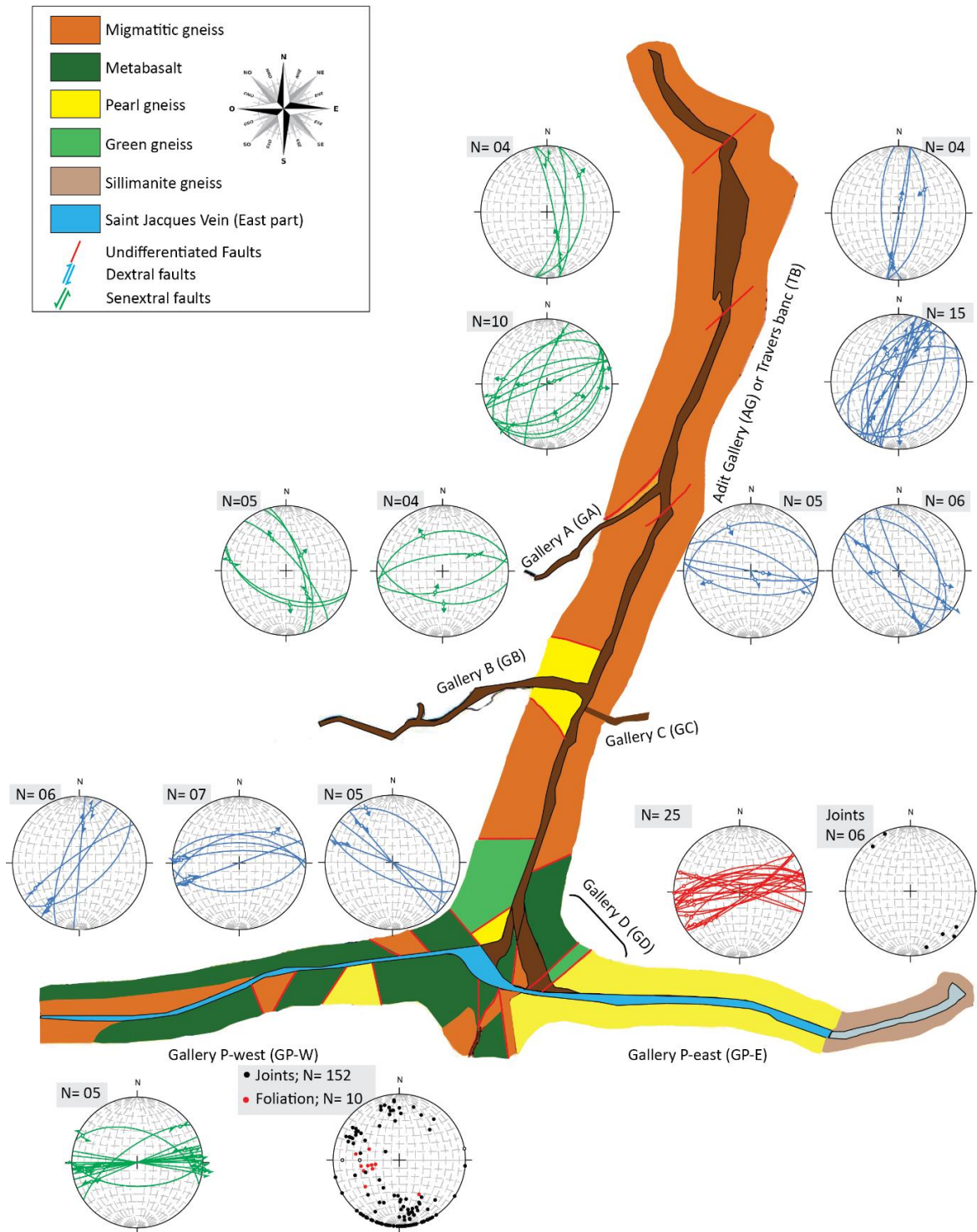


Figure 6-21. Geological map of the Gabe Gottes mine with fault analysis data

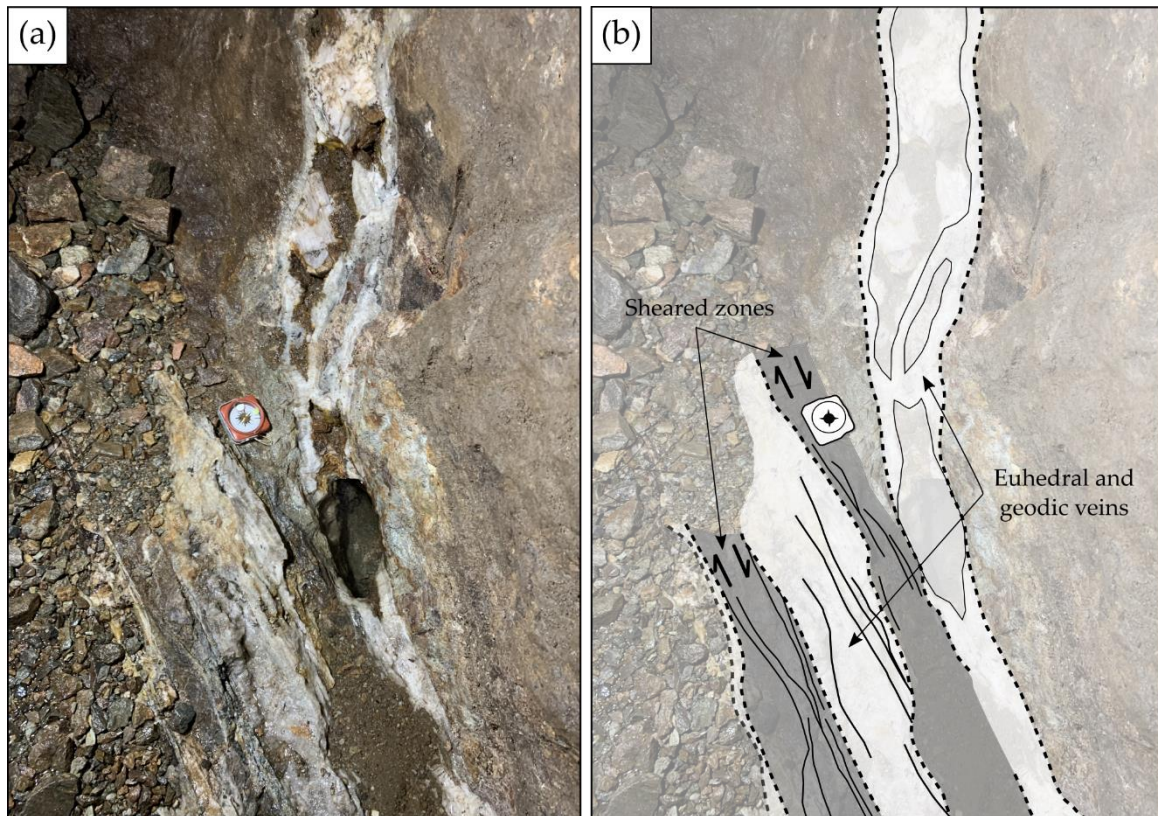


Figure 6-22. Interaction between a sheared zone and euheral-geodic veins

The shear zone is interlayered with euheral quartz veins of various width (Figure 6-23). Thinner veins were developed through these plans (Figure 6-24). Between these veins, veinlets crosscut the sheared zone making bridges between the larger veins (Figure 6-24). The interlayered veins are connected to wider vein orientated NW-SE found in the walls of the gallery. None of these veins present any sign of deformation (Figure 6-22) meaning that the outcrop is misleading. In the case of a vein offset by a strike-slip shear zone, its infill should have been deformed. However, the vein infills are automorph and do not present any signs of stretching. The strike slip fault zone must preexist before the vein formation, a feature independently confirmed by isotopic dating and considerations of regional geology. By following the wide vein on the gallery wall along the shear zone, it is observed that its direction is changing from NW-SE to E-W.

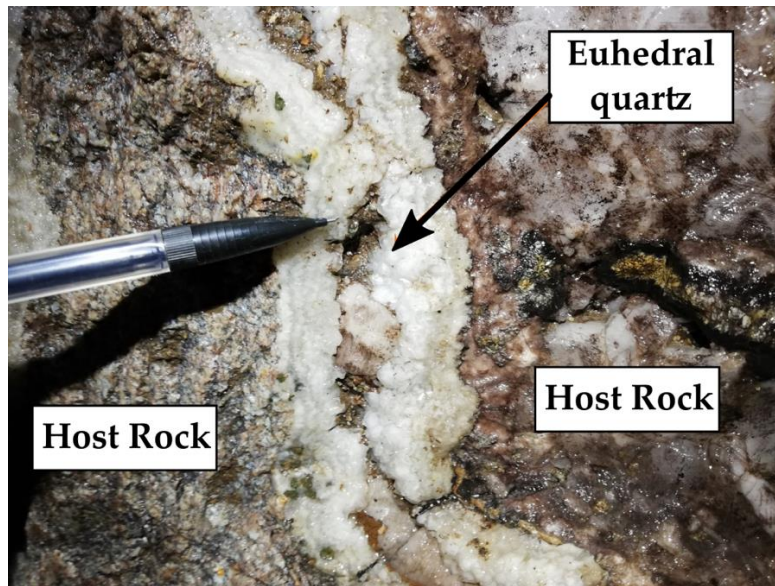


Figure 6-23. Development of euhehedral quartz within the shear zone, showing no sign of deformation

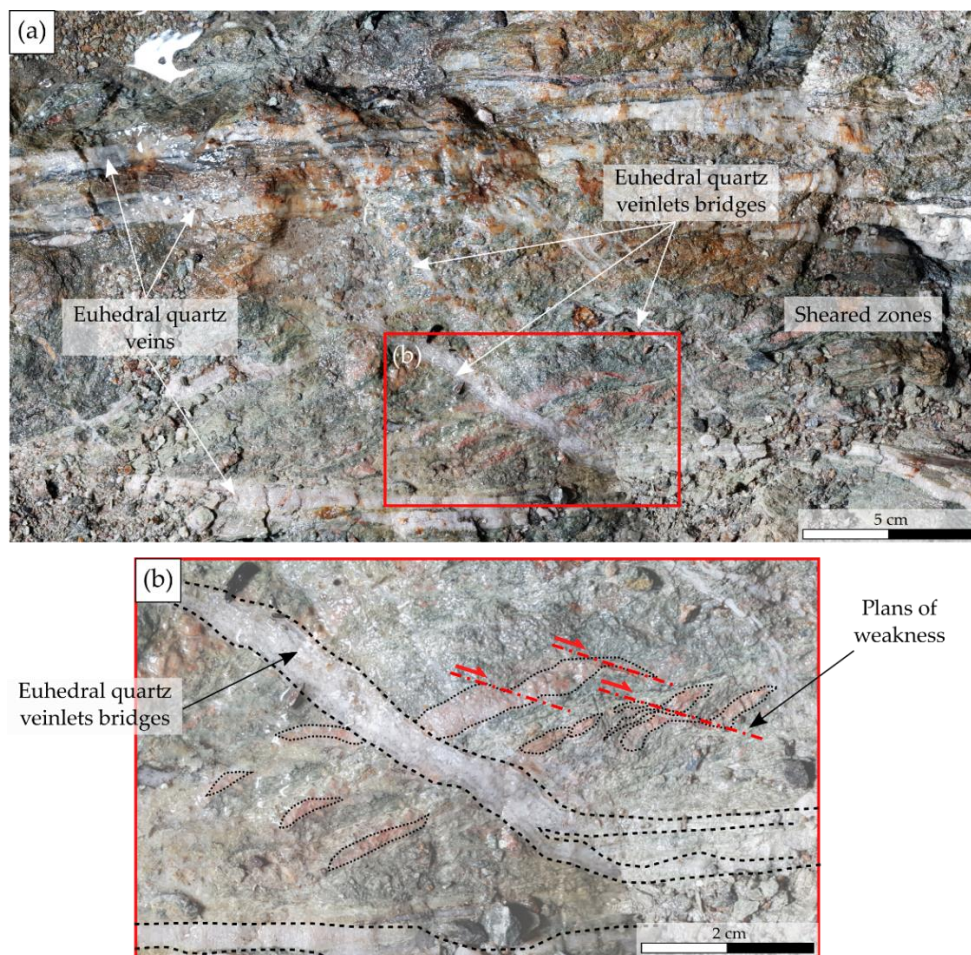


Figure 6-24. (a) Photograph of the sheared zone showing the euhehedral quartz veins interlayered and making bridges in the sheared basement. (b) Zoom showing an euhehedral quartz veinlets crosscutting the highly deformed basement using plans of weakness.

Petrographical analyses were performed on this sheared zone through thin sections from the surrounding rock to the core (Figure 6-25). The surrounding rock is altered but was affected by a low amount of deformation (Figure 6-25a). K-feldspar and plagioclase are altered into illite and few kaolinites. The brownish seems indicate the presence of carbonates mixed with the clay minerals. Biotite is also completely altered into illite and oxides but the shape and texture are still recognizable. Quartz is the only unaltered primary mineral. However, it presents signs of dynamic recrystallization at the border of the grains according to sub-grain rotation and grain boundary migration processes (Stipp and Kunze, 2008). Approaching the sheared zone, the rock appears highly deformed (Figure 6-25-d). Clay minerals and carbonates form layers presenting a crystallographic preferred orientation (CPO) and sigmoids interlayered with layers of quartz which have completely recrystallized according to grain boundary migrations and new formed grains. A new schistosity appears and mylonites can be sporadically recognized. In the core of the sheared zone, layers of clay-carbonates presenting a CPO and recrystallized quartz are visible (Figure 6-25e, f). However, veins and veinlets of secondary quartz are identified showing straight boundaries and following the schistosity (Figure 6-25e, f). Automorph minerals can also be present in these veins and veinlets as observed at outcrop scale. They show the growth of quartz crystals perpendicular to the vein borders, crystallization is starting from the border towards the center (Figure 6-25g). Veins of calcite are also identified in the sheared zone confirming a fluid rich in Ca. These Ca rich brines appear to be the latest brine circulation event.

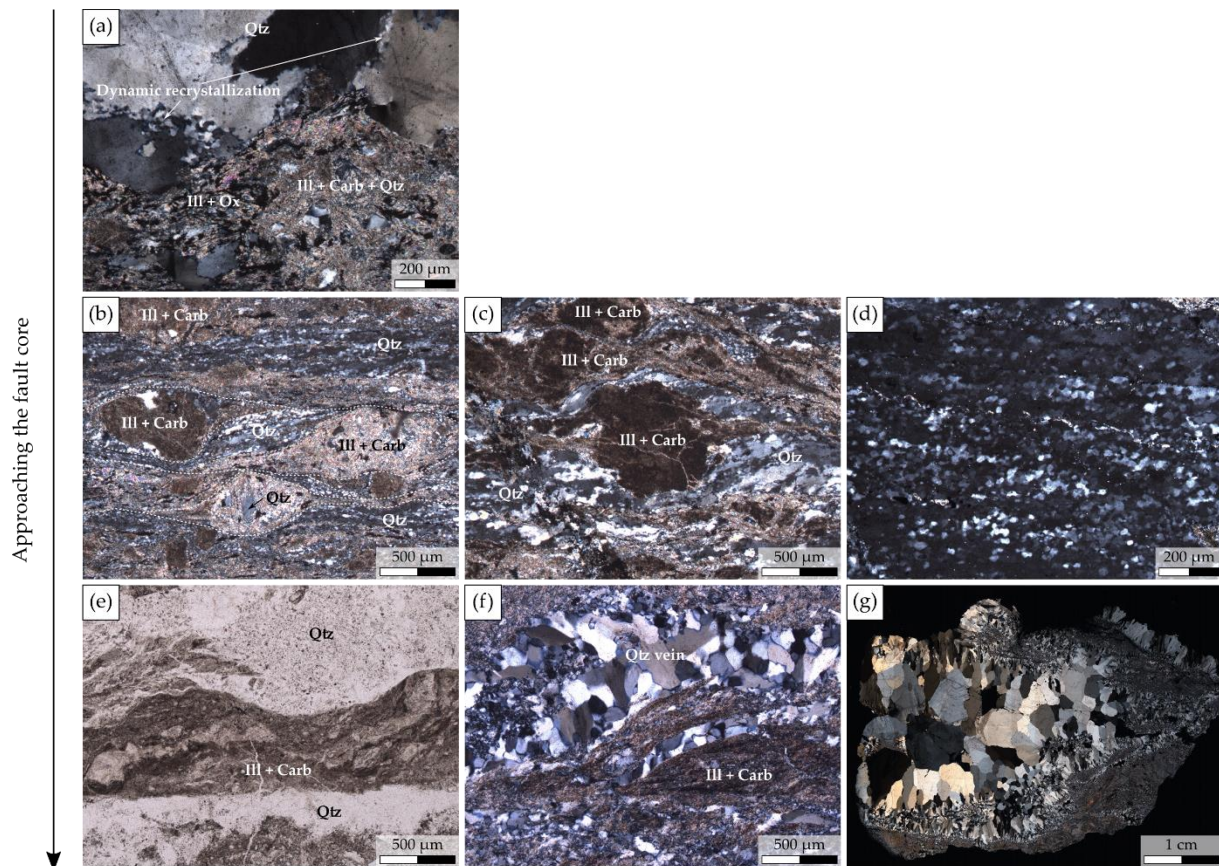


Figure 6-25. Microphotographs under optical microscope of samples collected according to a profile through a shear fault zone with (a) the wall rock, (b-d) the outer zone of the fault core and (e-g) the fault core. (a) The surrounding rock highly altered with feldspar transformed into illite associated to carbonates, altered biotite into illite and oxides and unaltered quartz partially dynamically recrystallized (grain boundary migration) at the grain borders. (b,c) Highly deformed basement showing sigma clasts of illite and carbonates, layers of dynamically recrystallized quartz by grain boundary migration and illite-carbonate rich layers. (d) Layer of recrystallized quartz by grain boundary migration. (e,f) Veins of euhedral secondary quartz crosscutting highly deformed zones of illite and carbonates presenting a CPO. (g) Example of a geode filled by quartz observed in the core of the high strain zone.

The vein observed in the gallery wall is originally orientated NW-SE and changes its orientation when encountering the sheared zone. The strike slip shear zone which was created before the vein development, induce an anisotropy in the form of a schistosity within the host rock. This schistosity is predominant along the inherited deformation zone but vanishes quickly when moving away from it.

Pronounced rock alteration within the strike slip zone changes their mechanical response to loading. Alteration drastically influences initial rock competence and occurrence of a clear brittle failure becomes less obvious as a component of rock bulk creeping can be expected (Genevois and Prestinzi, 1979). In addition, the earlier schistosity offers a preferential path to late fluid circulation.

It is proposed that the fluids circulating during the ore emplacement episode are deviated since fluid channeling along the planes of shistosity is easier than propagating a fracture across altered rocks.

### III.3. Black Forest – Schauinsland Mine

The other place of interest which was investigated is the Schauinsland mine (10km SE of Freiburg im Breisgau, Germany), located in the Black Forest mountain (Figure 6-26). The Black Forest corresponds to the Eastern shoulder of the URG. Its western border is delimited by a major normal fault with a NNE-SSW orientation (Figure 6-19). The mountain is mostly made of crystalline granitic basement rock as in the Vosges Mountain. The structure is covered by Cenozoic and Mesozoic sedimentary rocks on its Eastern part (Werner, 2004).

The Schauinsland mine was exploited from the 13th century to the 20<sup>th</sup> for Lead (galena), zinc (sphalerite) and native silver. The Schauinsland massif is made of Pre-Cambrian crystalline basement rocks with different compositions and a lot of mineral veins were mapped (Figure 6-27). The ore mineral can reach a thickness of several meters and present evidences of several brine circulation pulses (Figure 6-28). A high strain fault zone was studied in the mines with a well-developed core and damage zone containing abundant clay minerals deposit. This shear zones transects the whole set of exploited galleries (Figure 6-29) and has been given the name Schuhmachersche Ruschel by miners. Isotope dating ((Werner, 2002) and references therein) has shown multiple reactivation of this deformation zone, with a dominant activity phase during the Jurassic.

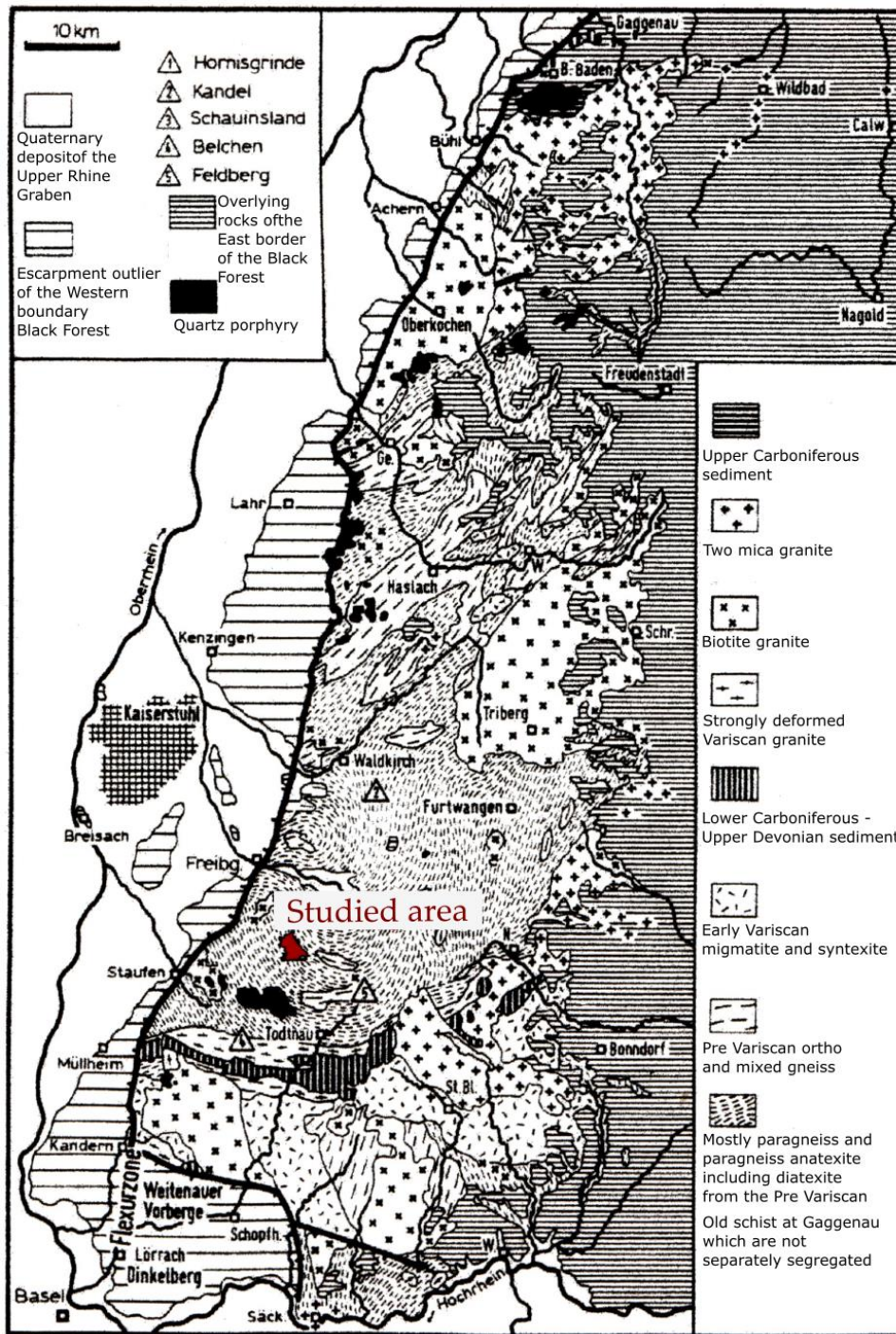


Figure 6-26. Geological map of the Black Forest. In red the location of the detailed geological map of the Schauinsland area, translated after Wittenbrink (1999)

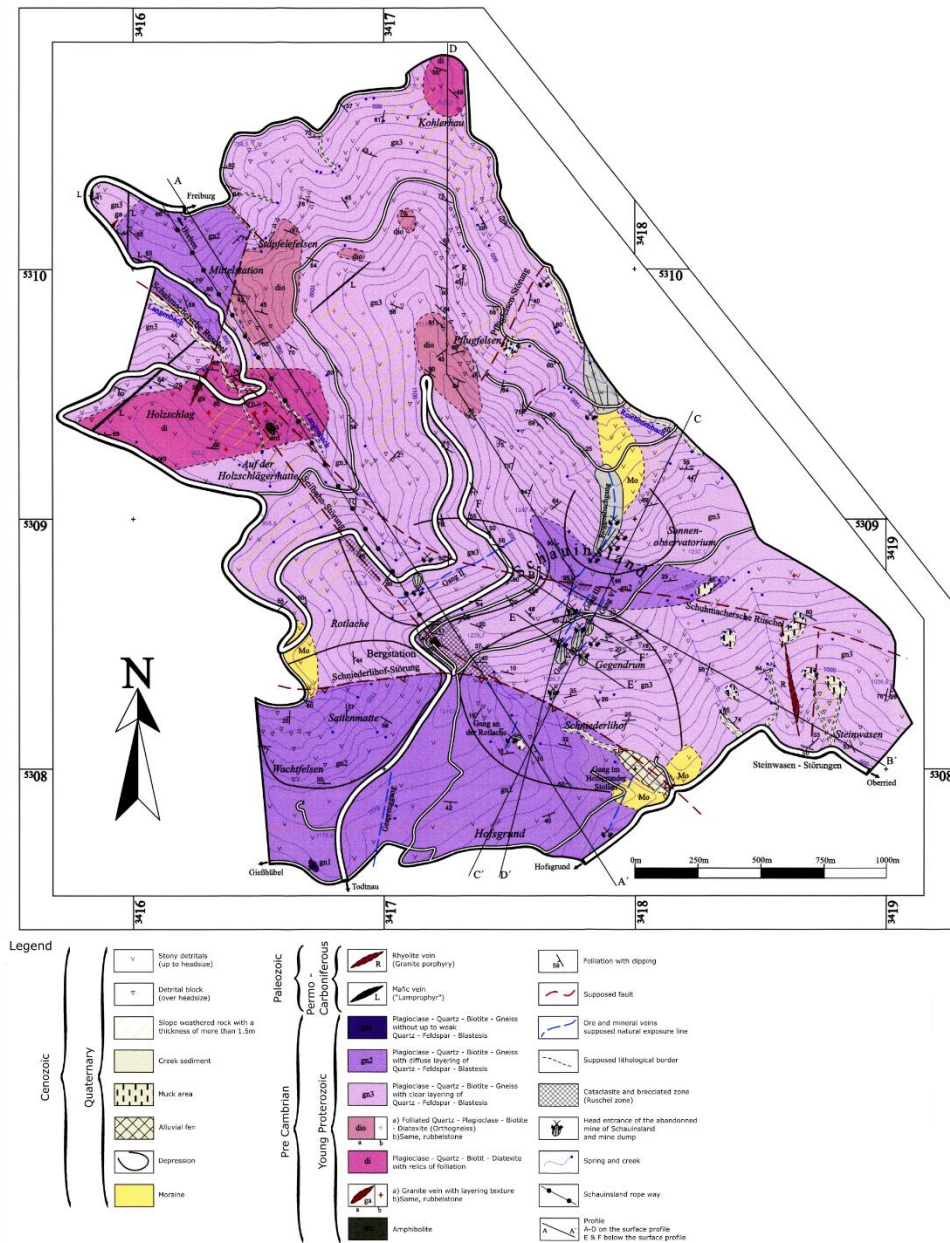


Figure 6-27. Geological map of Schauinsland mostly composed of pre-Cambrian gneissic rocks, the blue dotted lines correspond to the mineral veins, modified from Wittenbrink (1999).

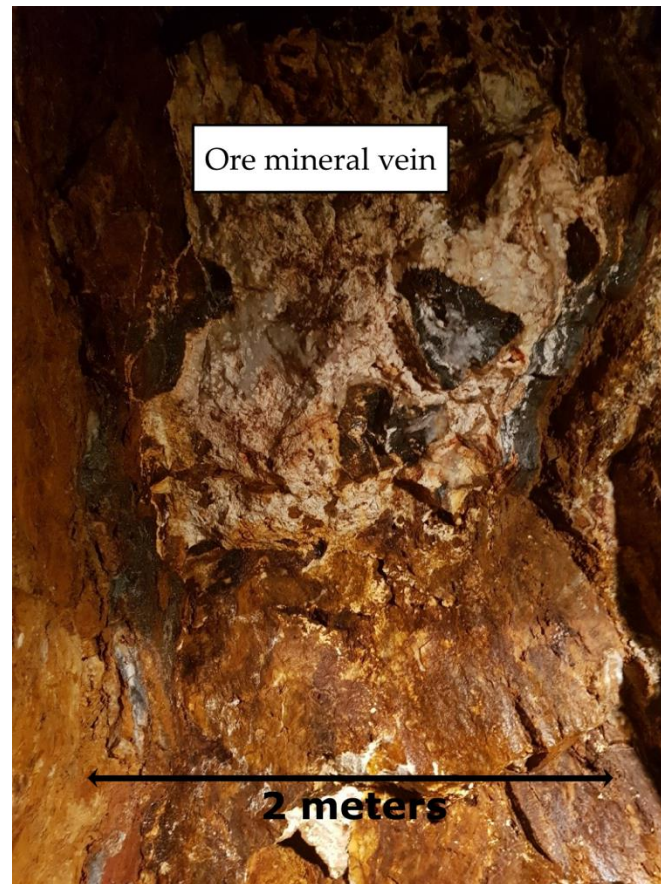


Figure 6-28. Ore mineral vein in Schauinsland showing evidence of brine circulation pulses

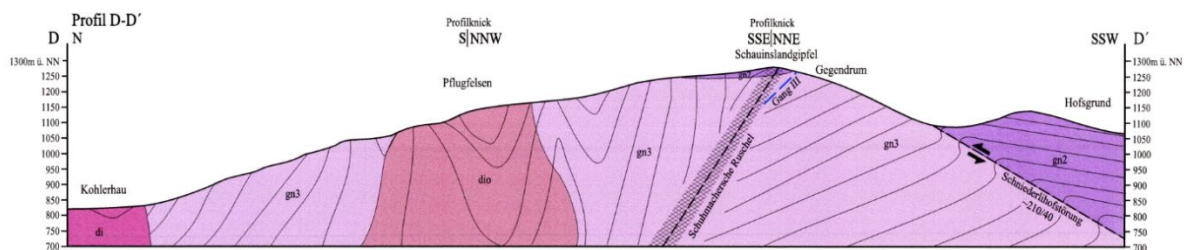


Figure 6-29. N-S cross-section of Schauinsland showing the Schumachersche Ruschel cross-cutting the Schauinsland massif, modified after Wittenbrink 1999).

A profile study was made along the gallery (Figure 6-30) where the highly sheared zone can be observed, the Schuhmachersche Ruschel (SR), presenting all the typical characteristics described by Choi et al. (2016) (Figure 6-31). At gallery entrance a pristine paragneiss and a vertical fault filled with baryte can be followed on the roof, following the gallery's orientation. The gallery was previously described by Werner (2002) where he documented the offset of a pre-existing high strain zone during a late phase of deformation responsible of ore mineral deposition (Figure 6-32). This chronology of polyphase deformation is confirmed by our observations. Evidences of clay smearing and ductile deformation features related to the SR

offset are ubiquitous. The offset of the SR which is syn-kinematic to ore veins formation reworks an already sheared clay rich fault core. This leads to spectacular, ductile driven, deformation features within the interference. The ore vein does not crosscut the SR zone and vanishes, it is only on the other side of the SR that the ore vein reappears.

Total XRD analysis was performed on the whole rock from the gouge revealing the presence of quartz (~30%), illite (~25%), paragonite (~10%), kaolinite (~10%), orthoclase (~8%), albite (~7%), apatite (~5%) and dolomite (~3%). The paragneiss is no longer recognizable and there are no mineral veins along the core and damage zone.

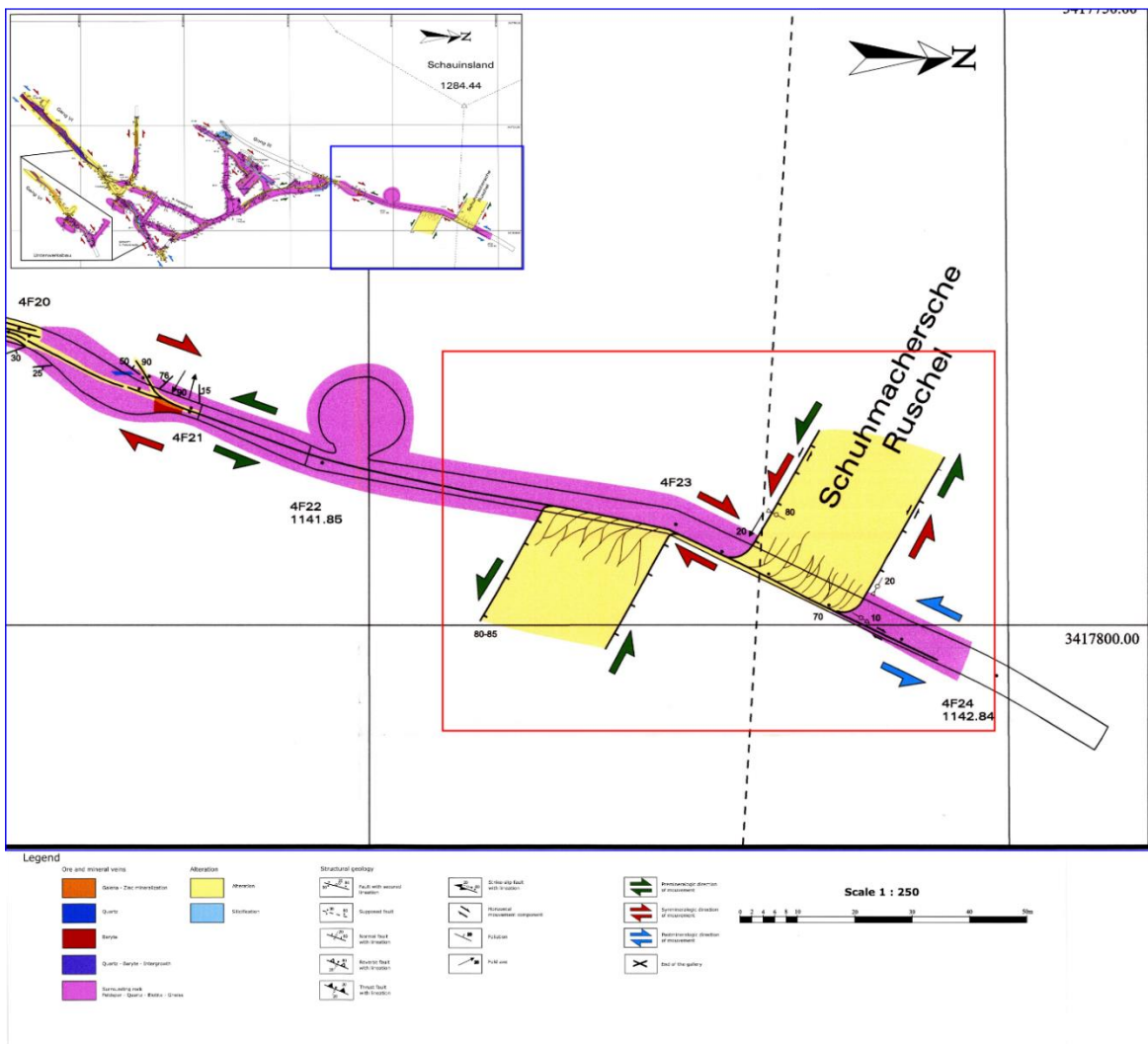


Figure 6-30. Geological map of the gallery, the studied area corresponds to the red rectangle where the beginning of the gallery is on the left, modified and translated after Wittenbrink (1999).



Figure 6-31. (a) Photogrammetric model of the portion of the gallery showing the fault gouge. (b) Photo of a branch of the fault gouge showing flows of hydrozincite.

The observation that ore mineral veins well developed in unaltered host rocks wedge out in map view when approaching inherited high strain zone is of primary concern when dealing with late brine circulations in a pre-structured reservoir. The situation is comparable to present day geothermal saline fluids circulations within fractured basements.

The development of ore veins in basement rocks imply a sudden release of accumulated elastic stress in a competent unit. In the case of Schauinsland, the paragneiss can accumulate elastic stress. Fluid overpressures combined to a critically loaded rocks induce rock fracturing by cross cutting the Mohr Coulomb failure envelope. Failure leads to void opening in a transtensive regime and formation of breccia (sometimes hydraulic breccia) can occur.

The same coeval stress field being applied to a highly pre-structured shear zone rich in clay minerals (the SR zone) induces a drastically different mechanical response. Shearing is accommodated by plasticity, related to the increasing amount of inherited clay minerals. Clay plasticity driven mechanisms are progressively replacing brittle behavior when entering the inherited SR deformation zone. The brittle behavior is replaced due to inherited clay minerals and elastic stress can no longer be accumulated. Brittle failure of the host rock becomes more and more difficult.

The onset of plasticity plays a crucial role in development of late fluid flow paths, hindering accumulation of elastic stresses. Under these mechanical conditions, vein opening by sudden rock failure becomes impossible and channeled brine circulation can be stopped as in Schauinsland or decreased and deviated as in Gabe Gottes.

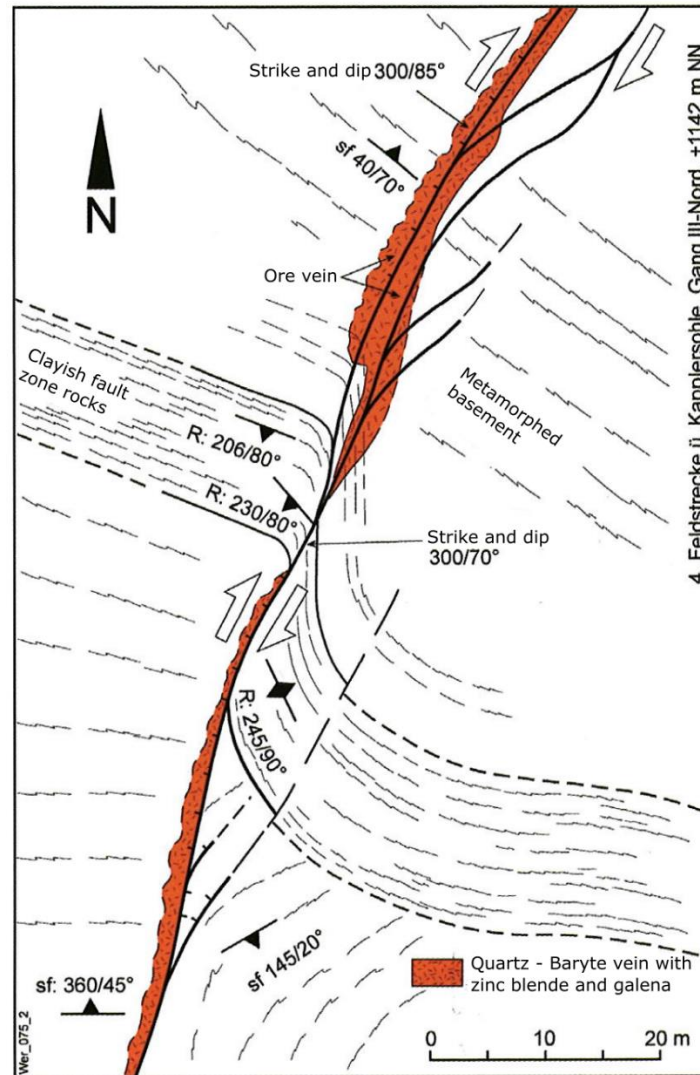


Figure 6-32. Scheme of the extinction of the mineral vein when encountering the highly strained shear zone (Werner, 2002).

### III.4. Conclusion

The shear zones were present before the deposit of mineral veins in the mines and play a role in their propagation. In Gabes Gottes mines, the presence of a pre-existing shear zone in the basement rock changed the direction of propagation of the mineral vein. The shear zone is used as a zone of weakness, the vein changes its direction according to the structure and uses natural planes of weaknesses inside the shear zone to crosscut it (Figure 6-33). In Schauinsland, the highly deformed shear zone has clay deposit inside which stops the propagation of mineral

veins. The basement rock can accumulate stress and when it breaks, create space for mineralization. However, the clay rich zone is hindering the accumulation of stress. In that way, clay is interpreted as a barrier which does not open to let the vein continue propagating. Such pre-existing structure must be identified for a better understanding of how fluids circulate inside a geothermal reservoir. More petrographical and geochemical studies will be made from various mines of the URG, focussing on the micro fabric of the rock to better understand the barrier behavior of the clay layers.

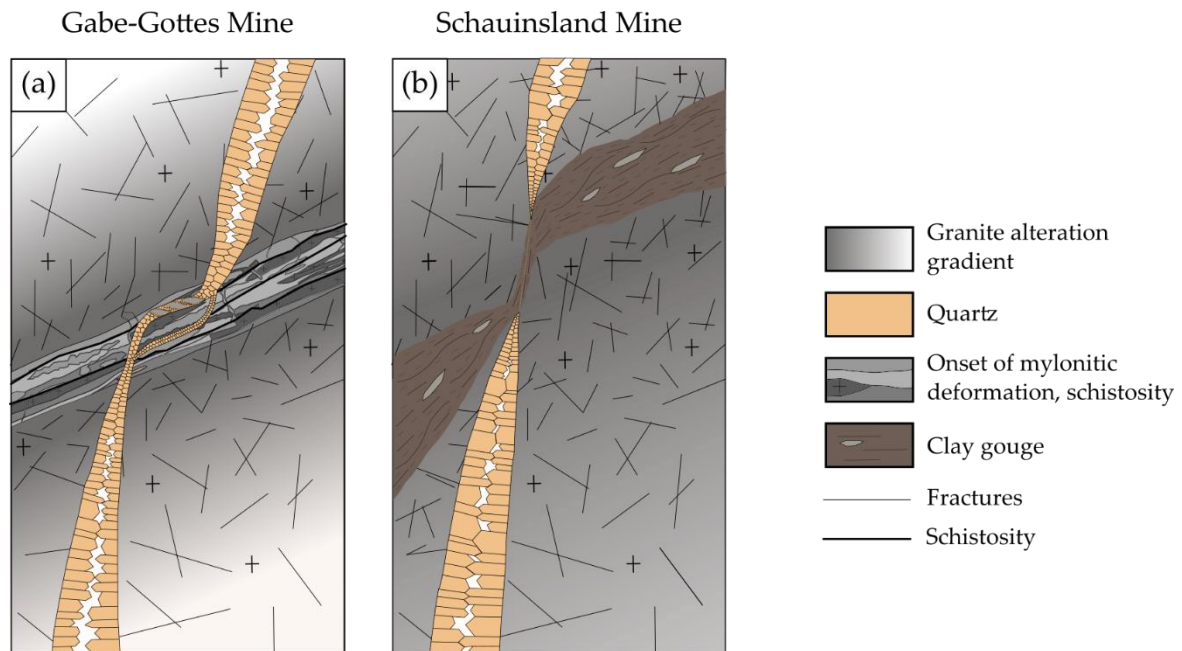


Figure 6-33. (a) Scheme of the interaction between the competent sheared zone and the vein observed in the Gabe-Gottes mine. (b) Scheme of the interaction between the sheared fault gouge and the vein observed in the Schauinsland mine.

#### IV. GENERAL CONCLUSION OF THIS CHAPTER 6

High strain zones have been described within several case studies. It has been shown that the structural heritage has an important control on the fluid circulation in a geothermal reservoir.

High strain fault zones should not always be considered as barriers even in the presence of a substantial amount of clay minerals. In the case of pinched sedimentary units high strain zones cross cutting sedimentary reservoirs act as drains and therefore enhance connectivity of the reservoir.

Depending on the total amount of accumulated strain, schistosity development can lead to a preferential channeling of brine flow and deviate fluid circulation within the reservoir. At the highest strain, the onset of creep deformation mechanisms in clay minerals prevents large

elastic stress accumulations and void opening. This in turn prevents flow circulation and inherited high strain zones become a barrier within the reservoir



# CHAPTER 7

## The Noble Hills granite and the Upper Rhine Graben shoulders crystalline basement: analogues of the Soultz-sous-Forêts geothermal reservoir

---

### I. INTRODUCTION

The NH range has been chosen as a far-field analogue for the Soultz-sous-Forêts (SsF) geothermal site because of its granitic (at least partially) nature, the trans-tensional context, the desertic conditions that allow very good observation because of the lack of vegetation, and the numerous deep canyons that crosscut the range and provide a 3D view of the structures. However, it is located far from the SsF site and thus in a different geological context. Thus, a close-field analogue was looked for in the Upper Rhine Graben (URG) to be exactly in a much more comparable structural and geodynamic context as at SsF. The shortage of good-quality outcrops made it necessary to look for mines and quarries on the shoulders of the graben to allow good observation. However, in that context, the basement is not made of granite but of gneiss, showing that it is difficult to find the ideal surface analogue and the necessity to study several of them, far-field and close-field when possible.

The fracture network in the URG, at outcrop scale and at the reservoir scale is the result of the Hercynian pre-structuration and of later reactivation processes (Illies, 1972; Schumacher, 2002). Inheritance may strongly influence the initiation of faults (Dezayes et al., 2021). Investigations made on the geothermal wells at SsF and Rittershoffen (RTH, 10km from SsF) have shown that the permeable structures intersected by the wells are open fractures related to the normal fault set formed during the rift activity. However, these structures need to be connected in order to let the fluid circulate. Based on indirect data, Edel et al. (2007) put in evidence an important strike-slip system, Variscan heritage, transversally oriented to the main normal fault system, which undergone several reactivations (Figure 7-1).

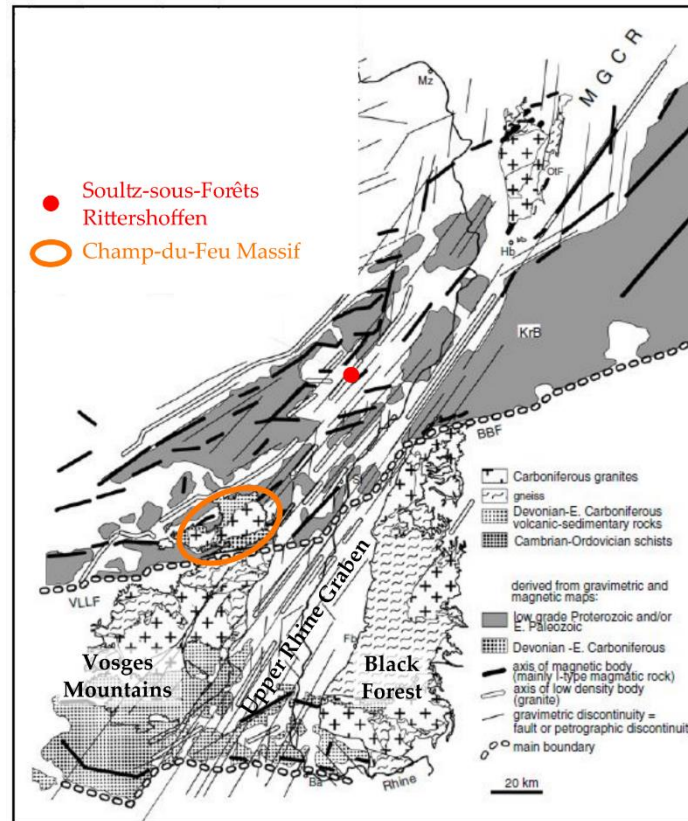


Figure 7-1. (a) Geological sketch map of the western Variscides. (b) Geological sketch map derived from the processed gravity maps illustrating the sinistral strike-slip motions along the NE-SW faults, modified after Edel et al. (2007).

An outcrop analogue study conducted in the Vosges Mountains by Dezayes et al. (2021) revealed the presence of some of these strike-slip zones identified by Edel et al. (2007), which show a low small amount of displacement (Dezayes et al., 2021). Recent fieldwork investigations in mines, as in Schauinsland in the Black Forest (Chapter 6), reveal the presence of highly strained shear zones rich in clay minerals which interfere with later fluid circulations

Here again, the reader is reminded that the outcrops investigated within the Vosges and Black Forest massifs do not necessarily represent the exact setting found in basement below the URG sedimentary cover. This is especially true regarding ore minerals deposits, which have only been documented at present in the shoulders of the URG massifs. Nevertheless, Variscan inherited high strain zones present in the mines predate the URG opening and it is therefore very likely that similar high strain zones are to be found within the graben basement itself.

The investigated analogy is to be found in the interferences between hypersaturated hot brines circulations (present saline brines at SsF and RTH, fluids responsible of ore mineral deposits) and a prestructured basement.

The hydrothermal alteration products and the composition of the geothermal brine circulating in the fracture/fault networks at SsF and RTH are similar, suggesting comparable pressure-temperature conditions (Glaas et al., 2021; Sanjuan et al., 2016) in these two sites. An interference study has also been conducted that has shown a connection between both sites (ÉSG personal communication). The initial idea of having two different reservoirs evolved towards a concept where SsF and RTH are a unique reservoir of several tens of square kilometers.

The aim of this chapter is (1) to compare the main findings from the far field and near field analogues to the SsF and RTH demonstrations sites and (2) give some insights about the influence of highly strained shear zones on fluid circulation.

## II. FRACTURE NETWORK CONNECTIVITY

The faults and fractures patterns play an important role in controlling the fluid circulation in crystalline rocks. Multiscale fracture organization studies are performed in order to establish hierarchical and mechanical relationships between fracture systems. They are based on the study of several orders of fault magnitude, which have been widely described in the literature in extensional context (Bertrand et al., 2015; Le Garzic et al., 2011; Morellato et al., 2003), and applied in transtensional context as the URG (Bertrand et al., 2018; Genter and Castaing, 1997). It consists of 4 order scales with specific fracture spacing (Le Garzic et al., 2011; Morellato et al., 2003):

- 1<sup>st</sup> order scale related to crustal faults longer than 100 km with 10-15 km spacing
- 2<sup>nd</sup> order scale refers to faults having a length between 20 and 30 km with 3-8 km spacing
- 3<sup>rd</sup> order scale refers to faults around 10 km length with 0.8-1.5 km spacing
- 4<sup>th</sup> order scale refers to faults under 1 km length with no defined spacing

The inherited faults were reactivated during the Tethyan rifting and the European Cenozoic Rift System (ECRIS) developed at the beginning of the Oligocene, opening the graben (Bertrand et al., 2018 and references therein). Through these tectonic events, the URG can be divided into first order blocks which can be divided into second and third order blocks with the respective fault orders (Bertrand et al., 2018) (Figure 7-2a). In the Vosges Mountains and the Champ-du-Feu massif (Figure 7-1), three order scale blocks have been highlighted: the N-S faults (border normal faults) and the ENE-SWS to E-W faults structured the graben following the 1<sup>st</sup> order scales blocks, poorly represented at regional scale (Edel et al., 2007), but predominating at outcrop scale (Dezayes et al., 2021). The N-S and NW-SE or NE-SW

(Hercynian fractures) structured the URG following the 2<sup>nd</sup> and 3<sup>rd</sup> order scales blocks (Bertrand, 2017).

Regarding the fracture densities at SsF geothermal site located north of the URG (Figure 7-1), the fracture density in the wells is around 1 frac/m (Dezayes et al., 2004), while at RTH, around 10 km away from SsF (Figure 7-1), the density of natural fracture ranges between 0.7 fracs/m to 1.78 fracs/m from the bottom of the well until the top of the granite (Vidal, 2017). In both geothermal sites (SsF and RTH), the fractures are grouped in clusters and control the reservoir permeability following the N-S direction (Baillieux, 2012). This N-S direction has been reactivated into normal movement due to the ECRIS, forms recharge drains and, promotes a large-scale vertical convective circulation system in the western part of the basin, and influences the organization (orientation and nature) of smaller structures (Bertrand, 2017; Dezayes and Lerouge, 2019b).

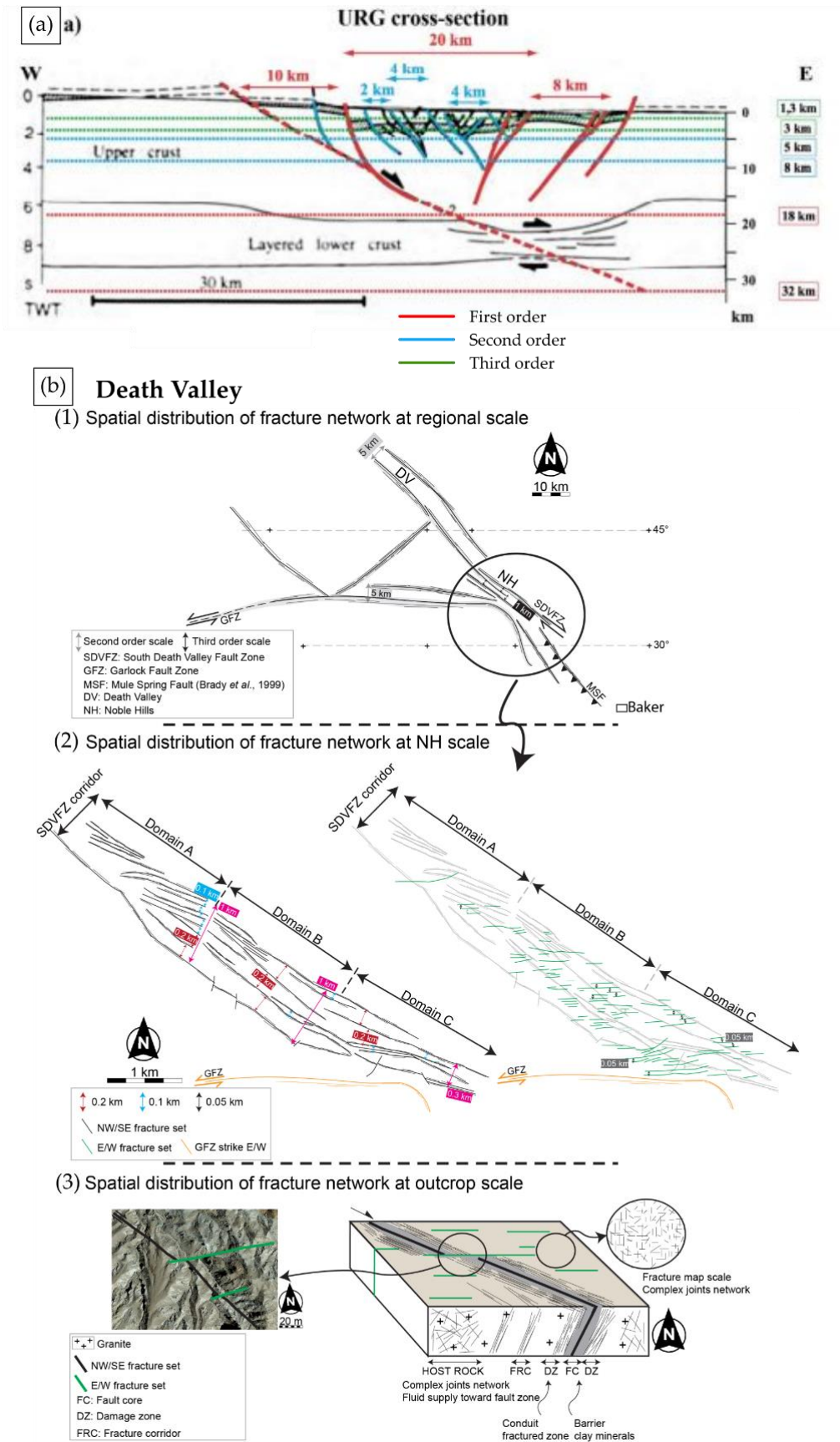


Figure 7-2. (a) Schematic large-scale W-E cross-section of the URG with interpretation of the fault orders from Bertrand et al. (2018). (b) Conceptual scheme presenting the spatial arrangement of the NH fracture network at (1) regional scale, (2) NH scale, (3) outcrop scale from Chabani et al. (2021).

The geometrical characteristics based on fault order magnitude were observed in the extensional regime and highlighted by Bertrand et al., 2015; Le Garzic et al., 2011; Morellato et al., 2003. Recently, Chabani et al. (2021) have used this approach to characterize the fracture organization in the NH range (see this co-author contribution in Appendix 1) within trans-tensional regime. They obtained the same geometrical characteristics as in extensional regime, and conclude that the second and third order scale spacing classification can be generalized to the trans-tensional regime (NH case study).

Indeed, the regional map shows that the geometry of NH is controlled by 2<sup>nd</sup> and 3<sup>rd</sup> orders faults following NW-SE and E-W trends (Figure 7-2b1). In addition, Chabani et al. (2021) highlighted at outcrop scale the fourth order scale faults ranging from 100 to 350m length and 100 to 200m spacing. This fourth order scale is available only in transtensional regime. Based on this fracture orders scales, a new spatial organization of the NH range has been proposed. Then, using the main dominant fracture orientations, the NH has been divided into three domains (Figure 7-2b2), each domain showing its own internal organization. One main deformation phase related to SDVFZ activity played a key role in the NH structuration. NW/SE trending fractures are found in the whole NH and dominates its geometry (Figure 7-2b2). The second main deformation episode consists in GFZ system trending E/W likely responsible for E/W fracturing episode and then controlled the NH geometry mostly in its internal part and the southeastern end (Chabani et al., 2021) (Figure 7-2b2).

Analyses at the outcrop scale confirmed the reproducibility and the consistency of all fracture sets defined at large scale (Chabani et al., 2021). Fractures parallel to SDVFZ and GFZ trend are represented as a complex network that can play a key role in the fracture connectivity (Figure 7-2b3). The fractures striking NW/SE (SDVFZ direction) affects the whole range, and represent the dominant structure in terms of length and density. They play a key role in the internal NH structuration. The fracture striking E-W, related to the GFZ direction, is the second main shear (sinistral) deformation episode controlling the NH geometry mainly in the southeastern part. Moreover, Chabani et al., (under review) highlighted fracture density ranges from 0.65 to 42.1 fracs/m at outcrop and NH scales, and from 8.4 to 31.8 fracs/m from field scanlines located in the central and southeastern domains. The fracture densities highlighted from NH range are in some cases equivalent and in other ones much higher than from the deepest boreholes of SsF and RTH geothermal sites. It seems to be related to bias in fractures sampling at depth because only imagery is available and direct observation is impossible. Most of the time, only the borehole logging data can help to quantify the fracturing and give an approximation of the fracture distribution variability in the reservoir. However, at SsF, the shallow EPS-1 borehole

(2220 m deep) was entirely cored and provided 800m of core in which about 3000 fractures were observed (Genter and Traineau, 1992), showing a fracture density up to 30 fracs/m (Ledéseret et al., 1993). Then, borehole logging data must be analyzed carefully and completed by analogue studies at different scales.

Deformation by fracturing occurred with a different intensity in the 3 domains of the NH (Figure 7-2b2) scale, which could influence the fluid circulation through the fracture network in those domains. A complex fracture network is highlighted at outcrop scale in the host rock which plays a key role in the fracture connectivity leading the fluid supply (Chabani et al., 2021). This fracture network is mainly filled with similar carbonates in the whole range, meaning that the same fluid has circulated through a well-connected fracture network.

In both sites, NH and URG, the fluid flow is mainly controlled by the major fractures composing the dominant fracture set in the areas. The multiscale analysis also put in evidence that structural blocks formed by faults of the 3<sup>rd</sup> and 4<sup>th</sup> order scale present minor fault zones and fracturing corridors that can modify the reservoir properties.

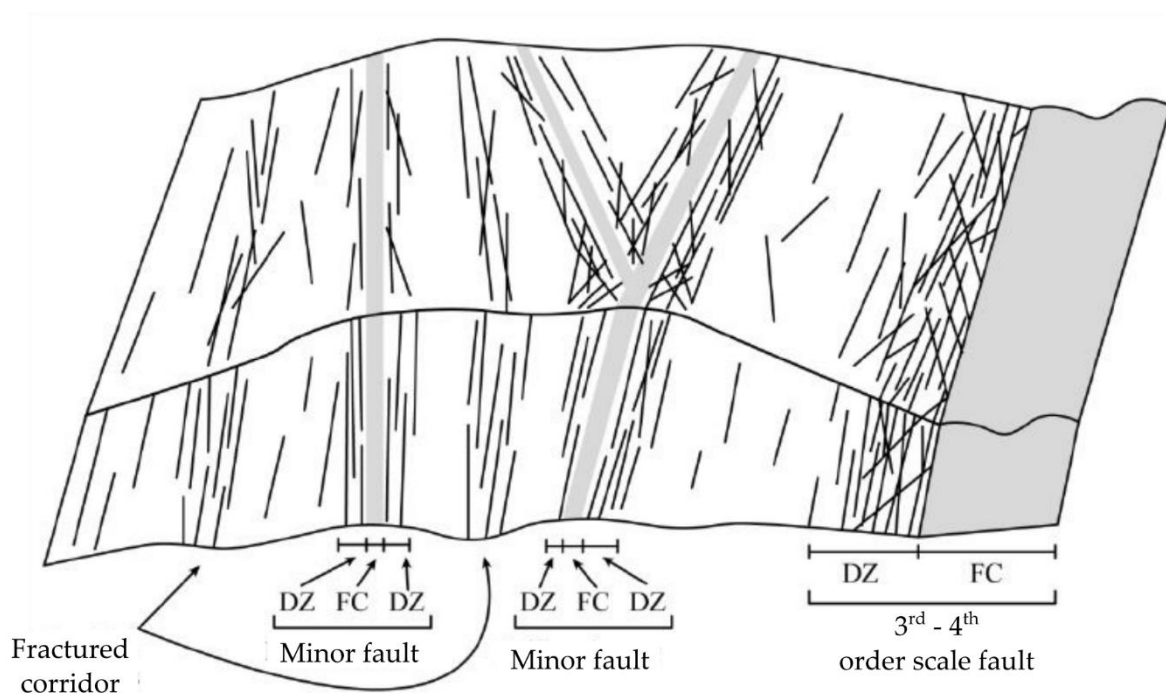


Figure 7-3. Scheme of a crystalline basement outcrop in the internal part of a 3<sup>rd</sup>-4<sup>th</sup> order structural block with the fault core (FC), the damage zone (DZ) and the intra-block fracturing corridor from Bertrand, 2017.

In addition, the hand-specimen and thin section scales also show the role of minor fractures for the conduction of fluids, as shown by the hydrothermal alteration of the wall-rocks related to fluid-rock interactions.

### III. ANALOGY IN TERMS OF HYDROTHERMAL ALTERATION BETWEEN THE UPPER RHINE GRABEN AND THE NOBLE HILLS RANGE

In SsF, as well as in RTH, and NH, the granite has a similar modal composition equivalent to a monzogranite with quartz, plagioclase (oligoclase), perthitic K-feldspar, biotite and few amphiboles in the case of the upper URG granite. URG and NH granites are both highly fractured and altered (Klee et al., 2021a, 2021b; Ledésert et al., 2010). The hydrothermal transformation of the granite begins with an early pervasive alteration having discrete effects but which occurred in the whole massif during the cooling of the pluton (Genter, 1989). It is representative of hydrothermal alteration in inactive flow regimes (Beaufort et al., 1990). In all granites, only biotite and plagioclase are partially affected. In the URG, the alteration products are chlorite, carbonates, epidote, corrensite and illite. Whereas no chlorite is observed in the NH (Klee et al., 2021a; Ledésert et al., 1999; Vidal et al., 2018). In both granites, carbonates are crystallized in microcracks or at the boundary between two grains without interaction with the surrounding rock. This pervasive alteration is called propylitic alteration (Traineau et al., 1991). In the URG and NH, this propylitic alteration is followed by a localized vein-related alteration organized along fractures in which fluids have circulated. In those zones, fluid-rock interactions are responsible for leaching and clay enrichment processes. giving the name of vein or argillic alteration (Genter, 1989; Klee et al., 2021a; Komninou and Yardley, 1997; Ledésert et al., 1999; Pauwels et al., 1993). It is responsible for secondary mineral crystallization as fracture infill and in the fracture walls (Genter, 1989). The vein alteration leads to the transformation of plagioclase and biotite of the whole rock into newly-formed minerals. In both granites, plagioclase can be completely altered (Genter, 1989; Klee et al., 2021a). The alteration products in common are (1) illite, (2) Illite-smectite mixed-layer and (3) calcite developing as patches, (4) opaque minerals and (5) quartz (Genter, 1989; Klee et al., 2021a; Traineau et al., 1991). However, the NH granite shows also an important amount of kaolinite, as a product of plagioclase transformation (Klee et al., 2021a, 2021b). In the SsF granite, instead of kaolinite, which was found in a single sample (Genter, 1989; Pauwels et al., 1992), tosudite was identified (Ledésert et al., 1999). Tosudite is considered as a geochemical analogue of kaolinite, but its occurrence can be explained by the amount of lithium present in the fluid at SsF (Ledésert et al., 1999). Note that Dezayes et al. (2021) identified the presence of kaolinite in an outcrop analogue in the Vosges Mountains which has been interpreted here as a product of weathering due to the exposure of the granite, which is not the case in the NH (Klee et al., 2021a). Biotite can be completely altered and transformed into illite in both granites, even if the SsF biotite was first at least partly chloritized. Moreover, secondary oxides crystallized along the clivage

planes (Genter, 1989; Klee et al., 2021a). K-feldspars are fractured but remain fresh in both granites (Bartier et al., 2008; Klee et al., 2021a, 2021b; Ledésert et al., 1999). They can be partially altered because the perthites or mineral inclusions transformed into illite (Genter, 1989; Klee et al., 2021b). Gresens method performed on the SsF granite and on the NH granite showed that major elements transfers occurred during the alteration of the granite (Genter, 1989; Jacquemont, 2002; Klee et al., 2021b). In both URG and NH granite, the K-feldspars being not altered or only slightly in some cases, the fluid enriched the system in potassium, which was fixed in the plagioclases during illitization processes (Jacquemont, 2002; Klee et al., 2021a, 2021b). In the URG, the source of K is supposed to be the sedimentary cover in which sylvite evaporitic layers are encountered and through which the meteoric fluid circulated before reaching the granitic reservoir. In the NH, the source of K is still unknown. MgO and FeO are released by the dissolution of ferro-magnesian minerals as biotite. MgO is fixed in both granites by carbonate precipitation and FeO by the precipitation of hematite and ankerite (Jacquemont, 2002; Klee et al., 2021a, 2021b). Carbonates being present in a high amount in the NH, the Ca source is considered as being the dolomitic Proterozoic series which was intruded by the granitic pluton and deformed by the SDVFZ activity in addition to the product of oligoclase alteration. This input of K and Ca show that both systems (URG and NH) are open. Even if a common secondary mineral assemblage in both granites was identified, the URG presents successive argillic alteration stages either in the central graben or in the shoulders (Dezayes et al., 2021; Genter, 1989; Vidal et al., 2018). This indicates different physico-chemical conditions. On the opposite, only one episode has been identified in the NH. The strong illitization of the URG granite, or kaolinization and illitization of the NH granite due to the vein alteration can overprint and even obliterate the early propylitic alteration when approaching the fracture zones (Klee et al., 2021a, 2021b; Vidal et al., 2018). A summary of the primary mineral composition, as well as the secondary minerals precipitated during the propylitic and the argillic alterations is shown in Table 7-1.

Table 7-1. Primary minerals, secondary minerals (from propylitic and argillic alterations) and fracture infills for both Upper Rhine Graben and Noble Hills range. Bold writing indicates the differences between SsF and NH.

	Upper Rhine Graben granite	Noble Hills granite
Primary minerals composition	Quartz, perthitic K-feldspar, Plagioclase (oligoclase), Biotite, <b>few Amphiboles</b>	Quartz, perthitic K-feldspar, Plagioclase (oligoclase), Biotite
Propylitic alteration secondary minerals	Illite, Corrensite, Epidote, Carbonates, <b>Chlorite</b>	Illite, Corrensite, Epidote, Carbonates
Argillic alteration secondary minerals	Illite, Illite/Smectite, Carbonates, Oxides, Quartz, <b>Tosudite</b>	Illite, Illite/Smectite, Carbonates, Oxides <b>Kaolinite</b>

Fluid circulating through the fractures can precipitate secondary minerals which clog the fracture. In the SsF-RTH reservoir, fracture fillings are heterogeneous, and polyphased, dominantly represented by quartz, barite, illite, carbonates, and iron oxides as hematite (Genter et al., 1995; Genter and Traineau, 1996). The fracture fillings present the same mineralogy in the whole granite. However, the mineral proportions vary according to the location in the granite body (Traineau et al., 1991; Vidal, 2017). Hematite is mainly found in joints and tension fractures at the top granite because of its weathering when exposed at surface. Illite is mainly found into fractures affected by shearing. Carbonates are mainly found in open fractures and the number of fractures filled by carbonates increases with depth. Quartz is present in the whole granite in open and sheared fractures (Vidal, 2017). It was found that secondary quartz precipitated in the fault core in its pseudo-hexagonal form, named geodic, drusy, or hydrothermal quartz (Glaas, 2021). Structural and mineralogical analysis of the secondary quartz in the vein revealed the successive crystallization of at least 7 generations of quartz, revealing a pulsed fluid flow system, probably due to several stress reactivations (Smith et al., 1998). The relative chronology of fracture fillings was determined from outcrop studies and consists into two major successive stages of filling: (1) a shearing/cataclase phase associated quartz and illite, followed by (2) a later precipitation of carbonates in tension fractures (Dezayes et al., 2013). Likewise, similar infills were observed in the NH granite also indicating a multi-stage paleo-fluid circulation, described in Klee et al. (2021b). Quartz veins and veinlets are rare but considered as the primary event. It is followed by the crystallization of illite in veinlets. However, illite is also present into a high amount in gouges identified in the area. Then come carbonates which constitute the major infills of fractures in the area and are considered as related to the SDVFZ activity (Klee et al., 2021b) and then oxides. Lately, barite precipitated as large pluri-decimetric veins mainly concentrated in the rear part of the range in the south-east

filling E-W fractures related to the activity of the GFZ. Small barite crystals are also present in the brecciated NH\_31 vein in the north-central part of the granite body (Klee et al., 2021b). Barite crystallization corresponds to the latest stage of fluid circulation. A summary of the nature of the fracture infills is given in Table 7-1.

In both URG and NH granites, alteration processes and secondary minerals are similar.

#### IV. ANALOGY IN TERMS OF FRACTURE ZONE PROPERTIES AT LOW TO MODERATE STRAIN

The fault and fracture networks of crystalline basement rocks are the main fluid flow conduits at depth in basins. All the wells in SsF or RTH exhibit at least one major permeable fracture with a natural fracture network acting as a natural heat exchanger. Indeed, most of the fractures are sealed. Thus, the hydraulic connection between the wells on each site is crucial to get an efficient geothermal heat exchanger (Hébert et al., 2010). The permeability can be increased by means of stimulation strategies. This permeability increase is also believed to be governed by shearing mechanism that occurred on pre-existing fracture planes and few by opening-mode fracturing (Genter et al., 2010). Indeed, recent induced seismic activity in the Rhine graben occurred during the stimulation of a geothermal borehole and has been related to strike-slip movements (EOST and CNRS, 2021).

The reservoir productivity at SsF and RTH is mainly taken up by a few opened fractures showing incipient geodic minerals precipitates, essentially quartz (Vidal and Genter, 2018). Vidal and Genter, 2018 have also shown that permeable fractures were intersected by the wells through the hydrothermally altered granite. Highly fractured and hydrothermally altered granitic basement is a higher potential reservoir than the other compartments (Vidal and Genter, 2018) (Figure 7-4).

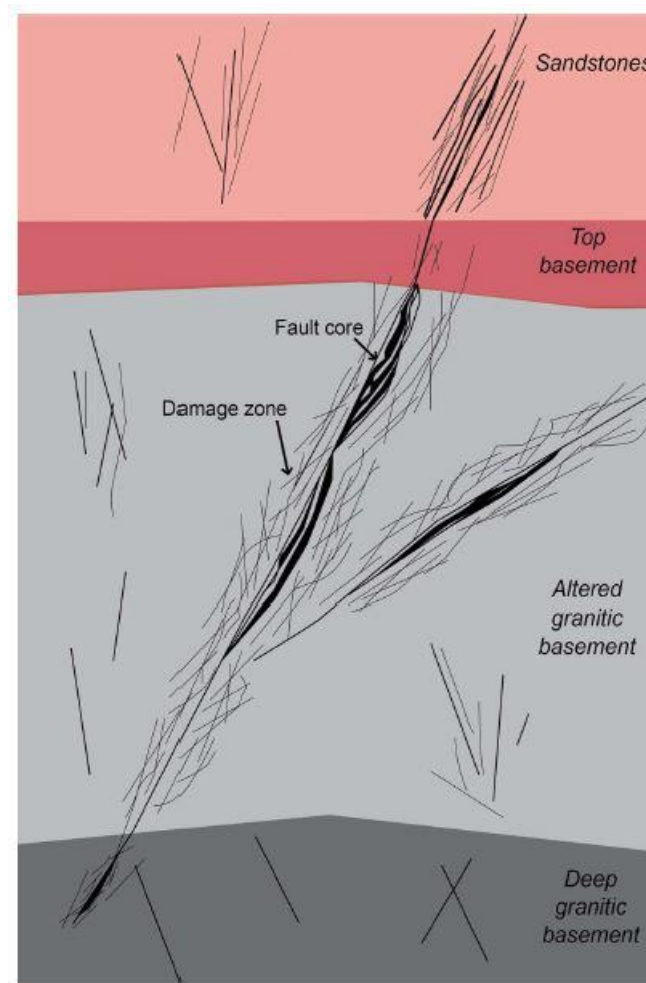


Figure 7-4. Fault zone architecture in sandstone, weathered top basement, hydrothermally altered granite and deep granite identified at Soultz-sous-Forêts in Vidal and Genter, 2018. FZ–Fault Zone, FC–Fault Core, DZ–Damage Zone

However, Glaas et al. (2021) have shown that, on the new geothermal site at Illkirch, moderately altered granite is more permeable than the intensely altered granite, because the latter corresponds to a zone sealed by a high amount of secondary minerals. The SsF boreholes intersect several thousands of fractures and only some of them are naturally permeable (Ledésert et al., 2010). They are organized in clusters at SsF, with a fault core filled most of the time by quartz or by a brecciated granite from successive stages of brittle deformation (Genter et al., 2000, 1995; Ledésert et al., 1999). This hydrothermal circulation occurs at several fracture scales (Vidal, 2017). Fractures were classified in different levels by Dezayes et al. (2010b) according to their relative scale and importance as fluid flow paths:

- Level 1 corresponds to naturally permeable major fracture zones located in the upper cluster in the altered porphyritic granite.
- Level 2 fracture zones are characterized by at least one thick fracture with a significant hydrothermal halo and showed a flow indication higher than 20% of fluid loss during

stimulation. They are present in the 2<sup>nd</sup> and 3<sup>rd</sup> cluster located respectively within the fractured and altered granite zone containing a high amount of clay and hydrothermal minerals and at the interface of two granite units.

- Level 3 fracture zones are found all along the wells and have a poorly developed alteration halo, as well as a fluid loss lower than 20% during stimulation.

However, this hydraulic connection can be hindered by the precipitation of secondary hydrothermal minerals such as illite, calcite or quartz.

RTH wells were drilled and investigated based on the knowledge from SsF. There is no further gain drilling at great depth: productivity is higher at shallower levels, the flow rate is two times higher and the GRT-2 trajectory is inclined in order to follow the damage zone of the Rittershoffen fault (Vidal and Genter, 2018). At RTH, GRT-1 well was subjected to thermal, chemical and hydraulic stimulations, even if it intersects one big fracture controlling 70% of the flow rate (Vidal et al., 2016; Vidal and Genter, 2018). Indeed, the nearly vertical GRT-1 well intersects the fracture network nearly connected to the fault zone only once. GRT-2 revealed a naturally good connection between the well and the fracture network with a productivity index of 4 L/s/bar (Baujard et al., 2017). The inclined trajectory of GRT-2 well, inside the fault zone, probably intersects several times the fracture network connected to the fault zone, enhancing the productivity (Baujard et al., 2017; Vidal, 2017). Thus, no stimulation was required, giving rise to the new hydrothermal concept, taking advantage of the naturally permeable and fractured reservoir at the top of the basement (Glaas, 2021; Vidal and Genter, 2018). Four major permeable fracture zones were identified in this well characterized as combined conduit-barrier fracture zones from the conceptual model of Caine et al. (1996). They act first as short-live conduit that then clogged to form a barrier to fluid flow (Vidal et al., 2017).

Glaas et al. (2019) mentioned that in a geothermal system without intense shear deformation (opening mode), fractures filled by different mineralizations are considered as paleo-permeable zones, which allow the fluid to circulate at present only on each side of the sealed fracture. Indeed, when fractures are completely sealed, only the open fractures present in the damage zone can act as fluid pathways (Figure 7-5). Glaas et al. (2019) also argue that in the case of an open fracture, the fluid is mainly channeled in the core fault and partially in the surrounding host rock.

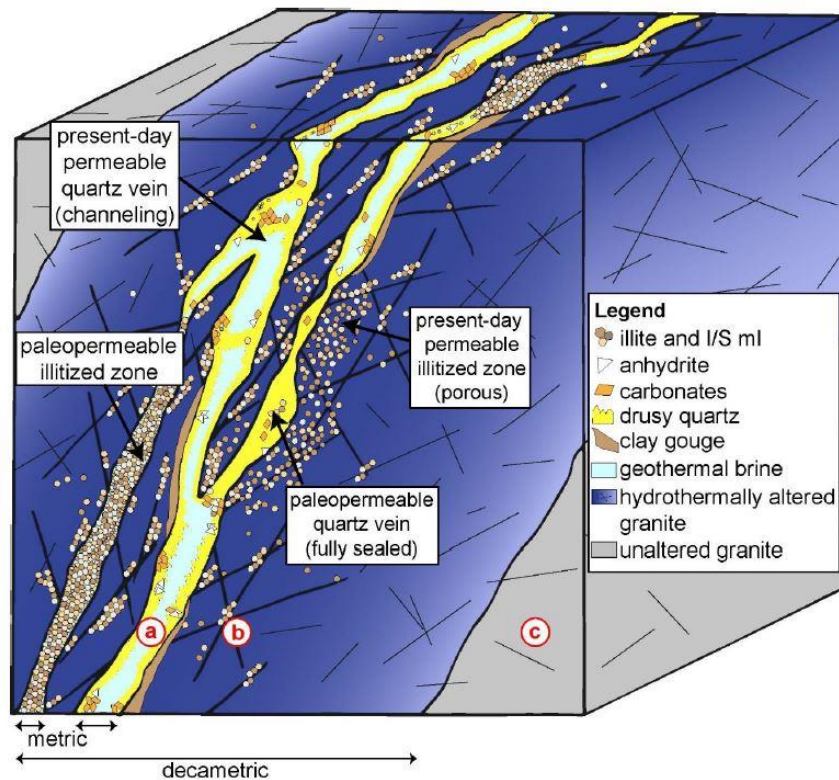


Figure 7-5. Block diagram from Glaas et al. (2019) representing the fluid circulation in a complex system of fracture zones. Three zones are distinguished: (a) the fault core, which can be a pathway for fluid if illite and quartz veins do not totally seal the zone, (b) the damage zone, which can be sealed or opened with small-scale fractures that act as fluid pathways, and (c) the unaltered granite, which generally shows very low matrix and fracture permeability.

At SsF and RTH sites, hydrothermal alteration grades in the granite are well known from core and cutting observation (Figure 7-6a) (Glaas, 2021; Ledésert et al., 1999; Meller and Kohl, 2014; Traineau et al., 1991; Vidal et al., 2018). There are six of these granite hydrothermal alteration grades, which are detailed by Glaas, 2021 and Vidal, 2017. The hydrothermal alteration increases when approaching fault cores.

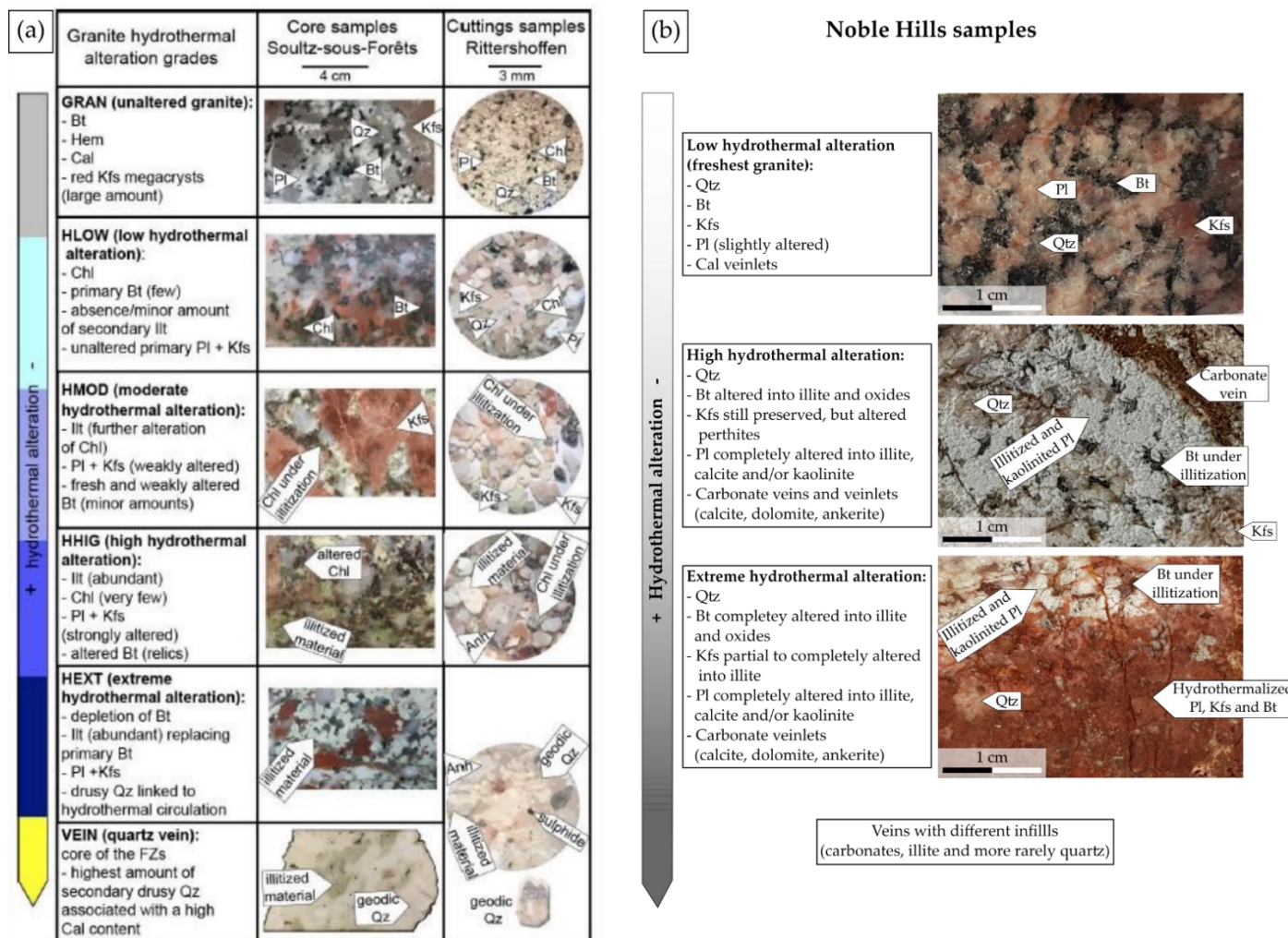


Figure 7-6. (a) Examples of mineralogical assemblages of the granitic basement observed in SsF cores (middle) and in RTH cuttings (right); these assemblages define the different hydrothermal alteration grades (left). GRAN: unaltered granite; HLOW: low hydrothermal alteration; HMOD: moderate hydrothermal alteration; HHIG: high hydrothermal alteration; HEXT: extreme hydrothermal alteration; VEIN: secondary drusy quartz vein from Glaas et al. (2019). (b) Examples of mineralogical assemblages of the granitic basement observed in the NH (right) defining different hydrothermal alteration grades (left).

An equivalent gradation, with 3 grades, is proposed for the NH granite (Figure 7-6b). The first grade is equivalent to the transition HLOW and HMOD (Figure 7-6). Indeed, as described by Klee et al. (2021a), the freshest granite found in the NH shows evidences of propylitic alteration. Small amounts of illite are found to replace chlorite. The second grade is equivalent to the HHIG grade (Figure 7-6), with abundant illite and kaolinite as a result of biotite and plagioclase complete alteration. Usually K-feldspar is unaltered in both facies. The last grade is equivalent to the HEXT (Figure 7-6), with a complete dissolution of all of the primary minerals except quartz. At this grade, the NH granite can even lose its magmatic texture due to a combination of incipient deformation and intense crystallization of clay minerals replacing primary minerals. Thus, approaching fracture zones in both sites, the argillic alteration overprints- completely the propylitic alteration.

Two samples, one from borehole EPS1 at SsF and one from the NH (NH\_31, (Klee et al., 2021b)), can be directly compared in terms of alteration gradient (Figure 7-7). The SsF core (Figure 7-7a) has been intensively investigated by Vidal and Genter (2018) and originates from a major permeable fracture zone. It shows a prominent alteration gradient decreasing from the quartz vein. Note that besides the vein opening, only a fine layer of cataclastic granite is observed. Away from the vein, the rock initial magmatic texture remains undisturbed. At the URG scale, major permeable fracture zones are around 10-40 m thick, consisting into multiple permeable drains that are around 10 cm thick Vidal and Genter (2018).

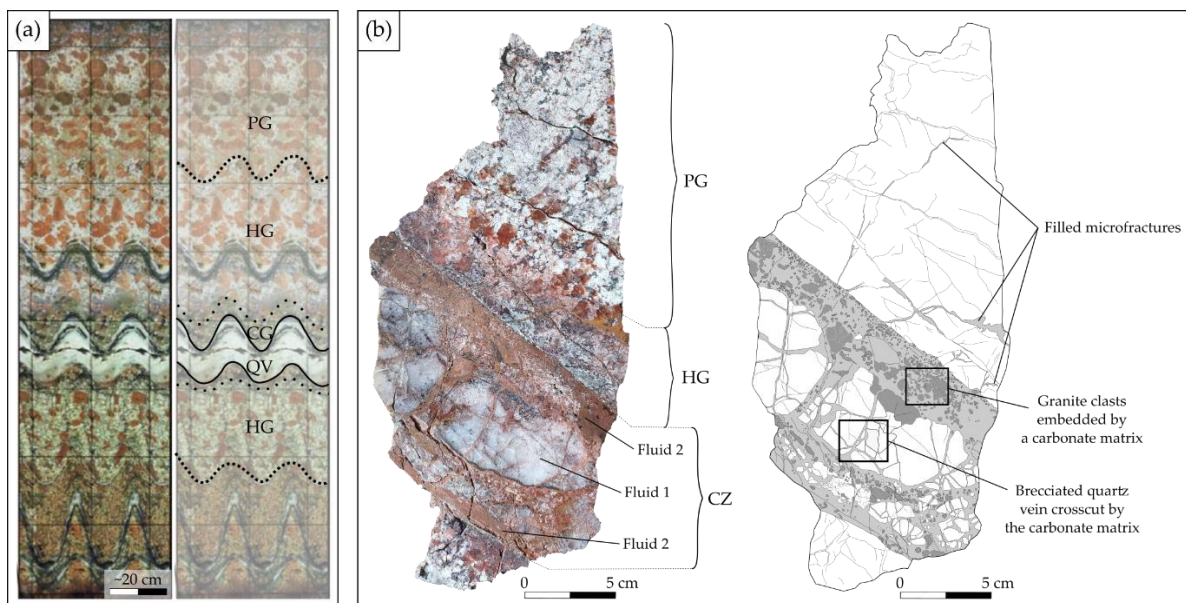


Figure 7-7. (a) Scan of a core (laid flat and doubled) of a major permeable fracture zone from EPS-1 well at SsF with the original scan and the zones characterizing the core (modified after Vidal and Genter (2018)). (b) Photo and respective digitization of the sample NH\_31 showing the different zones characterizing the

*sample. QV-Quartz vein, CG-Cataclased granite, HG-Hydrothermalized granite, PG-Porphyritic granite, CZ-Cataclastic Zone.*

A deformation gradient has been described in the NH by Klee et al. (2021b). Thus, in the area, low to moderate amount of strain is observed as in the sample presented in Figure 7-7b. Compared to SsF, this sample shows a fracture zone reactivated by shearing presenting a brecciated quartz vein crosscut by a carbonate material precipitated from a younger fluid circulation that occurred during the fracture reactivation and increased the fluid-rock interactions (Klee et al., 2021b). In that case, the deformation promoted the fluid circulation which was mostly concentrated in the fault core. Even if the amount of strain is slightly higher in the NH sample, both fracture zones (open and sheared) present similar characteristics in terms of alteration.

At SsF and RTH, despite the high porosity values in the damage zone, well tests revealed that a majority of the flow entered the rock mass only at discrete flow points corresponding to main open fractures observed on acoustic logs (Evans, 2005). EPS-1 core samples investigations also revealed that fault cores act as permeable drains and present a high density of fractures (Genter et al., 1995). The highest porosity in the fault zone is around 25%, found in the damage zone, due to the dissolution of primary minerals along fractures creating a secondary porosity (Ledésert et al., 2010, 1999). Plagioclase crystals being interconnected in 3D, they are considered as the main path for the fluid away from fracture planes as they get easily dissolved and porous, so fluids can circulate through them pervasively (Ledésert et al., 2010; Sardini et al., 1997). Apart from this fluid circulation possibility, microfracturing remains the main path for flow. This confirms the model of Caine et al. (1996) indicating that mineral precipitation yields fault cores with lower porosity and permeability. However, Géraud et al. (2005) and Ledésert et al. (2010) have shown that a fault core can present a low permeability, but can be highly fractured and porous.

As in SsF, it has been shown that in the NH granite, at large scale, porosity is also increasing towards the fracture zones due to the argillic hydrothermal alteration as a result of fluid circulation through the fracture network. The macrofracture and microfracture density is decreasing with distance to the fault core, linked to the decay of stress away from a fracture zone (Mitchell and Faulkner, 2012). Along the SsF and RTH wells and in the NH, closer to fracture zones, the fracture density increase is associated to the increase of the alteration intensity. However, the NH analogue study showed that this relation is not always applicable (Klee et al., 2021b). Indeed, Klee et al. (2021b) has shown that even if a granite is highly

brecciated with the presence of carbonates indicating fluid circulation, the alteration degree is very low. Likewise, samples, as that presented in Figure 7-7b, show a clear alteration gradient increasing towards the brecciated fault core, whereas no fracturing gradient was identified. The authors also showed an alteration gradient, as well as a fracturing gradient, both increasing towards a carbonate dominated mylonitized fault core.

Ledésert et al. (2009) have shown a relationship between fracture zones, flow zones and calcite content. In addition, Hébert et al. (2010) showed that the relationship between the fluid flow intensity and calcite content for fracture zones of GPK-3 and GPK-4 (a high fluid flow for a high calcite content) is opposed to that in GPK-2 (a high fluid flow for a low calcite content).

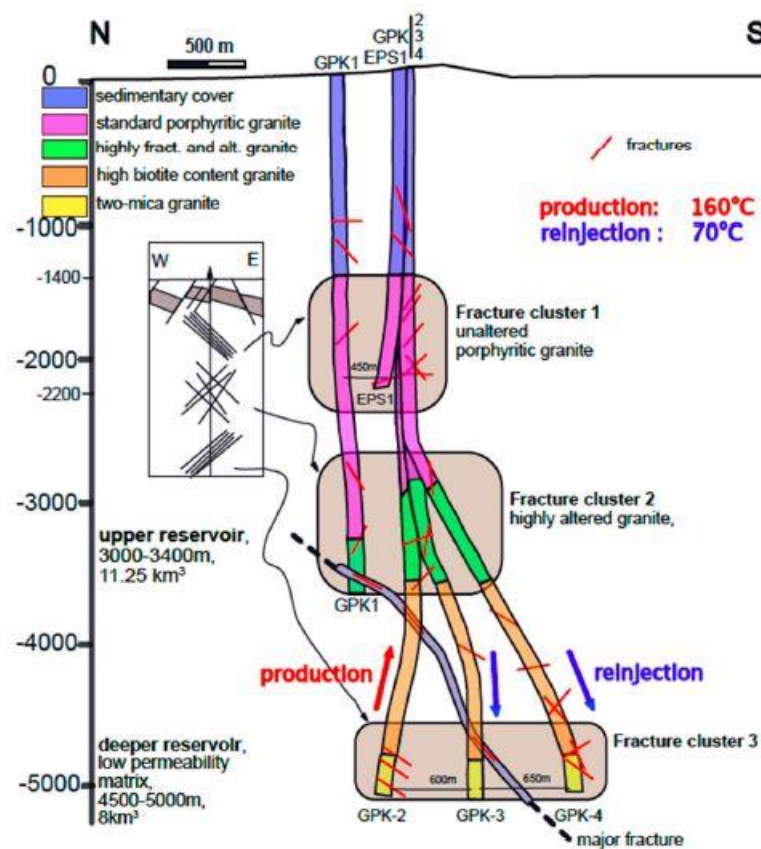


Figure 7-8. Cross-section of the Soultz-sous-Forêts geothermal system showing the different boreholes (EPS1, GPK1, GPK2, GPK3 and GPK4) from Ledésert and Hébert (2020)

This suggests that the fracture zones intersected by the wells are different between GPK-2 and both GPK-3 and GPK-4, and also that the fracture connectivity may be different (Hébert et al., 2010). Thus, these authors characterized GPK-2 by a structured network of medium-scale fractures not completely hydraulically connected, whereas GPK-3 and GPK-4 are characterized by a discrete fracture zone where the fluid is concentrated. Indeed, in 2005, production tests were performed showing an injection rate of 15L/s in GPK3 and a discrepancy between GPK2

and GPK4 showing production rates of 13 L/s and 2L/s respectively. The highest calcite content measured in the granite chips from each well was of 6.7%, 13.5% and 17.8% respectively (Ledésert et al., 2009). Thus, hydraulic and chemical stimulations were done to improve the hydraulic connectivity between the wells (Genter et al., 2010; Hébert et al., 2010). As described by Ledésert and Hébert (2012), calcite may represent a threat to the reservoir when the fracture connectivity is low while it does not impair the permeability when the fracture connectivity is high. Ledésert et al. (2009) also showed that stimulations, mainly chemical, are more efficient where high calcite contents occur. Thus, high calcite content reduces the ability of fracture network to conduct the fluid due to their sealing. However, calcite can be dissolved which enhances the hydraulic connectivity and the permeability. In the NH, a good fracture connectivity is suggested in the complex fracture network described by Chabani et al. (under review) (Figure 7-2b). Likewise, a good hydraulic connectivity is suggested from the predominance of carbonate fracture infills through the majority of the fracture network (Klee et al., 2021b). Thanks to the studies performed on SsF granitic reservoirs, it can be suggested that the fractures filled by carbonates in the NH could represent paleo-permeable fractures which could be stimulated if the reservoir was at depth.

In addition, illite can be considered as a potential indicator of fluid circulation and thus of reservoir permeability (Vidal et al., 2018). Indeed, a strong illitization indicates an intense paleo-circulation, which is observed in the vicinity of fracture zones in the SsF reservoir. Likewise, kaolinite, related the argillic alteration in the NH granite, shows its amount increasing towards fracture zones. This shows that in both sites, the fracture network controls the fluid circulation. In addition to precipitating mainly in the surrounding damage zone, by replacement of the primary minerals, clay minerals can also precipitate in the fault core, associated or not to deformation, and seal it (Figure 7-6).

## V. INFLUENCE OF HIGHLY SHEARED ZONES AND INHERITED STRUCTURES ON FLUID CIRCULATION

Several authors have shown that the URG tectonics has been controlled by the structural heritage of the Hercynian basement (Bertrand et al., 2018; Illies, 1972; Schumacher, 2002). Cores collected in the SsF granite show multiple brittle deformation stages from the simple fracture without any infill to the protomylonite, passing through the breccia (Genter, 1989). The main permeable fractures encountered in the SsF reservoir consist in open fractures which borders are cataclastic/brecciated, which reflect an extension regime. However, evidences of

shearing were also identified in the SsF boreholes as shown on the core from EPS-1 in Figure 7-9a. This core exhibits intense shearing accommodated along a foliated and anastomosed mylonitic fault zone surrounded by a highly hydrothermalized granite.

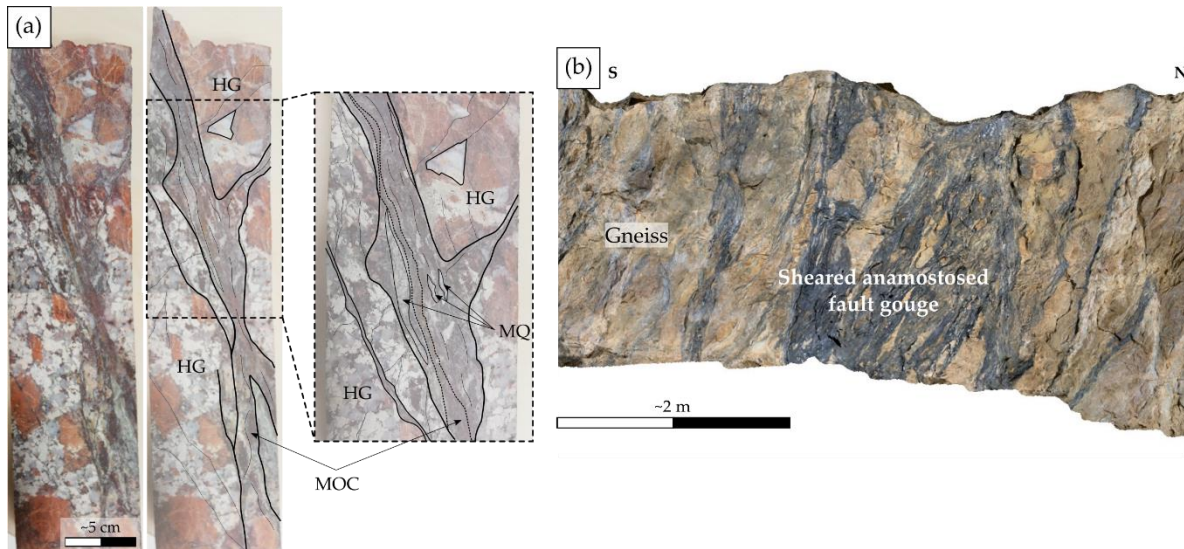


Figure 7-9. (a) Photographs of a longitudinal core section of a sheared and sealed fracture from EPS-1 well at SsF showing the different zonation characterizing the core. HG-Hydrothermalized granite; MQ-Mylonitic quartz as relicts; MOC-Mylonitic oxides and clays. (b) Photograph of an outcrop in the NH showing a high strain zone characterized as a fault gouge. (c) Photogrammetric model of a fault gouge from the Schauinsland mine in the Black Forest.

This deformation zone is considered as non-permeable for geothermal fluids as it is totally sealed by a large variety of dynamically recrystallized and newly-formed fine-grained minerals. Likewise, fieldwork in the Schauinsland mine in the Black Forest has shown an anastomosed clay-rich fault gouge formed from a unique protolith around 2 m wide (Figure 7-9b), in which later ore veins are abruptly stopped, not being able to develop within it (see Chapter 6) (Figure 7-12). These kind of structures shows that (1) they act as a barrier to fluid flow as demonstrated by Caine et al. (1996) in its model of fault zone and (2) inherited structures have an important impact on the recent fluid circulation.

A highly strained zone has also been investigated in the NH. However, compared to the previous high strain zones from the URG, this fault gouge is very heterogeneous presenting different types of fault rocks and lithologies. Indeed, the rocks constitutive of this fault core does not directly derive from the blocs in contact to the high strain zone itself but from an inherited stacked basement/sedimentary pile (see Chapter 6). Moreover, it has been shown that the clay fault gouge, contrary to the model of a fault zone established by Caine et al. (1996), presents a higher porosity than its damage zone. In the present case, the high porosity and the pronounced alteration degree being more suggest that this high strain zone can act as a drain

even if it contains a lot of illitic material (Figure 7-12). Such structures were not identified in the different wells in the SsF-RTH reservoir.

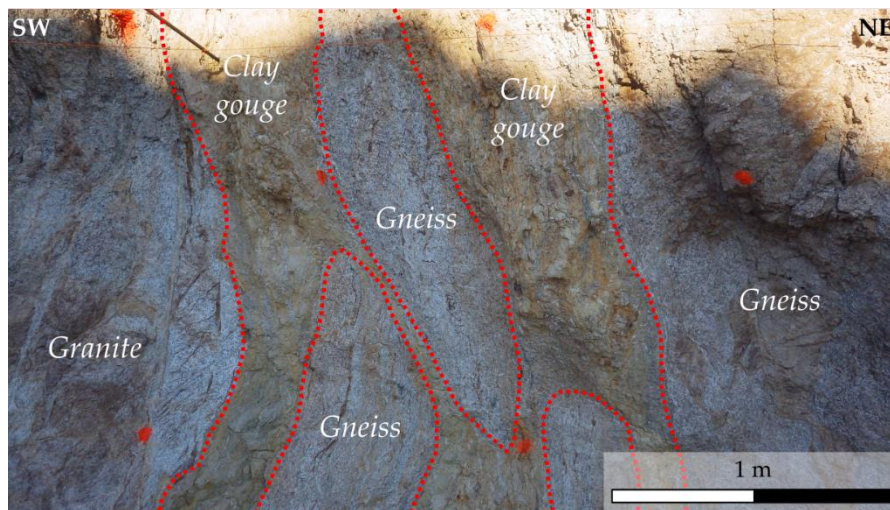


Figure 7-10. Fault gouge outcrop from in the Noble Hills range.

Finally, interference patterns between inherited high strain zones and later opening veins have been found at the Gabbe Gottes locality. Compared to Schauinsland, rock deformation and alteration at Gabbes Gottes is much less intense and purely ductile behavior within this shear zone is excluded. A schistosity is developed and is used by the late brines as a preferential path for percolation. This outcrop is crucial in the understanding of flow trajectories deviations within a basement reservoir having suffered polyphase deformation.



Figure 7-11. Geodic vein intersecting a shear zone by using weakness planes in the Gabe-Gottes mine (Vosges Mountains)

## VI. CONCLUSION TO CHAPTER 7

Available data from exploited geothermal reservoir as SsF and RTH are limited. However, the characterization of the reservoir is very important. A focus on sheared zones from analogue sites was done because these structures are poorly studied during reservoir exploration. Through the investigations performed on the Noble Hills granitic paleo-geothermal reservoir, which was perfectly exposed, and on crystalline basement outcropping in URG shoulders mines, it has been seen that the geology of a reservoir is very complex, especially due to inherited structures.

A synthetic scheme of the main structures found in the SsF reservoir has been proposed by Glaas et al. (2019) (Figure 7-5). Here we propose a new scheme improving previous ones by the new findings obtained about high strain zones (Figure 7-12). Indeed, such zones play an important role in the reservoir hydraulic connectivity. During a unique tectonic episode, dilatancy and shearing can occur together as new structures or by reactivating pre-existing structures (Glaas, 2021). However, inherited fault gouges, by their presence, can

compartmentalize the reservoir by acting as barriers. In the URG, fault zones/gouges are mainly formed from a unique protolith. The NH has shown that fault gouges can be formed from an inherited stacking of basement and sediments, which change drastically the fault core properties allowing it to act as a drain.

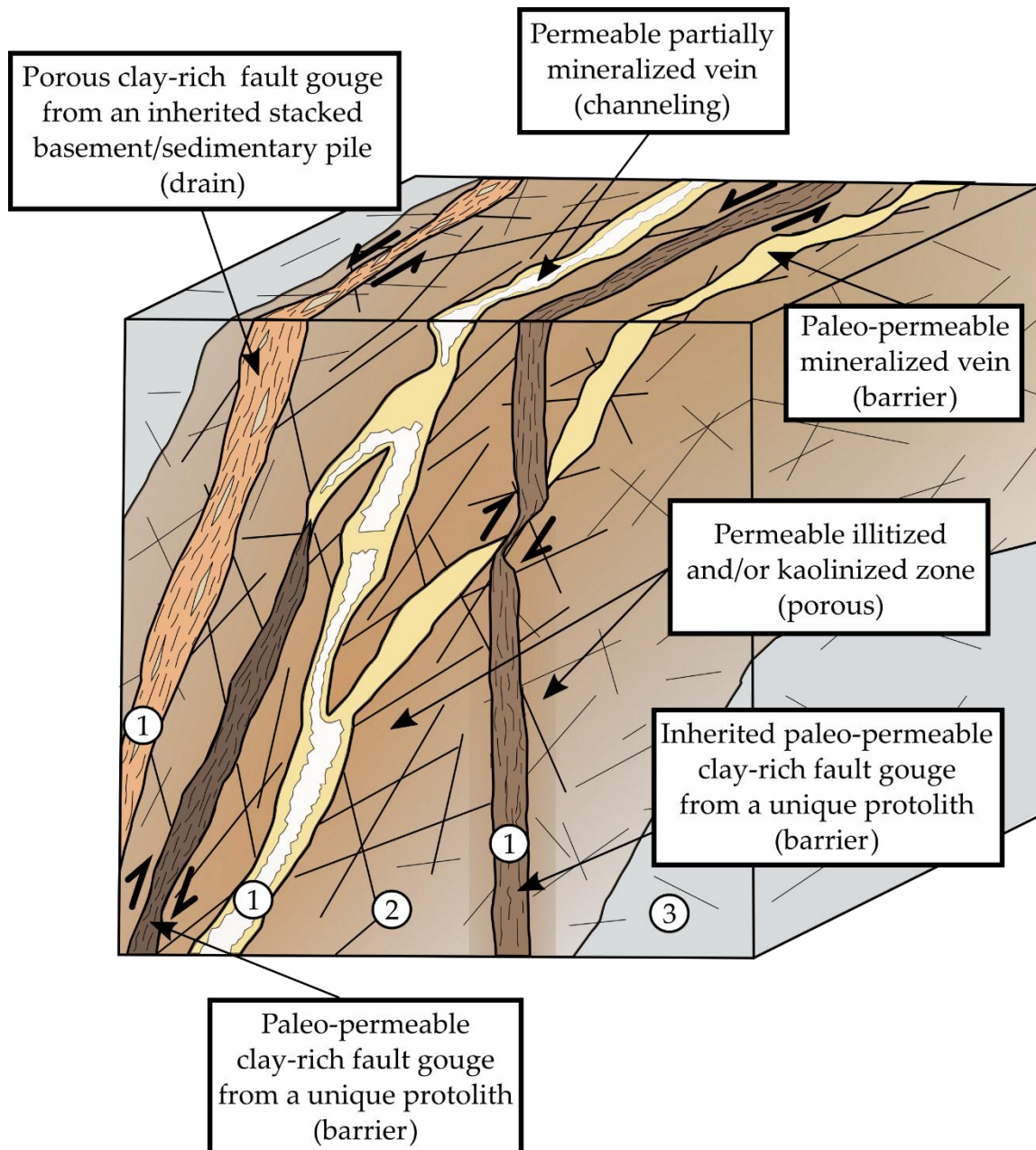


Figure 7-12. A synthetic scheme showing what might be the complexity of a granitic geothermal reservoir by representing the different types of fault zones and fractures that might exist, modified and enhanced after Glaas et al. (2019). Three zones are visible: (1) fault cores, which can be open or sealed by secondary minerals, (2) the damage zone which can be sealed or opened with small-scale fractures acting as fluid pathways, and (3) the unaltered granite showing generally a very low matrix and fracture porosity and permeability.

Shear zones can also act as a partial drain when an inherited shear zone is mylonitic and presents weakness planes that can be used by a later fluid circulation to intersect it even if the amount of flow is reduced as observed in the Gabe-Gottes mine.

It has been shown that depending on the strain the influence of sheared zone varies a lot. At low to moderate strain, fracture zones mostly identified as veins, reactivated or not, mainly acted as drains and connected the fractures. They have a similar impact on the reservoir properties whether the fracture zone is formed by opening or by shearing. Both can promote the fracture connectivity, even better when there is a combination of the two. Highly strained zones, which are usually not intensively investigated during geothermal exploration, play a major role in the hydraulic connectivity of the reservoir and need to be considered.

These observations and investigations have shown and confirmed (1) how heterogeneous a reservoir can be and (2) that deformation has an important impact on the evolution of the fault petrophysical properties (Wallace and Morris, 1986) and on the reservoir connectivity (Bailleux et al., 2011; Curewitz and Karson, 1997).

Analogues are really important in terms of insights to better understand the structure and the behavior of an active reservoir. Deformation is a crucial parameter influencing fault zone properties and which in turn modify substantially their permeability and so the geothermal exploitation potential. Analogue studies have shown that the complexity of a reservoir such as SsF and RTH sites is underestimated.

# CHAPTER 8

## Conclusions and Perspectives

---

This research work aims to provide new insights on the influence on fluid flow of strike-slip faults within crystalline basement rocks affected by varying amounts of deformation. Such structures are poorly studied in exploited geothermal as that they are considered most of the time as barriers to fluid flow. Investigations dedicated to strike slip deformation zones are needed as they participate to the Upper Rhine Graben (URG) structuration where the Soultz-sous-Forêts (SsF) demonstration site is located. The accessibility to the reservoir being limited on exploited sites, relevant naturally exhumed granitic reservoirs considered as analogues are studied. The chosen far-field analogue consists in a portion of the southern the Southern Death Valley Fault Zone (Noble Hills, CA, USA). The near-field analogues is located in the URG shoulders within abandoned mines of Vosges and Black Forest massifs.

### I. MAJOR OUTCOMES FOR RESEARCH

#### I.1. Hydrothermal alteration and its indicators

The NH range shows the following alteration stages:

- The propylitic alteration, considered as an earlier pervasive alteration stage, takes place at the end of the cooling and the crystallization of the granite. It results mainly in the partial recrystallization of primary biotite and plagioclase in secondary propylitic assemblage. This assemblage consists in: illite, epidote, corrensite (a chlorite/trioctahedral smectite mixed-layer) and calcite. Epidote and corrensite are the main indicators of the propylitic alteration. Calcite is only filling few microcracks or occurs at grain boundaries without interacting with the surrounding rock.
- The argillic alteration is considered as a localized alteration which overprints the propylitic alteration. Argillic alteration occurs in the vicinity of fractures where fluids have circulated. This alteration consists into the chemical leaching and clay enrichment processes produced at lower temperature (130-200°C). The newly formed mineral assemblage consists in illite, kaolinite, illite/smectite mixed-layer, calcite and oxide due to the complete alteration of plagioclase and biotite.

Weathering evidences (Montmorillonite and Vermiculite) were identified. Weathering evidences are scarce and considered negligible.

The propylitic and argillic mineral assemblages are comparable to those identified at SsF and Rittershoffen (RTH).

Approaching fracture zones, the alteration is more pronounced, a fact confirmed by the Loss of Ignition values increase. The fluid-rock interactions being more significant near fractures, argillic alteration is predominant and have almost completely overprinted the propylitic alteration. The similar observation has been done in the case of the SsF and RTH granites. Kaolinite is generally the dominant clay mineral near fracture zones, indicating either an important leaching or the circulation of an acidic fluid. KI values show a crystallization of illitic material at temperature around 200°C, confirming the predominance of the argillic alteration.

A multi-stage paleo-fluid circulation was put in evidence in the NH granite due to the various kinds of secondary minerals that precipitate in the fractures as quartz, illite, carbonates (calcite, dolomite, ankerite) and oxides. The source of Ca is interpreted to partly derive from plagioclase alteration and from Proterozoic dolomite. The calcite content has been measured and show an increase towards the fracture zones.

## 1.2. Relation between amount of deformation and fluid circulation

Bringing together the main findings from the NH range, the URG shoulders and data from the SsF and RTH granitic reservoirs, a synthetic scheme is proposed, summarizing (1) the evolution of strike-slip structure according to a gradient of deformation and (2) illustrating the relation between inherited shear zones and later fluid circulation (Figure 8-1).

Fracturing is initiated during the cooling of the granite which was pervasively affected by the propylitic alteration (Figure 8-1a). Under low to moderate strain, fractures open letting a fluid circulate. Two cases are to be considered:

1. In the case of a very low fluid/rock ratio, the fluid can circulate through the fracture network and secondary minerals can precipitate in the fracture producing a slight alteration of the granite (Figure 8-1b,c).
2. In the case of high fluid/rock ratio, the fluid circulates through the fractures affecting their walls and developing a gradient of alteration (Figure 8-1d). Through time, secondary minerals can precipitate from saturated brines, (e.g. quartz) and seal the fractures while increasing the alteration gradient (Figure 8-1e,f). Likewise, successive fault reactivations rework the initial vein content and further alter the host rocks. Depending on new fluid chemical composition, secondary minerals further develop in the host rock (here carbonates). Combined to the host grain size reduction, the amount

of these new minerals increases drastically through time. The newly formed rock presents a much lower competence compared to the initial protolith and promotes at first the development of a schistosity (Figure 8-1g) and finally the onset from creep deformation mechanism (Figure 8-1h).



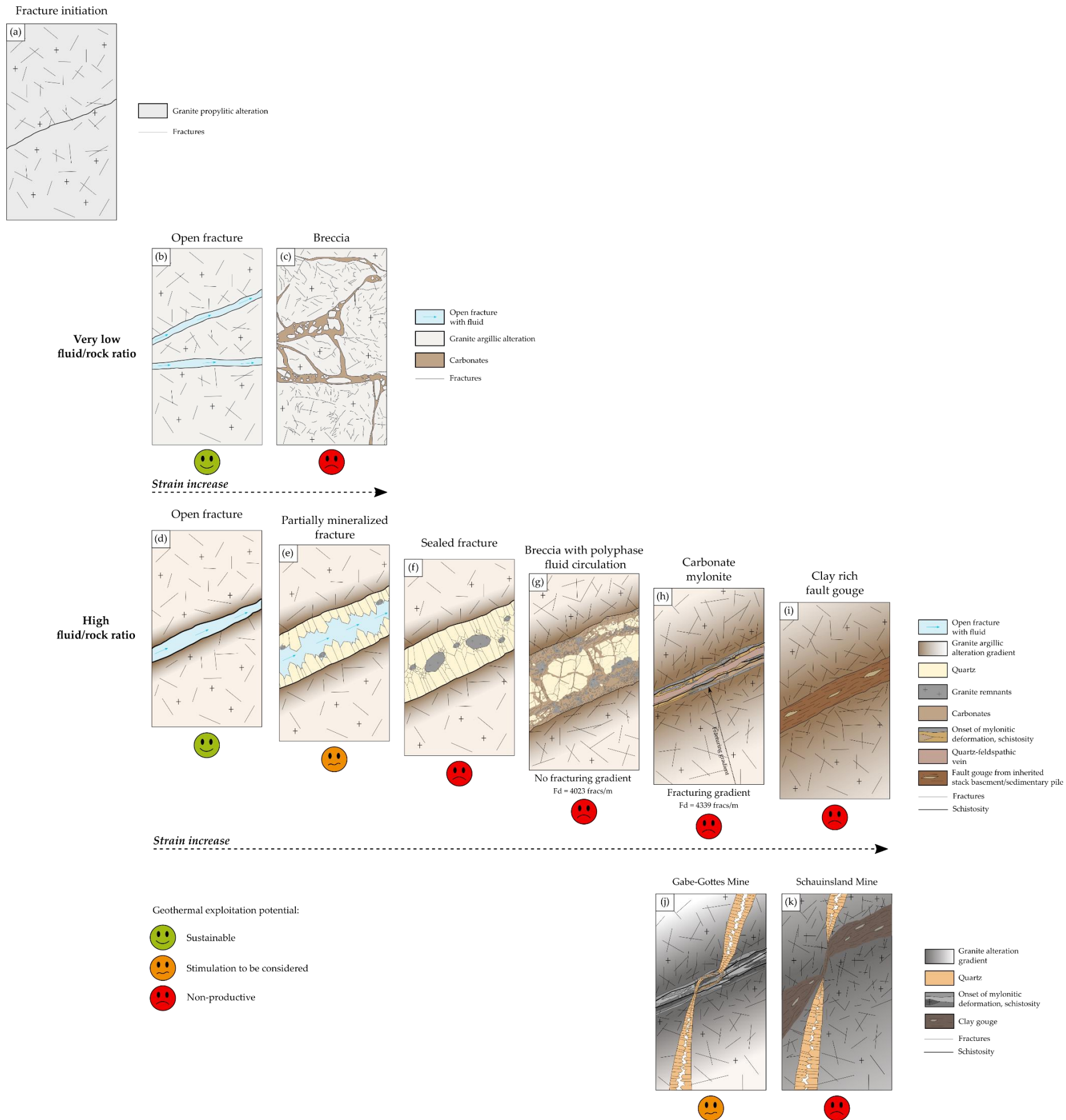


Figure 8-1. Synthetic scheme showing the interaction between the fluid and the granite at different amount of strain. (a) Initiation of a fracture in a granite affected by propylitic alteration. (b) Open fractures with an incipient alteration of the surrounding rock. (c) Brecciated zones with a carbonated matrix and no change of alteration degree. (d) An open fracture with an incipient alteration gradient at the border. (e) Mineral crystallization at the border of the vein. (f) A sealed fracture with a slight alteration gradient. (g) A brecciated vein induced from fracture reactivation and showing an alteration gradient but no fracturing gradient. (h) A mylonite made of carbonates and granitic lenses showing an alteration gradient and a fracturing gradient. (g) and (h) show a similar fracture density (Fd). (i) A fault gouge resulted into the deformation of inherited pinched Proterozoic basement and sediments. (j) Gabe-Gottes mine case, deviation of the vein with the shear zone. (k) Schauinsland case, the vein is stopped by the clay gouge. No scale is given for this scheme, because it can represent fracture zones of several order of magnitude. The supposed geothermal exploitation potential is indicated by smileys of different colors.



It has been shown that depending on the nature of the protolith composing the fault core, the fault gouge can act either as a drain (inherited heterogeneous protolith in the NH–Figure 8-1) or as a barrier (unique protolith Schauinsland–Figure 8-1k). The case of the gouge at Schauinsland shows that clay minerals tend to stop the development of recent mineralization due to their soft rheology (Figure 8-1k). However, in the case of a shear zone developing a schistosity, later veins can use these planes of weakness to propagate and crosscut the shear zone, even if the development of the vein is narrower (Figure 8-1j). Depending on the fault core composition and rheology, highly strained fault zones can have different behaviors and react differently to fluid flow.

At large scale, by approaching fracture zones, the fracture density increase, as well as the degree of alteration, the calcite content and the porosity. Sample scale and thin section scale have shown that this correlation is not always true.

## II. MAJOR OUTCOMES FOR THE GEOTHERMAL INDUSTRY

Due to the low matrix porosity of granitic rocks, fractures enhanced drastically the fluid circulation. Thus, the fluid interacts with the surrounding rock. The alteration processes related to chemical element transfers during the interaction of the fluid with the surrounding rock induce a global increase of the porosity and thus of the permeability. Fault zones composing of an open core and an altered damage zone become the major conduits. However, an abundance of newly-formed minerals can seal the fractures and clog the system.

Stimulations the SsF and RTH geothermal site have been performed in order to enhanced reservoir permeability. For example, carbonates having precipitated in the fractures were chemically dissolved in order to produce voids within fractures and let the fluid circulate. Investigations in the NH range show that carbonates are the most abundant secondary mineral filling the fractures in the whole area. As the fracture network filled by these carbonates is well geometrically connected (Chabani et al., 2021), it is suggested that the hydraulic connectivity was good.

The NH presenting a clear gradient of deformation along the range. The influence of deformation on fluid circulation has been investigated and allow to show the importance of the role of high strain zones in a reservoir. It has been shown that a high strain zone are not always following the classical model of a fault zone whose fault core is the product of a highly deformed unique protolith from (Caine et al., 1996) and which acts as a barrier due to the decrease of

porosity and permeability. In the case of the NH, a high strain zone, characterized as a fault gouge, can be a drain. It can be explained by (1) its heterogeneity resulting into the presence of inherited pinched and highly deformed Proterozoic sediments and basement in the fault core, (2) its high porosity in the fault core, (3) its high calcite content which can come from fluid circulation that precipitates carbonates and (4) a pronounced alteration. This fault gouge is also accommodating the deformation due to its composition. It is suggested that this kind of structure in the area divide the reservoir into relatively low strained blocs which glide next to each other without accumulated high elastic strain. This can explain why in the area large veins, corresponding to paleo-permeable fractures, are extremely rare. Thus, even if the fracture network in the NH is hydraulically connected, it might not be commercially exploitable due to this bloc system. However, by considering changing of the stress field, as the compression of the Avawatz Mountains against the NH, these low strained blocs are no more in the sliding configuration but stress can be accumulated and fractured consequently the blocs. Thus, pluri-decimeteric barite veins, oblique to the NH orientation, were identified as a result of this change of stress in the NH. These barite veins were not identified in the whole range certainly due to the influence of the transverse clay-rich fault zones which can stop or deviate the circulation.

Preliminary investigations performed in the mines in the URG shoulders have shown the important influence of the structural heritage on later fluid circulation. The Schauinsland mine in the Black Forest has shown that an inherited clay-rich gouge resulting into the deformation of a unique protolith act as a barrier. Clay material hindering the stress to accumulate, the gouge rapidly stopped the development of a vein. On the other side of the graben, in the Vosges Mountains, the Gabe-Gottes mine presents inherited shear zones in the basement rock through which veins can propagate by using the schistosity. Fluid circulation gets deviated by using the preferential orientation of inherited high strain zone schistosity. Such inherited structures identified in the URG shoulders must be considered when simulating fluid flow inside a geothermal reservoir.

Analogues allowed to show the real complexity of a geothermal reservoir which is most of the time underestimated. High strain zones can present different behaviors which influence directly the fluid circulation through the reservoir.

Strike-slip structures are not only important in the connectivity of the reservoir, but it can be also mentioned that these structures are subjected to reactivation during stimulation operations. Indeed, recent seismic events that occurred in Alsace in the vicinity of Strasbourg

were due to movements along the strike-slip structures oriented N309 during stimulations (EOST and CNRS, 2021).

The understanding through time of a reservoir needs to be considered by the industrials. The model of fracture evolution presented above (Figure 8-1) according to amounts of accumulated strain is directly related to reservoir evolution through geological time. Thus, a given reservoir commercially exploitable at a given time might not have been exploitable if missing one tectonic episode. At the opposite, one additional tectonic episode might prevent further exploitation of an reservoir active in the past. There is therefore, a geothermal exploitation time window where commercial exploitation is possible in the geological history of a reservoir. These geothermal windows providing a sustainable exploitation is represented by green smileys on Figure 8-1, which consist into fully open fractures. Orange smileys show the geothermal windows where exploitation is possible but will probably need some stimulation. Red smileys represent structural settings not compatible with geothermal exploitation.

### III. PERSPECTIVES

Although this PhD work helps somehow to improve the understanding about the influence of strike-slip structures in a granitic geothermal reservoir, the following points appear as the main remaining challenges that could be addressed in further works.

#### III.1. High strain zones in-depth characterization

This work put in evidence the major role that high strained shear zones play in the reservoir connectivity and productivity. However, more specific characterizations are needed to understand their mechanical and petrophysical behavior.

Thus, three topics deserve investigations in the future:

- Experimental deformation dealing with mechanical properties of reservoir rocks as a function of alteration, including acoustic emission monitoring. These experiments play a key role when relating stress and strain regime to the degree of rock alteration and potential occurrence of seismic event.
- Kinetics of fluid-rock interaction reactions and quantification of strain-enhanced effects on alteration minerals production rate in time.
- Multiscale characterization of clay mineral distributions across deformation zones to better understand the role drain/barrier of a highly strained fault core.

### III.2. Paleo-fluid characterization

In active geothermal the fluid composition and characterization are highly studied in order to better understand its interaction with the surrounding rock. Various methods are available in order to characterize the paleo-fluid that have circulated through the granite:

Fluid inclusion, provide a unique fossil record of the various fluid that have circulated through the granite. They can be used to determine the temperatures and physicochemical nature of the fluid at the time of trapping (Rankin, 2005). Analyses are ongoing on quartz, carbonate and barite veins from the NH.

Fluid isotopes can be used to characterize a fluid origin, age, and/or interaction with rocks or other fluids. As dating on illite has been performed through K/Ar isotopes, oxygen isotopes can give the origin of the fluid through its geochemical specific signature (Williams and McKibben, 1989). Likewise, carbonates can be dated, e.g. using the Sm-Nd system (Henjes-Kunst et al., 2014) and U/Pb, in order to determine the hydrothermal mineralization age and put it in relation with ages obtained on illite to decipher different generation of fluid circulation.

## REFERENCES

---

- Abad, I., 2007. Physical meaning and applications of the illite Kübler index: measuring reaction progress in low-grade metamorphism. *Diagenesis and Low-Temperature Metamorphism, Theory, Methods and Regional Aspects, Seminarios, Sociedad Espanola: Sociedad Espanola Mineralogia* 53–64.
- Alderton, D.H.M., Pearce, J.A., Potts, P.J., 1980. Rare earth element mobility during granite alteration: Evidence from southwest England. *Earth and Planetary Science Letters* 49, 149–165. [https://doi.org/10.1016/0012-821X\(80\)90157-0](https://doi.org/10.1016/0012-821X(80)90157-0)
- Altherr, R., Henes-Klaiber, U., Hegner, E., Satir, M., Langer, C., 1999. Plutonism in the Variscan Odenwald (Germany): from subduction to collision. *Int Journ Earth Sciences* 88, 422–443. <https://doi.org/10.1007/s005310050276>
- Altherr, R., Holl, A., Hegner, E., Langer, C., Kreuzer, H., 2000. High-potassium, calc-alkaline I-type plutonism in the European Variscides: northern Vosges (France) and northern Schwarzwald (Germany). *Lithos* 50, 51–73. [https://doi.org/10.1016/S0024-4937\(99\)00052-3](https://doi.org/10.1016/S0024-4937(99)00052-3)
- Andrew, J.E., Walker, J.D., Monastero, F.C., 2015. Evolution of the central Garlock fault zone, California: A major sinistral fault embedded in a dextral plate margin. *GSA Bulletin* 127, 227–249. <https://doi.org/10.1130/B31027.1>
- Aquilina, L., Pauwels, H., Genter, A., & Fouillac, C., 1997. Water-rock interaction processes in the Triassic sandstone and the granitic basement of the Rhine Graben: Geochemical investigation of a geothermal reservoir. *Geochimica et cosmochimica acta*, 61(20), 4281–4295. [https://doi.org/10.1016/S0016-7037\(97\)00243-3](https://doi.org/10.1016/S0016-7037(97)00243-3)
- Aretz, A., Bär, K., Götz, A.E., Sass, I., 2016. Outcrop analogue study of Permocarboniferous geothermal sandstone reservoir formations (northern Upper Rhine Graben, Germany): impact of mineral content, depositional environment and diagenesis on petrophysical properties [WWW Document]. URL <https://link.springer.com/article/10.1007/s00531-015-1263-2> (accessed 10.1.21).
- Árkai, P., Maehlmann, R., Suchy, V., Balogh, K., Sykorová, I., Frey, M., 2002. Possible effects of tectonic shear strain on phyllosilicates: A case study from the Kandersteg area, Helvetic domain, Central Alps, Switzerland. *TMPM Tschermarks Mineralogische und Petrographische Mitteilungen* 82, 273–290.
- Árkai, P., Sassi, F., Desmons, J., 2003a. Very low- to low-grade metamorphic rocks. *Metamorphic Rocks A Classification and Glossary Terms*.
- Árkai, P., Sassi, F., Desmons, J., 2003b. Very low- to low-grade metamorphic rocks. *Metamorphic Rocks A Classification and Glossary Terms*.
- Bächler, D., Kohl, T., Rybach, L., 2003. Impact of graben-parallel faults on hydrothermal convection—Rhine Graben case study. *Physics and Chemistry of the Earth, Parts*

- A/B/C, Heat Flow and the Structure of the Lithosphere 28, 431–441. [https://doi.org/10.1016/S1474-7065\(03\)00063-9](https://doi.org/10.1016/S1474-7065(03)00063-9)
- Baillieux, P., Schill, E., Dezayes, C., 2011. 3-D structural regional model of the EGS Soultz site (northern Upper Rhine Graben, France): insights and perspectives. Presented at the 36rd Workshop on Geothermal Reservoir Engineering, p. SGP-TR-191.
- Baillieux, P., 2012. Multidisciplinary approach to understand the localization of geothermal anomalies in the Upper Rhine Graben from regional to local scale.
- Baillieux, P., Schill, E., Edel, J.-B., Mauri, G., 2013. Localization of temperature anomalies in the Upper Rhine Graben: insights from geophysics and neotectonic activity. *International Geology Review* 55, 1744–1762. <https://doi.org/10.1080/00206814.2013.794914>
- Bard, J.P., 1980. *Microtextures des roches magmatiques et métamorphiques*. Masson Ed, Paris, New-York, Barcelone, Milan.
- Barrow, G., 1893. On an Intrusion of Muscovite-biotite Gneiss in the South-eastern Highlands of Scotland, and its accompanying Metamorphism. *Quarterly Journal of the Geological Society* 49, 330–358. <https://doi.org/10.1144/GSL.JGS.1893.049.01-04.52>
- Bartier, D., Ledésert, B., Clauer, N., Meunier, A., Liewig, N., Morvan, G., Addad, A., 2008. Hydrothermal alteration of the Soultz-sous-Forêts granite (Hot Fractured Rock geothermal exchanger) into a tosudite and illite assemblage. *European Journal of Mineralogy* 20, 131–142. <https://doi.org/10.1127/0935-1221/2008/0020-1787>
- Barton, C.A., Zoback, M.D., Moos, D., 1995. Fluid flow along potentially active faults in crystalline rock. *Geology* 23, 683–686. [https://doi.org/10.1130/0091-7613\(1995\)023<0683:FFAPAF>2.3.CO;2](https://doi.org/10.1130/0091-7613(1995)023<0683:FFAPAF>2.3.CO;2)
- Bauer, J.F., Meier, S., Philipp, S.L., 2015. Architecture, fracture system, mechanical properties and permeability structure of a fault zone in Lower Triassic sandstone, Upper Rhine Graben. *Tectonophysics* 647–648, 132–145. <https://doi.org/10.1016/j.tecto.2015.02.014>
- Baujard, C., Genter, A., Dalmais, E., Maurer, V., Hehn, R., Rosillette, R., Vidal, J., Schmittbuhl, J., 2017. Hydrothermal characterization of wells GRT-1 and GRT-2 in Rittershoffen, France: Implications on the understanding of natural flow systems in the rhine graben. *Geothermics* 65, 255–268. <https://doi.org/10.1016/j.geothermics.2016.11.001>
- Beaufort, D., Baronnet, A., Lanson, B., Meunier, A., 1997. Corrensite; a single phase or a mixed-layer phyllosilicate in saponite-to-chlorite conversion series? A case study of Sancerre-Couy deep drill hole (France). *American Mineralogist* 82, 109–124. <https://doi.org/10.2138/am-1997-1-213>
- Beaufort, D., Westercamp, D., Legendre, O., Meunier, A., 1990. The fossil hydrothermal system of Saint Martin, Lesser Antilles: geology and lateral distribution of alterations. *Journal of Volcanology and Geothermal Research* 40, 219–243. [https://doi.org/10.1016/0377-0273\(90\)90122-V](https://doi.org/10.1016/0377-0273(90)90122-V)

- Berg, S.S., Skar, T., 2005. Controls on damage zone asymmetry of a normal fault zone: outcrop analyses of a segment of the Moab fault, SE Utah. *Journal of Structural Geology* 27, 1803–1822. <https://doi.org/10.1016/j.jsg.2005.04.012>
- Berger, G., Velde, B., 1992. Chemical parameters controlling the propylitic and argillic alteration process. *ejm* 4, 1439–1456. <https://doi.org/10.1127/ejm/4/6/1439>
- Bertrand, L., 2017. Étude des réservoirs géothermiques développés dans le socle et à l'interface avec les formations sédimentaires (These de doctorat). Université de Lorraine.
- Bertrand, L., Géraud, Y., Le Garzic, E., Place, J., Diraison, M., Walter, B., Haffen, S., 2015. A multiscale analysis of a fracture pattern in granite: A case study of the Tamariu granite, Catalunya, Spain. *Journal of Structural Geology* 78, 52–66. <https://doi.org/10.1016/j.jsg.2015.05.013>
- Bertrand, L., Jusseaume, J., Géraud, Y., Diraison, M., Damy, P.-C., Navelot, V., Haffen, S., 2018. Structural heritage, reactivation and distribution of fault and fracture network in a rifting context: Case study of the western shoulder of the Upper Rhine Graben. *Journal of Structural Geology, Spatial arrangement of fractures and faults* 108, 243–255. <https://doi.org/10.1016/j.jsg.2017.09.006>
- Bestmann, M., Kunze, K., Matthews, A., 2000. Evolution of a calcite marble shear zone complex on Thassos Island, Greece: microstructural and textural fabrics and their kinematic significance. *Journal of Structural Geology* 22, 1789–1807. [https://doi.org/10.1016/S0191-8141\(00\)00112-7](https://doi.org/10.1016/S0191-8141(00)00112-7)
- Bisdorn, K., Gauthier, B.D.M., Bertotti, G., Hardebol, N.J., 2014. Calibrating discrete fracture-network models with a carbonate three-dimensional outcrop fracture network: Implications for naturally fractured reservoir modeling. *AAPG Bulletin* 98, 1351–1376. <https://doi.org/10.1306/02031413060>
- Blakely, R.J., Jachens, R.C., Calzia, J.P., Langenheim, V.E., 1999. Cenozoic basins of the Death Valley extended terrane as reflected in regional-scale gravity anomalies. <https://doi.org/10.1130/0-8137-2333-7.1>
- Bonorino, F.G., 1959. Hydrothermal alteration in the Front Range mineral belt, Colorado. *GSA Bulletin* 70, 53–90. [https://doi.org/10.1130/0016-7606\(1959\)70\[53:HAITFR\]2.0.CO;2](https://doi.org/10.1130/0016-7606(1959)70[53:HAITFR]2.0.CO;2)
- Bouchez, J.-L., Nicolas, A., 2018. *Principes de tectonique*. deBoeck.
- Bouchez, J. L., & Nicolas, A. (2021). *Principles of Rock Deformation and Tectonics*. Oxford University Press.
- Boynton, W.V., 1984. Cosmochemistry of the Rare Earth Elements: Meteorite Studies, in: *Developments in Geochemistry*. Elsevier, Amsterdam, The Netherlands, pp. 63–114. <https://doi.org/10.1016/B978-0-444-42148-7.50008-3>

- Brady III, R.H., 1986. Cenozoic Geology of the Northern Avawatz Mountains in Relation to the Intersection of the Garlock and Death Valley Fault Zones, San Bernardino County, California. University of California, Davis.
- Brady, R.H., 1984. Neogene stratigraphy of the Avawatz Mountains between the Garlock and Death Valley fault zones, southern Death Valley, California: Implications as to late Cenozoic tectonism. *Sedimentary Geology, Fluvial Sedimentation and Related Tectonic Framework, Western North-America* 38, 127–157. [https://doi.org/10.1016/0037-0738\(84\)90077-0](https://doi.org/10.1016/0037-0738(84)90077-0)
- Brady, R.H., Clayton, J., Troxel, B.W., Verosub, K.L., Cregan, A., Abrams, M., 1989. Thematic mapper and field investigations at the intersection of the Death Valley and Garlock fault zones, California. *Remote Sensing of Environment* 28, 207–217. [https://doi.org/10.1016/0034-4257\(89\)90114-4](https://doi.org/10.1016/0034-4257(89)90114-4)
- Brady, R.H., Troxel, B.W., 1986b. Stratigraphy and tectonics of the northern Avawatz Mountains at the intersection of the Garlock and Death Valley fault zones, San Bernardino County, California. *Quaternary tectonics of southern Death Valley, California - Field trip guide: Shoshone, California, Friends of the Pleistocene, Pacific Cell* 1–12.
- Bruhn, D., Manzella, A., Vuataz, F., Faulds, J., Moeck, I., Erbas, K., 2010. Exploration Methods, in: *Geothermal Energy Systems*. John Wiley & Sons, Ltd, pp. 37–112. <https://doi.org/10.1002/9783527630479.ch2>
- Bruhn, R.L., Parry, W.T., Yonkee, W.A., Thompson, T., 1994. Fracturing and hydrothermal alteration in normal fault zones. *PAGEOPH* 142, 609–644. <https://doi.org/10.1007/BF00876057>
- Buatier, M.D., Chauvet, A., Kanitpanyacharoen, W., Wenk, H.R., Ritz, J.F., Jolivet, M., 2012. Origin and behavior of clay minerals in the Bogd fault gouge, Mongolia. *Journal of Structural Geology* 34, 77–90. <https://doi.org/10.1016/j.jsg.2011.10.006>
- Burchfiel, B.C., Stewart, J.H., 1966. “Pull-apart” origin of the central segment of Death Valley, California. *GSA Bulletin* 77, 439–442. [https://doi.org/10.1130/0016-7606\(1966\)77\[439:POOTCS\]2.0.CO;2](https://doi.org/10.1130/0016-7606(1966)77[439:POOTCS]2.0.CO;2)
- Burkhard, M., 1990. Ductile deformation mechanisms in micritic limestones naturally deformed at low temperatures (150–350°C). *Geological Society, London, Special Publications* 54, 241–257. <https://doi.org/10.1144/GSL.SP.1990.054.01.23>
- Burnham, C.W., 1962. Facies and types of hydrothermal alteration. *Economic Geology* 57, 768–784. <https://doi.org/10.2113/gsecongeo.57.5.768>
- Butler, P.R., 1984. *Geology: Structural history and fluvial geomorphology of the southern Death Valley Fault Zone, Inyo and San Bernardino Counties, California*. University of California, Davis, CA, USA.

- Butler, P.R., Troxel, B.W., Verosub, K.L., 1988. Late Cenozoic history and styles of deformation along the southern Death Valley fault zone, California. *GSA Bulletin* 100, 402–410. [https://doi.org/10.1130/0016-7606\(1988\)100<0402:LCHASO>2.3.CO;2](https://doi.org/10.1130/0016-7606(1988)100<0402:LCHASO>2.3.CO;2)
- Caine, J., Forster, C., 1999. Fault Zone Architecture and Fluid Flow: Insights from Field Data and Numerical Modeling, in: *Faults and Subsurface Fluid Flow in the Shallow Crust*. pp. 101–127. <https://doi.org/10.1029/GM113p0101>
- Caine, J.S., Bruhn, R.L., Forster, C.B., 2010. Internal structure, fault rocks, and inferences regarding deformation, fluid flow, and mineralization in the seismogenic Stillwater normal fault, Dixie Valley, Nevada. *Journal of Structural Geology, Fault Zones* 32, 1576–1589. <https://doi.org/10.1016/j.jsg.2010.03.004>
- Caine, J.S., Evans, J.P., Forster, C.B., 1996. Fault zone architecture and permeability structure. *Geology* 24, 1025–1028. [https://doi.org/10.1130/0091-7613\(1996\)024<1025:FZAAPS>2.3.CO;2](https://doi.org/10.1130/0091-7613(1996)024<1025:FZAAPS>2.3.CO;2)
- Callahan, O.A., Eichhubl, P., Olson, J.E., Davatzes, N.C., 2019. Fracture Mechanical Properties of Damaged and Hydrothermally Altered Rocks, Dixie Valley-Stillwater Fault Zone, Nevada, USA. *Journal of Geophysical Research: Solid Earth* 124, 4069–4090. <https://doi.org/10.1029/2018JB016708>
- Calzia, J.P., Rämö, O.T., 2000. Late Cenozoic crustal extension and magmatism, southern Death Valley region, California. *GSA Field Guides* 2, 135–164. <https://doi.org/10.1130/0-8137-0002-7.135>
- Camacho, A., McDougall, I., Armstrong, R., Braun, J., 2001. Evidence for shear heating, Musgrave Block, central Australia. *Journal of Structural Geology* 23, 1007–1013. [https://doi.org/10.1016/S0191-8141\(00\)00172-3](https://doi.org/10.1016/S0191-8141(00)00172-3)
- Cassiaux, M., Proust, D., Siitari-Kauppi, M., Sardini, P., Leutsch, Y., 2006. Clay minerals formed during propylitic alteration of a granite and their influence on primary porosity: a multi-scale approach. *Clays and Clay Minerals* 54, 541–554. <https://doi.org/10.1346/CCMN.2006.0540502>
- Castaing, C., Rabu, D., 1981. Apports de la géologie à la recherche et à l'exploitation de pierres de taille (roches ornementales et de construction). *BULL BRGM,III, BULL BRGM* 1.
- Chabani, A., 2019. Analyse méthodologique et caractérisation multi-échelle des systèmes de fractures à l'interface socle/couverture sédimentaire – application à la géothermie (bassin de Valence, SE France) (These de doctorat). Paris Sciences et Lettres (ComUE).
- Chabani, A., Trullenque, G., Klee, J., Ledésert, B.A., under review. Fracture spacing variability and the distribution of fracture patterns in granitic geothermal reservoir: A case study in the Noble Hills range (Death Valley, CA, USA). *Geosciences* 33.
- Chabani, A., Trullenque, G., Ledésert, B.A., Klee, J., 2021. Multiscale Characterization of Fracture Patterns: A Case Study of the Noble Hills Range (Death Valley, CA, USA),

- Application to Geothermal Reservoirs. *Geosciences* 11, 280. <https://doi.org/10.3390/geosciences11070280>
- Chambefort, I., Moritz, R., von Quadt, A., 2007. Petrology, geochemistry and U–Pb geochronology of magmatic rocks from the high-sulfidation epithermal Au–Cu Chelopech deposit, Srednogorie zone, Bulgaria. *Mineralium Deposita* 42, 665–690. <https://doi.org/10.1007/s00126-007-0126-6>
- Chermak, J.A., Rimstidt, J.D., 1990. The hydrothermal transformation rate of kaolinite to muscovite/illite. *Geochimica et Cosmochimica Acta* 54, 2979–2990. [https://doi.org/10.1016/0016-7037\(90\)90115-2](https://doi.org/10.1016/0016-7037(90)90115-2)
- Chinn, L.D., 2013. Low-Temperature Thermochronometry of the Avawatz Mountains; Implications for the Eastern Terminus and Inception of the Garlock Fault Zone 48.
- Choi, J.-H., Edwards, P., Ko, K., Kim, Y.-S., 2016. Definition and classification of fault damage zones: A review and a new methodological approach. *Earth-Science Reviews* 152, 70–87. <https://doi.org/10.1016/j.earscirev.2015.11.006>
- Cloetingh, S., Ziegler, P.A., Beekman, F., Andriessen, P., Matenco, L., Bada, G., Garcia-Castellanos, D., Hardebol, N., Zes, P., Sokoutis, D., 2005. Lithospheric memory, state of stress and rheology: Neotectonic controls on Europe's intraplate continental topography. *Quaternary Science Reviews* 24, 241–304. <https://doi.org/10.1016/j.quascirev.2004.06.015>
- COP 21, 2015. Paris Agreement, united nations Framework convention on climate change, conference of the parties 21. *Int'l Legal Materials* 55, 743.
- Cox, K.G., 1979. *The Interpretation of Igneous Rocks*. Springer Science & Business Media, London.
- Cox, S.F., 2007. Structural and isotopic constraints on fluid flow regimes and fluid pathways during upper crustal deformation: An example from the Taemas area of the Lachlan Orogen, SE Australia. *Journal of Geophysical Research: Solid Earth* 112. <https://doi.org/10.1029/2006JB004734>
- Crawford, B. R., Faulkner, D. R., & Rutter, E. H., 2008. Strength, porosity, and permeability development during hydrostatic and shear loading of synthetic quartz-clay fault gouge. *Journal of Geophysical Research: Solid Earth*, 113(B3). <https://doi.org/10.1029/2006JB004634>
- Creasey, S.C., 1966. Hydrothermal alteration, in: *Geology of the Porphyry Copper Deposits Southwestern North America*. Tittley & Hicks, Tucson, pp. 51–74.
- Curewitz, D., Karson, J.A., 1997. Structural settings of hydrothermal outflow: Fracture permeability maintained by fault propagation and interaction. *Journal of Volcanology and Geothermal Research* 79, 149–168. [https://doi.org/10.1016/S0377-0273\(97\)00027-9](https://doi.org/10.1016/S0377-0273(97)00027-9)

- Dalmais, E., Genter, A., Trullenque, G., Leoutre, E., Leiss, B., Wagner, B., Mintsa, A.C., Bär, K., Rajsl, I., 2019. MEET Project: Toward the spreading of EGS across Europe. Presented at the European Geothermal Congress 2019, Den Haag, The Netherlands, p. 8.
- Davatzes, N.C., Hickman, S.H., 2005. Controls on fault-hosted fluid flow; Preliminary results from the Coso Geothermal Field, CA. Geothermal Resources Council 16.
- DeCelles, P.G., 2004. Late Jurassic to Eocene evolution of the Cordilleran thrust belt and foreland basin system, western U.S.A. *American Journal of Science* 304, 105–168. <https://doi.org/10.2475/ajs.304.2.105>
- Derer, C.E., Schumacher, M.E., Schäfer, A., 2005. The northern Upper Rhine Graben: basin geometry and early syn-rift tectono-sedimentary evolution. *Int J Earth Sci (Geol Rundsch)* 94, 640–656. <https://doi.org/10.1007/s00531-005-0515-y>
- Dezayes, C., Genter, A., Gentier, S., 2004. Fracture Network of the EGS Geothermal Reservoir at Soultz-sous-Forêts (Rhine Graben, France). *Geothermal Resources Council Transactions Vol. 28*, 7.
- Dezayes, C., Genter, A., Valley, B., 2010a. Overview of the Fracture Network at Different Scales Within the Granite Reservoir of the EGS Soultz Site (Alsace, France). Presented at the World Geothermal Congress 2010, p. 13 p.
- Dezayes, C., Genter, A., Valley, B., 2010b. Structure of the low permeable naturally fractured geothermal reservoir at Soultz. *Comptes Rendus Geoscience, Vers l'exploitation des ressources géothermiques profondes des systèmes hydrothermaux convectifs en milieu naturellement fracturés* 342, 517–530. <https://doi.org/10.1016/j.crte.2009.10.002>
- Dezayes, C., Lerouge, C., 2019a. Reconstructing Paleofluid Circulation at the Hercynian Basement/Mesozoic Sedimentary Cover Interface in the Upper Rhine Graben. *Geofluids* 2019, 1–30. <https://doi.org/10.1155/2019/4849860>
- Dezayes, C., Lerouge, C., 2019b. Reconstructing Paleofluid Circulation at the Hercynian Basement/Mesozoic Sedimentary Cover Interface in the Upper Rhine Graben [WWW Document]. *Geofluids*. <https://doi.org/10.1155/2019/4849860>
- Dezayes, C., Lerouge, C., Innocent, C., Lach, P., 2021. Structural control on fluid circulation in a graben system: Constraints from the Saint Pierre Bois quarry (Vosges, France). *Journal of Structural Geology* 146, 104323. <https://doi.org/10.1016/j.jsg.2021.104323>
- Dezayes, C., Lerouge, C., Ramboz, C., Wille, G., 2013. Relative chronology of deep circulations within the fractured basement of the Upper Rhine Graben 2.
- Dèzes, P., Schmid, S.M., Ziegler, P.A., 2004. Evolution of the European Cenozoic Rift System: interaction of the Alpine and Pyrenean orogens with their foreland lithosphere. *Tectonophysics* 389, 1–33. <https://doi.org/10.1016/j.tecto.2004.06.011>
- Dhansay, T., Navabpour, P., de Wit, M., Ustaszewski, K., 2017. Assessing the reactivation potential of pre-existing fractures in the southern Karoo, South Africa: Evaluating the

- potential for sustainable exploration across its Critical Zone. *Journal of African Earth Sciences* 134, 504–515. <https://doi.org/10.1016/j.jafrearsci.2017.07.020>
- Dokka, R.K., Travis, C.J., 1990. Role of the Eastern California Shear Zone in accommodating Pacific-North American Plate motion. *Geophysical Research Letters* 17, 1323–1326. <https://doi.org/10.1029/GL017i009p01323>
- Dubois, M., Ledésert, B., Potdevin, J.-L., Vançon, S., 2000. Détermination des conditions de précipitation des carbonates dans une zone d'altération du granite de Soultz (soubassement du fossé Rhénan, France) : l'enregistrement des inclusions fluides. *Comptes Rendus de l'Académie des Sciences - Series IIA - Earth and Planetary Science* 331, 303–309. [https://doi.org/10.1016/S1251-8050\(00\)01429-4](https://doi.org/10.1016/S1251-8050(00)01429-4)
- Dullien, F.A.L., 1979. *Porous Media: Fluid Transport and Pore Structure*. Academic Press, San Diego, USA.
- Eaton, G.P., 1982. The Basin and Range Province: Origin and Tectonic Significance. *Annual Review of Earth and Planetary Sciences* 10, 409–440. <https://doi.org/10.1146/annurev.ea.10.050182.002205>
- Edel, J.-B., Schulmann, K., 2009. Geophysical constraints and model of the “Saxothuringian and Rhenohercynian subductions – magmatic arc system” in NE France and SW Germany. *Bulletin de la Société Géologique de France* 180, 545–558. <https://doi.org/10.2113/gssgfbull.180.6.545>
- Edel, J.-B., Schulmann, K., Rotstein, Y., 2007. The Variscan tectonic inheritance of the Upper Rhine Graben: evidence of reactivations in the Lias, Late Eocene–Oligocene up to the recent. *International Journal of Earth Sciences* 96, 305–325. <https://doi.org/10.1007/s00531-006-0092-8>
- EOST, CNRS, 2021. Note d'information : Séisme du 26/6/2021 de magnitude M<sub>lv</sub> 3.9 à la Wantzenau (Nord de Strasbourg) [WWW Document]. URL <https://ites.unistra.fr/actualites/actualite/note-dinformation-seisme-du-26-6-2021-de-magnitude-mlv-39-a-la-wantzenau-nord-de-strasbourg> (accessed 9.27.21).
- European Commission, 2016. SET Plan - Declaration of intent on Strategic Targets in the context of an Initiative for Global Leadership in Deep Geothermal Energy [WWW Document]. URL [https://setis.ec.europa.eu/implementing-actions/set-plan-documents\\_da](https://setis.ec.europa.eu/implementing-actions/set-plan-documents_da) (accessed 10.3.21).
- Evans, J.P., Forster, C.B., Goddard, J.V., 1997. Permeability of fault-related rocks, and implications for hydraulic structure of fault zones. *Journal of Structural Geology* 19, 1393–1404. [https://doi.org/10.1016/S0191-8141\(97\)00057-6](https://doi.org/10.1016/S0191-8141(97)00057-6)
- Evans, K.F., 2005. Permeability creation and damage due to massive fluid injections into granite at 3.5 km at Soultz: 2. Critical stress and fracture strength. *Journal of Geophysical Research: Solid Earth* 110. <https://doi.org/10.1029/2004JB003169>

- Faulds, J., Coolbaugh, M., Bouchot, V., Moek, I., Oguz, K., 2010. Characterizing Structural Controls of Geothermal Reservoirs in the Great Basin, USA, and Western Turkey: Developing Successful Exploration Strategies in Extended Terranes 12.
- Faulds, J., Hinz, N., 2015. Favorable tectonic and structural settings of geothermal systems in the Great Basin region, western USA: Proxies for discovering blind geothermal systems. Proceedings World Geothermal Congress, Melbourne, Australia, 19-25 April 2015.
- Faulds, J.E., Coolbaugh, M., Blewitt, G., Henry, C.D., 2004. Why is Nevada in hot water? Structural controls and tectonic model of geothermal systems in the northwestern Great Basin. *Geothermal Resources Council Transactions* 28, 649–654.
- Faulds, J.E., Hinz, N., Kreemer, C., 2012. Structural and tectonic controls of geothermal activity in the Basin and Range Province, western USA. *New Zealand* 5.
- Faulds, J.E., Hinz, N.H., Dering, G.M., Siler, D.L., 2013. The Hybrid Model – The Most Accommodating Structural Setting for Geothermal Power Generation in the Great Basin, Western USA. *Geothermal Resources Council Transactions* 37, 3–10.
- Faulkner, D.R., Jackson, C.A.L., Lunn, R.J., Schlische, R.W., Shipton, Z.K., Wibberley, C.A.J., Withjack, M.O., 2010. A review of recent developments concerning the structure, mechanics and fluid flow properties of fault zones. *Journal of Structural Geology, Fault Zones* 32, 1557–1575. <https://doi.org/10.1016/j.jsg.2010.06.009>
- Ferreiro Mählmann, R., Bozkaya, Ö., Potel, S., Le Bayon, R., Šegvić, B., Nieto, F., 2012. The pioneer work of Bernard Kübler and Martin Frey in very low-grade metamorphic terranes: paleo-geothermal potential of variation in Kübler-Index/organic matter reflectance correlations. A review. *Swiss J Geosci* 105, 121–152. <https://doi.org/10.1007/s00015-012-0115-3>
- Ferreiro Mählmann, R., Frey, M., 2012. Standardisation, calibration and correlation of the Kübler-index and the vitrinite/bituminite reflectance: an inter-laboratory and field related study. *Swiss J Geosci* 105, 153–170. <https://doi.org/10.1007/s00015-012-0110-8>
- Fordham, A.W., 1989. Weathering of Biotite into D loctahedral Clay Minerals, *Clay Minerals*. ed. The Mineralogical Society of Great Britain and Ireland.
- Frankel, K., Glazner, A., Kirby, E., Monastero, F., Strane, M., Oskin, M., Unruh, J., Walker, J., Anandakrishnan, S., Bartley, J., Coleman, D., Dolan, J., Finkel, R., Greene, D., Kylander-Clark, A., Marrero, S., Owen, L., Phillips, F., 2008. Active tectonics of the eastern California shear zone. pp. 43–81. [https://doi.org/10.1130/2008.fld011\(03\)](https://doi.org/10.1130/2008.fld011(03))
- Frey, M., 1987. Very low-grade metamorphism of clastic sedimentary rocks. *Low Temperature Metamorphism* 9–58.
- Fridrich, C.J., Thompson, R.A., 2011. Cenozoic Tectonic Reorganizations of the Death Valley Region, Southeast California and Southwest Nevada, Professional Paper 1783. ed. U.S. Geological Survey, Reston, Virginia.

- Fuhrmann, U., Lippolt, H.J., Hess, J.C., 1987. Examination of some proposed K-Ar standards:  $^{40}\text{Ar}/^{39}\text{Ar}$  analyses and conventional  $^{K}/^{Ar}$  data. *Chemical Geology: Isotope Geoscience section* 66, 41–51. [https://doi.org/10.1016/0168-9622\(87\)90027-3](https://doi.org/10.1016/0168-9622(87)90027-3)
- Fulignati, P., 2020. Clay Minerals in Hydrothermal Systems. *Minerals* 10, 919. <https://doi.org/10.3390/min10100919>
- Garrels, R.M., MacKenzie, F.T., 1967. Origin of the Chemical Compositions of Some Springs and Lakes, in: *Equilibrium Concepts in Natural Water Systems, Advances in Chemistry. AMERICAN CHEMICAL SOCIETY*, pp. 222–242. <https://doi.org/10.1021/ba-1967-0067.ch010>
- Gates, W.P., Nefiodovas, A., Peter, P., 2004. Permeability of an Organo-Modified Bentonite to Ethanol-Water Solutions. *Clays and Clay Minerals* 52, 192–203. <https://doi.org/10.1346/CCMN.2004.0520205>
- Genevois, R., Prestininzi, A., 1979. Time-Dependent Behaviour Of Granitic Rocks Related To Their Alteration Grade. Presented at the 4th ISRM Congress, OnePetro.
- Genter, A., 1989. Géothermie roches chaudes sèches : le granite de Soultz-sous-Forêts (Bas-Rhin, France): fracturation naturelle, altérations hydrothermales et interaction eau-roche (PhD Thesis). Université d'Orléans, Orléans.
- Genter, A., Castaing, C., 1997. Effets d'échelle dans la fracturation des granites. *Comptes Rendus de l'Académie des Sciences - Series IIA - Earth and Planetary Science* 325, 439–445. [https://doi.org/10.1016/S1251-8050\(97\)81162-7](https://doi.org/10.1016/S1251-8050(97)81162-7)
- Genter, A., Evans, K., Cuenot, N., Fritsch, D., Sanjuan, B., 2010. Contribution of the exploration of deep crystalline fractured reservoir of Soultz to the knowledge of enhanced geothermal systems (EGS). *Comptes Rendus Geoscience, Vers l'exploitation des ressources géothermiques profondes des systèmes hydrothermaux convectifs en milieu naturellement fracturés* 342, 502–516. <https://doi.org/10.1016/j.crte.2010.01.006>
- Genter, A., Traineau, H., 1996. Analysis of macroscopic fractures in granite in the HDR geothermal well EPS-1, Soultz-sous-Forêts, France. *Journal of Volcanology and Geothermal Research* 72, 121–141. [https://doi.org/10.1016/0377-0273\(95\)00070-4](https://doi.org/10.1016/0377-0273(95)00070-4)
- Genter, A., Traineau, H., 1995. Fracture analysis in granite in the HDR geothermal EPS-1 well, Soultz-sous-Forêts, France.
- Genter, A., Traineau, H., 1992. Hydrothermally altered and fractured granite as an HDR reservoir in the EPS-1 borehole, Alsace, France. Presented at the Seventeenth Workshop on Geothermal Reservoir Engineering, p. 6.
- Genter, A., Traineau, H., Bourguin, B., Ledesert, B., Gentier, S., 2000. Over 10 years of geological investigations within the HDR Soultz Project, France.

- Genter, A., Traineau, H., Dezayes, C., Elsass, P., Ledésert, B., Meunier, A., Villemin, T., 1995. Fracture analysis and reservoir characterization of the granitic basement in the HRD Soultz project (France). *Geotherm. sci. technol* 4, 189–214.
- Gentier, S., Hopkins, D., Riss, J., 2000. Role of fracture geometry in the evolution of flow paths under stress, in: Faybishenko, B., Witherspoon, P.A., Benson, S.M. (Eds.), *Geophysical Monograph Series*. American Geophysical Union, Washington, D. C., USA, pp. 169–184. <https://doi.org/10.1029/GM122p0169>
- Gérard, A., Genter, A., Kohl, T., Lutz, P., Rose, P., Rummel, F., 2006. The deep EGS (Enhanced Geothermal System) project at Soultz-sous-Forêts (Alsace, France). *Geothermics* 35. <https://doi.org/10.1016/j.geothermics.2006.12.001>
- Géraud, Y., Rosener, M., Surma, F., Place, J., Le Garzic, É., Diraison, M., 2010. Physical properties of fault zones within a granite body: Example of the Soultz-sous-Forêts geothermal site. *Comptes Rendus Geoscience, Vers l'exploitation des ressources géothermiques profondes des systèmes hydrothermaux convectifs en milieux naturellement fracturés* 342, 566–574. <https://doi.org/10.1016/j.crte.2010.02.002>
- Géraud, Y., Surma, F., Rosener, M., 2005. Porosity network of Soultz-sous-Forêts granite: the importance of the damaged zone around faults and fractures. *Ecole et Observatoire des Sciences e le Terre: Strasbourg, France*.
- Gillespie, P.A., Holdsworth, R.E., Long, D., Williams, A., Gutmanis, J.C., 2020. Introduction: geology of fractured reservoirs. *Journal of the Geological Society* 178, jgs2020-197. <https://doi.org/10.1144/jgs2020-197>
- Gillespie, P.A., Howard, C.B., Walsh, J.J., Watterson, J., 1993. Measurement and characterisation of spatial distributions of fractures. *Tectonophysics, The origin of sedimentary basins: Inferences from quantitative modelling and basin analysis* 226, 113–141. [https://doi.org/10.1016/0040-1951\(93\)90114-Y](https://doi.org/10.1016/0040-1951(93)90114-Y)
- Glaas, C., 2021. Mineralogical and structural controls on permeability of deep naturally fractured crystalline reservoirs: Insights from geothermal wells (Upper Rhine Graben). *Université de Strasbourg, Strasbourg*.
- Glaas, C., Patrier, P., Vidal, J., Beaufort, D., Genter, A., 2021. Clay Mineralogy: A Signature of Granitic Geothermal Reservoirs of the Central Upper Rhine Graben. *Minerals* 11, 479. <https://doi.org/10.3390/min11050479>
- Glaas, C., Vidal, J., Patrier, P., Girard, J.-F., Beaufort, D., Petit, S., Genter, A., 2019. How Do Secondary Minerals in Granite Help Distinguish Paleo- from Present-Day Permeable Fracture Zones? Joint Interpretation of SWIR Spectroscopy and Geophysical Logs in the Geothermal Wells of Northern Alsace [WWW Document]. *Geofluids*. <https://doi.org/10.1155/2019/8231816>

- Glassley, W., Crossey, L., Montañez, I., 2016. Fluid–Rock Interaction, in: Encyclopedia of Geochemistry. Springer International Publishing, Switzerland. [https://doi.org/10.1007/978-3-319-39193-9\\_36-1](https://doi.org/10.1007/978-3-319-39193-9_36-1)
- Goddard, J.V., Evans, J.P., 1995. Chemical changes and fluid-rock interaction in faults of crystalline thrust sheets, northwestern Wyoming, U.S.A. *Journal of Structural Geology* 17, 533–547. [https://doi.org/10.1016/0191-8141\(94\)00068-B](https://doi.org/10.1016/0191-8141(94)00068-B)
- Goldich, S.S., 1938. A Study in Rock-Weathering. *The Journal of Geology* 46, 17–58. <https://doi.org/10.1086/624619>
- Götze, J., 2012. Application of Cathodoluminescence Microscopy and Spectroscopy in Geosciences. *Microscopy and Microanalysis* 18, 1270–1284. <https://doi.org/10.1017/S1431927612001122>
- Götze, J., 2000. Cathodoluminescence in Applied Geosciences, in: Pagel, M., Barbin, V., Blanc, P., Ohnenstetter, D. (Eds.), *Cathodoluminescence in Geosciences*. Springer, Berlin, Heidelberg, Germany. [https://doi.org/10.1007/978-3-662-04086-7\\_18](https://doi.org/10.1007/978-3-662-04086-7_18)
- Grammer, G.M., Harris, P., Eberli, G., 2004. Integration of outcrop and modern analogs in reservoir modeling / edited by G. Michael Grammer, Paul M. “Mitch” Harris, Gregor P. Eberli. SERBIULA (sistema Librum 2.0).
- Gresens, R.L., 1967. Composition-volume relationships of metasomatism. *Chemical Geology* 2, 47–65. [https://doi.org/10.1016/0009-2541\(67\)90004-6](https://doi.org/10.1016/0009-2541(67)90004-6)
- Griffiths, L., Heap, M.J., Wang, F., Daval, D., Gilg, H.A., Baud, P., Schmittbuhl, J., Genter, A., 2016. Geothermal implications for fracture-filling hydrothermal precipitation. *Geothermics* 64, 235–245. <https://doi.org/10.1016/j.geothermics.2016.06.006>
- Grimmer, J.C., Ritter, J.R.R., Eisbacher, G.H., Fielitz, W., 2017. The Late Variscan control on the location and asymmetry of the Upper Rhine Graben. *Int J Earth Sci (Geol Rundsch)* 106, 827–853. <https://doi.org/10.1007/s00531-016-1336-x>
- Haas, I.O., Hoffmann, C.R., 1929. Temperature Gradient in Pechelbronn Oil-Bearing Region, Lower Alsace: Its Determination and Relation to Oil Reserves1. *AAPG Bulletin* 13, 1257–1273. <https://doi.org/10.1306/3D932884-16B1-11D7-8645000102C1865D>
- Hadizadeh, J., Tullis, T.E., White, J.C., Konkachbaev, A.I., 2015. Shear localization, velocity weakening behavior, and development of cataclastic foliation in experimental granite gouge. *Journal of Structural Geology, Special Issue: Deformation of the lithosphere - How small structures tell a big story* 71, 86–99. <https://doi.org/10.1016/j.jsg.2014.10.013>
- Hafeznia, Y., Bourlange, S., Ohnenstetter, M., Flück, P., 2015. Post-meeting fieldtrip SGA 2015 meeting in Nacncy: Sainte-Marie-aux-Mines Gabe Gottes Mine.
- Heaman, L.M., Grotzinger, J.P., 1992. 1.08 Ga diabase sills in the Pahrump Group, California: Implications for development of the Cordilleran miogeocline. *Geology* 20, 637–640. [https://doi.org/10.1130/0091-7613\(1992\)020<0637:GDSITP>2.3.CO;2](https://doi.org/10.1130/0091-7613(1992)020<0637:GDSITP>2.3.CO;2)

- Hébert, R.L., Ledésert, B., Bartier, D., Dezayes, C., Genter, A., Grall, C., 2010. The Enhanced Geothermal System of Soultz-sous-Forêts: A study of the relationships between fracture zones and calcite content. *Journal of Volcanology and Geothermal Research* 196, 126–133. <https://doi.org/10.1016/j.jvolgeores.2010.07.001>
- Heinrichs, H., Herrmann, A.G., 2013. *Praktikum der Analytischen Geochemie*. Springer-Verlag.
- Henjes-Kunst, F., Prochaska, W., Niedermayr, A., Sullivan, N., Baxter, E., 2014. Sm–Nd dating of hydrothermal carbonate formation: An example from the Breitenau magnesite deposit (Styria, Austria). *Chemical Geology* 387, 184–201. <https://doi.org/10.1016/j.chemgeo.2014.07.025>
- Hill, M.L., Troxel, B.W., 1966. Tectonics of Death Valley Region, California. *GSA Bulletin* 77, 435–438. [https://doi.org/10.1130/0016-7606\(1966\)77\[435:TODVRC\]2.0.CO;2](https://doi.org/10.1130/0016-7606(1966)77[435:TODVRC]2.0.CO;2)
- Hoogland, O., Veenstra, E., Torres Vega, P.C., Saastamoinen, H., Kärki, J., 2019. Study on impacts of EU actions supporting the development of renewable energy technologies: Technology Sector Report, Bioenergy. European Commission EC.
- Huttrer, G., 2020. Geothermal Power Generation in the World 2015-2020 Update Report. Presented at the World Geothermal Congress, Reykjavik, p. 17.
- Ikari, M.J., Saffer, D.M., Marone, C., 2009. Frictional and hydrologic properties of clay-rich fault gouge. *Journal of Geophysical Research: Solid Earth* 114. <https://doi.org/10.1029/2008JB006089>
- Illies, J.H., 1972. The Rhine graben rift system-plate tectonics and transform faulting. *Geophysical Surveys* 1, 27–60. <https://doi.org/10.1007/BF01449550>
- Illies, J.H., Greiner, G., 1979. Holocene movements and state of stress in the rhinegraben rift system. *Tectonophysics, Recent Crustal Movements* 52, 349–359. [https://doi.org/10.1016/0040-1951\(79\)90245-2](https://doi.org/10.1016/0040-1951(79)90245-2)
- Inoue, A., 1995. Formation of Clay Minerals in Hydrothermal Environments, in: Velde, B. (Ed.), *Origin and Mineralogy of Clays*. Springer Berlin Heidelberg, Berlin, Heidelberg, Germany, pp. 268–329. [https://doi.org/10.1007/978-3-662-12648-6\\_7](https://doi.org/10.1007/978-3-662-12648-6_7)
- Ito, H., 2003. Inferred role of natural fractures, veins, and breccias in development of the artificial geothermal reservoir at the Ogachi Hot Dry Rock site, Japan. *Journal of Geophysical Research: Solid Earth* 108. <https://doi.org/10.1029/2001JB001671>
- Jacquemont, B., 2002. Etude des interactions eaux-roches dans le granite De Soultz-sous-Forets Quantification et modelisation des transferts de matiere par les fluides.
- Jagodzinski, H., 1949. Eindimensionale Fehlordnung in Kristallen und ihr Einfluss auf die Röntgeninterferenzen. I. Berechnung des Fehlordnungsgrades aus den Röntgenintensitäten. *Acta Cryst* 2, 201–207. <https://doi.org/10.1107/S0365110X49000552>
- Jennings, C.W., Burnett, J.L., Troxel, B.W., 1963. Geologic map of California: Trona sheet.

- Jensen, L.S., 1976. A new plot for classifying subalkalic volcanic rocks. Ontario Division of Mines, Miscellaneous Paper 66, 1–22.
- Kadko, D., Butterfield, D.A., 1998. The relationship of hydrothermal fluid composition and crustal residence time to maturity of vent fields on the Juan de Fuca Ridge. *Geochimica et Cosmochimica Acta* 62, 1521–1533. [https://doi.org/10.1016/S0016-7037\(98\)00088-X](https://doi.org/10.1016/S0016-7037(98)00088-X)
- Kajdas, B., Michalik, M.J., Migoń, P., 2017. Mechanisms of granite alteration into grus, Karkonosze granite, SW Poland. *CATENA* 150, 230–245. <https://doi.org/10.1016/j.catena.2016.11.026>
- Kanda, K., 1991. Energy dispersive X-ray spectrometer. U.S. Patent.
- Kanda, Kimio, 1991. Energy dispersive X-ray spectrometer. 5065020.
- Kisch, H.J., 1991. Illite crystallinity: recommendations on sample preparation, X-ray diffraction settings, and interlaboratory samples. *Journal of Metamorphic Geology* 9, 665–670. <https://doi.org/10.1111/j.1525-1314.1991.tb00556.x>
- Kisch, H.J., 1987. Correlation between indicators of very low-grade metamorphism. *Low temperature metamorphism* 227–300.
- Klee, J., Chabani, A., Ledésert, B.A., Potel, S., Hébert, R.L., Trullenque, G., 2021b. Fluid-Rock Interactions in a Paleo-Geothermal Reservoir (Noble Hills Granite, California, USA). Part 2: The Influence of Fracturing on Granite Alteration Processes and Fluid Circulation at Low to Moderate Regional Strain. *Geosciences* 11, 433. <https://doi.org/10.3390/geosciences11110433>
- Klee, J., Trullenque, G., Ledésert, B., Potel, S., Hébert, R., Chabani, A., Genter, A., 2020. Petrographic Analyzes of Fractured Granites used as An Analogue of the Soultz-sous-Forêts Geothermal Reservoir: Noble Hills, CA, USA. Presented at the Proceedings World Geothermal Congress 2020+1, Reykjavik, Iceland.
- Klee, Potel, S., Ledésert, B.A., Hébert, R.L., Chabani, A., Barrier, P., Trullenque, G., 2021a. Fluid-Rock Interactions in a Paleo-Geothermal Reservoir (Noble Hills Granite, California, USA). Part 1: Granite Pervasive Alteration Processes away from Fracture Zones. *Geosciences* 11, 325. <https://doi.org/10.3390/geosciences11080325>
- Koljonen, T., Rosenberg, R.J., 1974. Rare earth elements in granitic rocks. *Lithos* 7, 249–261. [https://doi.org/10.1016/0024-4937\(74\)90046-2](https://doi.org/10.1016/0024-4937(74)90046-2)
- Kominou, A., Yardley, B.W.D., 1997. Fluid-rock interactions in the Rhine Graben: A thermodynamic model of the hydrothermal alteration observed in deep drilling. *Geochimica et Cosmochimica Acta* 61, 515–531. [https://doi.org/10.1016/S0016-7037\(96\)00358-4](https://doi.org/10.1016/S0016-7037(96)00358-4)
- Kretz, R., 1983. Symbols for rock-forming minerals. *American Mineralogist* 68, 277–279.

- Kübler, B., 1967. La cristallinité de l'illite et les zones tout à fait supérieures du métamorphisme. *Etages tectoniques*, La Baconnière: Boudry, Switzerland 105–121.
- Kuncoro, G.B., 2015. Fluid-rock interaction studies on an enhanced geothermal system in the Cooper Basin, South Australia. (PhD Thesis). University of Adelaide, Adelaide, SA, Australia.
- Laubach, S., 2003. Practical approaches to identifying sealed and open fractures. *AAPG Bulletin* 87, 561–579. <https://doi.org/10.1306/11060201106>
- Laubach, S.E., Lamarche, J., Gauthier, B.D.M., Dunne, W.M., Sanderson, D.J., 2018. Spatial arrangement of faults and opening-mode fractures. *Journal of Structural Geology*, Spatial arrangement of fractures and faults 108, 2–15. <https://doi.org/10.1016/j.jsg.2017.08.008>
- Le Garzic, E., 2010. Distribution multi-échelle de la fracturation dans les réservoirs cristallins : influence de l'héritage structural. Exemples des marges obliques proximales du golfe d'Aden et de Catalogne (These de doctorat). Strasbourg.
- Le Garzic, E., de L'Hamaide, T., Diraison, M., Géraud, Y., Sausse, J., de Urreiztieta, M., Hauville, B., Champanhet, J.-M., 2011. Scaling and geometric properties of extensional fracture systems in the proterozoic basement of Yemen. Tectonic interpretation and fluid flow implications. *Journal of Structural Geology* 33, 519–536. <https://doi.org/10.1016/j.jsg.2011.01.012>
- Le Maître, R.W., Bateman, P., Dudek, A., Keller, J., Lameyre Le Bas, M.J., Sabine, P.A., Schmid, R., Sorensen, H., Streckeisen, A., Woolley, A.R., Zanettin, B., 1989. A classification of igneous rocks and glossary of terms. Blackwell, Oxford.
- Ledésert, B., Berger, G., Meunier, A., Genter, A., Bouchet, A., 1999. Diagenetic-type reactions related to hydrothermal alteration in the Soultz-sous-Forets Granite, France. *European Journal of Mineralogy* 11, 731–741.
- Ledésert, B., Dubois, J., Genter, A., Meunier, A., 1993. Fractal analysis of fractures applied to Soultz-sous-Forets hot dry rock geothermal program. *Journal of Volcanology and Geothermal Research* 57, 1–17. [https://doi.org/10.1016/0377-0273\(93\)90028-P](https://doi.org/10.1016/0377-0273(93)90028-P)
- Ledésert, B., Hébert, R., 2012. The Soultz-sous-Forêts' Enhanced Geothermal System: A Granitic Basement Used as a Heat Exchanger to Produce Electricity, in: *Heat Exchangers: Basics Design Applications*. Jovan Mitrovic, Rijeka, Croatia, pp. 477–504. <https://doi.org/10.5772/34276>
- Ledésert, B., Hébert, R., Genter, A., Bartier, D., Clauer, N., Grall, C., 2010. Fractures, hydrothermal alterations and permeability in the Soultz Enhanced Geothermal System. *Comptes Rendus Geoscience, Vers l'exploitation des ressources géothermiques profondes des systèmes hydrothermaux convectifs en milieux naturellement fracturés* 342, 607–615. <https://doi.org/10.1016/j.crte.2009.09.011>

- Ledésert, B., Hébert, R.L., Grall, C., Genter, A., Dezayes, C., Bartier, D., Gérard, A., 2009. Calcimetry as a useful tool for a better knowledge of flow pathways in the Soultz-sous-Forêts Enhanced Geothermal System. *Journal of Volcanology and Geothermal Research* 181, 106–114. <https://doi.org/10.1016/j.jvolgeores.2009.01.001>
- Ledésert, B.A., Hébert, R.L., 2020. How Can Deep Geothermal Projects Provide Information on the Temperature Distribution in the Upper Rhine Graben? The Example of the Soultz-Sous-Forêts-Enhanced Geothermal System. *Geosciences* 10, 459. <https://doi.org/10.3390/geosciences10110459>
- Li, X.-C., Fan, H.-R., Santosh, M., Hu, F.-F., Yang, K.-F., Lan, T.-G., 2013. Hydrothermal alteration associated with Mesozoic granite-hosted gold mineralization at the Sanshandao deposit, Jiaodong Gold Province, China. *Ore Geology Reviews* 53, 403–421. <https://doi.org/10.1016/j.oregeorev.2013.01.020>
- Lifton, Z.M., Newman, A.V., Frankel, K.L., Johnson, C.W., Dixon, T.H., 2013. Insights into distributed plate rates across the Walker Lane from GPS geodesy. *Geophysical Research Letters* 40, 4620–4624. <https://doi.org/10.1002/grl.50804>
- Liotta, D., Brogi, A., Ruggieri, G., Rimondi, V., Zucchi, M., Helgadóttir, H.M., Montegrossi, G., Friðleifsson, G.Ó., 2020. Fracture analysis, hydrothermal mineralization and fluid pathways in the Neogene Geitafell central volcano: insights for the Krafla active geothermal system, Iceland. *Journal of Volcanology and Geothermal Research* 391, 106502. <https://doi.org/10.1016/j.jvolgeores.2018.11.023>
- Liu, Y., Xie, C., Li, C., Li, S., Santosh, M., Wang, M., Fan, J., 2018. Breakup of the northern margin of Gondwana through lithospheric delamination: Evidence from the Tibetan Plateau. *GSA Bulletin* 131. <https://doi.org/10.1130/B31958.1>
- Long, J.C.S., Witherspoon, P.A., 1985. The relationship of the degree of interconnection to permeability in fracture networks. *Journal of Geophysical Research* 90, 3087. <https://doi.org/10.1029/JB090iB04p03087>
- Lopes Cardozo, G.G.O., Behrmann, J.H., 2006. Kinematic analysis of the Upper Rhine Graben boundary fault system. *Journal of Structural Geology, New dynamics in palaeostress analysis* 28, 1028–1039. <https://doi.org/10.1016/j.jsg.2006.03.010>
- Luckow, H., Pavlis, T., Serpa, L., Guest, B., Wagner, D., Snee, L., Hensley, T., Korjenkov, A., 2005. Late Cenozoic sedimentation and volcanism during transtensional deformation in Wingate Wash and the Owlshead Mountains, Death Valley. *Earth-Science Reviews* 73, 177–219. <https://doi.org/10.1016/j.earscirev.2005.07.013>
- Lund, J.W., Toth, A.N., 2021. Direct utilization of geothermal energy 2020 worldwide review. *Geothermics* 90, 101915. <https://doi.org/10.1016/j.geothermics.2020.101915>
- Lutz, S., Moore, J., Blamey, N., Norman, D., 2002. Fluid-inclusion gas chemistry of the Dixie Valley (NV) geothermal system. Presented at the Twenty-Seventh Workshop on Geothermal Reservoir Engineering, Stanford, California.

- Machette, M.N., Johnson, M.L., Slate, J.L., Klinger, R., Machette, M., Knott, J., Sarna-wojcicki, A., Block, D.L., Budahn, J.R., Crone, A.J., Dohrenwend, J.C., Fleck, R.J., Frankel, K., 2001. Quaternary and Late Pliocene Geology of the Death Valley Region: Recent Observations on Tectonics, Stratigraphy, and Lake Cycles (Guidebook for the 2001 Pacific Cell - Friends of the Pleistocene Fieldtrip), Chapter J.
- Mahon, R.C., Dehler, C.M., Link, P.K., Karlstrom, K.E., Gehrels, G.E., 2014a. Geochronologic and stratigraphic constraints on the Mesoproterozoic and Neoproterozoic Pahrump Group, Death Valley, California: A record of the assembly, stability, and breakup of Rodinia. *Geological Society of America Bulletin* 126, 652–664. <https://doi.org/10.1130/B30956.1>
- Mahon, R.C., Dehler, C.M., Link, P.K., Karlstrom, K.E., Gehrels, G.E., 2014b. Detrital zircon provenance and paleogeography of the Pahrump Group and overlying strata, Death Valley, California. *Precambrian Research* 251, 102–117. <https://doi.org/10.1016/j.precamres.2014.06.005>
- Maria Tartarello, Johnson, G., 2019. How do we see fractures? Quantifying subjective bias in fracture data collection. *Solid Earth* 10, 487–516. <https://doi.org/10.5194/se-10-487-2019>
- Marques, J.M., Matias, M.J., Basto, M.J., Carreira, P.M., Aires-Barros, L.A., Goff, F.E., 2010. Hydrothermal alteration of Hercynian granites, its significance to the evolution of geothermal systems in granitic rocks. *Geothermics* 39, 152–160. <https://doi.org/10.1016/j.geothermics.2010.03.002>
- McDonough, W., Sun, S.-S., Ringwood, A., Jagoutz, E., Hofmann, A., 1992. Potassium, rubidium, and cesium in the Earth and Moon and the evolution of the mantle of the Earth. *Geochimica et Cosmochimica Acta* 56, 1001–1012. [https://doi.org/10.1016/0016-7037\(92\)90043-I](https://doi.org/10.1016/0016-7037(92)90043-I)
- McGill, S.F., Wells, S.G., Fortner, S.K., Kuzma, H.A., McGill, J.D., 2009. Slip rate of the western Garlock fault, at Clark Wash, near Lone Tree Canyon, Mojave Desert, California. *Geological Society of America Bulletin* 121, 536–554. <https://doi.org/10.1130/B26123.1>
- Meller, C., Kohl, T., 2014. The significance of hydrothermal alteration zones for the mechanical behavior of a geothermal reservoir. *Geotherm Energy* 2, 12. <https://doi.org/10.1186/s40517-014-0012-2>
- Merriman, R.J., Frey, M., 1998. Patterns of Very Low-Grade Metamorphism in Metapelitic Rocks, in: Frey, Martin, Robinson, D. (Eds.), *Low-Grade Metamorphism*. Blackwell Publishing Ltd., Oxford, UK, pp. 61–107. <https://doi.org/10.1002/9781444313345.ch3>
- Meunier, A., 1995. Hydrothermal Alteration by Veins, in: Velde, B. (Ed.), *Origin and Mineralogy of Clays: Clays and the Environment*. Springer, Berlin, Heidelberg, pp. 247–267. [https://doi.org/10.1007/978-3-662-12648-6\\_6](https://doi.org/10.1007/978-3-662-12648-6_6)

- Meunier, A., Velde, B.D., Dudoignon, P., Beaufort, D., 1983. Identification of weathering and hydrothermal alteration in acidic rocks : petrography and mineralogy of clay minerals. *Sciences Géologiques, bulletins et mémoires* 72, 93–99.
- Miller, M., 2005. Geological landscapes of the Death Valley region☆. *Earth-Science Reviews* 73, 17–30. <https://doi.org/10.1016/j.earscirev.2005.07.010>
- Miller, M.B., Wright, L.A., 2015. *Geology of Death Valley National Park*. Kendall Hunt publishing company, Dubuque, IA, USA.
- Miller, M.M., Johnson, D.J., Dixon, T.H., Dokka, R.K., 2001. Refined kinematics of the eastern California shear zone from GPS observations, 1993–1998. *Journal of Geophysical Research: Solid Earth* 106, 2245–2263. <https://doi.org/10.1029/2000JB900328>
- Mitchell, T.M., Faulkner, D.R., 2012. Towards quantifying the matrix permeability of fault damage zones in low porosity rocks. *Earth and Planetary Science Letters* 339–340, 24–31. <https://doi.org/10.1016/j.epsl.2012.05.014>
- Mitchell, T.M., Faulkner, D.R., 2009. The nature and origin of off-fault damage surrounding strike-slip fault zones with a wide range of displacements: A field study from the Atacama fault system, northern Chile. *Journal of Structural Geology* 31, 802–816. <https://doi.org/10.1016/j.jsg.2009.05.002>
- Moeck, I.S., 2014. Catalog of geothermal play types based on geologic controls. *Renewable and Sustainable Energy Reviews* 37, 867–882. <https://doi.org/10.1016/j.rser.2014.05.032>
- Moir, H., Lunn, R.J., Shipton, Z.K., Kirkpatrick, J.D., 2010. Simulating brittle fault evolution from networks of pre-existing joints within crystalline rock. *Journal of Structural Geology, Fault Zones* 32, 1742–1753. <https://doi.org/10.1016/j.jsg.2009.08.016>
- Moore, D.M., Reynolds, R.C., 1989. *X-ray diffraction and the identification and analysis of clay minerals*. Oxford University PRes, Oxford, UK.
- Morellato, C., Redini, F., Doglioni, C., 2003. On the number and spacing of faults. *Terra Nova* 15, 315–321. <https://doi.org/10.1046/j.1365-3121.2003.00501.x>
- Mukherjee, S., 2011. Mineral fish: their morphological classification, usefulness as shear sense indicators and genesis. *Int J Earth Sci (Geol Rundsch)* 100, 1303–1314. <https://doi.org/10.1007/s00531-010-0535-0>
- Mullis, J., Mählmann, R.F., Wolf, M., 2017. Fluid inclusion microthermometry to calibrate vitrinite reflectance (between 50 and 270°C), illite Kübler-Index data and the diagenesis/anchizone boundary in the external part of the Central Alps. *Applied Clay Science* 143, 307–319. <https://doi.org/10.1016/j.clay.2017.03.023>
- Nagorsen-Rinke, S., Lee, J., Calvert, A., 2013. Pliocene sinistral slip across the Adobe Hills, eastern California–western Nevada: Kinematics of fault slip transfer across the Mina deflection. *Geosphere* 9, 37–53. <https://doi.org/10.1130/GES00825.1>

- Navelot, V., Géraud, Y., Favier, A., Diraison, M., Corsini, M., Lardeaux, J.-M., Verati, C., Mercier de Lépinay, J., Legendre, L., Beauchamps, G., 2018. Petrophysical properties of volcanic rocks and impacts of hydrothermal alteration in the Guadeloupe Archipelago (West Indies). *Journal of Volcanology and Geothermal Research* 360, 1–21. <https://doi.org/10.1016/j.jvolgeores.2018.07.004>
- Niemeijer, A.R., Spiers, C.J., Peach, C.J., 2008. Frictional behaviour of simulated quartz fault gouges under hydrothermal conditions: Results from ultra-high strain rotary shear experiments. *Tectonophysics* 460, 288–303. <https://doi.org/10.1016/j.tecto.2008.09.003>
- Niles, J.H., 2016. Post-middle pliocene tectonic development of the Noble Hills, southern Death Valley, California (PhD Thesis). San Francisco State University, San Francisco, CA, USA.
- Nishimoto, S., Yoshida, H., 2010. Hydrothermal alteration of deep fractured granite: Effects of dissolution and precipitation. *Lithos* 115, 153–162. <https://doi.org/10.1016/j.lithos.2009.11.015>
- Norton, I., 2011. Two-stage formation of Death Valley. *Geosphere* 7, 171–182. <https://doi.org/10.1130/GES00588.1>
- Numelin, T., Marone, C., Kirby, E., 2007. Frictional properties of natural fault gouge from a low-angle normal fault, Panamint Valley, California. *Tectonics* 26. <https://doi.org/10.1029/2005TC001916>
- Olasolo, P., Juárez, M.C., Morales, M.P., D'Amico, S., Liarte, I.A., 2016. Enhanced geothermal systems (EGS): A review. *Renewable and Sustainable Energy Reviews* 56, 133–144. <https://doi.org/10.1016/j.rser.2015.11.031>
- Olson, J.E., 1993. Joint pattern development: Effects of subcritical crack growth and mechanical crack interaction. *Journal of Geophysical Research: Solid Earth* 98, 12251–12265. <https://doi.org/10.1029/93JB00779>
- Parneix, J.C., Petit, J.C., 1991. Hydrothermal alteration of an old geothermal system in the Auriat granite (Massif Central, France): Petrological study and modelling. *Chemical Geology* 89, 329–351. [https://doi.org/10.1016/0009-2541\(91\)90023-K](https://doi.org/10.1016/0009-2541(91)90023-K)
- Parsons, T., 2006. Chapter 7 The basin and range province, in: Olsen, K.H. (Ed.), *Developments in Geotectonics, Continental Rifts: Evolution, Structure, Tectonics*. Elsevier, pp. 277–XV. [https://doi.org/10.1016/S0419-0254\(06\)80015-7](https://doi.org/10.1016/S0419-0254(06)80015-7)
- Passchier, C.W., Trouw, R.A.J., 2005. *Microtectonics*. Springer Science & Business Media.
- Pauwels, H., Fouillac, C., Criaud, A., 1992. Water-rock interactions during experiments within the geothermal Hot Dry Rock borehole GPK1, Soultz-sous-Forêts, Alsace, France. *Applied Geochemistry* 7, 243–255.
- Pauwels, H., Fouillac, C., Fouillac, A.-M., 1993. Chemistry and isotopes of deep geothermal saline fluids in the Upper Rhine Graben: Origin of compounds and water-rock

- interactions. *Geochimica et Cosmochimica Acta* 57, 2737–2749. [https://doi.org/10.1016/0016-7037\(93\)90387-C](https://doi.org/10.1016/0016-7037(93)90387-C)
- Pavlis, T.L., Trullenque, G., 2021. Evidence for 40–41 km of dextral slip on the southern Death Valley fault: Implications for the Eastern California shear zone and extensional tectonics. *Geology* 49, 767–772. <https://doi.org/10.1130/G48528.1>
- Place, J., 2010. Caractérisation des chemins de circulations de fluides dans le réseau poreux d'un batholite granitique: application au site géothermique de Soultz-sous-Forêts (These de doctorat). Strasbourg.
- Plumper, O., Putnis, A., 2009. The Complex Hydrothermal History of Granitic Rocks: Multiple Feldspar Replacement Reactions under Subsolidus Conditions. *Journal of Petrology* 50, 967–987. <https://doi.org/10.1093/petrology/egp028>
- Pribnow, D., Schellschmidt, R., 2000. Thermal tracking of upper crustal fluid flow in the Rhine graben. *Geophysical Research Letters* 27, 1957–1960. <https://doi.org/10.1029/2000GL008494>
- Priest, S.D., Hudson, J.A., 1976. Discontinuity spacings in rock. *International Journal of Rock Mechanics and Mining Sciences & Geomechanics Abstracts* 13, 135–148. [https://doi.org/10.1016/0148-9062\(76\)90818-4](https://doi.org/10.1016/0148-9062(76)90818-4)
- Que, M., Allen, A.R., 1996. Sericitization of plagioclase in the Rosses Granite Complex, Co. Donegal, Ireland. *Mineralogical Magazine* 60, 927–936. <https://doi.org/10.1180/minmag.1996.060.403.07>
- Quick, H., Michael, J., Huber, H., 2010. History of International Geothermal Power Plants and Geothermal Projects in Germany. Presented at the World Geothermal Congress, Bali, Indonesia, p. 5.
- Rämö, T.O., Calzia, J.P., Kosunen, P.J., 2002. Geochemistry of Mesozoic plutons, southern Death Valley region, California: Insights into the origin of Cordilleran interior magmatism. *Contrib Mineral Petrol* 143, 416–437. <https://doi.org/10.1007/s00410-002-0354-9>
- Rankin, A.H., 2005. Fluid inclusions, in: Selley, R.C., Cocks, L.R.M., Plimer, I.R. (Eds.), *Encyclopedia of Geology*. Elsevier, Oxford, pp. 253–260. <https://doi.org/10.1016/B0-12-369396-9/00097-6>
- Reinert, E., 2004. Low-temperature thermochronometry of the Avawatz Mountains, California: Implications for the inception of the Eastern California Shear Zone (PhD Thesis). University of Washington, Seattle, WA, USA.
- Rollinson, H.R., 1993. *Using Geochemical Data: Evaluation, Presentation, Interpretation*. Routledge, Abingdon, UK.
- Rosener, M., Géraud, Y., 2007. Using physical properties to understand the porosity network geometry evolution in gradually altered granites in damage zones. *Geological Society, London, Special Publications* 284, 175–184. <https://doi.org/10.1144/SP284.12>

- Rotstein, Y., Edel, J.-B., Gabriel, G., Boulanger, D., Schaming, M., Munsch, M., 2006. Insight into the structure of the Upper Rhine Graben and its basement from a new compilation of Bouguer Gravity. *Tectonophysics* 425, 55–70. <https://doi.org/10.1016/j.tecto.2006.07.002>
- Sanderson, D.J., Peacock, D.C.P., 2019. Line sampling of fracture swarms and corridors. *Journal of Structural Geology* 122, 27–37. <https://doi.org/10.1016/j.jsg.2019.02.006>
- Sanjuan, B., Millot, R., Dezayes, C., & Brach, M., 2010. Main characteristics of the deep geothermal brine (5 km) at Soultz-sous-Forêts (France) determined using geochemical and tracer test data. *Comptes Rendus Geoscience*, 342(7-8), 546-559. <https://doi.org/10.1016/j.crte.2009.10.009>
- Sanjuan, B., Millot, R., Innocent, C., Dezayes, C., Scheiber, J., Brach, M., 2016. Major geochemical characteristics of geothermal brines from the Upper Rhine Graben granitic basement with constraints on temperature and circulation. *Chemical Geology* 428, 27–47. <https://doi.org/10.1016/j.chemgeo.2016.02.021>
- Sardini, P., Ledésert, B., Touchard, G., 1997. Quantification of Microscopic Porous Networks By Image Analysis and Measurements of Permeability in the Soultz-Sous-Forêts Granite (Alsace, France), in: Jamtveit, B., Yardley, B.W.D. (Eds.), *Fluid Flow and Transport in Rocks: Mechanisms and Effects*. Springer Netherlands, Dordrecht, pp. 171–189. [https://doi.org/10.1007/978-94-009-1533-6\\_10](https://doi.org/10.1007/978-94-009-1533-6_10)
- Schleicher, A. V., van der Pluijm, B. A., & Warr, L. N. (2010). Nanocoatings of clay and creep of the San Andreas fault at Parkfield, California. *Geology*, 38(7), 667-670. <https://doi.org/10.1130/G31091.1>
- Schmid, S.M., Panozzo, R., Bauer, S., 1987. Simple shear experiments on calcite rocks: rheology and microfabric. *Journal of Structural Geology* 9, 747–778. [https://doi.org/10.1016/0191-8141\(87\)90157-X](https://doi.org/10.1016/0191-8141(87)90157-X)
- Schmidt, D., Schmidt, S.T., Mullis, J., Ferreiro Mählmann, R., Frey, M., 1997. Very low grade metamorphism of the Taveyanne formation of western Switzerland. *Contrib Mineral Petrol* 129, 385–403. <https://doi.org/10.1007/s004100050344>
- Schumacher, E., 1975. Herstellung von 99, 9997% <sup>38</sup>Ar für die <sup>40</sup>K/<sup>40</sup>Ar Geochronologie. *Geochronologia Chimia* 24, 441–442.
- Schumacher, M.E., 2002. Upper Rhine Graben: Role of preexisting structures during rift evolution. *Tectonics* 21, 6–1. <https://doi.org/10.1029/2001TC900022>
- Seebeck, H., Nicol, A., Walsh, J.J., Childs, C., Beetham, R.D., Pettinga, J., 2014. Fluid flow in fault zones from an active rift. *Journal of Structural Geology* 62, 52–64. <https://doi.org/10.1016/j.jsg.2014.01.008>
- Sidle, R. E., & Lee, W. J., 2010. An update on the use of reservoir analogs for the estimation of oil and gas reserves. In *SPE Hydrocarbon Economics and Evaluation Symposium*. OnePetro. <https://doi.org/10.2118/129688-MS>

- Smith, M.P., Savary, V., Yardley, B.W.D., Valley, J.W., Royer, J.J., Dubois, M., 1998. The evolution of the deep flow regime at Soultz-sous-Forêts, Rhine Graben, eastern France: Evidence from a composite quartz vein. *Journal of Geophysical Research: Solid Earth* 103, 27223–27237. <https://doi.org/10.1029/98JB02528>
- Song, S.J., Choo, C.O., Chang, C.J., Jang, Y.D., 2017. A microstructural study of the fault gouge in the granite, Yangbuk, Gyeongju, southeastern Korea, with implications for multiple faulting. *Geosci J* 21, 1–19. <https://doi.org/10.1007/s12303-016-0021-1>
- Spencer, J.E., 1990. Late Cenozoic extensional and compressional tectonism in the southern and western Avawatz Mountains, southeastern California, in: *Basin and Range Extensional Tectonics near the Latitude of Las Vegas, Nevada: Geological Society of America Memoir*. Boulder, CO, USA, pp. 317–333.
- Środoń, J., 1999. Nature of mixed-layer clays and mechanisms of their formation and alteration. *Annual Review of Earth and Planetary Sciences* 27, 19–53. <https://doi.org/10.1146/annurev.earth.27.1.19>
- Stamm, J.F., 1981. *Geology at the intersection of the Death Valley and Garlock fault zones, southern Death Valley, California*. Pennsylvania State University.
- Staněk, M., Géraud, Y., 2019. Granite microporosity changes due to fracturing and alteration: secondary mineral phases as proxies for porosity and permeability estimation. *Solid Earth* 10, 251–274. <https://doi.org/10.5194/se-10-251-2019>
- Starkey, H.C., Blackmon, P.D., Hauff, P.L., 1984. *The routine mineralogical analysis of clay-bearing samples (No. 1563)*. U.S. G.P.O., Washington, DC, USA. <https://doi.org/10.3133/b1563>
- Steiger, R.H., Jäger, E., 1977. Subcommission on geochronology: Convention on the use of decay constants in geo- and cosmochronology. *Earth and Planetary Science Letters* 36, 359–362. [https://doi.org/10.1016/0012-821X\(77\)90060-7](https://doi.org/10.1016/0012-821X(77)90060-7)
- Steiner, A., 1968. Clay Minerals in Hydrothermally Altered Rocks at Wairakei, New Zealand. *Clays Clay Miner.* 16, 193–213. <https://doi.org/10.1346/CCMN.1968.0160302>
- Stewart, J.H., 1983. Extensional tectonics in the Death Valley area, California: Transport of the Panamint Range structural block 80 km northwestward. *Geology* 11, 153–157. [https://doi.org/10.1130/0091-7613\(1983\)11<153:ETITDV>2.0.CO;2](https://doi.org/10.1130/0091-7613(1983)11<153:ETITDV>2.0.CO;2)
- Stewart, J.H., Ernst, W.G., 1988. Tectonics of the Walker Lane belt, western Great Basin: Mesozoic and Cenozoic deformation in a zone of shear. *Metamorphism and crustal evolution of the western United States* 7, 683–713.
- Stipp, M., Kunze, K., 2008. Dynamic recrystallization near the brittle-plastic transition in naturally and experimentally deformed quartz aggregates. *Tectonophysics* 448, 77–97. <https://doi.org/10.1016/j.tecto.2007.11.041>

- Streckeisen, A., 1973. Classification and Nomenclature of Plutonic Rocks: Recommendations of the IUGS Subcommittee on the Systematics of Igneous Rocks. *GeoTimes* 18, 26–30. <https://doi.org/10.1007/BF01820841>.
- Sun, S.-., McDonough, W.F., 1989. Chemical and isotopic systematics of oceanic basalts: implications for mantle composition and processes. Geological Society, London, Special Publications 42, 313–345. <https://doi.org/10.1144/GSL.SP.1989.042.01.19>
- Tardy, Y., Paquet, H., Millot, G., 1970. Trois modes de genèse des montmorillonites dans les altérations et les sols. *Bulletin du Groupe français des Argiles* 22, 69–77. <https://doi.org/10.3406/argil.1970.1120>
- Terzaghi, R.D., 1965. Sources of Error in Joint Surveys. *Géotechnique* 15, 287–304. <https://doi.org/10.1680/geot.1965.15.3.287>
- Tilley, C.E., 1925. A Preliminary Survey of Metamorphic Zones in the Southern Highlands of Scotland. *Quarterly Journal of the Geological Society* 81, 100–112. <https://doi.org/10.1144/GSL.JGS.1925.081.01-04.05>
- Tomasini-Montenegro, C., Santoyo-Castelazo, E., Gujba, H., Romero, R.J., Santoyo, E., 2017. Life cycle assessment of geothermal power generation technologies: An updated review. *Applied Thermal Engineering* 114, 1119–1136. <https://doi.org/10.1016/j.applthermaleng.2016.10.074>
- Traineau, H., Genter, A., Cautru, J.P., Fabriol, H., Chevremont, P., 1991. Petrography of the granite massif from drill cutting analysis and well log interpretation in the geothermal HDR borehole GPK1 (Soultz, Alsace, France). *Geotherm. sci. technol* 3, 1–29.
- Troxel, B.W., 1994. Right-lateral offset of ca. 28 km along a strand of the southern Death Valley fault zone. *California: Geological Society of America Abstracts with Programs* 26, 99.
- Troxel, B.W., Butler, P.R., 1979. Rate of Cenozoic Slip on Normal Faults, South-central Death Valley, California. Department of Geology, University of California, Berkeley, CA, USA.
- Trullenque, G., Genter, A., Leiss, B., Wagner, B., Bouchet, R., Leoutre, E., Malnar, B., Bär, K., Rajšl, I., 2018. Upscaling of EGS in Different Geological Conditions: a European Perspective. *Proceedings, 43rd Workshop on Geothermal Reservoir Engineering* Stanford University, Stanford, CA, USA 10.
- Turpault, M.-P., Berger, G., Meunier, A., 1992. Dissolution-precipitation processes induced by hot water in a fractured granite Part 1: Wall-rock alteration and vein deposition processes. *ejm* 4, 1457–1476. <https://doi.org/10.1127/ejm/4/6/1457>
- Ukar, E., Laubach, S. E., & Hooker, J. N., 2019. Outcrops as guides to subsurface natural fractures: Example from the Nikanassin Formation tight-gas sandstone, Grande Cache, Alberta foothills, Canada. *Marine and Petroleum Geology*, 103, 255-275. <https://doi.org/10.1016/j.marpetgeo.2019.01.039>
- Van der Pluijm, B.A., Marshak, S., 2004. *Earth structure: an introduction to structural geology and tectonics*, 2nd ed. ed. W.W. Norton, New York.

- Van Driessche, A.E.S., Stawski, T.M., Kellermeier, M., 2019. Calcium sulfate precipitation pathways in natural and engineered environments. *Chemical Geology* 530, 119274. <https://doi.org/10.1016/j.chemgeo.2019.119274>
- Velde, B., 1977. *Clays and Clay Minerals in Natural and Synthetic Systems, Development in sedimentology*. ed. Elsevier, Amsterdam, Oxford, New-York.
- Verosub, K.L., Brady, R.H., III, Abrams, M., 1989. Kinematics at the intersection of the Garlock and Death Valley fault zones, California: Integration of TM data and field studies.
- Vidal, J., 2017. *Altérations hydrothermales associées aux zones de fractures à l'interface de la couverture sédimentaire et du socle cristallin dans le Fossé rhénan supérieur : application aux forages géothermiques de Rittershoffen (Alsace, France) (These de doctorat)*. Strasbourg.
- Vidal, J., Genter, A., 2018. Overview of naturally permeable fractured reservoirs in the central and southern Upper Rhine Graben: Insights from geothermal wells. *Geothermics* 74, 57–73. <https://doi.org/10.1016/j.geothermics.2018.02.003>
- Vidal, J., Genter, A., Chopin, F., 2017. Permeable fracture zones in the hard rocks of the geothermal reservoir at Rittershoffen, France - Vidal - 2017 - *Journal of Geophysical Research: Solid Earth* - Wiley Online Library. *Journal of Geophysical Research: Solid Earth* 4864–4887. <https://doi.org/10.1002/2017JB014331>
- Vidal, J., Genter, A., Schmittbuhl, J., 2016. Pre- and post-stimulation characterization of geothermal well GRT-1, Rittershoffen, France: insights from acoustic image logs of hard fractured rock. *Geophysical Journal International* 206, 845–860. <https://doi.org/10.1093/gji/ggw181>
- Vidal, J., Patrier, P., Genter, A., Beaufort, D., Dezayes, C., Glaas, C., Lerouge, C., Sanjuan, B., 2018. Clay minerals related to the circulation of geothermal fluids in boreholes at Rittershoffen (Alsace, France). *Journal of Volcanology and Geothermal Research* 349, 192–204. <https://doi.org/10.1016/j.jvolgeores.2017.10.019>
- Villemin, T., Bergerat, F., 1987. L'évolution structurale du fosse rhenan au cours du Cenozoïque ; un bilan de la déformation et des effets thermiques de l'extension. *Bulletin de la Société Géologique de France* III, 245–255. <https://doi.org/10.2113/gssgfbull.III.2.245>
- Wallace, R.E., Morris, H.T., 1986. Characteristics of faults and shear zones in deep mines. *PAGEOPH* 124, 107–125. <https://doi.org/10.1007/BF00875721>
- Warr, L.N., Cox, S.C., 2016. Correlating illite (Kübler) and chlorite (Árkai) “crystallinity” indices with metamorphic mineral zones of the South Island, New Zealand. *Applied Clay Science, Clay mineral indices in palaeo-geothermal and hydrothermal studies* 134, 164–174. <https://doi.org/10.1016/j.clay.2016.06.024>
- Warr, L.N., Mählmann, R.F., 2015. Recommendations for Kübler Index standardization. *Clay Minerals* 50, 283–286. <https://doi.org/10.1180/claymin.2015.050.3.02>

- Warr, L.N., Rice, A.H.N., 1994a. Interlaboratory standardization and calibration of day mineral crystallinity and crystallite size data. *Journal of Metamorphic Geology* 12, 141–152. <https://doi.org/10.1111/j.1525-1314.1994.tb00010.x>
- Warr, L.N., Rice, A.H.N., 1994b. Interlaboratory standardization and calibration of day mineral crystallinity and crystallite size data. *Journal of Metamorphic Geology*.
- Wemmer, K., 1991. K/Ar-Altersdatierungsmöglichkeiten für retrograde Deformationsprozesse im spröden und duktilen Bereich--Beispiele aus der KTB-Vorbohrung (Oberpfalz) und dem Bereich der Insubrischen Linie (N-Italien). Im Selbstverlag der Geologischen Institute der Georg-August-Universität Göttingen, Göttingen.
- Werner, W., 2004. Lagerstätten und Bergbau im Schwarzwald: ein Führer unter besonderer Berücksichtigung der für die Öffentlichkeit zugänglichen Bergwerke. Landesamt für Geologie, Rohstoffe und Bergbau Baden-Württemberg.
- Werner, W., 2002. Die Erzlagerstätte Schauinsland bei Freiburg im Breisgau: Bergbau, Geologie, Hydrogeologie, Mineralogie, Geochemie, Tektonik und Lagerstättenentstehung, Aedificatio-Verlag. ed.
- Wernicke, B., Axen, G.J., Snow, J.K., 1988. Basin and Range extensional tectonics at the latitude of Las Vegas, Nevada. *GSA Bulletin* 100, 1738–1757. [https://doi.org/10.1130/0016-7606\(1988\)100<1738:BARETA>2.3.CO;2](https://doi.org/10.1130/0016-7606(1988)100<1738:BARETA>2.3.CO;2)
- Wernicke, B., Spencer, J.E., Burchfiel, B.C., Guth, P.L., 1982. Magnitude of crustal extension in the southern Great Basin. *Geology* 10, 499–502. [https://doi.org/10.1130/0091-7613\(1982\)10<499:MOCEIT>2.0.CO;2](https://doi.org/10.1130/0091-7613(1982)10<499:MOCEIT>2.0.CO;2)
- White, A.F., Schulz, M.S., Lowenstern, J.B., Vivit, D.V., Bullen, T.D., 2005. The ubiquitous nature of accessory calcite in granitoid rocks: Implications for weathering, solute evolution, and petrogenesis. *Geochimica et Cosmochimica Acta* 69, 1455–1471. <https://doi.org/10.1016/j.gca.2004.09.012>
- White, A.J.R., Chappell, B.W., 1983. Granitoid types and their distribution in the Lachlan Fold Belt, southeastern Australia, in: *Circum-Pacific Plutonic Terranes*. Geological Society of America, Boulder, CO, USA, pp. 21–34. <https://doi.org/10.1130/MEM159-p21>
- Williams, A.E., McKibben, M.A., 1989. A brine interface in the Salton Sea Geothermal System, California: Fluid geochemical and isotopic characteristics. *Geochimica et Cosmochimica Acta* 53, 1905–1920. [https://doi.org/10.1016/0016-7037\(89\)90312-8](https://doi.org/10.1016/0016-7037(89)90312-8)
- Williams, C.F., Reed, M.J., Anderson, A.F., 2011. Updating the classification of geothermal resources. *Proceedings, Thirty Sixth Workshop on Geothermal Reservoir Engineering* Stanford University, Stanford, CA, USA.
- Wilson, M., 1989. Review of igneous petrogenesis: A global tectonic approach. *Terra Nova* 1, 218–222. <https://doi.org/10.1111/j.1365-3121.1989.tb00357.x>
- Winkler, H.G.F., 1979. Anatexis, Formation of Migmatites, and Origin of Granitic Magmas, in: Winkler, H.G.F. (Ed.), *Petrogenesis of Metamorphic Rocks*, Springer Study Edition.

- Springer, New York, NY, pp. 283–339. [https://doi.org/10.1007/978-1-4757-4215-2\\_18](https://doi.org/10.1007/978-1-4757-4215-2_18)
- Wittenbrink, J., 1999. Diplomkartierung (Teil A) Petrographische und tektonische Kartierung des Zentralschwarzwälder Gneiskomplexes im Bereich der Blei – Zink – Lagerstätte Schauinsland bei Freiburg i. Br./Schwarzwald.
- Woodcock, N.H., Dickson, J.A.D., Tarasewicz, J.P.T., 2007. Transient permeability and reseat hardening in fault zones: evidence from dilation breccia textures. *Geological Society, London, Special Publications* 270, 43–53. <https://doi.org/10.1144/GSL.SP.2007.270.01.03>
- Wooden, J.L., Miller, D.M., 1990. Chronologic and isotopic framework for Early Proterozoic crustal evolution in the eastern Mojave Desert Region, SE California. *Journal of Geophysical Research: Solid Earth* 95, 20133–20146. <https://doi.org/10.1029/JB095iB12p20133>
- Wright, L., 1976. Late Cenozoic fault patterns and stress fields in the Great Basin and westward displacement of the Sierra Nevada block. *Geology* 4, 489–494. [https://doi.org/10.1130/0091-7613\(1976\)4<489:LCFPAS>2.0.CO;2](https://doi.org/10.1130/0091-7613(1976)4<489:LCFPAS>2.0.CO;2)
- Wright, L.A., Troxel, B.W., Williams, E.G., Roberts, M.T., Diehl, P.E., 1974. Precambrian Sedimentary Environments of the Death Valley Region, Eastern California [WWW Document]. URL [http://www.muststayawake.com/SDAG/library/Wright\\_etal\(CDMG-SR106\).pdf](http://www.muststayawake.com/SDAG/library/Wright_etal(CDMG-SR106).pdf) (accessed 10.5.21).
- Zhou, W., Wang, Z.L., 2007. *Scanning Microscopy for Nanotechnology: Techniques and Applications*. Springer Science & Business Media, Berlin/Heidelberg, Germany.
- Ziegler, P.A., 1992. European Cenozoic rift system. *Tectonophysics, Geodynamics of rifting, volume 1 Case history studies on rifts: Europe and Asia* 208, 91–111. [https://doi.org/10.1016/0040-1951\(92\)90338-7](https://doi.org/10.1016/0040-1951(92)90338-7)

## APPENDICES

---

The following pages provide the captions of two appendices presented in the manuscript, and then the associated content on the remainder of the pages.

**Appendix 1:** A co-author contribution written as first author by Arezki Chabani in the *Geosciences Journal*, in the 2021 special issue “Enhanced Geothermal Systems and other Deep Geothermal Applications throughout Europe: The MEET Project”.

*Reference:* Chabani, A., Trullenque, G., Ledésert, B.A., Klee, J., 2021. Multiscale Characterization of Fracture Patterns: A Case Study of the Noble Hills Range (Death Valley, CA, USA), Application to Geothermal Reservoirs. *Geosciences* 11, 280. <https://doi.org/10.3390/geosciences11070280>.

**Appendix 2:** The Geological map of the Noble Hills, Southern Death Valley, California realized by John H. Niles and S. John Caskey in 2014.

**Appendix 3:** The preliminary work conducted on the Noble Hills granite and accepted for presentation at the *World Geothermal Congress 2020*. This work is the preliminary petrographical characterization of the Noble Hills granite compared to the Soultz-sous-Forêts granite.

*Reference:* Klee, J., Trullenque, G., Ledésert, B., Potel, S., Hébert, R., Chabani, A., Genter, A., 2020. Petrographic Analyzes of Fractured Granites used as An Analogue of the Soultz-sous-Forêts Geothermal Reservoir: Noble Hills, CA, USA. Presented at the Proceedings World Geothermal Congress 2020+1, Reykjavik, Iceland.



*APPENDIX 1*

Original paper



## Article

# Multiscale Characterization of Fracture Patterns: A Case Study of the Noble Hills Range (Death Valley, CA, USA), Application to Geothermal Reservoirs

Arezki Chabani <sup>1,\*</sup> , Ghislain Trullenque <sup>1</sup>, Béatrice A. Ledéseret <sup>2</sup>  and Johanne Klee <sup>1</sup> 

<sup>1</sup> UniLaSalle, UPJV, B2R UMR 2018.C100, U2R 7511, 19 rue Pierre Waguët, F-60026 Beauvais, France; ghislain.trullenque@unilasalle.fr (G.T.); johanne.klee@unilasalle.fr (J.K.)

<sup>2</sup> Geosciences and Environnement Cergy, CY Cergy Paris Université, 1 rue Descartes, F-95000 Neuville sur Oise, France; beatrice.ledesert@cyu.fr

\* Correspondence: arezki.chabani@unilasalle.fr; Tel.: +33-6-58-07-14-14

**Abstract:** In the basement fractured reservoirs, geometric parameters of fractures constitute the main properties for modeling and prediction of reservoir behavior and then fluid flow. This study aims to propose geometric description and quantify the multiscale network organization and its effect on connectivity using a wide-ranging scale analysis and orders scale classification. This work takes place in the Noble Hills (NH) range, located in the Death Valley (DV, USA). The statistical analyses were performed from regional maps to thin sections. The combination of the length datasets has led to compute a power law exponent around  $-2$ , meaning that the connectivity is ruled by the small and the large fractures. Three domains have been highlighted in the NH: (1) domain A is characterized by a dominance of the NW/SE direction at the fourth order scale; (2) domain B is characterized by a dominance of the E/W and the NW/SE directions at respectively the fourth and third order scales; (3) domain C is also marked by the E/W direction dominance followed by the NW/SE direction respectively at the fourth and third order scale. The numerical simulations should consider that the orientation depends on scale observation, while the length is independent of scale observation.

**Keywords:** fracture network; Death Valley; Noble Hills; power law distribution; multiscale analysis; geothermal reservoir characterization



**Citation:** Chabani, A.; Trullenque, G.; Ledéseret, B.A.; Klee, J. Multiscale Characterization of Fracture Patterns: A Case Study of the Noble Hills Range (Death Valley, CA, USA), Application to Geothermal Reservoirs. *Geosciences* **2021**, *11*, 280. <https://doi.org/10.3390/geosciences11070280>

Academic Editors: Jesus Martinez-Frias and Gianluca Groppelli

Received: 10 June 2021

Accepted: 30 June 2021

Published: 3 July 2021

**Publisher's Note:** MDPI stays neutral with regard to jurisdictional claims in published maps and institutional affiliations.



**Copyright:** © 2021 by the authors. Licensee MDPI, Basel, Switzerland. This article is an open access article distributed under the terms and conditions of the Creative Commons Attribution (CC BY) license (<https://creativecommons.org/licenses/by/4.0/>).

## 1. Introduction

Fluid flow in fractured rocks of very low matrix permeability is localized mainly in few fractures [1]. The complex geometry of fracture and fault patterns is the main cause of the complexity of fluid flow. In that case, numerous studies have been undertaken worldwide to show the control of the fracture network on the fluid circulations especially in hydrocarbon and aquifers reservoirs [2–5], in heat transfer [6], and thus also in geothermal reservoirs [7–9].

A fracture system is characterized by geometrical parameters as fracture lengths, spacings, orientations, and relations between them [1,10–12]. In order to access hierarchical and mechanical relationships between fracture systems, many authors undertook a multiscale approach, in sedimentary [2,12–15], and in Crystalline [16–20] rocks. This approach allows to model and predict hydraulic reservoir properties, by studying several geometric attributes, such as the distribution of orientations, lengths, widths, spacings and densities classically considered in spatial arrangement analysis [21–24].

The geometric parameters are commonly collected for (1) explicitly constructing deterministic models (Discrete Fracture Network: DFNs, [2]) or (2) ensuring inputs of stochastic simulations by determining fracture distribution functions from sampled fracture networks [23,25–27]. The main goal is to better understand the fracture network connectivity and then the fluid flow patterns [3,22,28]. Subsequently, the main question is whether

data correspond to scale-limited lognormal or exponential distributions, or scale-invariant power laws, corresponding to fractal patterns? Several orders of magnitude based on length and spacing characteristics are thus mandatory to establish scaling laws from statistical distributions [29]. These orders of magnitude have been widely described in the literature in extensional [17,20,30] and trans-tensional [17] contexts. It consists of: (1) first order scale related to the crustal faults larger than 100 km length, (2) second order scale refers to the faults comprised between 20 and 30 km length, (3) third order scale refers to faults around 10 km length, (4) and the fourth order refers to faults under 1 km length [20]. In the extensional regime, [30] having defined a spacing characteristic for the two first order scales, with a 10 to 15 km spacing for first order and 3 to 8 km for the second order scale; while [20] have defined 0.8 to 1.5 km spacing for the third order scale. However, the fourth order spacing characteristic is not defined in the literature.

Fracture networks impact the fluid flow in reservoirs [23]. The 2D/3D seismic lines and 1D borehole data cannot detect respectively the fracture geometries and the spatial arrangement at the reservoir scale due to the lack of information [31]. Then, the spatial arrangement of fracture networks are widely studied from field analogues [16,23,29,32], as they give access to 2D and 3D distributions. In geothermal basement setting, the analogues are chosen according to the lithology and geological context to get closer to the reservoir conditions. Sometimes, the analogue is chosen in desert conditions, without vegetation, perfectly suited for realistic multiscale fracture network reconstructions in 2D, and in 3D in case of modeling canyons with photogrammetric [33] or lidar [34] approaches.

The present work is part of the MEET project (Multidisciplinary and multi-context demonstration of EGS exploration and Exploitation Techniques and potentials, [35]), which aims to develop geothermal exploitation at European scale by applying Enhanced Geothermal System (EGS) technology to different geological contexts. This study aims to propose geometric description and quantify the multiscale network organization and its effect on connectivity. A wide-ranging scale analysis from the microscopic scale to the regional scale was conducted in the desert environment of Noble Hills (NH) fractured granitic basement. It is located in the southern termination of Death Valley (DV, California, USA) and assimilated to a paleo geothermal analogue. The NH range is considered as analogue to the Soultz-sous-Forêts (SsF) geothermal electricity producing system, due to the granitic nature, the alteration and the trans-tensional tectonic setting of the DV region [36,37].

Measurements have been performed at various scales using the DV regional map [38] at 1:250,000, NH regional map based on previous studies undertaken by [37,39] and orthophoto images taken for the present day. At outcrop scale, fractures are digitized thanks to the photogrammetric models. Several 2D fracture maps are also used, as well as additional scales on samples and in thin sections. This allows to integrate fracture lengths ranging from micrometer to kilometer scales.

In this study, the multiscale approach is used to better understand the spatial arrangement of the fracture networks which aims at producing the necessary data for DFN modeling. This helps to better characterize reservoirs in response to the developing geothermal exploration and exploitation by EGS. This study is conducted through:

1. a 2D characterization of the NH fracture network;
2. a multiscale evolution of length distributions;
3. evaluate the fracture system in the complex tectonic and geometrical setting;
4. present a conceptual scheme of the NH fracture network organization, and the role of each fracture order of magnitude on the connectivity.

## 2. Geological Setting

The present study takes place in the NH fractured granitic zone, located at the southern termination of the Death Valley (DV, California, USA) (Figure 1a). The NH range is assimilated to a paleo geothermal analogue [37]. Indeed, Reference [37] confirmed the analogy between the DV region and Soultz-sous-Forêts reservoir (Rhine graben, East of France), with many similarities, especially: (1) the trans-tensional tectonic setting of the DV,

and (2) the granitic nature and hydrothermal alteration of the central part of the NH range. Furthermore, the desert conditions of the NH range make this analogue perfectly suited for multiscale characterization of fracture networks dedicated to the global understanding of the spatial arrangement in granitic reservoir affected by trans-tensional tectonics [35].

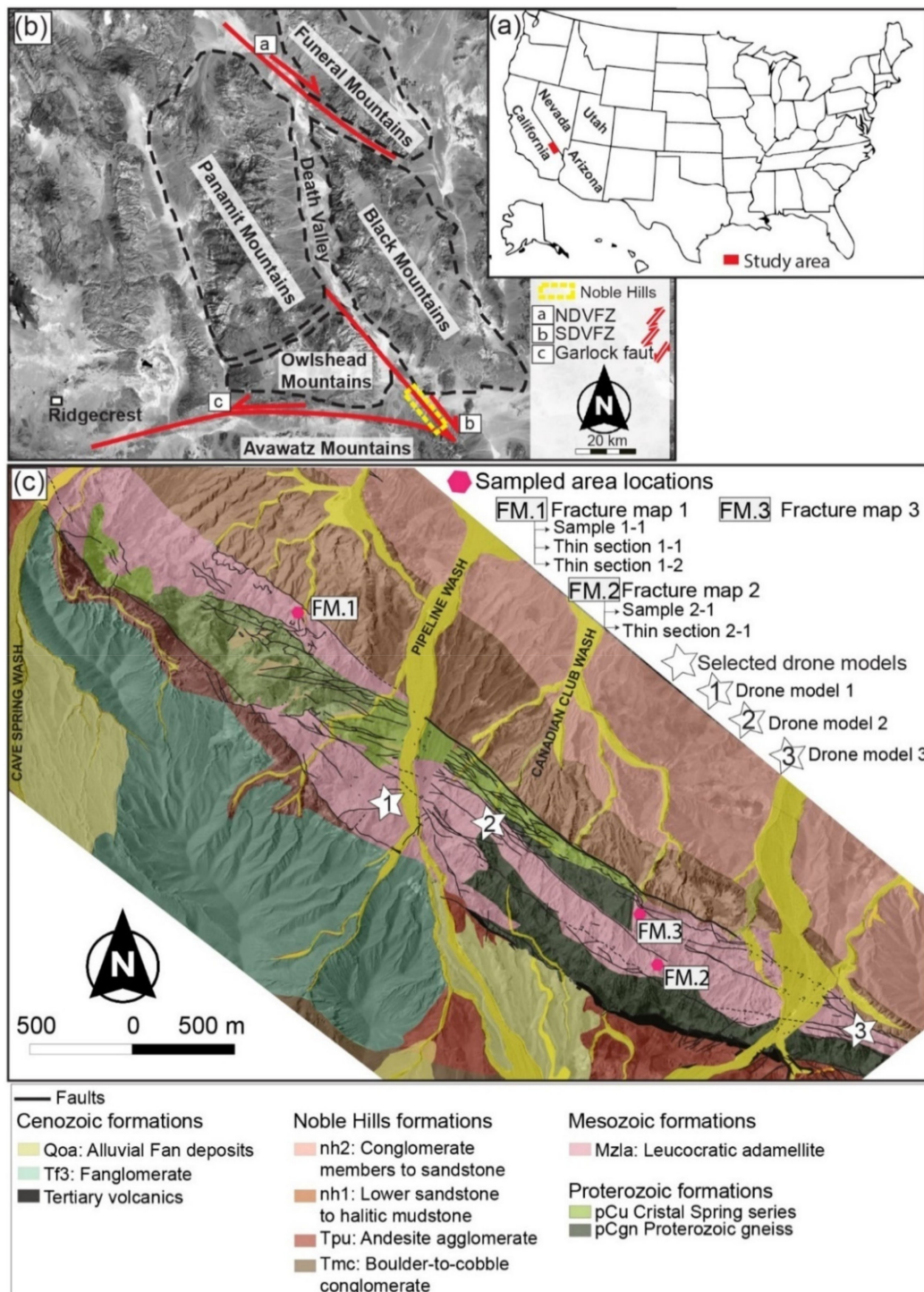


**Figure 1.** (a,b) Location and geological setting of DV, NDVFZ: Northern Death Valley Fault Zone, SDVFZ: Southern Death Valley Fault Zone; (c) Structural scheme of the NH range built using high-resolution digital mapping techniques modified after [37,39]. Additional digitized fractures were performed using orthophotos. The aerial picture in (b) was extracted from Google Earth®. The samples location was reported in the structural scheme. FM: fracture map.

The DV region has been characterized by a complex structural and tectonic history which includes the overprinting of Mesozoic to early Cenozoic contractional structures by late Cenozoic extensional and trans-tensional features [40–42]. The northwest trending contractional structures of the DV are at the origin of the Cordilleran orogenic belt of North America, which extends more than 6000 km from southern Mexico to the Canadian Arctic and Alaska [43]. Their age is estimated around 100 Ma and coincides with the Sevier orogenic belt [43,44]. The northeast trend is related to a thrust faults system [41].

The Mesozoic period was marked by the beginning of pluton emplacement in DV along the development of contractional structures. Then, during the Cenozoic period, the DV extension episode occurred [45,46], but there is no general agreement about its timing, e.g. [45,47]. The Miocene period was characterized by a trans-tensional regime. The opening of the DV region as a pull-apart basin began around 5 Ma [41,48–50]. A recent study done by [51] challenges this, mentioning that the opening of DV region into pull-apart basin started around 12 Ma ago.

Located in the southernmost part of the DV, the NH range trends parallel to, and then forms, the main topographic features aligned with components of the right-lateral Southern Death Valley Fault Zone (SDVFZ) [37] (Figure 1b). This SDVFZ is part of the Death Valley fault system (DVFS) [52], and its net dextral strike-slip displacement has been estimated around 40–41 km [51]. The northeast-vergent contractional deformation has been characterized along the length of the NH and constitutes the dominant structural style [48,53,54]. In the NH foreland basin, compressional structures have been characterized by [39] near the Canadian Club Wash (Figure 1c). An entire compressional region has also been created by the interaction between the SDVFZ and the GF zone, which is responsible for shortening within the Avawatz Mountains [55,56]. Furthermore, the reverse displacement of the GF was identified in the front of the Avawatz [57]. The E/W fractures observed mainly in the southeast end of the NH show an identical orientation to GF. Given this similarity in orientation and the close vicinity to the GF, it is tempting to relate the E/W trending fracturing to GF zone activity.

Recent work by [37] using high-resolution digital mapping techniques reveals the dominance of basement rocks in the central part of the NH (Figure 1c). Indeed, the granitic rocks are mostly represented and related to the Mesozoic granitic intrusion (Mzla, Figure 1c) [58]. Proterozoic formations characterized by gneiss in the bottom have been defined in the center part and the southeast end of the NH (pCgn, Figure 1c). The Proterozoic Crystal Spring sedimentary series defined in the northwestern part of the NH are mainly composed of carbonates and quartzites facies (pCu, Figure 1c). Some tertiary volcanic series have also been mapped in the southeastern end of the NH.

Outside the center part, Reference [39] has widely studied the Cenozoic NH formations mainly composed of Fanglomerate and alluvial fan deposits.

### 3. Materials and Methods

#### 3.1. Materials

##### 3.1.1. Large Scale Characterization

The analysis of large scale fracture attributes was performed on fractures digitized from DV regional map at 1:250,000 scale (geological map of California, Trona Sheet [38]) (Figure 2a). In the central part of the NH range, the main structures were mapped during 2018 and 2019 field campaigns published by Klee et al. [37]. In addition, in this present study, orthophoto images of 1 m resolution were used to digitalize and then complete the fractures sampling (Figure 2b).

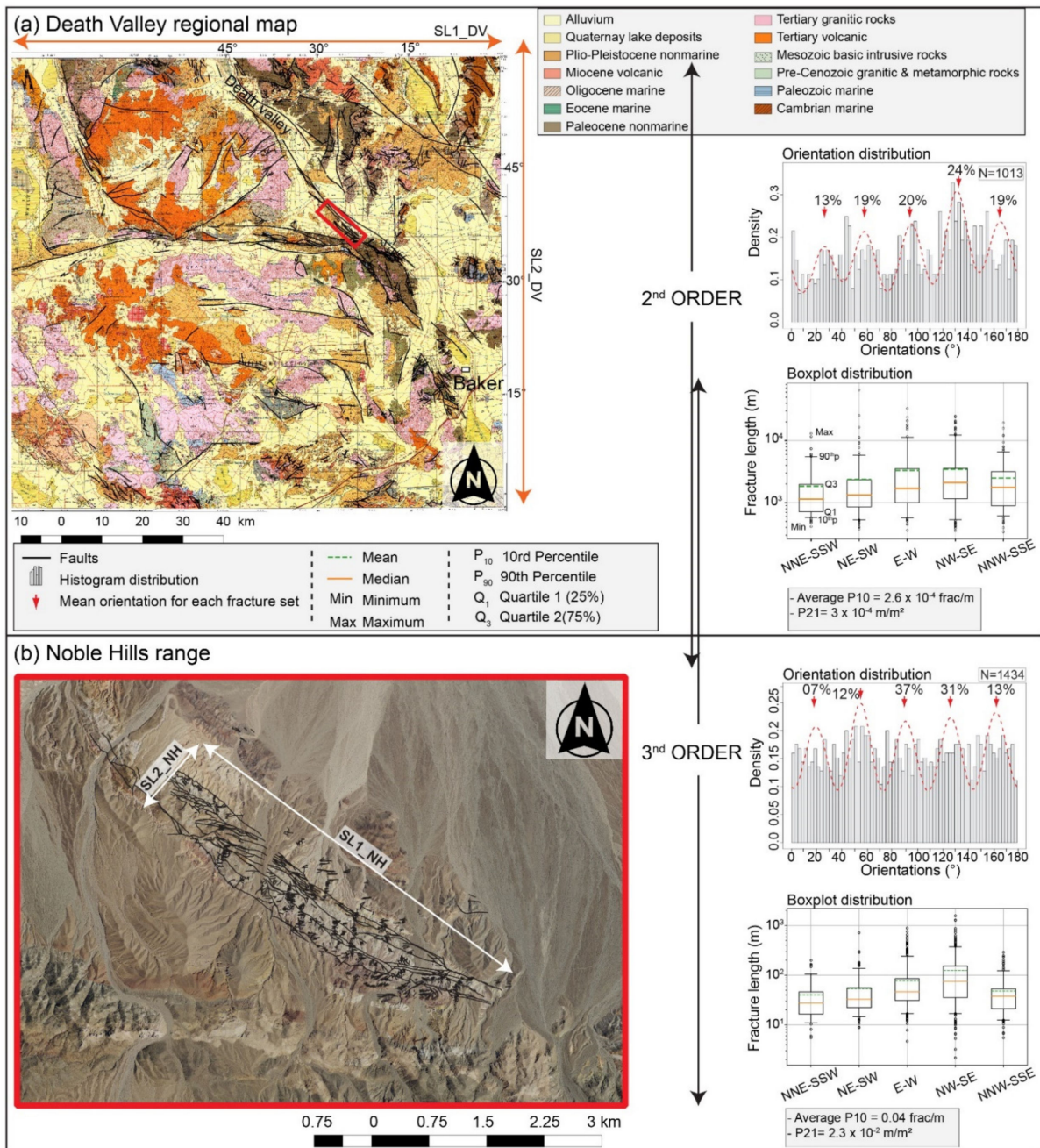


**Figure 2.** Fracture traces, orientation, and boxplot distributions from (a) DV geological map and (b) NH range map (in red rectangle for large scale location). The order of fractures magnitude were referred to the classification detailed in [30]. The first order referred to the faults larger 100 km length is not detected in this study. Each fracture map dataset is expressed in histogram for orientation distribution, and into boxplot for length distribution, according to the fracture orientations. Two scanlines (SL) were taken for every map.

With the aim of pinpointing the likely fracture variability, the NH range map has been divided into three domains (Figure 3). The sampling strategy along domains is detailed below. In total, 1013 fractures are extracted from the DV geological map, 1434 fractures from the NH map with 306 from domain A, 522 from domain B, and 606 from domain C.

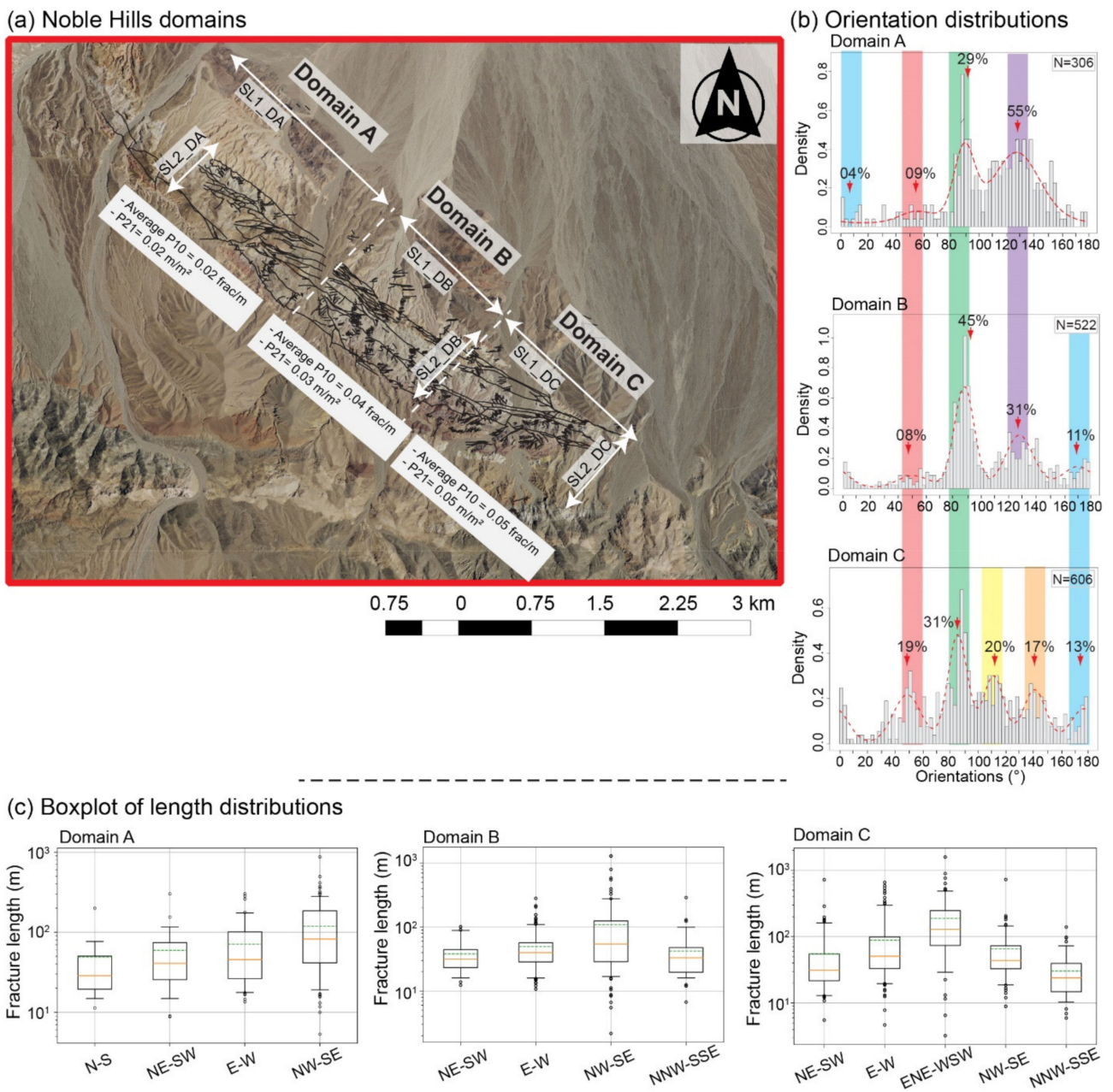


**Figure 3.** Fracture traces from the NH range divided into 3 domains. (a) NH domains: A, B, and C, (b) orientation distributions, and (c) boxplot of length distributions according to the fracture orientations. Two scanlines (SL) were taken for every domain. For boxplot and orientation distribution legend, see Figure 2.

Orientation and length distributions were collected and 1D/2D densities were calculated from them. All of these data are summarized in Table 1.

**Table 1.** Spatial statistics of 2D samples acquired at large scale (DV and NH regional maps) and outcrop scale (Drone models). Two Scanlines (SL) at least were generated for calculating the fracture density (P10). The length average is provided.

	Nb of Fractures	Mean Orientation	Average SL Length (m)/Area (m <sup>2</sup> )	Fracture Density (P10) (frac/m)	Fracture Density (P21) (m/m <sup>2</sup> )
DV regional map	133	N025	$10^5/1.3 \times 10^{10}$	$2 \times 10^{-4}$	$3 \times 10^{-4}$
	188	N058			
	199	N096			
	248	N132			
	197	N167			
NH regional map	97	N020	$4.7 \times 10^3/4.4 \times 10^6$	$2.6 \times 10^{-4}$	$3 \times 10^{-4}$
	168	N054			
	535	N090			
	441	N126			
	192	N163			
NH domain A	13	N010	$1.5 \times 10^3/1.9 \times 10^6$	$2 \times 10^{-2}$	$2 \times 10^{-2}$
	26	N055			
	89	N091			
	168	N132			
NH domain B	43	N050	$1.7 \times 10^3/1.2 \times 10^6$	$4 \times 10^{-2}$	$3 \times 10^{-2}$
	233	N088			
	164	N128			
	59	N171			
NH domain C	113	N049	$2 \times 10^3/1.2 \times 10^6$	$5 \times 10^{-2}$	$5 \times 10^{-2}$
	191	N085			
	119	N111			
	103	N141			
	77	N177			
Drone model 1	235	N025	$3.5 \times 10^2/1.4 \times 10^4$	$6.5 \times 10^{-1}$	$2 \times 10^{-1}$
	208	N055			
	183	N085			
	112	N115			
	281	N142			
	214	N174			
Drone model 2	681	N022	$1.7 \times 10^2/5.8 \times 10^3$	1.28	$7 \times 10^{-1}$
	767	N043			
	642	N085			
	616	N108			
	722	N142			
	637	N171			
Drone model 3	2968	N018	$2.8 \times 10^2/1.7 \times 10^4$	$9 \times 10^{-1}$	1
	2531	N038			
	1993	N079			
	2127	N109			
	2232	N140			
	3084	N169			

### 3.1.2. Photogrammetric Study/Analysis

In order to combine the widest fracture network analysis, three photogrammetric models, localized only in the granitic facies and alongside the major faults that structure the NH range (see Figure 1 for the location), are considered in this study to extract the fractures ranging approximatively from  $10^{-2}$  m to 20 m. A photogrammetric campaign was carried out in October 2018 with a high-resolution 3D point cloud and large collection of photographs.

Drone model 1 is sized approximately 350 m per 46 m and is located in the granitic facies (Figure 1); 1271 fractures are traced. Drone model 2 is located in the granitic facies

within a high deformation zone, and is sized approximately 172 m per 44 m (Figure 1). In total, 4196 fractures are traced. Finally, drone model 3 is located in the southeast termination of NH, and is sized approximately 280 m per 70 m. 15,594 fractures are traced.

The main statistical characteristics are summarized in Table 1.

### 3.1.3. Fracture Map Characterization

To complete the multiscale analysis with the small fractures, fracture maps were created with a resolution of  $2 \times 10^{-4}$  m. The fracture map 1 (see Figure 1c for location) is sized at 3.4 m per 3.1 m and is located between the granitic facies and the tertiary sediments, near the influence of the SDVFZ (see Figure 1b for the SDVFZ location). It is composed of quartzite boudin facies (part of Crystal Spring series) and granitic rocks, which respectively represent approximately 20% and 80% of occurrences.

In order to include the very small fractures in this study, additional fracture sets were collected from this fracture map with sample 1-1 sized 17 cm per 12 cm (resolution of  $10^{-4}$  m) and thin sections 1-1 and 1-2 (resolution of  $10^{-5}$  m), both sized 3.5 per 2.5 cm (see Figure 1c for location). Both sections are composed mainly of Plagioclase, Quartz, K-Feldspar, and Biotite representing respectively 35%, 30%, 25%, and 10% of occurrences.

Fracture map 2 (Figure 1c) is sized 1.7 m per 1.6 m and is located in the granitic facies, near the SDVFZ deformation corridor. This map includes sample 2-1 and thin section 2-1 which size respectively 15 cm per 5.2 cm and 3.5 cm per 2.5 cm. Thin section 2-1 represents the same mineral composition as thin sections 1-1 and 1-2 with approximately the same occurrences. Fracture map 3 (Figure 1c) is sized 1.8 m per 1.7 m and is located also in the granitic facies.

Table 2 summarizes the main statistical characteristics.

**Table 2.** Spatial statistics of 2D samples acquired from outcrop scale (fracture maps) to thin section scale. Two Scanlines (SL) at least were generated for calculating the fracture density (P10); the length average is provided.

	Nb of Fractures	Mean Orientation	Average SL Length (m)/Area (m <sup>2</sup> )	Fracture Density (P10) (frac/m)	Fracture Density (P21) (m/m <sup>2</sup> )
Fracture map 1	1133 631	N005 N083	3.1/7.94	12	12
Sample 1-1	104 115 117 51	N018 N053 N090 N126	$15 \times 10^{-2}/2.2 \times 10^{-2}$	184	118
Thin section 1-1	723 754 751 730	N018 N053 N090 N126	$3 \times 10^{-2}/8 \times 10^{-4}$	5140	715
Thin section 1-2	612 659 444 512 623	N020 N051 N088 N128 N162	$3 \times 10^{-2}/8 \times 10^{-4}$	4525	702
Fracture map 2	36 34 98 32 83	N005 N038 N070 N110 N145	1.7/1.91	18	13

Table 2. Cont.

	Nb of Fractures	Mean Orientation	Average SL Length (m)/Area (m <sup>2</sup> )	Fracture Density (P10) (frac/m)	Fracture Density (P21) (m/m <sup>2</sup> )
Sample 2-1	75	N017	$10^{-1}/10^{-2}$	177	240
	145	N057			
	101	N092			
	116	N130			
	135	N157			
Thin section 2-1	201	N014	$3 \times 10^{-2}/8 \times 10^{-4}$	517	1064
	213	N059			
	170	N097			
	221	N140			
Fracture map 3	149	N009	1.7/3	20	12
	88	N033			
	119	N071			
	70	N104			
	146	N149			

### 3.2. Methods

#### 3.2.1. Fractures Acquisition

In this study, fracture digitization was performed manually by tracing every fracture segment from entire 2D maps in QGIS<sup>®</sup> software v.2.18.17. Only fractures reported as full solid lines on the DV geological map were considered for statistical analysis (Figure 2a).

Regarding the procedure of fracture digitization, the fractures extending out of the sampling domain were considered as one continuous feature [16,23,59] (Figure 2b). The digitization of fractures consists of an extraction of the end point coordinates of each fracture using the QGIS<sup>®</sup> software v.2.18.17. Each extracted fracture is characterized by the X and Y coordinates of each of the two end points, which help to compute the orientations and the length of segments. In case of curved fractures, a straight segment line was automatically traced between the end of point coordinates, and then the mean directions and lengths were computed.

As described above, the NH fracture data were acquired during the field mapping campaign and then completed by orthophoto image analysis. The data were analyzed in the entire area (Figure 2b). However, the complexity in loading history within NH widely discussed in the literature [48,54,60] makes the analysis of the fracture geometries difficult. Furthermore, the field observations and the new geological map done by [37] reveal additional complexities inside this area, and show a stacking of different Crystal Spring series (pCu, Figure 1c), intruded by the Mesozoic granite (Mzla, Figure 1c). This observation was highlighted in the northwest part of the NH. In center part, Crystal Spring series thicknesses were reduced, dragged, and stretched against the granite due to the SDVFZ activity (pCu, Figure 1c). The southeast of the NH is characterized by the absence of the Crystal Spring series. To better characterize the fracture variability, it is prime of interest to consider the facies variability and the deformation intensity within NH, because they influence the fracture evolution [23,59]. In this sense, we decided to divide the NH range into three domains according to the facies variability and change in range trend orientation variation (Figure 3): (1) Domain A is located northwestward, highlighted by thick Crystal Spring sediments and granitic rocks; (2) Domain B is in the central part of NH, highlighted by reduced thickness of Crystal Spring sediments, granitic and gneissic rocks, and (3) Domain C is located in the southeastern part of the NH and is characterized by granite, gneiss, and Tertiary volcanism. Note that Domain B and C are composed approximately of the same facies. However, range orientation in domain B is NW/SE, while in domain C it is toward E/W. This general E/W trend is puzzling as it is similar to the GF (see Figure 1b for location). Therefore, this difference in orientation constitutes an additional argument to better delimitate domain B and C. Figure 3 shows the fracture

distributions within each domain. Some more work based on field analyses could more precisely delimitate the domains.

The photogrammetric models undertaken in this work were performed using a 3DR Solo drone with 4k cameras and DJI Phantom drone provided by University of Texas at El Paso (UTEP), Texas, USA. The videos were recorded between the late morning and the early afternoon during seven days with a manual mode camera setting to reduce the effects of lighting condition. Pictures were then extracted every second from the recorded drone videos using ffmpeg software v.4.5. The extracted pictures with a sufficient overlapping were aligned in Agisoft Metashape software (2020, Version 1.6.5). The obtained 3D models are georeferenced and then imported in CloudCompare software (version 2.9.1; [GPL software] (2017)) to begin the fracture extraction process. A workflow explaining the procedure of the models construction and the fractures extraction is detailed in [36]. In this study, the digitized fractures are projected on a 2D map to make the work only in 2D in order to keep data homogenous at different scales.

The 2D fracture maps at outcrop scale were performed in the field using a DSLR high resolution camera provided by UniLaSalle (Beauvais, France), with a 50 mm focal lens to minimize distortion. Pictures were taken vertically, with the same distance, and in the absence of sunlight to avoid the light effects in the fracture digitization [12]. From each fracture map, several pictures were taken with a sufficient overlapping. Then, pictures were aligned using the Agisoft Metashape software with the same procedure detailed in [36]. The maps are georeferenced and then used to extract the fractures in QGIS<sup>®</sup> with the same technique as for large scale maps.

Additional fracture datasets are used in this study by adding samples. These samples were taken directly from fracture maps. Then, a high-resolution picture was taken for each sample using a DSLR camera. With the same procedure as large-scale fractures acquisition, the sample was added in QGIS<sup>®</sup> to extract the fractures.

Thin section mosaics are also added to this study, made from samples as described earlier to keep a consistent sampling strategy. These mosaics were taken under an optical microscope Leica DM4500-P provided also by UniLaSalle (Beauvais, France), using a  $\times 5$  magnification and polarized non-analyzed light mode. A Leica DFC450C high resolution camera provided also by UniLaSalle (Beauvais, France) and Leica application Suite v.4.11.0 were used to take pictures. Every mosaic was relatively oriented using the corresponding sample. Then, with the same fracture digitization procedure described earlier, fracture parameters were extracted under QGIS<sup>®</sup> v.2.18.17.

### 3.2.2. Fractures Analysis

Different geometrical parameters were then collected from each fracture database at different scales. Detailed orientation distributions and classification into fracture sets were performed using the mixture of von Mises distribution (MvM) [61]. This approach consists of a semi-automated procedure based on appraisal tests in order to avoid any subjectivity in fracture sets analysis. For each fracture set, three output parameters were considered: (1) mean orientation ( $\mu$ ) around which the distribution is centered, (2) kappa ( $\kappa$ ) which controls the concentration of the orientation's values around the mean, and (3) weight ( $\omega$ ) corresponding to the relative contribution of each fracture set to the model. Then, we are able to check the best number of fracture sets from the distributions using the goodness of fit parameters (e.g., Likelihood). For more details, see [62] who describe and adapt the methodology for structural data. The standard of deviation of  $\pm 10^\circ$  was calculated for each given mean orientation value in this study.

Fracture length is the most used geometrical parameter to characterize the spatial organization in the natural fracture networks [4,25,63]. This characterization is performed using a statistical distribution as the Power law distributions widely used in structural data from field analogue [4,25,26,63,64]. The power law is often used to describe the distribution of fracture parameters such as length and aperture [25]. It is recognized that power law and fractal geometry provide widely applicable descriptive tools for fracture system

characterization. This is due to the absence of characteristic length scales in the fracture growth process. The power law exponent  $\alpha$  provides a real significance on the fracture connectivity. Indeed, for an exponent comprised between 2 and 3, fracture connectivity is ruled by both small and large fractures [65]. In addition, fractal analyses using Cantor's dust method allow the quantification of fracture distribution in clusters or, in the opposite, with a homogeneous distribution [66] and prediction of the fracture occurrence [7]. The exponential law is also used to describe the size of discontinuities in rocks [67–69], and to incorporate a characteristic scale that reflects a physical length in the system, such as thickness of a sedimentary layer [70].

However, fitting the geometric attributes to the statistical distributions suffers from a lot of biases, such as truncation and censoring biases [25]. Truncation effects are caused by resolution limitations of a field observation such as from satellite images, the human eye, or microscopes [63]. Censoring effects are associated with the probability that a long fracture intersecting the boundary of the sampling area is not sampled, and to the subjective choice of the sampling area which tends to exclude very long fractures [63,71]. Then, censoring effects cause an overestimation of fracture density. In this study, the truncation and censoring effects were automatically excluded from the distributions. Length distribution in Figure 4 shows the data excluded from the distribution (grey color) due to the impact of truncation and censoring effects.

The fracture length distributions are analyzed using the cumulative distribution. Statistical distributions used in this study were adjusted after corrections from the truncated and censoring effects. Research for truncation and censoring thresholds was performed using the « powerLaw: Analysis of Heavy Tailed Distributions » package from Rstudio® v.1.3.1056 [72]. We also used the coefficient of determination ( $R^2$ ) to estimate the goodness of fit of the power law to the length distribution. This coefficient is comprised between 0 and 1. A high  $R^2$  for a given number of degrees of freedom means that the regression is a statistically meaningful description of the data.

Fracture densities are computed in this study. They consist of fracture density ( $P_{10}$ ), defined as the number of fracture intersections along a 1D virtual scanline traced on every analyzed 2D map [59,73]. The scanline methodology is widely used to describe the fracture variability in 1D [73]. In this study, the linear fracture density  $P_{10}$  was obtained from two virtual scanlines, orientated perpendicular to the main structures.

Finally, the surface fracture density ( $P_{21}$ ) is defined as the total sum of fracture lengths within the area [59,73].

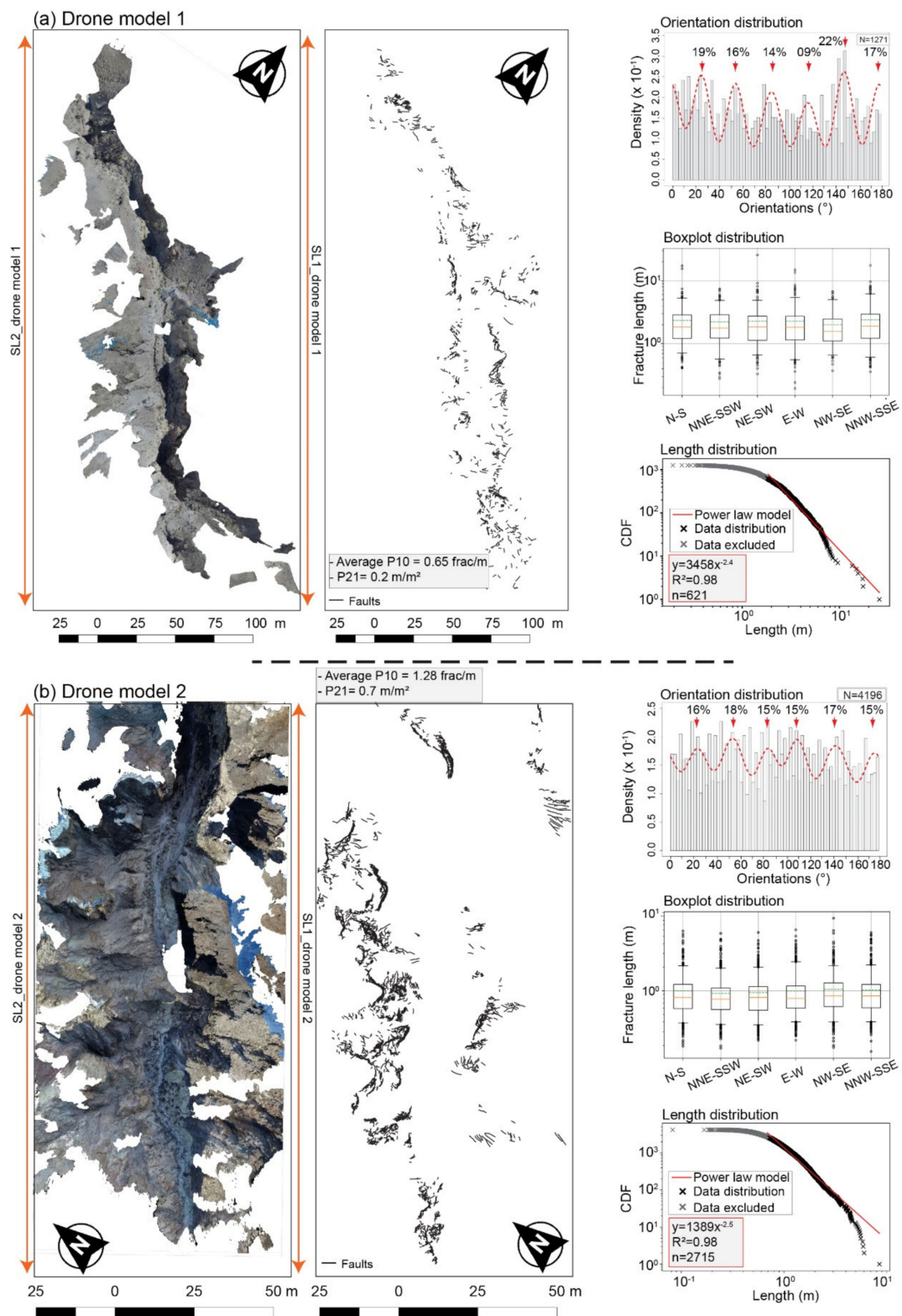


**Figure 4.** Fracture traces, orientation, boxplot length distributions from (a) drone model 1 and (b) drone model 2. Each fracture map data is expressed into histogram for orientation distribution, boxplot of length distribution according to the fracture orientations, and cumulative distribution function (CDF) of lengths. Two scanlines (SL) were taken along the left and the right side of the canyon. For the boxplots and orientation distributions legend, see Figure 2.

## 4. Results

### 4.1. Large Scale Domains

The mean orientation ( $\mu$ ) N095° (E/W trend) and N132° (NW/SE trend) trending fractures occur at the largest length scale, with a 20 and 24% of whole fractures, and about 3300 to 4400 m mean length (Figure 2a). Both directions are well expressed following the DV and Garlock strike slip trend faults (See Figure 1b for location) [39,48]. The largest fracture length is recorded within the NE/SW fracture set with 65 km length. The other recorded fracture sets are relatively equivalent (around 20%), except for the N025° fracture set which is less dominant, with 13% and 1900 m mean length.

At NH scale, the same dominance of N090° and N126° fracture sets with respectively 37% and 31% are observed (Figure 2b). The other fracture sets are poorly expressed (<15%). The boxplot distribution in Figure 2b showed also the dominance of the E/W and NW/SE fracture sets with respectively 80 m and 125 m mean length. The other fracture sets did not exceed the 50 m mean length.

The occurrence of two prominent fracture sets is shown in the NH domains A and B (Figure 3a,b). Domain A is characterized by two main fracture sets striking N091° and N132° representing respectively 29% and 55% of occurrences (Figure 3b). The N091° fracture set lengths range from 30 m to 300 m, while the N132° fracture set length ranges from 5 m to 800 m, meaning that the NW/SE is the most dominant fracture set in domain A (Figure 3b).

Orientation and length data of domain B shows an equivalent distribution as in domain A (Figure 3b). Indeed, two main fracture sets striking also N088° and N128° are mostly representative with respectively 45% and 31%. The fractures are much longer within NW/SE trend, ranging from 2 m to 1300 m (mean is of 108 m). The other fracture sets show an intermediate length with a 50 m mean value.

Fracture geometry in Domain C shows immediately a different distribution with four main fracture sets striking N050° (19%), N085° (31%), N111° (20%), and N141° (17%) (Figure 3b). The NW/SE fracture set mainly sampled and representative in the domain A and B is split into N111° and N141° fracture sets in domain C, with respective lengths ranging from 3 to 1600 m (mean is 190 m) and from 8 m to 730 m (mean is 65 m).

The fracture densities are increasing considerably from domain A to C with  $2 \times 10^{-2}/3 \times 10^{-2}$  m/m<sup>2</sup> in the domain A and B, and  $5 \times 10^{-2}$  m/m<sup>2</sup> in the domain C.

### 4.2. Photogrammetric Models

NH canyons modeled with photogrammetric method provide fractures from centimetric to decametric scale. Fracture distributions are displayed by drone model 1 for both sides of the canyon walls (Figure 4a). Six fracture sets are recorded and strike N025°, N055°, N085°, N115°, N142°, and N174°. The N142° is also the most dominated fracture set with 22%. The E/W fracture set is the less expressed (14%) at outcrop scale. An equivalent mean length of fractures is shown by the boxplot distribution graphic with 2.3 m, whatever the fracture set (Figure 4a).

The exponent of power law (red line in the length distribution, Figure 4) is of  $\alpha = -2.4$  for length distribution of the drone model 1, outside lengths affected by truncation and censoring bias (data mentioned in the length distribution graphic with grey color, Figure 4). The range of length values performed by the power law is 1.85 m to 25 m.

Finally, fracture densities  $P_{21}$  and  $P_{10}$  are of respectively  $2 \times 10^{-1}$  m/m<sup>2</sup> and  $6.5 \times 10^{-1}$  frac/m.

Fractures from drone model 2 are mainly distributed along the left side of the canyon (Figure 4b). The same fracture sets as drone model 1 are recorded with an equivalent percentage (between 15 and 18%) (Figure 4b). Fracture lengths are highlighted by the boxplot distribution and are also equivalent with 1 m mean length, whatever the fracture set. The largest fractures are recorded within the NW/SE fracture set (maximum of 8.5 m), and then confirm the consistency of the NW/SE direction at outcrop scale.

The fracture length range modeled by the power law is of 0.69 m to 8.5 m, for exponent  $\alpha = -2.5$  and  $R^2 = 0.97$  (Figure 4b). Fracture lengths under 0.69 m are excluded automatically from the distribution (truncation effects).

Fracture densities are quite high in comparison with Drone model 1, with  $7 \times 10^{-1} \text{ m}^2$  and 1.28 frac/m for respectively  $P_{21}$  and  $P_{10}$ .

Drone model 3 is the largest studied model with 15594 traced fractures (Figure 5). Six fracture sets are highlighted also in this canyon. Their proportions range from 13% (N079° and N109°), 14–16% (N140° and N038°), to 19–20% (N018 and N169°). The fracture lengths are equivalent, once again, with a 1.2 m mean length.

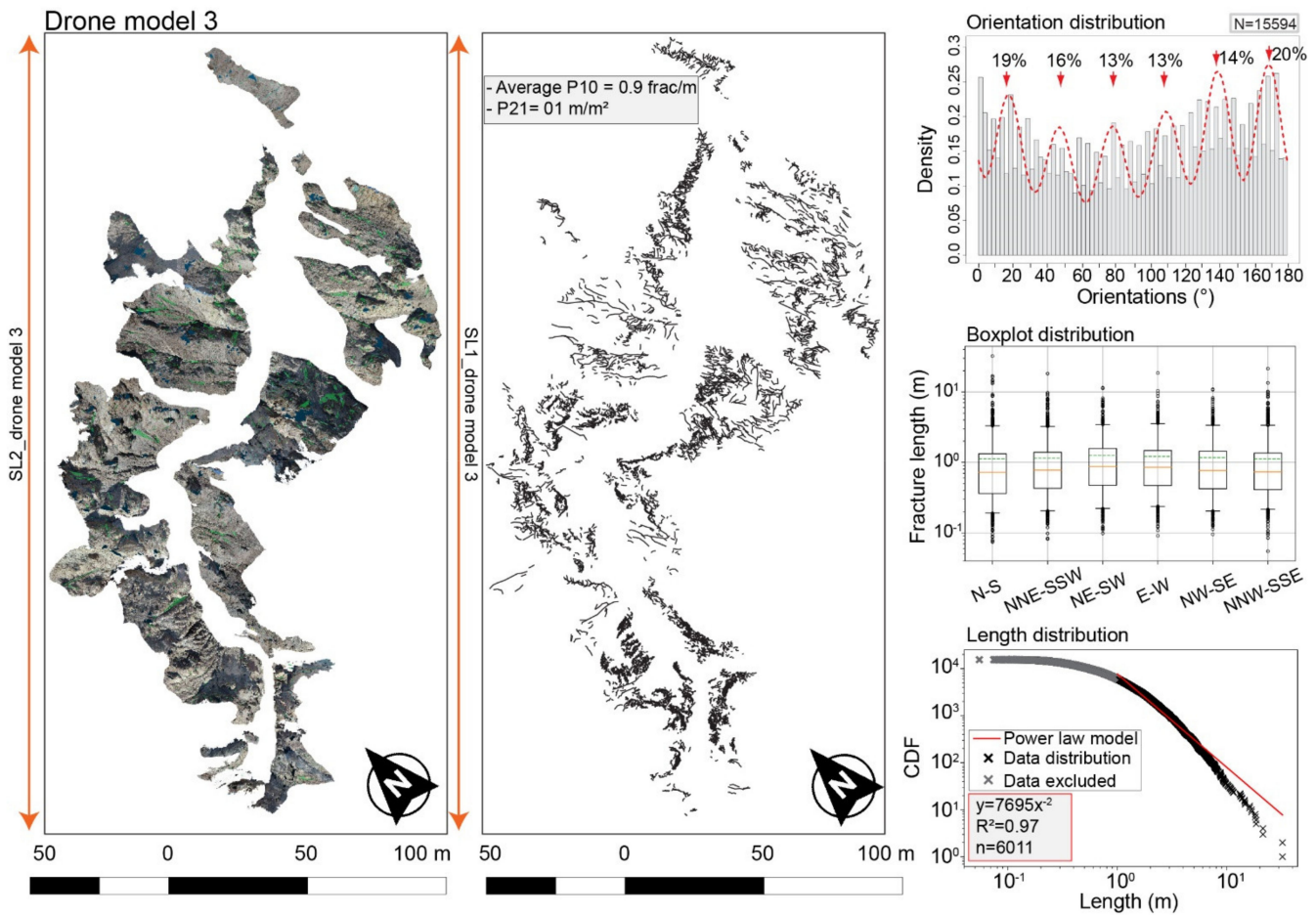


**Figure 5.** Fracture traces, orientation, boxplot length distributions from drone model 3. Different Datasets are expressed into histogram for orientation distribution, boxplot of length distribution according to the fracture orientations, and cumulative distribution function (CDF) of lengths. Two scanlines (SL) were taken along the left and the right side of the canyon. For Boxplot and orientation distribution legend, see Figure 2.

The power law exponent for drone model 3 length distribution is of  $\alpha = -2$ , outside lengths affected by truncation and censoring effects (Figure 5).  $R^2$  value is of 0.97, indicating a good fit of the power law to the data. Fracture density  $P_{21}$  is of 1  $\text{m}^2$ , increasing by a factor 5 compared to drone model 1 fracture density.

#### 4.3. Fracture Maps

Fracture map 1 is characterized by intense fracture areas, especially along the center part (Highly fractured area, Figure 6). The high fracture density is located mainly in the quartzite boudin, while the less fractured zone is related to the granitic rocks.

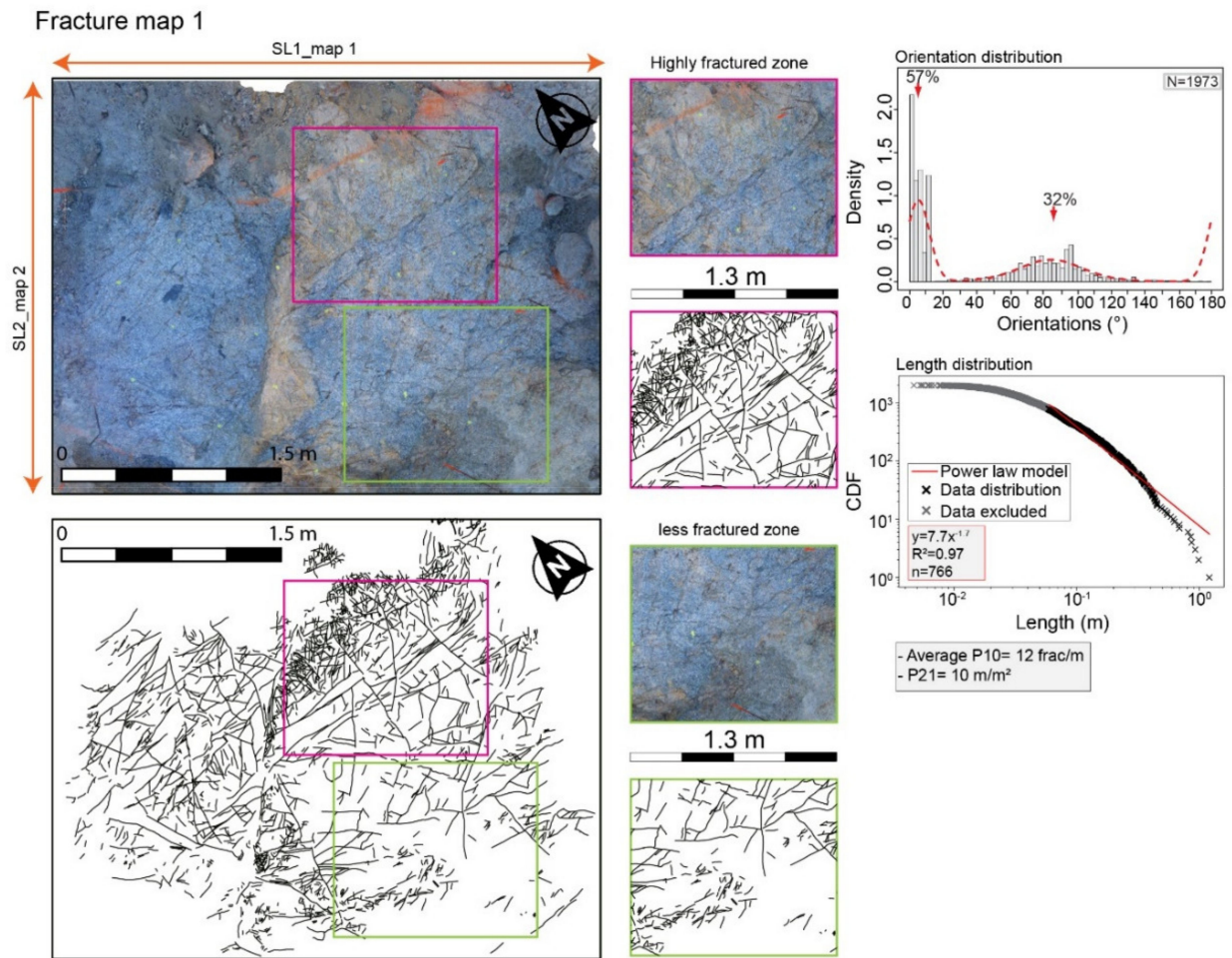


**Figure 6.** Fracture traces, orientation and length distributions from fracture map 1. Different datasets are expressed into histogram for orientations distribution, and into cumulative distribution function (CDF) of lengths. Two scanlines (SL) were taken for every domain. For orientation distribution legend, see Figure 2.

For the rest of the fracture map, average  $P_{10}$  of 12 frac/m is computed from two scanlines (SL1\_map1 and SL2\_map 2, Figure 6), while  $P_{21}$  is of 10 m/m<sup>2</sup>. Two main fracture sets are highlighted: N005° and N083°, with respectively 57% and 32% (Figure 6). Outside fracture lengths affected by truncation and censoring bias, the power law exponent is of  $\alpha = -1.7$  for values ranging from  $6 \times 10^{-2}$  m to 1.2 m.

Sample 1-1 is characterized by homogeneous fracture distribution with four main fracture sets: N018°, N053°, N090°, and N126° representing respectively 27%, 30%, 30%, and 13% (Figure 7a). The largest veins visible in the sample map are characterized by carbonate mineralizations in two directions: N053° and N126°.  $P_{10}$  and  $P_{21}$  fracture densities are of 184 frac/m and 118 m/m<sup>2</sup> respectively. Regarding the length distribution, the power law exponent is of  $\alpha = -1.43$ , with thresholds of  $3 \times 10^{-3}$  m and  $7 \times 10^{-2}$  m.

Four main fracture sets are highlighted in thin section 1-1: N018°, N053°, N090°, and N126° with a comparable fracture proportion (around 25%). Additional fracture set is detected in thin section 1-2: N162°. Regarding the densities,  $P_{21}$  is of 715 m/m<sup>2</sup> and 702 m/m<sup>2</sup>, while  $P_{10}$  is of 5140 frac/m and 4525 frac/m respectively for thin section 1-1 and 1-2 (Figure 7b,c). The power law exponents are quite higher with  $\alpha = -1.95$  (modeled range from  $2.2 \times 10^{-4}$  m to  $4.63 \times 10^{-3}$  m) and  $\alpha = -1.7$  (modeled range from  $2.2 \times 10^{-4}$  m to  $7 \times 10^{-3}$  m) respectively for thin section 1-1 and 1-2.

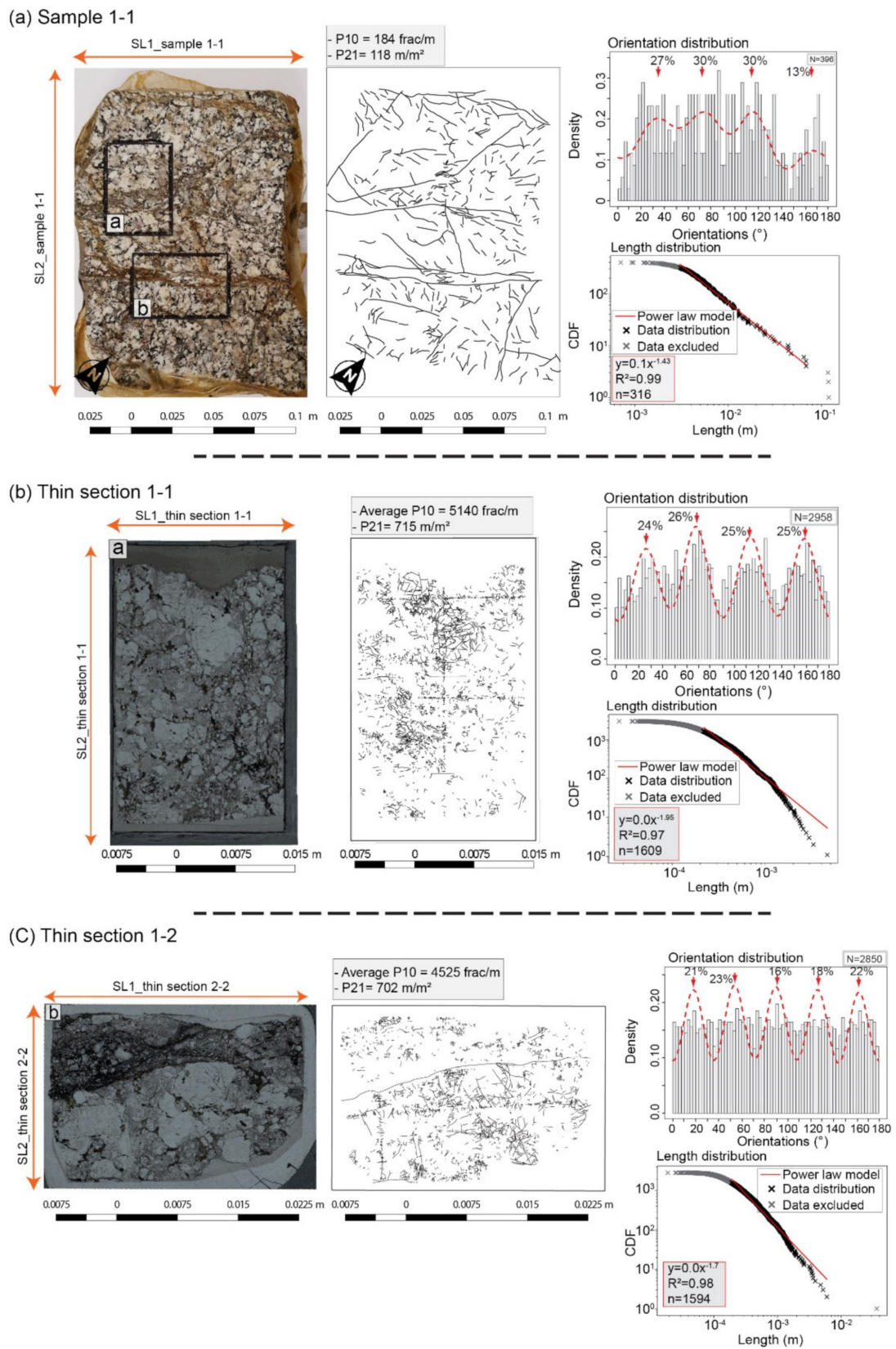


**Figure 7.** Fracture traces, orientation and length distributions from (a) sample 1-1, (b) thin section 1-1, and (c) thin section 1-2 sampled from fracture map 1. Different datasets are expressed into histograms for orientations distribution, and into cumulative distribution function (CDF) of lengths. Two scanlines (SL) were taken for each map. For orientation distribution legend, see Figure 2.

Fracture densities of fracture map 2 are comparable with fracture map 1 with average  $P_{10} = 18 \text{ frac/m}$  and  $P_{21} = 13 \text{ m/m}^2$  (Figure 8a). Five fracture sets are highlighted:  $N005^\circ$ ,  $N038^\circ$ ,  $N070^\circ$ ,  $N110^\circ$ , and  $N145^\circ$ . The  $N070^\circ$  and  $N145^\circ$  are the most recorded fracture sets with respectively 32% and 27%.

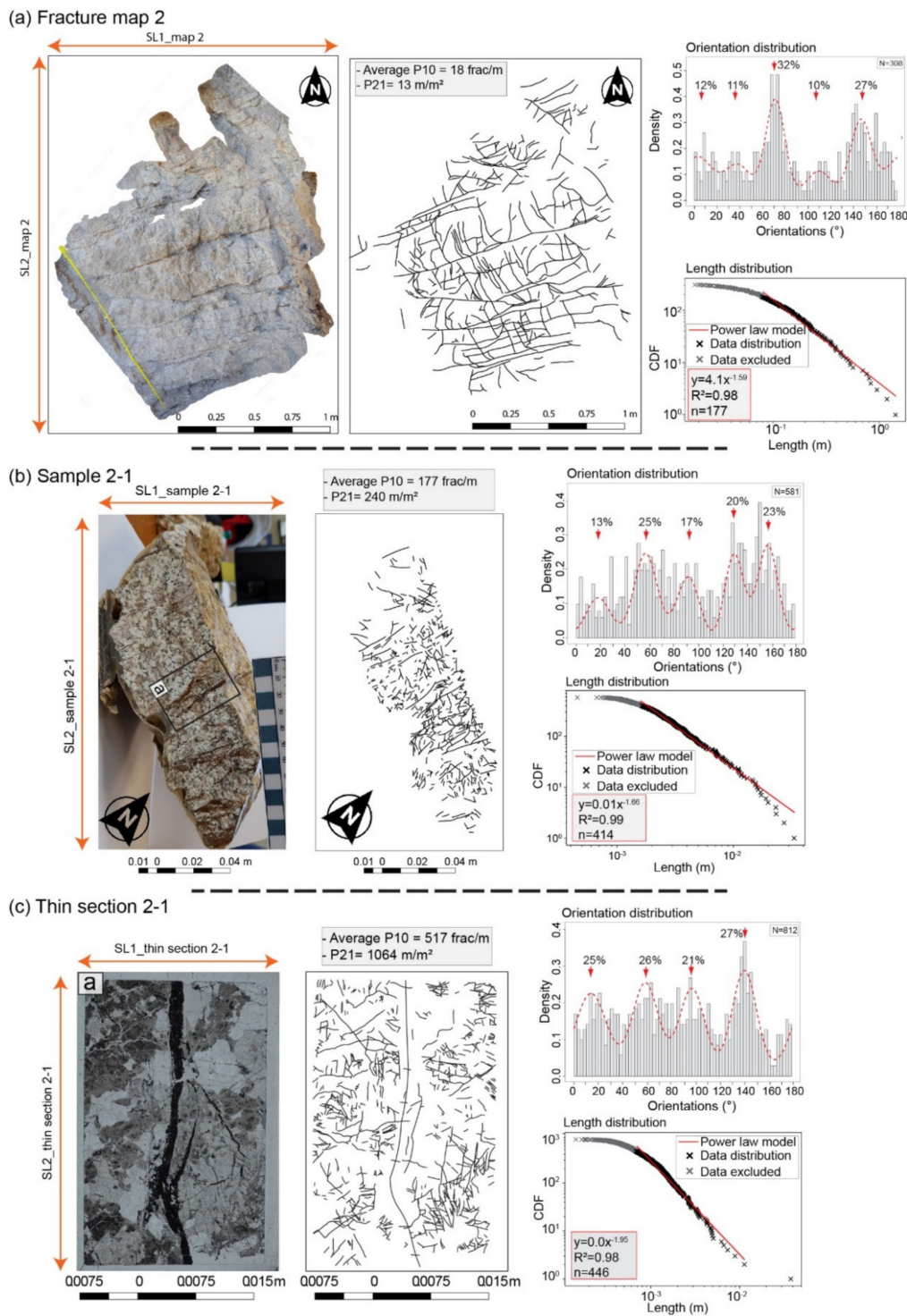


**Figure 8.** Fracture traces, orientation, and length distributions from (a) fracture map 2, (b) sample 2-1, and (c) thin section 2-1, located in sample 2-1. Different datasets are expressed into histogram for orientations distribution, and into cumulative distribution function (CDF) of lengths. Two scanlines (SL) were taken for each map. For orientation distribution legend, see Figure 2.

The power law exponent is also comparable to that of fracture map 1 ( $\alpha = -1.59$ ), with the thresholds of  $8 \times 10^{-2}$  m and 1.43 m (Figure 8a).

Sample 2-1 is characterized by a fracture density of  $P_{10} = 177$  frac/m and  $P_{21} = 240$  m/m<sup>2</sup> (Figure 8b). In total, five fracture sets are highlighted: N017°, N057°, N092°, N130°, and N157°. Three fracture sets are the most recorded: N057°, N130° and N157°, with 20% to 25%. The power law exponent is of  $\alpha = -1.66$ , thresholds from  $1.6 \times 10^{-3}$  m to  $3.33 \times 10^{-2}$  m.

Thin section 2-1 trans-cutting a large carbonate vein in the central part (Figure 8c), is characterized by a fracture density  $P_{21} = 1064$  m/m<sup>2</sup> higher than in thin section 1-1 and 1-2. Only four fracture sets are highlighted: N014°, N059°, N097° and N140°, with an equivalent fracture proportion. Outside the lengths affected by sampling bias, the exponent is of  $\alpha = -2$ , thresholds of  $7 \times 10^{-4}$  m to  $3.5 \times 10^{-2}$  m.

Finally, fracture map 3 is characterized by a comparable fracture density as in fracture map 2 with  $P_{10} = 20$  frac/m and  $P_{21} = 12$  m/m<sup>2</sup> (Figure 9). Five fracture sets are also detected with a high proportion of 26% for N009° and N149°. Fracture sets N033°, N077°, N104° showed an abundance of 15%, 21%, and 12% respectively. The power law exponent is of  $\alpha = -1.53$  for lengths data ranging from  $4 \times 10^{-2}$  m to 1.21 m.

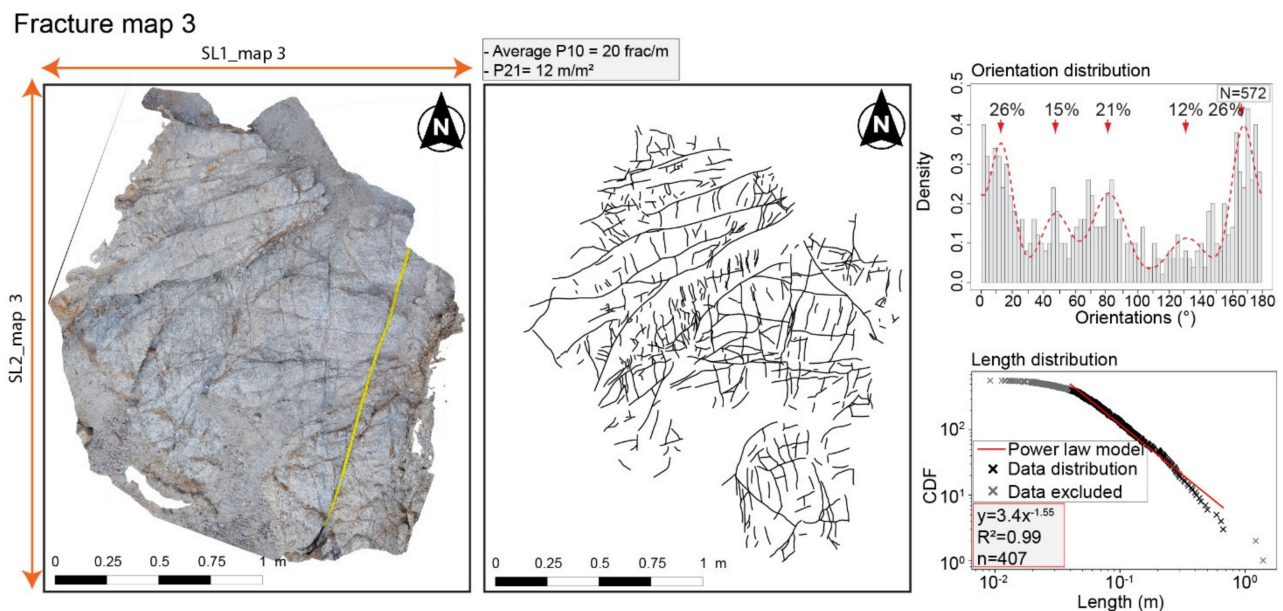


**Figure 9.** Fracture traces, orientation and length distributions from fracture map 3. The computed dataset is expressed into histogram for orientations distribution, and into cumulative distribution function (CDF) of lengths. Two scanlines (SL) were taken. For orientation distribution legend, see Figure 2.

## 5. Discussion

The combination of data at various scales in this study allowed to propose a new interpretation of the fracture network in the NH range, based on multiscale evolution of fractures length and orientation. A conceptual scheme of the NH structuration is created and discussed in terms of fracture network connectivity and its influence of fluid flow.

### 5.1. Multiscale Length Characterization

The cumulative length distributions of each fracture map from the DV regional map scale to thin section scale are plotted in Figure 10. All length datasets have been fitted to the power law distribution, outside lengths affected by truncation and censoring bias.

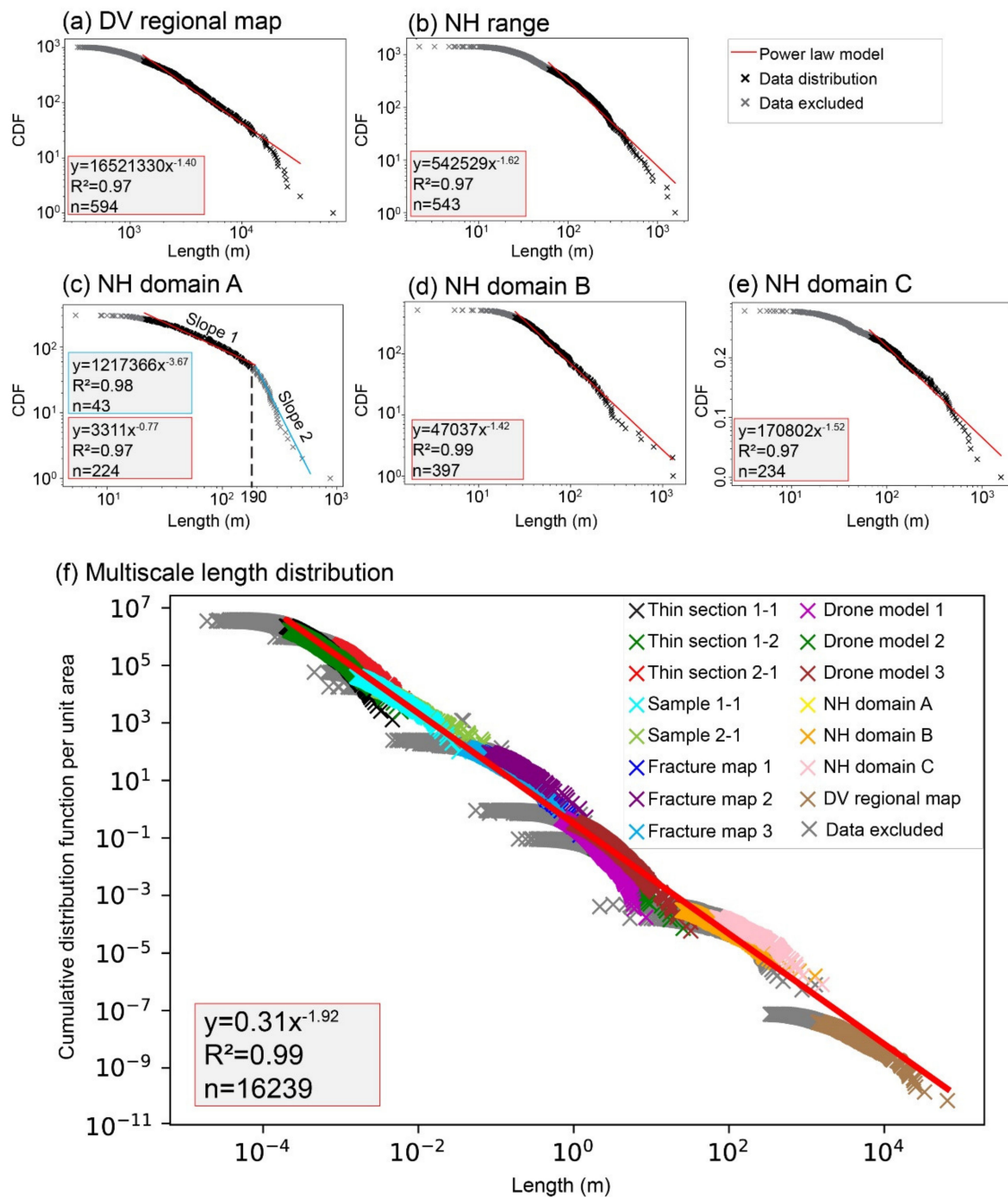


**Figure 10.** Fracture length distribution from (a) DV geological map, (b) NH range, (c) NH map domain A, (d) NH map domain B, and (e) NH map domain C, and (f) Multiscale length distribution obtained from the combination of the whole data.

DV regional map exponent is quite low, around  $\alpha = -1.40$ , and gradually increase to around  $\alpha = -1.62$  in NH map (Figure 10a,b). The division of the NH into 3 domains according to the facies variability and the change in range trend orientation showed a disparity in power law exponent values. Indeed, the exponent  $\alpha = -0.83$  in the domain A (values ranging from 21 m to 230 m), while  $\alpha = -1.42$  (values ranging from 25 m to 1283 m) and  $\alpha = -1.52$  (values ranging from 70 m to 1500 m) respectively in domain B and C (Figure 10c–e). The lowest  $\alpha$  value in domain A can be explained by the dependence of fracture lengths on scale of observation for fractures ranging from 5 m to 870 m. In addition, the domain A is composed of granitic rocks and Crystal Spring sedimentary series with carbonates and quartzites (Figure 1), meaning that the sedimentary rocks can

have a different behavior from that of basement rocks during the fracture growth and propagation process.

Cumulative distribution of fracture lengths in the domain A showed also two different trend slopes (Figure 10c), with a failure slope quantified around 230 m. Distribution into two slopes has been largely discussed in the literature [25,67,70], and can be explained by the fracture growth process which has been divided into two trends. However, this result and interpretation cannot allow to determine if these two trends correspond to a single or to two different regional directions. Cumulative distribution of fracture lengths according to their orientations and the nature of rocks could help to resolve the episodes of deformation challenge, together with some more work in the field (e.g., looking for evidences of displacement).

The cumulative fracture length from all maps has been plotted in a single graphic, normalized by surface area of each map [63] (Figure 10f). The power law distribution included fracture lengths from  $2.2 \times 10^{-4}$  m to 65 km scale. Power law distribution was performed over 6 orders of magnitude. Two length ranges were not represented in this study. The first one corresponds to the fracture lengths over 100 km and related to the first order fracture defined by [30]. This absence can be explained by: (1) a different evolution stage and opening mechanism of faults [30,74], (2) a structural heritage which controls the reactivation during the DV trans-tensional tectonic setting. The second one corresponds to the length ranging from 1 km to 5 km length (Figure 10f). The Basin and Range regional map and the geological map at 1:25,000 scale could help to resolve both gaps.

The power law distribution gives an exponent  $\alpha = -2$  for the whole 2D fracture lengths analyzed in this study (Figure 10f), which suggests the 2D representation is self-similar [4,16,23,26]. The probability to detect fracture of the size of the sampling window is the same at all scales. Then, the fracture connectivity is ruled by the small and large fractures [65], meaning that the large fractures detected and studied at large scale in the NH play the same role as any fracture at millimeter scale in fracture network connectivity.

### 5.2. Spatial Organization of NH Fracture Network

The fracture densities and the main dominant orientations on the regional maps show the control of NH geometry by NW/SE and E/W trends. Both trends are associated to the second order scale faults over 20 km length, well expressed in terms of abundance (DV regional map, Figure 11). The third order scale detected along NE/SW trend is characterized by faults around 10 km length. Spacing values were computed and correspond to 5 km and 1 km respectively for the second and the third order scale (Figure 12a). The same geometrical characteristics (detailed in the introduction) were approved in the extensional regime [20,30], meaning that the second and third order scale spacing classification can be generalized to the trans-tensional regime studied in the present work.

At NH scale, the fracture densities and the main dominant orientations approve the separation of the NH into three domains:

1. The first domain referred to the NH domain A is characterized by a specific spatial arrangement with a NW/SE direction dominance (Domain A, Figure 11). This direction is marked by the SDVFZ bordering fault of the strike-slip corridor, and is mostly dominated the NH fracture network in terms of length and abundance. It approved the importance of the NW/SE deformation episode at the fourth order scale. These fractures are the longest ones and also control the internal structuration inside the domain (Figure 12b). The E/W direction is less represented in comparison with domains B and C (Figure 11), but still the second most dominated fracture set, with less control on the NH geometry. Regarding the spacing characteristics, the NW/SE fractures set are regularly spaced from 0.1 to 0.2 km, while the E/W fractures set did not exceed 0.1 km spacing (Figure 12b).
2. The central domain (domain B, Figure 3) is characterized by several short segments of fractures. Indeed, the E/W direction is also dominated by short fractures with 60 m mean length, while the NW/SE direction is the second dominated system with long

fracture of 100 m mean length (Figure 11). Then, NW/SE and E/W directions control the NH geometry respectively following the third and fourth order scale length. In this case, the spacing related to the third order scale is around 1 km between the SDVFZ bordering faults and regularly spaced at 0.2 km (Figure 12b). A spacing of 0.05 km is defined along the E/W fracture set (Figure 12b).

3. The southeastern end area corresponding to the domain C (Figure 3) highlights a specific spatial arrangement with an additional fracture set (yellow color, Figure 11), the longest one with 200 m mean length. Indeed, the NW/SE direction is split into N111° and N141° fracture sets thus highlighting the influence of both NW/SE and E/W deformation episodes in this area. Once again, the E/W direction is more expressed, with a 100 m mean length (Figure 11). The ENE/WSW, E/W and also NW/SE directions control the NH geometry and structuration respectively following the third and fourth order scale. The spacing of 0.3 km defined for the third order scale in domain C between the SDVFZ bordering faults is under the third order spacing characteristic. Indeed, the NW/SE direction has been deviated and then the relative spacing is reduced. Regarding the internal organization, the NW/SE and E/W fractures are also regularly spaced with 0.1–0.2 km and 0.05 km, respectively (Figure 12b).

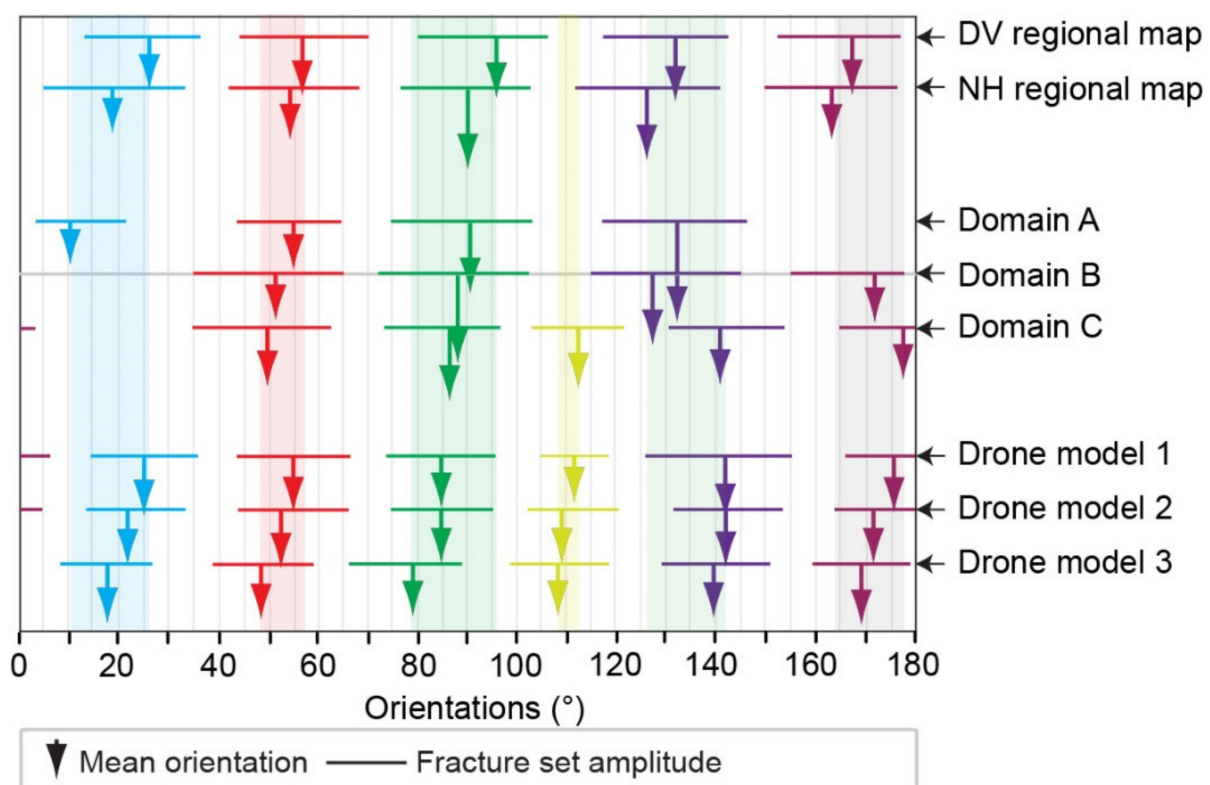


**Figure 11.** Orientation plot representing mean orientation of each fracture set from DV regional map, NH regional map, NH domains and drone models at outcrop scale. Each arrow corresponds to the mean orientation. The length of each arrow corresponds to the fracture set abundance. The horizontal line above each arrow corresponds to the fracture set standard deviation within an interval of confidence of 75% (see [62] for more explanations). Each color arrow corresponds to fracture set: Blue arrow corresponds to NNE/SSW fracture set, red arrow corresponds to the NE/SW fracture set, green arrow corresponds to the E/W fracture set, yellow arrow corresponds to the NNW/SSE fracture set, purple arrow corresponds to the NW/SE fracture set, and marron arrow corresponds to the N/S fracture set.

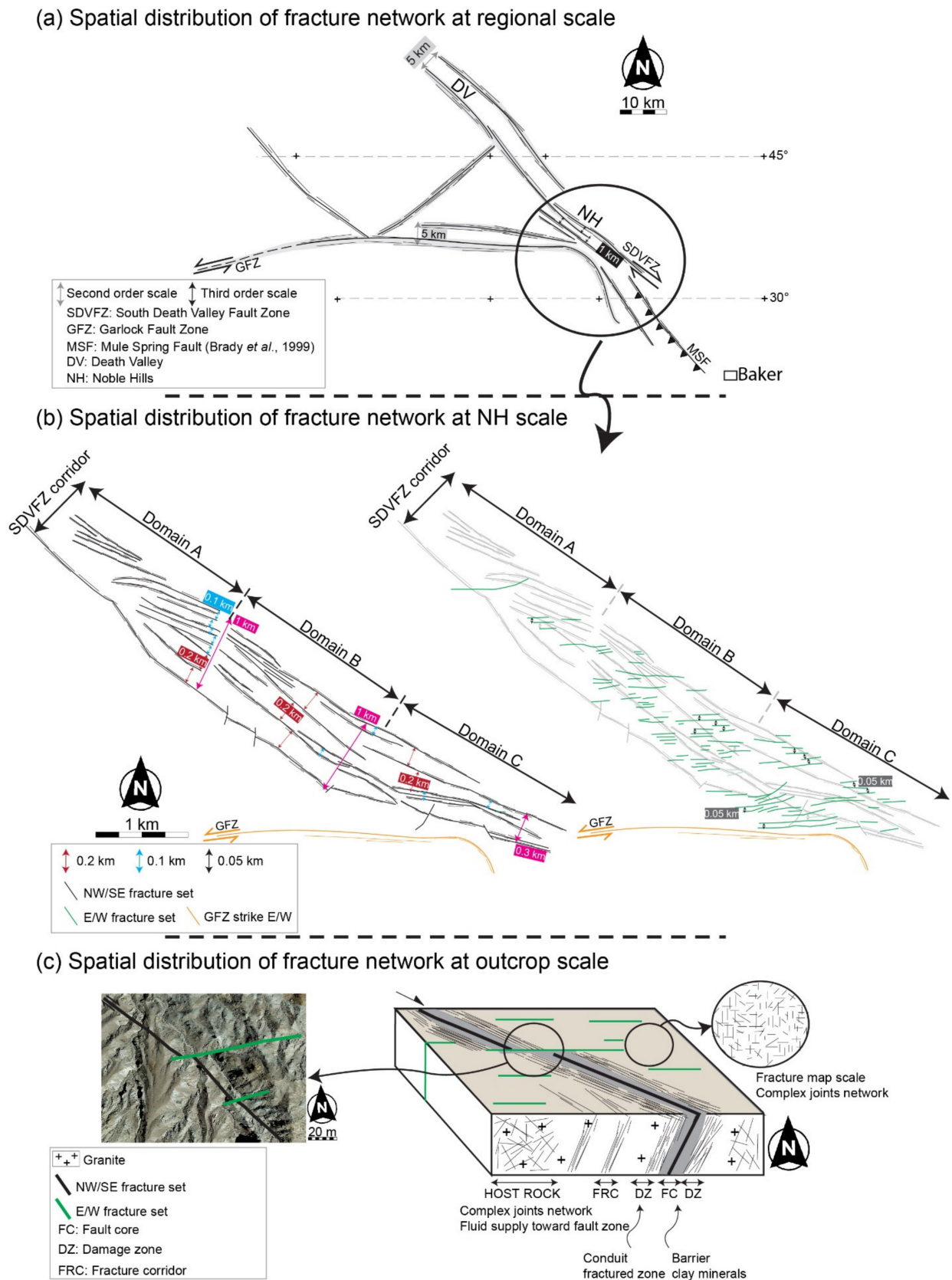


**Figure 12.** Conceptual scheme presenting the spatial arrangement of the NH fracture network at (a) regional scale, (b) NH scale, and (c) outcrop scale. The organization is based on scale orders referring to the [16,17,20,30] classification, and their associated spacing characteristics referring to [20,30]. The picture presented in (c) is provided by GoogleEarth®.

In the present work, the spacing characteristics of 0.05 km to 0.1–0.2 km computed in the three internal domains are attributed to the fourth order scale (Figure 12b). These values vary according to their directions and also lengths. Two spacing characteristics can be highlighted from this study: (1) spacing of 0.05 km corresponding to the fractures comprised between 0.1 and 0.35 km (percentile 90 values), (2) spacing of 0.1–0.2 m corresponding to the fractures comprised between 0.35 and 0.5 km. Further work on the fourth order scale spacing characteristics will obviously be needed in order to generalize them to the trans-tensional regime.

At outcrop scale, the drone models highlighted the reproducibility and the consistency of the whole fracture sets defined at large scale (Figure 11). However, N111° fracture set, detected only in domain C, is less expressed in domain A (drone model 1, 9%) (Figure 11). The E/W direction trend is more expressed in the drone models 2 and 3 respectively in the domain B and C. This observation is confirmed by the fracture maps 2 and 3, sample 2-1 and thin section 2-1 (Figures 8 and 9), highlighting a consistent fracturing episode. In the previous works, [39,55–57] mentioned the presence of the compression signature at the southeastern end of the NH and the front of the Avawatz mountains. According to these studies and our current observations, a hypothesis of fracturing intensity which affected up to the internal domain can explain the consistency of the E/W direction.

A special fracture arrangement was observed in fracture map 1 (Figure 6). The length distribution is characterized by a high density of short fractures in the quartzite boudin rocks, while the granitic part is characterized by a lower density of long fractures. This leads to a change in the power law and orientation distributions and then makes a bias. Indeed, only N/S and E/W directions are recorded, while the sample 1-1, thin sections 1-1 and 1-2 have recorded the whole fracture sets.

Fractures are organized along SDVFZ direction as fault zone segments with a highly mineralized (clay minerals) fault core (FC) which can act as a barrier and damage zone (DZ), acting as a conduit (Figure 12c). A complex joint network that can play a key role in the fracture connectivity is highlighted in the host rock. A petrographic study focusing on these fault zones is required to better characterize the fluid circulation potential.

The N/S to NNE/SSW and the NE/SW fracture sets are less expressed and are attributed to the fourth order scale with 40 m mean length on NH map, while they are still very important and consistent at outcrop, sample, and thin section scales, regardless of domain (Figures 2–5). These trends are highly dependent on the scale of observation and have no influence on the NH geometry.

To summarize, a new spatial organization of the NH range based on second, third, and fourth order scales has been proposed with length, spacing, density, and orientation distributions. Each NH domain shows its own internal organization. Variability in between recorded fracture sets from different areas is a marker of a complex tectonic and geometrical setting. One main deformation episode played a key role in the NH structuration: SDVFZ trending NW/SE affected whole NH and then controlled its geometry. The second main deformation episode is in the GF system trending E/W, likely responsible for E/W fracturing episode, and controlled the NH geometry mostly in its internal part and the southeastern end.

The identical orientation of GF and the E/W structures could suggest that the GF was responsible for the E/W fracturing in the internal and southeastern end domains (Figure 12b). Furthermore, the E/W structures are characterized by a sinistral strike-slip displacement, highlighted by the movement of the tertiary volcanic blocks in the back of the NH. This sinistral strike-slip movement has been characterized along the GF zone, widely described in the literature [55,57]. The similarities on the strike-slip nature can help to consider that the E/W fractures are related to GF activity which plays a key role on the NH geometry. In addition, the lower dominance of the NW/SE direction in the central and the southeastern end of the NH can be explained by the overprinting of the E/W fracturing, highlighting that these structures are posterior to the SDVFZ system (Figure 12c).

Regarding the fracture distributions, the fracture density is higher in the domain C with a factor 2.5 and 1.5, in comparison respectively with domain A and B (Figure 3). At outcrop scale, fracture densities raise from domains A and B to domain C with a factor 0.5 and 1.4, approving the localization of the fracture intensity in this area due to the complex tectonic setting [39]. Furthermore, a gradient of deformation has been observed in the field along the entire NH length with evidence of extreme shearing, notably in the internal domain. Boudinage structures and brittle shearing are prevalent within Crystal Spring series. A future publication will be planned to better characterize this deformation.

### 5.3. Fracture Network Impact on Flow

The deformation occurred with a different intensity at the whole NH scale. This can influence the fluid circulation through the fracture network following the domains. Even if the connectivity in the reservoir analogue is ruled by the large and small fractures (Figure 10f), some domains, such as domain A, had a different behavior insofar as the connectivity was ruled by only the large fractures. A complex joint network is highlighted at outcrop scale in the host rock and plays a key role in the fracture connectivity leading the fluid supply toward the fault zone.

The fluid flow modeling in this reservoir analogue should consider that the orientation parameter depends on scale observation and then should be modeled differently at each scale, while the length parameter is independent of the observation scale in the case of NH geothermal reservoir analogue.

Flow simulations will be planned in the future publications, based on photogrammetric models acquired from different NH domains. This study can help to approve the sensitivity of the fluid circulations to the gradient of strike-slip deformation and the spatial arrangement of NH fracture network. The sensitivity of the deterministic models on resulting permeability will be tested according to the directional dependence and their corresponding length distribution.

## 6. Conclusions

This study is part of the MEET project (Multidisciplinary and multi-context demonstration of EGS exploration and Exploitation Techniques and potentials), aiming at developing geothermal exploitation at European scale by applying Enhanced Geothermal System (EGS) technology to different geological settings. NH range, assimilated to a paleo geothermal reservoir analogue, gives an opportunity to study the basement rocks in trans-tensional context. This study proposes geometric description and quantifies the multiscale network organization and its effect on connectivity using a wide-ranging analysis scale from the microscopic scale to the regional scale. We used 2D fracture maps at different scales. We have shown a power law distribution for six orders of scales. Then, a power law exponent of  $\alpha = -2$  was computed by combining the whole datasets, meaning that the connectivity is ruled by the small and the large fractures.

A new spatial arrangement of the fracture network at different scales has been proposed for the NH range, based on densities, spacings, orientations, and length distributions. The SDVFZ controls the NH geometry at large scale within the second order scale, while the E/W directions—whose origin remains to be determined—controls the NH geometry within the third order scale. The spacing characteristics are of 5 and 1 km for respectively the second and the third order scale, and correspond to the spacings highlighted in the extensional regime.

The division into three domains according to the facies variability and the change in range trend orientation has been approved by statistical analysis. Indeed, domain A is characterized by a dominance of the NW/SE direction in terms of length and abundance at the fourth order scale with a regular fracture spacing of 0.1–0.2 km. Then, NW/SE direction controls the internal structuration of this domain. Domain B is structured by the second and third orders of fractures scales following the E/W and NW/SE direction with regular spacing of 0.2 km and 0.005 km, respectively. Domain C was also characterized by

the structuration of a specific spatial arrangement with the dominance of short fractures following E/W direction, which highlight the persistence of the E/W fracturing episode. The ENE/WSW, E/W, and also NW/SE directions control the NH geometry and structuration in this area. A regular spacing of 0.2 km and 0.005 km is computed inside the domain at fourth order scale. Therefore, two spacing characteristics have been highlighted in this study at fourth order scale: 0.1–0.2 km and 0.05 km spacing for fractures length of 0.1–0.35 km and 0.005 km, respectively.

Each internal domain described in this study proposes its own spatial arrangement of fracture network. Indeed, two main deformation episodes referring to the SDVFZ striking NW/SE and fractures system striking E/W play a key role in the structuration of the NH range. However, the SDVFZ deformation affected the whole NH, whereas the E/W fracturing affected only the central and the southeastern area.

Fluid flow modeling will be planned and will take into consideration that orientation parameters should be modelled differently at each scale, while length parameters modelled by the power law should be considered as homogenous at different scales.

**Author Contributions:** Conceptualization, A.C., G.T. and B.A.L.; methodology, A.C.; software, A.C.; validation, G.T., B.A.L. and J.K.; formal analysis, A.C.; investigation, A.C., G.T., B.A.L. and J.K.; resources, A.C.; data curation, A.C.; writing—original draft preparation, A.C.; writing—review and editing, G.T., B.A.L. and H2020 MEET consortium; visualization, G.T., B.A.L. and J.K.; supervision, G.T.; project administration, G.T.; funding acquisition, G.T. and H2020 MEET consortium. All authors have read and agreed to the published version of the manuscript.

**Funding:** This project has received funding from the European Union’s Horizon 2020 research and innovation program under grant agreement No 792037 (MEET project).

**Data Availability Statement:** Not applicable.

**Acknowledgments:** This work is part of postdoctoral contribution, prepared at Institut Polytechnique UniLaSalle Beauvais, which was funded by European Union’s Horizon 2020 research (H2020 MEET project). We are grateful to Armand Pomart and Ruben Attali for their help for analyses. We also wish to thank the H2020 MEET consortium for their helpful comments and manuscript validation. We also thank the Assistant Editor Sorin Hadrian Petrescu and the anonymous reviewers for the relevant remarks that significantly approved the article.

**Conflicts of Interest:** The authors declare no conflict of interest.

## References

1. Bour, O.; Davy, P. Connectivity of Random Fault Networks Following a Power Law Fault Length Distribution. *Water Resour. Res.* **1997**, *33*, 1567–1583. [[CrossRef](#)]
2. Gillespie, D.T. Approximate Accelerated Stochastic Simulation of Chemically Reacting Systems. *J. Chem. Phys.* **2001**, *115*, 1716–1733. [[CrossRef](#)]
3. Berkowitz, B. Characterizing Flow and Transport in Fractured Geological Media: A Review. *Adv. Water Resour.* **2002**, *25*, 861–884. [[CrossRef](#)]
4. Odling, N.E.; Gillespie, P.; Bourguine, B.; Castaing, C.; Chiles, J.P.; Christensen, N.P.; Fillion, E.; Genter, A.; Olsen, C.; Thrane, L. Variations in Fracture System Geometry and Their Implications for Fluid Flow in Fractured Hydrocarbon Reservoirs. *Pet. Geosci.* **1999**, *5*, 373–384. [[CrossRef](#)]
5. Johnston, J.D.; McCaffrey, K.J.W. Fractal Geometries of Vein Systems and the Variation of Scalingrelationships with Mechanism. *J. Struct. Geol.* **1996**, *18*, 349–358. [[CrossRef](#)]
6. Geiger, S.; Emmanuel, S. Non-Fourier Thermal Transport in Fractured Geological Media. *Water Resour. Res.* **2010**, *46*, W07504. [[CrossRef](#)]
7. Ledésert, B.; Dubois, J.; Genter, A.; Meunier, A. Fractal Analysis of Fractures Applied to Soultz-Sous-Forets Hot Dry Rock Geothermal Program. *J. Volcanol. Geotherm. Res.* **1993**, *57*, 1–17. [[CrossRef](#)]
8. Dezayes, C.; Genter, A.; Valley, B. Structure of the Low Permeable Naturally Fractured Geothermal Reservoir at Soultz. *Comptes Rendus Géosciences* **2010**, *343*, 517–530. [[CrossRef](#)]
9. Valley, B.; Dezayes, C.; Genter, A.; Maqua, E.; Syren, G. Main Fracture Zones in GPK3 and GPK4 and Cross-Hole Correlations. In Proceedings of the EHDRA Scientific Conference, Soultz-sous-Forêts, France, 17–18 March 2005.
10. Bour, O.; Davy, P. On the Connectivity of Three-dimensional Fault Networks. *Water Resour. Res.* **1998**, *34*, 2611–2622. [[CrossRef](#)]

11. Darcel, C.; Bour, O.; Davy, P.; de Dreuzy, J.R. Connectivity Properties of Two-Dimensional Fracture Networks with Stochastic Fractal Correlation: Connectivity of 2D Fractal Fracture Networks. *Water Resour. Res.* **2003**, *39*, 1272. [[CrossRef](#)]
12. Odling, N.E. Scaling and Connectivity of Joint Systems in Sandstones from Western Norway. *J. Struct. Geol.* **1997**, *19*, 1257–1271. [[CrossRef](#)]
13. Castaing, C.; Halawani, M.A.; Gervais, F.; Chilès, J.P.; Genter, A.; Bourguine, B.; Ouillon, G.; Brosse, J.M.; Martin, P.; Genna, A. Scaling Relationships in Intraplate Fracture Systems Related to Red Sea Rifting. *Tectonophysics* **1996**, *261*, 291–314. [[CrossRef](#)]
14. Marrett, R.; Ortega, O.J.; Kelsey, C.M. Extent of Power-Law Scaling for Natural Fractures in Rock. *Geology* **1999**, *27*, 799–802. [[CrossRef](#)]
15. Soliva, R.; Schultz, R.A.; Benedicto, A. Three-dimensional Displacement-length Scaling and Maximum Dimension of Normal Faults in Layered Rocks. *Geophys. Res. Lett.* **2005**, *32*, L16302. [[CrossRef](#)]
16. Bertrand, L.; Géraud, Y.; Le Garzic, E.; Place, J.; Diraison, M.; Walter, B.; Haffen, S. A Multiscale Analysis of a Fracture Pattern in Granite: A Case Study of the Tamariu Granite, Catalunya, Spain. *J. Struct. Geol.* **2015**, *78*, 52–66. [[CrossRef](#)]
17. Bertrand, L.; Jusseume, J.; Géraud, Y.; Diraison, M.; Damy, P.-C.; Navelot, V.; Haffen, S. Structural Heritage, Reactivation and Distribution of Fault and Fracture Network in a Rifting Context: Case Study of the Western Shoulder of the Upper Rhine Graben. *J. Struct. Geol.* **2018**, *108*, 243–255. [[CrossRef](#)]
18. Ehlen, J. Fractal Analysis of Joint Patterns in Granite. *Int. J. Rock Mech. Min. Sci.* **2000**, *37*, 909–922. [[CrossRef](#)]
19. Genter, A.; Castaing, C. Effets d'échelle Dans La Fracturation Des Granites. *Comptes Rendus de l'Académie des Sci. Ser. IIA Earth Planet. Sci.* **1997**, *325*, 439–445. [[CrossRef](#)]
20. Le Garzic, E.; de L'Hamaide, T.; Diraison, M.; Géraud, Y.; Sausse, J.; De Urreiztieta, M.; Hauville, B.; Champanhet, J.-M. Scaling and Geometric Properties of Extensional Fracture Systems in the Proterozoic Basement of Yemen. Tectonic Interpretation and Fluid Flow Implications. *J. Struct. Geol.* **2011**, *33*, 519–536. [[CrossRef](#)]
21. De Dreuzy, J.-R.; Davy, P.; Bour, O. Hydraulic Properties of Two-dimensional Random Fracture Networks Following Power Law Distributions of Length and Aperture. *Water Resour. Res.* **2002**, *38*, 12-1–12-9. [[CrossRef](#)]
22. Davy, P.; Le Goc, R.; Darcel, C.; Bour, O.; de Dreuzy, J.R.; Munier, R. A Likely Universal Model of Fracture Scaling and Its Consequence for Crustal Hydromechanics. *J. Geophys. Res.* **2010**, *115*, B10411. [[CrossRef](#)]
23. Hardebol, N.J.; Maier, C.; Nick, H.; Geiger, S.; Bertotti, G.; Boro, H. Multiscale Fracture Network Characterization and Impact on Flow: A Case Study on the Latemar Carbonate Platform. *J. Geophys. Res. Solid Earth* **2015**, *120*, 8197–8222. [[CrossRef](#)]
24. McCaffrey, K.J.W.; Sleight, J.M.; Pugliese, S.; Holdsworth, R.E. Fracture Formation and Evolution in Crystalline Rocks: Insights from Attribute Analysis. *Geol. Soc. Lond. Spec. Publ.* **2003**, *214*, 109–124. [[CrossRef](#)]
25. Bonnet, E.; Bour, O.; Odling, N.E.; Davy, P.; Main, I.; Cowie, P.; Berkowitz, B. Scaling of Fracture Systems in Geological Media. *Rev. Geophys.* **2001**, *39*, 347–383. [[CrossRef](#)]
26. Bour, O.; Davy, P.; Darcel, C.; Odling, N. A Statistical Scaling Model for Fracture Network Geometry, with Validation on a Multiscale Mapping of a Joint Network (Hornelen Basin, Norway). *J. Geophys. Res. Solid Earth* **2002**, *107*, ETG 4-1–ETG 4-12. [[CrossRef](#)]
27. Bonneau, F.; Caumon, G.; Renard, P.; Sausse, J. Stochastic Sequential Simulation of Genetic-like Discrete Fracture Networks. *Proceeding 32nd Gocad Meeting, Nancy, France*. 2012. Available online: <https://www.ring-team.org/component/liad/?view=pub&id=2214> (accessed on 3 July 2021).
28. de Dreuzy, J.-R.; Méheust, Y.; Pichot, G. Influence of Fracture Scale Heterogeneity on the Flow Properties of Three-Dimensional Discrete Fracture Networks (DFN): 3D Fracture Network Permeability. *J. Geophys. Res.* **2012**, *117*, B11207. [[CrossRef](#)]
29. Chabani, A. Analyse Méthodologique et Caractérisation Multi-Échelle Des Systèmes de Fractures à l'interface Socle/Couverture Sédimentaire Application à La Géothermie (Bassin de Valence, SE France). These de Doctorat, Paris Sciences et Lettres (ComUE), Paris, France, 2019. Available online: <http://www.theses.fr/2019PSLEM046> (accessed on 3 July 2021).
30. Morellato, C.; Redini, F.; Doglioni, C. On the Number and Spacing of Faults. *Terra Nova* **2003**, *15*, 315–321. [[CrossRef](#)]
31. Bourbiaux, B.; Basquet, R.; Daniel, J.M.; Hu, L.Y.; Jenni, S.; Lange, G.; Rasolofosaon, P. Fractured Reservoirs Modelling: A Review of the Challenges and Some Recent Solutions. *First Break* **2005**, *23*. [[CrossRef](#)]
32. Gillespie, P.; Monsen, E.; Maerten, L.; Hunt, D.; Thurmond, J.; Tuck, D.; Martinsen, O.J.; Pulham, A.J.; Haughton, P.D.W.; Sullivan, M.D. Fractures in Carbonates: From Digital Outcrops to Mechanical Models. *Outcrops Revital.—Tools Tech. Appl. Tulsa Okla. SEPM Concepts Sedimentol. Paleontol.* **2011**, *10*, 137–147.
33. Vollgger, S.A.; Cruden, A.R. Mapping Folds and Fractures in Basement and Cover Rocks Using UAV Photogrammetry, Cape Liptrap and Cape Paterson, Victoria, Australia. *J. Struct. Geol.* **2016**, *85*, 168–187. [[CrossRef](#)]
34. Biber, K.; Khan, S.D.; Seers, T.D.; Sarmiento, S.; Lakshminantha, M.R. Quantitative Characterization of a Naturally Fractured Reservoir Analog Using a Hybrid Lidar-Gigapixel Imaging Approach. *Geosphere* **2018**, *14*, 710–730. [[CrossRef](#)]
35. Trullenque, G.; Genter, A.; Leiss, B.; Wagner, B.; Bouchet, R.; Léoutre, E.; Malnar, B.; Bär, K.; Rajšl, I. Upscaling of EGS in Different Geological Conditions: A European Perspective. In Proceedings of the Proceedings 43rd Workshop on Geothermal Reservoir Engineering, Stanford, CA, USA, 12–14 February 2018.
36. Chabani, A.; Trullenque, G.; Rishi, P.; Pomart, A.; Attali, R.; Sass, I. Modelling of Fractured Granitic Geothermal Reservoirs: Use of Deterministic and Stochastic Methods in Discrete Fracture Networks and a Coupled Processes Modeling Framework. In Proceedings of the Extended Abstract, Reykjavik, Iceland, 2 May 2021.

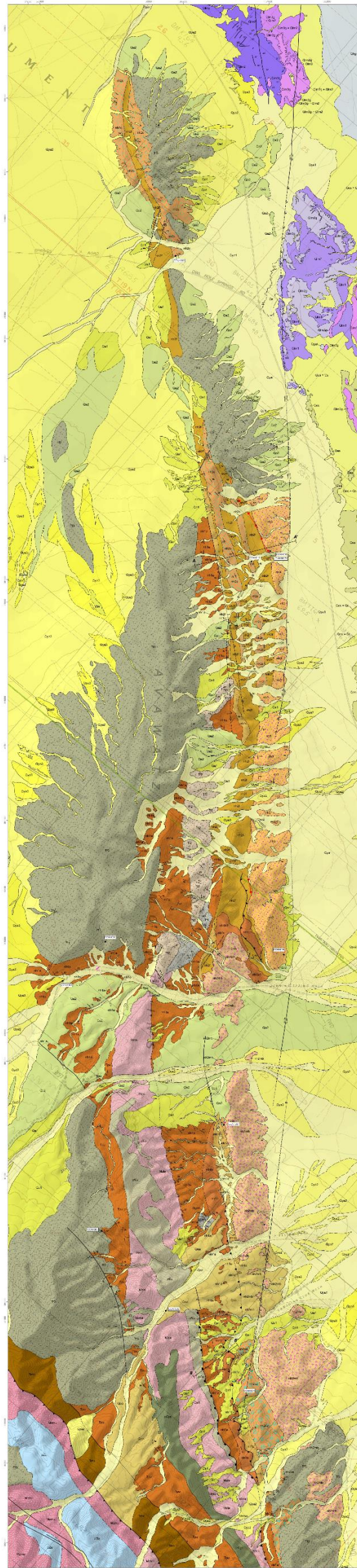
37. Klee, J.; Trullenque, G.; Ledésert, B.; Potel, S.; Hébert, R.; Chabani, A.; Genter, A. Petrographic Analyzes of Fractured Granites Used as An Analogue of the Soultz-Sous-Forêts Geothermal Reservoir: Noble Hills, CA, USA. In Proceedings of the Extended Abstract, Reykjavik, Iceland, 26 May 2021.
38. Jennings, C. Geologic Map of California, Scale 1: 250,000. Olaf P. Jenkins Edition, Long Beach Sheet. *Calif. Div. Mines Geol, Serie No 33, List No 6347.033*; CA, USA, 1962. Available online: [https://www.davidrumsey.com/luna/servlet/detail/RUMSEY~8~1~324920~90093990:Geologic-Map-of-California,-Long-Be?sort=Pub\\_List\\_No\\_InitialSort%2CPub\\_Date%2CPub\\_List\\_No%2CSeries\\_No](https://www.davidrumsey.com/luna/servlet/detail/RUMSEY~8~1~324920~90093990:Geologic-Map-of-California,-Long-Be?sort=Pub_List_No_InitialSort%2CPub_Date%2CPub_List_No%2CSeries_No) (accessed on 3 July 2021).
39. Niles, J.H. Post-Middle Pliocene Tectonic Development of the Noble Hills, Southern Death Valley, California. Doctoral Dissertation, San Francisco State University, San Francisco, CA, USA, 2016.
40. Miller, M.; Pavlis, T. The Black Mountains Turtlebacks: Rosetta Stones of Death Valley Tectonics. *Earth-Sci. Rev.* **2005**, *73*, 115–138. [[CrossRef](#)]
41. Pavlis, T.L.; Rutkofske, J.; Guerrero, F.; Serpa, L.F. Structural Overprinting of Mesozoic Thrust Systems in Eastern California and Its Importance to Reconstruction of Neogene Extension in the Southern Basin and Range. *Geosphere* **2014**, *10*, 732–756. [[CrossRef](#)]
42. Snow, J.K.; Wernicke, B. Uniqueness of Geological Correlations: An Example from the Death Valley Extended Terrain. *Geol. Soc. Am. Bull.* **1989**, *101*, 1351–1362. [[CrossRef](#)]
43. DeCelles, P.G. Late Jurassic to Eocene Evolution of the Cordilleran Thrust Belt and Foreland Basin System, Western U.S.A. *Am. J. Sci.* **2004**, *304*, 105–168. [[CrossRef](#)]
44. Walker, J.D.; Burchfiel, B.; Davis, G.A. New Age Controls on Initiation and Timing of Foreland Belt Thrusting in the Clark Mountains, Southern California. *Geol. Soc. Am. Bull.* **1995**, *107*, 742–750. [[CrossRef](#)]
45. Stewart, J.H. Possible Large Right-Lateral Displacement along Fault and Shear Zones in the Death Valley-Las Vegas Area, California and Nevada. *Geol. Soc. Am. Bull.* **1967**, *78*, 131–142. [[CrossRef](#)]
46. Stewart, J.H. Extensional Tectonics in the Death Valley Area, California: Transport of the Panamint Range Structural Block 80 Km Northwestward. *Geology* **1983**, *11*, 153–157. [[CrossRef](#)]
47. Snow, J.K. Cenozoic Tectonism in the Central Basin and Range; Magnitude, Rate, and Distribution of Upper Crustal Strain. *Am. J. Sci.* **2000**, *300*, 659–719. [[CrossRef](#)]
48. Brady, R. Cenozoic Geology of the Northern Avawatz Mountains in Relation to the Intersection of the Garlock and Death Valley Fault Zones, San Bernardino County, California. Doctoral Dissertation, University of California, Davis, CA, USA, 1987.
49. Norton, I. Two-Stage Formation of Death Valley. *Geosphere* **2011**, *7*, 171–182. [[CrossRef](#)]
50. Burchfiel, B.C.; Stewart, J.H. “Pull-Apart” Origin of the Central Segment of Death Valley, California. *Geol. Soc. Am. Bull.* **1966**, *77*, 439–442. [[CrossRef](#)]
51. Pavlis, T.L.; Trullenque, G. Evidence for 40–41 Km of Dextral Slip on the Southern Death Valley Fault: Implications for the Eastern California Shear Zone and Extensional Tectonics. *Geology* **2021**, *49*, 767–772. [[CrossRef](#)]
52. Machette, M.N.; Klinger, R.E.; Knott, J.R.; Wills, C.J.; Bryant, W.A.; Reheis, M.C. *A Proposed Nomenclature for the Death Valley Fault System. Quaternary and Late Pliocene Geology of the Death Valley Region: Recent Observations on Tectonics, Stratigraphy, and Lake Cycles (Guidebook for the 2001 Pacific Cell—Friends of the Pleistocene Fieldtrip)*; US Department of the Interior, US Geological Survey: Reston, VA, USA, 2001; p. 173.
53. Troxel, B.W.; Butler, P.R. Rate of Cenozoic Slip on Normal Faults, South-Central Death Valley, California. Doctoral Dissertation, Department of Geology, University of California, Office of Scholarly Communication (OSC), Irvine, CA, USA, 1979.
54. Brady III, R.H. Neogene Stratigraphy of the Avawatz Mountains between the Garlock and Death Valley Fault Zones, Southern Death Valley, California: Implications as to Late Cenozoic Tectonism. *Sediment. Geol.* **1984**, *38*, 127–157. [[CrossRef](#)]
55. Reinert, E. Low Temperature Thermochronometry of the Avawatz Mountains, California: Implications for the Inception of the Eastern California Shear Zone. Doctoral Dissertation, University of Washington, Washington, DC, USA, 2004. Available online: [https://www.ess.washington.edu/content/people/student\\_publications\\_files/reinert--erik/Reinert\\_2004.pdf](https://www.ess.washington.edu/content/people/student_publications_files/reinert--erik/Reinert_2004.pdf) (accessed on 3 July 2021).
56. Spencer, J.E. *Late Cenozoic Extensional and Compressional Tectonism in the Southern and Western Avawatz Mountains, Southeastern California. Basin and Range Extensional Tectonics near the Latitude of Las Vegas, Nevada: Geological Society of America Memoir*; Geological Society of America: Las Vegas, NV, USA, 1990; Volume 176, pp. 317–333. [[CrossRef](#)]
57. Chinn, L.D. *Low-Temperature Thermochronometry of the Avawatz Mountains; Implications for the Eastern Terminus and Inception of the Garlock Fault Zone*; University of Washington: Washington, DC, USA; Available online: [https://www.ess.washington.edu/content/people/student\\_publications\\_files/chinn--logan/chinn--logan\\_ms\\_2013.pdf](https://www.ess.washington.edu/content/people/student_publications_files/chinn--logan/chinn--logan_ms_2013.pdf) (accessed on 3 July 2021).
58. Rämö, T.O.; Calzia, J.P.; Kosunen, P.J. Geochemistry of Mesozoic Plutons, Southern Death Valley Region, California: Insights into the Origin of Cordilleran Interior Magmatism. *Contrib. Mineral. Petrol.* **2002**, *143*, 416–437. [[CrossRef](#)]
59. Bisdom, K.; Gauthier, B.D.M.; Bertotti, G.; Hardebol, N.J. Calibrating Discrete Fracture-Network Models with a Carbonate Three-dimensional Outcrop Fracture Network: Mplcations for Naturally Fractured Reservoir Modeling. *AAPG Bull.* **2014**, *98*, 13511376. [[CrossRef](#)]
60. Brady, R.H.; Troxel, B.W.; Wright, L.A. The Miocene Military Canyon Formation: Depocenter Evolution and Constraints on Lateral Faulting, Southern Death Valley, California. *Spec. Pap. Geol. Soc. Am.* **1999**, *277*–288. [[CrossRef](#)]
61. von Mises, R. Über Die “Ganzzahligkeit” Der Atomgewicht Und Verwandte Fragen. *Physikal. Z.* **1918**, *19*, 490–500.

62. Chabani, A.; Mehl, C.; Cojan, I.; Alais, R.; Bruel, D. Semi-Automated Component Identification of a Complex Fracture Network Using a Mixture of von Mises Distributions: Application to the Ardeche Margin (South-East France). *Comput. Geosci.* **2020**, *137*, 104435. [[CrossRef](#)]
63. Pickering, G.; Bull, J.M.; Sanderson, D.J. Sampling Power-Law Distributions. *Tectonophysics* **1995**, *248*, 1–20. [[CrossRef](#)]
64. Pickering, G.; Peacock, D.C.; Sanderson, D.J.; Bull, J.M. Modeling Tip Zones to Predict the Throw and Length Characteristics of Faults. *AAPG Bull.* **1997**, *81*, 82–99.
65. Davy, P.; Bour, O.; De Dreuzy, J.-R.; Darcel, C. Flow in Multiscale Fractal Fracture Networks. *Geol. Soc. Lond. Spec. Publ.* **2006**, *261*, 31–45. [[CrossRef](#)]
66. Ledésert, B.; Dubois, J.; Velde, B.; Meunier, A.; Genter, A.; Badri, A. Geometrical and Fractal Analysis of a Three-Dimensional Hydrothermal Vein Network in a Fractured Granite. *J. Volcanol. Geotherm. Res.* **1993**, *56*, 267–280. [[CrossRef](#)]
67. Cruden, D.M. *Describing the Size of Discontinuities*; Elsevier: Amsterdam, The Netherlands, 1977; Volume 14, pp. 133–137.
68. Priest, S.D.; Hudson, J.A. *Estimation of Discontinuity Spacing and Trace Length Using Scanline Surveys*; Elsevier: Amsterdam, The Netherlands, 1981; Volume 18, pp. 183–197.
69. Priest, S.D.; Hudson, J.A. Discontinuity Spacings in Rock. *Int. J. Rock Mech. Min. Sci. Geomech. Abstr.* **1976**, *13*, 135–148. [[CrossRef](#)]
70. Cowie, P.A.; Sornette, D.; Vanneste, C. Multifractal Scaling Properties of a Growing Fault Population. *Geophys. J. Int.* **1995**, *122*, 457–469. [[CrossRef](#)]
71. Priest, S.D. *Discontinuity Analysis for Rock Engineering*; Springer Science & Business Media: Berlin/Heidelberg, Germany, 1993.
72. Gillespie, C.S. The PowerLaw Package: A General Overview. Newcastle, UK. Available online: [https://cran.r-project.org/web/packages/poweRlaw/vignettes/a\\_introduction.pdf](https://cran.r-project.org/web/packages/poweRlaw/vignettes/a_introduction.pdf) (accessed on 3 July 2021).
73. Gillespie, P.A.; Howard, C.B.; Walsh, J.J.; Watterson, J. Measurement and Characterisation of Spatial Distributions of Fractures. *Tectonophysics* **1993**, *226*, 113–141. [[CrossRef](#)]
74. Bertrand, L. *Etude Des Réservoirs Géothermiques Développés Dans Le Socle et à l'interface Avec Les Formations Sédimentaires*. Doctoral Dissertation, Université de Lorraine, Lorraine, France, April 2017; p. 492.

GEOLOGIC MAP OF THE NOBLE HILLS, SOUTHERN DEATH VALLEY, CALIFORNIA

By John H. Niles and S. John Caskey

2014  
Department of Geosciences, 500 Thomson Hall, San Francisco State University, 1600 Holloway Ave., San Francisco, CA 94132



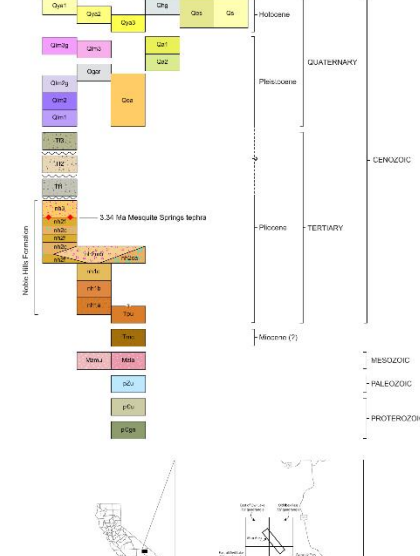
DESCRIPTION OF MAP UNITS

- Surficial Deposits**
- Qm** Modern Eolian Sand Deposits (Green, 2009) - Coe deposits consist of well-sorted windblown light brown very fine-grained sand and silt.
  - Qs** Modern Playa Deposits (Green, 2009) - The deposit is light gray to light brown and consists of silt, clay, and minor sand.
- Amargosa River Deposits**
- Dm** Modern Amargosa River deposits (Green, 2009) - Qm consists of fluvial deposits within the active, natural stream channels of the Amargosa River. The deposits consist primarily of loose sand, gravel, boulders, and silt and mud/clay.
  - Qgr** Late-Middle Pleistocene(?) Fluvial Gravels of the Amargosa River (Green, 2009) - Qgr deposits consist of subangular to subrounded, moderately-sorted, pebble-cobble gravel. Age of deposit is constrained to be post ~90 ka and pre ~30-24 ka (Green, 2009).
- Alluvial Fan Deposits**
- Qa1** Latest Holocene Alluvial Fan Deposits - Qa1 deposits have the active to recently active channels. Deposits are abundant bar and scum fan surface topography with no rounded clasts or desert pavement. Vegetation is abundant on Qa1 deposits. Qa1 deposits are readily identifiable in aerial photographs by their light color.
  - Qa2** Late Holocene Alluvial Fan - Qa2 deposits are the first surface above the active channels. Bar and scum fan surface topography is present. Desert scum and desert pavement are absent to weakly developed. Vegetation is abundant on Qa2 surfaces.
  - Qa3** Middle Holocene Alluvial Fan Deposits - Surfaces have pronounced bar and scum fan surface topography and are typically more than one Qa1 surface. Qa2 surfaces contain weakly rounded clasts and no desert pavement. There is a moderate amount of vegetation on the surface. Qa3 deposits are typically 8000-15 ka.
  - Qa4** Late Pleistocene Alluvial Fan Deposits - Qa4 surfaces are typically very flat, stratified, elongate surfaces that are light gray to black depending on source lithology. The surfaces contain well-sorted clasts that form flat surfaces with moderate to strong pavement. Vegetation is sparse due to the tightly packed nature of cobbles in the pavement. Qa4 deposits range in age from about 100 ka to 40 ka.
  - Qa5** Middle Pleistocene Alluvial Fan Deposits - These deposits are found at higher elevations than other alluvial deposits. Surfaces contain well-sorted clasts. The deposits are deeply dissected, forming linear whaleback-shaped ridges, with strongly rounded shoulders. Qa5 deposits are 70-400 ka.
  - Qa6** Middle-Early Pleistocene Alluvial Fan Deposits - Surfaces contain well-sorted clasts. The deposits are deeply dissected, forming linear whaleback-shaped ridges, with strongly rounded shoulders. Qa6 deposits contain distally Awasatz Mountains sourced durite and intermediate rocks, as well as volcanic and granitic rocks likely reworked from the post-Military Canyon Formation. Qa6 deposits are 800-500 ka.
- Lacustrine/Fluvial Deposits**
- Qm1** Late Pleistocene Deposits of Lake Manly (Green, 2009) - Qm1 consists of moderately-to-well rounded, moderately-sorted, pebble gravel, clasts are one foot or below an elevation of 40 ft. The unit is light-gray-to-gray and contains primary quartzite and granite, with some gneiss, volcanic, metamorphic rocks. Qm1 correlates to the late-Pleistocene Qm1 lacustrine phase of Lake Manly.
  - Qm2** Late Pleistocene Deposits of Lake Manly (Green, 2009) - Qm2 consists of interbedded sand, silt, and clay and exhibits a strong, well-indicated salt crust with opogonite features formed on surface exposures. The deposits are found at or below an elevation of 40 ft and lack significant dissection. Qm2 is correlated to the late-Pleistocene Qm2 lacustrine phase of Lake Manly (~30-24 ka).
  - Qm3** Middle Pleistocene Gravel Deposits of Lake Manly (Green, 2009) - Qm3 consists of interbedded sand and gravel. The interbedded beds contain well-sorted, subrounded clasts to coarse-grained sand and very fine pebble gravel. The top of the unit contains ~15-20 cm thick pebble-cobble gravel.
  - Qm4** Early-Middle Pleistocene Deposits of Lake Manly (Green, 2009) - Qm4 consists of interbedded sand, silt, and clay with minor boulders (masses of conglomerate) and a few trace thin lignite layers.
  - Qm5** Early Pleistocene(?) Deposits of Lake Manly (Green, 2009) - Qm5 deposits are generally poorly exposed and were therefore not studied in detail. The unit consists of light brown to tan, moderately to poorly indurated sand, silt, and clay.
  - Qm6** Late Pleistocene-Early Pleistocene Fungiformites - Matrix supported gravel-to-boulder fungiformites; light brown to gray, weakly indurated, moderately to poorly sorted. Clasts are subangular to subrounded. This unit is locally indurated. This unit is most uniformly on the Noble Hills Formation, the undifferentiated units of Tm, and the Military Canyon Formation. Clast cores from these locations are shown in Fig. CCH001, CCH002, CCH003.
  - Qm7** Late Pleistocene-Early Pleistocene Fungiformites - Matrix supported gravel-to-cobble fungiformites; light brown to gray, weakly indurated, poorly sorted. Clasts are subangular to subrounded. This unit was unconformably on the Noble Hills Formation, and T1 fungiformites.
  - Qm8** Late Pleistocene-Early Pleistocene Fungiformites - Matrix supported gravel-to-cobble fungiformites; light brown to gray, weakly indurated, poorly sorted. Clasts are subangular to subrounded. T1 beds unconformably on, and is channelled into the Noble Hills Formation.
- Noble Hills Formation**
- NH1** Granite Bearing Conglomerate of the Noble Hills Formation - Matrix supported gravel-to-boulder conglomerate. Light gray, moderately to poorly to moderately indurated, poorly sorted. Clasts are subangular to subrounded. This unit contains predominantly (90-95%) granitic clasts with lesser volcanic and quartzite (see clast count table CCH009, CCH010, Figure 10 in text).
  - NH2** Mesozoic Member of the Noble Hills Formation - Coarsely graded blocks of Precambrian Kingston Peak and Crystal Springs Formation, granitic gneiss, and Mesozoic granitic rocks. Block size on the order of tens of meters. Poorly indurated and moderately faulted.
  - NH3** Upper Sandstone, Siltstone and Gypsiferous Member of the Noble Hills Formation - Fine-grained sandstone, siltstone, and gypsiferous sandstone, light gray-to-white. Moderately to well-sorted, weakly indurated. Unit is highly indurated, and contains Durite clasts of quartzite, limestone, marble, and dolomite, with lesser clasts of granite and schist. Unit is a poorly-sorted, subangular to angular pebble-to-boulder conglomerate consisting of clasts derived from the Awasatz Mountains.
  - NH4** Halite Mudstone Member of the Noble Hills Formation - Poorly indurated, medium brown halite muds, silt, and siltstone with angular pebble conglomerate. Where exposed by strong erosion, massive crystalline halite displays fine weathering features. Seeps form small scale salt topography.
  - NH5** Gypsiferous Member of the Noble Hills Formation - Light gray-to-white to light greenish-white evaporitic siltstone, and sand and brown siltstone. Unit is highly indurated and cleaved by desiccation, but where exposed in the vicinity of thrust faults, Gypsiferous intervals contain secondary vuggy porosity.
  - NH6** Lower Sandstone and Siltstone Member of the Noble Hills Formation - Well-sorted fine-grained arkose sandstone and siltstone, matrix supported pebble conglomerate, siltstone, gypsiferous, and well-indurated limestone. Fine grained beds are usually thinly laminated. Graded bedding, trough, and trough cross-beds are common in sandstone and siltstone lenses. Limestones display cleaved laminae, crystalline texture, and secondary terrar and nodular chert.
- Older Sediments of the Noble Hills**
- U1** Undifferentiated Pliocene (?) Brine - The central belt of Brady (1986). Consists of anoxic agglomerate, which locally is gypsiferous shale, red-brown, pebble-conglomerate, granitic megacrysts, halite, and limestone.
  - U2** Miocene (?) Military Canyon Formation (Brady, 1986a) - Fine grained sequence consisting of boulder-to-cobble conglomerate, coarse sandstone, sandstone, siltstone, claystone, fine-grained limestone, gypsiferous, and halite (Brady, 1986a).
- Older Rocks of the Noble Hills and Awasatz Mountains**
- M1** Mesozoic lacustrine sediment - Brine to clay, medium to coarse grained sedimentary to evaporitic sediment; calcareous (quartz monazite) (Starnes, 1981).
  - M2** Mesozoic undifferentiated monodioritic rocks - The Awasatz quartz monodiorite of Spencer (1981). Variable in composition. Ranges from diorite to quartz monodiorite, granite and quartz monzonite (Spencer, 1981).
  - P1** Undifferentiated Precambrian and Paleozoic (?) rocks - Primarily consists of Precambrian Crystal Springs Formation and associated schist and gneiss (Starnes, 1981).
  - P2** Undifferentiated Precambrian metamorphic and intrusive rocks.
  - G1** Gneiss - Granitic gneiss present as roof pendants in M2 (Starnes, 1981).

MAP SYMBOLS

- Contact between map units - Solid where accurately located, dashed where approximately located, when well and spaced contact type (i.e. dip-slip or fault) is uncertain.
- Inset channel contact - Characterized by conglomerate unconformably inset into older Noble Hills Formation. Identity and existence certain, location accurate. Numerous pebbles into channel.
- Fault - Solid where accurately located, dashed where approximately located, dotted where concealed, spaced where uncertain. Arrows show relative motion.
- Normal fault - Solid where accurately located, dashed where approximately located, dotted where concealed, quartered where anticlinal, roll and bar on downthrow.
- Hawassa fault - Solid where accurately located, dashed where approximately located, dotted where concealed, quartered where anticlinal, half-sphere on downthrow.
- Thrust fault - Solid where accurately located, dashed where approximately located, dotted where concealed, quartered where anticlinal, sawtooth on upper (tectonically higher) plate.
- Syncline - Dashed where approximately located, dotted where concealed.
- Anticline - Dashed where approximately located, dotted where concealed.
- Tectonics - Strike and dip of inclined bedding, Strike and dip of overturned bedding, Approximate strike and dip of contorted bedding.
- Figure - Clast count location, Figure 11 in text for lithologic descriptions.
- Trapezoid - Trapezoid sample location, number.
- Cross section line - See text for cross sections.

CORRELATION OF MAP UNITS



- REFERENCES TO GEOLOGIC MAPPING**
- Geor, H.L., 2005. Biostratigraphic investigation of the southern Death Valley fault zone, southern California. San Francisco State University, 131 pp.
  - This report.
  - Brady, R.L., 1986. Geologic geology of the northern Awasatz Mountains in relation to the intersection of the Carlock and Death Valley fault zones, San Bernardino County, California. Ph.D. thesis, University of California, 292.
  - Jimwings, C.W., Stead, R.G., and Rogers, T.H., 1977. Geologic map of California. California Division of Mines and Geology, scale 1:750,000.
  - Spencer, J.C., Geology and geomorphology of the Awasatz Mountains, San Bernardino County, California. Ph.D. dissertation, 140 pp. Also, in: Tuller, Cambridge, 1981.
  - Starnes, J.T., 1981. Geology of the intersection of the Death Valley and Carlock fault zones, southern Death Valley, California. Pennsylvania State University.





*APPENDIX 3*

Extended abstract (WGC 2020+1)



## **Petrographic Analyzes of Fractured Granites used as An Analogue of the Soultz-sous-Forêts Geothermal Reservoir: Noble Hills, CA, USA**

Johanne Klee<sup>1\*</sup>, Ghislain Trullenque<sup>1</sup>, Béatrice Ledésert<sup>2</sup>, Sébastien Potel<sup>1</sup>, Ronan Hébert<sup>2</sup>,  
Arezki Chabani<sup>1</sup>, Albert Genter<sup>3</sup>,

<sup>1</sup>Institut Polytechnique UniLaSalle, 19 rue Pierre Waguet, F-60000, Beauvais, France

<sup>2</sup>Université de Cergy-Pontoise, 1 rue Descartes, F-95000, Neuville sur Oise

<sup>3</sup>ES-Géothermie, 5 rue André Marie Ampère, F-67450, Mundolsheim

\*johanne.klee@unilasalle.fr, others: ghislain.trullenque@unilasalle.fr, beatrice.ledesert@cyu.fr, sebastien.potel@unilasalle.fr,  
ronan.hebert@cyu.fr, arezki.chabani@unilasalle.fr, albert.genter@es.fr

**Keywords:** EGS system, analogue, fractured granite, rock/fluid interaction

### **ABSTRACT**

The work presented here is part of the European MEET project (Multidisciplinary and multi-context demonstration of EGS exploration and Exploitation Techniques and potentials), which aims to enhance demonstration of geothermal energy production throughout Europe. Petrographic analyzes of a geothermal reservoir are key issues for the understanding of fluid circulation in granitic rocks. Through field work, microscopical observations (optical microscope, SEM) and XRD analyzes, we aim at characterize a fractured and altered granitic body found in the Noble Hills (NH, Southern Death Valley, CA, USA) chosen as an analogue of the Soultz-sous-Forêts (SsF) geothermal reservoir (Upper Rhine Graben, Alsace, France). Our current state of knowledge reveals that the NH range is composed of a fractured and altered Mesozoic granitic body intruding Proterozoic sedimentary series. The composition of the granite and its alteration processes present similarities with the ones at SsF: oligoclase is transformed into kaolinite (tosudite at SsF) / illite/calcite and biotite into chlorite/illite. The whole range suffers a substantial amount of shear deformation linked to the activity of the Southern Death Valley Fault Zone (SDVFZ) possibly much higher compare to SsF. A gradient of deformation can be followed through the range and along which samples were collected. Those ones reveal that the shear deformation can either reactivate mineralized fractures and create new drains for fluid circulation at low strain or promote the plugging of fractures due to the development of a high amount of clay minerals at high strain. Through analogue studies we here aim at 1) better understand the geometry of fluid circulation paths in the granitic fractured reservoirs and 2) gain insights in fluid rock interaction processes as these can drastically modify fractures properties through time.

### **1. INTRODUCTION**

The H2020 MEET European project (Multidisciplinary and multi-context demonstration of EGS exploration and Exploitation Techniques and potentials) aims at improving of a deep geothermal reservoir by new exploitation and energy production techniques while continuing to explore and exploit the EGS (Enhanced Geothermal System) technology. In order to lower the cost and develop the use of geothermal energy in Europe the EGS technology must be developed in large variety of geological environments like intra-cratonic sedimentary basins and Variscan orogeny related terrains. Applying EGS techniques to Variscan domains are particularly challenging for a variety of reasons like 1) the complex geological history of the Variscan orogeny itself, 2) possible Alpine tectonic overprint and 3) the high anisotropy of the metamorphics rocks.

Reservoir understanding at depth is a prerequisite for a successful application of EGS technique. In the present study we aim at understanding fluid/rock interaction processes taking into consideration the amount of deformation affecting the reservoir. Our work is focused on the petrographical and petrophysical characterization of fractured granitic reservoirs and the SsF site is used as the demonstration site. Unfortunately access to the SsF reservoir is reduced to a limited amount of cores preventing a global geological understanding of the reservoir. Studies on analogues, i.e. exhumed fossil reservoir in which fluids have circulated are necessary to understand the evolution of fractured granitic reservoirs at large scale. In the following, we consider an analogue of a reservoir not as a true copy of the reference site but as an entity having similarities in term of structural and geological context and also in term of type of rocks. The main chosen analogue is the NH range located in the Death Valley in California (USA). It is proposed that progressive fracture sealing involving a combination of 1) fluid/rock interaction and precipitation of clay minerals and 2) deformation and associated dynamic recrystallization processes lead to variations in reservoir productivity at geological scale. Our model of evolution has important consequences in terms of targeting potential fractures systems at depth and adapting stimulation strategies.

### **2. THE MEET VARISCAN OROGENY APPROACH**

The Variscan domain very often outcrops in Europe and is recognized for its good geothermal potential. Some gas wells crossing it have shown the occurrence of a geothermal resource. In order to structure our approach, the Variscan domain has been divided in two main parts depending on the nature of the encountered rocks (Variscan metasediments and metavolcanics versus Variscan granitic basement) themselves divided in two groups depending on their tectonic history: Variscan domains affected by post Variscan extensional tectonics versus Variscan domains not affected by post Variscan extensional tectonics.

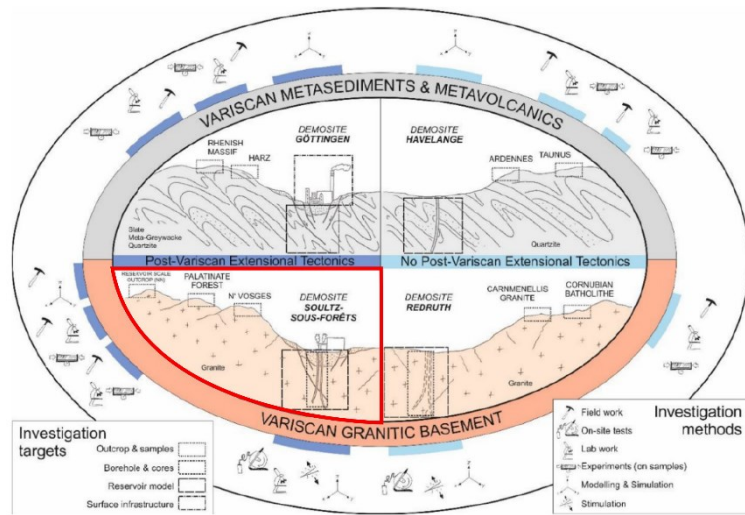


**Figure 1: Schematic overview of the four representative European Variscan geotectonic settings including the demonstration sites, the analogue sites and the investigation methods according to (Trullenque et al., 2018). Our case study is framed in red.**

The MEET project has a demonstration site each of these contexts (Figure 1) (Trullenque et al., 2018):

- Variscan metamorphic (metasedimentary and metavolcanic) successions overprinted by younger (mostly Cenozoic) extensional tectonics (rift system): demonstration site University of Göttingen (Germany)
- Variscan metamorphic (metasedimentary and metavolcanic) successions not overprinted by younger extensional tectonics: demonstration site Havelange (Belgium)
- Variscan crystalline basement overprinted by post-variscan extensional faults: demonstration site Soultz-sous-Forêts (France), which is our study (fig. 1)
- Variscan basement not overprinted by younger extensional faults: demonstration site Redruth (United Kingdom)

### 3. PRESENTATION OF THE DEMONSTRATION AND ANALOGUE SITES

#### 3.1. Demonstration site: Soultz-sous-Forêts

##### 3.1.1. Geological context

The SsF site is located within the Upper Rhine Graben (URG), which forms the central most conspicuous segment of the European Cenozoic Rift System (Ziegler, 1992), near its major western boundary fault (Figure 2a).

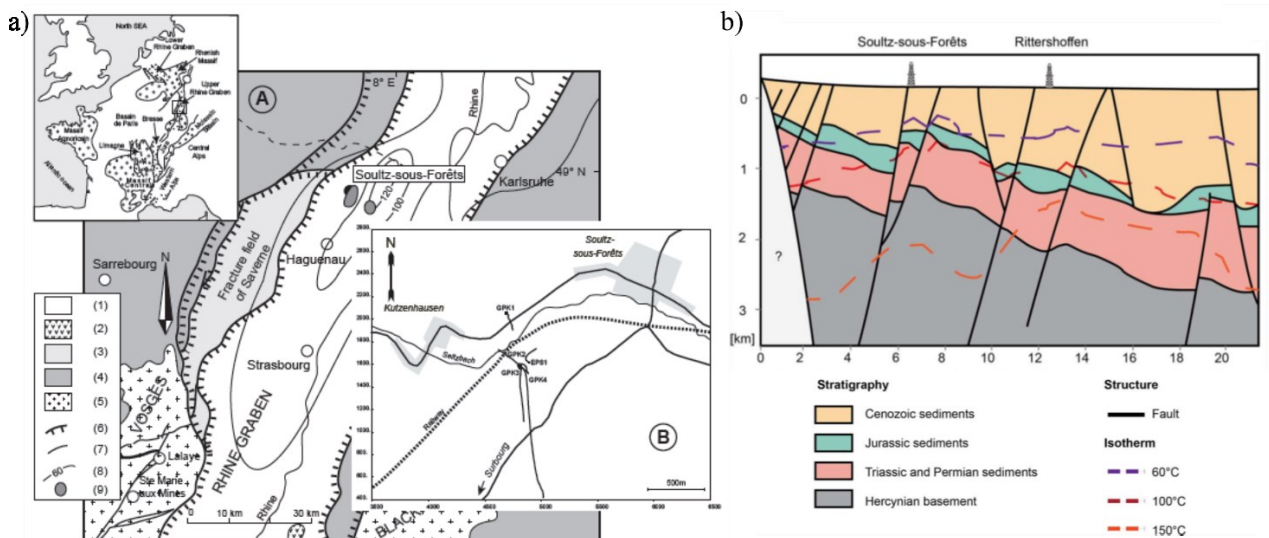


**Figure 2: Figures presenting a) A: the location of the EGS Soultz-sous-Forêts site and geology of the URG and B: a local map of the Soultz-sous-Forêts site with the well trajectories. According to (Dezayes et al., 2004) and b) a simplified geological cross section and isotherms across Soultz-sous-Forêts and Rittershoffen geothermal plants (Vidal and Genter, 2018)**

The URG originates in Paleogene times from the Alpine collision due to the build-up of far-field intraplate compressional stresses and is described as a typical example of syn-orogenic, intra-continental foreland rifting affected by Variscan crustal pre-

discontinuities (Ziegler, 1992; Dèzes et al., 2004). It has a NNE-trending which is limited by the Rhenish Massif to the north and the Jura Mountains to the south and has a length of some 300 km and a width of 30-40 km.

Three major terranes oriented NE to NNE characterize the Variscan crystalline basement of the URG. They are intruded by carboniferous granitoids (Visean (-340 Ma) and Permian (-270 Ma)) which are emplaced following the URG trending related to primary weakness zones such as collisional or shear zones. These Paleozoic crystalline basement rocks do not outcrop but are overlain by 1400 m of Mesozoic (Triassic and Jurassic) and Cenozoic sediments (Figure 2b). Rifting occurred during the Tertiary between the end of the Eocene and the beginning Miocene (Schumacher, 2002; Dezayes and Lerouge, 2019; Edel and Schulmann, 2009).

### 3.1.2. Soultz-sous-Forêts site

After an initial Hot Dry Rock (HDR) concept, SsF has evolved to an EGS technology which consists in hydraulic and/or chemical stimulations to increase the permeability and allow transport of the geothermal brine (Dezayes et al., 2010). In total five boreholes have been drilled but only three of them are used for reservoir development and heat exploitation. Those ones reach a depth of approximately 5000 m with temperatures up to 200°C.

All the wells exhibit at least one permeable fracture zone and the natural fracture network acts as a natural heat exchanger. The top of the granite is highly fractured with a fracture density average of 1 fr/m above 2000 m. Below, the fracture density decrease to 0.4 fr/m and in the deep part it increases to 0.6 fr/m between 4600 and 5100 m (Dezayes et al., 2004).

The SsF reservoir is characterized by the presence of highly fractured fault cores, which are surrounded by altered, porous and fractured damage zones. Through these fractures a highly saline fluid (100 g/L) circulates at a temperature between 130 and 150°C. Fault zones present a higher permeability for hydrothermally altered granitic basement than for hard fractured sandstones or poorly altered deep granitic basement (Vidal and Genter, 2018). Fracture fillings are heterogeneous, and polyphased, dominantly represented by quartz, barite, illite, carbonates, and iron oxides (Genter et al., 1995). Quartz veins are mainly localized into the fault core and correspond to the precipitation of silica-rich fluids derived from the dissolution of primary silicate minerals during vein alteration (Vidal and Genter, 2018). The hydrothermal alteration of the SsF granite is characterized by specific mineral assemblages and changes in bulk-rock chemical composition. It presents two major kinds of alteration: 1) a propylitic alteration linked to the cooling of the pluton, characterized by the partial transformation of biotite into chlorite and plagioclase into illite and newly formed epidote (Genter, 1989) and 2) a vein alteration due to fluid flowing within the fracture network which induces chemical leaching and clay enrichment processes (Genter, 1989; Ledesert et al., 1999; Pauwels et al., 1993). Alteration of primary minerals related to these water-rock interactions leads to the breakdown of: 1) plagioclase mainly into illite but also into tosudite in the SsF granite (Ledesert et al., 1999). Tosudite is considered as a geochemical analogue of kaolinite, but the occurrence of tosudite instead of the kaolinite can be explained by the amount of lithium present in the fluid (Pauwels et al., 1992) and 2) biotite into chlorite and illite. Primary K-feldspar and quartz are not affected by this alteration (Traineau et al., 1991). The URG granite has been affected during the Tertiary by several compressional and extensional tectonic phases developing a multiscale fracture network (Schumacher, 2002). This latter having suffered no more deformation let geothermal fluid flow through those open fractures. Glaas et al., (2019) argue that in the case of an open fracture, the fluid is mainly channeled in the core fault, precipitating drusy quartz and partially in the walls. However, when this fracture or vein is completely sealed by quartz or illite, only the open fractures present in the damage zone can act as fluid pathways (Figure 3).

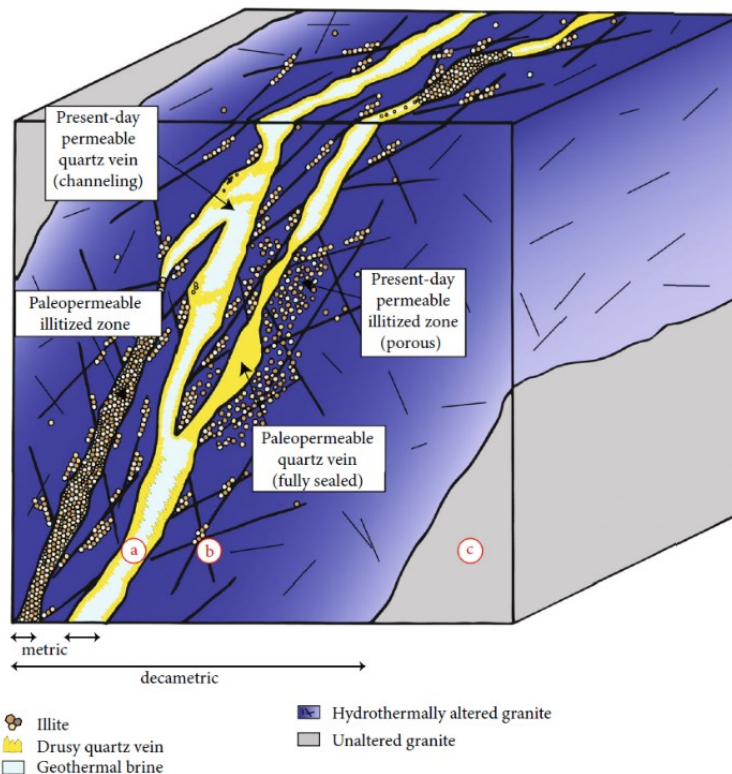
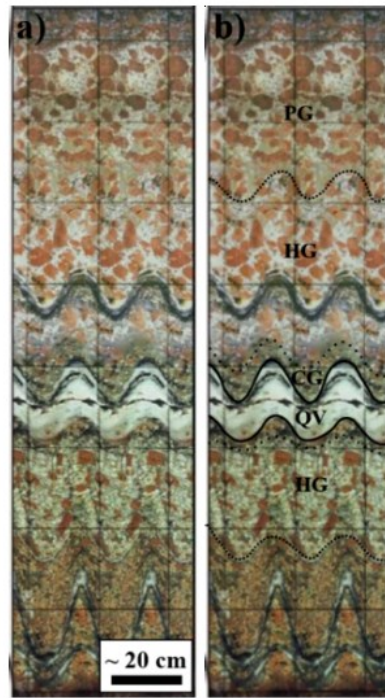


Figure 3: Block diagram from Glaas et al. (2019) representing the fluid circulation in a complex system of fault zones

In order to illustrate the above mentioned deformation and alteration features we present two core samples, SsF1 and SsF2, from borehole EPS1 taken at a depth of 2160 m (Measure Depth) and around 1400 meters respectively. Sample SsF1 (Figure 4) has been intensively investigated by Vidal and Genter, (2018) and originates from a major permeable fracture zone. It shows a prominent alteration gradient from the walls of the granitic veins away from it. Note that besides the vein opening and associated fluid circulation related alteration, the rock initial magmatic texture remains undisturbed. We notice in particular the lack of any cataclastic nor mylonitic deformation implying that no strain was applied along the vein walls after vein opening.



**Figure 4: Sample SsF1. Scan of a core (laid flat and doubled) of major permeable fracture zones from EPS1 well at Soultz-sous-Forêts with a) the original scan and b) the different zonation characterizing the core. QV: Quartz vein; CG: Cataclased granite; HG: Hydrothermalized granite; PG: Porphyritic granite (modified after Vidal and Genter, 2018).**

As described by (Glaas et al., 2019), only opened or filled fractures are investigated in the SsF reservoir. However, there is evidences of shearing as shown by the sample SsF2 (Figure 5). It exhibits intense shearing accommodated along a foliated and anastomosing cataclastic gouge with a clear gradient of alteration affecting the rest of the sample. Note the impressive stretching of the oxide precipitates and quartz ribbons related to post vein formation strain. This deformation zone is non-permeable for geothermal fluids as totally sealed by a large variety of dynamically recrystallized and neo-formed fine-grained minerals.

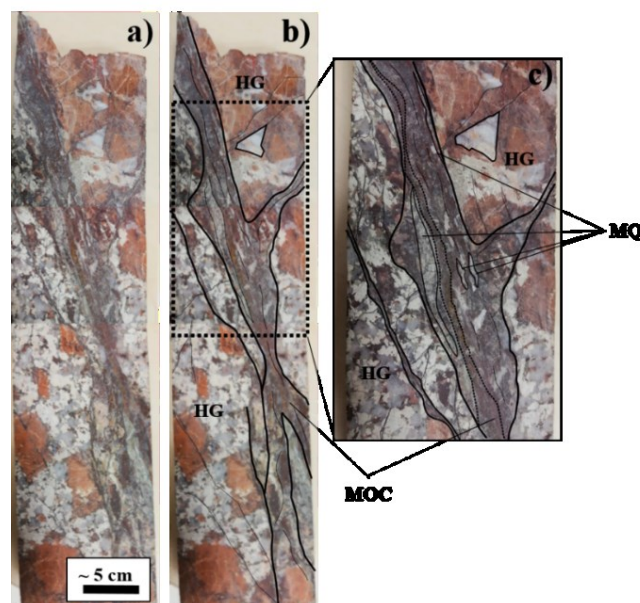


**Figure 5: Sample SsF2. Picture of a longitudinal core cut section of a sheared and sealed fracture from EPS1 well at Soultz-sous-Forêts with a) the original picture, b) the different zonation characterizing the core and c) a zoom on the core. HG: Hydrothermalized granite; MQ: Mylonitic quartz as relicts; MOC: Mylonitic oxides and clays.**

Deformation has an important impact on the evolution of the fault petrophysical properties (Wallace and Morris, 1986) and on the reservoir connectivity (Bailleux et al., 2011; Curewitz and Karson, 1997). That is why one part of this study focuses on varying deformation amounts accumulated on faults and their impact on fluid circulation and fluid/rock interaction processes.

### 3.2. Analogue site: Noble Hills

#### 3.2.1. Death Valley geological context

The Death Valley region is located in the southwestern part of the Basin and Range province of southeastern California and southern Nevada (Figure 6) and is bounded on the west by the Panamint Range and the south by the Providence Mountains. The Death Valley region is one of the youngest regions of large-scale crustal extension within the Basin and Range province. This extension occurred from the Miocene to the Holocene. Normal and associated strike-slip faulting accompanied by the extensional basin formation began < 15 Ma and continues today (Calzia and Rämö, 2000).

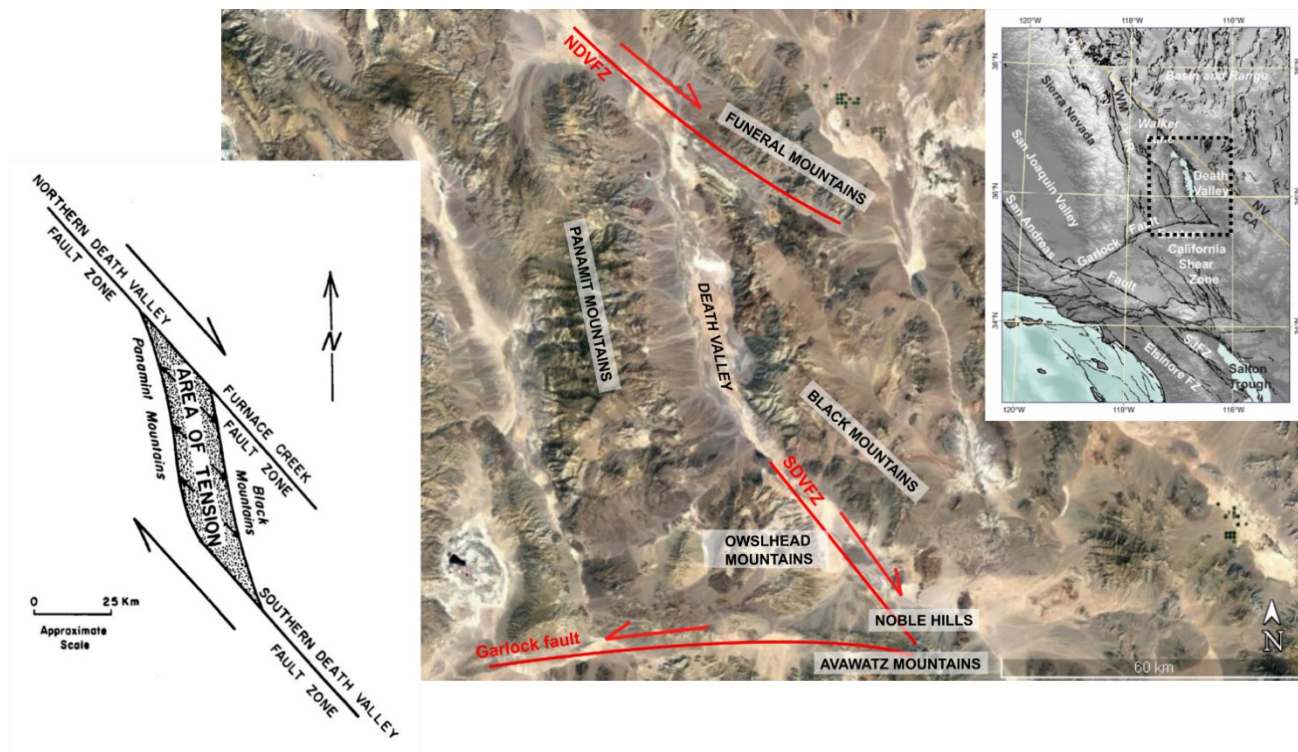


**Figure 6: Location of Death Valley and tectonic domains modified after ((Burchfiel and Stewart, 1966; Norton, 2011) NDFVZ – Northern Death Valley Fault Zone; SDVFZ – Southern Death Valley Fault Zone**

The Southern Death Valley Fault Zone (SDVFZ) is part of the northwest-trending, right-lateral, strike-slip system of faults located in southern Death Valley. Along with the Northern Death Valley-Furnace Creek Fault Zone (NDFVZ), the SDVFZ appears to be related to extension within the southern Basin and Range province (Stewart, 1983) and so makes up the southern component of the Death Valley fault system (DVFS) (Machette et al., 2001). Near its southern end, the fault zone intersects the east-trending, left-lateral Garlock fault which is linked to the San Andreas Fault (Calzia and Rämö, 2000). A right-lateral offset of ~35 km has been defined, based on matching offset alluvial fan ravel with its source area. It refined earlier estimates of 8 to 80 km of movement for the SDVFZ (Butler et al., 1988) and is consistent with the geometry of a pull-apart basin model for central Death Valley defined by Burchfiel and Stewart, 1966. Recently, (Pavlis and Trullenque, Submitted) have proposed a net amount of 40 to 41 km strike-slip along the SDVFZ based on correlation of a set of geological markers between the Owshead and the southern termination of the Noble Hills.

In this region the pre-Cenozoic stratigraphy consists of Early Proterozoic cratonic rocks and Middle Proterozoic sedimentary paragneiss, schist, and quartzite intruded by ca.1700 Ma orthogneiss and 1400 Ma anorogenic granites (Wooden and Miller, 1990). The Middle Proterozoic Pahrump Group unconformably overlies the cratonic rocks and is overlain by 3000-5000 m of Late Proterozoic and Paleozoic miogeoclinal deposits. It consists of ~2100 m of conglomerate, sandstone, shale, and carbonate rocks divided into three formations: the Crystal Spring Formation, Beck Spring Dolomite, and Kingstone Peak Formation. The first one, Crystal Spring Formation, is intruded by 1068 Ma and 1087 Ma diabase sills. Most of the Proterozoic and Paleozoic rocks are intruded by Mesozoic and Tertiary plutons. All these rocks are overlain by later Tertiary sedimentary and volcanic rocks and Quaternary alluvial deposits. Note that numerous granitic plutons, dikes, and sills are synchronous with extension (Calzia and Rämö, 2000).

#### 3.2.2. The Noble Hills range.

The Noble Hills (NH) are located in the southernmost part of the Death Valley region and trend parallel to the SDVFZ at its southern end (Figure 6). Troxel and Butler, (1979) characterized the SDVFZ as a zone of multiple, subparallel, overlapping right-lateral fault strands extending northwest the length of the NH from the foothills of the Avawatz. In the NH, the SDVFZ juxtaposes Tertiary and Quaternary strata against crystalline basement rocks also called “axial crystalline ridge” (Brady III, 1986). This one comprises

Precambrian Crystal Springs Formation of the Pahrump Group and is intruded by undifferentiated Mesozoic granitic rocks which crop out and locally by 1.1 Ga diabase sills (Troxel and Butler, 1979).

A combination of GIS assisted field work mapping and intensive sampling of the area were realized. Regarding mapping we revisited the work of Niles, 2016. It was conducted in the field by using satellite imagery and supported by our own observations. Structural data were collected on all the area to have a general overview of the kinematic of the NH. The mapping revealed a complex geometry with several repetitions of the Proterozoic sedimentary cover. A perfect continuity of those series as well as granite is observed southeastward together with an impressive stretching linked to the dextral shear activity of the SDVFZ, which shows an increasing deformation gradient toward the south east (Figure 7).

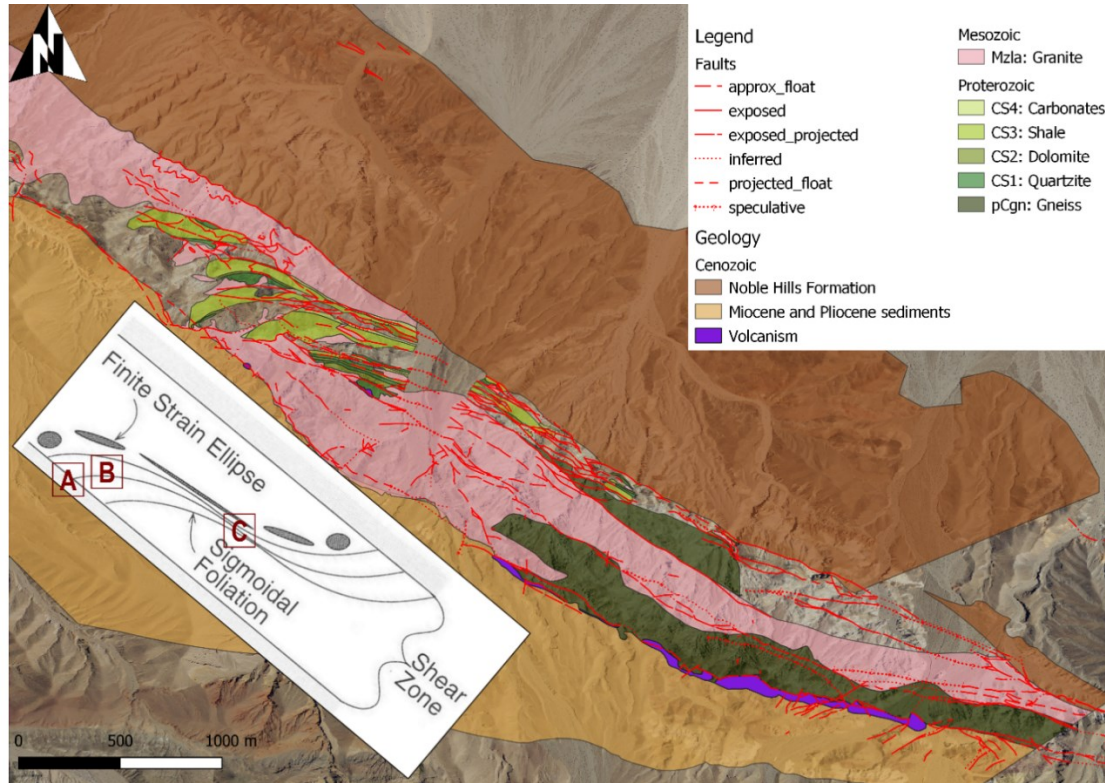


**Figure 7: Geological map of the Noble Hills range realized from field investigations (ongoing work) and after Niles (2016) compared to a scheme of a shear zone (<https://slideplayer.com/slide/3405849>). A, B and C correspond to samples collected along the deformation gradient.**

#### 4. PETROGRAPHIC CHARACTERIZATION

##### 4.1 Hydrothermal alteration of the granitic basement

The sampling was done 1) in a homogeneous way to cover the study area as much as possible and 2) following the gradient of deformation. Thin sections were investigated for each of the 37 samples collected in the field. An accurate optical microscopic study allowed to determine the mineralogical composition of each sample. The main primary minerals are feldspars (plagioclases and K-feldspars), quartz and biotite. More precisely, plagioclase, in our case oligoclase, are the most abundant. According to (Streckeisen, 1973) the composition corresponds to a granite/granodiorite. Moreover, it has been observed that the samples present signs of alteration due to a fluid circulation. This alteration affects plagioclase and sometimes biotite. Quartz and K-feldspar remain intact. Plagioclase alteration initiates at the center of the mineral (Figure 8a and b) and spreads to the edge. They are transformed into kaolinite (Figure 8c) and into illite (Figure 8d). Cathodoluminescence observations (Figure 8b) show that plagioclase can present a Na-rich rim (in blue) attributed to albite, and can contain calcite.

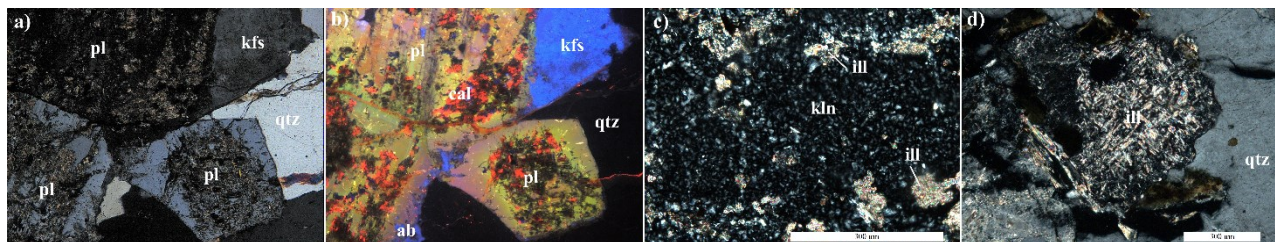


**Figure 8: Images a) of altered plagioclases under optical microscope in polarized and analyzed light, b) of the same plagioclases than a) under cathodoluminescence presenting the calcite in red, in pink-green the plagioclases with a blueish albite rim and also in blue the K-feldspars, c) kaolinite and illite as plagioclase pseudomorphosis products under optical**

**microscope in cross polarized light and d) of an altered plagioclase with illite precipitation under optical microscope in cross polarized light**

When observed with a scanning electron microscope coupled with an energy dispersive spectrometer (SEM-EDS), plagioclase shows corrosion pits and zones where kaolinite has crystallized, replacing plagioclase. A focus on kaolinite is given in Figure 9, showing hexagonal particles organized in fan shape. Illite (Figure 8d) and also calcite are precipitating. During the alteration of plagioclase Ca was released which contributed to the precipitation of carbonates, here nearly pure calcite. The samples generally have a high amount, up to 10% of carbonates (calcite and dolomite) occurring mainly as veinlets. However, it is unlikely that such a high amount of calcite is only related to the alteration of the plagioclases. Since Precambrian age dolomites crop out within the Noble Hills, i.e. in direct vicinity of the granite. It is conceivable that the fluid got enriched in Ca and Na while crossing the dolomite units to finally precipitate carbonates in the fracture network affecting the granitic basement.

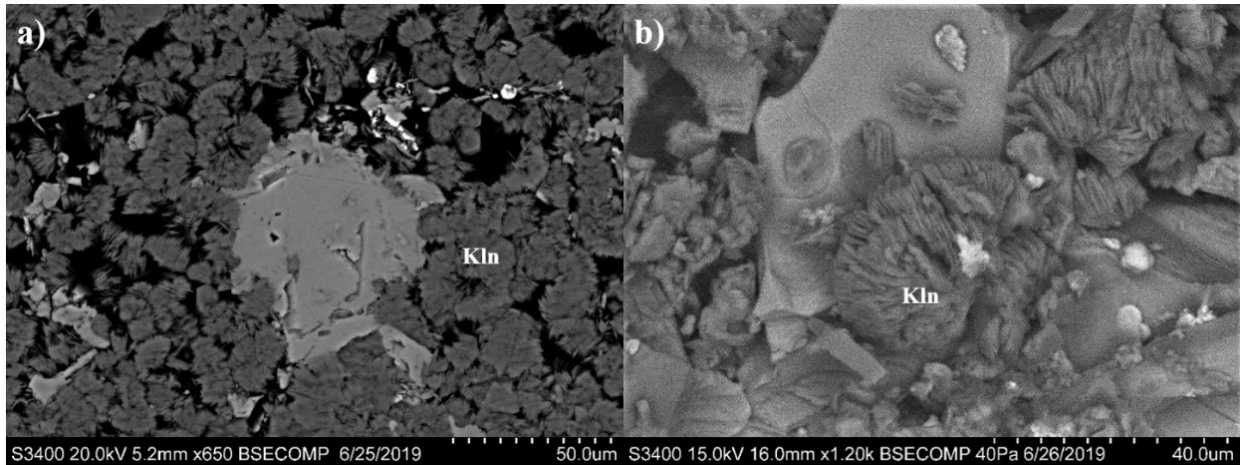


**Figure 9: Images of kaolinite of the same sample under SEM of a) the thin section and b) a piece of the sample**

Biotite alteration is less pronounced than that of plagioclase. Large patches of biotite are indeed still recognizable in thin sections (Figure 10). According to SEM-EDS analyzes, the product of biotite alteration contains only K, Al, Si and O (no Mg and Fe) and corresponds to illite. This type of transformation is also observed on biotite in the SsF granite (Bartier et al., 2008; Ledesert et al., 1999). The lack of Mg and Fe could be due to the extraction from biotite during alteration and seems to be confirmed by the occurrence of oxides surrounding altered biotite as visible in Figure 10. Further SEM investigations and Mass Balance Calculations are planned to confirm this hypothesis in other samples.

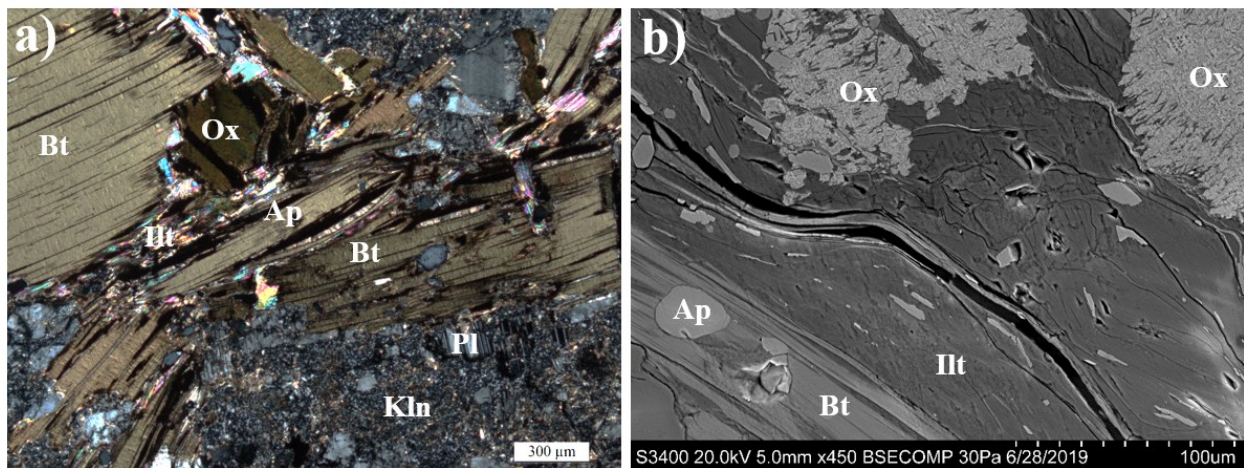


**Figure 10: Images of slightly altered biotite, a) under polarized and analyzed light and b) under SEM**

Samples present sign of dynamic recrystallization processes affecting quartz. Bulging recrystallization develop at the boundary between quartz crystals indicating a temperature around 300°C (Stipp et al., 2002). XRD analyzes were performed on these samples and, based on the illite crystallinity (Kübler, 1968), data show a low degree of metamorphism with temperature lower than 300°C. This apparent contradiction in term of temperature can be explained by the fact that the system has been potentially reset with time due to fluid circulation and deformation. K/Ar dating on illite is underway to replace the fault within the historical context and answer to this question.

#### 4.2 Fault zones fluid circulation associated to the amount of deformation

As already announced, the Noble Hills granite present an intense gradient of deformation. Three zones (A, B and C on Figure 7) were chosen along this gradient in order to describe the response of granitic rock to strain. The aim is to see the influence of the deformation on the fluid circulation.

The zone A is characterized by a granite presenting incipient signs of deformation. Fractures are filled by secondary mineral precipitations as carbonates (Figure 11a), oxides, barite (Figure 11b). Those fractures had to act as the main fluid channels before their complete sealing. Due to this concentrated fluid flow in the fracture, the walls develop a decreasing alteration halo by moving away from the fracture.



**Figure 11: Pictures from zone A presenting a) an altered granite rich in carbonates veins and b) a fracture filled by automorphy barite**

The zone B (Figure 7) manifests a low strain illustrated by the sample presented in Figure 12. This sample shows: 1) a pronounced alteration gradient from either side of the fracture and 2) a sharp contact marking the border between the granite and the deformed quartz vein relict. This vein is reduced to fractured, rounded shape quartz blocks interpenetrated by carbonates veinlets. A centimetric scale ultracataclastic layer consisting in a mix of carbonates, clays and granitic clasts marks the border with the host rock. Those observations indicate that a Ca rich fluid has circulated during the reactivation of the fracture, precipitating carbonates which were crushed due to ongoing shearing.

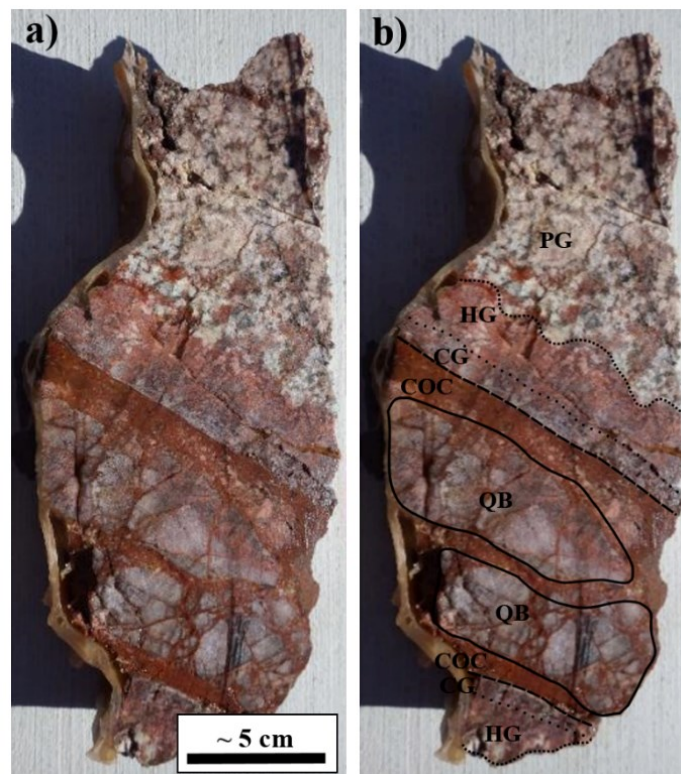


**Figure 12: Pictures from zone B of a quartz vein slice from Death Valley with a) the original picture and b) the different zones characterizing the slice. QB: Quartz blocks; COC: Cataclastic oxides/clays layer; CG: Cataclased granite; HG: Hydrothermalized granite; PG: Porphyritic granite**

Finally, high strain is highlighted in the zone C (Figure 7) and characterized by two meters width clay gouge. The sample from this gouge (Figure 13) presents a global matrix rich in clay minerals, mainly illite, but also some reworked clasts of quartz, carbonates and oxides. Microscopic and SEM observations show signs of intense shearing as sigma clasts. In both sides of the gouge the host rock is highly fractured and altered.



**Figure 13: Picture from zone C of a sample from a clay gouge presenting signs of a high amount of dextral shear deformation**

Complementary analyses are performed as SEM analyses supported by XRD and cathodoluminescence analyses to better characterize the mineralogical, structural and chemical composition of the samples. Geochemical analyses are also performed in order to better quantify the chemical composition of the bulk rock and to characterize the possible chemical elements transfer. Others analyzes are planned: 1) fluid inclusions analyses in quartz crystals in order to obtain information on the pressure, temperature and salinity of the fluid which has circulated, 2) calcimetry analyses to determine the proportion of carbonates in the samples and 3) goniometry and EBSD to investigate microfabric characteristics of fault core zones.

## 6. DISCUSSION AND CONCLUSION

### 6.1 Comparison of granite alteration between NH and SsF

The vein emplacement alteration leads to the transformation of primary minerals of the whole rock into neo-formed minerals. In both SsF and NH granite, the same primary minerals are altered. Plagioclase is transformed into illite an kaolinite or locally into tosudite in the case of SsF (Bartier et al., 2008) and biotite is transformed into chlorite (propylitic alteration) and then illite (vein alteration). Those veins are composed of different mineralization as carbonates, oxides, clays, quartz and barite and found in both granites. It shows that different generation of fluid have circulated. However, in the Noble Hills, the propylitic alteration, well described in the SsF granite, is probably almost totally overprinted by the vein alteration due to the nearly total absence of chlorite and epidote.

### 6.2 Impact of the deformation on fluid circulation

The reservoir productivity at SsF is mainly taken up by a few opened fractures showing incipient geodic minerals, essentially quartz precipitations (Vidal and Genter, 2018 and references therein). Glaas et al., (2019) mentioned that in geothermal system without shear deformation (opening mode), fractures filled by different mineralization are considered as paleo-permeable zones, which allow the fluid to circulate only in the walls (Figure 3). Compare to SsF, the NH granite undergone a higher amount of shear deformation due to the recent activity of the SDVFZ. By considering this deformation, some mineralized fractures can be reworked allowing the fluid to circulate in the fracture and the increase of fluid/rock interactions (Figure 12). In that case, deformation promotes fluid circulation which is mostly concentrated in the fault core. However, a high amount of deformation associated to fluid circulation can increase the fluid/rock interaction to such a way that a significant amount of clay minerals will be produced (Figure 13). As described by Glaas et al., (2019), fractures filled by clay minerals act as a barrier concentrating the fluid in the walls. This can be applied in the case of the clay gouge presenting in Figure 13, but we suggest here that the fault plugging was promoted by the shear deformation. Depending on the amount of deformation and associated to fluid circulation, fault zone behavior can be drastically modified (Wallace and Morris, 1986).

This work has shown 1) that analogue studies are important to enhance the understanding of the reservoir in its entirety and 2) through the SsF granite knowledges and the field observations in the NH, we see that both granites react similarly to this alteration. Moreover, we conclude that deformation is a crucial parameter influencing fault zone properties and which in turn modify substantially their permeability and so the geothermal exploitation potential.

To enrich the panel of possible analogues to SsF, so to granitic reservoirs and confirm our preliminary interpretations, analogues in the URG shoulders (Black Forest, Germany and Vosges Mountains, France) will come in complement to get information about the importance of the structural inheritance and how those structures influence the fluid circulation.

## ACKNOWLEDGMENTS

This work was performed in the framework of the H2020 MEET EU project which has received funding from the EU framework program for research and innovation under grant agreement No 792037. The authors acknowledge the GEIE Exploitation Minière de la Chaleur for accessing to the Soultz core samples data and informations. We acknowledge our American colleagues Prof. Terry

Pavlis and Dr. Zachariah D. Fleming for their help and advices on the field. We would like to thank our partners from CY Cergy Paris Université and the University of Göttingen for their contributions to fieldwork and lab analyzes. We acknowledge Thi Tuyen NGUYEN and Elena PAVLOVSKAIA for their help on XRD analyses. We also acknowledge Dr. Jeanne VIDAL and Carole GLAAS for their help on the comparison between the SsF reservoir and the NH. We finally thank Damien PAISNEL and Eric GONTHIER for the production of the thin sections.

## REFERENCES

- Bailleux, P., Schill, E., Dezayes, C., 2011. 3-D structural regional model of the EGS Soultz site (northern Upper Rhine Graben, France): insights and perspectives. Presented at the 36rd Workshop on Geothermal Reservoir Engineering, p. SGP-TR-191.
- Bartier, D., Ledésert, B., Clauer, N., Meunier, A., Liewig, N., Morvan, G., Addad, A., 2008. Hydrothermal alteration of the Soultz-sous-Forêts granite (Hot Fractured Rock geothermal exchanger) into a tosudite and illite assemblage. *Eur. J. Mineral.* 20, 131–142. <https://doi.org/10.1127/0935-1221/2008/0020-1787>
- Brady III, R.H., 1986. Cenozoic Geology of the Northern Avawatz Mountains in Relation to the Intersection of the Garlock and Death Valley Fault Zones, San Bernardino County, California. University of California, Davis.
- Burchfiel, B.C., Stewart, J.H., 1966. “Pull-apart” origin of the central segment of Death Valley, California. *GSA Bull.* 77, 439–442. [https://doi.org/10.1130/0016-7606\(1966\)77\[439:POOTCS\]2.0.CO;2](https://doi.org/10.1130/0016-7606(1966)77[439:POOTCS]2.0.CO;2)
- Butler, P.R., Troxel, B.W., Verosub, K.L., 1988. Late Cenozoic history and styles of deformation along the southern Death Valley fault zone, California. *GSA Bull.* 100, 402–410. [https://doi.org/10.1130/0016-7606\(1988\)100<0402:LCHASO>2.3.CO;2](https://doi.org/10.1130/0016-7606(1988)100<0402:LCHASO>2.3.CO;2)
- Calzia, J.P., Rämö, O.T., 2000. Late Cenozoic crustal extension and magmatism, southern Death Valley region, California. *GSA Field Guid.* 2, 135–164. <https://doi.org/10.1130/0-8137-0002-7.135>
- Curewitz, D., Karson, J.A., 1997. Structural settings of hydrothermal outflow: Fracture permeability maintained by fault propagation and interaction. *J. Volcanol. Geotherm. Res.* 79, 149–168. [https://doi.org/10.1016/S0377-0273\(97\)00027-9](https://doi.org/10.1016/S0377-0273(97)00027-9)
- Dezayes, C., Genter, A., Gentier, S., 2004. Fracture Network of the EGS Geothermal Reservoir at Soultz-sous-Forêts (Rhine Graben, France). *Geotherm. Resour. Counc. Trans.* Vol. 28, 7.
- Dezayes, C., Genter, A., Valley, B., 2010. Structure of the low permeable naturally fractured geothermal reservoir at Soultz. *Comptes Rendus Geosci., Vers l’exploitation des ressources géothermiques profondes des systèmes hydrothermaux convectifs en milieux naturellement fracturés* 342, 517–530. <https://doi.org/10.1016/j.crte.2009.10.002>
- Dezayes, C., Lerouge, C., 2019. Reconstructing Paleofluid Circulation at the Hercynian Basement/Mesozoic Sedimentary Cover Interface in the Upper Rhine Graben [WWW Document]. *Geofluids*. <https://doi.org/10.1155/2019/4849860>
- Dèzes, P., Schmid, S.M., Ziegler, P.A., 2004. Evolution of the European Cenozoic Rift System: interaction of the Alpine and Pyrenean orogens with their foreland lithosphere. *Tectonophysics* 389, 1–33. <https://doi.org/10.1016/j.tecto.2004.06.011>
- Edel, J.-B., Schulmann, K., 2009. Geophysical constraints and model of the “Saxothuringian and Rhenohercynian subductions – magmatic arc system” in NE France and SW Germany. *Bull. Société Géologique Fr.* 180, 545–558. <https://doi.org/10.2113/gssgfbull.180.6.545>
- Genter, A., 1989. Géothermie roches chaudes sèches : le granite de Soultz-sous-Forêts (Bas-Rhin, France) : fracturation naturelle, altérations hydrothermales et interaction eau-roche. Université d’Orléans.
- Genter, A., Traineau, H., Dezayes, C., Elsass, P., Ledésert, B., Meunier, A., Villemin, T., 1995. Fracture analysis and reservoir characterization of the granitic basement in the HRD Soultz project (France). *Fract. Anal. Reserv. Charact. Granitic Basement HRD Soultz Proj.* Fr. 4, 189–214.
- Glaas, C., Vidal, J., Patrier, P., Girard, J.-F., Beaufort, D., Petit, S., Genter, A., 2019. How Do Secondary Minerals in Granite Help Distinguish Paleo- from Present-Day Permeable Fracture Zones? Joint Interpretation of SWIR Spectroscopy and Geophysical Logs in the Geothermal Wells of Northern Alsace [WWW Document]. *Geofluids*. <https://doi.org/10.1155/2019/8231816>
- Kübler, B., 1968. La cristallinité de l’illite et les zones tout à fait supérieures du métamorphisme. *Etages Tecton.* 105–1021.
- Ledesert, B., Berger, G., Meunier, A., Genter, A., Bouchet, A., 1999. Diagenetic-type reactions related to hydrothermal alteration in the Soultz-sous-Forêts Granite, France. *Eur. J. Mineral.* 11, 731–741.
- Machette, M.N., Johnson, M.L., Slate, J.L., Klinger, R., Machette, M., Knott, J., Sarna-wojcicki, A., Block, D.L., Budahn, J.R., Crone, A.J., Dohrenwend, J.C., Fleck, R.J., Frankel, K., 2001. Quaternary and Late Pliocene Geology of the Death Valley Region: Recent Observations on Tectonics, Stratigraphy, and Lake Cycles (Guidebook for the 2001 Pacific Cell - Friends of the Pleistocene Fieldtrip), Chapter J.
- Norton, I., 2011. Two-stage formation of Death Valley. *Geosphere* 7, 171–182. <https://doi.org/10.1130/GES00588.1>
- Pauwels, H., Fouillac, C., Criaud, A., 1992. Water-rock interactions during experiments within the geothermal Hot Dry Rock borehole GPK1, Soultz-sous-Forêts, Alsace, France. *Appl. Geochem.* 7, 243–255.
- Pauwels, H., Fouillac, C., Fouillac, A.-M., 1993. Chemistry and isotopes of deep geothermal saline fluids in the Upper Rhine Graben: Origin of compounds and water-rock interactions. *Geochim. Cosmochim. Acta* 57, 2737–2749. [https://doi.org/10.1016/0016-7037\(93\)90387-C](https://doi.org/10.1016/0016-7037(93)90387-C)

- Pavlis, T.L., Trullenque, G., Submitted. Evidence for 40-41 km of dextral slip on the southern Death Valley fault zone: Implications for the Eastern California Shear Zone and Extensional Tectonics. *Geology*.
- Schumacher, M.E., 2002. Upper Rhine Graben: Role of preexisting structures during rift evolution. *Tectonics* 21, 6–1. <https://doi.org/10.1029/2001TC900022>
- Stewart, J.H., 1983. Extensional tectonics in the Death Valley area, California: Transport of the Panamint Range structural block 80 km northwestward. *Geology* 11, 153–157. [https://doi.org/10.1130/0091-7613\(1983\)11<153:ETITDV>2.0.CO;2](https://doi.org/10.1130/0091-7613(1983)11<153:ETITDV>2.0.CO;2)
- Stipp, M., Stünitz, H., Heilbronner, R., Schmid, S.M., 2002. The eastern Tonale fault zone: a ‘natural laboratory’ for crystal plastic deformation of quartz over a temperature range from 250 to 700°C. *J. Struct. Geol.* 24, 1861–1884. [https://doi.org/10.1016/S0191-8141\(02\)00035-4](https://doi.org/10.1016/S0191-8141(02)00035-4)
- Streckeisen, A., 1973. Classification and Nomenclature of Plutonic Rocks: Recommendations of the IUGS Subcommittee on the Systematics of Igneous Rocks. *GeoTimes* 18, 26–30. <https://doi.org/10.1007/BF01820841>.
- Traineau, H., Genter, A., Cautru, J.P., Fabriol, H., Chevremont, P., 1991. Petrography of the granite massif from drill cutting analysis and well log interpretation in the geothermal HDR borehole GPK1 (Soultz, Alsace, France). *Petrogr. Granite Massif Drill Cut. Anal. Well Log Interpret. Geotherm. HDR Boreh. GPK1 Soultz Alsace Fr.* 3, 1–29.
- Troxel, B.W., Butler, P.R., 1979. Rate of Cenozoic Slip on Normal Faults, South-central Death Valley, California. Department of Geology, University of California.
- Trullenque, G., Genter, A., Leiss, B., Wagner, B., Bouchet, R., Leoutre, E., Malnar, B., Bär, K., Rajšl, I., 2018. Upscaling of EGS in Different Geological Conditions: a European Perspective. *Proc. 43rd Workshop Geotherm. Reserv. Eng. Stanford Univ. Stanford Calif.* 10.
- Vidal, J., Genter, A., 2018. Overview of naturally permeable fractured reservoirs in the central and southern Upper Rhine Graben: Insights from geothermal wells. *Geothermics* 74, 57–73. <https://doi.org/10.1016/j.geothermics.2018.02.003>
- Wallace, R.E., Morris, H.T., 1986. Characteristics of faults and shear zones in deep mines. *Pure Appl. Geophys.* 124, 107–125. <https://doi.org/10.1007/BF00875721>
- Wooden, J.L., Miller, D.M., 1990. Chronologic and isotopic framework for Early Proterozoic crustal evolution in the eastern Mojave Desert Region, SE California. *J. Geophys. Res. Solid Earth* 95, 20133–20146. <https://doi.org/10.1029/JB095iB12p20133>
- Ziegler, P.A., 1992. European Cenozoic rift system. *Tectonophysics, Geodynamics of rifting, volume 1 Case history studies on rifts: Europe and Asia* 208, 91–111. [https://doi.org/10.1016/0040-1951\(92\)90338-7](https://doi.org/10.1016/0040-1951(92)90338-7)



## RÉSUMÉ ÉTENDU

---

Le présent travail de thèse a été effectué à UniLaSalle Beauvais, dans l'unité de recherche U2R 7511 Basins-Reservoirs-Resources (B2R), dans le cadre d'un projet européen H2020 intitulé MEET (Multidisciplinary and multi-context demonstration of EGS exploration and Exploitation Techniques and potentials) (<https://www.meet-h2020.com>). Ce projet rassemble 16 partenaires (centres de recherche et industriels) de France, Allemagne, Belgique, Croatie et Islande.

Le projet et donc ce travail de recherche, ont reçu un financement de l'Union européenne dans le cadre du programme de recherche et d'innovation Horizon 2020, sous l'accord de financement No. 792037.

Ce mémoire de thèse est organisé en huit chapitres.

Il comprend deux articles publiés en première auteure dans un journal international à comité de lecture *Geosciences*, numéro spécial (Klee et al. 2021a) et (Klee et al. 2021b). Ces articles sont intégrés en tant que chapitres dans le corps de ce manuscrit (chapitres 4 et 5). Ces chapitres ainsi que les chapitres 6 et 7 sont relatifs à deux articles en tant que co-auteur, l'un publié (Annexe 1), l'autre en processus de « review ».

### I. CHAPITRE 1 : INTERET DE L'ETUDE ET OBJECTIFS SCIENTIFIQUES

Ce chapitre donne dans un premier temps une vue générale des concepts et de la production d'énergie géothermique dans le monde et en Europe. Un focus est fait sur les réservoirs géothermiques profonds.

L'Europe dort sur une gigantesque ressource d'énergie géothermique, largement sous-employée. La quantité importante de chaleur naturelle venant de la Terre gît sous terre, sous les pieds des citoyens européens. Afin de développer la pénétration du marché de l'énergie géothermique en Europe, le projet MEET a été créé avec pour objectif principal de démontrer la viabilité des Systèmes Géothermiques Stimulés (en Anglais : Enhanced Geothermal System, EGS) avec la production d'électricité et d'énergie thermique dans tous types de contextes géologiques hercynien (volcanique, métamorphique, sédimentaire et cristallin). Le concept EGS vise à exploiter la chaleur contenue dans tous les environnements géologiques, avec différentes configurations de composition lithologique, de contexte géologique et de champ de contraintes.

Les principaux objectifs du projet MEET sont :

- Collecter des connaissances sur la production de chaleur et d'énergie électrique dans des contextes géologiques variés,
- Augmenter la production de chaleur à partir de centrales existantes et convertir des puits pétroliers en puits géothermiques,
- Développer la conversion de la chaleur en électricité à faible température (60-90°C) en utilisant des centrales mobiles intelligentes basées sur le cycle organique de Rankine,
- Répliquer la technologie en promouvant la pénétration de production de chaleur et d'électricité à partir de centrales EGS.

Appliquer les techniques EGS aux domaines hercyniens est un défi pour de nombreuses raisons telles que (1) l'histoire géologique complexe de l'orogénèse hercynienne elle-même, (2) la succession d'événements orogéniques post-hercyniens et (3) la forte anisotropie des roches métamorphiques.

Le domaine hercynien affleure largement en Europe et n'est pas encore reconnu pour son potentiel géothermique important. Afin de structurer l'approche du projet, le domaine hercynien a été divisé en quatre parties principales dépendant de la nature des roches rencontrées (Figure A) :

- Successions métamorphiques (métasédimentaires et métavolcaniques) suivies de tectonique en extension (rift) principalement cénozoïque,
- Successions métamorphiques (métasédimentaires et métavolcaniques) non suivies de tectonique en extension (rift),
- Socle granitique affecté par de la tectonique en extension post-varisque,
- Socle granitique non affecté par de la tectonique en extension post-varisque.

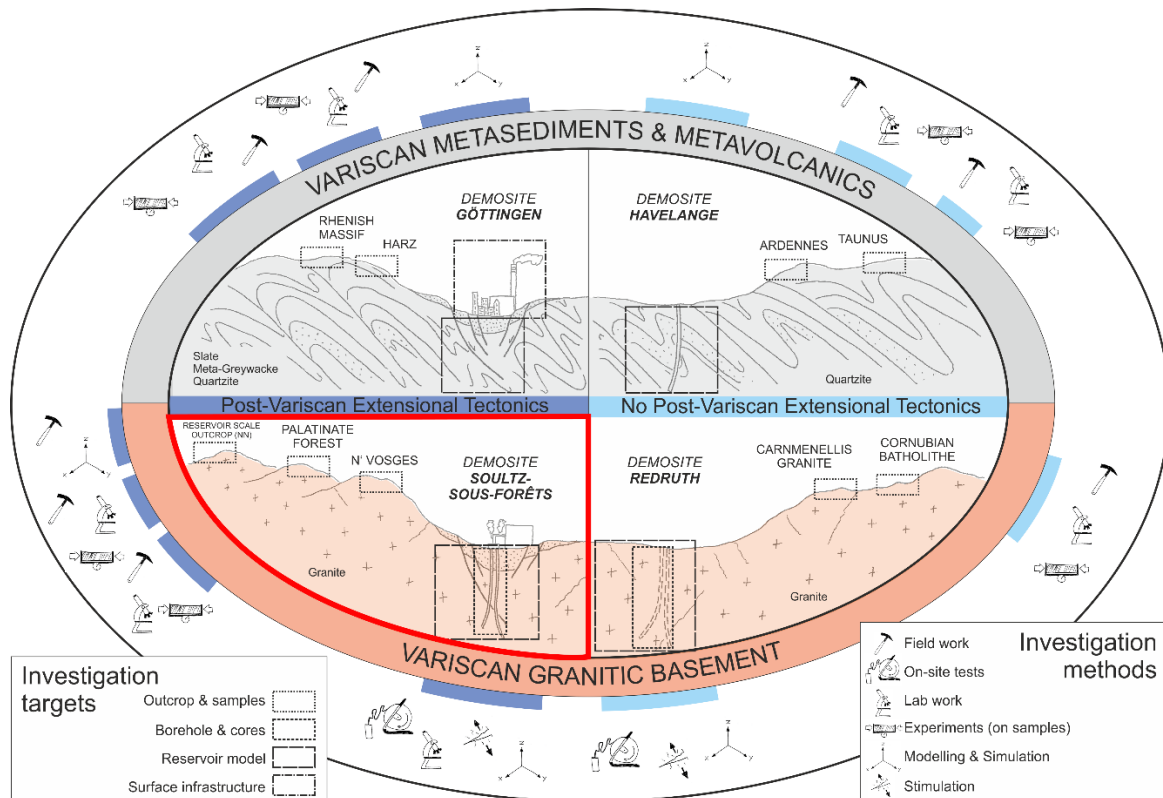


Figure A. Aperçu schématique des quatre contextes géotectoniques européens représentatifs du Varisque, y compris les sites de démonstration, les sites analogues et les méthodes d'investigation selon (Trullenque et al., 2018). Notre étude de cas est encadrée en rouge.

Une approche multidisciplinaire est choisie et les géologues de réservoir jouent ici un rôle de la plus grande importance. Les plus grandes difficultés pour eux résident dans le manque d'affleurements à grande échelle puisque les informations sont réduites aux données de forages et aux méthodes géophysiques, indirectes. Malgré plusieurs décennies d'efforts de recherche et de développement, la structure à grande échelle des réservoirs géothermiques n'est pas encore totalement comprise à l'heure actuelle.

Ce travail se concentre sur l'étude des réservoirs granitiques affectés par la tectonique d'extension comme encadré en rouge sur la Figure A. Le Graben du Rhin Supérieur (GRS, France), avec le site géothermique actif de Soutz-sous-Forêts, a été considéré comme la référence pour cette étude en termes de réservoir granitique exploité.

Des failles normales, liées à la formation du graben, sont les structures principales ciblées pour l'exploitation géothermique dans le GRS puisque ce sont les principaux drains dans le réservoir granitique (Genter, 1989; Glaas, 2021; Vidal, 2017). Jusqu'à présent, le modèle conceptuel des zones de faille comprend le développement d'un cœur de faille imperméable, qui ne favorise pas la connectivité et agit comme une barrière à la circulation des fluides (Caine et al., 1996). Ces zones de forte déformation peuvent être associées à tout type de faille.

Il est connu que le GRS est affecté par des décrochements réactivés (Edel et al., 2007). Dans les zones en trans-tension, la connectivité des failles est naturellement favorisée par des relations entre les failles normales et les décrochements (Bailleux et al., 2011; Curewitz and Karson, 1997). L'évolution, dans le temps et l'espace, de ces décrochements dans le socle cristallin affecté par des quantités variables de déformation et d'interactions fluide-roche associées paraît de la plus grande importance pour la compréhension du réservoir.

Le présent travail de recherche vise à répondre aux questions suivantes :

- Quels sont les effets des processus d'altération en termes de propriétés du réservoir en approchant des zones de fractures ?
- Quelle est la relation entre densité de fractures, altération et circulation de fluides ?
- Quelle relation existe entre l'intensité de la déformation et les propriétés pétrophysiques des zones de failles ?
- Comment l'héritage structural impacte-t-il les propriétés du réservoir et la connectivité ?

Il y a donc un besoin crucial d'explorer au-delà de la vision 1D permise par les forages profonds, en évaluant des réservoirs granitiques exhumés considérés comme analogues. Cette approche est assez commune dans la littérature au sujet des réservoirs géothermaux (Aretz et al., 2016; Bertrand, 2017; Chabani, 2019; Le Garzic, 2010; Place, 2010) et d'hydrocarbures (Grammer et al., 2004) et a montré qu'elle peut apporter une contribution notable à la compréhension des réservoirs. Dans le domaine du pétrole et du gaz, l'analogie est appliquée dans l'estimation et la classification des réserves pétrolières et utilisée dans l'évaluation des ressources (Sidle et Lee, 2010). Un réservoir analogue doit avoir des propriétés similaires en termes de roches et fluides, ainsi que des conditions de réservoir, une formation géologique, une structure et des mécanismes d'entraînement similaires (Sidle et Lee, 2010). En géothermie, les analogues consistent en des affleurements permettant la caractérisation du réseau de fractures à grande échelle, car certains attributs ne peuvent pas être mesurés à l'aide de puits, mais aussi les minéralisations, les interactions fluide-roche et les propriétés pétrophysiques (Bertrand, 2017 ; Chabani, 2019 ; Ukar et al., 2019, Dezayes et al., 2021). Les analogues sont également précieux car (1) ils fournissent des jeux de données 2D et 3D de haute qualité non affectés par les biais d'échantillonnage des forages, (2) ils sont beaucoup moins coûteux, (3) ils nécessitent des moyens simples pour l'acquisition des données et (4) l'étude peut se faire à différentes échelles, de l'imagerie satellitaire aux lames minces.

Le concept d'analogie peut donc avoir différentes approches. **L'accent est mis ici sur la définition adoptée pour un analogue, comme étant un site permettant la compréhension de l'évolution de processus-clés en profondeur pour certains types de structures géologiques. Il est envisagé que l'un de ces processus est relatif aux interactions fluide-roche et leur évolution en fonction de la quantité de déformation dans les structures décrochantes affectant le socle cristallin.**

**Selon un tel concept, les sites "de démonstration" et "analogues" n'ont pas besoin d'être directement comparables en termes de paramètres géologiques spécifiques tels que la période des événements tectoniques considérés ou la quantité de déformation. L'étude n'a jamais eu pour objectif d'établir une comparaison directe entre deux objets à l'échelle régionale.**

Un analogue devrait au moins satisfaire les trois conditions principales suivantes :

1. Présenter un faisceau de similarités en termes de contexte géologique à grande échelle ;
2. Avoir des caractéristiques pétrographiques de roches cristallines similaires ;
3. Permettre l'accès à des conditions d'affleurement de bonne/excellent qualité dans lesquelles les gradients de déformation et les processus d'interaction fluide-roche sont particulièrement bien développés et préservés.

Le réservoir géothermique de Soultz-sous-Forêts (SsF, Alsace, GRS, France) est considéré dans cette étude comme le site de démonstration localisé dans un socle granitique ayant subi une extension tectonique postérieure (Figure A, encadré rouge). La chaîne des Noble Hills (NH), localisée le long d'une portion de la zone de faille sud de la Vallée de la Mort (Southern Death Valley Fault Zone, SDVFZ, Californie, USA) a été choisie comme analogue principal. L'objectif est d'établir un modèle montrant l'évolution des structures cisailantes en termes d'interactions fluide-roche et de quantité de déformation en tenant compte de l'héritage géologique et structural. Connaissant la présence de failles cisailantes dans les épaulements du GRS, il est très probable que ces structures se trouvent dans le graben même. Ainsi, les mines existantes dans les épaulements du GRS (Vosges et Forêt Noire) ont fait l'objet d'une étude préliminaire afin de transposer les observations faites dans les NH.

## II. CHAPITRE 2 : CONTEXTE GEOLOGIQUE

Ce chapitre présente les fondements du contexte géologique d'un part de la Vallée de la Mort (Death Valley, DV) avec l'accent mis sur (1) la faille cisailante sud de la Vallée de la Mort qui a permis la formation du pull-apart de la Vallée de la Mort et (2) sur la chaîne des Noble Hills (NH) qui s'est formée le long de cette zone de faille. D'autre part, il présente un résumé du contexte

géologique du graben du Rhin supérieur (GRS), avec quelques précisions sur le réservoir géothermique de Soultz-sous-Forêts (SsF).

### III. CHAPITRE 3 : ETAT DE L'ART

Le chapitre 3 présente un aperçu général (1) des mécanismes de déformation dans le domaine cassant et le domaine ductile, (2) de la composition d'une zone de faille avec un accent sur les zones cisailantes et les débris de roches broyés par l'action mécanique dans le plan de faille, (3) des interactions fluide-roche en milieu granitique et (4) des propriétés pétrophysiques des zones de failles.

### IV. CHAPITRE 4 : INTERACTIONS FLUIDE-ROCHE DANS UN RESERVOIR PALEO-GEOTHERMIQUE (GRANITE DE NOBLE HILLS, CALIFORNIE, USA). PARTIE 1 : PROCESSUS D'ALTERATION GENERALISEE DU GRANITE LOIN DES ZONES DE FRACTURES

Ce chapitre présente des processus d'interaction fluide-roche qui ont eu lieu à distance des zones de fractures dans le granite des NH. Une description est donnée de (1) la pétrogenèse et les paragenèses d'altération du granite des NH par comparaison au protolithe non déformé trouvé dans les Owshead plus au nord et (2) des effets de l'altération sur son comportement pétrographique et pétrophysique.

Les résultats montrent deux types d'altérations hydrothermales du granite ont été identifiées : une altération propylitique pervasive et une altération argillique locale qui surimpose l'altération propylitique. Des signes d'altérations météorique ont été identifiés mais considérés comme négligeable. Ces altérations se traduisent par la transformation de minéraux primaires en minéraux secondaires via le transfert d'éléments chimiques, ainsi que par l'augmentation du pourcentage de la perte au feu. Le gradient de température dans le corps granitique est établi. Cela a permis de définir le granite des NH comme un paléo réservoir géothermique.

Ce chapitre est une contribution publiée en premier auteur dans le volume spécial du journal *Geosciences* intitulé « Les systèmes géothermaux stimulés et autres applications géothermales profondes en Europe : le projet MEET » ("Enhanced Geothermal Systems and other Deep Geothermal Applications throughout Europe : The MEET Project"). Le titre de cette contribution est : « Fluid-Rock Interactions in a Paleo-Geothermal Reservoir (Noble Hills Granite, California, USA). Part 1: Granite Pervasive Alteration Processes away from Fracture Zones ».

## V. CHAPITRE 5 : INTERACTIONS FLUIDE-ROCHE DANS UN RESERVOIR PALEO-GEOTHERMIQUE (GRANITE DE NOBLE HILLS, CALIFORNIE, USA). PARTIE 2 : L'INFLUENCE DE LA FRACTURATION SUR LES PROCESSUS D'ALTERATION DU GRANITE ET LA CIRCULATION DES FLUIDES A UNE DEFORMATION REGIONALE FAIBLE A MODEREE

Ce chapitre donne un aperçu de la structure des NH et étudie l'influence des zones de fractures à déformation faible voire modérée sur les circulations de fluides et les interactions fluide-roche au travers des NH. Dans ce chapitre, un accent particulier est mis sur (1) les relations entre densité de fractures, processus d'altération et circulations de fluides et (2) les implications en termes de réservoir géothermique.

Les résultats montrent des signes de circulation de plusieurs générations de fluides dans le granite des NH de part la présence de veines de différentes natures. De plus, à l'approche des zones de fractures, l'interaction fluide-roche est beaucoup plus importante, ainsi l'altération argillique est dominante. La relation circulation de fluide, altération et fracturation est visible à différentes échelles, à l'échelle de l'affleurement et celle de l'échantillon. Une augmentation de la densité de fracture s'accompagne souvent d'une altération prononcée, mais des exceptions ont été observées. Ainsi, le taux d'altération ne dépend pas toujours du gradient de déformation ou de la densité de fractures.

Ce chapitre est publié sous la forme d'un deuxième article en premier auteur dans le volume spécial du journal *Geosciences*. Son titre est : « Fluid-Rock Interactions in a Paleo-Geothermal Reservoir (Noble Hills Granite, California, USA). Part 2: The Influence of Fracturing on Granite Alteration Processes and Fluid Circulation at Low to Moderate Regional Strain ».

## VI. CHAPITRE 6 : LE ROLE DE LA STRUCTURATION HERITEE SUR LA CIRCULATION DES FLUIDES A DANS UN RESERVOIR PRE-STRUCTURE SOUS FORTE CONTRAINTE.

Ce chapitre est relatif à l'impact des zones de forte déformation et l'influence des structures héritées sur les circulations de fluides dans un réservoir en termes de circulation de fluides et de connectivité. Cette étude est basée sur deux études de cas d'affleurement : (1) dans les NH et (2) dans des mines localisées dans les épaules du GRS. L'étude réalisée dans les mines est principalement basée sur la littérature et est complétée par une étude préliminaire de terrain et des analyses pétrographiques.

La partie dédiée aux investigations d'un affleurement situé dans les NH est en préparation pour une future publication dans un journal international à comité de lecture.

## VII. CHAPITRE 7 : LE GRANITE DE NOBLE HILLS ET LE SOCLE CRISTALLIN DES EPAULES DU FOSSE DU RHIN SUPERIEUR : DES ANALOGUES DU RESERVOIR GEOTHERMIQUE DE SOULTZ-SOUS-FORETS

Ce chapitre présente une synthèse des principaux résultats de cette étude sur les NH et les compare aux données disponibles dans la littérature sur le réservoir géothermique de SsF et de Rittershoffen (RTH) situé à quelques kilomètres de SsF. Dans cette discussion, l'accent est mis sur l'importance de la connectivité des fractures et sur la complexité des réservoirs au travers de (1) l'analyse géométrique de réseaux de fractures, (2) les produits d'altération hydrothermale et leur influence sur les propriétés des zones de fracture présentant des quantités différentes de déformation, et (3) l'influence de l'héritage structural. Ce chapitre amène à la compréhension des réservoirs granitiques en régime de trans-tension, dans un but d'explorations géothermiques futures. Un effort particulier est porté pour inclure les données nouvelles représentant la complexité d'un réservoir dans un modèle conceptuel actualisé.

## VIII. CHAPITRE 8 : CONCLUSIONS ET PERSPECTIVES

Ce chapitre présente les principales conclusions de ce travail de recherche afin d'apporter une nouvelle connaissance de l'influence des décrochements sur la circulation des fluides en milieu granitique affecté par des niveaux de déformation variés. De telles structures sont peu étudiées dans les réservoirs géothermaux granitiques car elles sont généralement considérées comme des barrières aux écoulements de fluides. Or ces failles participent à la structuration du GRS où se situe le site de démonstration de SsF qui produit de l'électricité à partir d'un EGS. L'accès au réservoir y est limité aux forages, si bien qu'il a paru judicieux d'étudier des analogues naturels de surface. L'analogue lointain (du point de vue géographique) est situé en Californie (USA) le long de la SDVFZ, dans la chaîne des NH. Les analogues proches géographiquement sont situés dans des mines localisées dans les épaules du GRS, dans les massifs des Vosges (France) et de la Forêt Noire (Allemagne). Il s'agit de mines dont l'exploitation est arrêtée. Ce travail apporte des résultats majeurs pour la recherche mais aussi pour l'industrie :

### VIII.1. Résultats majeurs pour la recherche

#### VIII.1.1. Les altérations hydrothermales et leurs indicateurs dans les NH

Les NH montrent plusieurs types d'altération successives :

- L'altération propylitique est considérée comme une altération précoce et pervasive, prenant place à la fin du refroidissement et de la cristallisation du granite. Elle résulte principalement d'une transformation partielle des biotites et plagioclases primaires en un assemblage d'illite, épidote, corrensite (minéraux interstratifiés chlorite/smectite trioctaédrique) et calcite. Epidote et corrensite sont les témoins les plus caractéristiques de l'altération propylitique. La calcite est seulement trouvée en remplissage de fissures et de joints de grains, sans interaction avec la roche encaissante.
- L'altération argillique, ou filonienne, se superpose localement à l'altération propylitique. Elle intervient à proximité de fractures dans lesquelles des fluides hydrothermaux ont circulé. Cette altération consiste en une hydrolyse des minéraux et la cristallisation massive de minéraux argileux, à température plus faible (130-200°C) que dans le stade propylitique. Les produits d'altération consistent en assemblages minéraux néoformés d'illite, kaolinite, interstratifiés illite/smectite, calcite and oxydes et résultent de l'altération totale des biotites et plagioclases.
- De rares signes d'altération météorique (Montmorillonite and Vermiculite) ont été observés et sont considérés comme étant négligeables.

Les assemblages minéralogiques des épisodes propylitique et argillique sont comparables à ceux identifiés à SsF et RTH.

En s'approchant des zones de fractures, l'altération devient plus intense, ainsi que le montre l'augmentation des valeurs de perte au feu (LOI, Loss On Ignition). Les interactions fluide-roche étant plus prononcées à proximité des fractures, l'altération argillique y oblitère presque complètement l'altération propylitique. Ce phénomène a également été observé à SsF et RTH. La kaolinite est généralement le minéral argileux dominant près des zones de fractures, indiquant un lessivage important ou la circulation d'un fluide acide. Les valeurs d'indice de Kübler (KI) montre une température de cristallisation de l'illite proche de 200°C. Une circulation de paléo-fluides hydrothermaux polyphasée a été mise en évidence dans les NH du fait des minéraux néoformés variés qui ont précipité dans les fractures (quartz, illite, carbonates tels que calcite, dolomite, et ankérite and oxydes). La quantité de calcite a été estimée : elle augmente en se rapprochant des fractures.

#### VIII.1.2. Relation entre la quantité de déformation et les circulations de fluides

Lorsque les données relatives aux NH, aux épaules du GRS et à SsF et RTH sont réunies, il est possible de présenter un schéma synthétique qui (1) résume l'évolution de la structure

décrochante selon un gradient de déformation et (2) illustre la relation entre zone de cisaillement héritée et circulation de fluide postérieure (Figure B).

La fracturation est initiée durant le refroidissement du granite alors affecté par l'altération propylitique pervasive (Figure Ba). Sous une déformation faible à modérée, les fractures s'ouvrent et laissent circuler un fluide. Deux cas doivent être considérés :

1. Dans le cas d'un très faible ratio fluide/roche, le fluide circule dans le réseau de fractures et des minéraux secondaires y précipitent, induisant une faible altération du granite (Figure b et c).
2. Dans le cas d'un fort ratio fluide/roche, le fluide circule dans le réseau de fractures, affecte leurs épontes et développe un halo d'altération montrant un gradient (Figure Bd). Avec le temps, des minéraux secondaires précipitent depuis la saumure saturée (quartz, par exemple) et scellent les fractures pendant que le gradient d'altération s'intensifie (Figure Be et f). Des réactivations de failles successives mobilisent et modifient les dépôts de veine et amplifient l'altération de la roche encaissante. En fonction de la nature des nouveaux fluides, de nouveaux minéraux secondaires peuvent se former, tels des carbonates. Combiné à la réduction de taille des grains de la roche hôte du fait du cisaillement, la quantité de ces minéraux néoformés augmente de façon importante au cours du temps. La nouvelle roche ainsi obtenue montre une compétence diminuée par rapport au protolithe et le développement d'une schistosité est initié (Figure Bg) qui mène à un mécanisme de fluage (Figure Bh).

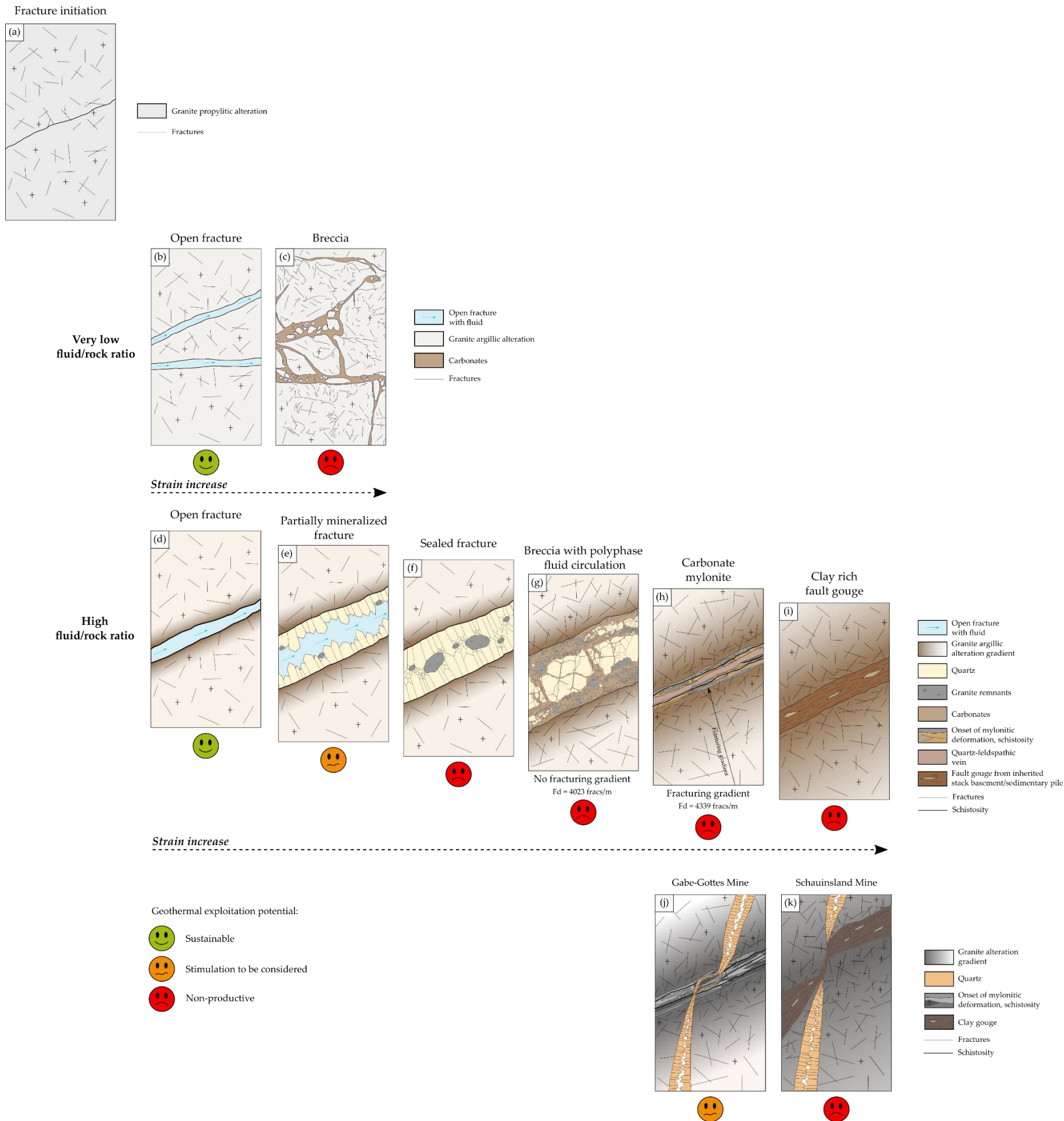


Figure B. Schéma synthétique montrant l'interaction entre le fluide et le granite à différents niveaux de déformation. (a) Initiation d'une fracture dans un granite affecté par une altération propylitique. (b) Fractures ouvertes avec une altération argilique naissante de la roche environnante. (c) Zones bréchifiées avec une matrice carbonatée et aucun changement du degré d'altération. (d) Une fracture ouverte avec un gradient d'altération naissant à la limite. (e) Cristallisation minérale à la limite de la veine. (f) Une fracture fermée avec un léger gradient d'altération. (g) Une veine bréchifiée issue de la réactivation d'une fracture et présentant un gradient d'altération mais pas de gradient de fracturation. (h) Une mylonite constituée de carbonates et de lentilles granitiques présentant un gradient d'altération et un gradient de fracturation. (g) et (h) présentent une densité de fractures (Fd) similaire. (i) Une gouge de faille a entraîné la déformation du socle protérozoïque et des sédiments pinces hérités. (j) Cas de la mine de Gabe-Gottes, déviation de la veine avec la zone de cisaillement. (k) Cas de Schauinsland, la veine est arrêtée par la gouge argileuse. Aucune échelle n'est donnée pour ce schéma, car il peut représenter des zones de fractures de plusieurs ordres de grandeur. Le potentiel supposé d'exploitation géothermique est indiqué par des smileys de différentes couleurs.



Il a été montré que selon la nature du protolithe composant le cœur de la faille, la gouge de faille peut agir soit comme un drain (protolithe hétérogène hérité dans le NH, Figure Bi), soit comme une barrière (protolithe unique comme décrit sur les mines de Schauinsland, Figure Bk). Le cas de la gouge de Schauinsland montre que les minéraux argileux ont tendance à stopper le développement de la minéralisation récente en raison de leur plasticité qui est un frein au développement de fractures ouvertes par déformation cassante (Figure Bk). Cependant, dans le cas d'une zone de cisaillement développant une schistosité, les veines ultérieures peuvent utiliser ces plans de faiblesse pour se propager et recouper la zone de cisaillement (Figure Bj). Selon la composition et la rhéologie du cœur de faille, les zones de faille fortement déformées peuvent avoir des comportements différents et réagir différemment à l'écoulement des fluides.

A grande échelle, en se rapprochant des zones de fractures, la densité des fractures augmente, ainsi que le degré d'altération, la teneur en calcite et la porosité. L'échelle de l'échantillon et celle de la lame mince ont montrées que cette corrélation n'est pas toujours vraie.

## VIII.2. Résultats majeurs pour les industriels

En règle générale, la présence de fractures ouvertes augmente considérablement la perméabilité d'un réservoir. Ces fractures jouent un rôle d'autant plus important en termes d'exploitation lorsque la porosité initiale des roches constituant le réservoir est faible, comme cela est le cas des granites. Lors de son passage, le fluide interagit avec la roche environnante. Les processus d'altération liés aux transferts d'éléments chimiques lors de l'interaction du fluide avec la roche environnante induisent une augmentation globale de la porosité et donc de la perméabilité. Les zones de failles composées d'un cœur ouvert et d'une zone endommagée altérée deviennent les principaux conduits. Cependant, une abondance de minéraux nouvellement formés peut aussi sceller les fractures et obstruer le système.

Les études menées dans les NH montrent que les carbonates sont les minéraux secondaires les plus abondants qui remplissent les fractures dans toute la région. Comme le réseau de fractures déposé par ces carbonates est bien connecté géométriquement (Chabani et al., 2021), il est suggéré que la connectivité hydraulique était bonne lors de la phase de circulation de fluides saturés.

Les NH présentant un gradient clair de déformation le long de la chaîne. L'influence de la déformation sur la circulation des fluides a été étudiée et permet de montrer l'importance du rôle des zones de failles intensément déformées dans un réservoir. Il a été démontré qu'une

zone de faille dont le cœur est le produit d'un protolithe unique fortement déformé (Caine et al., 1996) ne suit pas toujours le modèle classique d'une zone de faille. Dans le modèle de (Caine et al., 1996) le cœur est considéré comme une barrière en raison de la diminution de la porosité et de la perméabilité. Dans le cas des NH cependant, une zone de faille intensément déformée, caractérisée comme une gouge de faille, peut constituer un drain. Elle peut s'expliquer par (1) son hétérogénéité résultant de la présence de sédiments protérozoïques hérités et fortement déformés et du socle dans le cœur de la faille, (2) sa porosité élevée dans le cœur de la faille, (3) sa teneur élevée en calcite qui peut provenir d'une circulation de fluide qui précipite les carbonates et (4) une altération prononcée. Il est suggéré que ce type de structure dans la zone divise le réservoir en blocs relativement peu déformés qui glissent les uns par rapport aux autres sans accumuler eux-mêmes de forte déformation élastique. Cela peut expliquer pourquoi dans la zone, les larges veines, correspondant à des fractures paléo-perméables, sont extrêmement rares. Ainsi, même si le réseau de fractures dans le NH est hydrauliquement connecté, il pourrait ne pas être commercialement exploitable en raison de ce système de blocs. Cependant, en considérant le changement du champ de contrainte, comme la compression des Montagnes Avawatz contre le NH, ces blocs faiblement déformés ne sont plus dans la configuration de glissement mais la contrainte peut être accumulée et, par conséquent, fracturer les blocs. Ainsi, des veines de barytine pluri décimétriques, obliques par rapport à l'orientation des NH, ont été identifiées suite à ce changement de contrainte dans le NH. Ces veines de barytine n'ont pas été identifiées dans l'ensemble du massif certainement en raison de l'influence des zones de failles transversales riches en argile qui peuvent arrêter ou dévier la circulation.

Des études préliminaires réalisées dans les mines des épaules du GRS ont montré l'influence importante de l'héritage structural sur la circulation ultérieure des fluides. La mine de Schauinsland dans la Forêt Noire a montré qu'une gouge riche en argile héritée de la déformation d'un protolithe unique agit comme une barrière. Le matériau argileux empêchant l'accumulation des contraintes, la gouge a rapidement arrêté le développement d'une ouverture par fracturation et donc d'un filon exploitable. De l'autre côté du graben, dans les Vosges, la mine de Gabe-Gottes présente des zones de cisaillement héritées dans le socle rocheux à travers lesquelles les veines peuvent se propager en utilisant la schistosité. La circulation des fluides est déviée en utilisant l'orientation préférentielle de la schistosité héritée des zones de forte déformation. Ces structures héritées identifiées dans les épaules du GRS doivent être prises en compte lors de la simulation de l'écoulement des fluides dans un réservoir géothermique.

Les analogues ont permis de montrer la complexité réelle d'un réservoir géothermique qui est la plupart du temps sous-estimée. Les zones de faille intensément déformées peuvent présenter différents comportements qui influencent directement la circulation des fluides dans le réservoir.

Les structures décrochantes ne sont pas seulement importantes pour la connectivité du réservoir, mais on peut également mentionner que ces structures (1) peuvent perturber la stabilité du forage en raison de leur compétence lorsqu'elles sont constituées de gouge d'argile molle et (2) sont soumises à une réactivation pendant les opérations de stimulation. En effet, les récents événements sismiques qui se sont produits en Alsace à proximité de Strasbourg étaient dus à des mouvements le long des structures décrochantes orientées N309 pendant les stimulations (EOST and CNRS, 2021).

La compréhension de l'évolution d'un réservoir dans le temps doit être prise en compte par les industriels. Le modèle d'évolution des fractures présenté ci-dessus (Figure B) en fonction des quantités de déformation accumulées est directement lié à l'évolution du réservoir à travers les temps géologiques. Ainsi, un réservoir commercialement exploitable à un moment donné pourrait ne pas l'être s'il manquait un épisode tectonique. À l'inverse, un épisode tectonique supplémentaire pourrait empêcher l'exploitation d'un réservoir actif avant cet épisode. Il existe donc une fenêtre temporelle d'exploitation géothermique où l'exploitation commerciale est possible dans l'histoire géologique d'un réservoir. Ces fenêtres géothermiques permettant une exploitation durable sont représentées par des smileys verts sur la Figure B, qui correspondent à des fractures totalement ouvertes. Les smileys oranges montrent les fenêtres géothermiques où l'exploitation est possible mais nécessitera probablement une stimulation. Les smileys rouges représentent les contextes structuraux non compatibles avec une exploitation géothermique.

### VIII.3. Perspectives

Le chapitre 6 propose des perspectives de recherche qui pourraient permettre d'améliorer encore la connaissance des réservoirs géothermiques en milieu granitique.

#### VIII.3.1. Caractérisation approfondie des zones de forte déformation

Ces travaux mettent en évidence le rôle majeur que jouent les zones de cisaillement fortement déformées dans la connectivité et la productivité des réservoirs. Cependant, des caractérisations plus spécifiques sont nécessaires pour comprendre leur comportement mécanique et pétrophysique.

Ainsi, trois sujets méritent d'être étudiés à l'avenir :

- La déformation expérimentale traitant des propriétés mécaniques des roches réservoirs en fonction de l'altération, y compris le suivi des émissions acoustiques. Ces expériences jouent un rôle clé lorsqu'il s'agit de relier le régime de contrainte et de déformation au degré d'altération de la roche et à l'occurrence potentielle d'un événement sismique,
- La cinétique des réactions d'interaction fluide-roche et la quantification des effets de la contrainte sur le taux de production de minéraux d'altération dans le temps,
- La caractérisation multi-échelle des distributions de minéraux argileux à travers les zones de déformation pour mieux comprendre le rôle de drain/barrière d'un coeur de faille fortement déformé.

### VIII.3.2. Caractérisation des paléo-fluides

En géothermie active, la composition et la caractérisation des fluides sont très étudiées afin de mieux comprendre leur interaction avec la roche environnante ainsi que leurs origines. Plusieurs méthodes sont disponibles pour caractériser les paléo-fluides qui ont circulé dans le granite :

Les inclusions fluides, fournissent un enregistrement fossile unique des différents fluides qui ont circulé dans le granite. Elles peuvent être utilisées pour déterminer les températures et la nature physico-chimique du fluide au moment du piégeage (Rankin, 2005). Des analyses sont en cours sur des veines de quartz, de carbonate et de barytine provenant des NH.

Les isotopes des fluides peuvent être utilisés pour caractériser l'origine d'un fluide, son âge, et/ou son interaction avec les roches ou d'autres fluides. Comme la datation de l'illite a été réalisée grâce aux isotopes K/Ar, les isotopes de l'oxygène peuvent donner l'origine du fluide par sa signature géochimique spécifique (Williams and McKibben, 1989). De même, les carbonates peuvent être datés, par exemple en utilisant le système Sm-Nd (Henjes-Kunst et al., 2014) et U/Pb, afin de déterminer l'âge de la minéralisation hydrothermale et de le mettre en relation avec les âges obtenus sur l'illite pour déchiffrer les différentes générations de circulation des fluides.





JOHANNE KLEE



## **Influence of fluid-rock interaction processes and strain on strike-slip zones properties: An analogue-based multidisciplinary approach. Fractured granitic geothermal reservoirs applications.**

### **ABSTRACT**

---

This contribution aims at a better understanding of basement rock petrophysical properties evolution affected by progressive deformation along strike slip structures. The chosen approach is based on analogue studies, an analogue being a geological object dedicated to the understanding processes of particular interest. We have chosen a portion of the Southern Death Valley Fault Zone (Noble Hills, CA, USA) as an analogue. A comparison to structures found within the Upper Rhine Graben area and Soultz-sous-Forêts demonstration site is proposed. Our findings indicate that two stages of alteration can affect granitic basement rocks. A pervasive propylitic alteration, affecting the whole granitic body is overprinted by an argillic alteration mainly concentrated in the vicinity of fracture zones. At low to moderate strain a progressive increase of alteration degree, porosity values and calcite content are observed. Interestingly, the degree of alteration is not directly linked to the fracture density. It is demonstrated that high strain zones can but do not necessarily represent a barrier to geothermal brines circulation. Mechanical properties of high strained fault rocks play a crucial role in hindering the development of openings necessary to channel the flow within the reservoir. These properties are involving in time and space depending on accumulated deformation and fluid-rock interaction processes. A conceptual model of fault zone evolution and reservoir architecture is proposed. Geothermal exploration and exploitation must consider the role of geological heritage in order to warranty sustainable and safe operations.

**Keywords:** Fractured granite, Fluid-rock interaction, Deformation gradient, Geothermal reservoirs, Analogue

### **RÉSUMÉ**

---

Cette contribution a pour objectif de mieux comprendre l'évolution des propriétés pétrophysiques des roches de socles affectées par une déformation progressive le long de structures décrochantes. L'approche choisie est basée sur des études d'analogues, un analogue étant un objet géologique dédié à la compréhension de processus d'intérêt spécifique. Nous avons choisi pour analogue une portion de la partie sud de la zone faillée de la Vallée de la Mort (Noble Hills, CA, USA). Une comparaison avec les structures trouvées dans le graben du Rhin supérieur et au site de démonstration de Soultz-Sous-Forêts est proposée. Nos résultats indiquent que deux étapes d'altération peuvent affecter les roches du socle granitique. Une altération argillique principalement concentrée aux environs des zones de fractures se superpose à une altération propylitique pervasive affectant l'ensemble du corps granitique. Dans le cas de déformations de faible à moyenne intensité, une augmentation progressive du degré d'altération, de la porosité et de la teneur en calcite est observée. Curieusement, le degré d'altération n'est pas directement lié à la densité de fractures. Il est démontré que les zones de fortes déformations peuvent représenter une barrière à la circulation de saumures géothermales sans toutefois l'être nécessairement. Les propriétés mécaniques des roches faillées ayant accumulé une forte déformation ont un rôle crucial en empêchant le développement d'ouvertures nécessaires à l'écoulement dans le réservoir. Ces propriétés évoluent dans le temps et l'espace en fonction de la déformation accumulée et des processus d'interaction entre le fluide et la roche. Un modèle conceptuel de l'évolution d'une zone faillée et de l'architecture d'un réservoir est proposé. L'exploration et l'exploitation géothermiques doivent prendre en compte le rôle de l'héritage géologique afin de garantir des opérations sécurisées et durables.

**Mots clés :** Granite fracturés, Interaction fluide-roche, Gradient de déformation, Réservoirs géothermiques, Analogue